Internal Report
DESY F35-92-02
January 1992

The Uranium Scintillator Calorimeter for the ZEUS Detector at the Electron–Proton Collider HERA

— The Heart of ZEUS —

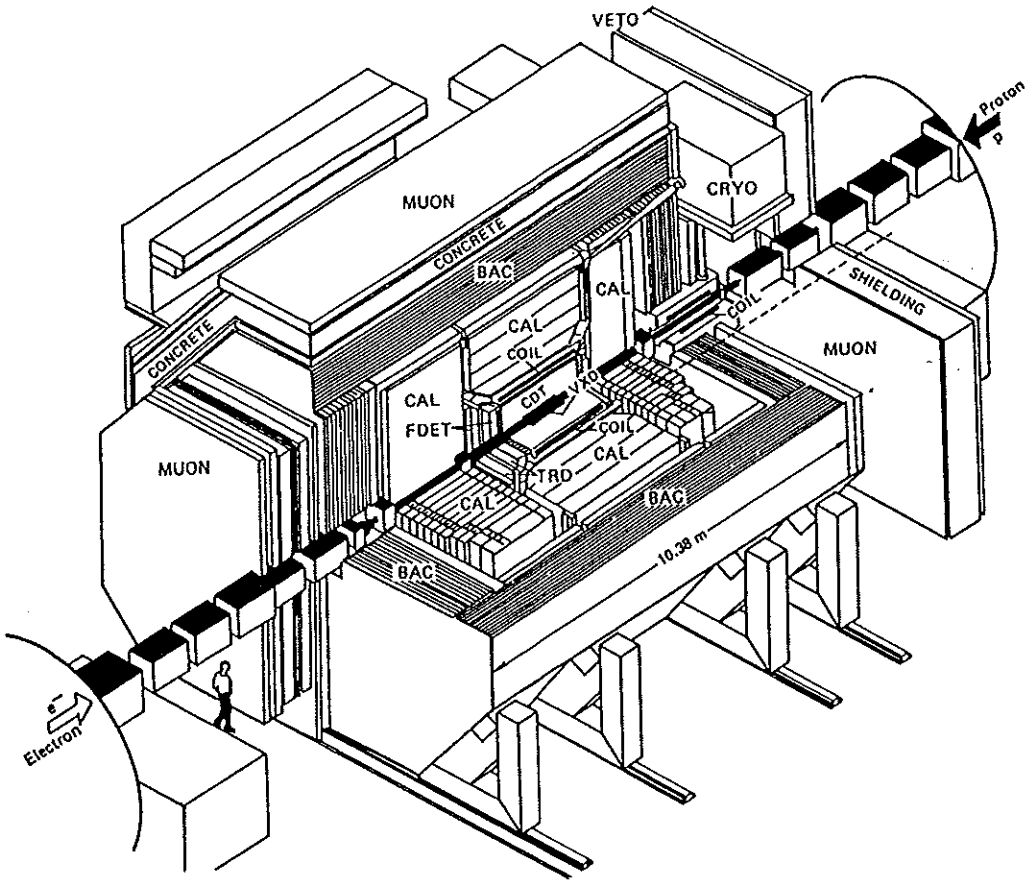

Jürgen Krüger

The Uranium Scintillator Calorimeter for the ZEUS Detector at the Electron–Proton Collider HERA

— The Heart of ZEUS —

Jürgen Krüger

II. Institut für Experimentalphysik, Universität Hamburg

and

Deutsches Elektronen–Synchrotron DESY, Hamburg

Habilitationsschrift, vorgelegt dem Fachbereich Physik der Universität Hamburg, Januar 1992

Abstract

For experimentation at HERA, the ZEUS collaboration has put a major effort into calorimeter research and has developed a high resolution uranium scintillator calorimeter, which represents the main component of the ZEUS detector.

Physics requirements call for a calorimeter with the best possible energy resolution, equal response for hadrons and electrons and a stability and uniformity at the one–percent level.

This report describes the principles of calorimetry and their application for the ZEUS calorimeter. A detailed test program has led to a calorimeter with a depth of up to 7λ, consisting of a sampling structure of 3.3mm thick uranium plates interleaved with 2.6mm thick plastic scintillator tiles and wavelength shifter readout with photomultipliers. The 700t calorimeter is hermetic and covers about 99.8% of the solid angle. An energy resolution of $35\%/\sqrt{E}$ has been measured for single hadrons and jets, and equal response to electrons and hadrons to within 2% between 2 and 100GeV. The angular resolution for hadrons is better than 10mrad. Special readout electronics has been developed for coping with the short time between bunch crossings at HERA leading to a time resolution of 1ns for energy deposits of more than 15GeV.

HERA physics requires a precise calibration of the calorimeter. Several calibration methods have been developed and are presented. The main method uses the signal from the uranium radioactivity, which has been calibrated against the response to electrons, hadrons and muons with well known energies in test experiments at fixed target accelerators. The quality control of the calorimeter fabrication has allowed us to achieve an absolute calibration throughout the calorimeter of 1% from the uranium signal alone. The uranium signal also provides a longterm calibration at the 1% level.

Contents

Chapter 1

Introduction

At the new electron–proton collider HERA at DESY, which has successfully produced the first ep collisions, interactions between 30GeV electrons and 820GeV protons will be studied. For this purpose two large detectors, H1 and ZEUS, have been built.

For measuring with high precision the energies and directions of single particles and particle jets, created in electron–proton collisions, the ZEUS collaboration has constructed a high resolution uranium scintillator calorimeter.

This report describes the systematic development of a hermetic uranium scintillator calorimeter, which provides excellent energy resolution and good angular resolution for jets and hadrons as well as sufficient electron resolution. Then it presents the tests and calibration of the calorimeter modules and the installation of the complete calorimeter into the ZEUS detector.

In order to understand the demands on a detector at HERA, a short introduction is given to the parameters of the collider. Then a selection of exciting topics of HERA physics and the requirements on the detector are presented, followed by a description of the main characteristics of the individual components of the ZEUS detector (chapter 2).

In chapter 3 an introduction to the fundamentals of calorimetry is given and the basic physical processes and compensation in hadron calorimeters are described.

The research in calorimetry performed by the ZEUS calorimeter group over many years and the systematic development of the high resolution ZEUS uranium scintillator calorimeter are presented in chapter 4. The optimization of the parameters of the calorimeter is described. In addition to the development of the high precision calorimeter, new experimental results in hadron calorimetry have been attained, providing a deeper understanding of the physical processes which dominate hadron calorimetry and which should be useful for the design of the next generation of calorimeters.

The experimental results gained from the various tests of the forward calorimeter prototype performed at the Proton–Synchrotron (PS) and the Super–Proton–Synchrotron (SPS) at CERN (Conseil Européen pour la Recherche Nucléaire, Geneva) and the verification and optimization of the parameters for the final construction of the ZEUS calorimeter are presented in chapter 5. Not described will be the results on the barrel calorimeter modules which have been tested with beam particles at FNAL (Fermi National Accelerator Laboratory, near Chicago).

In chapter 6 the thorough quality control of all individual components of the calorimeter and the different quality checks and measurements of the final ZEUS forward and rear calorimeter modules are presented. The excellent calibration results achieved with different methods, in particular the calibration using the signal of the radioactivity of the uranium and the high precision in the uniformity of the calorimeter in position and time are presented and discussed.

In chapter 7 the most important characteristics of the ZEUS uranium scintillator calorimeter are summarized and final conclusions are drawn.

Chapter 2

The ZEUS Detector at HERA

2.1 The Electron–Proton Collider HERA

2.1.1 Overview of HERA

The Hadron Electron Ring Accelerator, HERA, is the first electron–proton collider in the world and will be the only one for many years. It offers for the first time the unique possibility to study, at very high energies, deep inelastic scattering between electrons of 30 GeV and protons of 820 GeV. The construction of this two–ring accelerator took from May 1984 until November 1990 followed by the commissioning of the machine in 1991. The experiments will start in April 1992.

The HERA tunnel runs for the most of its length of 6.3km outside the Deutsches Elektronen–Synchrotron DESY, Hamburg (Fig. 2.1) 10m – 25m deep under a large city park and residential and industrial buildings. The four experimental halls are completely underground and have only small access buildings above ground.

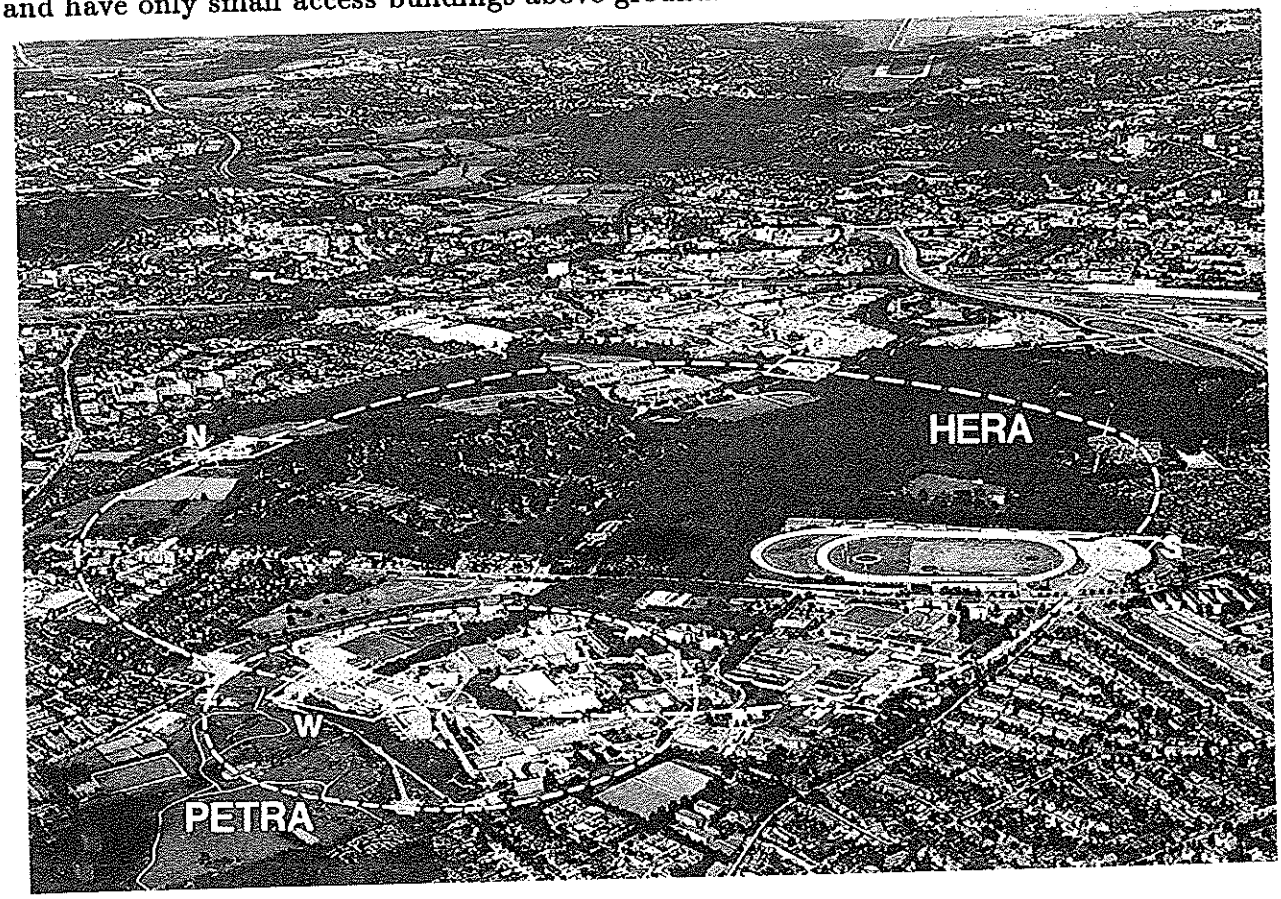

Fig. 2.1 HERA at DESY, Hamburg.

HERA was built at DESY in international collaboration with institutes in Canada, France, Israel, Italy, Netherlands, USA and manpower from PR China, CSFR, former GDR, Poland and United Kingdom. The main parameters of HERA are summarized in Tables 2.1 – 2.3. For details see [HER81], [VOS87], [WII90] and [KOS92]. Status reports and further articles on HERA can be found in [LOH87], [BRI88], [WII89], [POE89], [KRÜ89d], [SÖD90] and [SCH90].

Figure 2.2 presents the layout of the electron–proton collider HERA, including the pre–accelerator system and the three interaction points where the two large experiments H1 and ZEUS, each consisting of many individual components, are presently under construction and a third experiment, HERMES, is planned for the future.

A detailed description of the HERA injection scheme is presented in Fig. 2.3.
The proton injection starts with negative hydrogen ions (H^-) from the 50 MeV Proton Linac, followed by acceleration in the proton synchrotron DESY III to 7.5 GeV. From there the protons are transferred via PETRA at an energy of 40 GeV to the HERA proton storage ring. The electrons or positrons are pre–accelerated first in a linear accelerator, LINAC I (220 MeV, e^-) or LINAC II (450 MeV, e^+) and at DESY II to 7.5GeV. Then the particles are injected via PETRA at an energy of 14 GeV into the HERA electron storage ring.

Figure 2.4 shows a view into the 25m deep HERA ring tunnel with an inner diameter of 5.2m. The two storage rings are mounted on top of each other. The magnets of the electron storage ring (lower) are normal conducting and operate at room temperature. The magnets of the proton storage ring (upper) have to produce a magnetic field of 4.7 Tesla to bend the high momentum proton beam in the arcs of the ring. Therefore superconducting (s.c.) magnets were developed which are operated at a temperature of 4.2^0K (Fig. 2.4).

A cross section of the HERA tunnel is given in Fig. 2.5. In addition to the proton and electron magnets there are transfer lines for helium and pressure of gas, a quench pipe, cooling water, a shielded cavity for electronics and there is space for a transport vehicle (HERA "Tram").

Main General Parameters of HERA	
Construction time	May 1984 – November 1990
Costs of the HERA collider	1010 mio Deutsch–mark
Countries involved in the construction of the collider	12
Commissioning	1991
Circumference of the HERA tunnel	6336m
Depth underground	10m – 25m
Inner diameter of the tunnel	5.2m
Thickness of the tunnel walls	30cm
Number of pre–accelerators for HERA	6
Number of experimental halls	4
Size of the experimental halls	25m x 43m
Number of experiments (1st stage)	2 (H1 and ZEUS)
Costs of the 2 experiments (1st stage)	240 mio Deutsch–mark
Countries involved in the 2 experiments	17
Beginning of the experiments	April 1992
Number of interaction points	3

Table 2.1 Main general parameters of the electron–proton collider HERA.

The HERA Beams	Electron	Proton
Nominal energy	30 GeV	820 GeV
Centre of mass energy	314 GeV	
Injection energy	14 GeV	40 GeV
Luminosity per interaction point	$1.5 \times 10^{31} cm^{-2} s^{-1}$	
Particle current	60 mA	160 mA
Particles per bunch	3.5×10^{10}	10^{11}
Number of bunch buckets	220	220
Maximum number of bunches	210	210
Beam crossing angle	head–on collision,	0 mrad
Bunch distance	28.8m (96ns)	
Bunch length (at maximum energy)	30mm	440mm
Beam width at the interaction points	0.264mm	0.300mm
Beam height at the interaction points	0.017mm	0.095mm
Radiation energy loss per revolution	70.38 MeV	1.4×10^{-10} MeV
Polarization time at 30 GeV	27 min	—
Filling time	15 min	20 min

Table 2.2 Main parameters of the HERA beams.

The HERA Storage Rings	Electron	Proton
Total number of magnets	2009	1833
Main dipoles	465	422 (s.c.)
Main quadrupoles	605	224 (s.c.)
Field strength of the main dipoles	0.16 T	4.68 T
Number of conventional rf cavities	82	2 (4)
Number of superconducting rf cavities	16	—
Frequency of the rf cavities	500 MHz	52 (208) MHz

Table 2.3 Main parameters of the HERA storage rings.

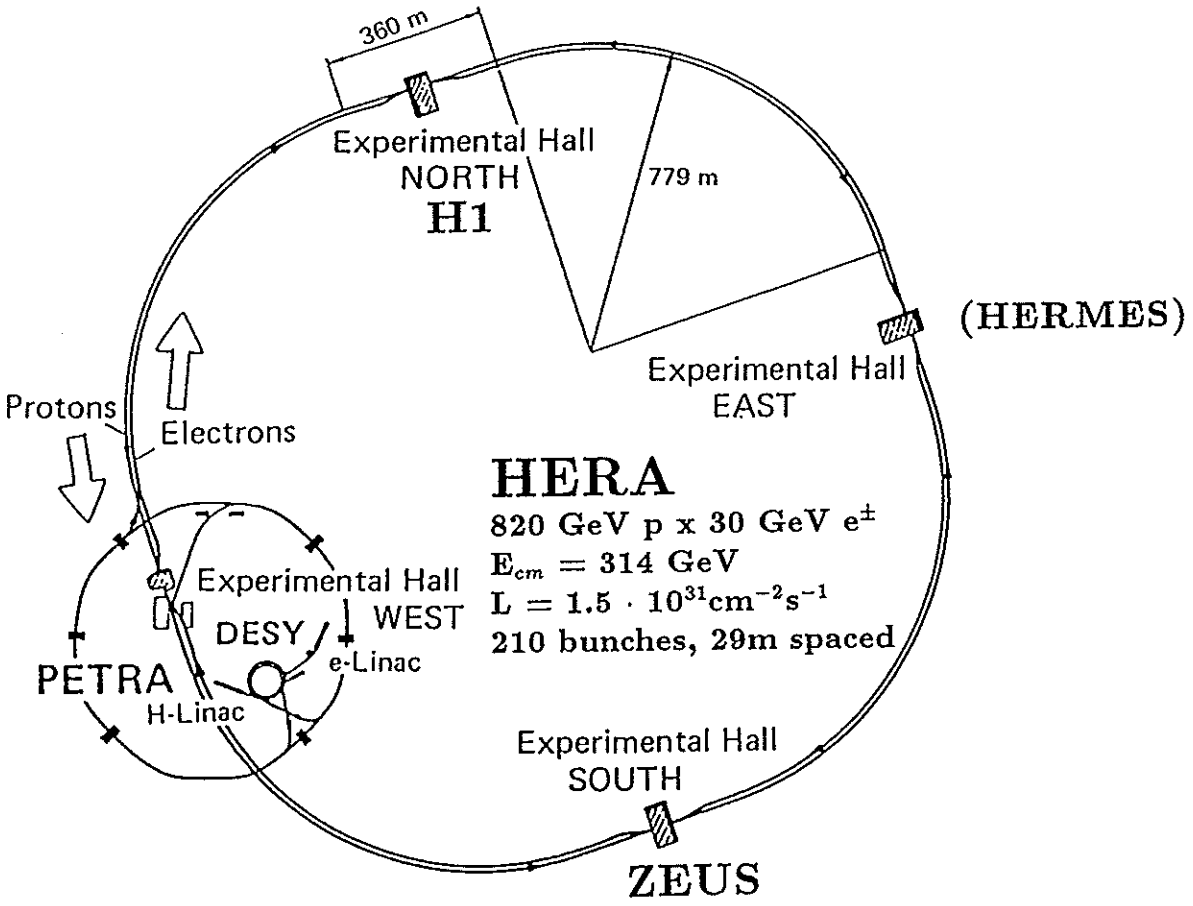

Fig. 2.2 Layout of the HERA electron–proton collider.

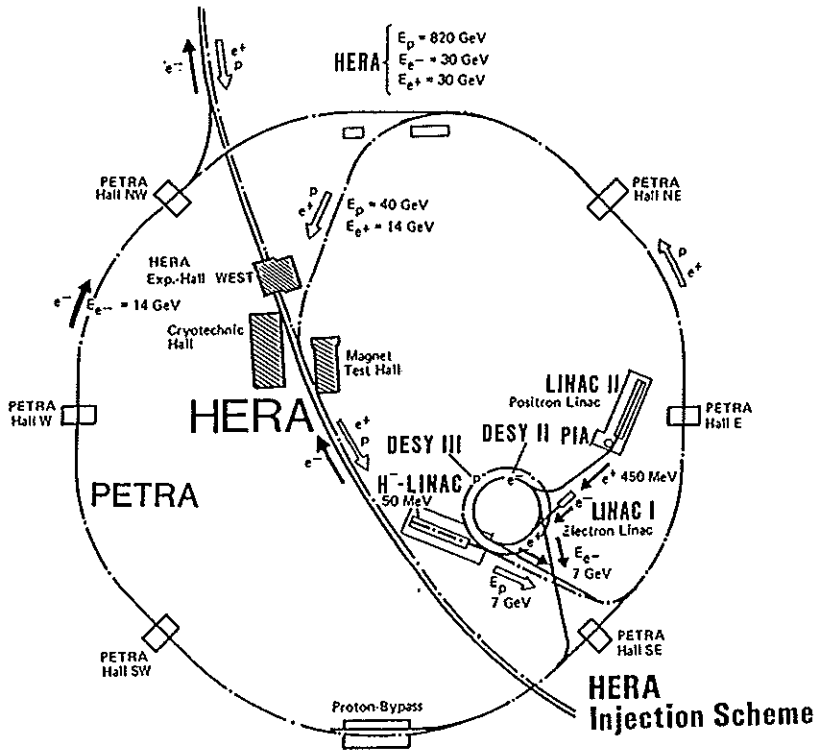

Fig. 2.3 The HERA injection scheme.

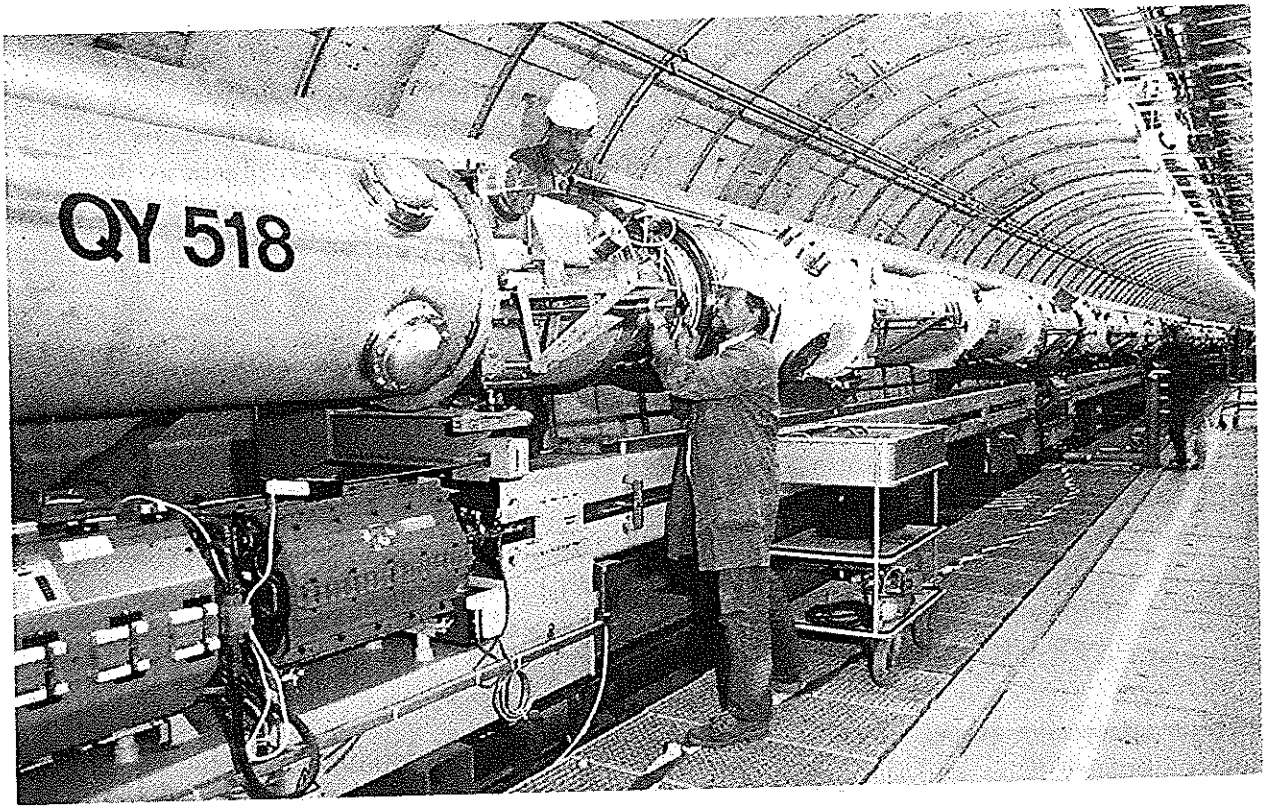

Fig. 2.4 View of the HERA ring tunnel.

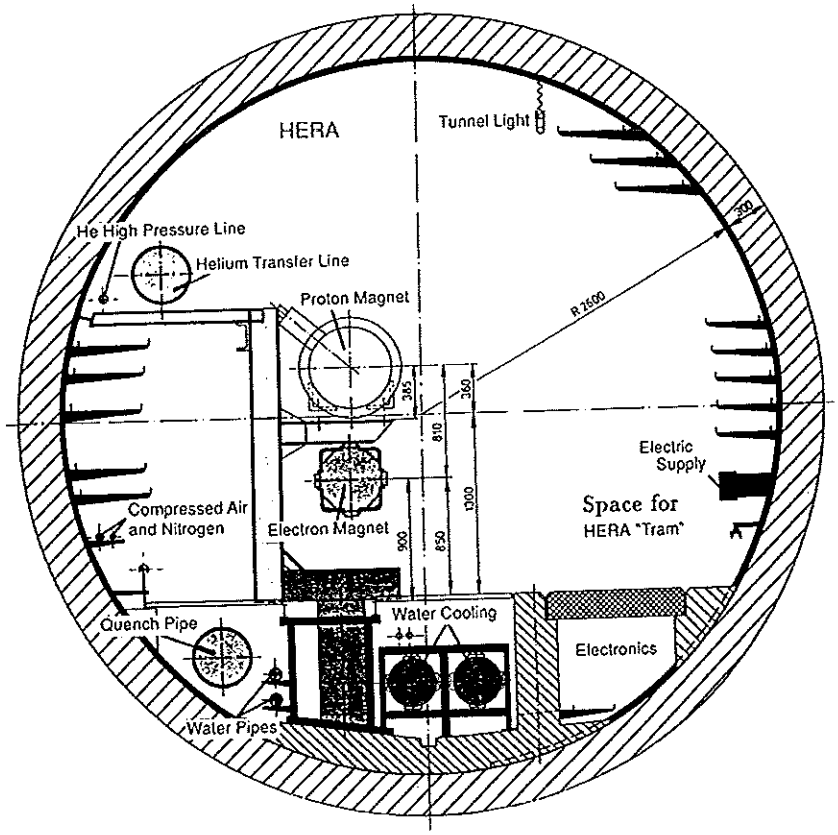

Fig. 2.5 Cross section through the HERA ring tunnel.

2.1.2 The HERA Electron Storage Ring

Figure 2.7 shows one of the 12 m long magnet modules of the electron ring, the cross sections through the different magnet types and a summary of the main magnet data. Each module consists of a 9 m long dipole magnet supplying a field of 0.16 Tesla at 30GeV, one quadrupole, one or two sextupole and several correction magnets preassembled on a common girder. The main parameters of the electron beam and the electron storage ring are summarized in Tables 2.2 and 2.3.

In August, 1988 for the first time electrons were injected and successfully stored in HERA. Single electron bunch currents have been accumulated at the design value of 0.3 mA and a maximum energy of 14 GeV has been reached limited by the radio frequency (rf) system used at this stage. In a second run in September 1989 electrons were accelerated to an energy of 27.5 GeV and stored with lifetimes of up to 5 hours. The maximum single bunch current reached was 2.49 mA corresponding to 3.26 x 10^{11} electrons per bunch. In the multibunch mode 2.87 mA was reached (design value: 58 mA) mainly limited by low accumulation rate and poor lifetime at high currents. A feed back system has been developed and successfully tested in PETRA [WII90].

The successive stages of the rf system are described in Fig. 2.6, where the maximum electron energy E_{max} and the polarization time τ_{Pol} are plotted as a function of the electron current [POE89]. Sixteen superconducting 4–cell cavity structures assembled pairwise into 8 cryostats were built by industry and tested at DESY. The design goal for the gradient is 5MV/m. These cavities were installed in the straight sections of HERA early 1991.

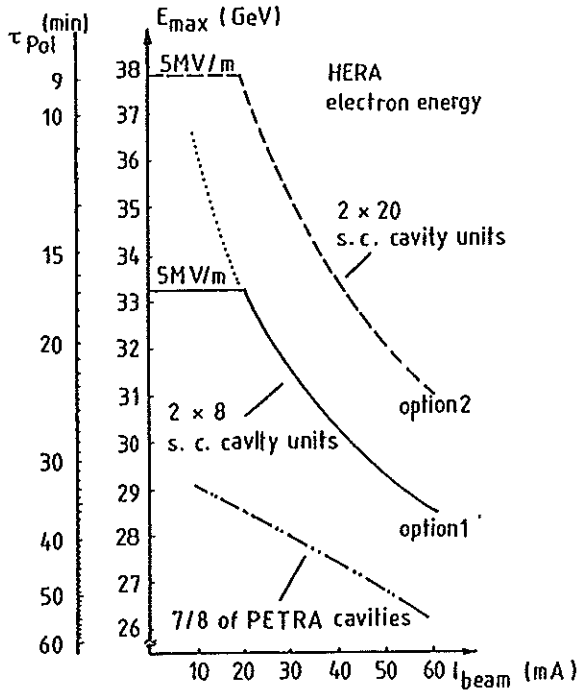

Fig. 2.6 Maximum electron energy E_{max} and polarization time τ_{Pol} in HERA as a function of the electron current for 3 options of cavity configurations.

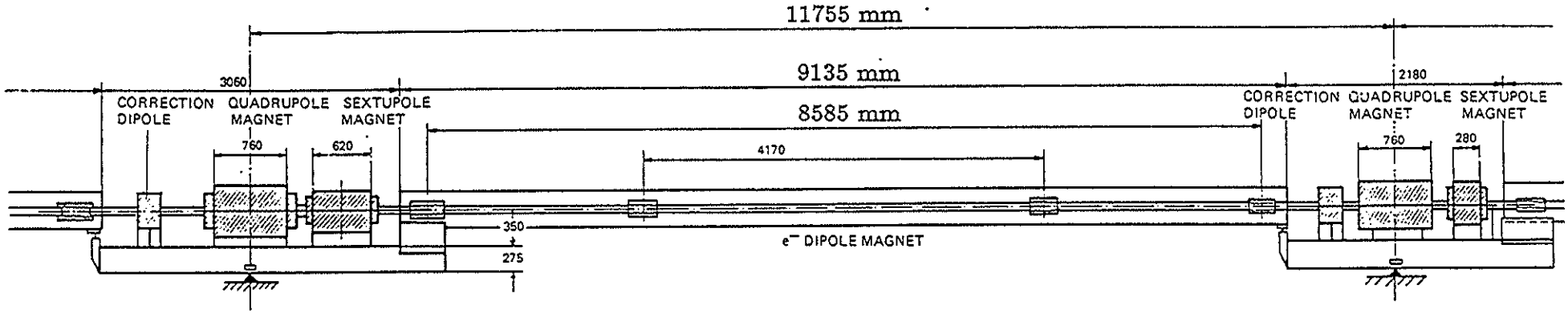

HERA: MAGNETMODULES for the ELECTRON RING

QUADRUPOLE MAGNET

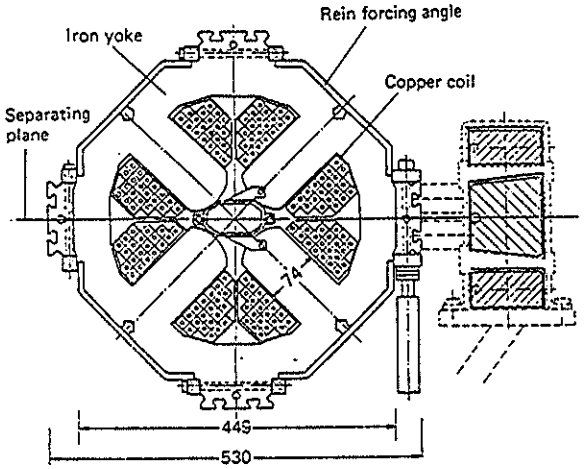

TECHNICAL DATA at 30 GeV

field gradient	0.1314 T/cm
bore diameter	74 mm
conductor (copper)	13.3x13.3 mm^2
hole diameter	5.7 mm
turns per coil	20
current	358 A
power	2.73 kW
mass	1020 kg

SEXTUPOLE MAGNET

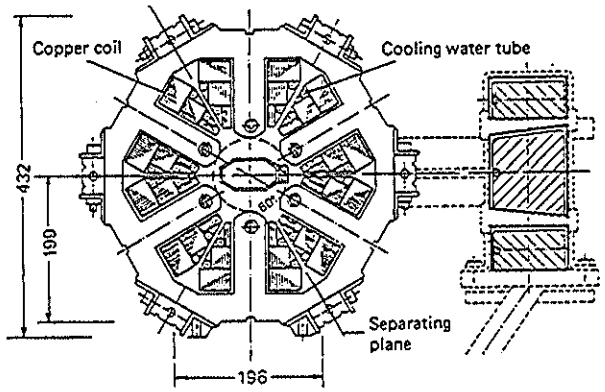

TECHNICAL DATA at 30 GeV

Sextupole strength	0.0409 T/cm^2
bore diameter	96 mm
conductor ribbon (copper)	28x0.5 mm^2
turns per coil	138
current	45 A
power (620 mm long magnet)	3.5 kW
mass (620 mm long magnet)	550kg

DIPOLE MAGNET

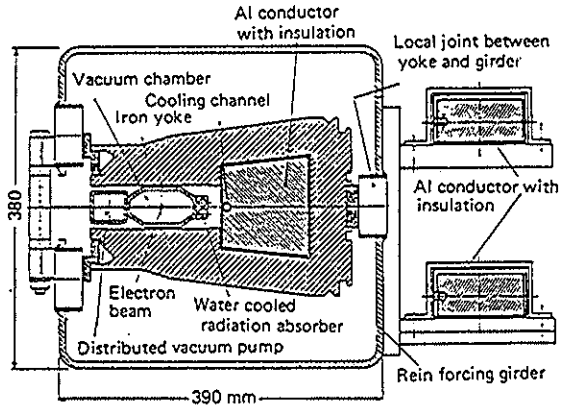

TECHNICAL DATA at 30 GeV

Field strength	0.1638 T	Number of turns in coil	1
Bending radius	610.4 m	Current	6767 A
Gapheight	51.5 mm	Power	2.57 kW
Good field cross section	40x80 mm^2	Mass (including girder for quadrupole and sextupole	4200 kg
Conductor (aluminum)	100 cm^2		

Fig. 2.7 Magnet module for the HERA electron ring and magnet cross sections.

2.1.3 The HERA Proton Storage Ring

The 416 main dipoles and 224 main quadrupoles of the proton ring are superconducting magnets [WOL86b], [KAI86], [WII88]. The basic design of a superconducting (s.c.) dipole magnet coil is shown in Fig. 2.8 [MES88]. A s.c. HERA dipole has a length of 9.8 m and a nominal current of 5027 A for 820 GeV protons leading to a central field of 4.682 T.

The wires developed for the s.c. magnets consist of niobium–titanium alloy fibres embedded in copper (Fig. 2.9). Twentyfour wires, each consisting of 1230 filaments with a diameter of 0.014 mm in a 0.8mm diameter, are combined to form the superconducting cable.

The cross sections of dipole and quadrupole magnets for the proton ring are shown in Fig. 2.10. The superconducting dipoles have been tested and achieve very high current densities of about 2800 A/mm^2 at 4.2 K. The mechanical tolerances are very tight, in the order of 10–20μ, the forces acting on the mechanical structures are extremely high, about 100–200to/m and the stored energy is 210 kJ/m at a temperature of 6.2 K. The main parameters of a superconducting HERA dipole magnet are summarized in Table 2.4.

The s.c. magnets are extremely well insulated against the outside world. For a dipole this is shown in Fig. 2.11. The two layer Nb–Ti–coil, clamped by aluminium alloy collars, contains spacers for improving the field homogenity. The coil is cooled by one–phase helium at 4.4 K. The helium returns in two phase condition through pipes in the cold iron yoke. The superinsulation of the 4 K parts of the magnets consists of 10 layers of aluminium coated mylar foils interleaved with glass net spacers. The 40 K shield is wrapped with 30 layers.

The superconducting parts of the proton ring are supplied with liquid helium by a large liquid helium refrigerator plant. It consists of 3 units with a total power consumption of 3 x 2845 kW and a cooling capacity of 3 x 6.6 kW at 4.3 K plus 20.4 g/s liquid He.

All s.c. dipoles and quadrupoles have been fabricated in industry and tested at DESY. The high quality of the s.c. cables and s.c. magnets is documented in Fig. 2.12 and 2.13.

Figure 2.12 shows the critical currents I_c of the s.c. cables (BBC) at a magnetic field of 5.5 T and a temperature of 4.6 K versus the cable identifying number [WIP90]. Each dipole cable has a length of usually 1910 m comprising 2 x 585 m and 2 x 372 m for the two inner and outer coils of a complete magnet. The cable length necessary for all dipoles is 874 km and for all quadrupoles 109 km. The critical currents of nearly all dipole cables are far above the nominal value of 5027 A and fulfil the selection criterion to carry at least 8000 A.

The s.c. magnets have been quenched several times to study their properties and maximum quench currents [MEI90]. Figure 2.13 presents the distributions of quench currents of all dipoles and all quadrupoles at a temperature of 4.72 K. The average quench currents are also indicated. At the HERA operational temperature of <4.5 K the quench currents will be higher by more than 400 A compared to the values shown in Fig. 2.13. Corrected to 4.4 K the quench currents of the dipoles will be about 6910A, far above the nominal value of 5027A and for the quadrupoles about 7840A, thus safe operation of the proton storage ring should be possible at 1 TeV. In addition the field quality of both dipoles and quadrupoles, was measured and gave excellent results.

All magnets of the proton ring have been installed in the HERA tunnel and cooled down. One octant has been ramped up to 6000 A, the other octants up to 3000 A (Sept. 91).

Superconducting Dipole Magnet	
Type	cold bore, cold yoke
Nominal field for 820 GeV	4.682 T
Nominal current for 820 GeV	5027 A
Maximum field at the conductor	4.914 T
Stored energy	762 kJ
Yoke length	8.736 m
Cryostat length	9.766 m
Cryostat diameter (outer)	0.61 m
Inner diameter of beam pipe	55.3 mm
Number of dipoles (horizontal)	416

Table 2.4 Main parameters of a superconducting HERA dipole magnet.

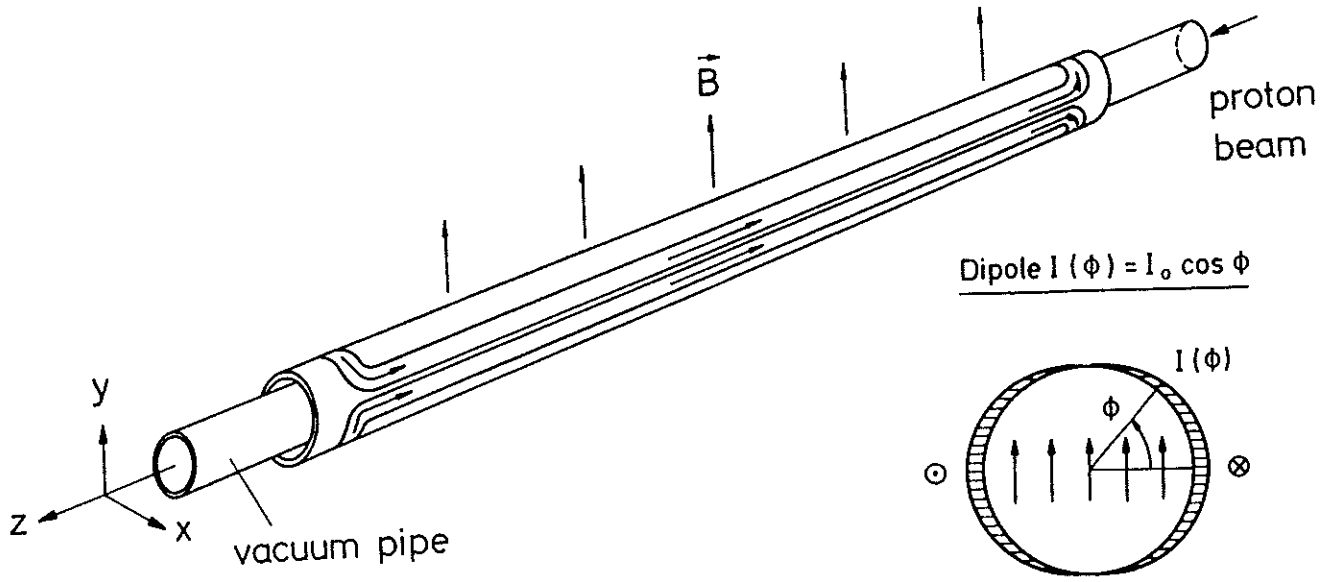

Fig. 2.8 Schematic view of a superconducting dipole magnet coil.

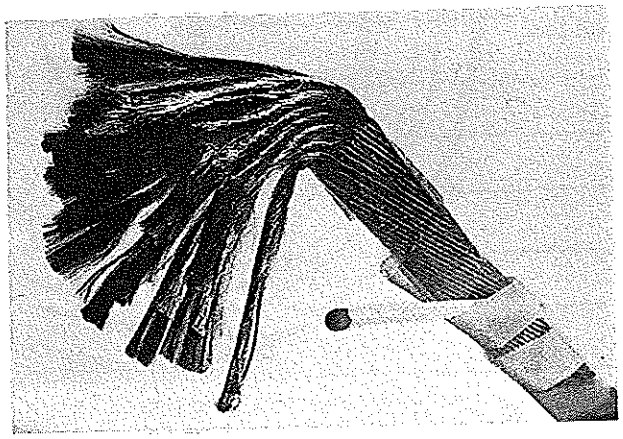

Fig. 2.9 Superconducting cable for the magnets of the HERA proton storage ring.

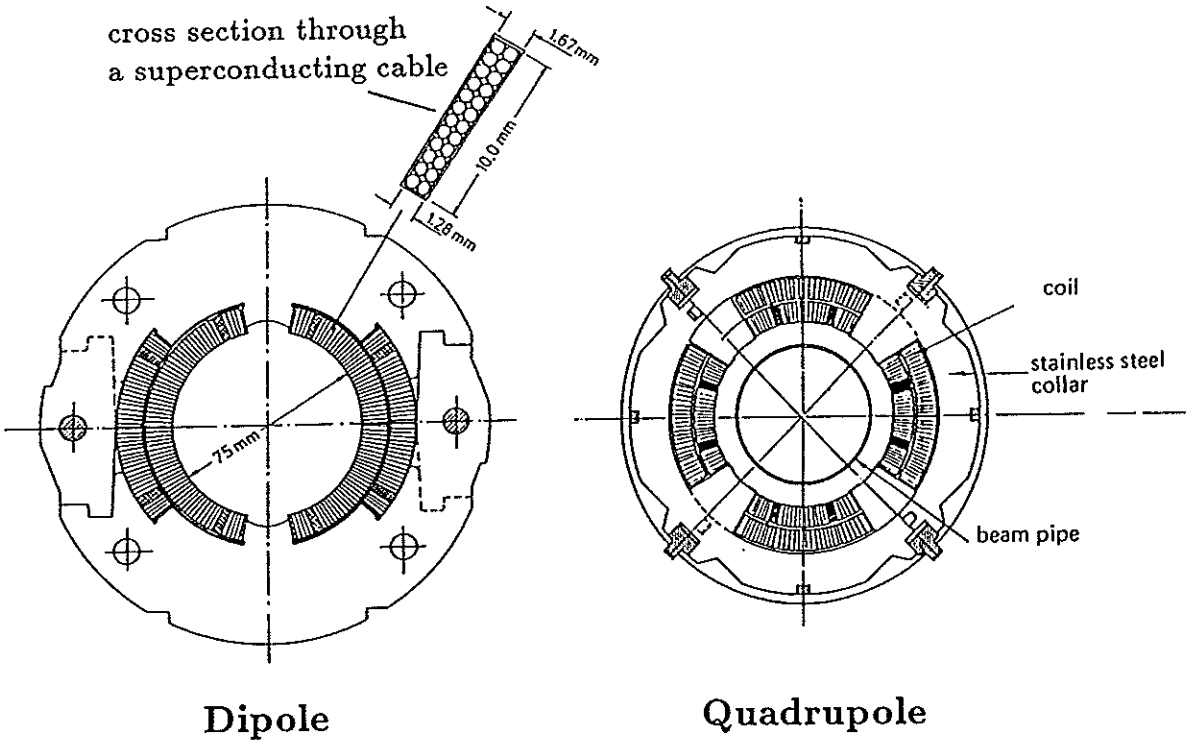

Fig. 2.10 Cross sections through the superconducting coils of the HERA proton ring.

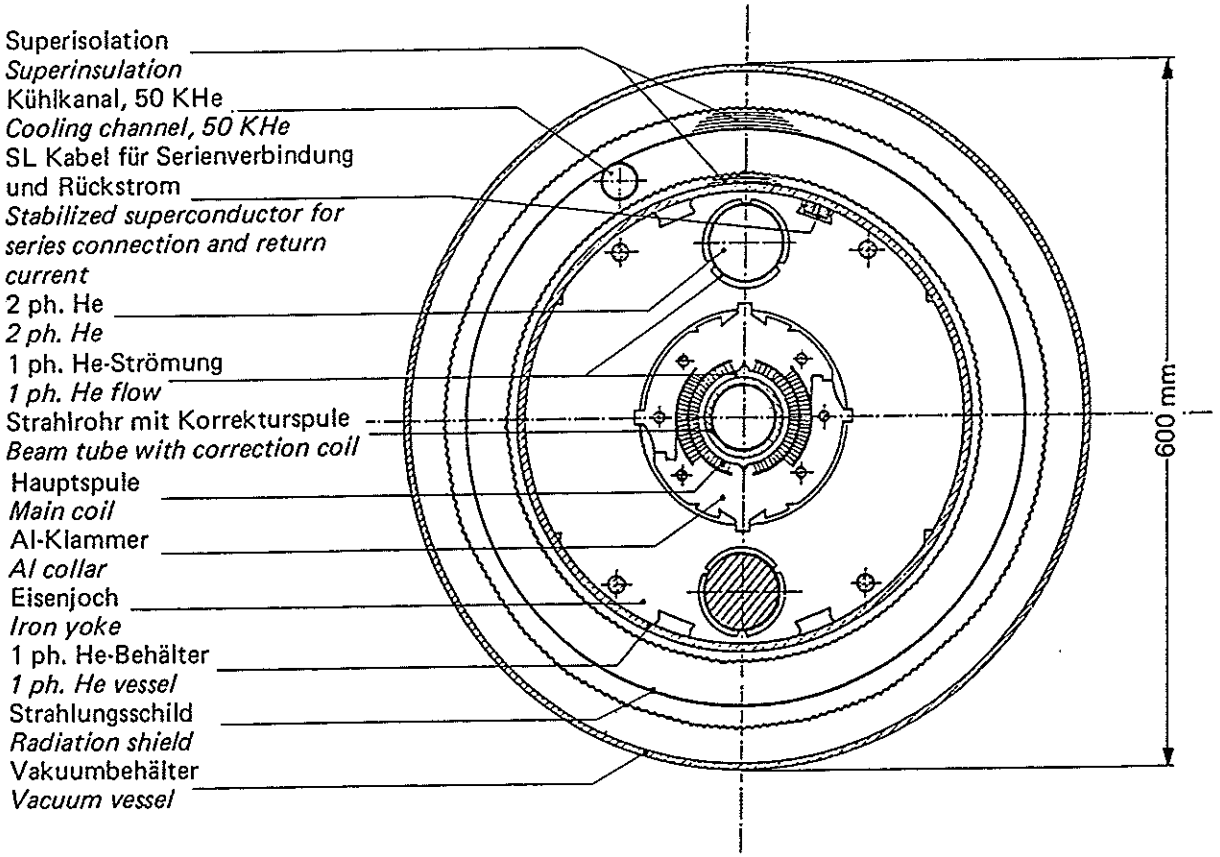

Fig. 2.11 Cross section through a superconducting HERA dipole magnet with cryogenic.

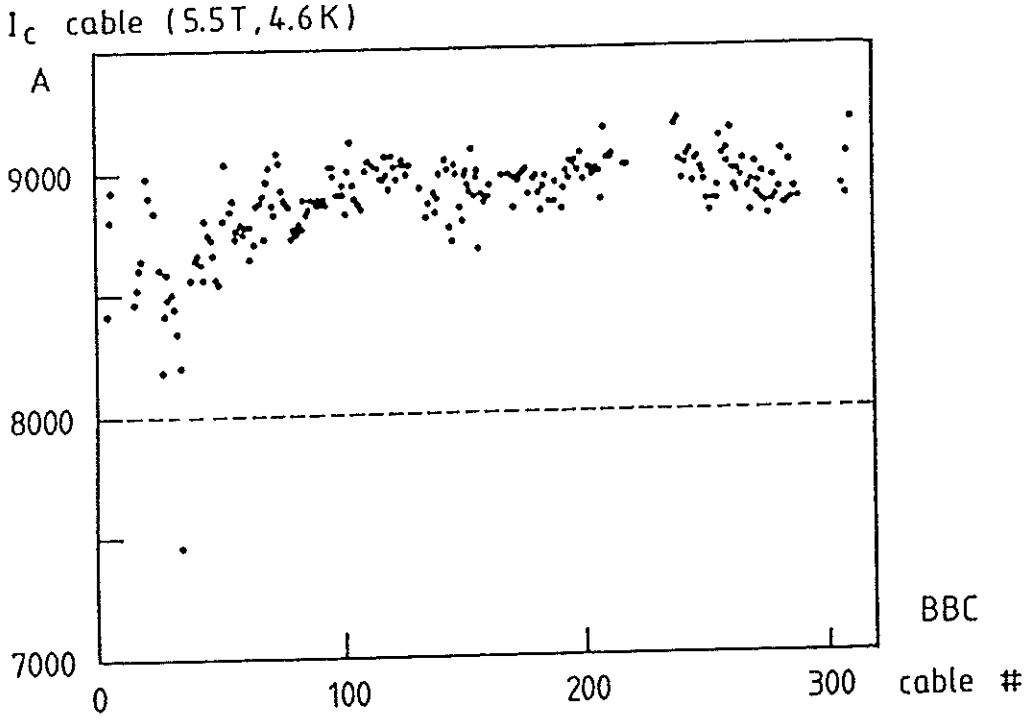

Fig. 2.12 Critical current I_c of the superconducting cables (BBC) at a magnetic field of 5.5 T and a temperature of 4.6 K versus the cable identifying number.

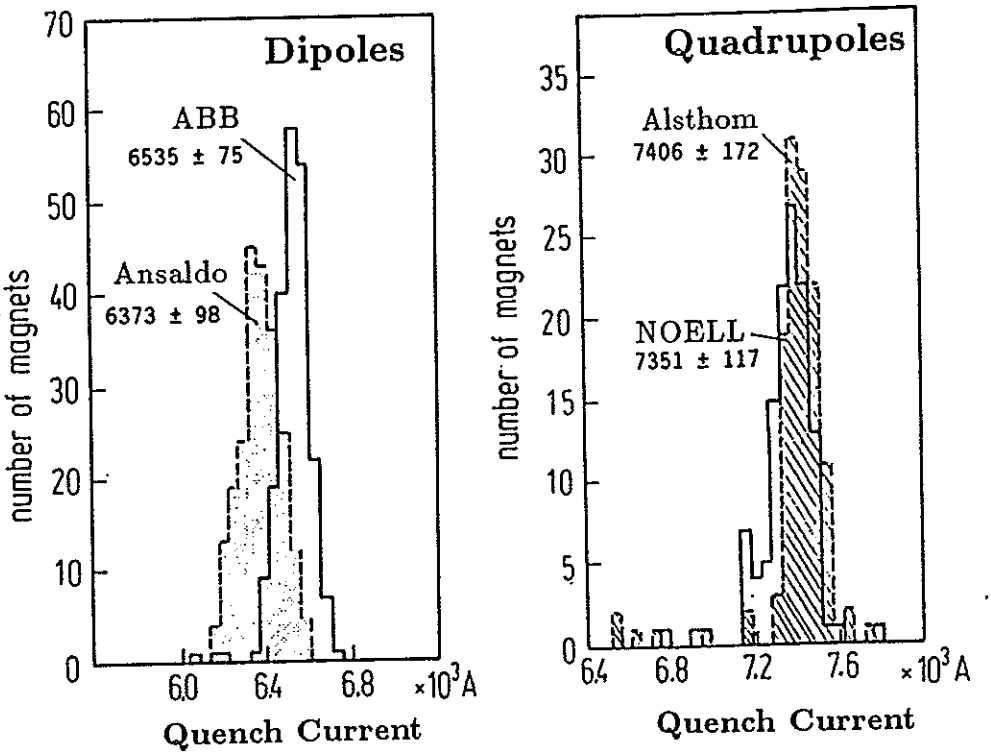

Fig. 2.13 Quench current distributions of the s.c. dipoles and quadrupoles at 4.72 K. The nominal current for 820 GeV protons is 5027 A at <4.5 K.

2.1.4 The Interaction Region

Side and top views of an interaction region are shown schematically in Fig. 2.14 [BUO86]. In the straight sections close to the interaction region the electron and proton bunches run in the same vacuum pipe at an angle of 0 mrad and pass through one another for head–on collisions. For the electron and proton bunches to be in the middle of the same straight line, the proton beam is smoothly bent down by about 80cm (Fig. 2.14, side view). After the protons have passed the interaction region they are brought back to the level of the proton ring. To solve this task 123 conventional magnets are installed in the straight sections to guide the protons.

At the interaction point (IP) the beam sizes are very small. For electrons the beam width is 0.26mm and the beam height 0.017mm. For protons the beam width is 0.3mm and the beam height 0.095mm.

The maximum number of beam buckets is 220 for each beam. Of these 10 are left empty. The distance between bunches is about 29m and the bunch length is 30mm for electrons and 440mm for protons at maximum energy (Table 2.2).

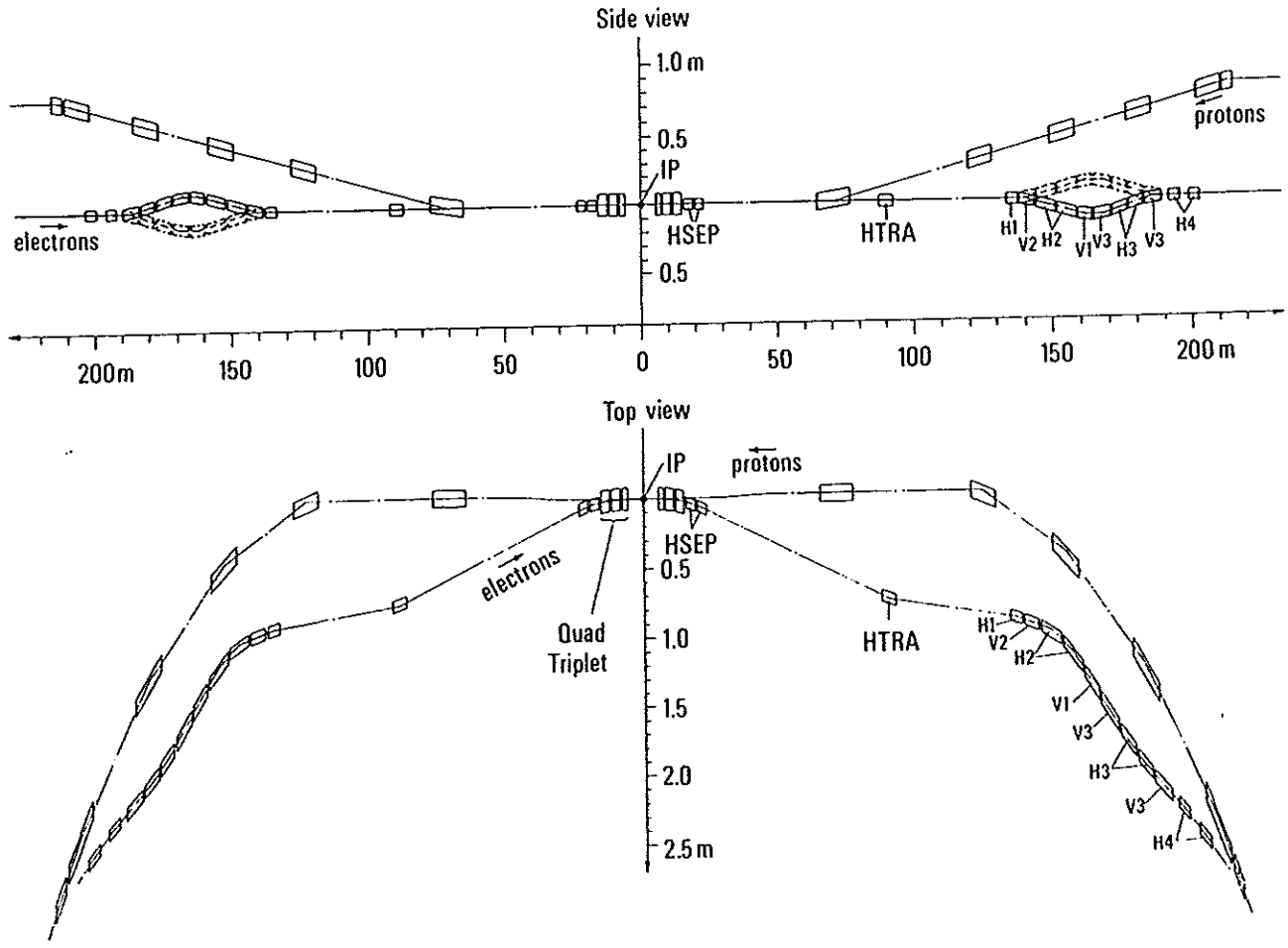

Fig. 2.14 Interaction region of the HERA electron–proton collider.

2.2 Physics at HERA

2.2.1 Overview of HERA Physics

Deep inelastic lepton nucleon scattering has played an important role in probing the structure of the proton and has made significant contributions for understanding the fundamental electromagnetic, weak and strong interactions of leptons and quarks.

A figure of merit for lepton nucleon interactions is the maximum four momentum transfer squared, Q^2, that can be explored. Before HERA Q^2_{max} has been $\approx 300 - 400 GeV^2$; with HERA it will increase by two orders of magnitude to $\approx 30000 - 40000 GeV^2$.

Under specific assumptions the building blocks of matter can be studied down to substructures of 3×10^{-18}cm corresponding to $\sim 10^{-4}$ of the proton radius. The forces at such small distances are of particular interest.

There are several reports, talks and lectures presenting overviews of the physics accessible at HERA, e.g. [LLE77], [ECF79-83], [CAS85], [LOH83], [WOL86], [HER87+91], [SÖD90], [ALI90].

A comprehensive overview can be found in the "Proceedings of the HERA Workshop", Hamburg, October 12–14, 1987 (Vol.1+2, 940 p.) [HER87] and in the forthcoming proceedings of the 1991 workshop.

In the present work only a small selection of primary topics of HERA physics will be presented. After a description of the kinematics of deep inelastic ep–scattering and an overview of selected topics of HERA physics, the physics requirements on the ZEUS detector are formulated.

The range of the region which can be investigated, critically depends on the accuracy to which the energies and angles of the particles and jets resulting from the interactions can be measured.

The main topics of HERA physics discussed in this section are

- Neutral and Charged Current Processes
- Test of Quantum Chromodynamics
- Substructure of Quarks and Electrons
- Search for New Currents
- Search for New Particles.

2.2.2 Deep Inelastic Electron–Proton Scattering

Due to the large momentum transfer with Q^2 up to $10^5 GeV^2$ HERA becomes an electron–quark collider. The fundamental electron–proton scattering process is described in lowest order by the diagram shown in Fig. 2.15 with j = photon.

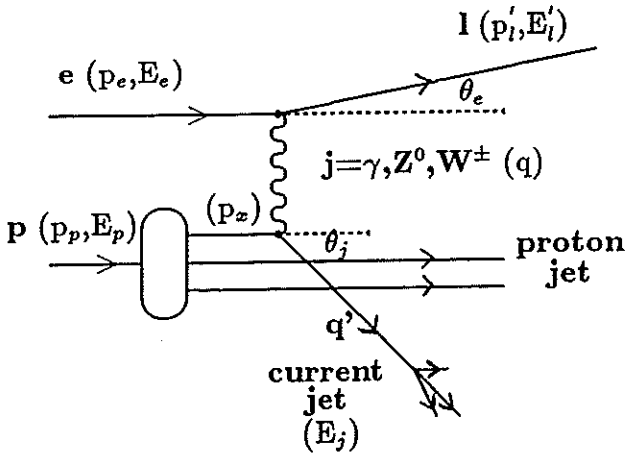

p_e, E_e = four momentum and energy of the incoming lepton (electron beam)

p_l', E_l' = four momentum and energy of the outgoing lepton

θ_e = scattering angle of the outgoing electron

q = four momentum of the current j = γ,Z^0,$W^\pm$

p_p, E_p = four momentum and energy of the incoming proton (beam)

x = fraction of the proton momentum carried by the struck quark

E_j, θ_j = energy and scattering angle of the current jet

Fig. 2.15 Diagram of the deep inelastic electron–proton scattering process.

The incoming electron (lepton) exchanges a neutral (γ, Z^0) or charged ($W^\pm$) current j with one of the quarks of the proton. The struck quark q', called the current quark, fragments into a jet of particles (current jet). The remaining quarks of the proton (spectator quarks) fragment into the proton jet mainly disappearing into the beam pipe. The outgoing lepton is an electron (e) or a neutrino (ν) depending on whether a neutral (NC) or charged (CC) current is exchanged.

In the quark–parton model the current j couples to a quark with four momentum $p_x \equiv \xi(E_p,0,0,-E_p)$. Assuming the initial and final quark to be massless, $p_x^2=p_f^2=0$, then

$$0 = p_f^2 = (p_x+q)^2 = p_x^2+2p_xq+q^2 = \xi 2p_pq-Q^2 \quad \Rightarrow \quad \xi = Q^2/(2p_pq) \equiv x \; .$$

Neglecting QCD corrections the Bjorken scaling variable x can be interpreted as the fraction of the proton momentum carried by the struck quark.

The basic kinematical variables of the deep inelastic electron–proton scattering are summarized in Table 2.5. The inclusive scattering process is completely described by two independent kinematical variables as e.g. the two Lorentz invariant quantities Q^2 and ν or equivalently the dimensionless scaling variables x and y.

	Kinematical variables Q^2 and ν:		
Q^2	$\equiv$	$-q^2 = -(p_e - p_l')^2 = sxy$	four momentum transfer of the current squared
ν	$\equiv$	$\frac{p_p \cdot q}{m_p} \simeq 2E_p(E_e - E_l\cos^2\frac{\theta_e}{2})$	energy of the current in the target rest frame
	or equivalently x and y in the range $0 \leq (x,y) \leq 1$:		
x	$\equiv$	$\frac{Q^2}{2(p_p \cdot q)} = \frac{Q^2}{2m_p\nu}$	Bjorken scaling variable ($\approx$fraction of the proton momentum carried by the struck quark)
y	$\equiv$	$\frac{(p_p \cdot q)}{(p_p \cdot p_e)} = \frac{2(p_p \cdot q)}{s} = \frac{\nu}{\nu_{max}}$	and $Q^2 = sxy$
	and		
s	$\equiv$	$(p_e + p_p)^2 \simeq 4E_eE_p$	total invariant mass squared
W^2	$\equiv$	$(q + p_p)^2 = Q^2(1/x - 1) + m_p^2$	invariant mass squared of the hadronic system

Table 2.5 Kinematical variables of the deep inelastic ep scattering events.

The total invariant mass squared is called s and the invariant mass squared of the hadronic system W^2, which ranges from m_p^2 to s. The approximate ($\simeq$) sign results from the fact that the masses of electron (m_e), proton (m_p) and the scattered lepton have been neglected which is a very good approximation at HERA energies.

The maximum possible energy of the current in the proton rest frame is:

$$\nu_{max} = \frac{s - (m_e + m_p)^2}{2m_p} \simeq \frac{s}{2m_p} = \frac{2E_eE_p}{m_p}$$

From this follows that collisions at HERA correspond to a fixed target experiment with an electron beam of 52TeV.

The event topologies of the scattering process (Fig. 2.15) in the laboratory system are presented in Fig. 2.16 before and after the deep inelastic scattering process.

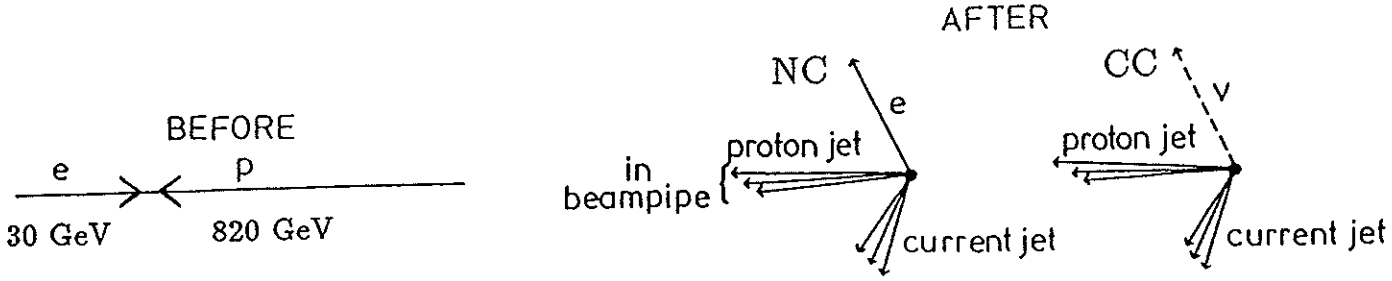

Fig. 2.16 Event topology of deep inelastic ep scattering events.

The kinematical variables of an event can be determined from a measurement of the following quantities (Table 2.6):

1) from the scattered electron [NC]:
   E_l' and θ_e — energy and scattering angle of the outgoing electron;
2) from the current jet [NC, CC]:
   E_j and θ_j — energy and production angle of the current jet;
3) from the final state hadrons [NC, CC]:
   $p_{z,i}$, $p_{T,i}$ and $E_{h,i}$ — parallel and transverse momenta w.r.t. the beam axis and energy of the i-th final hadron (Jacquet Blondel Method [JAC79]).

Kinematical Variable	Scattered Electron E_e, θ_e	Current Jet E_j, θ_j	Hadronic System $p_{z,i}$, $p_{T,i}$, $E_{h,i}$, i=1...n
$Q^2 \simeq$	$4\,E_e\,E_e'\,\sin^2\frac{\theta_e}{2}$	$\frac{E_j^2\,\sin^2\theta_j}{1-\frac{E_j}{E_e}\cos^2\frac{\theta_j}{2}}$	$\frac{(\sum_i p_{T,i})^2}{1-y}$
$x \simeq$	$\frac{E_e'\,\sin^2\frac{\theta_e}{2}}{E_p\left(1-\frac{E_e'}{E_e}\cos^2\frac{\theta_e}{2}\right)}$	$\frac{E_j\,\sin^2\frac{\theta_j}{2}}{E_p\left(1-\frac{E_j}{E_e}\cos^2\frac{\theta_j}{2}\right)}$	$\frac{Q^2}{s\,y}$
$y \simeq$	$1-\frac{E_e'}{E_e}\cos^2\frac{\theta_e}{2}$	$\frac{E_j}{E_e}\cos^2\frac{\theta_j}{2}$	$\frac{\sum_i(E_{h,i}-p_{z,i})}{2\,E_e}$

Table 2.6 Experimental determination of the kinematical variables Q^2, x and y from the scattered electron, the current jet or the hadronic system.

2.2.3 Neutral and Charged Current Processes

The most important processes contributing to deep inelastic electron proton scattering can be described by Feynman diagrams presented in Fig. 2.17 [HIL87]. In particular photon gluon fusion plays an important role at HERA and is the main source for heavy quark production (Q=c, b, t, ...).

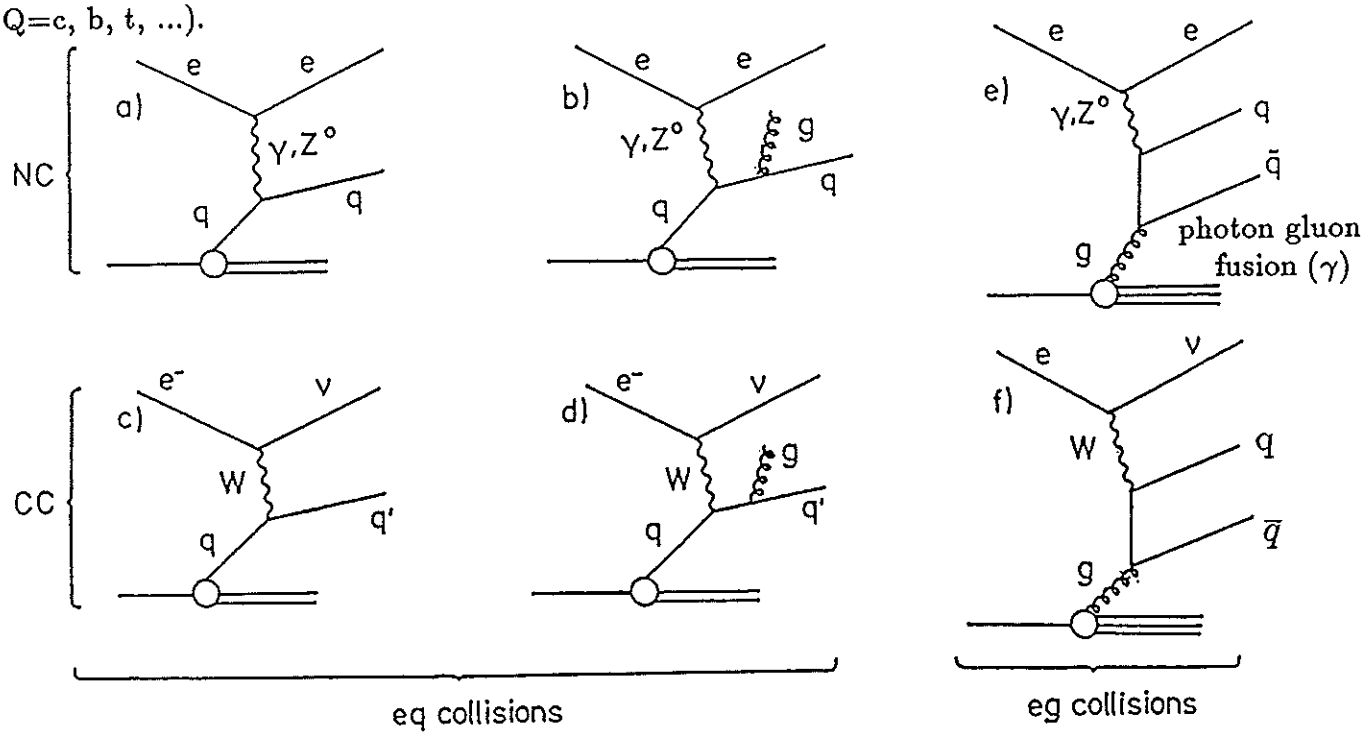

Fig. 2.17 Processes (Feynman diagrams) contributing to deep inelastic ep scattering.

The contributions from neutral and charged current processes to the scattering cross section in ep scattering, taking into account only pure γ and pure W exchange, can be approximately described [WOL86] by:

$$\frac{d\sigma(\gamma p)}{dxdy} \sim \alpha^2 \left(\frac{1}{Q^2}\right)^2 F(x,y) \qquad \text{NC}$$

$$\frac{d\sigma(Wp)}{dxdy} \sim \alpha^2 \frac{1}{(Q^2+M_W^2)^2} F(x,y) \qquad \text{CC}$$

assuming the same coupling constant α for γ and W to leptons and quarks and the structure function F(x,y). Only the propagator terms $1/Q^4$ and $1/(Q^2+M_W^2)^2$, with M_W=82GeV the mass of the W, differ for the two processes.

Figure 2.18 shows qualitatively the behaviour of the cross sections for γ and W exchange as a function of Q^2. At $Q^2 \approx 1$ the cross section for neutral currents (γ) is about 10^8 times larger than the cross section for charged currents (W). For $Q^2 > 10^4 GeV^2$ weak and electromagnetic cross sections have the same magnitude.

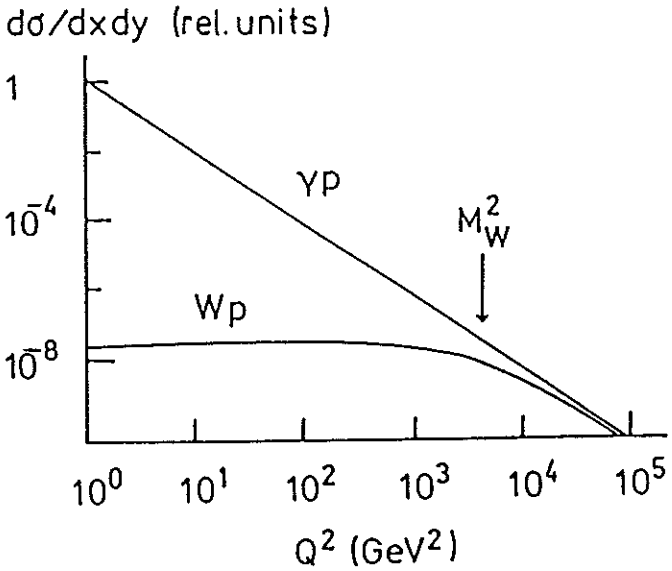

Fig. 2.18 Qualitative behaviour of NC scattering by γ exchange and CC scattering by W exchange.

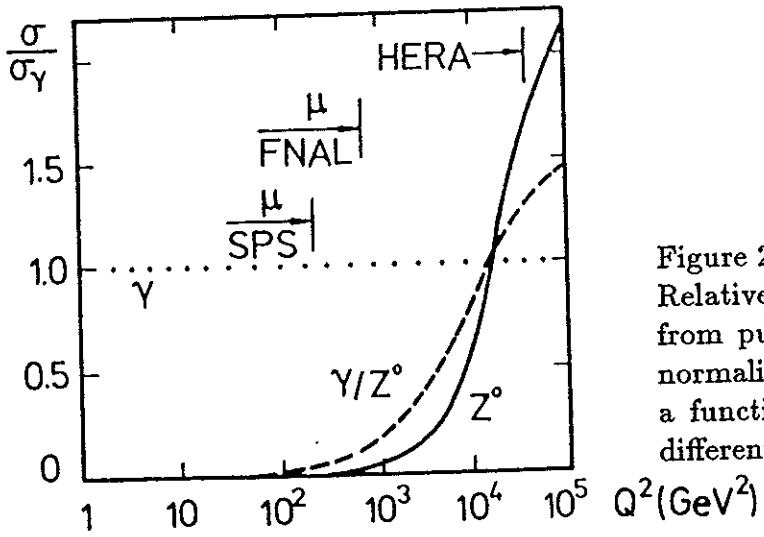

Figure 2.19
Relative size of the cross section contributions from pure γ, pure Z^0 and γ/Z^0 interference normalized to the γ exchange cross section as a function of Q^2. The regions accessible to different accelerators are also indicated.

Figure 2.19 shows the relative size of the cross section from pure γ, pure Z^0 and γ/Z^0 interference as a function of Q^2. The γ/Z^0 interference and the pure Z^0 term become important in the upper HERA Q^2–range and finally dominate at Q^2 above 10^4 GeV^2 [ING87].

Neutral Current Processes

The differential neutral current cross section is given in leading order standard electroweak theory by

$$\frac{d^2\sigma_{NC}(e^{\mp}p)}{dxdQ^2} = \frac{4\pi\alpha^2}{xQ^4}\left[y^2xF_1(x,Q^2) + (1-y)F_2(x,Q^2) \pm (y - y^2/2)xF_3(x,Q^2)\right]$$

where F_1, F_2, F_3 are structure functions. F_1 and F_2 are related through the Callan–Gross relation, $2xF_1=F_2$, which is approximately valid for spin 1/2 quarks.

The double differential cross section for the one–photon exchange ($e^-p \to e^-X$) can be expressed by two dimensionless structure functions $F_1(x,Q^2)$ and $F_2(x,Q^2)$:

$$\frac{d^2\sigma(\gamma)}{dxdy} = \frac{4\pi\alpha^2}{sx^2y^2}\left[(1-y)F_2(x,Q^2) + xy^2F_1(x,Q^2)\right]$$

Introducing the Callan–Gross relation this formula can be abbreviated:

$$\frac{d^2\sigma(\gamma)}{dxdy} \approx \frac{4\pi\alpha^2}{sx^2y^2}(1 - y + y^2/2)F_2(x,Q^2)$$

The structure functions can be expressed in the standard quark parton model by quark distribution functions $q_f(x,Q^2)$ and $\overline{q}_f(x,Q^2)$ which measure the probability for finding a quark or an antiquark carrying the momentum fraction x of the proton. The structure functions can be expressed in terms of the q, $\overline{q}$ as follows:

$$F_2(x,Q^2) = 2xF_1(x,Q^2) = x\left[q(x,Q^2) + \overline{q}(x,Q^2)\right]$$

where e.g. $q(x,Q^2)=\frac{4}{9}u(x,Q^2)+\frac{1}{9}d(x,Q^2)+\frac{1}{9}s(x,Q^2)+\frac{4}{9}c(x,Q^2)+\frac{1}{9}b(x,Q^2)$ for the em current.

The cross section with additional Z^0 exchange can be written in the same form as for the one photon exchange; $F_1(x,Q^2)$ and $F_2(x,Q^2)$ now contain contributions from γ and Z^0 exchange and γ, Z^0 interference terms.

In the upper Q^2–range of HERA, above 10^4GeV^2, γ/Z^0 interference and pure Z^0 exchange start to dominate the pure γ exchange as mentioned above (Fig. 2.19).

Charged Current Processes

The differential charged current cross section for left handed $e_L^{\mp}$ ($e_L^{\mp}p \rightarrow \nu X$) through W exchange can be described by

$$\frac{d^2\sigma_{CC}(e_L^{\mp}p)}{dxdQ^2} = \frac{1}{2sin^4\Theta_W}\frac{4\pi\alpha^2}{x(Q^2+M_W^2)^2}\left[y^2xF_1(x,Q^2)+(1-y)F_2(x,Q^2)\pm(y-y^2/2)xF_3(x,Q^2)\right]$$

where $F_1(x,Q^2)$, $F_2(x,Q^2)$ and $F_3(x,Q^2)$ are three structure functions.
For right handed electrons:

$$\frac{d^2\sigma_{CC}(e_R^{\mp}p \rightarrow \nu X)}{dxdQ^2} = 0$$

since the neutrino is left handed.

In the quark–parton model these structure functions can be expressed by

$$F_2(x,Q^2) = 2xF_1(x,Q^2) = x\left[q(x,Q^2)+\overline{q}(x,Q^2)\right] \quad and \quad xF_3(x,Q^2) = x\left[q(x,Q^2)-\overline{q}(x,Q^2)\right]$$

where

$$q(x,Q^2) = u(x,Q^2)+c(x,Q^2)+... \quad and \quad \overline{q}(x,Q^2) = \overline{d}(x,Q^2)+\overline{s}(x,Q^2)+...$$

If higher quark masses are omitted the cross section for left handed $e_L^{\mp}$ is approximately described by

$$\frac{d^2\sigma_{CC}(e_L^{\mp}p \rightarrow \nu X)}{dxdQ^2} \approx \frac{1}{2sin^4\Theta_W}\frac{4\pi\alpha^2}{(Q^2+M_W^2)^2}\left[u(x,Q^2)+(1-y)^2\overline{d}(x,Q^2)\right]$$

The accessible region of x and Q^2 at HERA depends on the structure of events and the detector design. Figure 2.20 shows the accessible domains in the x,Q^2–plane where x and Q^2 can be well measured a) for NC scattering from either the scattered electron or the jets and b) for CC scattering only from the jets [WOL90a]. The main limitations result from the precision with which the energy of the scattered electron or the jets can be measured, and on the size of the beam hole. For NC scattering, precise measurements of the structure functions should be possible for the full range of x and Q^2 over which the event rate is sufficient. For CC scattering this will be difficult for y>0.6 ($y=Q^2/xs$). The well measurable region can be extended by operating HERA at lower beam energies.

Figure 2.21 points out how wide the accessible range at HERA is for measurements of the structure function $F_2(x,Q^2)$ at $s \approx 10^4 GeV^2$ and $10^5 GeV^2$ extending over almost 5 orders of magnitude in Q^2 [BLÜ87]. For comparison data of charged lepton–proton scattering from SLAC and the CERN SPS muon experiments are superimposed.

For one year of data taking an integrated luminosity of $100pb^{-1}$ is expected. For the structure function measurements an integrated luminosity of $500pb^{-}$ is assumed. Figures 2.22 and 2.23 present the event rates in the x,Q^2–plane expected at HERA for NC and CC scattering with $L = 500pb^{-1}$ calculated with Lund–LEPTO and EHLQ structure functions [WOL90a]. At low Q^2 the large NC event rate stems from photon exchange. At Q^2 above the mass squared of the Z^0 (m_Z), the contribution of Z^0 exchange has the same magnitude as pure photon exchange. The CC event rate at low Q^2 is much smaller than for NC scattering, but exceeds the NC event rate at $Q^2 > m_W^2$.

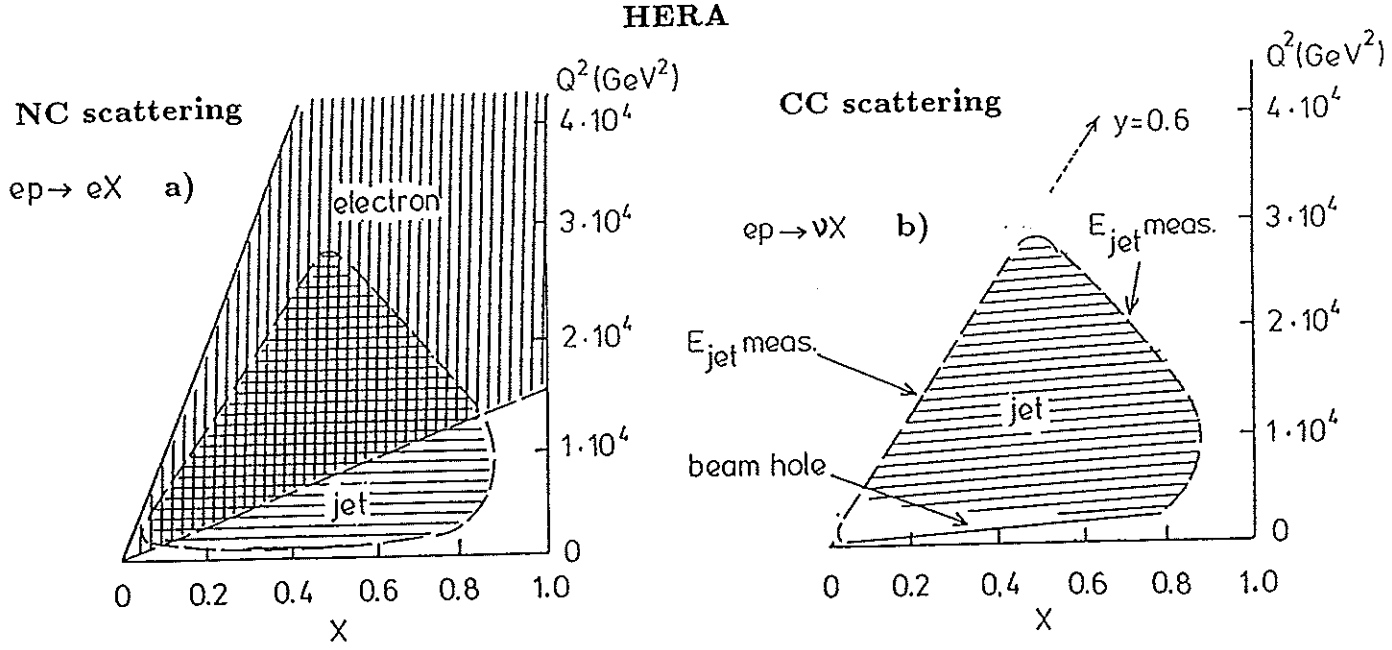

Fig. 2.20 The accessible regions at HERA where x and Q^2 can be well measured:
a) for NC scattering from either the electron or the jets and
b) for CC scattering only from the jets.

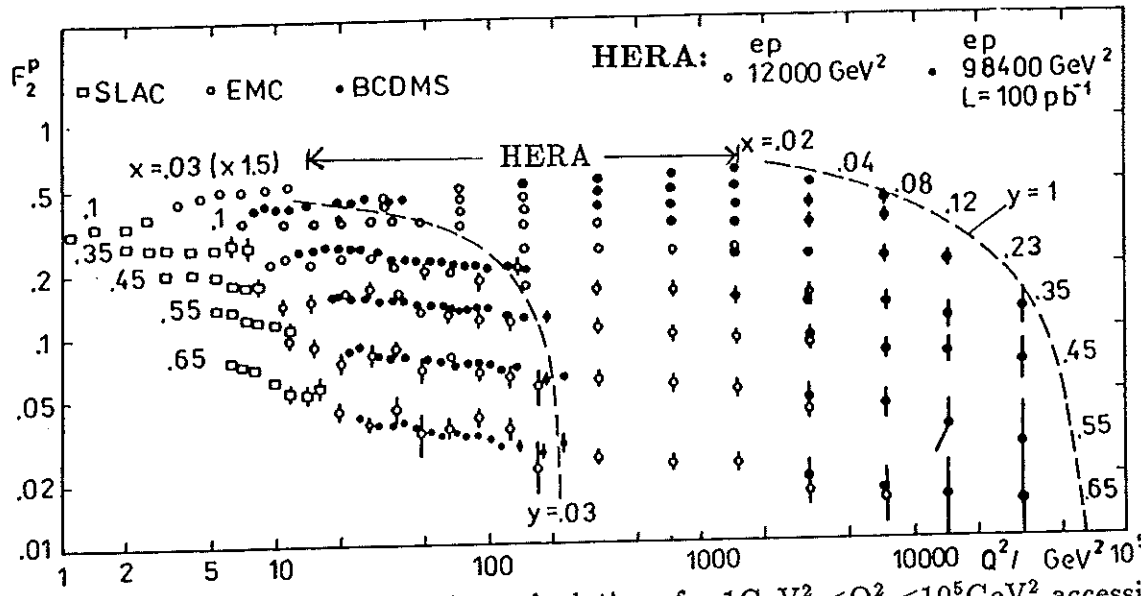

Fig. 2.21 $F_2(x,Q^2)$ structure function calculations for $1\text{GeV}^2 < Q^2 < 10^5\text{GeV}^2$ accessible at HERA compared to measurements of different fixed target experiments.

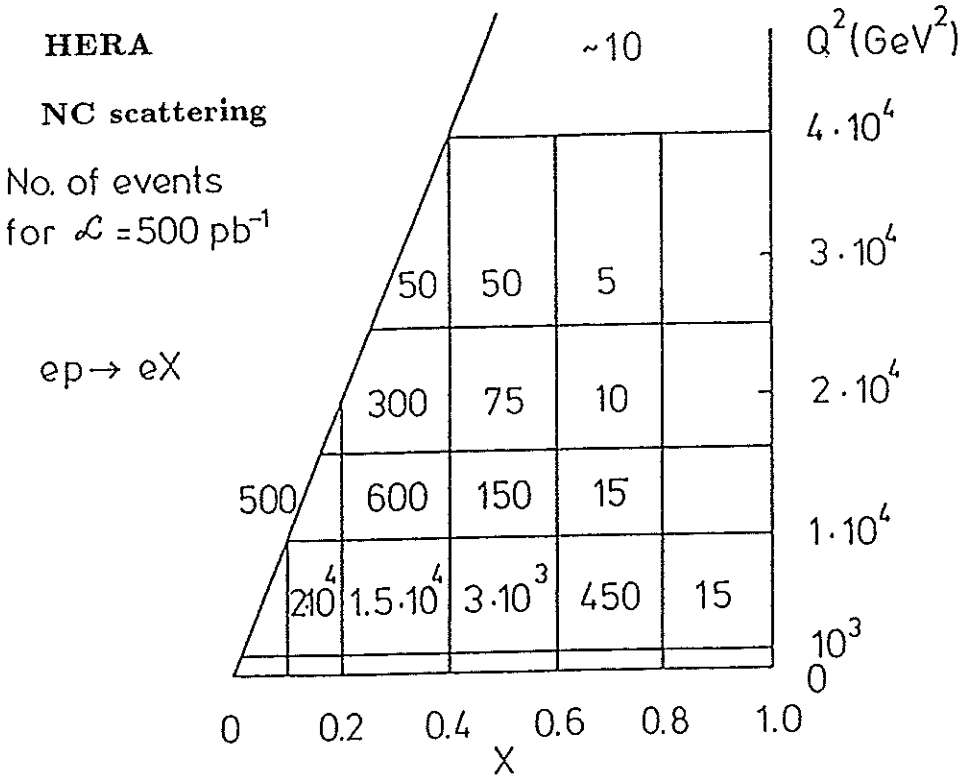

Fig. 2.22 Event rates for NC scattering at HERA with L = 500pb^{-1} calculated with Lund–LEPTO and EHLQ structure functions.

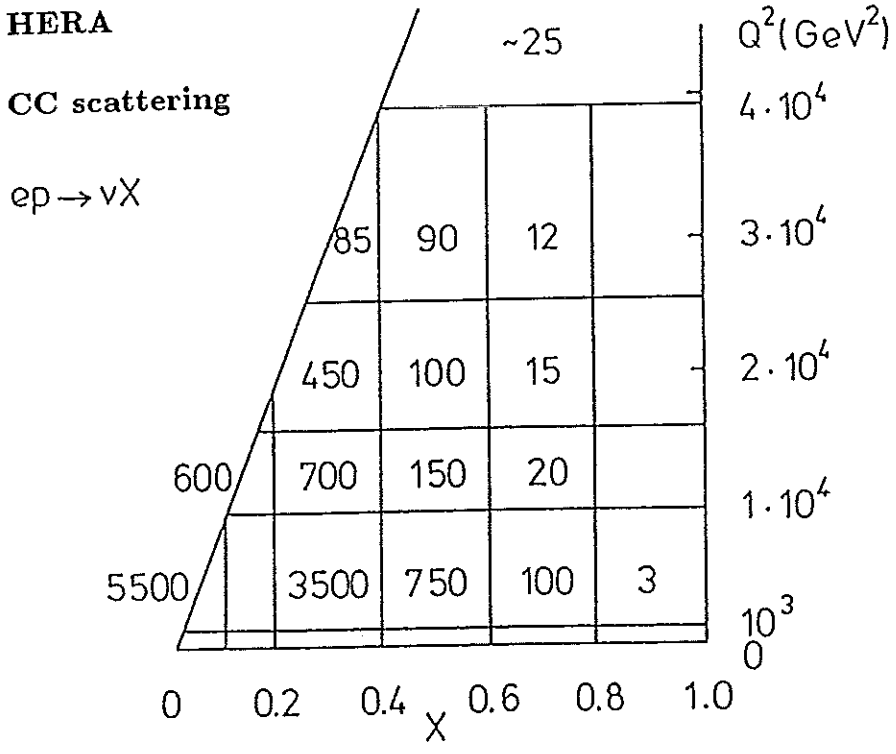

Fig. 2.23 Event rates for CC scattering at HERA with L = 500pb^{-1} calculated with Lund–LEPTO and EHLQ structure functions.

2.2.4 Test of Quantum Chromodynamics

Stringent tests of Quantum Chromodynamics (QCD) will be possible at HERA due to the large accessible Q^2–range. One of the primary physics goals at HERA is to make precise measurements of the deep inelastic structure functions at high Q^2, where logarithmically falling structure functions are predicted by QCD as already indicated in Fig. 2.21.

The structure functions measured at SLAC and the CERN SPS muon experiments up to 300 GeV^2 will be extended with sufficient statistics up to $4 \cdot 10^4$ GeV^2.

Gluon radiation as described for example from the scattered quark in Fig. 2.24 leads to scale breaking of the form

$$F(x) \rightarrow \frac{F(x)}{1 + c\ ln(Q^2/\Lambda^2)}$$

and can be studied in full detail.

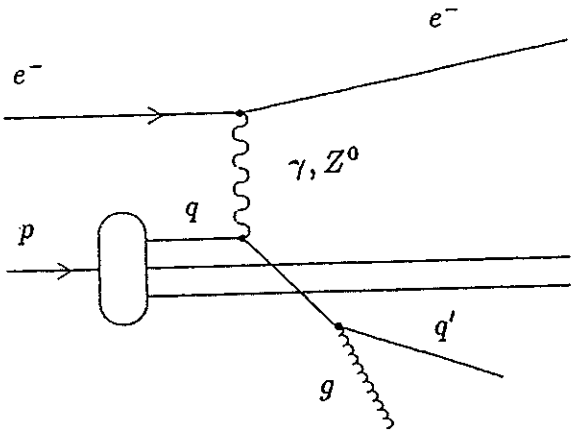

Figure 2.24
Gluon bremsstrahlung in eq–scattering.

The QCD scale parameter, Λ_{QCD}, is expected to be determined with an accuracy of about $\pm$40MeV for Λ_{QCD}=200MeV.

The HERA experiments can be expected to provide for the first time a precise measurement of the gluon structure function $G(x,Q^2)$ of the proton. Measurement of the gluon distribution at small x will be possible from the longitudinal structure function $F_L \equiv F_2 - 2xF_1$ [COO87]. The question of the rise of $G(x,Q^2)$ – a hotly discussed subject will be answered.

Figure 2.25 shows two different gluon distributions which are both compatible with present data. They are of the form
(A) $xG(x,Q^2) = 0.676\ x^{-1/2}(1-x)^5$ and
(B) $xG(x,Q^2) = 5\ (1-x)^9$.
Superimposed are the measured data expected from HERA. The error bars and shaded bands illustrate the statistical and systematic errors for 100pb^{-1} corresponding to one standard year of data taking.

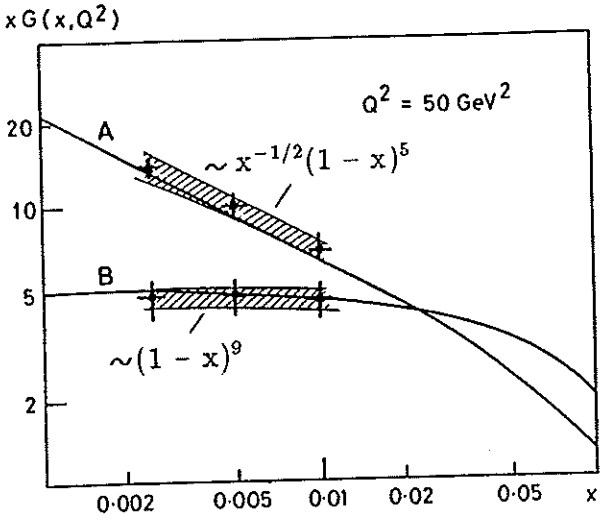

Figure 2.25
Two different gluon distributions superimposed on measurements expected for data from the ZEUS detector (Q^2 = 50GeV^2).

2.2.5 Substructure of Quarks and Electrons

There are models considering quarks and/or electrons as composite objects, with common constituents [EIC83], [CAS83], [CAS85], [MAR87] as illustrated in Fig. 2.26. These substructures of quarks and/or electrons would produce deviations from the QCD predicted structure functions. The interchange of common constituents leads to a contact interaction (C.I.), which is a function of the mass parameter Λ describing the strength of the compositness scale. The contact term L is proportional to $L \sim g^2/\Lambda^2$, where g measures the coupling strength and $g^2/4\pi = 1$ is assumed.

If such new physics exists the new physical phenomena will differ from the predictions of the standard model for $Q^2 > \Lambda^2$. At $Q^2 \leq \Lambda^2$ the interference between the standard processes and the new physics would lead to contact interactions resulting in observable deviations from the standard model expectations.

Figure 2.26c shows the ratio between the structure function F_2 for γ exchange alone and with the contributions from Z^0, together with the additional contribution from a contact interaction with Λ=1TeV [CAS83]. For Q^2 above $10^4 GeV^2$ large deviations from the standard model are predicted. After two years of data taking the measurements will be sensitive to $\Lambda \approx 7$TeV corresponding to distances of about $3 \cdot 10^{-18}$cm.

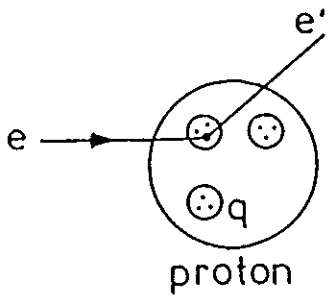

Fig. 2.26a Electron scattering on composite quarks.

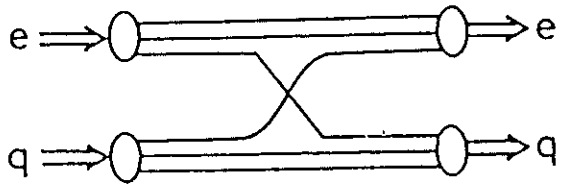

Fig. 2.26b Composite electron and quark scattering by constituent interchange.

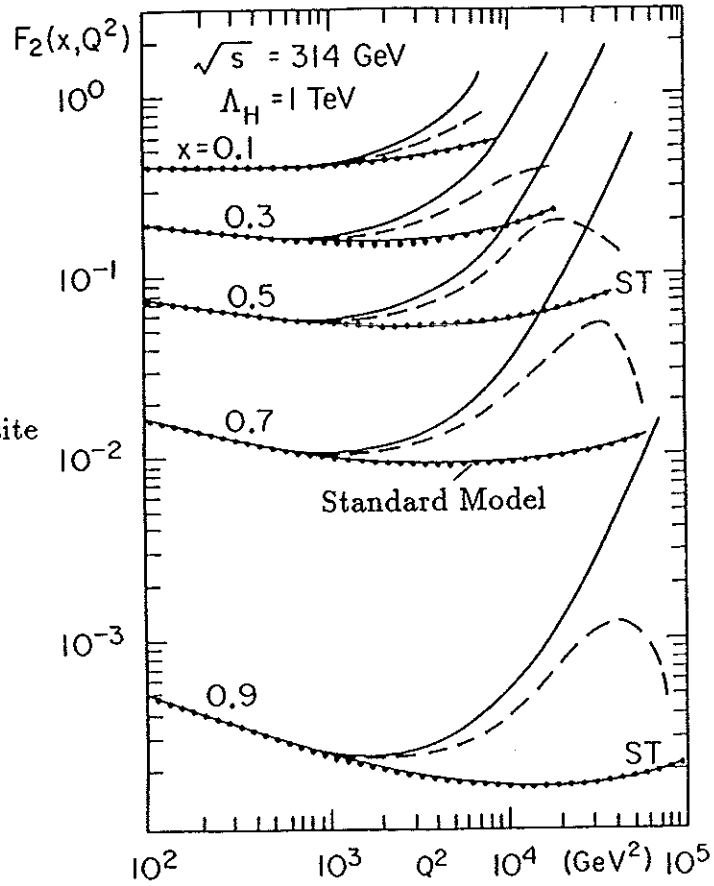

Figure 2.26c
Influence of a contact interaction with Λ_H = 1 TeV on the structure function $F_2(x,Q^2)$ compared to the standard model. The full curves correspond to $(V-A)_l \times (V-A)_q$, the dashed one to $(V-A)_l \times (V+A)_q$.

2.2.6 Search for New Currents

Electroweak theories can be tested at HERA simultaneously by measurements of deep inelastic neutral current and charged current processes. In addition there is the possibility to measure with e^- and e^+ beams. Furthermore there is the expectation that the measurements eventually can be performed with longitudinally polarized $e^{\pm}$'s.

In addition to processes with the known $W(W_1)$ and $Z(Z_1)$ vector bosons, the sensitivity of deep inelastic ep scattering to effects of hypothetical second W_2 and Z_2 bosons has been studied. The explorable mass range was estimated for different interesting models and the additional physical power of longitudinally polarized beams for W_2 and Z_2 searches was pointed out. An example for estimation of the sensitivity to a second W_2 at HERA is given in the following.

The amplitude for the exchange of the standard $W(W_1)$ is given by

$$A(Q^2) \sim \frac{g_2}{(Q^2 + M_W^2)}$$

If a hypothetical W_2 couples in the same way to leptons and quarks and if the coupling constants g_1 and g_2 for W_1 and W_2 are chosen such that the low Q^2 region remains unchanged, the ratio of the cross sections of $\sigma(W_1+W_2)$ to $\sigma(W_1)$ can be written as:

$$\frac{\sigma(W_1 + W_2)}{\sigma(W_1)} = \left[1 - r\frac{m_1^2}{m_2^2} + r\frac{m_1^2}{m_2^2}\ \frac{1 + Q^2/m_1^2}{1 + Q^2/m_2^2}\right]$$

with $m_1=M_W$ and $r=g_2^2/g^2$.

Figure 2.27 shows this ratio with r=1. After two years of HERA running W_2 masses can be investigated up to $\approx$ 700GeV.
Corresponding estimations exist also for neutral currents and Z^0 production.

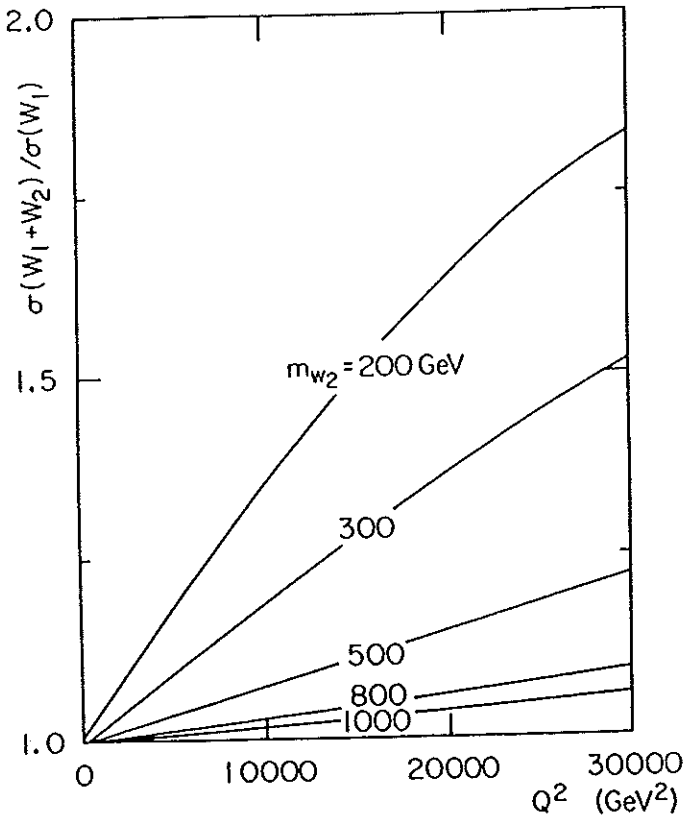

Fig. 2.27 Ratio of the cross sections of $\sigma(W_1 + W_2)$ to $\sigma(W_1)$.

Right Handed Currents

A search for right handed currents is of prime interest. This is best done using longitudinally polarized electrons.

Any nonzero cross section of $e_R^-p \rightarrow \nu X$ or $e_L^+p \rightarrow \bar{\nu}X$ scattering signals the existence of a right handed charged current.

For neutral current reactions a difference between the cross sections for $e_{L,R}^-$ and $e_{L,R}^+$ scattering is expected due to the different contributions of the Z^0 exchange. Figure 2.28 presents the magnitude of weak interaction effects in NC reactions which amount to about 60% at $Q^2 \approx 10^4 GeV^2$.

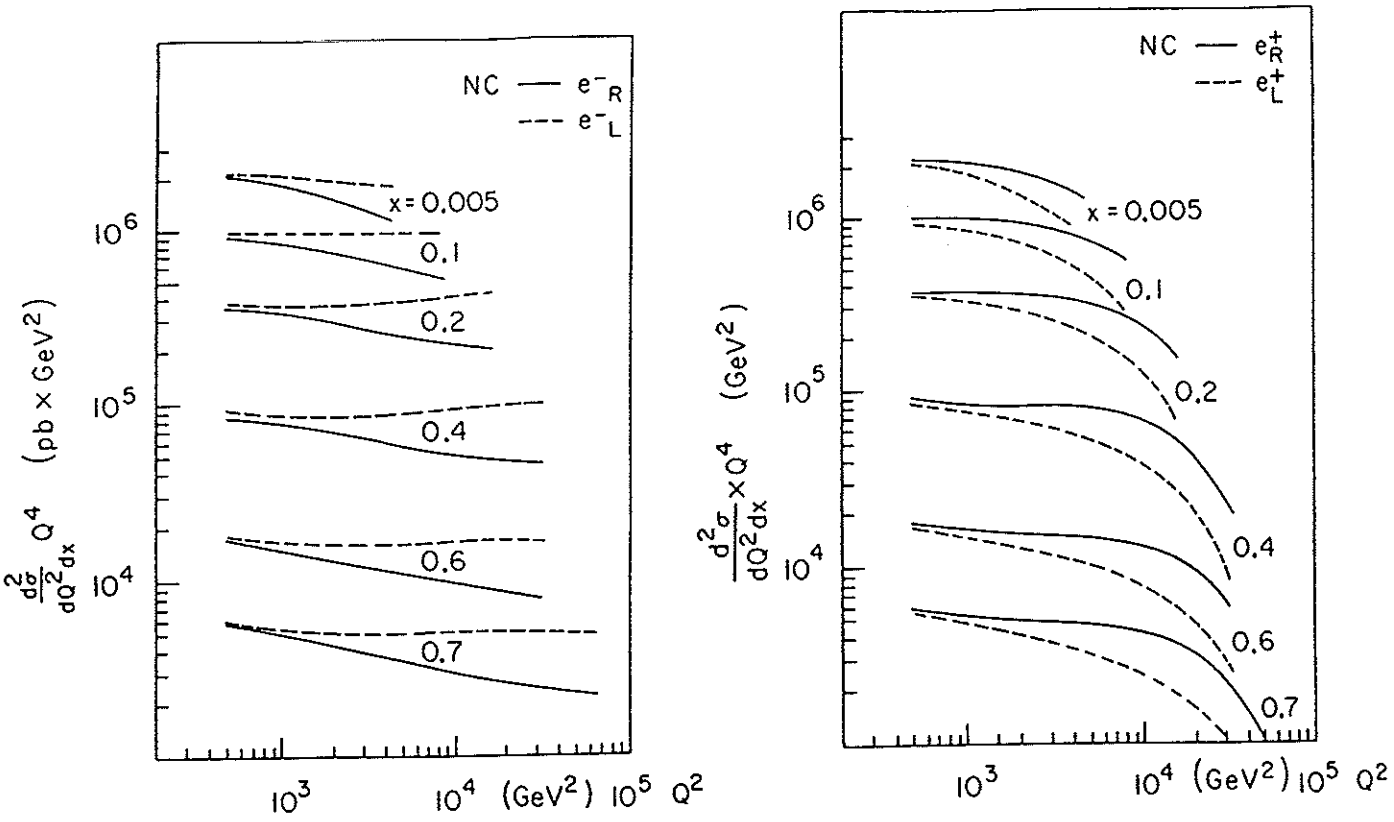

Fig. 2.28 Neutral current cross sections for left and right handed $e^{\mp}$.

2.2.7 Search for New Particles

At HERA the main source of heavy quark production will be photon gluon fusion (Fig. 2.17). The total cross section is of the form

$$\sigma(eq \to Q\overline{Q}X) \sim M_Q^{-4}$$

with M_Q = mass of the heavy quark.

Figure 2.29 describes the contributions of photon gluon fusion in neutral current events as a function of Q^2 [ZEU85]. It shows that the production of heavy quarks can be expected essentially at low Q^2.

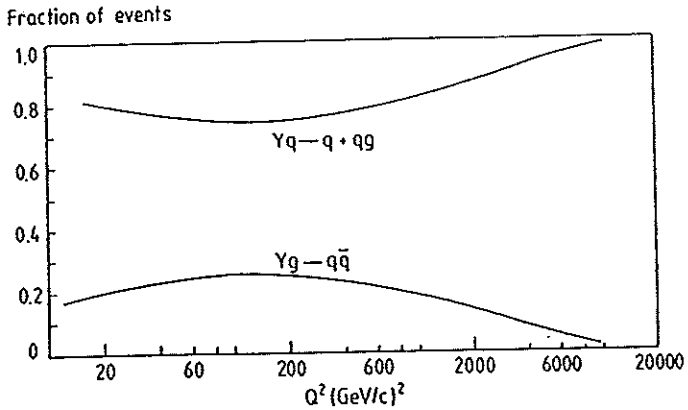

Fig. 2.29 Contributions of photon gluon fusion in NC events.

At HERA, searches are possible in particular [SÖD90] for:

$Z^{0\prime}$	up to a mass of	700 GeV	contact int.	up to a mass of	4–7 TeV
$W^{\pm}_R$		400 GeV	leptoquarks		300 GeV
SUSY		180 GeV	leptogluons		280 GeV
e^*		200–250 GeV			

2.2.8 Physical Requirements on the Detector Performance

The detector requirements for calorimetry, tracking devices and particle identification, depend on the momenta and angles of the particles and jets of the final state produced in the ep scattering [ZEU85], [WOL86], [KRÜ87a]. The kinematics of deep inelastic scattering between 30GeV electrons and 820GeV protons is shown in Fig. 2.30. The transverse momentum is plotted w.r.t. the beam axis versus the longitudinal momentum. The elongated shape of the phase space of the scattered lepton and the quark is due to the different electron and proton beam energies. The events are in general very asymmetric, with most of the final state hadrons in the forward proton direction [ING87].

In Fig. 2.31 two Monte Carlo simulated events are shown in a typical HERA detector design, one neutral current event [NC] with x=0.25 and Q^2=5000GeV^2 in the upper plot and a charged current event [CC] with x=0.35 and Q^2=16000GeV^2 in the lower plot. For the NC event the scattered electron has an energy of 64GeV and the current jet an energy of 160GeV. The proton remnants jet disappears essentially in the beam pipe. The kinematical quantities x and Q^2 of this event can either be determined from a measurement of energy and angle of the scattered electron (E'_e,θ_e) or from energy and scattering angle of the current jet (E_j, θ_j). In the CC event the outgoing lepton is a neutrino ν, which carries away an energy of 50GeV, the current jet has an energy of 170GeV and again the proton remnants jet disappears essentially in the beam pipe. The neutrino is not detected, thus for CC events the kinematical variables x and Q^2 can be determined precisely only from the energy and the scattering angle of the current jet (E_j, θ_j), or from the total hadron flow [JAC79].

These two typical examples for NC and CC events show, that the precision with which the kinematical variables x and Q^2 can be determined depends strongly on precise energy and angular measurements. In particular for CC events x and Q^2 can be determined only from a measurement of the energies and angles of the produced hadrons. A closer inspection reveals that in most cases it is the precision of the energy measurement which determines the accuracy of x, Q^2. Consequently a high precision energy measurement is of primary physical interest for a HERA detector and requires the implementation of a high resolution calorimeter.

Figure 2.32 shows the kinematical region accessible in the x,Q^2–plane at HERA for CC events assuming the Longo criteria [LON83]. The dashed line describes the measurable area for a high resolution calorimeter with an energy resolution of $35\%/\sqrt{E}\oplus 1\%$ for single hadrons and jets, and equal response to electrons and hadrons (e/h=1), the full line correspondingly for a standard hadron calorimeter with a typical resolution of $60\%/\sqrt{E}\oplus 1\%$ and e/h=1.4. The Longo criteria require for the well measurable region, that if the x,Q^2–plane is divided into small bins, after reconstruction more than 60% of the events stay in the original bin and less than 40% of the events migrate from outside into that bin. This plot shows the power of a high resolution calorimeter: it extends significantly the accessible kinematical region in particular at low x, and towards large Q^2.

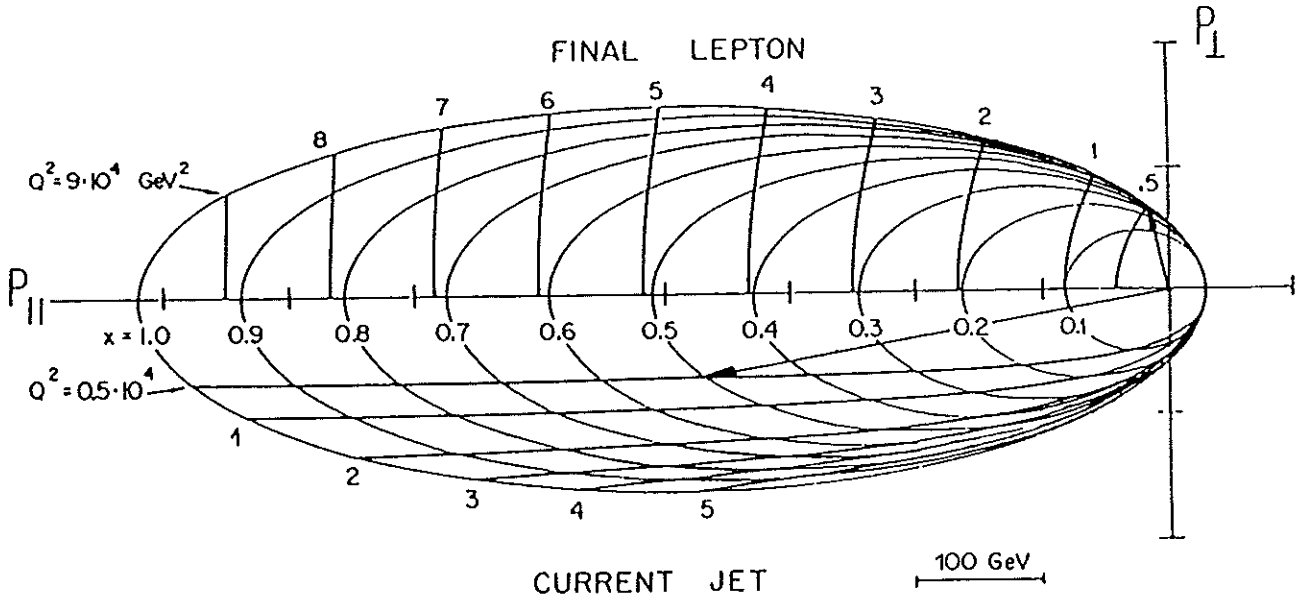

Fig. 2.30 Polar diagram of the kinematics for the final lepton and the current jet with lines of constant x and Q^2. Connecting a given (x,Q^2) point with the origin gives the laboratory momentum vectors, as shown by the example for x=0.5, Q^2=5000GeV^2.

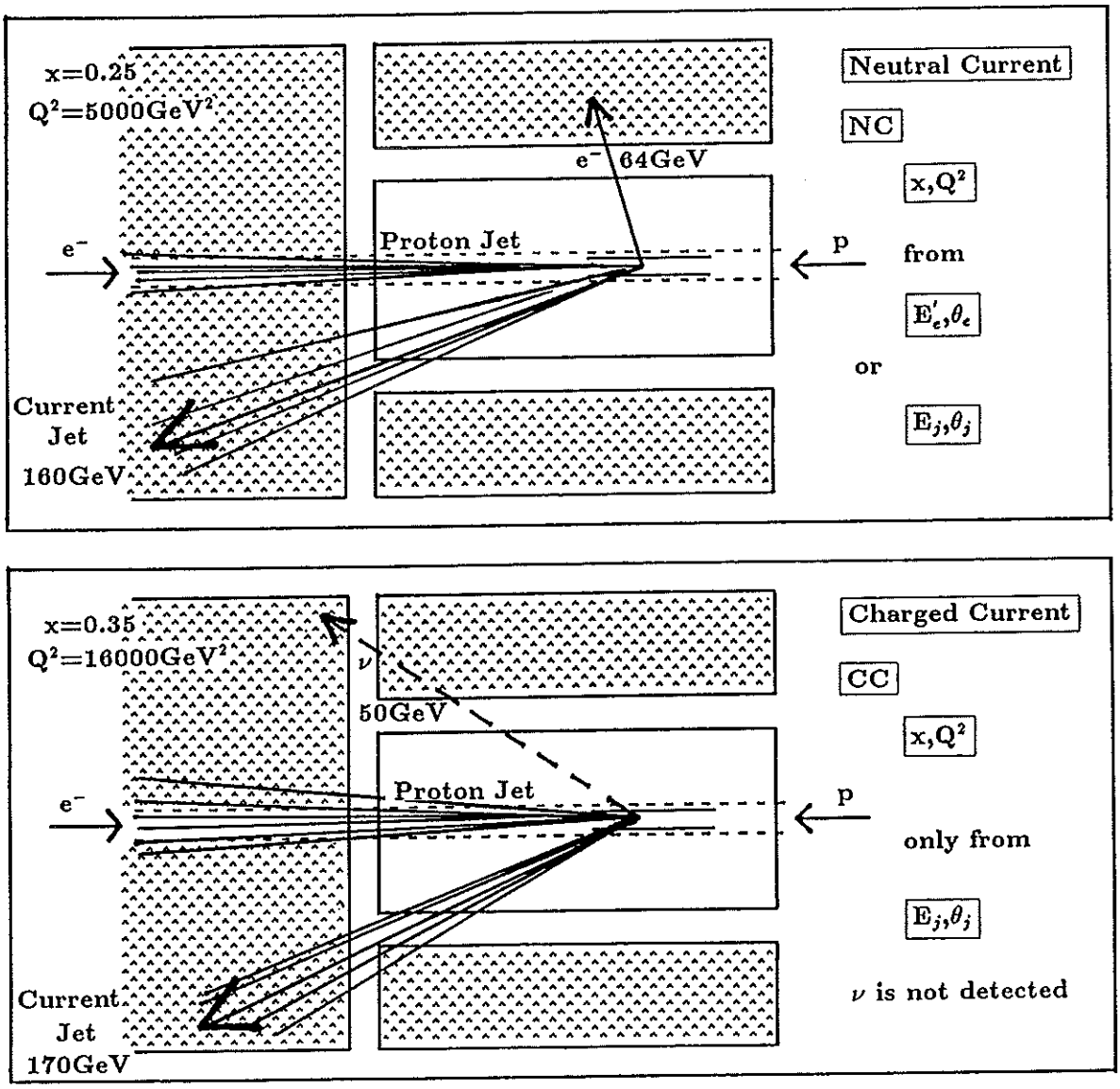

Fig. 2.31 Monte Carlo simulated neutral current (NC) and charged current (CC) events.

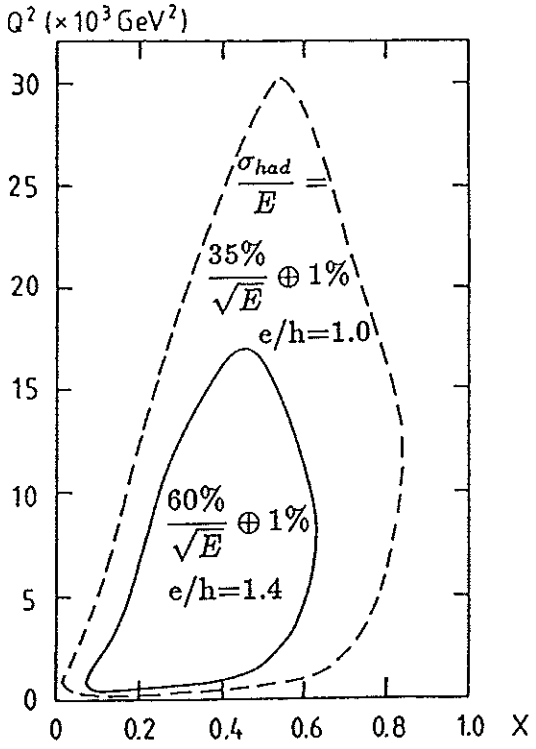

Figure 2.32
Areas in the x,Q^2–plane that can be well measured with calorimeters of indicated resolution assuming the Longo criteria.

The ZEUS collaboration started in 1984 a comprehensive program of research and development in calorimetry to gain the knowledge and experience for design and construction of a calorimeter with the best possible energy resolution for hadrons and jets.

The primary goals for the ZEUS hadron calorimeter can be summarized as follows:

- Compensation (e/h=1) and best possible energy resolution for hadrons and jets
- 4π hermeticity
- Precise angular resolution for particles and jets ($\leq$10mrad)
- Precise energy calibration ($\leq$1%)
- Handling of short times between bunch crossings, 96ns

For the tracking devices one of the most important tasks is the determination of the sign of the charge of the particles in the final state, in particular for single electrons and muons. The essential requirements can be summarized as follows:

- High transverse momentum resolution $\frac{\sigma(p_T)}{p_T} \approx 0.003 p_T$
- High density of points along each track for dE/dx measurement and electron recognition
- Two track angular resolution $\approx$ 4mrad
- Tracking down close to the beam line ($\approx$ 100mrad)
- Precise vertex detection

For lepton identification the requirements are as follows:

- Identification of leptons and momentum and angle measurements over the entire angular range

2.3 The ZEUS Detector

2.3.1 Overview of the ZEUS Detector

About 450 scientists are taking part in the ZEUS collaboration. They come from 50 institutions (Table 2.7) in ten countries: Canada, Germany, Israel, Italy, Japan, The Netherlands, Poland, Spain, United Kingdom and the USA [ZEU85...91]. The composition of the ZEUS collaboration can be found at the end of this report (p.8–31). In addition an organigram of the Hamburg ZEUS members is added indicating their activities (p.8–35).

Figure 2.33 shows an artist view of the ZEUS detector and its internal structure. Sections of ZEUS along and perpendicular to the beam are presented in Fig. 2.34 and 2.35 and the main parameters of the detector are summarized in Table 2.8. The dimensions of the ZEUS detector are 11.6m x 10.8m x 20.0m (x, y, z) and its total weight is 3600t.

The heart of the ZEUS detector is the uranium scintillator calorimeter (CAL) which measures with high precision energies and directions of particles and particle jets. It has a layered structure and is built from depleted uranium (DU) plates interleaved with sheets of plastic scintillator. Readout of the light from the scintillator is achieved by means of plastic wavelength shifters with associated photomultipliers.

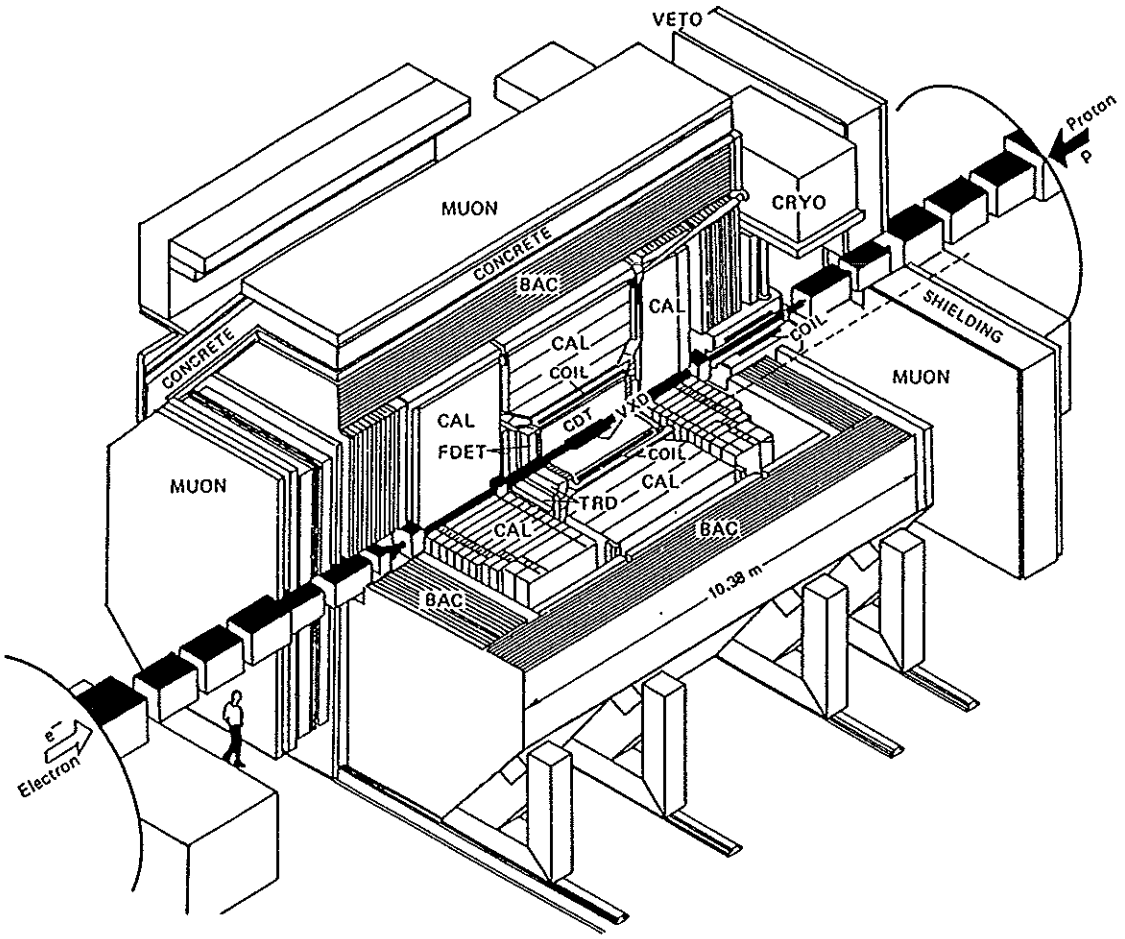

Fig. 2.33 Artist view of the ZEUS detector showing its internal structure.

The uranium scintillator calorimeter totally encloses the tracking detectors. These detectors measure the tracks of charged particles using wire chambers and consist of: a vertex detector (VXD), the central drift chamber (CTD), forward (FTD) and backward (RTD) drift chambers and in the forward direction a transition radiation detector (TRD) to identify high energy electrons. These chambers are surrounded by a thin superconducting solenoid coil producing an axial field of 1.8 Tesla for determining the momenta of charged particles from their curvature in the magnetic field.

Behind the third and sixth DU layers of the calorimeter a detector of 3cm x 3cm silicon diodes is foreseen in order to improve the hadron electron separation (HES) and in addition the spatial resolution.

The CAL is surrounded by the backing calorimeter (BAC) which is constructed from the 7.3cm thick iron plates of the return yoke and read out by means of proportional tube chambers. With the BAC the energy of events not completely absorbed by the CAL can be measured.

Particles which traverse the large amount of material and are not absorbed in the uranium scintillator or backing calorimeter are identified as muons and their tracks are measured before and after the iron yoke by special muon track chambers (MUON). The muon momenta are determined by the deflection of their tracks in the iron yoke which is magnetized toroidally by copper coils to 1.6 Tesla. In the forward direction additional magnetized iron toroids and muon chambers are installed to cope with very energetic muons (up to 150GeV). Also, the path of muons through the yoke can be followed with BAC.

In the far forward direction a leading proton spectrometer (LPS) is installed consisting of six pots distributed over 100 m along the beam pipe to detect, with high resolution silicon strip detectors, forward scattered protons.

In the direction of the electron beam photons and electrons are detected in coincidence in the luminosity detector (LUMI) at distances of 35m and 106m from the interaction point.

ZEUS – COLLABORATION	
CANADA	Manitoba, McGill, Toronto, York
GERMANY	Bonn, DESY, DESY–Zeuthen, Freiburg, Hamburg I, Hamburg II, Jülich, Siegen
ISRAEL	Tel Aviv, Weizmann Institute
ITALY	Bologna, Cosenza, Florence, Frascati, L'Aquila, Padua, Rome, Turin I, Turin II
JAPAN	Tokyo–INS, Tokyo–Metropolitan
THE NETHERLANDS	NIKHEF–Amsterdam
POLAND	Cracow, Warsaw
SPAIN	Madrid
UNITED KINGDOM	Bristol, Glasgow, London (I.C.), London (U.C.), Oxford, Rutherford
USA	Argonne, Brookhaven, Columbia, Iowa, Louisiana State, Ohio State, Pennsylvania State, U.C. Santa Cruz, Virginia Tech, Wisconsin

Table 2.7 Institutes of the ZEUS Collaboration.

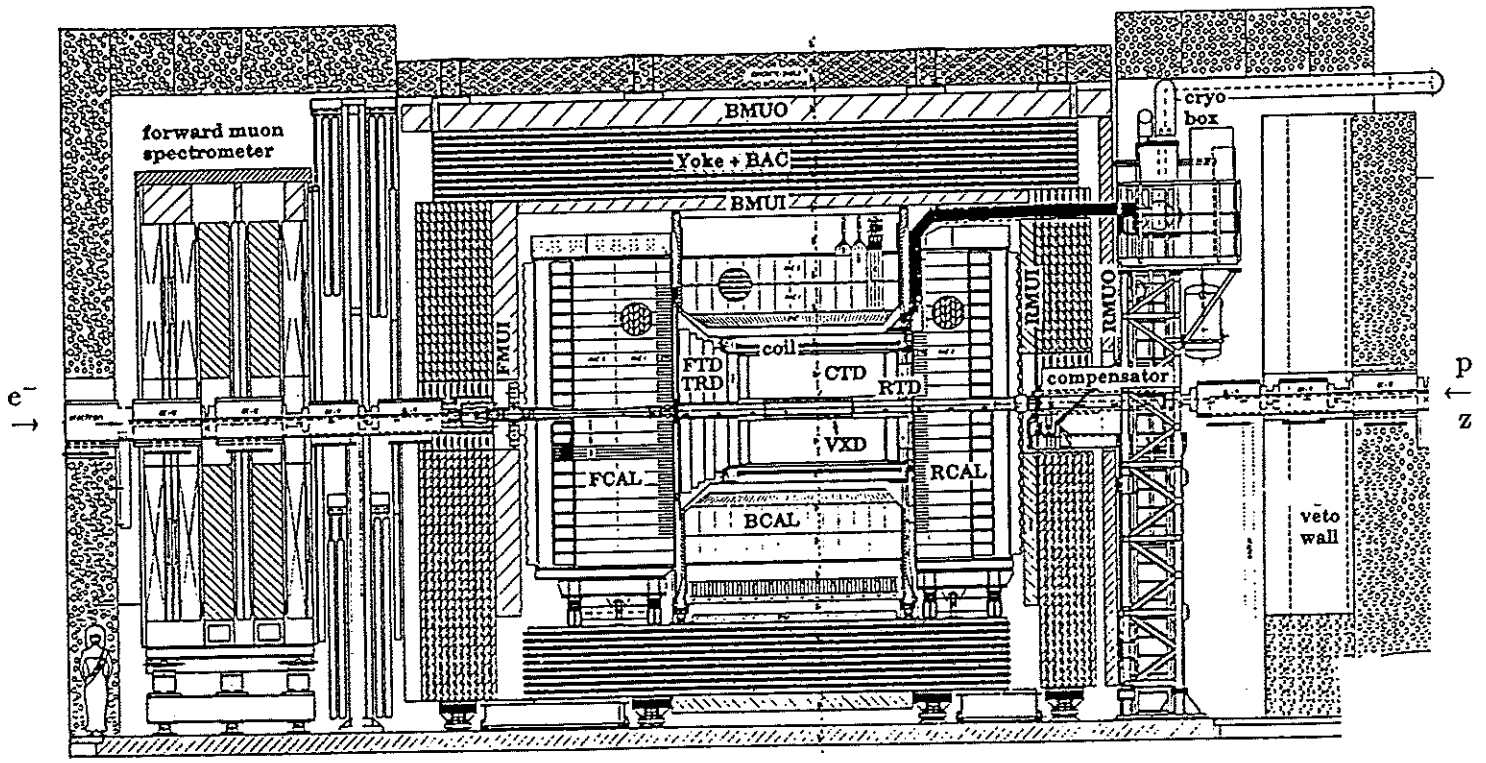

Fig. 2.34 Section of the ZEUS detector along the beam.

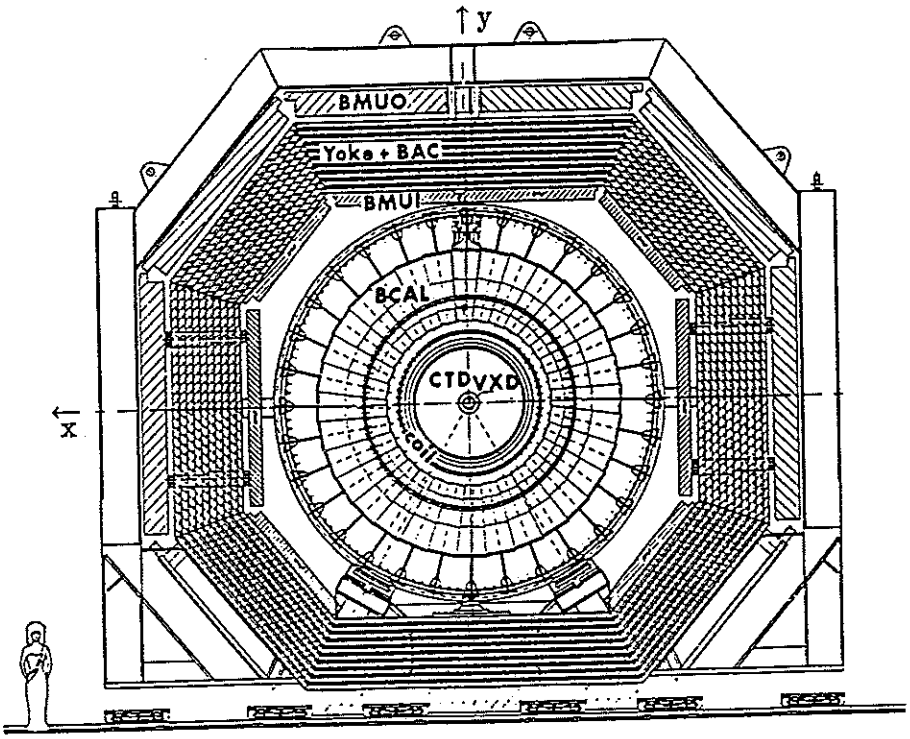

Fig. 2.35 Section of the ZEUS detector perpendicular to the beam.

PARAMETERS OF THE ZEUS DETECTOR			
Dimensions	11.6m x 10.8m x 20.0m		
Total weight	3600t		
Magnets: **Solenoid** (s.c.)	1.8T, 86cm<R<111cm, L=280cm		
Compensator (s.c.)	5T, 37cm<R<47cm, L=120cm		
Yoke Coils	1.6T in the iron yoke		
Uranium Scintillator Calorimeter (CAL)			
Total weight	700t		
Layer structure	3.3mm DU + 2.6mm Scint.		
Structure of CAL	FCAL	BCAL	RCAL
Number of modules	24	32	24
Longitudinal segmentation	EMC	EMC	EMC
	HAC1,2	HAC1,2	HAC1
Max. number of layers	185	119	105
Max. depth in absorption length	7.1	5.3	4
EMC transverse segmentation	5 x 20	5 x 24	10 x 20cm^2
HAC transverse segmentation	20 x 20	20 x 28	20 x 20cm^2
Number of photomultipliers	12000		
Silicon detector (HES)	FCAL	BCAL	RCAL
Number of layers / Si-diodes	2 / 20000	1 / 20000	1 / 10000
Diode area	20	20	10 m^2
Backing Calorimeter (BAC)			
Active area	2980 m^2		
Number of layers / signal wires	7 – 10 / 40000		
Size of towers / Number of towers	50 x 50cm^2 / 1700		
Tracking Detectors (VXD, CTD, FTD, RTD, TRD)			
Vertex detector (VXD) / number of signal wires	9.9cm<R<15.9cm / 1440		
Central drift chamber (CTD)	16.2cm<R<85.0cm		
Superlayers / wire layers per superlayer	9 / 8		
Number of signal wires	4608		
Forward/backward detector (FTD, RTD)	12.4–16.4cm<R<62–121cm		
Drift layers / signal wires	12 / 5544		
RTD drift layers / signal wires	3 / 1008		
Number of TRD planes	4		
Number of TRD signal wires / cathode strips	1056 / 1056		
Muon Detector (MUON)			
Forward: Number of signal layers / channels	26 / 18400		
Central: Number of signal layers / channels	16 / 70400		
Leading Proton Spectrometer (LPS)			
Position of detectors	z = 24, 41, 44, 63, 81, 90m		
Luminosity Detector (LUMI)			
Position of detectors	z = –35, –106m		
Performance:			
Energy resolution for hadrons and jets	$\sigma(E)/E = 35\%/\sqrt{E} \oplus 2\%$		
Energy resolution for electrons	$\sigma(E)/E = 18\%/\sqrt{E} \oplus 1\%$		
Momentum resolution for charged particles	$\sigma(p)/p = 0.002 \cdot p \oplus 0.003$		
Hadron misidentification probability P(h→e)	$5 \cdot 10^{-4} - 10^{-5}$		
Pion misidentification probability P($\pi \rightarrow \mu$)	10^{-3}		

Table 2.8 Parameters of the ZEUS detector.

2.3.2 Magnet System and Iron Yoke

The momenta of charged particles are determined by measuring the deflection of their tracks in the 1.8 Tesla axial field of the thin, superconducting solenoid which is located between CTD and CAL. The coil of the solenoid has a length of 2.46m and an inner/outer diameter of 1.85m/1.91m (Table 2.9). It is installed in a 2.8m long cryostat with an inner/outer diameter of 1.72m/2.22m. The inner wall of the vacuum vessel supports the CTD.

The material thickness of the solenoid was minimized to about 0.9 radiation lengths X_0 ($\hat{=}$8cm Al) to reduce the degradation of the energy measurement of electrons, photons and hadrons in the high resolution calorimeter. The field inhomogenity defined by $\frac{1}{L}\int_0^L \frac{(B_z - B_{z0})}{B_{z0}} dl$, with a magnetic field B_{z0} at the origin and a track length L should be less than 8% in the central region.

Figure 2.36 shows a picture of the opened iron yoke during installation of the solenoid. The solenoid has been tested and cooled down to 5 K in 66 hours (Jan. 90) and the design field of 1.8 T has been reached. Field measurements have been performed with a precision better than 0.2% in the central region. They are in good agreement (<1%) with the predicted values. Figure 2.37 shows results of the magnetic field measurements. The axial field B_z and the radial field B_r are plotted as a function of z. Results from detailed 3-dimensional magnetic field calculations with the program package TOSCA are superimposed for comparison [COR90].

Superconducting Solenoid	Coil	Cryostat
Inner diameter	1850mm	1720mm
Outer diameter	1914mm	2220mm
Length	2.46 m	2.80 m
Forward length	1.3 m	1.45 m
Backward length	-1.2 m	-1.35 m
B_{max} (z=0)	1.8 Tesla	—
Nominal current	5 kA	—

Table 2.9 Parameters of the thin superconducting solenoid.

To compensate for the influence of the magnetic field of the thin solenoid on the beam dynamics a superconducting solenoid (compensator) creating the same opposite integrated field length of $\int B_z dz = 6.0$ Tm along the beam axis is installed in the rear end cap of the iron yoke. The compensation coil has a length of 1.2m, an inner diameter of 0.37m and reaches a maximum field B_{max} of 5T on axis.

The two solenoids are treated as a whole system. They have the same cooling system and are supplied with He at a temperature of 4.4K and a pressure of 1 bar and gaseous He at 40K. Both solenoids are charged or discharged simultaneously during beam operation.

The iron yoke returns part of the flux of the thin solenoid and represents the biggest part of the detector. It has the shape of an octagonal cylinder, closed by two end caps, with overall dimensions of 10.4m x 9.1m x 8.6m (l,w,h) and a weight of 1962 tons. It is built from 7.3cm thick iron plates with 3.7cm gaps for insertion of the multiwire proportional chambers of the backing calorimeter. The iron yoke is split into 3 parts and can be opened for access to the inner components of the detector (see Fig. 2.36).

In order to enable a precise muon momentum measurement the yoke is magnetized by normal conducting coils generating a toroidal magnetic field of 1.6T in the iron yoke (Fig. 2.36).

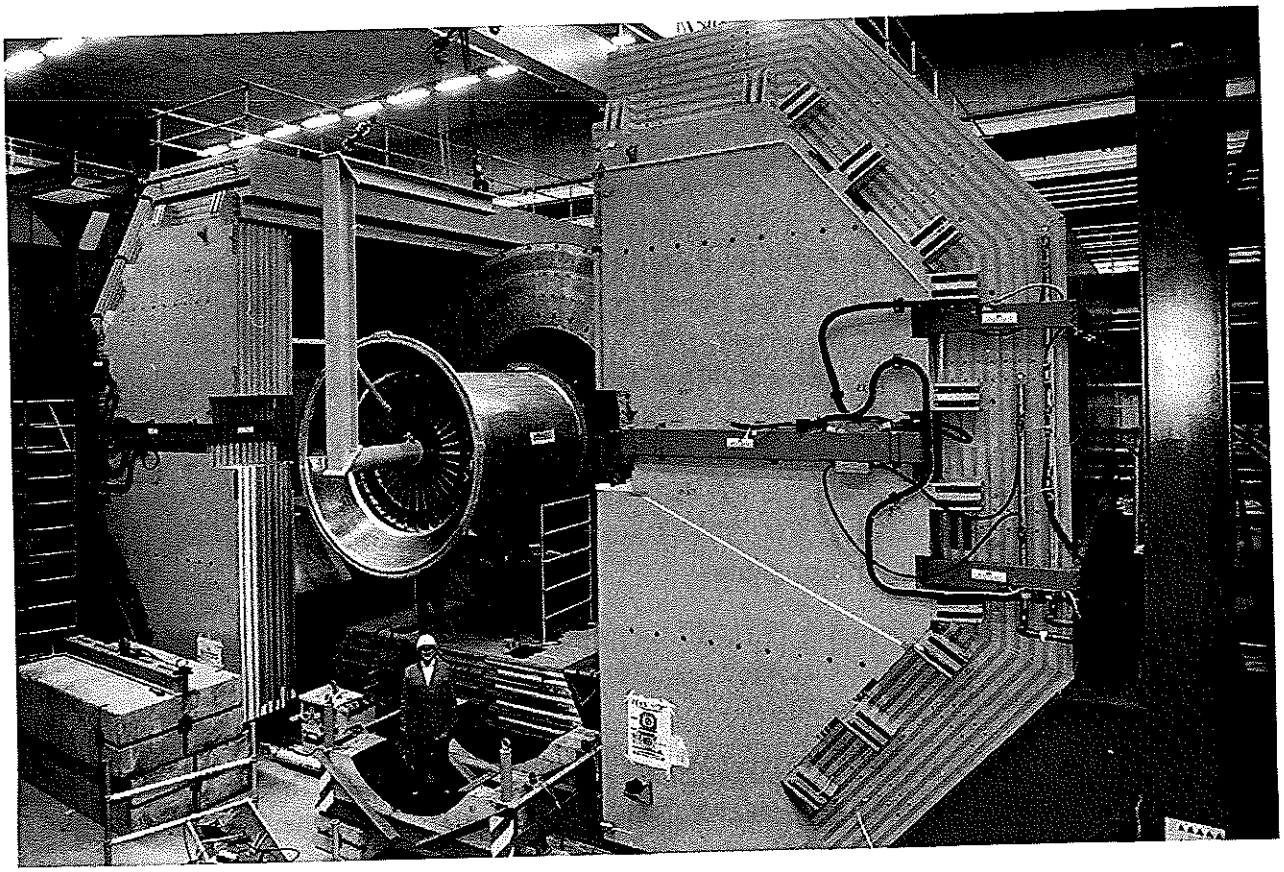

Fig. 2.36 Installation of the superconducting solenoid.

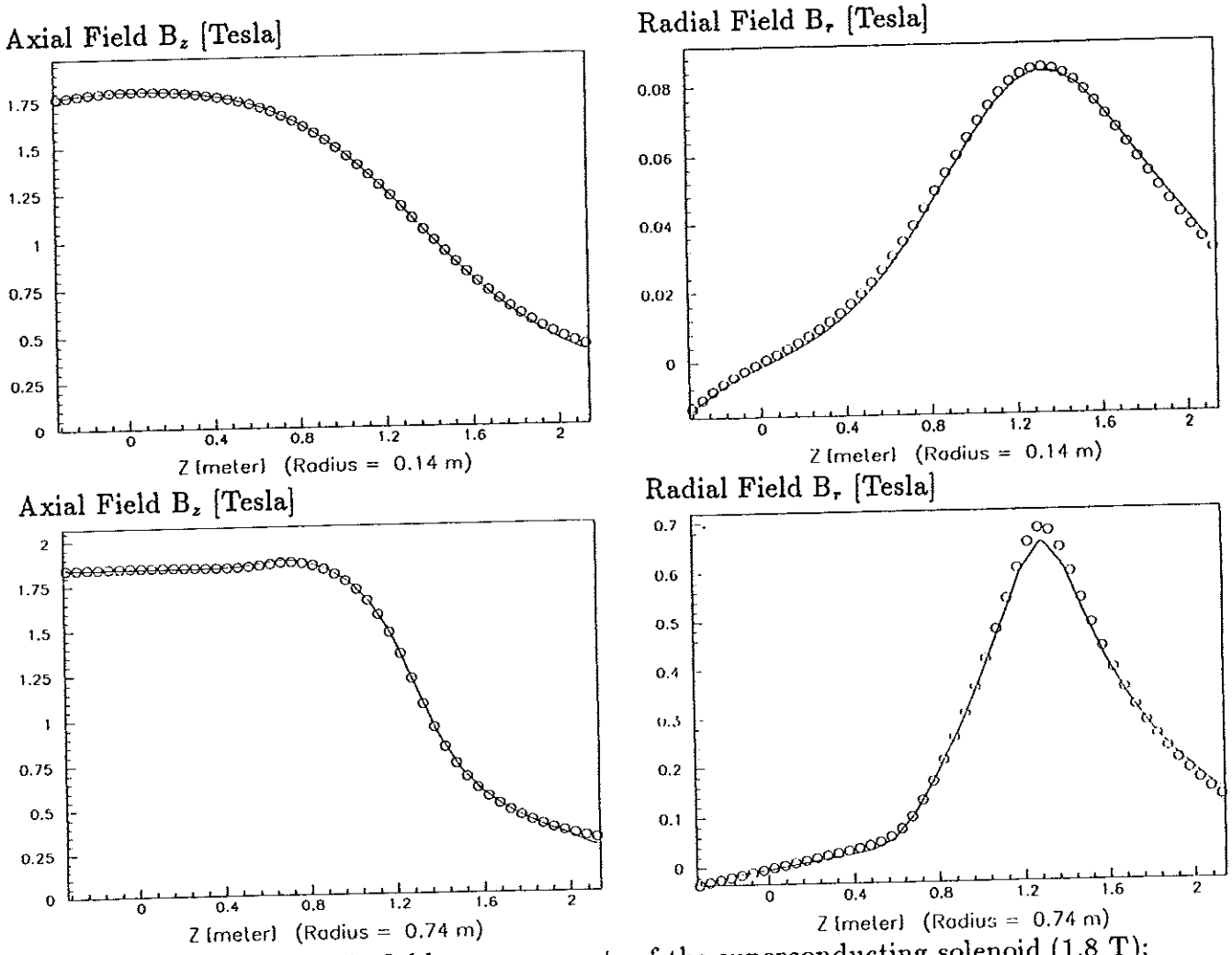

Fig. 2.37 Magnetic field measurements of the superconducting solenoid (1.8 T); open circles measured, full lines calculated with TOSCA.

2.3.3 High Resolution Calorimeter (CAL)

The most important characteristics of the calorimeter can be summarized as follows: full containment of all particles in the entire angular range (solid angle coverage 99.8% in the forward and 99.5% in the backward hemisphere), linear and equal response for electrons and hadrons up to the highest energies (e/h=1.0 (compensation)), precise energy measurement for hadrons and jets with an energy resolution of $35\%/\sqrt{E} \oplus 2\%$ and $18\%/\sqrt{E} \oplus 1\%$ for electrons, an angular resolution for jets better than 10mrad, a time resolution of a few ns compared to a bunch–crossing time of 96 ns, the ability to discriminate between hadrons and electrons because of their different energy depositions and a calibration accuracy of about 1%.

Figure 2.38 shows the layout of the calorimeter. It totally encloses the inner tracking detectors (VXD, CTD, FTD, RTD, TRD) and the superconducting solenoid and consists mechanically of three main components:

Forward Calorimeter (FCAL)	(	$2.2^0 < \theta < 39.9^0$),
Central or Barrel Calorimeter (BCAL)	(	$36.7^0 < \theta < 129.1^0$),
Rear Calorimeter (RCAL)	(	$128.1^0 < \theta < 176.5^0$).

The depths of these three calorimeter parts were optimized w.r.t. the kinematically maximum possible jet energy E(θ). In units of absorption lengths FCAL has a maximum depth of 7.1λ, BCAL of 5.3λ and RCAL of 4λ. The total weight of the uranium scintillator calorimeter is 707t (517t DU, 52t steel boxes, 23t scintillator, plus mechanical structures).

FCAL and BCAL are segmented longitudinally into three sections, an electromagnetic (EMC) with a depth of 25 radiation lengths (X_0) or 1 interaction length (λ) and two hadronic sections (HAC1,2) with a depth of 2 x 3.1λ in the FCAL and 2 x 2.1λ in the BCAL. The RCAL is divided longitudinally into two sections, one EMC (1λ) and one HAC section (3.1λ).

Figure 2.39 shows a front view of the FCAL with its modular structure as seen from the interaction point. Its front face approximates a circle with a radius of 2.5m and its depth for vertical incidence varies from 7.1λ in the central region to 5.6λ in the outer horizontal regions. The different depths are indicated in Fig. 2.39. The FCAL is assembled from a total of 24 modules each having a width of 20cm, an active depth up to 1.53m, a height varying from 2.2m to 4.6m and a weight of up to 12t. The transverse internal segmentation of the FCAL as seen from the interaction point is presented in Fig. 2.40. The fine granularity in the central region is achieved by a finer transverse segmentation of the EMC section which extends up to the region of the shadow of the BCAL. The different FCAL and RCAL module types and compositions are summarized in Table 2.10.

Figure 2.41 indicates the internal structure of an FCAL module. The FCAL modules have a non–projective tower structure with a size of 5cm x 20cm in the EMC and 20cm x 20cm in HAC1 and HAC2.

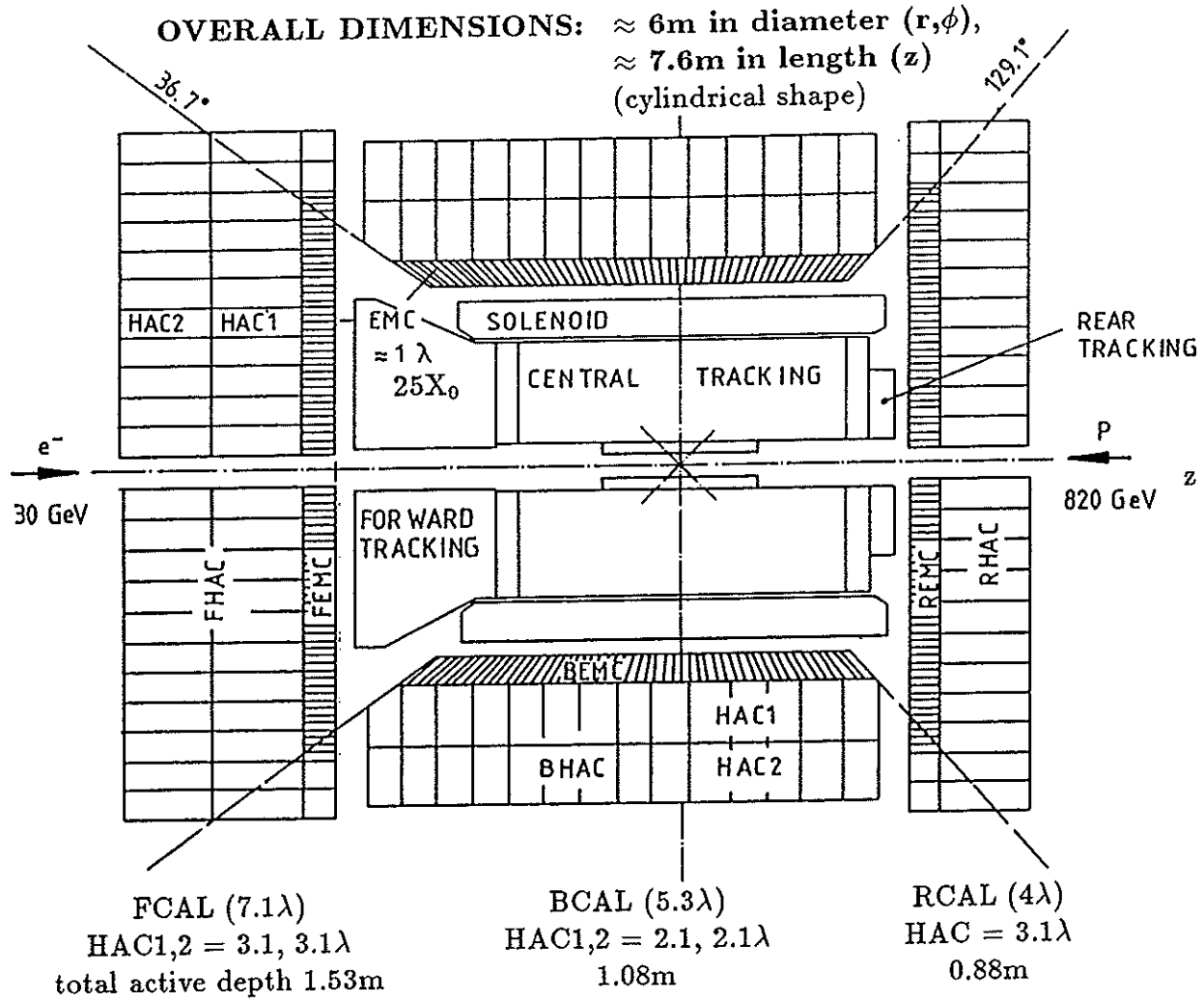

Fig. 2.38 Layout of the ZEUS Uranium Scintillator Calorimeter; FCAL = Forward Calorimeter, BCAL = Central Calorimeter, RCAL = Rear Calorimeter, EMC and HAC = electromagnetic and hadronic sections.

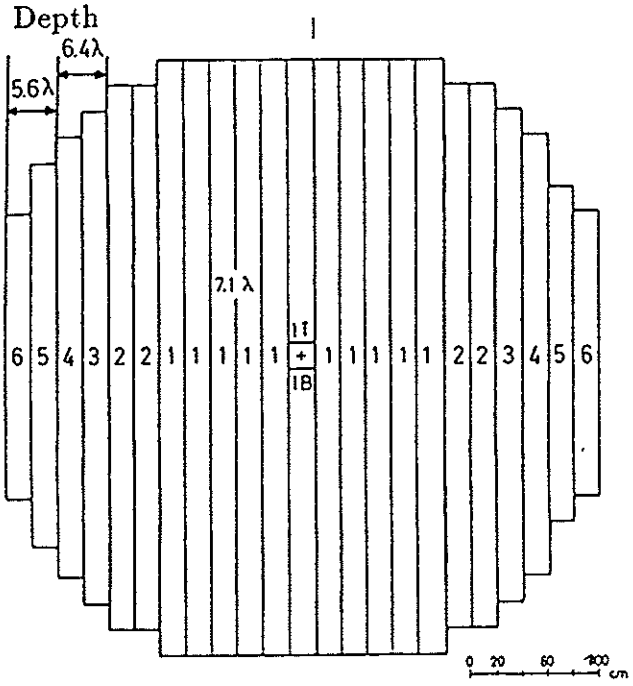

Fig. 2.39 Front view of FCAL assembled from 24 modules of various depth in λ.

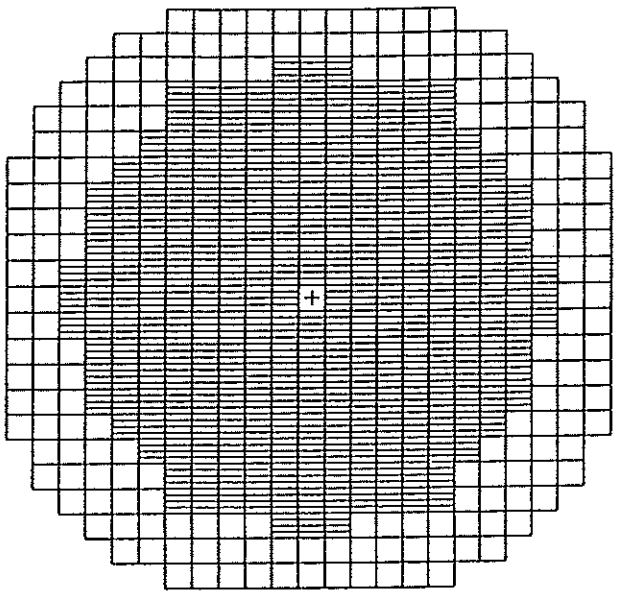

Fig. 2.40 Front view of FCAL with transverse segmentation seen from the IP.

FCAL module type	F1T	F1B	F11	F12	F21	F22	F3	F4	F5	F6
number of modules	1	1	2	8	2	2	2	2	2	2
active height (cm)	220	220	460	460	420	420	380	340	300	220
total weight (t)	5.9	5.9	12.4	12.4	11.3	11.3	9.3	8.8	6.6	4.8
towers (20x20cm^2)	11	11	23	23	21	21	19	17	15	11
depth (λ)	7.1	7.1	7.1	7.1	7.1	7.1	6.4	6.4	5.6	5.6
EMC sections (5x20)	36	36	76	68	52	44	36	12	–	–
HAC0 sections (20x20)	2	2	4	6	8	10	10	14	15	11
HAC1 sections (20x20)	11	11	23	23	21	21	19	17	15	11
HAC2 sections (20x20)	11	11	23	23	21	21	19	17	15	11
EMC channels (XP1911)	72	72	152	136	104	88	72	24	–	–
HAC channels (R580)	48	48	100	104	100	104	96	96	90	66

RCAL module type	R1T	R1B	R11	R12	R21	R22	R23	R3	R4	R5	R6
number of modules	1	1	2	6	2	2	2	2	2	2	2
active height (cm)	220	220	460	460	420	420	420	380	340	260	220
total weight (t)	3.3	3.7	7.7	7.7	7.0	7.0	7.0	6.4	5.7	3.7	3.0
towers (20x20cm^2)	11	11	23	23	21	21	21	19	17	13	11
depth (λ)	4.0	4.0	4.0	4.0	4.0	4.0	4.0	4.0	4.0	3.3	3.3
EMC sections (10x20)	10	18	38	34	30	26	22	18	6	–	–
HAC0 sections (20x20)	–	2	4	6	6	8	10	10	14	13	11
HAC1 sections (20x20)	11	11	23	23	21	21	21	19	17	13	11
EMC channels (R580)	20	36	76	68	60	52	44	36	12	–	–
HAC channels (R580)	22	26	54	58	54	58	62	58	62	52	44

T and B modules are special modules above and below the beam pipe.

Table 2.10 FCAL and RCAL module types and compositions.

material	EMC			HAC		
	thickness (mm)	thickness (X_0)	thickness (λ)	thickness (mm)	thickness (X_0)	thickness (λ)
steel	0.2	0.011	0.0012	0.4	0.023	0.0024
DU	3.3	1.000	0.0305	3.3	1.000	0.0305
steel	0.2	0.011	0.0012	0.4	0.023	0.0024
paper	0.2			0.2		
SCI	2.6	0.006	0.0033	2.6	0.006	0.0033
paper	0.2			0.2		
contingency	0.9			0.9		
sum	7.6	1.028	0.0362	8.0	1.052	0.0386
effective X_0	0.74 cm			0.76 cm		
effective λ	21.0 cm			20.7 cm		
effect. Moliere radius	2.02 cm			2.00 cm		
effect. critical energy	10.6 MeV			12.3 MeV		
effective density	8.7 g/cm^3			8.7 g/cm^3		

Table 2.11 Layer structure of the EMC and HAC calorimeter sections.

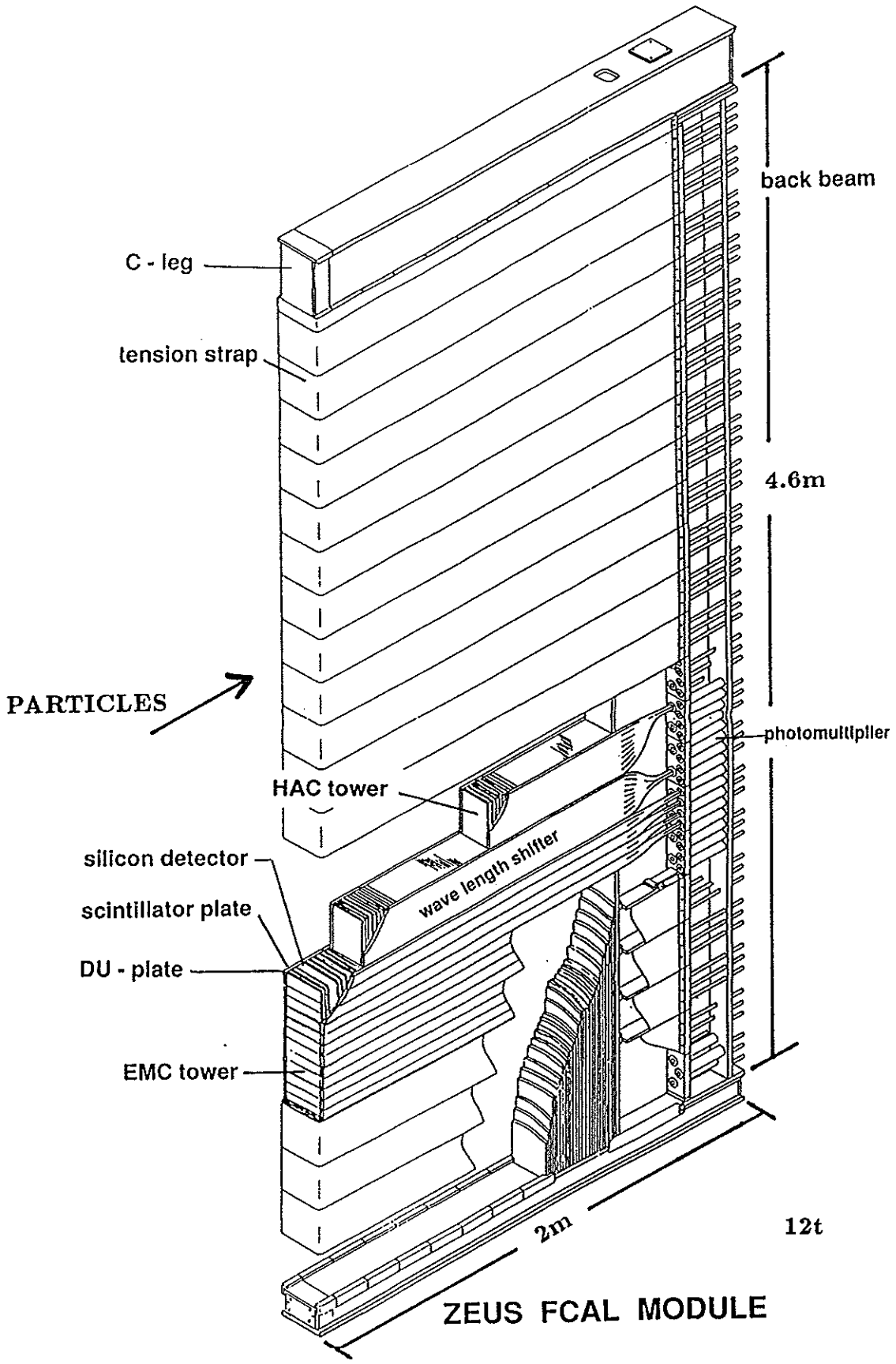

Fig. 2.41 Internal structure of an FCAL module.

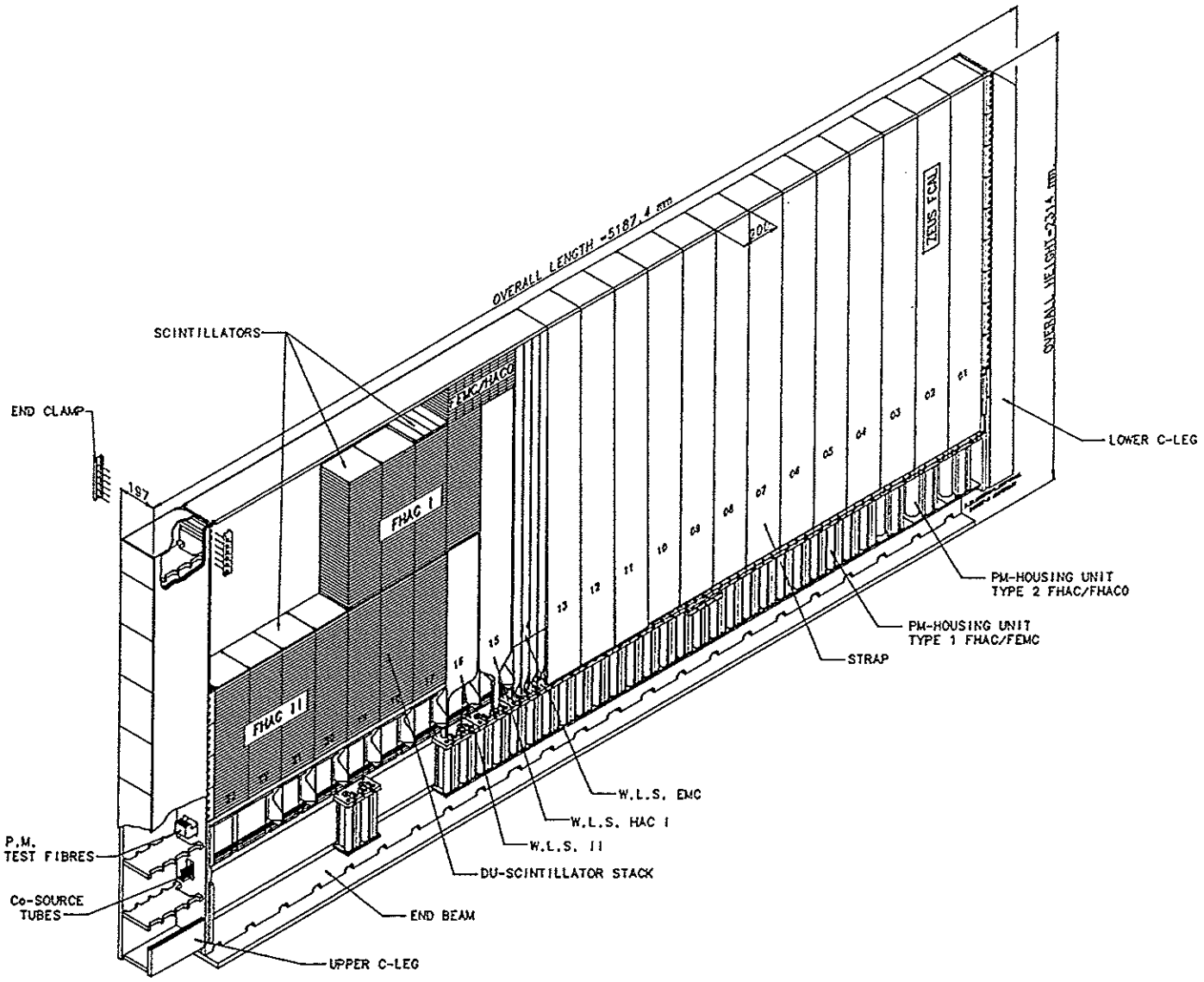

Fig. 2.42 Mechanical details of a large FCAL module.

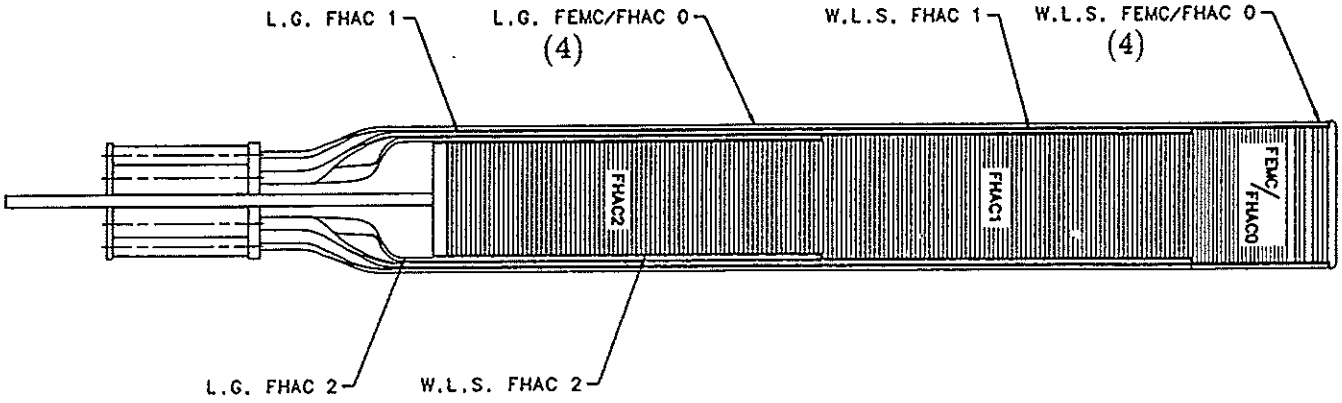

Fig. 2.43 Details of the optical readout scheme.

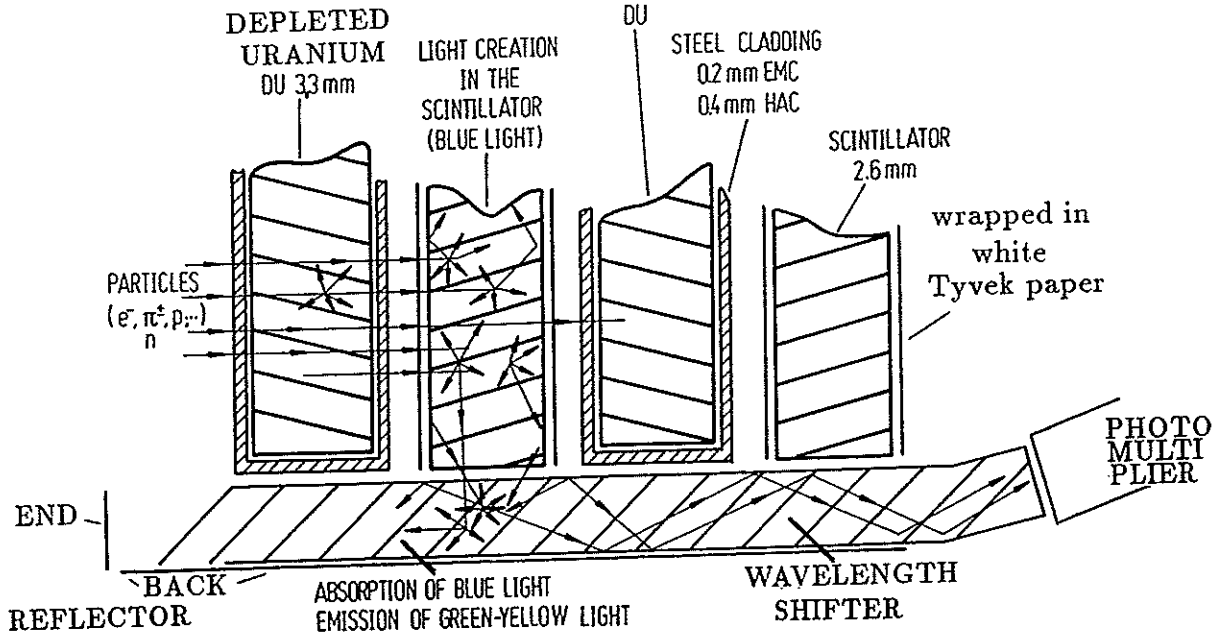

Fig. 2.44 Readout of the scintillator light with wavelength shifters.

The sandwich sampling structure is the same throughout the whole calorimeter: 3.3mm thick depleted uranium plates (DU) corresponding to one radiation length ($1X_0$) and 2.6mm thick scintillator plates. The DU plates are clad with 0.2mm (EMC) or 0.4mm (HAC) steel foils for ease of handling and reduction of noise from the radioactivity of the uranium. Table 2.11 gives detailed information on the layer structure of the EMC and HAC sections.

In order to the uranium plates not exerting pressure on the scintillator plates the distance between the uranium plates is kept by small 3.9mm thick spacers of 5mm x 6mm (TiC) in the EMC and 5mm x 10mm (WC) in the HAC. The spacers are placed every 20cm along both edges between two DU plates. Special gaps of 15mm are provided after the 4th and 7th scintillator layer ($3.3X_0$ and $6.3X_0$; the first layer consists of scintillator plates) for insertion of the silicon pad arrays (3cm x 3cm Si diodes) of the hadron electron separator (HES). BCAL and RCAL have only one gap, namely after the 4th scintillator layer. A fully stacked module equipped with wavelength shifters is compressed to a solid mechanical unit by 196mm wide and 0.25mm thick stainless steel straps tensioned with 15–20kN/strap. The mechanical details of an FCAL module are seen in Fig. 2.42 showing a large FCAL module in the stacking position.

Each longitudinal section (EMC, HAC1, HAC2) is read out on both sides by plastic wavelength shifter plates (WLS, 2mm thick), light guides (LG) and associated photomultipliers (PMs). Details of the mechanical design and the optical readout scheme are presented in Fig. 2.43 for a cut along one calorimeter stack. In total the calorimeter requires about 12000 photomultipliers.

The calorimeter roughly works as follows (Fig. 2.44): particles entering the calorimeter interact with the absorber plates (DU) producing a "shower" of particles. The charged particles of such a shower produce light in the scintillator which propagates by reflection to the wavelength shifters where it is converted to light of a longer wavelength. This light again propagates by reflection to the photomultiplier which generates an electrical signal that can be measured and recorded. A detailed description of the physical processes and the development of the high resolution ZEUS calorimeter are given in chapter 3 and 4.

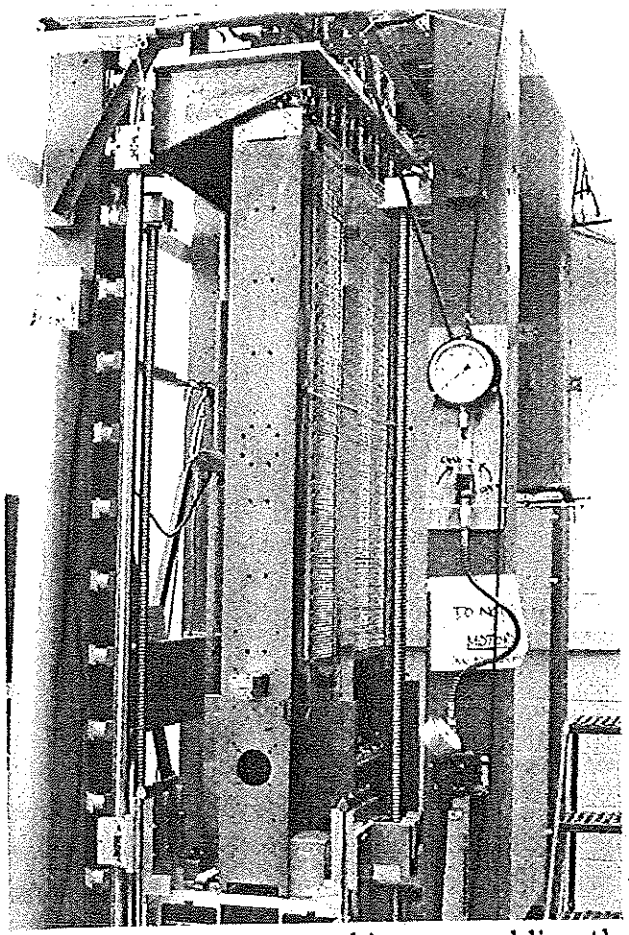

Fig. 2.45 The stacking machine, assembling the first FCAL prototype module, in York(Canada).

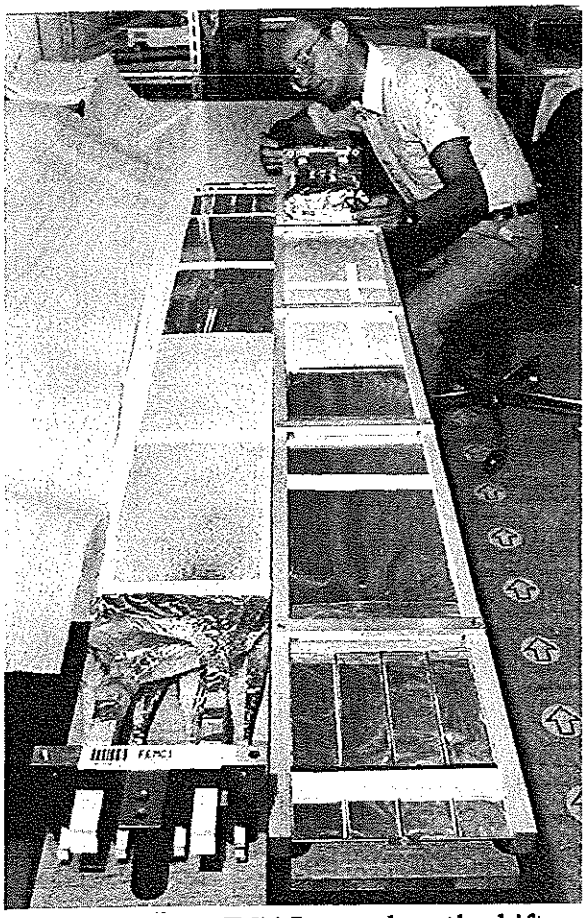

Fig. 2.46 Two FCAL wavelength shifter cassettes ready for installation.

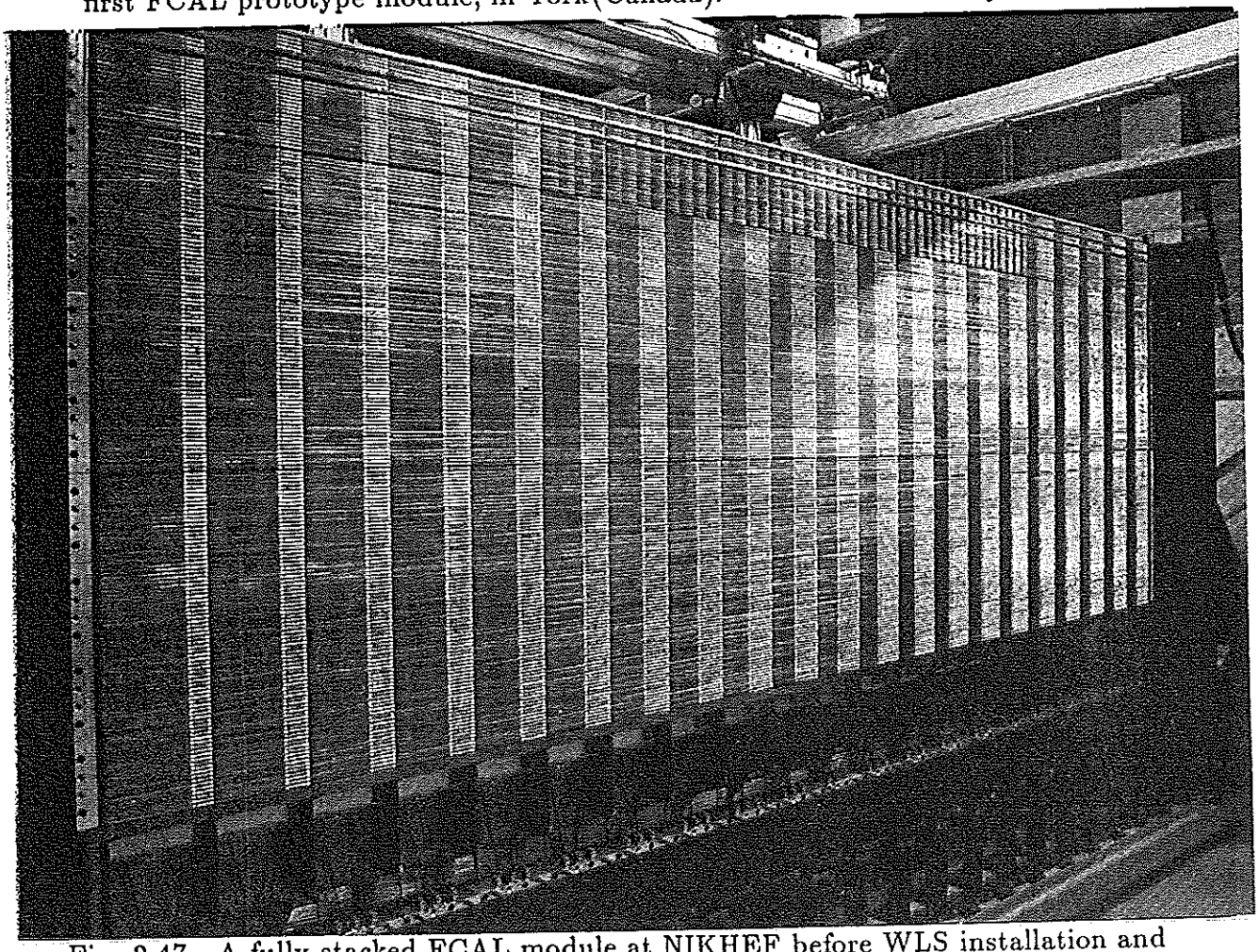

Fig. 2.47 A fully stacked FCAL module at NIKHEF before WLS installation and mounting of the tension straps.

The depth of the calorimeter is sufficient to absorb in most cases the full electron showers in the EMC and the hadron showers in the EMC and HAC sections. The signal produced in the photomultipliers is proportional to the energy of the incident particles.

The thickness of the uranium and scintillator plates of the ZEUS calorimeter has been optimized to give equal signals for electrons and hadrons of equal energy (e/h=1). Such a calorimeter is called compensating calorimeter. It has the advantage that for all jets of the same energy (ignoring muons and ν's in the jet) it produces the same signal size irrespective of their electromagnetic (electrons, photons) and hadronic (e.g. pions, protons) composition. A compensating calorimeter gives the best energy resolution for hadrons. In ZEUS this amounts to $35\%/\sqrt{E} \oplus 2\%$ while for typical noncompensating calorimeters $50\text{–}60\%/\sqrt{E} \oplus$ 4% is typically observed (see, however, the noncompensating calorimeter of H1 in weighting mode (p. 3–27)). The principle of operation of a compensating calorimeter is discussed in full detail in chapter 3 and 4.

The better energy resolution of such a compensating calorimeter increases the number of well measured events by a factor of 1.7, expands the Q^2 range by 50%, and allows events with very small x–values ($x \approx 0.01$) to be measured. For comparison see Fig. 2.32.

Figure 2.45 shows a photo of the stacking machine in York (CDN) assembling the first FCAL prototype module. These prototype modules have the same internal structure as the final FCAL modules and a height of 80cm. The comprehensive FCAL prototype calorimeter test program is presented and discussed in chapter 5.

Figure 2.46 presents a photo of two FCAL wavelength shifter cassettes ready for installation into a fully stacked calorimeter module. At the front left side two light guides of HAC1 and HAC2 and, below, four smaller EMC light guides can be seen. At the front right side four EMC wavelength shifters of the other cassette are visible. In order to get uniform response along the WLS special absorption patterns for the back reflector have been individually calculated based on uniformity measurements. They were printed under computer control for each WLS and put at the backside.

Figure 2.47 shows a picture of a fully stacked FCAL module at NIKHEF (Amsterdam, NL) before WLS installation and mounting of the tension straps. The uranium scintillator sampling structure can be well seen. At the central front face of the module (top side) the finer transverse segmentation of the EMC section and the two gaps after 3 and 6 DU layers for the silicon pad arrays of the HES are also visible.

The RCAL like the FCAL consists of 24 modules. In comparison to the FCAL the RCAL differs mainly in a coarser tower structure of 10cm x 20cm in the EMC having only one HAC section and a total depth of 4λ.

The Barrel Calorimeter is constructed from 32 identical modules each covering an angle wedge of 11.25^0. Figure 2.48 shows a section through the BCAL perpendicular w.r.t. the beam axis. The inner/outer radius of the BCAL is 1.22m/2.29m. All modules are (near–) projective in ϕ, but tilted by 2.5^0 to avoid projective module boundaries. The whole BCAL can be rotated around its central axis to allow insertion and removal of modules from above.

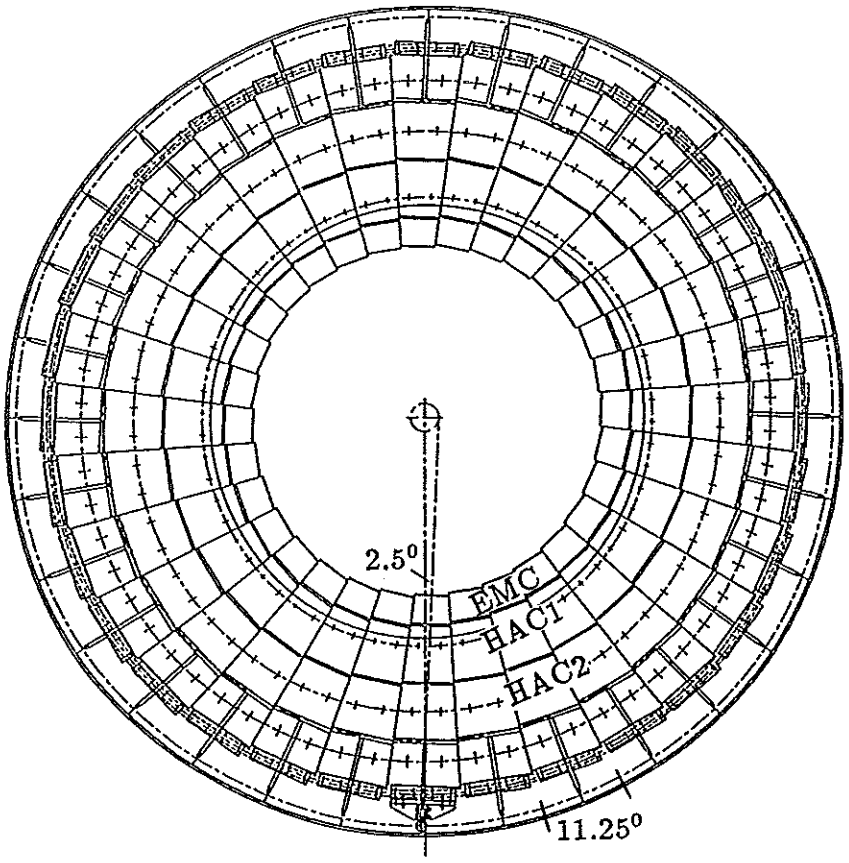

Fig. 2.48 Section through the BCAL perpendicular to the beam axis. Each BCAL module covers an angle wedge of 11.25^0 in ϕ and is tilt by 2.5^0.

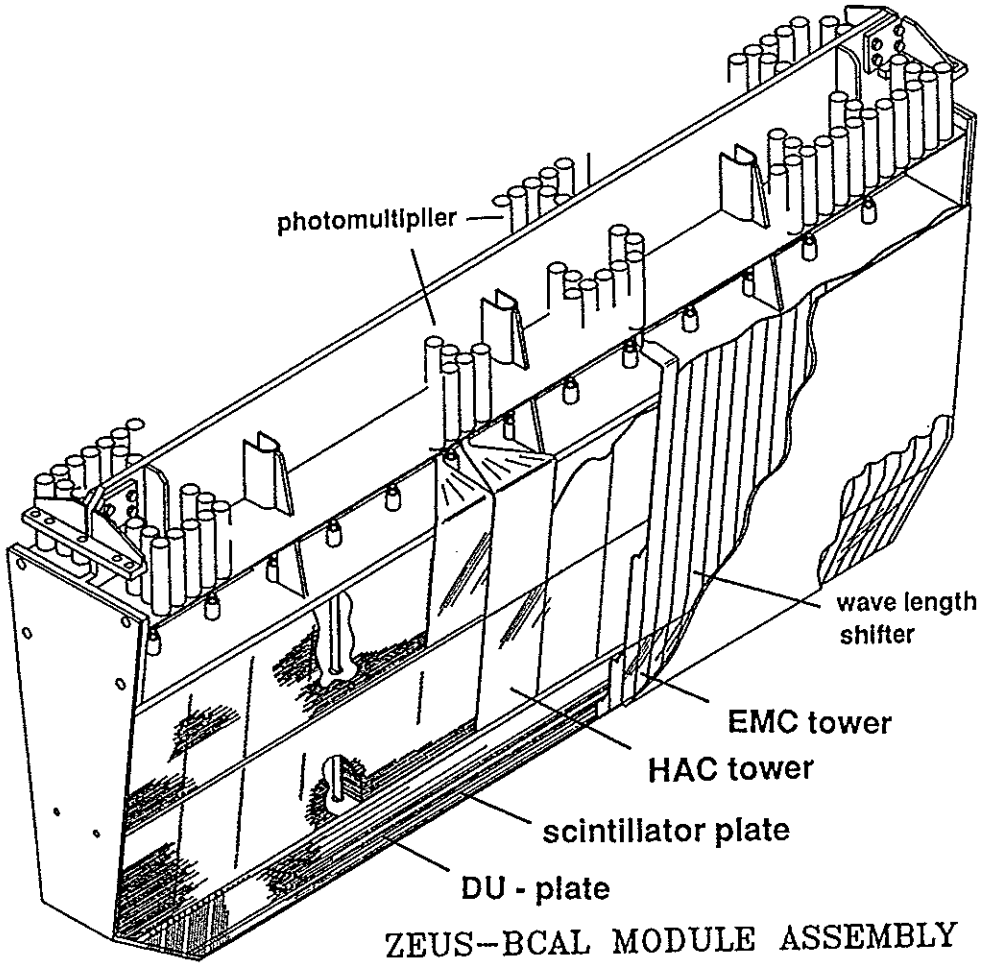

Fig. 2.49 Internal structure of a BCAL module.

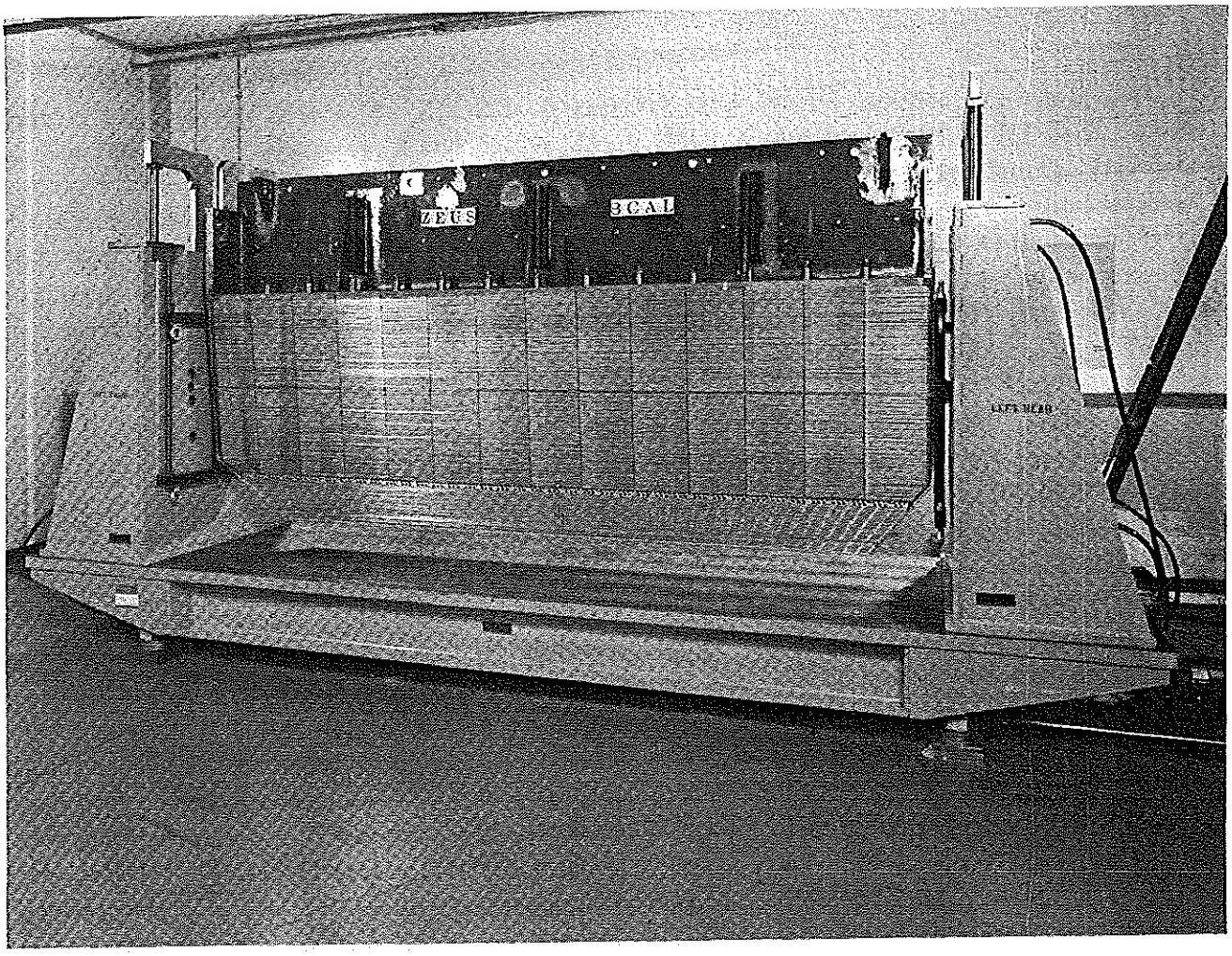

Fig. 2.50 The BCAL stacking machine at Argonne containing a fully stacked module.

Figure 2.49 shows the internal structure of a BCAL module; each module has a length of 3.3m and a total weight of about 10t. The EMC towers of a BCAL module are projective in ϕ and θ and have a size of 5cm x 24cm at the front face. The HAC towers are projective in ϕ, but non–projective in θ.

Figure 2.50 shows the BCAL stacking machine at ANL (Argonne, USA) containing a fully stacked BCAL module before installation of the WLS. The uranium scintillator sandwich sampling structure and the EMC towers, projective in θ, can be seen as well.

In order to achieve the desired characteristics for the final ZEUS calorimeter, in particular the excellent energy resolution for hadrons and particle jets, extreme care has been taken in the design and fabrication of all individual components: the optical readout comprising scintillator plates, wavelength shifters, light guides, photomultipliers, PM–shielding against the magnetic field and also the calorimeter electronics, depleted uranium plates etc...

The depleted uranium plates have a material composition of 98.1% ^{238}U, 1.7% Nb and less than 0.2% ^{235}U and the density is about 18.9g/cm^3. One radiation length of pure ^{238}U is 3.2mm and one absorption length 10.5cm. The density of DU is less and the chosen thickness of 3.3mm corresponds to one radiation length. The maximum allowed tolerances on the nominal DU plate thickness of 3.3mm are $\pm$0.15mm in the EMC, $\pm$0.20mm in the HAC1, $\pm$0.25mm in the HAC2 section and the r.m.s. spread of the thickness is about 2% [AND91].

The plastic scintillator plates were fabricated of SCSN–38, a cast polystyrene material doped with 1% p–PBD and 0.02% BDB fluors, which has a relatively high light yield and stability against aging and radiation. Only scintillator plates with a thickness of 2.6±0.2mm were accepted. To get uniform light output over the entrance surface the scintillator tiles were wrapped in white Tyvek paper with correction pattern printed on. Figure 2.51 shows the correction pattern of an EMC scintillator tile and the improvement on the uniformity in light response. The light output combined from both readout edges yields a uniformity of ±2.5%.

The plastic wavelength shifters (2.0±0.2mm thick) were made of PMMA (polymethyl methacrylate) doped with fluorescent dye Y7 with an ultraviolet absorbant for wavelengths below 360nm. They were equipped with back and end reflectors to give a uniform light collection along the WLS, this means throughout the total calorimeter depth. In Fig. 2.46 the small black dots of a correction pattern are visible through the upper HAC wavelength shifter close to the HAC light guide of the left cassette. Figure 2.52 shows the improvement by the correction pattern along the WLS. After correction by this graded pattern the response is uniform. It improves from 12% to 3% nonuniformity.

Figure 2.53 presents the emission spectrum of SCSN–38, absorption and emission spectra of K27 and Y7 in PMMA and the spectral sensitivity of a trialcali photocathode. The ZEUS calorimeter has been equipped with XP1911 (ϕ=19mm) and R580 (ϕ=38mm) photomultipliers which have bi–alkaline photocathodes with a spectral response (similar to that of the trialkali photocathodes) well suited to match the spectrum of the Y7 WLS. This shows that the chosen optical components match well.

Each single piece of the various components has been fully tested and measured under all relevant aspects as for example dimensions, weight, uniformity etc...

The large amount of individual pieces: The largest FCAL modules contain 185 DU plates, 5980 scintillator plates, 9024 spacers and 46 wavelength shifter cassettes. Overall, there are 156000 FCAL/RCAL scintillator plates, 12000 wavelength shifters and 12000 photomultipliers. The tight quality control required, made it necessary to automatize the quality control and have it done under computer control. Such systems were developed and setup at several institutions.

A degradation of the uniformity at the boundaries between two calorimeter modules has been avoided or minimized by adding 2.6mm thick lead sheets between the modules. The thickness of the lead sheets has been optimized in the FCAL prototype calorimeter tests at CERN. The measurement results of these tests are presented in chapter 5.

As shown by extensive tests, by careful fabrication of all calorimeter components and the subsequent high quality control the design requirements of ±2% signal uniformity over the entrance surface and in the calorimeter depth were achieved. A light yield of $\geq$2 photoelectrons per scintillator layer per minimum ionizing particle (mip) was measured.

For global calorimeter calibration and monitoring the uranium radioactivity offers a superior feature. Test measurements have shown a long term stability of better than 0.5% and the absolute energy scale to be known to better than 1%. For details see chapters 5 and 6.

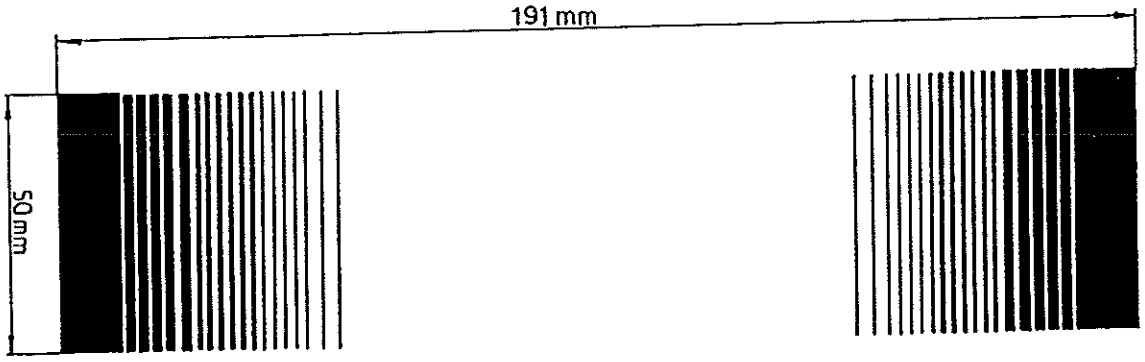

a) uncorrected

	0.989	0.981	0 984	0 984	0.970	0.981	0.994	0.979
1.035	1.012	1.000		0.996	0.991	0.993	0.988	0.994
1.113	1.075	1.025	1.010	0.993	1.000	1.013	1.004	1.006
1.111	1.100	1.050	1.015	1.009	1.013	1.009	1.005	0.997
1.133	1.096	1.067	1.027	1.016	1.010	1.004	0.993	1.000
1.142	1.108	1.070	1.036	1.029	1.009	1.000	1.001	1.000
1.136	1.101	1.076	1.037	1.024	1.019	1.007	1.003	0.999
1.126	1.109	1.071	1.045	1.030	1.018	1.006	0.995	0.993
1.100	1.080	1.064	1.036	1.025	1.013	0.990	0.990	0.972
1.109	1.086	1.061	1.050	1.019	1.017	0.991	0.986	0.974

45 35 25 15 5 — 10 30 50 70 90 (mm)

b) corrected

	0.960	0.972	0.972	0.985	0.996	0.989	0.996	0.985
0.960	0.973	0.964	0.968	0.985	0.990	0.997	0.998	0.996
0.980	0.995	0.975	0.965	0.978	1.006	0.999	1.002	0.995
0.982	1.006	0.994	0.977	0.989	1.005	1.002	1.001	1.004
0.980	1.000	0.996	0.990	0.987	1.001	1.009	1.001	1.004
0.974	1.005	0.996	0.991	0.995	1.013	1.012	1.010	1.000
0.972	0.995	0.993	0.987	0.996	1.000	1.006	1.002	0.998
0.960	0.989	0.983	0.976	0.991	0.998	0.990	0.984	0.989
0.937	0.966	0.971	0.970	0.976	0.988	0.979	0.986	0.975

45 35 25 15 5 — 15 35 55 75 95 (mm)

——nonuniformity < 5.0 % ——nonuniformity < 25 %

Fig. 2.51 Black printed correction pattern for an EMC scintillator tile and the uniformity before and after correction.

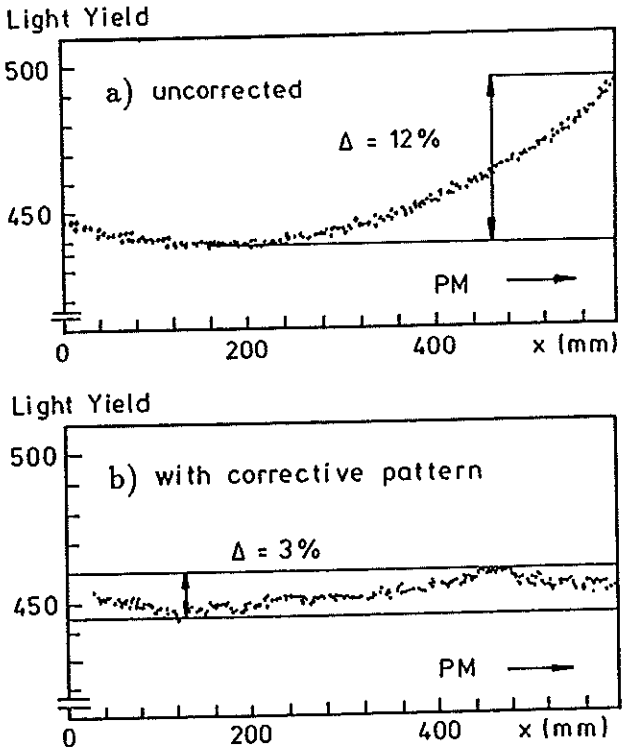

Figure 2.52
Uniformity of a FHAC1 WLS measured with a xenon lamp a) before and b) after correction.

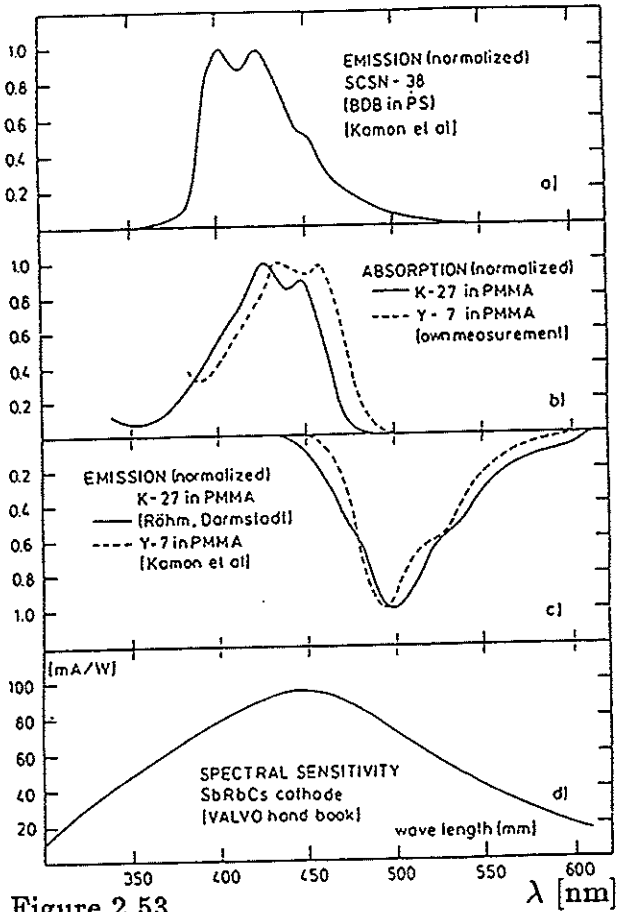

Figure 2.53
Emission spectrum of SCSN–38; Absorption spectra of K27 and Y7 in PMMA; Emission spectra of K27 and Y7 in PMMA and spectral sensitivity of a trialcali photocathode.

Ten of the FCAL/RCAL modules or 30% of all FCAL/RCAL towers have been tested at the CERN SPS with hadrons, electrons and muons in the momentum range from 15GeV/c to 100GeV/c and calibrated to an absolute energy scale of about 1%. These results are statistically relevant and can be used for an absolute energy calibration of all 48 FCAL/RCAL modules by the uranium radioactivity. A detailed description of these tests and the subsequent analysis of the data are presented in chapter 6.

The performance of the calorimeter can be checked by radioactive sources (^{60}Co), which are moved along the edges of the calorimeter towers. Direct calibration of the photomultipliers is possible by a light flasher system consisting of a laser set up and optical fibres.

Before installation in the ZEUS detector each fully equipped calorimeter module has been checked for light tightness, scanned with ^{60}Co sources to check the correct local uranium scintillator plate structure and calibrated with cosmic muons.

Figure 2.54 shows a picture of the complete forward calorimeter after installation in the ZEUS detector. At the backside of the 24 FCAL modules photomultipliers, cables etc... are visible. The two FCAL parts can be retracted, by ≈40cm also when the iron yoke is closed, to avoid excessive irradiation during HERA machine development.

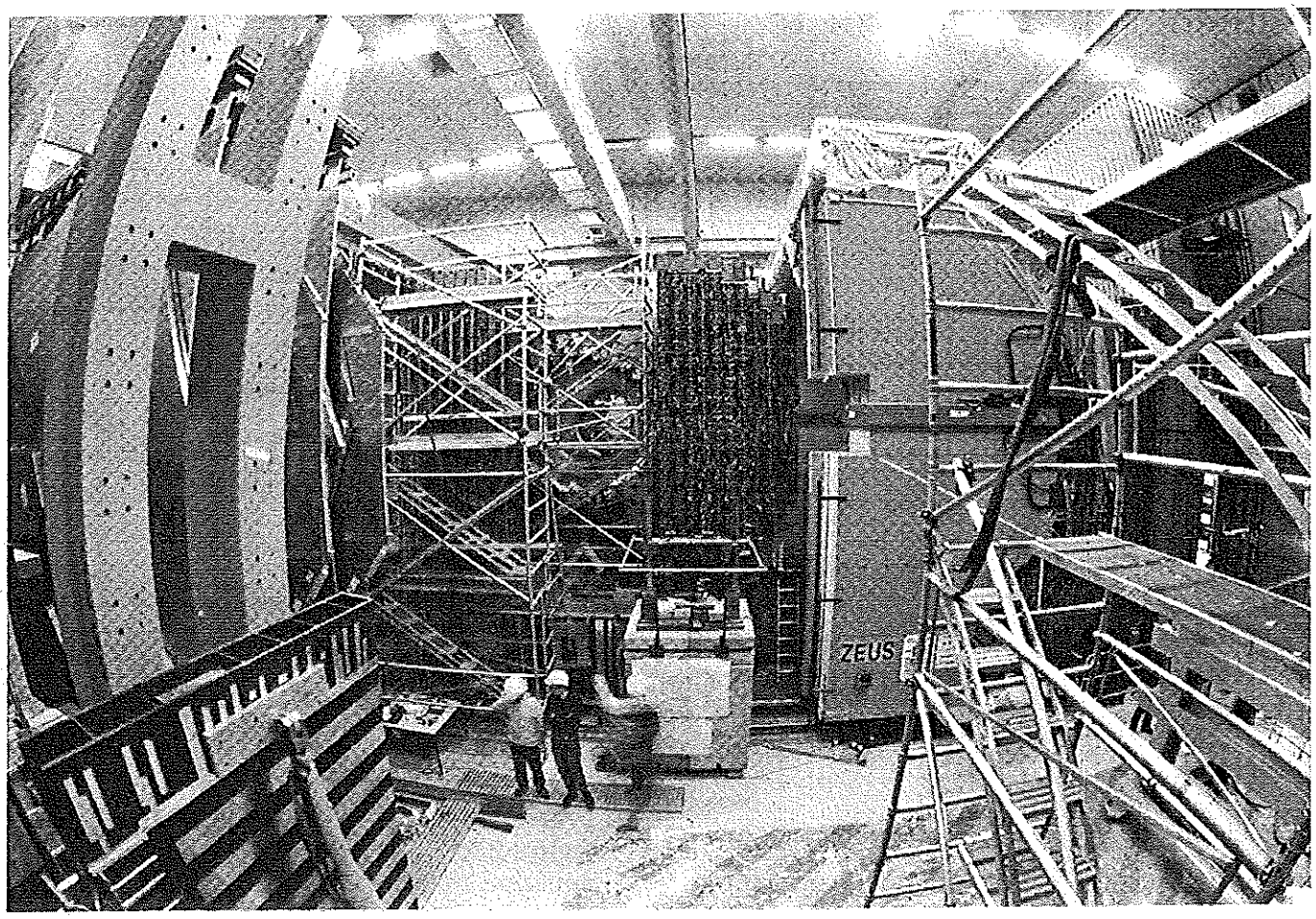

Fig. 2.54 View into the ZEUS detector after installation of the FCAL.

Hadron Electron Separator (HES)

The main task of the Hadron Electron Separator is to achieve a significant improvement of the identification of single electrons and electrons in jets compared to the calorimeter alone. In jets the prompt electron to hadron ratio is expected to be in the order of 10^{-3}. The identification is possible due to the different development of electromagnetic and hadronic showers in the calorimeter [ZEU91a].

The HES consists of one or two planes of silicon pad arrays of $\approx$ 3cm x 3cm Si diodes. FCAL has two 15mm deep gaps for the Si diode planes after the 4th and 7th scintillator layer ($3.3X_0$ and $6.3X_0$; the first layer consists of scintillator plates), BCAL and RCAL have one plane after the 4th scintillator layer ($\approx 4X_0$).

Combining the information from a single Si plane with that from the calorimeter a hadron rejection of 75 to 200 is achieved at 90% electron efficiency between 10 and 75GeV. For two Si planes the hadron rejection is further improved by a factor 5.

Test measurements with various Si diodes have been performed together with the ZEUS FCAL prototype calorimeter tests at CERN. Figure 2.55 shows for example the different pulseheight spectra of hadrons and electrons at 5GeV in one silicon pad detector placed after $3.3X_0$ in the FCAL prototype [ERN91].

Figure 2.56 presents a scatter plot of 5GeV beam particles, where the calorimeter information ($E_{HAC1}/E_{HAC1+EMC}$) is plotted versus the energy measured in the HES. Cuts are indicated by which clean electron and hadron samples can be selected.

The hadron misidentification at an electron efficiency of 90% for one Si diode plane after $3.3X_0$ is summarized in Table 2.12 for particle energies of 2, 5 and 9 GeV. Different combinations of the information available from the HES and from one or nine calorimeter towers are presented.

Energy [GeV]	HES [%]	1 CAL Tower [%]	1 CAL Tower + HES [%]	9 CAL Towers [%]	9 CAL Towers + HES [%]
2	3.8±0.4	7.79±0.45	1.47±0.24	4.28±0.35	0.98±0.21
5	3.5±0.2	0.65±0.09	0.22±0.06	0.36±0.07	0.17±0.06
9	3.6±0.2	0.37±0.08	0.15±0.06	0.23±0.07	0.11±0.06

Table 2.12 Hadron misidentification at 90% electron efficiency for one Si diode plane placed after $3.3X_0$ in the FCAL prototype calorimeter.

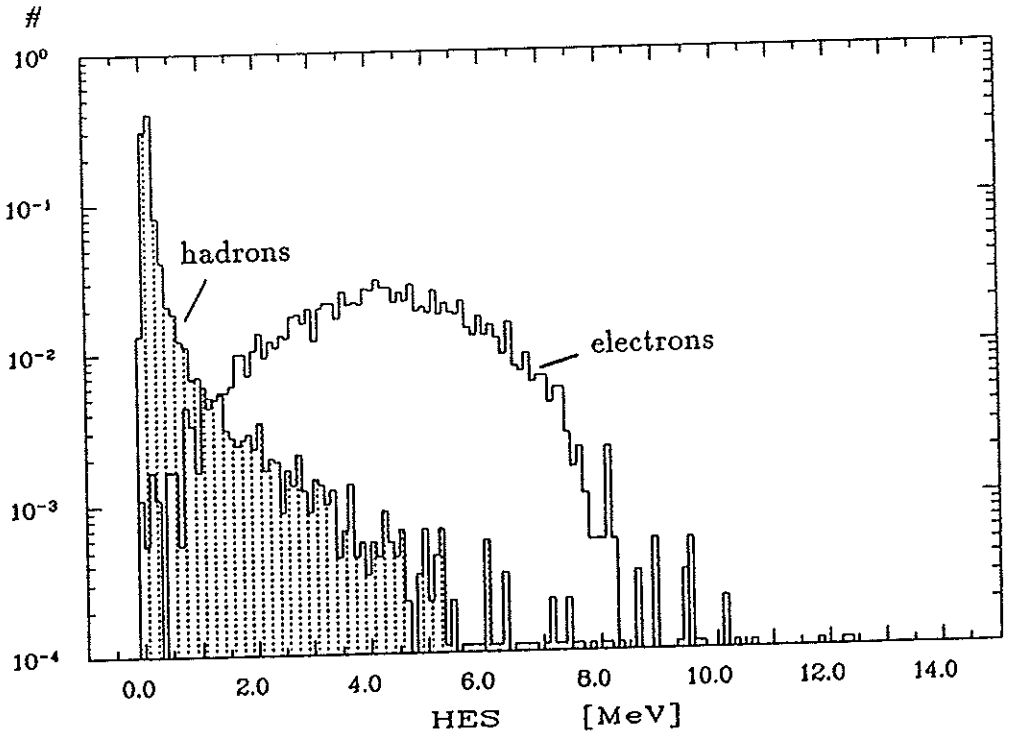

Fig. 2.55 Pulse height distributions measured in one Si diode plane after $3.3X_0$ in the FCAL prototype for 5 GeV hadrons and electrons identified by Cherenkov counters.

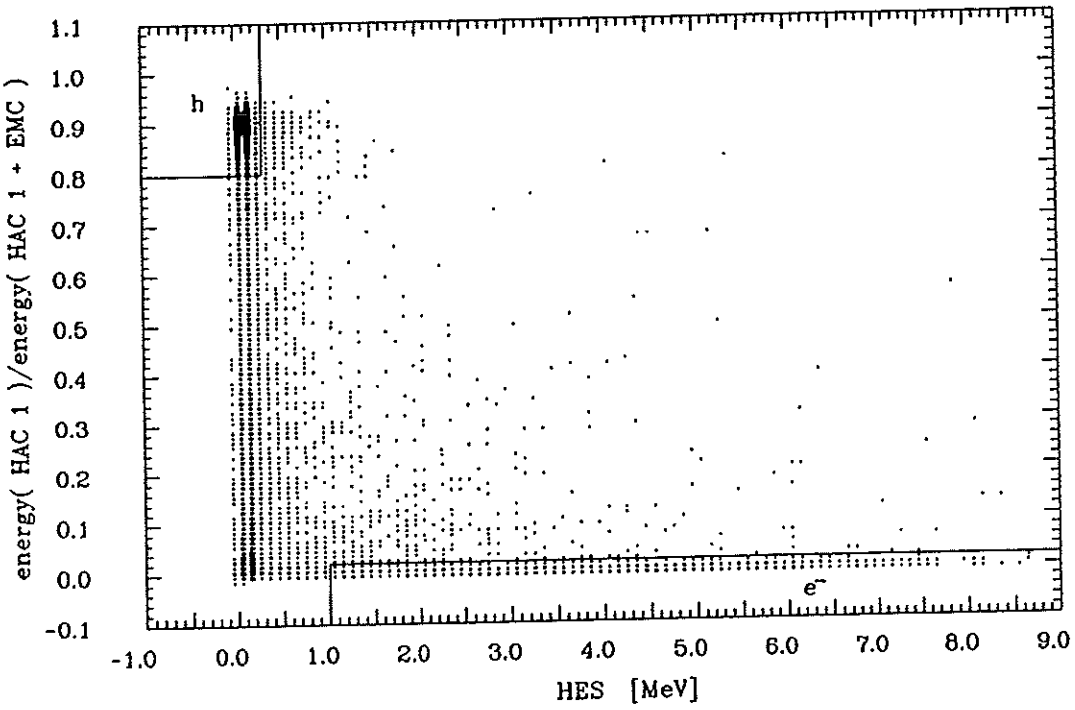

Fig. 2.56 Scatter plot of calorimeter information versus HES energy for 5 GeV beam particles. The indicated cuts yield clean electron and hadron samples.

2.3.4 Backing Calorimeter (BAC)

The Backing Calorimeter complements the energy measurement of hadron showers leaking out of the high resolution calorimeter and acts as veto counter selecting precisely measured events fully contained in the uranium scintillator calorimeter. The BAC energy resolution is about $1.1/\sqrt{E}$ for hadrons. It also measures in three layers with high spatial precision muons traversing the bottom yoke.

The BAC totally surrounds the inner detector and the high resolution uranium scintillator calorimeter. It consists of the 7.3cm thick plates of the iron yoke with 3.7cm gaps equipped with aluminium proportional tubes filled with 87%Ar + 13%CO_2 and operated at 1.8kV.

Figure 2.57 shows the various elements of a BAC chamber module. The main components are an Al extrusion and an Al coverplate which form 15mm x 11mm cells. Each cell is read out by a gold plated tungsten wire of 50μm diameter.

The signals of wires and cathode pads are added to form non–projective pad towers of about 50cm x 50cm. Special cathode pads are installed in layers 1, 5 and 9 of the bottom yoke achieving a spatial resolution of about 1mm along the tube direction.

In forward direction 10 module layers are installed, in the barrel and bottom region 9 and in the rear direction 7 layers with a total area of about 3000m^2. The main parameters of the Backing Calorimeter are summarized in Table 2.13.

A BAC prototype consisting of eleven 7.3cm thick iron absorber plates and ten chamber planes with transverse dimensions of 2m x 2m, a depth of 4.9λ (46X_0, 115cm) and a weight of 26t has been built and extensively tested at the CERN–SPS without and with the FCAL prototype calorimeter in front [ABR90].

Figure 2.58 shows for 100 GeV hadrons the correlation between the energy measured in the Backing Calorimeter prototype and the Forward Calorimeter prototype. For most hadrons the energy is almost completely contained in the FCAL as expected [KRÜ86a,b], [KRÜ90e] (for details see chapter 4.2). A strong correlation is found between events with energy leakage out of the FCAL prototype and the energy measured in the BAC prototype. The prototype tests have shown, that the Backing Calorimeter fulfils its tasks very well.

	Barrel	Bottom	Forward	Rear	Total
Number of layers	9	9	10	7	
Area [m^2], Gas volume [m^3]	1902, 38.0	296, 5.9	460, 9.2	322, 6.4	2980, 59.6
Number of 8, 7–tube modules	2246, 658	193, 120	840, 280	572, 112	3891, 1170
Module lengths [m]	4.5, 5.5	7.3	1.8, 3.6	1.8, 3.6	
Number of wires	22574	2384	7980	5360	38298
Wire, pad towers	100, 1100	10, 150	32, 222	36, 230	178, 1702

Table 2.13 Parameters of the Backing Calorimeter (BAC).

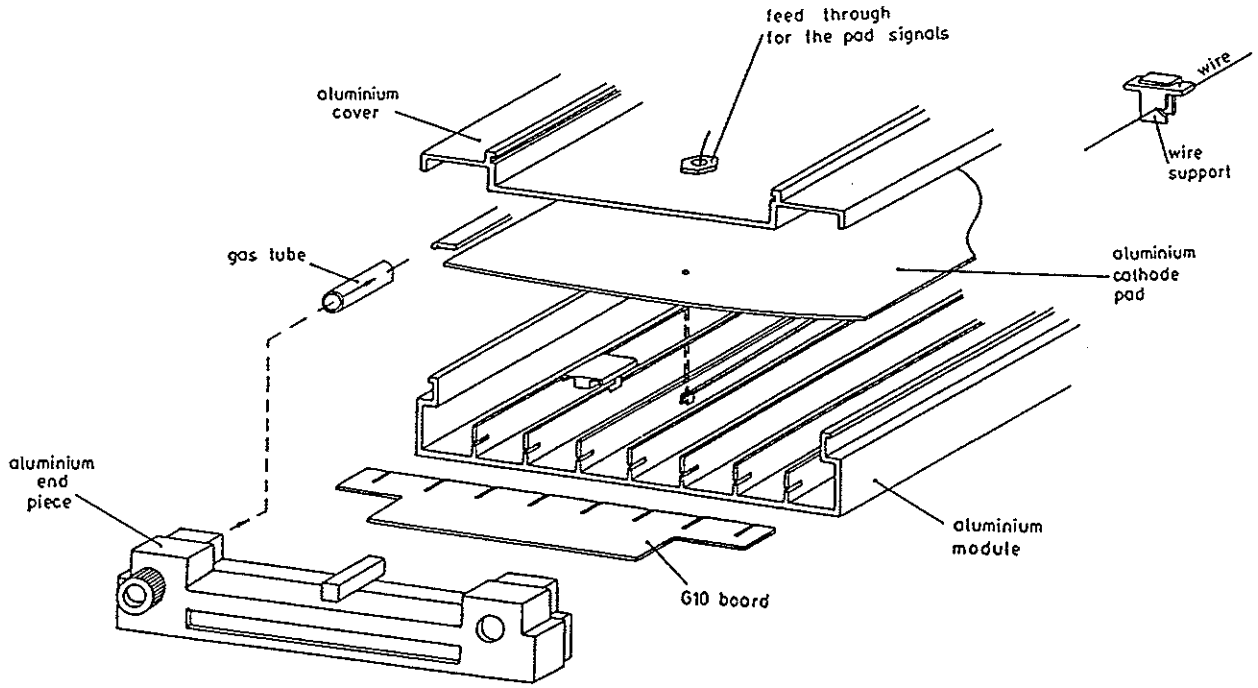

Fig. 2.57 Elements of the Backing Calorimeter module assembly.

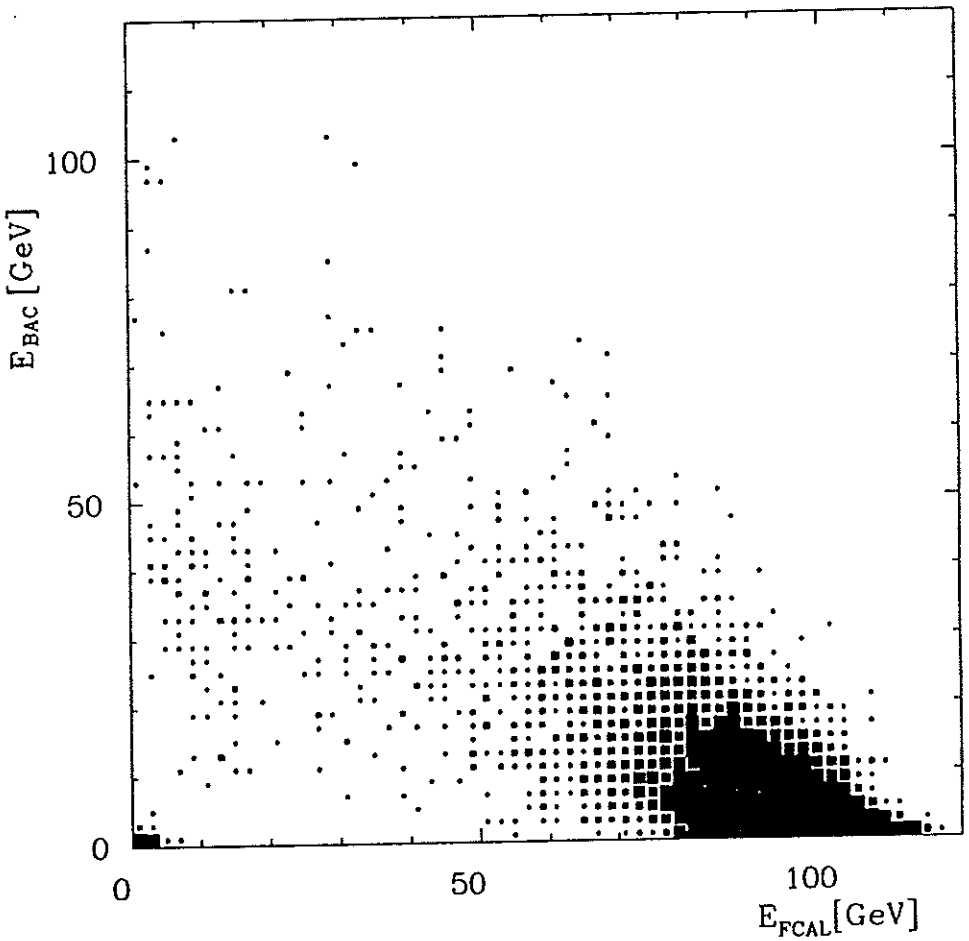

Fig. 2.58 Correlation between the energy measured in the BAC prototype calorimeter E_{BAC} and the FCAL prototype calorimeter E_{FCAL} for 100 GeV hadrons.

2.3.5 Tracking System

The inner detector of ZEUS is positioned inside the superconducting solenoid. It consists of different tracking devices: the Vertex Detector (VXD), the Central (CTD), Forward (FTD) and Rear Tracking Detector (RTD) and the Transition Radiation Detector (TRD) and is dedicated for charged particle detection.

The main tasks of the inner detector are summarized in the following:

- Separation and reconstruction of charged and neutral current events
- Reconstruction of final state hadrons and electrons with $\sigma(p_t)/p_t<0.003 \cdot p_t$; electron tagging by dE/dx and TRD; suppression of muons from hadron decays
- Reconstruction of tracks close to the primary vertex
- Trigger rejection of events which do not come from the primary vertex.

Figure 2.59 shows a vertical section through the inner detector along the beam axis. The various detector components of the tracking system are described in the following from inside to outside starting with the Vertex Detector.

Vertex Detector

The primary tasks of the Vertex Detector are the detection of short–lived particles and the improvement of the momentum and angular resolution of charged particles measured in the CTD.

The VXD is a cylindrical drift chamber filled with dimethyl ether (DME) and placed in the limited space available between the beam pipe and the CTD (88mm<R<162mm). It represents a combination of a Jet Chamber and a Time Expansion Chamber (TEC). It has 120 drift cells; each cell has 12 sense wires with a length of 1.6m, 3mm apart alternating with field wires. The structure and dimensions of one cell are presented in Fig. 2.60. Parameters of the VXD are summarized in Table 2.14.

Wire length	1.6 m
Diameter of sense, field, drift wires	20, 50, 50 μm
Maximum drift space	3.6 mm
Drift gas ("slow")	dimethyl ether
Drift velocity at 2 kV/cm	5 μm/ns
Maximum drift time	500 ns

Table 2.14 Parameters of the Vertex Detector (VXD).

The Vertex Detector has a high spatial resolution of 35–70μm and achieves a double track resolution of 500μm. Calculations on the vertex position and momentum resolution of the CTD at a polar angle of 90^0 with and without VXD information are presented in Table 2.15. Measurement errors of 100μm are taken into account for the CTD and 35μm or 55μm for the VXD. The precision of the determined vertex position, where d_0 indicates the closest distance between the true production point and the fitted track in the x,y–plane, improves for example for 50 GeV particles from $\sigma(d_0)$=91μm using only CTD information to 25 μm with additional VXD information (σ_{VXD} = 35μm) and the momentum resolution $\sigma(1/p)$ [GeV/c] improves from $1.5 \cdot 10^{-3}$ to $8.7 \cdot 10^{-4}$. These results show a significant improvement of both the determination of the vertex position and the momentum resolution.

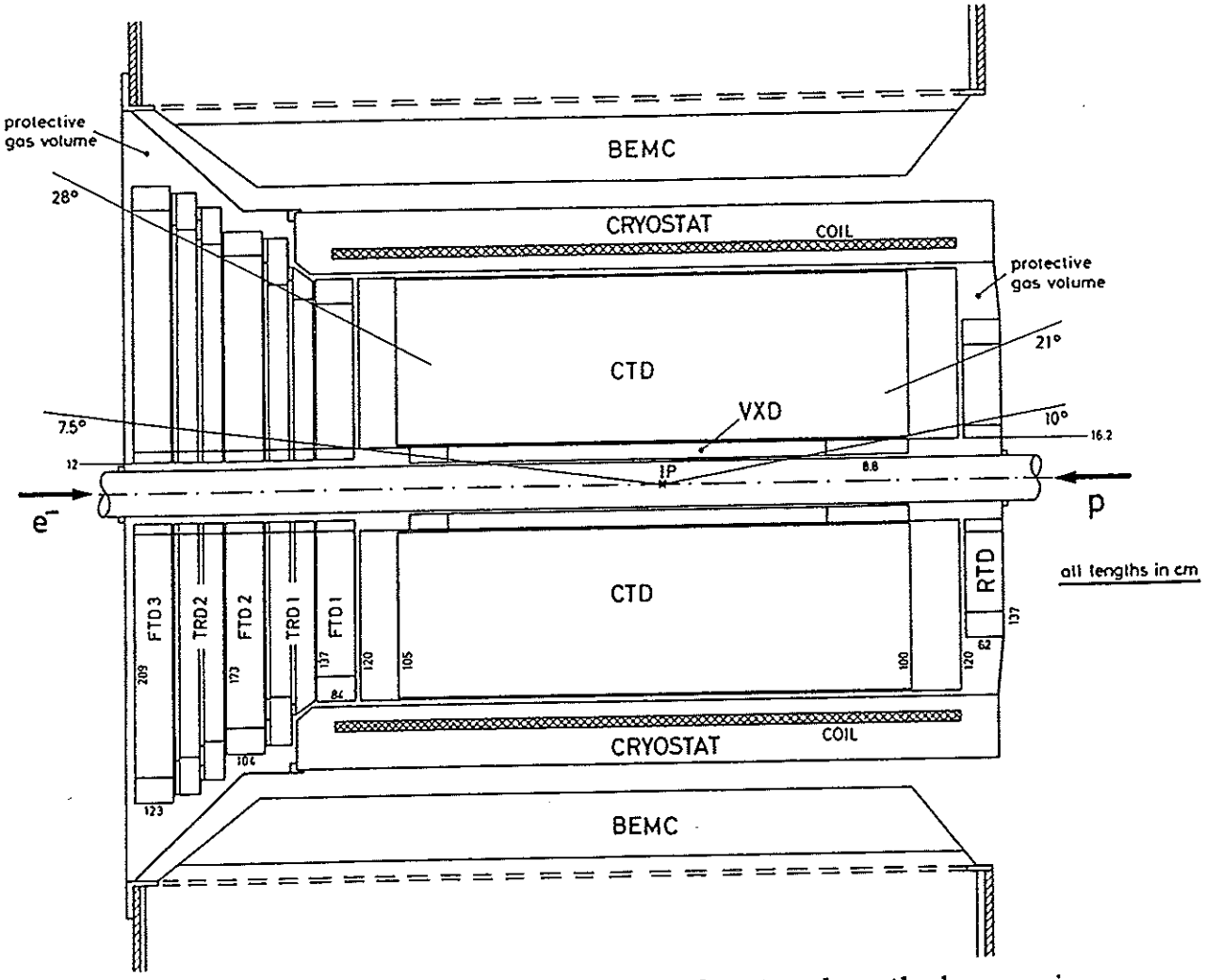

Fig. 2.59 Vertical section through the inner detector along the beam axis.

Cell Structure of the Vertex Detector

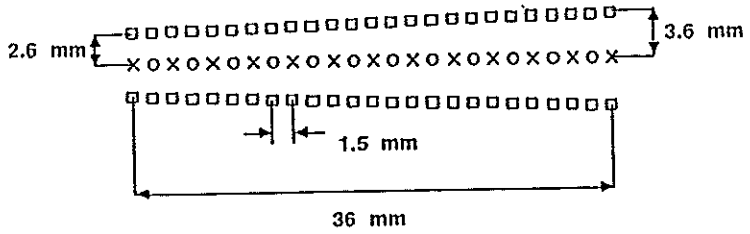

o Sense wires Ø = 20 µm
× Field wires Ø = 50 µm
□ Drift wires Ø = 50 µm

Fig. 2.60 Cell structure of the Vertex Detector.

p [GeV/c]	Resolution of d_0 and p	CTD only	CTD+VXD (σ_{VXD}=35μm)	CTD+VXD (σ_{VXD}=55μm)
50	$\sigma(d_0)$	91	25	33
1	[μm]	230	77	85
50	$\sigma(1/p)$	$1.5 \cdot 10^{-3}$	$8.7 \cdot 10^{-4}$	$9.2 \cdot 10^{-4}$
1	[GeV/c]	$5.6 \cdot 10^{-3}$	$4.3 \cdot 10^{-3}$	$4.4 \cdot 10^{-3}$

Table 2.15 Vertex and momentum resolution at 90^0 polar angle.

Central Tracking Detector (CTD)

In the Central Tracking Detector the trajectories of charged particles are reconstructed in a polar angle region from $15^0 < \theta < 164^0$ surrounding the interaction region.

The CTD is positioned inside the superconducting solenoid and is built as a cylindrical drift chamber with a length of 241cm and an inner/outer radius of 16cm/85cm (Fig. 2.59).

The layout of the wires and the equipotentials and electron drift trajectories in the CTD are presented in Fig. 2.61 and 2.62. The inner structure of the CTD consists of 9 superlayers with 8 sense wires per superlayer. Five superlayers run parallel to the beam and four are tilted by a stereo angle of 5^0 or 7^0 for z–measurement of the tracks.

The CTD is equipped with 576 drift cells with overall 4608 sense wires and 19584 field wires and is filled with a gas mixture of $Ar:CO_2:C_2H_6$ (90:8:2) (in addition about 0.84% ethanol) at atmospheric pressure bubbled through ethanol. The active wire length is about 2 m. The maximum drift path is 2.56 cm and the maximum drift time is about 500 ns. The main parameters of the Central Tracking Detector are summarized in Table 2.16.

The CTD achieves a spatial resolution of 100–120 μm in the (x, y)–plane depending on the polar angle θ and in z–direction of 1.0–1.4 mm. The two track resolution is in the order of < 2.5 mm.

A momentum resolution of $\sigma(p)/p = 0.0021 \cdot p \oplus 0.003$ (p in GeV/c) is expected at a polar angle of 90^0. In addition particle identification is possible by dE/dx with $\sigma(dE/dx)/dE/dx$ better than $< 6\%$ (e^-).

For the first level trigger information is used from the first 3 axial superlayers of the CTD.

Figure 2.63 shows a picture taken of the Central Tracking Detector during preparation of the chamber in a clean room.

Overall dimensions	L=241cm, R_{in}=16cm, R_{out}=85cm
Inner structure	9 superlayers, 8 sense wires / superl.
Number of cells, sense, field wires	576, 4608, 19584
Gas / Lorentz Angle at 1.8T	argon/ethane 50:50 / 45^0
Maximum drift time	$\approx$ 500 ns
Position resolution in (x, y)–plane	100–120 μm (θ–dependent)
Resolution in z by stereo wires (by timing)	1.0–1.4mm ($<$ 3cm)
Two–track resolution	< 2.5 mm
Momentum resolution at 90^0	$\sigma(p)/p = 0.0021 \cdot p \oplus 0.0029$
Particle identification by dE/dx	$\sigma(dE/dx)/(dE/dx) < 6\%$ (e^-)

Table 2.16 Parameters of the Central Tracking Detector (CTD).

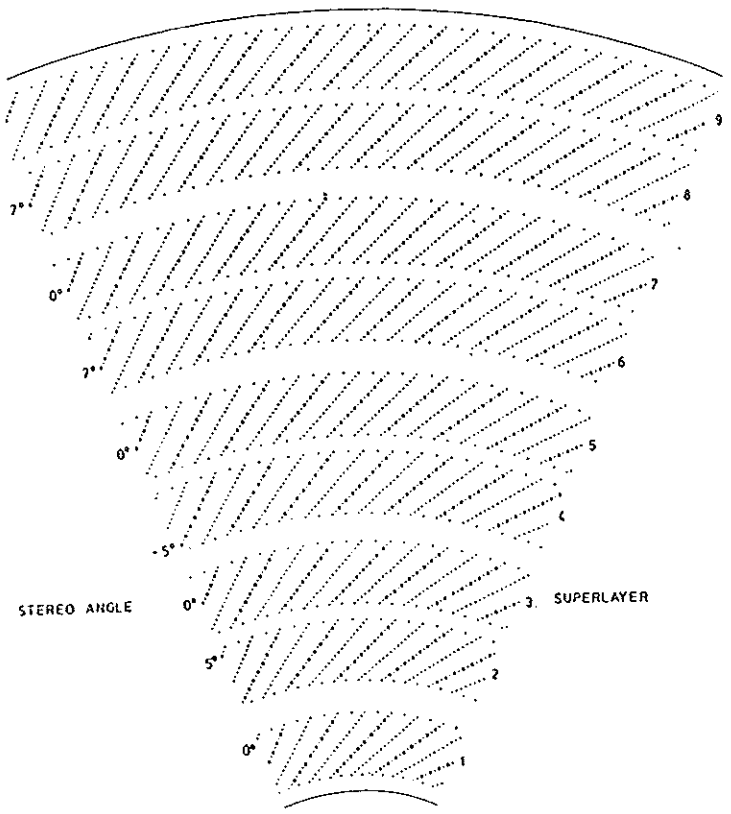

Figure 2.61
A 45^0 sector of the CTD consisting of 9 superlayers with 8 sense wires per superlayer.

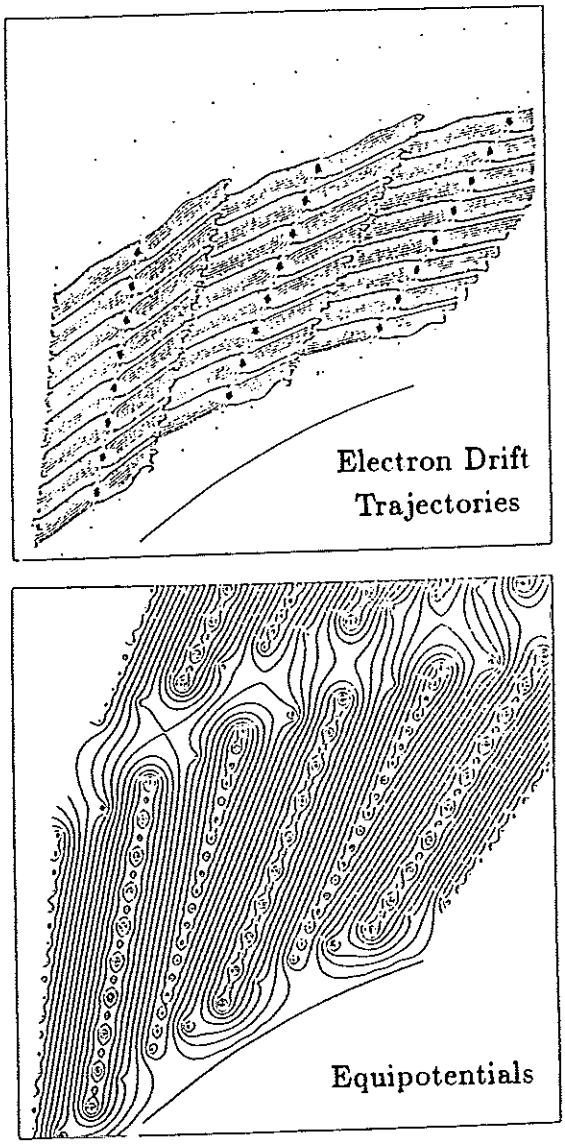

Figure 2.62
Equipotentials and electron drift trajectories in superlayer 1.

Figure 2.63
The assembled vessel of the CTD at Oxford.

Forward and Rear Tracking Detector (FTD, RTD)

The Forward Tracking Detector consists of 3 planar drift chambers and extends the tracking region in the forward direction to $7.5^0 < \theta < 28^0$, where high particle rates are expected due to the jet topology and the Lorentz boost (Fig. 2.59). The 3 FTD chambers are separated by 21cm leaving space for the Transition Radiation Detector (TRD).

The Rear Tracking Detector consists of 1 planar drift chamber covering an angle of $160^0 < \theta < 170^0$ in the backward direction (Fig. 2.59). Its main task is to measure the direction of scattered primary electrons in low Q^2 events.

Each of the 4 planar drift chambers has the same internal structure. It consists of 3 layers of drift cells, positioned perpendicular to the beam with wire orientations of 0^0, $+60^0$ and -60^0 with respect to the horizontal plane. The layout of one FTD chamber is presented in Fig. 2.64 indicating the 3 different wire orientations.

Figure 2.65 shows the structure of two drift cells of an FTD layer with a depth of 50mm and a width of 25mm. Each drift cell contains 6 sense wires and 7 potential wires and is filled with a gas mixture of argon/ethane at atmospheric pressure ($Ar/C_2H_6/C_2H_5OH$ (49/49/2)). The amount of material per chamber has been minimized to a radiation thickness of $0.09X_0$ for the sensitive area and $0.13X_0$ for the outer rim. The main parameters of the FTD and RTD are summarized in Table 2.17.

Figure 2.66 indicates the number of sense wires hit by a track going in forward direction as a function of the polar angle θ using only the CTD and CTD + FTD in combination. It shows, that more than 50 sense wires are hit in the forward direction down to θ angles >120mrad and that a precise track measurement is possible down to very small angles. For single wires a spatial resolution of about 120–130μm is achieved and a two track resolution of $\leq$ 2.4mm.

The momentum resolution is better than $\sigma(p)/p<0.01 \cdot p$ down to θ angles of 150mrad.

Parameters of	FTD1	FTD2	FTD3	RTD
Overall Dimensions R_{in}, R_{out} [mm]	124, 820	124, 1030	144, 1210	164, 620
Angular acceptance [mrad]	140 – 470	122 – 489	105 – 489	175 – 350
Number of sense, potential wires	1224, 1428	1512, 1764	1800, 2100	1008, 1176
Gas volume [m^3]	0.25	0.40	0.60	0.14
R.l. of sens. area, outer rim [X_0]	0.09, 0.13	0.09, 0.13	0.09, 0.13	0.09, 0.13
Total no. of channels, gas volume	5544, 1.39m^3			
Number (diameter) of sense, pot. wires/cell	6 (30μm), 7 (121μm)			
Gas mixture at atm. pressure	Ar/ethane/ethanol (49:49:2)			
Drift field, nominal drift velocity	$\approx$ 1250V/cm, 52μm/ns			
Single wire resolution	120–130μm			
Two track resolution	$\leq$ 2.4mm			

Table 2.17 Parameters of the Forward and Rear Tracking Detectors (FTD, RTD).

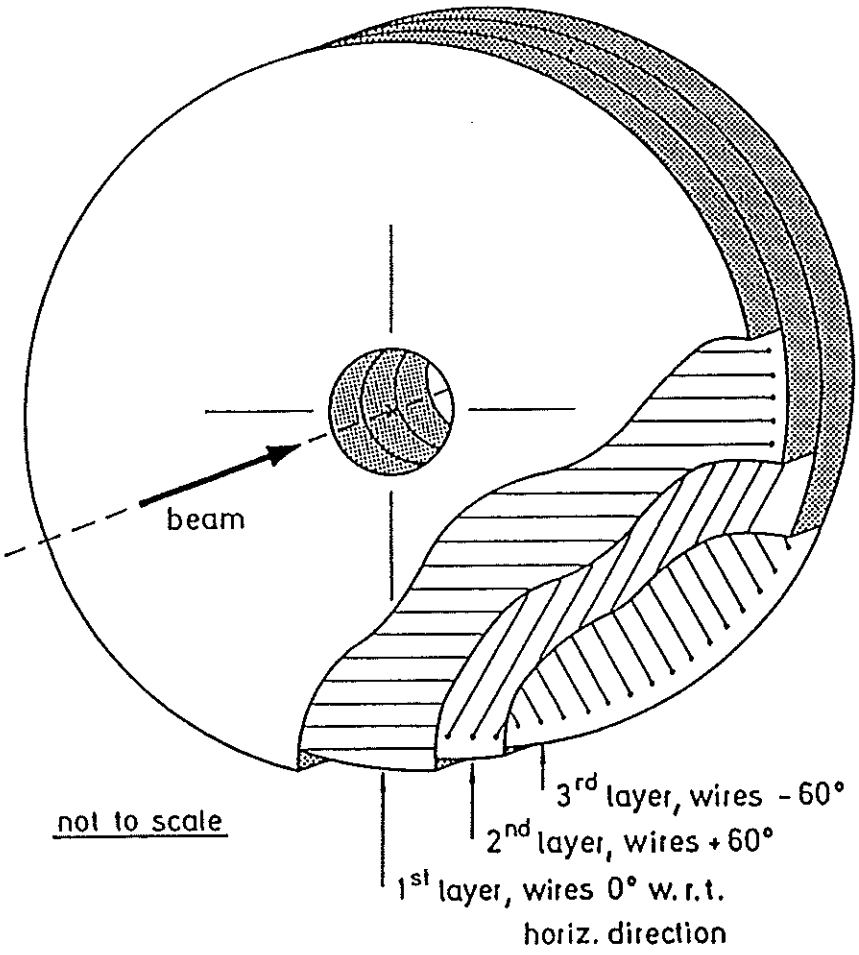

Fig. 2.64 Internal structure of one FTD chamber consisting of 3 layers.

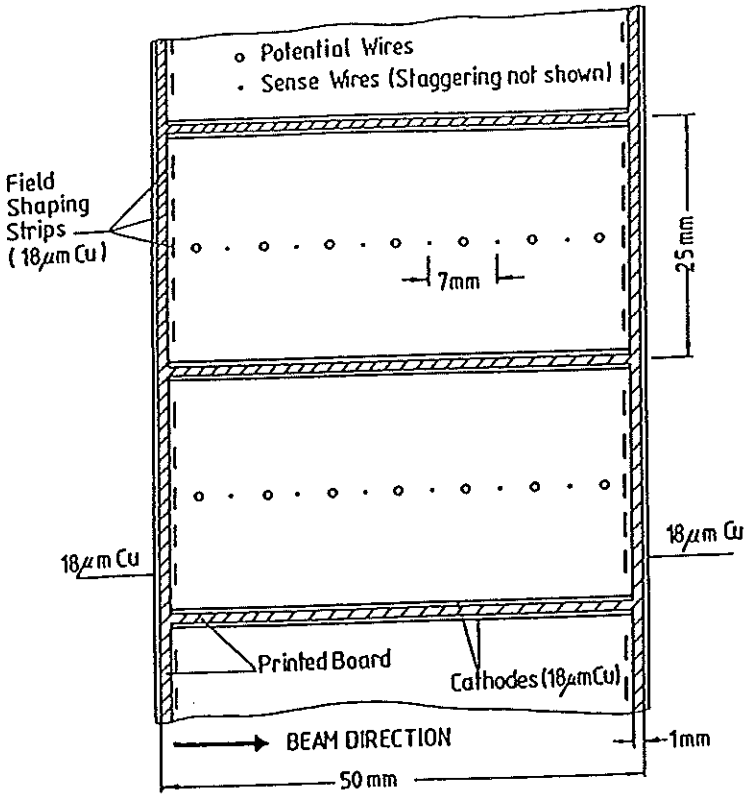

Figure 2.65
Cell structure of one FTD layer.

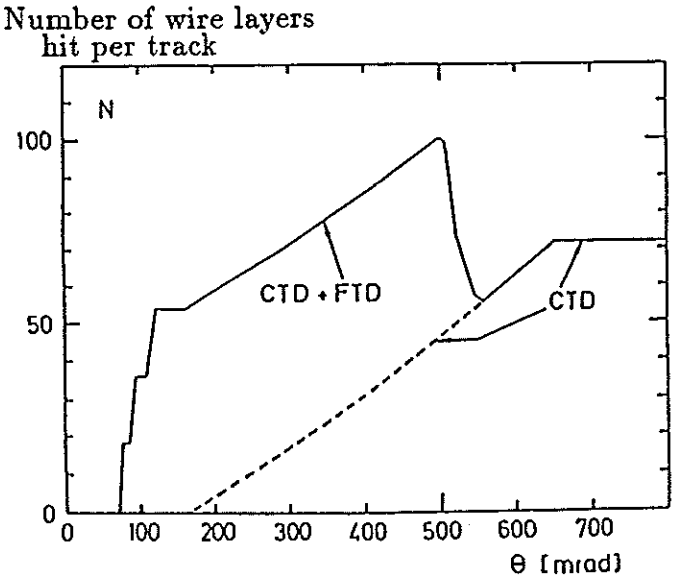

Figure 2.66
Number of wire layers hit per track in CTD and CTD+FTD as a function of the θ angle.

Transition Radiation Detector (TRD)

The Transition Radiation Detector was optimized for electron identification, especially for electrons in jets, in the momentum range from 1 to 30GeV/c. A probability for misidentifying pions as electrons P($\pi \rightarrow$ e) of about $2{\cdot}10^{-2}$ is achieved.

Transition radiation is created by charged particles passing the boundary of two materials with different dielectrical constants. This effect starts above a certain γ–threshold (γ=E/mc^2), even below the Cherenkov threshold, thus charged particles of the same momentum, but different mass can be distinguished due to their different γ's. The opening angle of the radiation cone is $\theta = 1/\gamma$. To increase the light output a periodical layer structure is chosen for the radiator.

The TRD consists of two packages of two modules positioned in the two 21cm wide gaps between the three FTD chambers and covers an angular range from 7^0 to 26^0 in forward direction (Fig. 2.59). Each of the four TRD modules has a depth of 10cm and overall outer dimensions of R_{in}=12.5cm and R_{out}=82.5–109.5cm. It is built of a 7cm thick radiator stack followed by a drift chamber as detector filled with Xe gas with 10% admixture of quench gas (CO_2 and iso–C_4H_{10}). The radiator stack is built of polypropylene (PP) fibres with a diameter of ϕ=20μm and a density of ρ=0.101g/cm^3.

Figure 2.67 shows a sketch of one TRD module indicating the radiator and the drift chamber layout. The internal structure is described in Fig. 2.68, where a radial cut through a TRD module is presented.

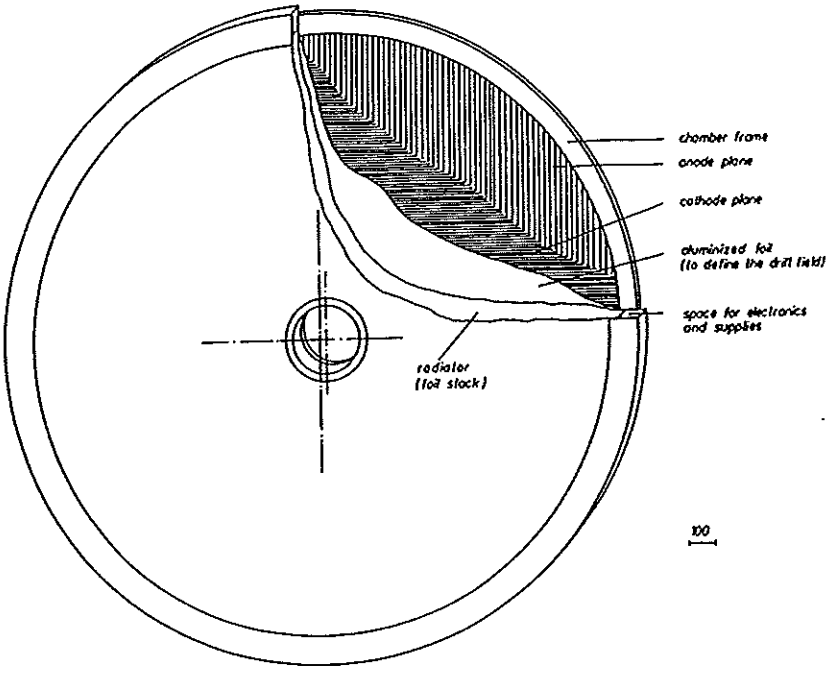

Figure 2.67
Internal structure of one TRD module.

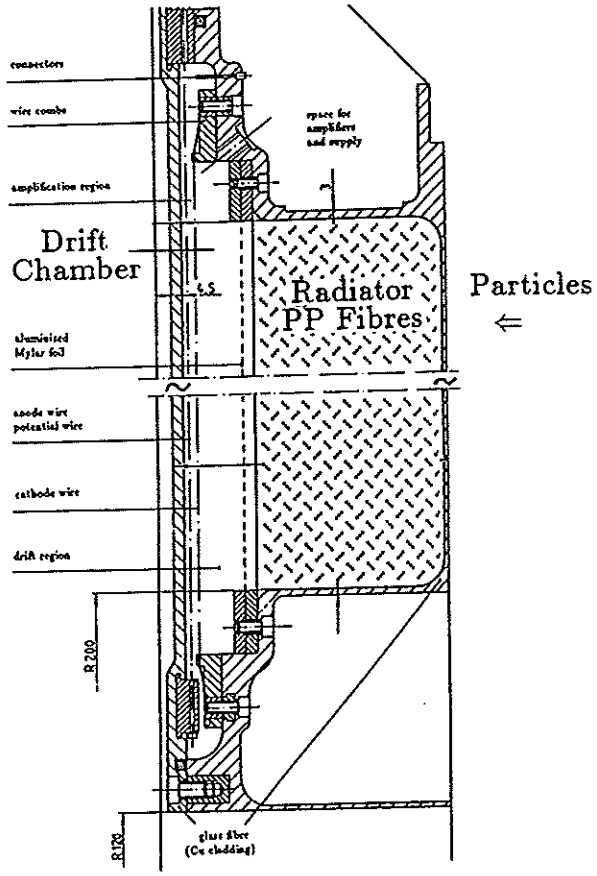

Figure 2.68
Radial cut through one TRD module.

2.3.6 Muon Detectors (MUON)

Forward Muon Detector (FMUON)

The Forward Muon Detector identifies muons in the forward hemisphere down to very small angles close to the beam axis (Fig. 2.34). It offers a completely independent measurement of muon momenta up to at least 100GeV/c. This is in particular important at small angles (<200mrad) where the momentum resolution of the CTD + FTD deteriorates. In addition an independent vertex reconstruction is possible.

The Forward Muon Spectrometer consists of Drift Chambers (DC) and Limited Streamer Tubes (LST) plus two magnetized iron toroids. A vertical section through the detector along the beam axis is presented in Fig. 2.69.

Figure 2.70 shows a photo of the front face of the FMUON toroids. The two external iron toroids, 6m in diameter with a total depth of 0.9m and a weight of about 200 tons are placed in front of the iron yoke (1.6T) and are magnetized by 8 normal conducting coils per toroid to an internal field of 1.7 Tesla. Together with the magnetized iron yoke they provide the bending power for a precise momentum measurement and improved muon identification.

Four planes of Drift Chambers (DC1,...,DC4) provide precise position and angular measurements of the outgoing muons. The positions of the DC–planes in the FMUON are indicated in Fig. 2.69. Figure 2.71 shows one full FMUO plane, 5.7–6.9m in diameter with 8 drift chambers and the support structure. In total there are 32 'octant' chambers with trapezoidal shape.

Four planes of Limited Streamer Tubes (LT1,...,LT4) with $\rho - \phi$ strip readout yield information for muon triggering and good tracking and momentum measurement. The positions of the LT–planes are also given in Fig. 2.69. Figure 2.72 presents the layout of one full LT–plane with a diameter of about 6.6m. Each plane is built of 4 quadrants consisting of two layers of plastic LSTs fabricated of Noryl and displaced by a half cell width (5mm). In total there are 16 'quadrant' chambers.

Two additional planes of Limited Streamer Tubes (LW) with an angular range from 18^0 to 36^0 plus the Inner Forward Muon chamber FMUI ensure the overlap coverage between the Forward and Barrel Muon Detector.

Figure 2.73 shows a photo of the Forward Muon Spectrometer installation in the ZEUS detector.

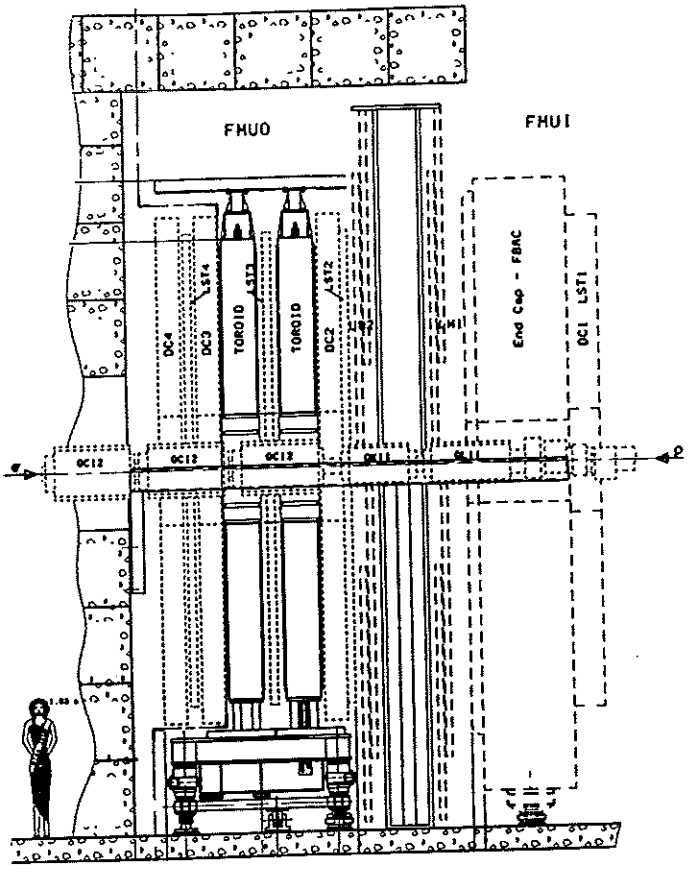

Figure 2.69
Vertical section through the Forward Muon Detector along the beam axis.

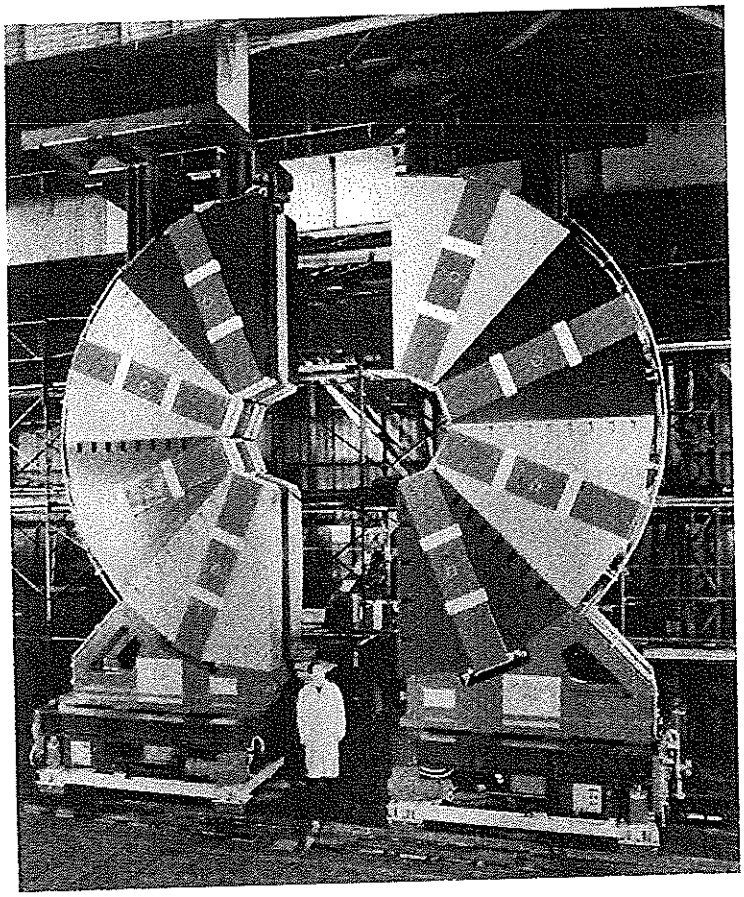

Figure 2.70
Photo of the opened FMUON toroids.

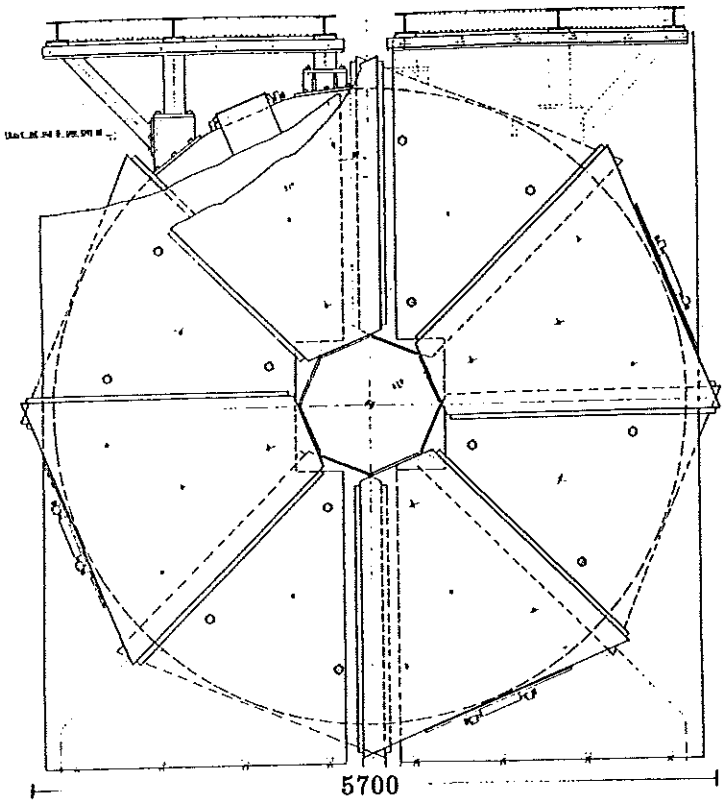

Figure 2.71
One full plane of FMUON drift chambers (DC1, DC2, DC3, DC4).

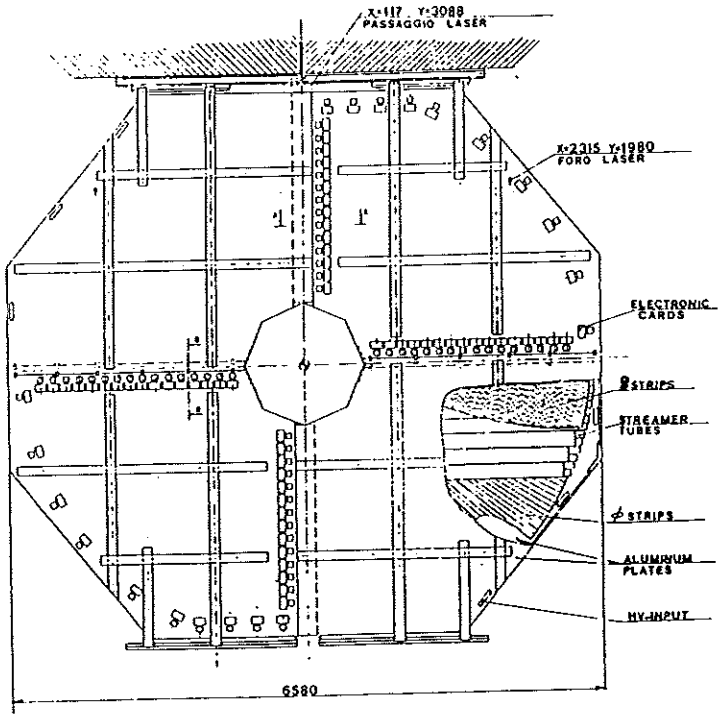

Figure 2.72
One full plane of FMUON limited streamer tubes (LT1, LT2, LT3, LT4).

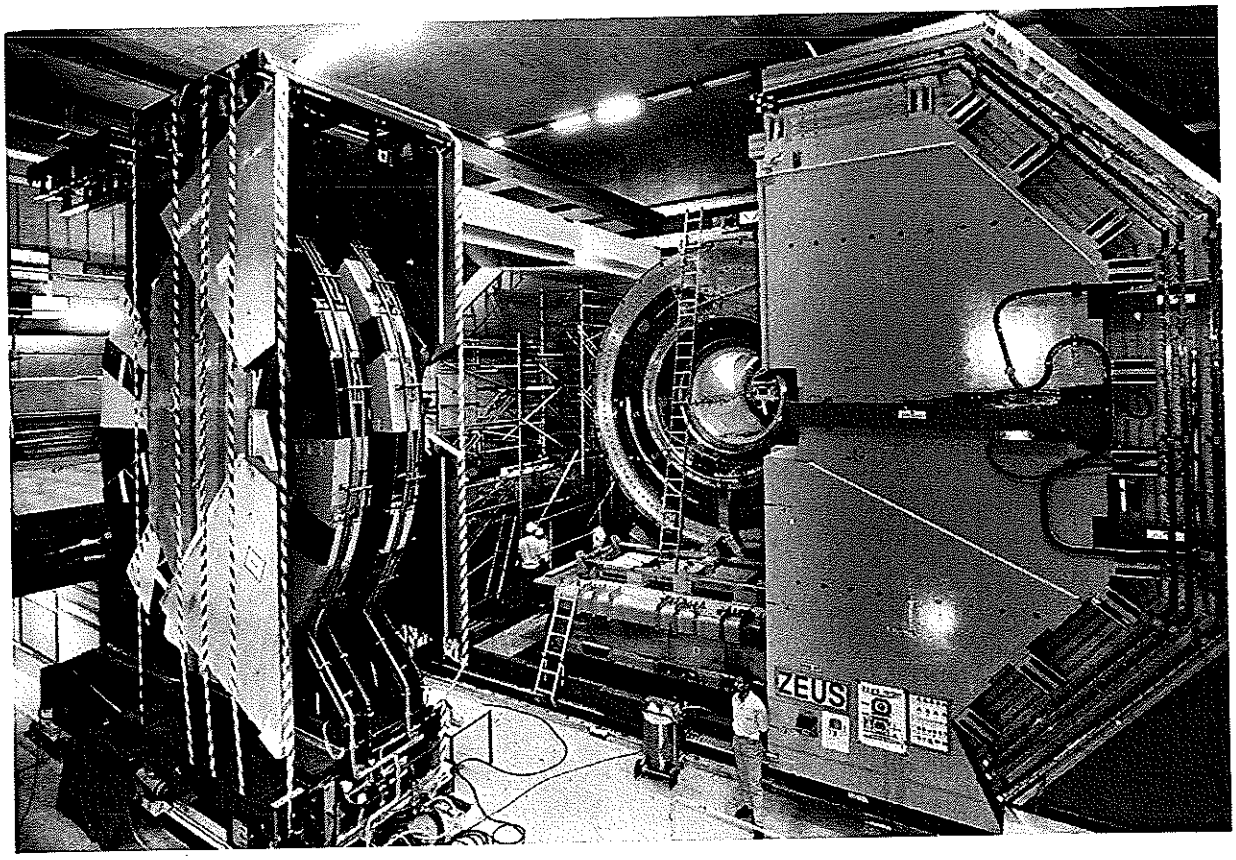

Fig. 2.73 Photo of the Forward Muon Spectrometer installation in the ZEUS detector.

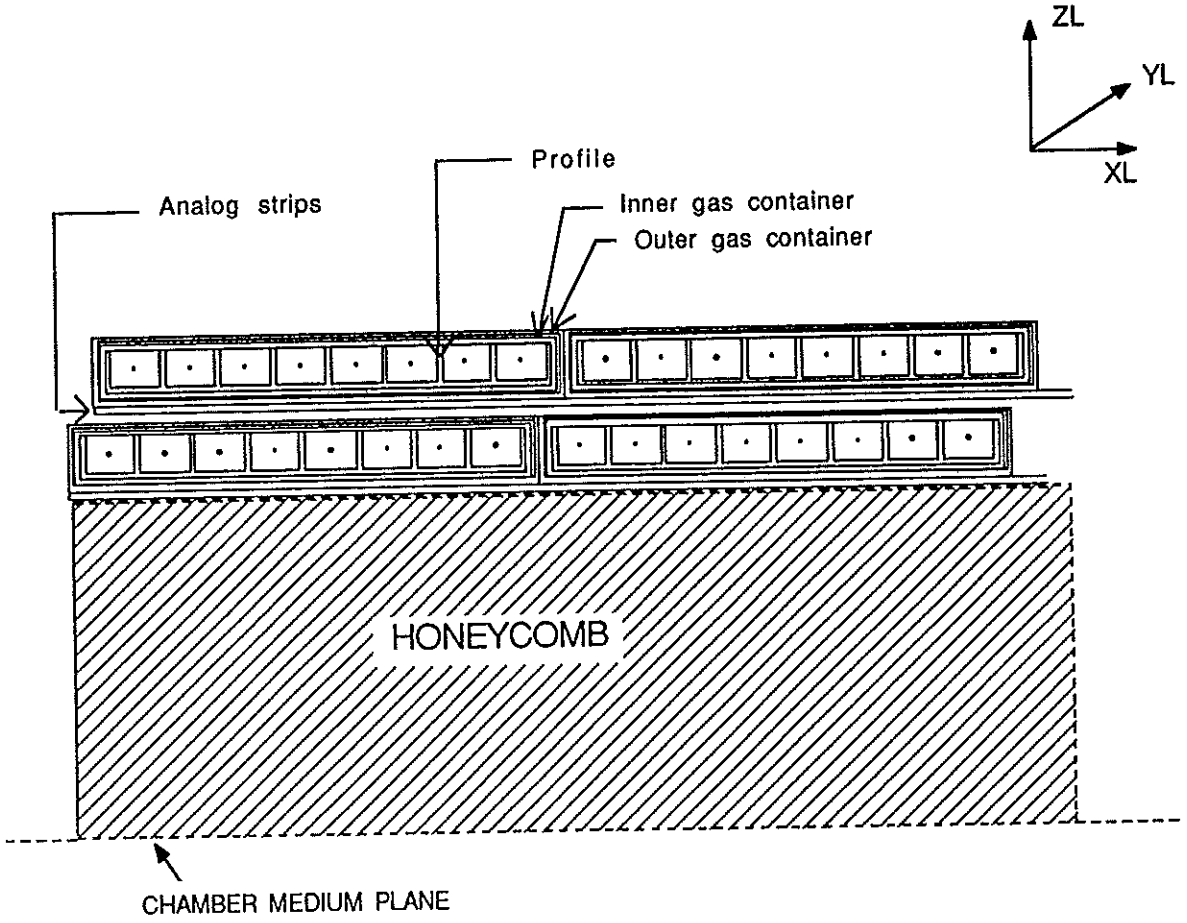

Fig. 2.74 Cross section of a half BMUON chamber.

Barrel and Rear Muon Detector (BMUON, RMUON)

The main task of the Barrel and Rear Muon Detectors is to identify muon tracks penetrating the calorimeter and the iron yoke.

The momentum determination is achieved by measuring the direction of the particle tracks before and after the magnetized iron yoke by two chambers of two double layers of limited streamer tubes placed inside (BMUI, RMUI) and outside (BMUO, RMUO) of the iron yoke. These detectors cover a large area of about 2000m^2 and have a fine granularity necessary for a point resolution better than 1mm. Typical dimensions of the chambers are 3m x 8m.

Each chamber consists of 2 double layers of LSTs separated by an aluminium honeycomb structure with a depth of 20cm in BMUI and 40cm in BMUO, which provides the mechanical stability for the chamber with minimum weight and offers the lever arm necessary for a precise angular measurement.

Figure 2.74 shows a cross section of a half BMUON chamber. The LSTs are placed in horizontal positions. They are equipped with external orthogonal readout strips (analog readout) and run parallel w.r.t. the beam axis in BMUON. They are placed in double gas containers. One LST module is built of 8–fold plastic profiles and jackets, both made of Noryl.

The RMUON has a corresponding structure, but the LSTs run perpendicular w.r.t. the beam axis. The main parameters of the muon detectors are summarized in Table 2.18.

FMUON	DC1,...,DC4	Number of planes, drift chambers/plane	4, 8
		Total active area	111m^2
		Total number of sense wires, cells	4064, 1016
		Gas mixture at atm. pressure	90%Ar+9%CO_2 +1%CH_4
	LT1,...,LT4	Number of planes, LST chambers/plane	4, 4
		Number of layers/chamber	2
		Number of profiles (8 wires)/layer	34
		Total number of profiles	1088
	LW1, LW2	Profile length	3.22–3.34m
		Gas mixture	30%Ar+70%C_4H_{10}
BMUON, RMUON	LSTs	Active area	$\approx$ 2000m^2
		Total number of digital, analog channels	27840, 42496
		BMUON + RMUON angular acceptance	$34^0 < \theta$
		Gas mixture	25%Ar+75%C_4H_{10}

Table 2.18 Parameters of the Muon Detectors (FMUON, BMUON, RMUON).

2.3.7 Leading Proton Spectrometer (LPS)

The Leading Proton Spectrometer measures forward scattered protons with transverse momenta p_T <1GeV/c and momenta p/p_{beam}=0.3–1.0 with an acceptance of $\approx$ 10% – 40%.

The LPS consists of six detector stations S1,...,S6 using 'Roman pots' positioned 24m, 41m, 44m, 63m, 81m and 90m down the proton beam line. Figure 2.75 shows the positions of the LPS detector stations along the outgoing proton beam line. The first three detectors S1, S2, S3 are built of single pots and S4, S5, S6 of double pots.

There are six silicon strip detector planes per pot with 2 x–planes, 2 u– and 2 v–planes at $\pm 45^0$ w.r.t. the x–plane with the x strips parallel to the direction of magnetic deflection. In addition at stations S4, S5 and S6 there are extra, small trigger planes. The shapes of the detector planes are different for each station and optimized w.r.t. the least area of 10σ around the beam profile.

Each detector plane consists of silicon strips with a readout pitch of width of 115μm. Two planes of the same coordinate in a detector provide a spatial resolution of $\pm$25μm. The total number of strips is about 50000 with a total area of 1560cm^2. The main parameters of the Leading Proton Spectrometer are summarized in Table 2.19.

At least two horizontal and two vertical position measurements together with the assumed point–like interaction region in combination with the bending power of the beam magnets yield a very precise momentum determination. At high momenta the resolution varies from 0.9% with information of only two detectors to 0.15% with information of S4, S5 and S6.

Number of detector stations, 'Roman pots'	6, 9
Number of pots per station	1 (S1,S2,S3), 2 (S4,S5,S6)
Position of station S1,...,S6 [m]	24, 41, 44, 63, 81, 90
Detector planes per pot	6 strip planes
Strip width	115μm
Total number of Si–strips	$\approx$ 50000
Total area of strips, large–area Si	1560cm^2, 260cm^2
Spatial resolution	$\pm$25μm
Momentum resolution	< 1%

Table 2.19 Parameters of the Leading Proton Spectrometer (LPS).

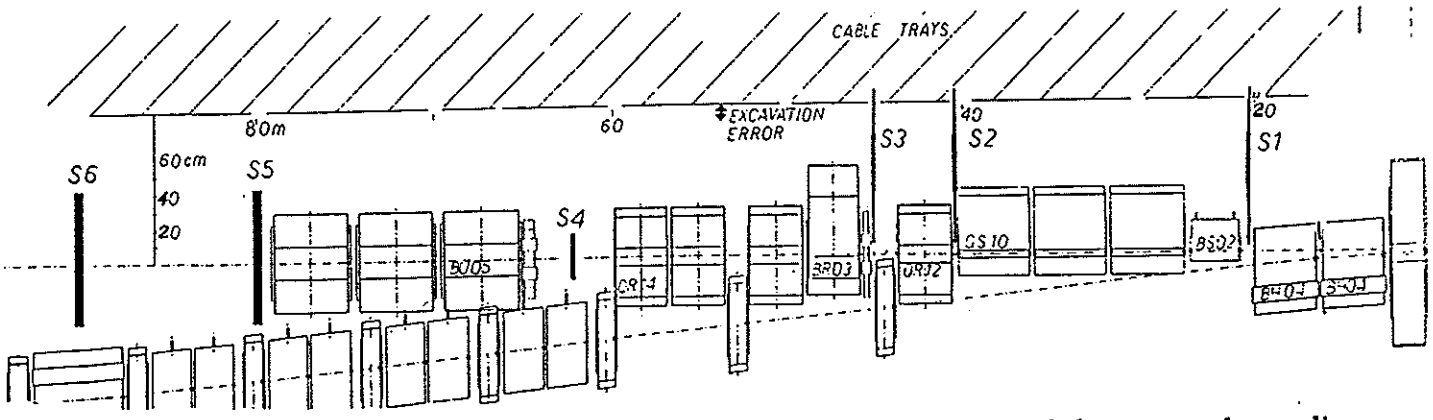

Fig. 2.75 Positions of the LPS stations along the straight section of the proton beam line.

2.3.8 Luminosity Monitor

The main tasks of the Luminosity Monitor are a precise measurement of the luminosity and tagging of electrons emitted at very low angles.

For determination of the absolute luminosity the preferred process of small angle, high energy bremsstrahlung ep $\rightarrow$ epγ is measured by tagging e and γ in coincidence. The cross section of this process is described by the Bethe–Heitler formula:

$$\frac{d\sigma}{dk} = 4\alpha r_e^2 \frac{E'}{kE}\left(\frac{E}{E'} + \frac{E'}{E} - \frac{2}{3}\right)\left(\ln\frac{4E_pEE'}{Mmk} - \frac{1}{2}\right)$$

with k = photon energy, E, E' = primary and secondary electron energy, E_p = proton energy, M, m = mass of proton and electron, α = fine structure constant, r_e = classical radius of electron. Since the energy transfer to the proton is negligible, $E' = E - k$.

The Luminosity Monitor consists of two detectors: an electron detector and a photon detector. Figure 2.76 shows the positions of these two detectors at the electron and proton beam lines.

The electron detector is placed about 35m from the interaction point close to the electron beam line behind the bending magnet BH04, which acts as beam spectrometer for off beam energy electrons. It is built of an electromagnetic lead scintillator sampling calorimeter surrounded by lead shielding and tags electrons scattered under very small angles θ_e <0.5mrad. For position measurement of the electron provisions are made for inserting scintillating finger counters into this calorimeter.

The photon detector is positioned at a distance of 104m to 107m from the interaction point close to the proton beam line. It consists of three components: 1) an adjustable 0.5 – 3.5X_0 thick carbon filter absorbing synchrotron radiation, 2) an air filled Cherenkov counter vetoing electrons mainly from γ conversion in the filter and 3) a photon lead scintillator sampling calorimeter. The photon detector measures the energy of photons in the energy intervall of 16GeV>E_γ >11GeV with full geometrical acceptance of the scattered electrons with energies of 14GeV<E_e <19GeV.

The bremsstrahlung cross section integrated over the photon energies amounts to 15.4mb. The event detection rate for this cross section will be in the order of 230kHz assuming a luminosity of L = $1.5 \cdot 10^{31} cm^{-2} s^{-1}$. This event rate is more than sufficient for a fast and continuous monitoring of the luminosity.

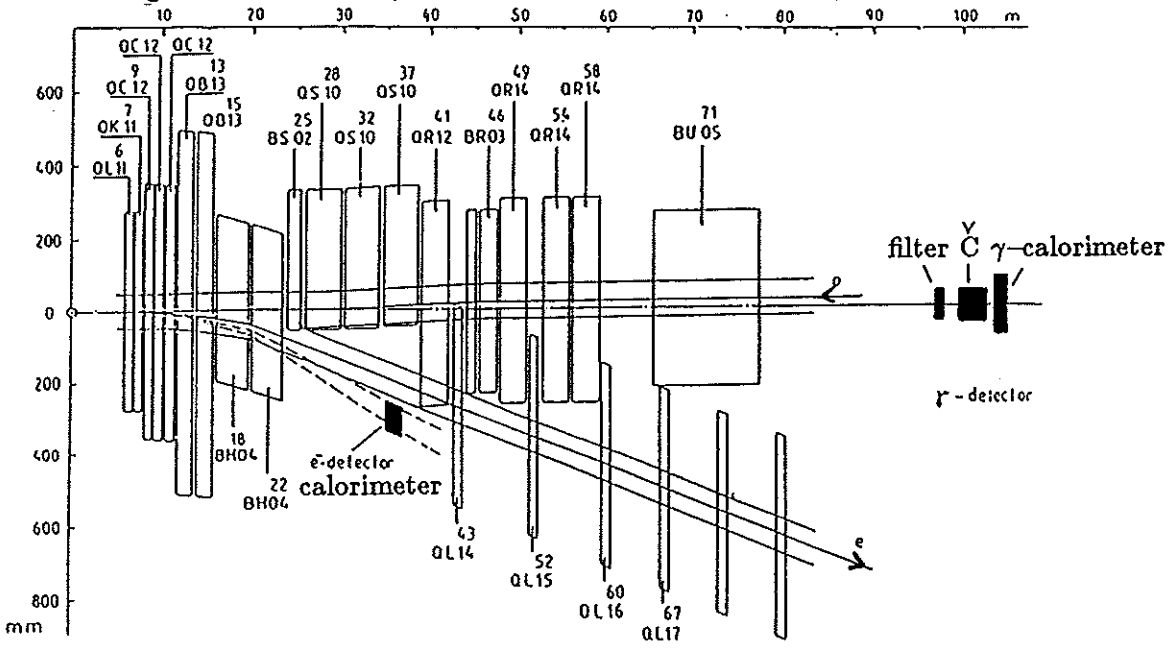

Fig. 2.76 Positions of the Luminosity Monitor detectors at the electron and proton beam.

2.3.9 Trigger, Data Acquisition and Physics Detection

The short bunch–crossing time of 96 ns demands a pipeline, in which the data of the subdetectors is kept to permit a decision in the first–level trigger (FLT). The decision of the FLT is taken 4.4μs after the crossing [ZEU85...91].

The task of the FLT is to reduce the incoming events (almost all from background) to a level of 1kHz. At the second–level trigger the digitized data of the detector components are analysed and cross checked and the rate is reduced at least to about 100Hz. At the third–level trigger the whole event is reconstructed and the rate is further reduced to around 3Hz. The trigger logic is built in a VME environment. In addition test and calibration triggers are set up, e.g. for the uranium noise, light flashers, luminosity etc... The various triggers can enforce the readout by the data acquisition (DAQ) system.

The main goal of the DAQ is to collect and store the event data from the ZEUS detector. Important tasks of the DAQ are readout and recording of data, monitoring of hardware and software performance, collection and storage of calibration constants, control of dataflow and reconstruction, testing of hardware and software functions. The dataflow in the DAQ for the various components is described in Fig. 2.77.

In the first step of the off–line analysis detector oriented entities, like tracks, energy deposition in the calorimeter etc... will be reconstructed. Then the physical objects such as momentum vectors, particle identities etc... are determined by combining the information from the individual detector components.

Correct pattern recognition and event reconstruction represent a very complex task. Comprehensive program packages were developed and implemented in the ZEUS analysis chain. Figure 2.78 shows a simulated deep inelastic scattering event in the CTD. Figure 2.79 represents the graphic display of a generated event in a vertical section through the inner tracking detectors and the uranium scintillator calorimeter of the ZEUS detector along the beam axis [LEI92]. Both pictures illustrate the complexity of event reconstruction.

An overview of possible HERA physics processes and their typical physical signatures related to the ZEUS detection methods and detector specifications is presented in Table 2.20 [STR91].

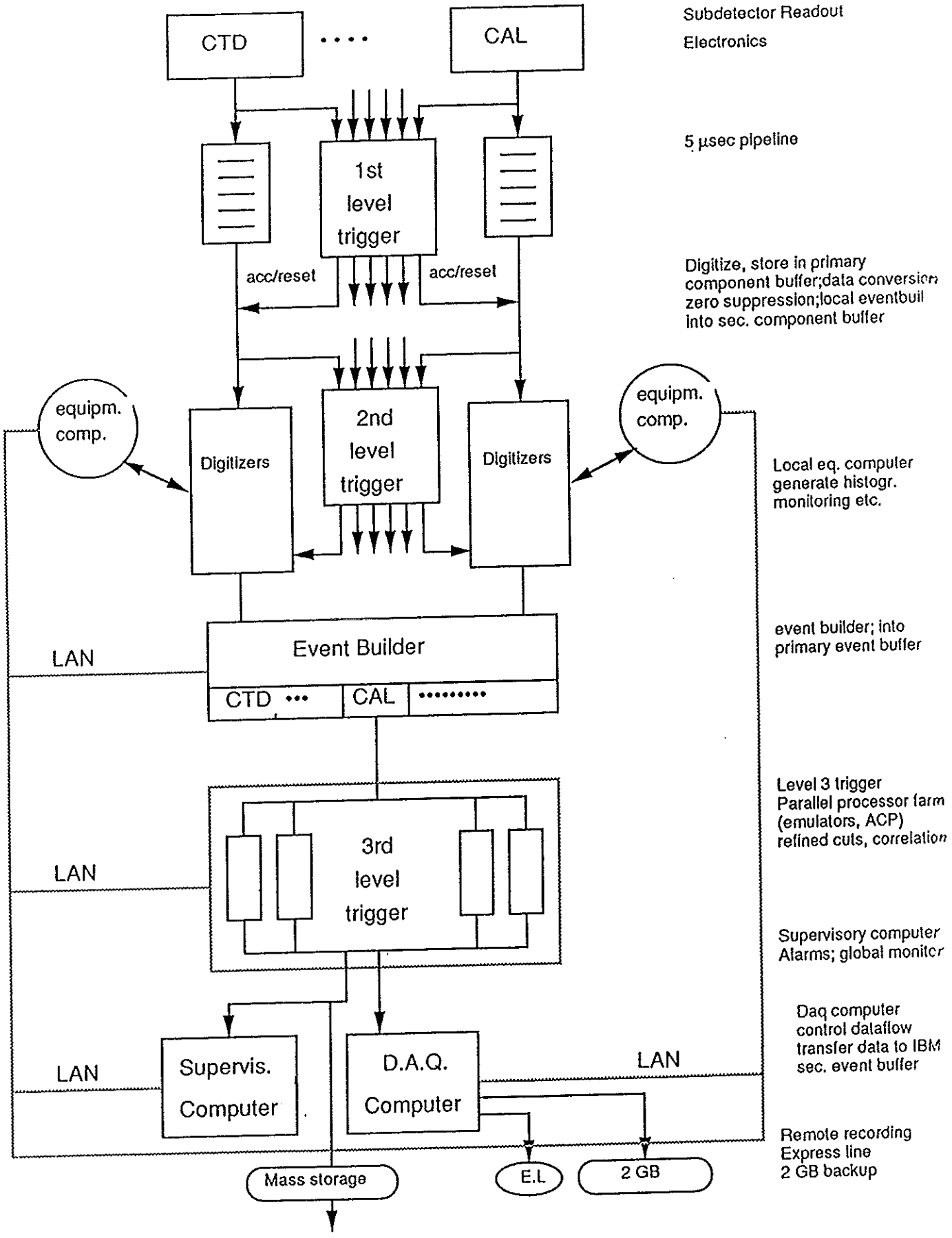

Fig. 2.77 Outline of the ZEUS Data Acquisition System.

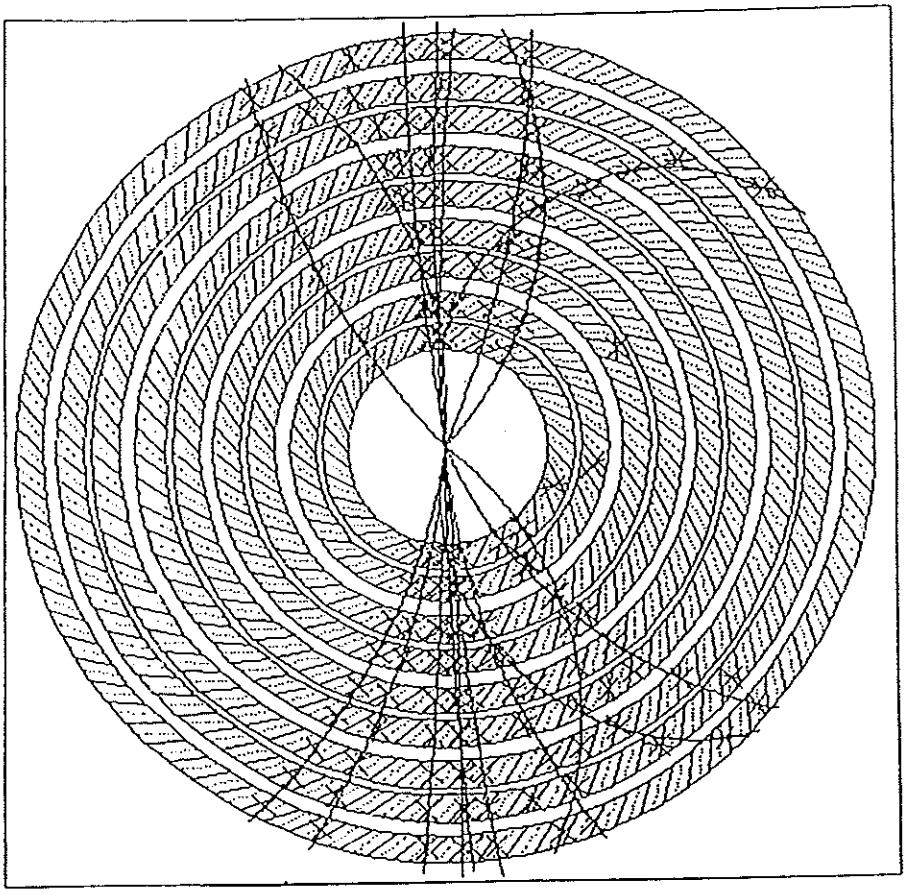

Fig. 2.78 A generated deep inelastic scattering event in the CTD.

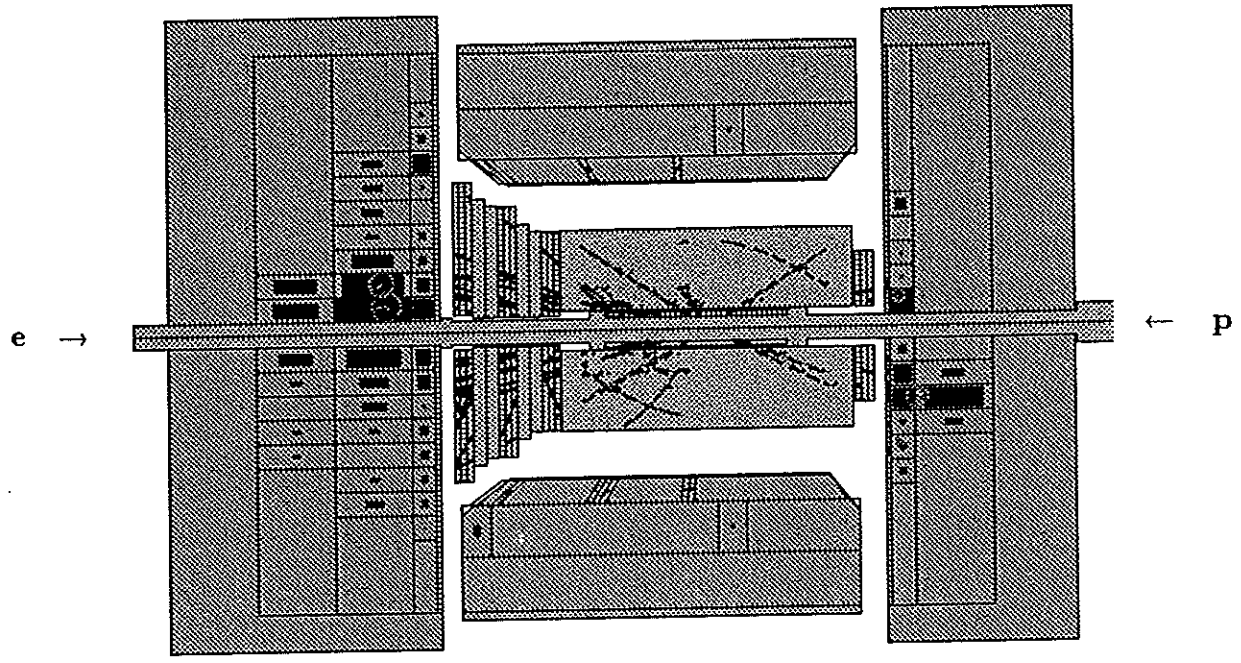

Fig. 2.79 Graphic display of a generated event simulated in the inner tracking detectors and the uranium scintillator calorimeter of the ZEUS detector.

Production process(es)	typical signature	detector	ZEUS specifications
neutral current	isolated electrons	EM. calorimeter	$\sigma(E_e)/E_e = 18\%/\sqrt{E_e} \oplus 1\%$
		central tracking	$\sigma(p_T)/p_T < 0.003 \cdot p_T$
charged current	hadron jets	HAD. calorimeter	$\sigma(E_h)/E_h = 35\%/\sqrt{E_h} \oplus 2\%$
supersymmetry	missing p_T	hermetic calorimeter	solid angle coverage: forward: 99.8 %, backward: 99.5 %
heavy flavour exotics	electrons in jets	central tracking	dE/dx for $E < 6 - 10\,GeV$ two track resolution < 2.5mm
		calorimeter	longitudinal segmentation and HES
		forward transition radiation detector	h misidentification P(h→e) $\approx 2 \cdot 10^{-2}$ for 1GeV<E_e <30GeV
	isolated muons and muons in jets	muon chambers	forward: $\sigma(p)/p = 23\%$ at $100\,GeV$ barrel: $\sigma(p)/p = 30\%$ at $20\,GeV$
	sign of charge	magnetic field	$1.8\,T$ central tracking region $1.6\,T$ iron yoke (μ chamber)
	secondary vertices	vertex detector	$\sigma_{spatial} \approx 30 - 70\mu m$ $\sigma_{twotrack} \approx 500\mu m$
photoproduction	electron detection at small angles	small angle electron tagger	zero angle electron tagger 14GeV<E_e <19GeV
bremsstrahlung for luminosity monitoring	photon detection at small angles	small angle photon tagger	zero angle γ tagger 16GeV>E_γ >11GeV

Table 2.20 Overview of possible HERA physics processes and their typical physical signatures related to the ZEUS detection methods and detector specifications.

Chapter 3

Fundamental Physics of Hadron Sampling Calorimeters

3.1 Energy Measurement of High Energy Particles and Jets

In order to measure the energy of particles and jets with high precision, calorimeters become more and more the central component of large detectors at the new generation of particle accelerators.

In contrast to wire detectors positioned in a magnetic field, where the momenta of charged particles can be measured, and where the momentum resolution scales as

$$\frac{\sigma(p)}{p} \sim \mathrm{p}$$

and so degrades with increasing momentum, the energies of both charged and neutral particles can be measured with calorimeters and the energy resolution of well designed calorimeters scales as

$$\frac{\sigma(E)}{E} \sim \frac{1}{\sqrt{E}}$$

and so improves with increasing energy.

A further striking advantage of calorimeters is that the depth L necessary to absorb electrons and hadrons increases only logarithmically with the energy E of the incoming particle or jet:

$$\mathrm{L} \sim \mathrm{a} + \mathrm{b} \cdot \ln \mathrm{E} \ .$$

Particle identification is also possible in a spatially (longitudinally and transversally) segmented calorimeter due to the spatially different energy deposits of different particle types. In addition, a calorimeter such as that built for the ZEUS detector offers a high time resolution of better than 1ns for energy deposits above 15GeV. It can handle high event rates and provides fast information for the trigger and timing to a few ns.

There are various excellent reviews and publications providing overviews of calorimetry. Only a few are mentioned here, e.g. [AMA81], [FAB85], [BRÜ86,87], [WIG87,91], [FAB89]. Calorimeters have been used for more than 20 years. A major break through in the understanding of hadron calorimeters was achieved in the mid eighties.

Hadron calorimetry is one of the most complex and exciting fields of detector research and development in high energy physics. There are various new ideas, developments and tests in calorimetry. Comprehensive and excellent overviews of the present status of the different fields in calorimetry can be found e.g. in [ECF89], [LHC90], [COL90] and [PIS91].

The topics on calorimetry selected in this chapter are chosen in particular with respect to the basic understanding of the high resolution ZEUS uranium scintillator calorimeter. Intensive research and systematic development were performed for the ZEUS calorimeter during 1984–1991. The most important results of the ZEUS calorimeter research, development and tests are presented in the following chapters. Overviews and special topics on the ZEUS calorimeter can be found e.g. in [ZEU85...91], [WOL86], [KRÜ87a...90b], [BER87], [KLA89] and on the ZEUS calorimeter tests in particular in [CAT87], [AND86], [BER87a], [AGO89], [DRE90], [BEH90], [AND90] and [AND91].

The central ideas of a perfect calorimeter are, that:

1) the particle or particle jet is completely absorbed in the calorimeter
   and
2) the absorbed energy is converted into a measurable signal, which is proportional to the energy of the incident particle and independent of its type.

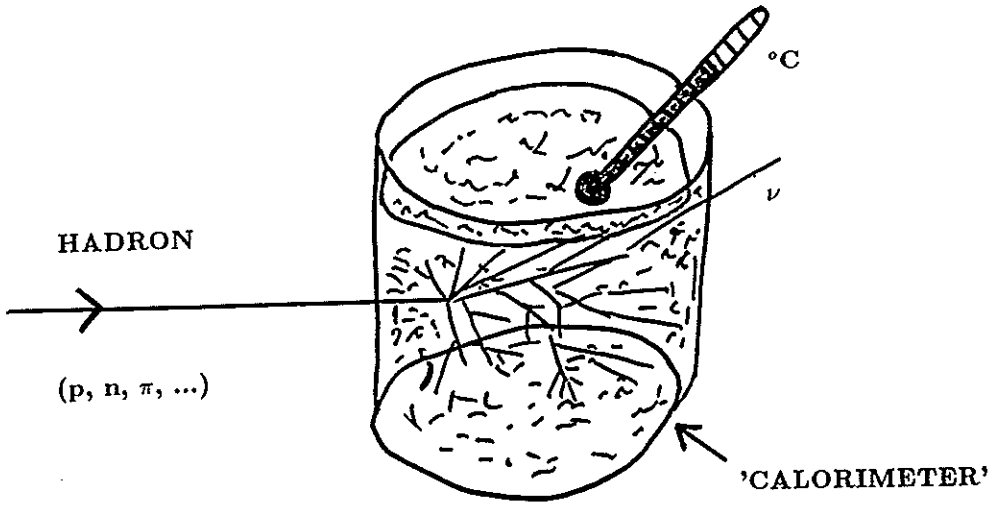

Fig. 3.1 Principal ideas of a 'calorimeter'.

Figure 3.1 illustrates the idea of a 'calorimeter'. From the left a particle, e.g. a hadron (p, $\pi^{\pm}$, ...) enters a vessel filled with a liquid. It interacts with the atoms of the liquid and deposits its energy by creating a shower of particles. The shower is almost completely absorbed in the liquid, only neutrinos will leave the vessel undetected. The temperature of the liquid will increase with the deposited energy. But due to the small change in temperature the energy can not be measured by a normal thermometer. For example cosmic protons with an energy of 10^{20}eV which are totally absorbed in a 10^{8}g massive block of material increase the temperature of the block only by 10^{-8}K, an undetectable amount.

Next best would be to use an active medium like scintillator and measure the generated light as energy measure. But the density is too small and the calorimeter would become too big.

Finally the best choice is to build a sampling calorimeter. This is the preferred way for hadron calorimeters in the multi–GeV region.

Homogeneous calorimeters consist of an absorbing part which represents simultaneously also the active medium. Examples of homogeneous electromagnetic calorimeters are e.g. that of L3 using a device of BGO ($Bi_4Ge_3O_{12}$) crystals with transverse dimensions of about 3cm x 3cm and a depth of 24cm readout by photodiodes [L3Y83], [BAK88] or that of OPAL using lead glass blocks, with transverse dimensions of 11cm x 11cm and a depth of about 37cm readout by associated photomultipliers [OPA83].

In order to realize a compact sampling hadron calorimeter usually absorber plates are interleaved with detector layers, forming the sampling (sandwich) calorimeter. But there are also other geometries used for sampling calorimeters, e.g. that of the spaghetti type with scintillating plastic fiber readout or the accordion type liquid argon calorimeter. Construction and operation of sampling (sandwich) calorimeters are described in the following section.

3.2 Structure and Operation of Sampling Calorimeters

In contrast to homogeneous calorimeters, which are fully sensitive detectors, sampling calorimeters are built of passive absorber alternating with an active medium. Common sampling sandwich calorimeters consist of absorber plates of material with a short interaction length such as Fe, Cu, Pb, U, ... interleaved with active detector layers e.g. scintillator or liquid argon.

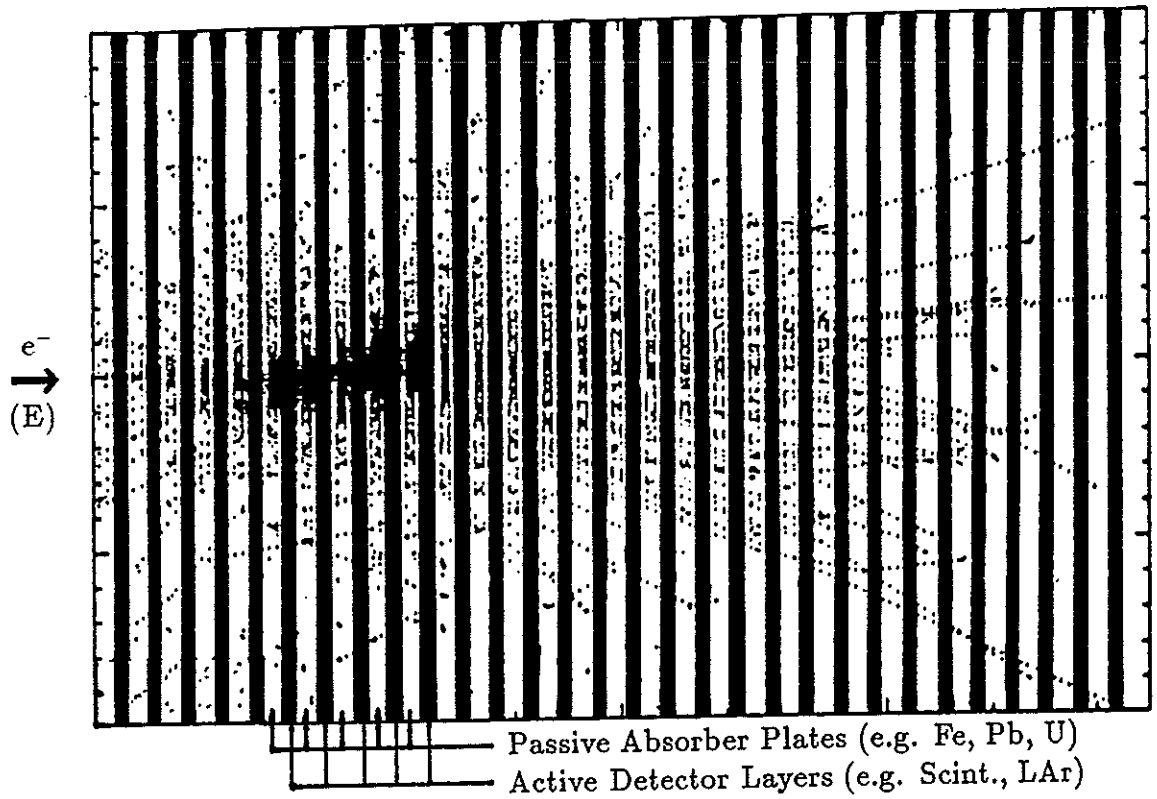

Fig. 3.2 An electromagnetic shower simulated in a sampling calorimeter.

Figure 3.2 shows the principle of a sampling calorimeter. It consists of passive absorber plates (Pb, U, ...) and active layers of scintillator plates, which detect the traversing particles and which can be read out by wavelength shifters and associated photomultipliers (see also Fig. 2.43 and 2.44). An electromagnetic shower has been simulated with the Monte Carlo program package EGS4 (Electron Gamma Shower Simulation, Version 4) [NEL85]: an electron enters the calorimeter and creates an electromagnetic shower. The shower is almost completely contained in the calorimeter volume apart from a few particles leaving the calorimeter in the backward direction (albedo).

Only a small fraction (4% for electrons in the ZEUS calorimeter) of the particle energy is deposited in the active medium of a sampling calorimeter. A small fraction of this energy is converted to light and yields a measurable signal in the photomultipliers. In standard sampling calorimeters this signal is approximately proportional to the energy of the incoming particle.

The ratio of energy of a particle of type i visible in the active medium to the totally absorbed energy in the calorimeter is called the sampling fraction R_i. It depends on the material and the thicknesses of the absorber and detector plates of the calorimeter as well as on the particle type. It is defined as:

$$R_i = \frac{E_{vis,i}}{E_{abs,i}} = \frac{E_{vis,i}}{E_{invis,i} + E_{vis,i}} ,$$

where i = particle type e.g. e, h, mip (shower component)
$E_{vis,i}$ = visible (measurable) energy in the active layers for i
$E_{invis,i}$ = invisible energy in the active and passive layers for i
$E_{abs,i}$ = totally absorbed energy in the calorimeter for i .

To compare the sampling fractions of different calorimeters, R_i is often normalized to the sampling fraction of a hypothetical minimum ionizing particle, called mip. R_{mip} (=:mip as abbreviation) is defined as

$$\text{mip} = \frac{(dE/dx)_s}{(dE/dx)_s + R(dE/dx)_t} ,$$

where $(dE/dx)_s$ and $(dE/dx)_t$ are the minimum ionizing losses per unit length of the active medium and the absorber, and $R = t/s$, where t and s are the thicknesses of an absorber plate and an active medium layer. The mip value is independent of the energy and depends only on the material. Figure 3.3 shows the minimum energy losses of different particle types which are all about equal. Muons at a fixed energy of about 200 – 300MeV behave similarly to minimum ionizing particles. They usually have a pulse height distribution with a long tail towards high pulses due to δ–rays, known as Landau distribution. To obtain an approximately energy independent signal the most probable value of the muon pulse height spectrum is used (for more details see chapter 4.2.5).

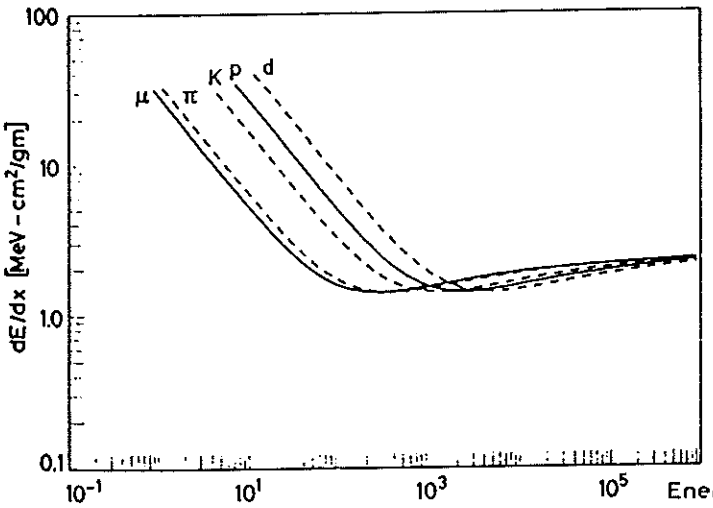

Figure 3.3
Energy loss dE/dx as a function of the energy for different particles.

The relative sampling fraction R_i/R_{mip} (=: i/mip as abbreviation) represents the ratio of the measurable fraction of the deposited energy of particle type i to that of a minimum ionizing particle. Typical e/mip (:=R_e/R_{mip}) –ratios for heavy absorbers and light readout media are between 0.6 and 0.7 [WIG87].

Fluctuations in the energy measurement are expected due to the sampling structure of a sampling calorimeter and the statistical nature of the physical processes. Because of the statistical nature of the physical processes that play a role in calorimeter measurements, the relative energy resolution improves with increasing energy.

Fluctuations of the sampling fractions, denoted by Δe, $\Delta\pi$, etc., where e (:=R_e), π (:=R_π) etc. represent the sampling fractions, produce the so–called "sampling fluctuations". They can be reduced by increasing the sampling frequency.

Fluctuations of the shower components, ΔE_{em}, ΔE_π, etc., where E_{em}, E_π, etc. represent the energy fractions of the different shower components in the shower, through the different sampling fractions, produce the so–called "intrinsic fluctuations" [TIE89], [DRE90].

3.3 Electromagnetic Showers

3.3.1 Physical Description of Electromagnetic Showers

Electromagnetic showers consist of e^-'s, e^+'s, γ's. They are created by the interaction of a high energetic electron, positron or photon with matter. e^+e^-–pairs and bremsstrahlung γ's are produced, which in turn produce particles themselves. This cascade continues until the total energy of the primary particle has been transformed into low energetic secondary particles which loose their energy predominantly by ionization.

Figure 3.4a shows the cross sections of the different physical processes of electrons and positrons in lead as a function of their energy. The physical processes for photons in lead are presented in Fig. 3.4b.

At energies above 1 GeV bremsstrahlung ($\sim Z^2$) for electrons and positrons and pair production ($\sim Z^2$) for photons are the dominating processes and become energy independent. At low energies ionisation loss ($\sim Z\cdot\log(Z)$) plays the dominant role for electrons and positrons, and photo effect ($\sim Z^4$–Z^5) for photons.

The development of electromagnetic showers is very well described by quantum electrodynamics (QED) [TSA74]. The energy–loss mechanisms depend essentially on the electron density in the absorber. At low energies ($\lesssim$10MeV) nuclear reactions, e.g. γn, γp or photonuclear fission, may also play a certain role. But these usually do not exceed 1% of the cross sections [FAB89]. The radiation length X_0 sets the typical scale for electromagnetic showers. The scale for electromagnetic showers expressed in units of X_0 is material independent.

X_0 is defined as the energy loss of electrons by bremsstrahlung at energies above 1GeV:

$$\frac{dE}{dx}_{brems} = -\frac{E}{X_0} ,$$

where x represents the thickness of the material in units of radiation lengths X_0 and E the energy of the incident electron or positron in MeV.

The radiation length X_0 can be calculated with high precision from the formula [ROS52]:

$$\frac{1}{X_0} = \frac{4\,\alpha\,\frac{N_A}{A}\,Z\,(Z+1)\,r_e^2\,\ln(183\,Z^{-1/3})}{(1+0.12\,(Z/82)^2)}\;[\frac{cm^2}{g}] ,$$

where $\alpha = \frac{e^2}{\hbar c}$, A = mass number of the material in $[g]$, Z = atomic number of the material, N_A = Avogadro number and r_e = classical electron radius in $[cm]$.

The radiation lengths of a few materials are summarized in Table 3.1 [PDG90]. A good approximation for the radiation length X_0 is given by [AMA81]:

$$X_0 \approx 180\,\frac{A}{Z^2}\,[\frac{g}{cm^2}] ,$$

with a precision of $\pm$20% for $13 \leq Z \leq 92$.

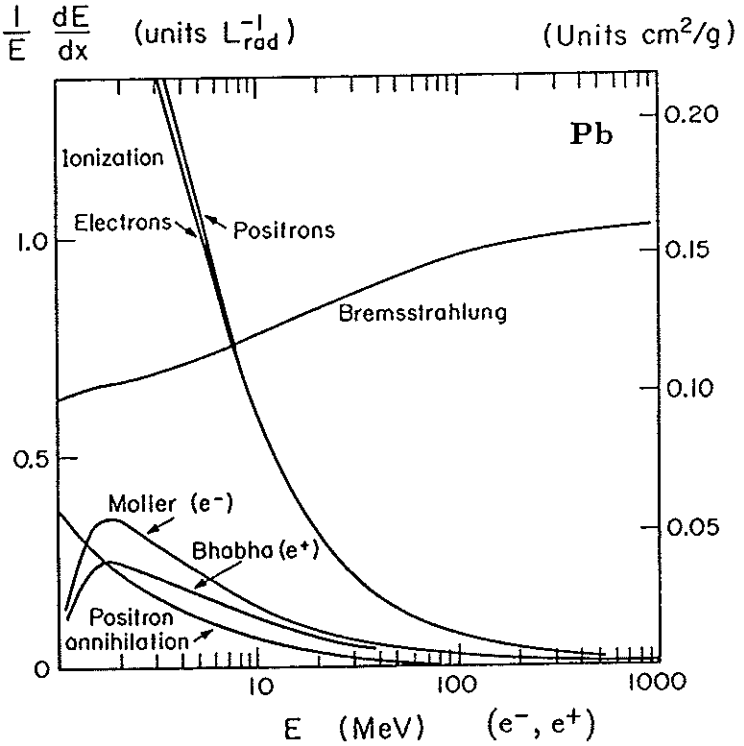

Figure 3.4a
Fractional energy loss per radiation length in Pb as a function of electron or positron energy [PDG90]. The longitudinal development of electron–photon cascades is approximately independent of the absorber when the results are expressed in units of inverse radiation lengths.

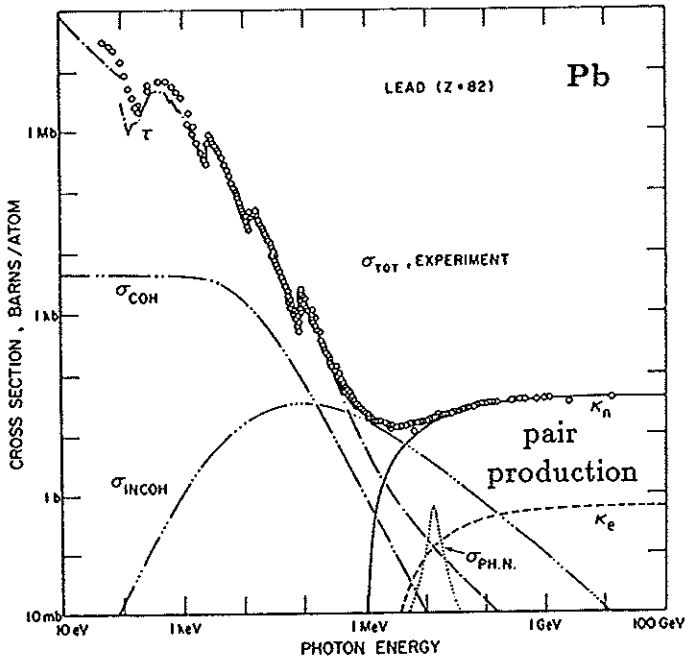

Figure 3.4b
Photon cross sections σ in Pb as a function of the photon energy, showing the contributions of different processes [PDG90].
τ = atomic photo-effect (electron ejection, photon absorption), σ_{COH} = coherent scattering (Rayleigh scattering – atom neither ionized nor excited), σ_{INCOH} = incoherent scattering (Compton scattering off an electron), κ_n = pair production (nuclear field), κ_e = pair production (electron field), $\sigma_{PH.N.}$ = photonuclear absorption
The intensity of photons can be expressed as $I=I_0e^{-\sigma x}$, where x [X_0] is the path length and σ [$1/X_0$] the photon cross section.

Material	Z	A [g]	$\rho[\frac{g}{cm^3}]$	$X_0[\frac{g}{cm^2}]$	X_0[cm]	R_M[cm]	$\lambda[\frac{g}{cm^2}]$	λ[cm]	λ/X_0
Polystyrene	≈3.4	-	1.060	43.8	41.3	14.7	82.0	77.4	1.87
Al	13	26.98	2.70	24.01	8.89	5.38	106.4	39.4	4.43
Fe	26	55.85	7.87	13.84	1.76	1.91	131.9	16.8	9.53
Pb	82	207.19	11.35	6.37	0.56	1.56	194.0	17.1	30.45
U	92	238.03	18.95	6.00	0.32	0.96	199.0	10.5	33.17

Table 3.1 Values of radiation lengths X_0 and interaction lengths λ for a few materials.

The energy loss by ionisation of an electron traversing one radiation length is called the critical energy ϵ_0:

$$\frac{dE}{dx}_{ion} = -\frac{\epsilon_0}{X_0},$$

where $\epsilon_0 \approx \frac{550}{Z}$ [MeV] with a precision of $\pm 10\%$ for $13 \leq Z \leq 92$.

For an electron with an energy ϵ_0 the energy loss by ionization and bremsstrahlung are approximately equal:

$$\left.\frac{dE}{dx}\right|_{ion} = \left.\frac{dE}{dx}\right|_{brems}.$$

In an electromagnetic shower ϵ_0 defines the dividing line between shower multiplication and energy dissipation through ionization.

A simplified consideration of the electromagnetic shower development at high energies taking into account only bremsstrahlung and pair production is described in [ROS52].

Precise calculations of electromagnetic showers, taking into account all known physical processes, cross sections and the detailed calorimeter configuration, can be performed using the Monte Carlo program EGS4 [NEL85], yielding reliable results in comparison to real measurements with a precision at the percent level.

Precise calculations of the maximum number of particles N_{max} in an electromagnetic shower and the depth t_{max} after which the shower maximum is reached yield [LOH90]:

$$N_{max} \approx \frac{0.31}{\sqrt{ln(E/\epsilon_0) - 0.25}} \frac{E}{\epsilon_0} \quad \text{and} \quad t_{max}[X_0] \approx ln(E/\epsilon_0) - \begin{cases} 1.1 & for\ electrons \\ 0.5 & for\ photons \end{cases}$$

Some fundamental properties of electromagnetic showers calculated and experimentally verified are indicated here and will be discussed in more detail later:

1) the energy measured in the calorimeter is proportional to the particle energy
2) the energy resolution $\sigma(E)/E$ is proportional to $1/\sqrt{E}$
3) longitudinal shower dimensions are proportional to a + b·lnE
   (e.g. at 10GeV, >98% of the shower is contained in $20X_0$)

3.3.2 Electromagnetic Shower Dimensions

Longitudinal Development of Electromagnetic Showers

The average longitudinal profile of electromagnetic showers can be approximately (analytically) described with Rossi's approximations [ROS52]:

1) the cross section for ionisation is energy independent ($dE/dx = -\epsilon_0/X_0$),
2) multiple scattering is neglected and the shower is treated one–dimensionally,
3) Compton–scattering is neglected.

A good parametrization of the longitudinal energy deposition $dE/dt(t)$ is given by [LON75]:

$$\frac{dE}{dt}(t) = E\frac{b^{\alpha+1}}{\Gamma(\alpha+1)}t^{\alpha}e^{-bt} ,$$

where E = the energy of the primary particle, $t = x/X_0$ depth from the calorimeter front face in units of X_0, t_{max} = position of the shower maximum, $\alpha = b \cdot t_{max}$ and $b \approx 0.5$. The parametrization for 1 GeV photons in Pb has for example the following form: $dE/dt(t) = E \cdot 0.06 \cdot t^2 e^{-t/2}$ [KLE84].

Figure 3.5 presents the longitudinal shower profiles of 6 GeV/c electrons in Al, Cu, Pb and U, showing the approximate scaling in units of radiation lengths X_0 [FAB85]. The deviation from exact scaling in X_0 is essentially due to the fact that X_0 is defined for GeV–type particles. The shift of the shower maximum to greater depths for high–Z absorbers is a result of particle multiplication down to lower energies and the shower decay beyond the shower maximum is due to lower–energy electrons which still radiate [FAB89].

The depth t_{med}, at which half of the energy of the incident particle is deposited is:

$$t_{med} = [\ln(\frac{E}{\epsilon_0}) + a] \text{ (with a = 0.4 or 1.2 for e's or } \gamma\text{'s)} .$$

The depths t_{med} and t_{max} are related approximately by [AMA81]: $t_{max}[X_0] \approx t_{med} - 1.5$.

The length L after which 98% of an electromagnetic shower is contained in a calorimeter is approximately [FAB85]:

$$L(98\%) \approx t_{max} + 4\lambda_{att} ,$$

where $\lambda_{att} \approx (3.4 \pm 0.5)[X_0]$ describes the exponential decrease of the shower after its maximum t_{max}. λ_{att} is almost energy independent, but material dependent.

Another approximation for the electromagnetic shower containment is given by [LOH83]:

$$L(98\%) \approx 3 \cdot t_{max} \quad \text{and} \quad L(90\%) \approx 2 \cdot t_{max} .$$

Transverse Development of Electromagnetic Showers

The transverse development of electromagnetic showers in the first, high energetic core of the shower, is characterized by both the emission of bremsstrahlung photons and multiple scattering. Multiple scattering of $e^{\pm}$ increases with decreasing energy of the shower particles and contributes to the lateral spread of the shower. The peripheral part of the shower is mainly dominated by the propagation of photons, that are less attenuated in matter in the region where the total cross section is minimal (e.g. at about 10–20MeV in lead) [AMA81].

The Molière Radius R_M gives a measure for the radial shower development and describes the average lateral deflection of electrons with an energy ϵ_0 after one radiation length X_0:

$$R_M = E_S \frac{X_0}{\epsilon_0} ,$$

where $E_S = 21\text{MeV}$ from multiple scattering theory.

An approximation of R_M is given by:

$$R_M \approx 7 \frac{A}{Z} \left[\frac{g}{cm^2}\right]$$

with a precision of $\pm 10\%$ for $13 \leq Z \leq 92$.

Figure 3.5 indicates for 6 GeV/c electrons on the right ordinate the radius R [R_M] for 90% shower containment as a function of the shower depth in X_0. It shows, that the lateral shower development scales approximately with the Molière radius R_M.

An electromagnetic shower is contained with a certain fraction of its energy in a cone with a mean radius R of about [KLE84]:

$$R(95\%) \approx 2 \cdot R_M \quad \text{and} \quad R(99\%) \approx 3 \cdot R_M .$$

The lateral spread of a shower grows with Z of the absorber material because R_M increases almost linearly with Z if R_M is measured in units of X_0:

$$R_M / X_0 = 21\text{MeV}/\epsilon_0 \approx 0.04 \cdot Z .$$

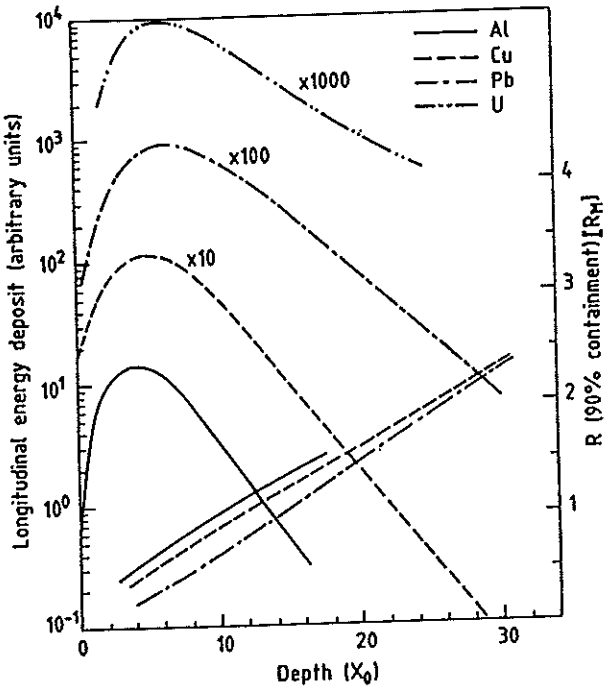

Figure 3.5
Longitudinal shower development (left ordinate) of 6 GeV/c electrons in Al, Cu, Pb and U, showing the scaling in units of X_0. The shower radius (right ordinate and lower curves) in units of R_M for 90% shower containment as a function of the shower depth [FAB85].

The radial shower distribution d(r) can be approximated by the sum of two exponential functions with r in units of R_M.

The transverse shower profile $dE/dx(x)$, where x describes the transverse horizontal coordinate in cm from the shower maximum, can be parametrized also by a combination of two exponential functions:

$$\frac{dE}{dx}(x) = A_1 e^{-|x|/B_1} + A_2 e^{-|x|/B_2} ,$$

with the parameters A_1, A_2 for the contributions and B_1, B_2 for the slopes of the two exponential functions. The spatial energy deposition $f(x,y,z)$ is integrated over the whole calorimeter depth $dE/dx(x) = \int f(x,y,z)dydz$, with y [cm] and z [cm] the vertical and longitudinal coordinates. The first exponential describes the high energetic core of the shower and the second one the low energetic halo.

3.4 Energy Resolution of Electromagnetic Sampling Calorimeters

For electromagnetic showers in sampling calorimeters the following relation is valid [DRE90]:

$$E_{vis} = eE \ ,$$

where E is the energy of the incident particle, E_{vis} the visible energy in the readout medium and e (:=R_e) the electromagnetic sampling fraction.

The electromagnetic energy resolution of sampling calorimeters can be expressed by:

$$\frac{\Delta E_{vis}}{E_{vis}} = \frac{\Delta e}{e} = \frac{a}{\sqrt{E}} \quad (E \text{ in GeV}) \ ,$$

where ΔE_{vis} represents the fluctuations of E_{vis} and Δe the fluctuations of the electromagnetic sampling fraction e (:=R_e), which produce the so–called electromagnetic sampling fluctuations.

All experimental data indicate that the parameter a is energy–independent and approximately proportional to $\sqrt{t}$, with t the thickness of an absorber plate. A parametrization of a is given by [FAB85]:

$$a = 3.2\%\sqrt{\Delta\epsilon[MeV]} \quad \text{with} \quad \Delta\epsilon = \mathrm{t}(\frac{dE}{dx})_t + \mathrm{s}(\frac{dE}{dx})_s \ ,$$

where $\Delta\epsilon$ represents the energy loss per sampling layer (t,s) in MeV.

The electromagnetic energy resolution of sampling calorimeters is usually dominated by sampling fluctuations. It can be improved by increasing the sampling frequency. Other effects such as photoelectron statistics σ_{pe} and light attenuation in the scintillator σ_λ degrade the energy resolution. For several ZEUS test calorimeters the influence of these effects is discussed in detail in chapter 4.5.3.

The energy resolutions for electrons measured with different electromagnetic sampling calorimeters are summarized in Table 3.2 [AMA81].

Calorimeter pas/act [mm]	Al/Scint 89/30	Fe/LAr 1.5/2.0	Cu/Scint 5/2.5	W/Si det. 7.0/0.2	Pb/Ar/CO_2 2.0/10.0	U/Scint 1.6/2.5
Energy resolution meas. at 1GeV [%]	20	7.5	13.0	25.0	$\leq$ 20.0	11.0

Table 3.2 Energy resolutions for electrons measured with different electromagnetic sampling calorimeters [FAB85].

3.5 Hadron Showers

3.5.1 Physical Description of Hadron Showers

A hadron shower or cascade is a series of successive hadronic interactions induced by a strongly interacting particle (p, n, $\pi^{\pm}$, ...).

The composition of hadron showers is much more complex in comparison to electromagnetic showers. Due to this complexity no simple analytic description exists for hadron showers and up to now their simulation is only approximate although detailed and complex Monte Carlo program packages have been developed e.g. CALOR, GHEISHA and HERMES.

A detailed qualitative description of the development of hadron showers can be found in [FAB85], [BRÜ86,87], [WIG87,91], [BER87] and [FAB89].

The elementary physical processes contributing to a hadron shower are illustrated by a simplified presentation in Fig. 3.6. The main characteristic properties of a hadronic cascade in the multi–GeV region are summarized in Table 3.3.

With high probability a charged hadron (p, $\pi^{\pm}$, ...), entering a calorimeter, will first lose energy by ionisation of the material before a hadronic interaction takes place.

For energies above 50 MeV the hadronic interaction of the incoming hadron with the nucleons of the absorber material will induce a spallation process. This process consists of many independent particle collisions inside the nucleus followed by a deexitation through p, n, $\pi^{\pm}$, π^0, γ, ... particle emission and evaporation. By this intranuclear cascade new particles are emitted if their kinetic energy is above the binding energy. Further intranuclear cascades may be induced along the shower axis.

High energy ($\gtrsim$50MeV) pions, protons and neutrons can additionally induce a fission of heavy nuclei.

Nuclear fragments and excited nuclei are produced thus nuclear binding energy is lost in the absorber and is no longer available for a measurable signal.

Deexitation will also proceed via γ–emission. Most γ's are prompt, whereas neutron capture of ^{238}U leads to a delayed γ–radiation up to 1 μs [ARM83].

In addition to the pure hadronic process a significant electromagnetic contribution to the hadron shower is produced by neutral pions, η's etc decaying into photons ($\pi^0 \rightarrow \gamma\gamma$). The electromagnetic fraction of a hadron induced shower increases with incident energy. This increase is due to the secondary π^0's which will propagate electromagnetically without any further nuclear interactions. This electromagnetic fraction fluctuates strongly from event to event.

Neutrinos leave the calorimeter volume undetected; muons behave in many cases similar to minimum ionizing particles and may leave the calorimeter after deposition of a certain fraction (e.g. a few GeV) of their initial energy.

The hadronic cascade starts to die out, when the energies of the shower particles become so small, that they are completely absorbed.

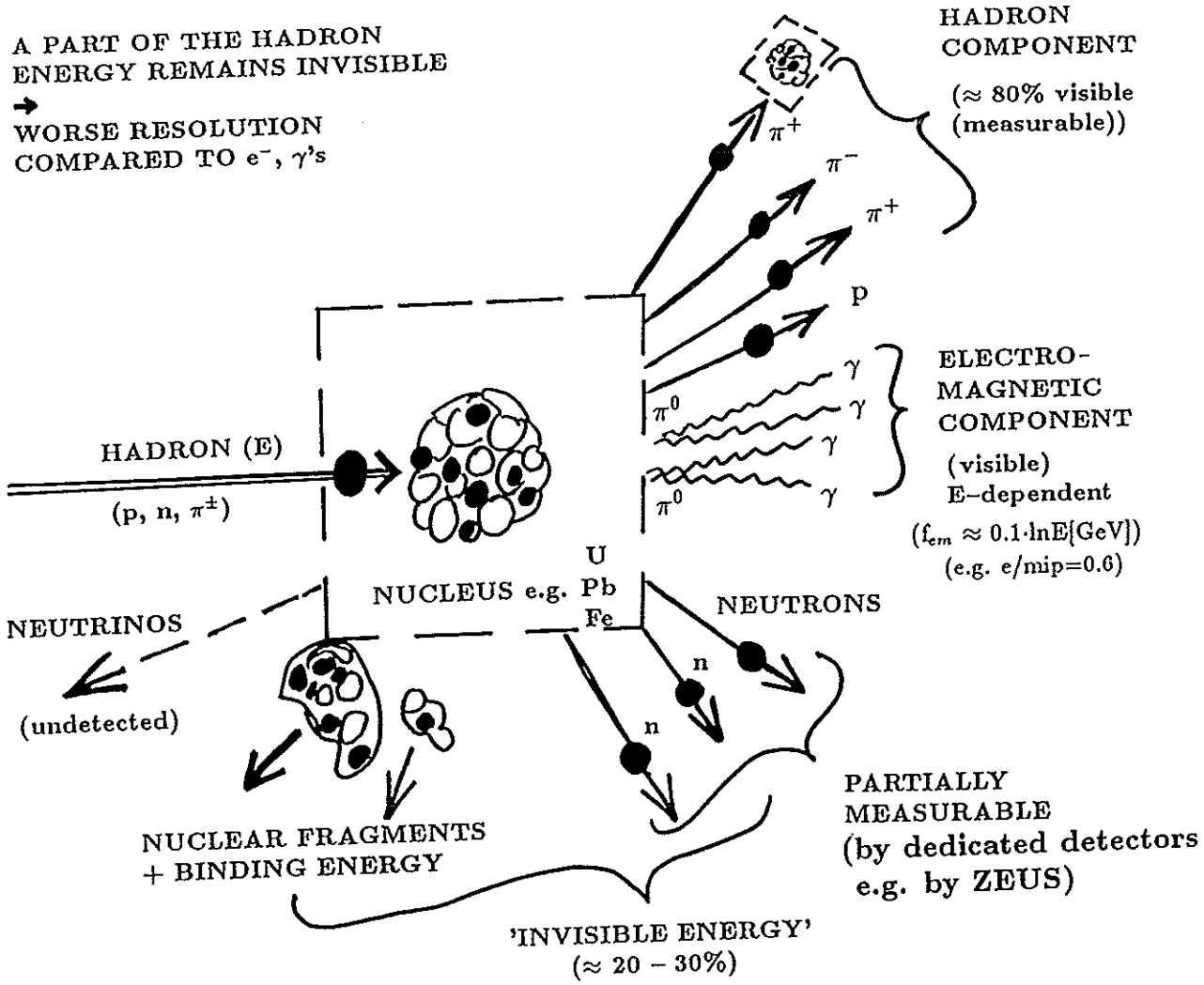

Fig. 3.6 'Elementary physical process' in a hadron shower.

Reaction	Properties	Influence on energy resolution	Characteristic time (s)	Characteristic length (g/cm^2)
Hadron production	Multiplicity $\simeq A^{0.1} \ln s$	π^0/π^+ ratio Binding energy loss.	10^{-22}	Abs. length $\lambda \simeq 35\frac{A^{1/3}}{\rho}$
Nuclear de-excitation	Evaporation energy ≃ 10% Binding energy ≃ 10% Fast neutrons ≃ 40% Fast protons ≃ 40%	Binding energy loss. Poor or different response to n, charged particles, and γ's.	10^{-18}–10^{-13}	Fast neutrons $\lambda_n \simeq 100$ Fast protons $\lambda_p \simeq 20$
Pion and muon decays	Fractional energy of μ's and ν's ≃ 5%	Loss of ν's partial loss of μ's	10^{-8}–10^{-6}	$\gg \lambda$
Decay of c, b particles produced in multi-TeV cascades	Fractional energy of μ's and ν's at percent level	Loss of ν's, part. μ's Tails in resolution function.	10^{-12}–10^{-10}	$\ll \lambda$

Table 3.3 Characteristic properties of the hadronic cascade [FAB85].

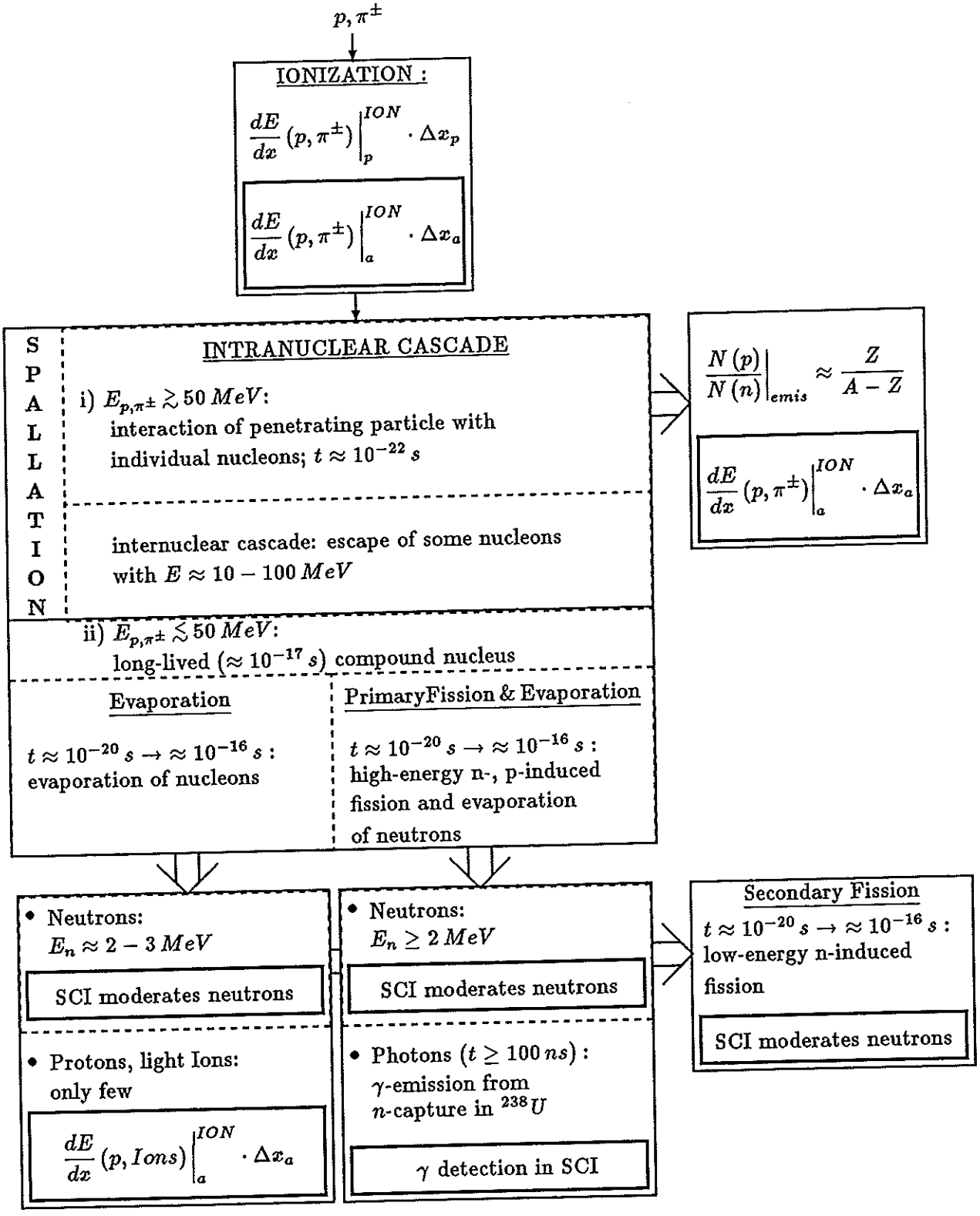

Figure 3.7
Block diagram of the simplified pure hadronic part of a hadron shower in a uranium scintillator calorimeter [BER87]; the bold frames indicate the sources of measurable signals; $dE/dx\,(p,\pi^{\pm},Ions)|^{ION}\,\Delta x_{a\,(p)}$ = ionization loss in the scintillator (a) or the uranium (p); $N\,(p)/N\,(n)$ = number of protons to number of neutrons released during the intranuclear cascade; Z and A = atomic and mass number; SCI = scintillator.

The subsequent processes of the purely hadronic part of the shower in a uranium scintillator calorimeter are described in Fig. 3.7. Spallation is essentially considered as a process, which happens in two phases. The time scales for the individual physical processes are indicated and the sources for a measurable signal in the scintillator are pointed out by bold frames.

Figure 3.8a presents the results of Monte Carlo calculations on the energy fractions of the different physical processes contributing to the hadronic shower as a function of the energy of the incoming hadron (proton) [GAB89]. It shows, that the electromagnetic fraction increases approximately logarithmically (0.1·lnE[GeV]) with the energy of the primary particle.

Figure 3.8b presents the energy fractions w.r.t. the hadronic energy (B+C+D of Fig. 3.8a) as a function of the energy of the incoming hadron. It illustrates, that the fractions of hadronic energy (f_{ion}, $f_{B,\nu,\gamma}$, f_n) are approximately independent of the energy of the incoming hadron for energies above $\approx$ 2GeV.

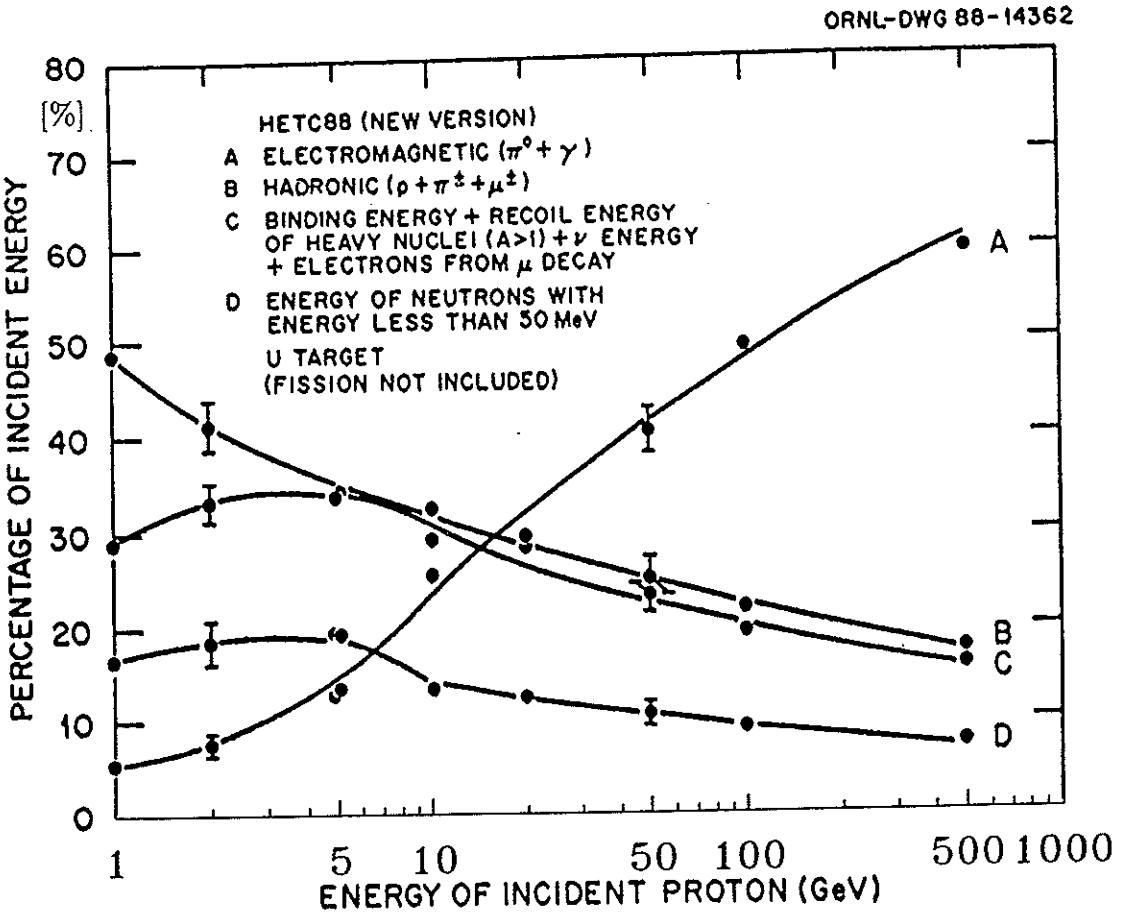

Fig. 3.8a Fractions of the deposited energy (A+B+C+D) for an infinite uranium block as a function of the incident proton energy [GAB89].

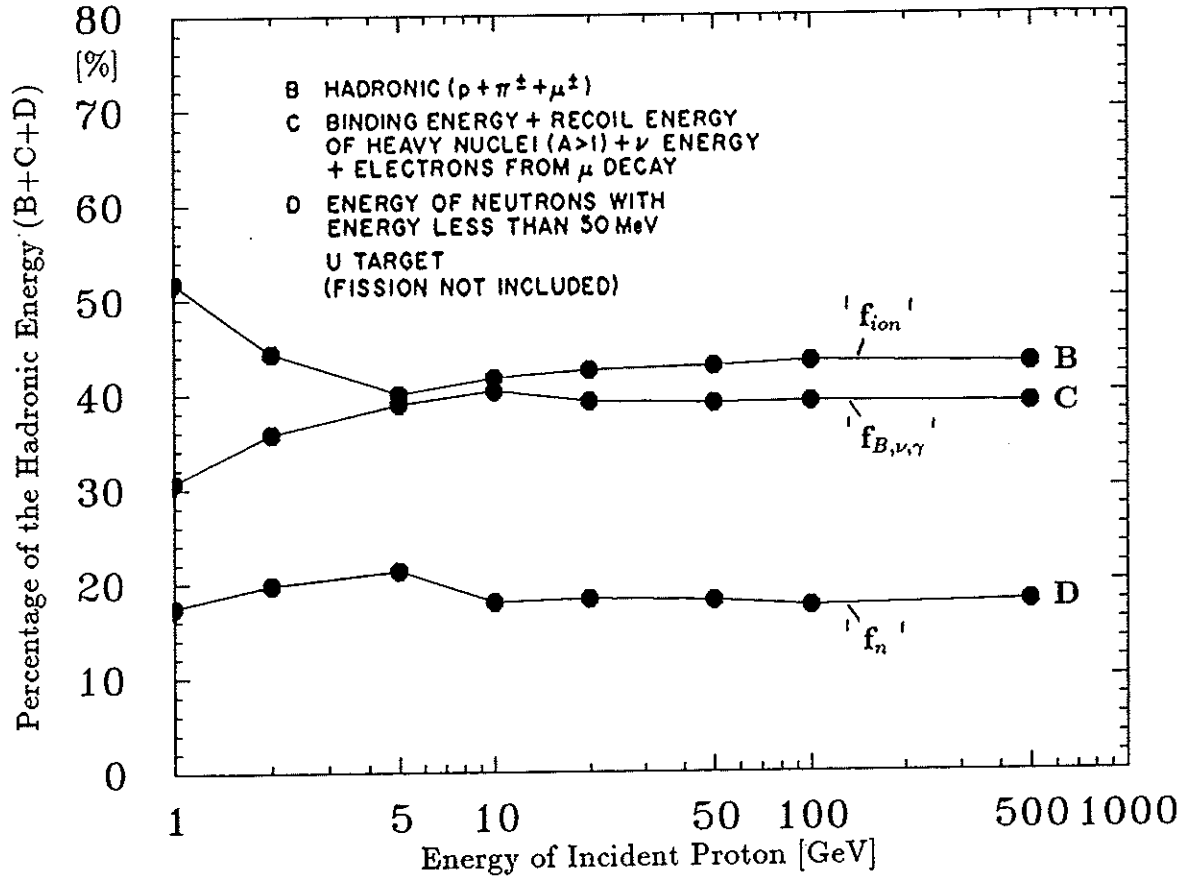

Fig. 3.8b Fractions of the deposited hadronic energy (B+C+D) for an infinite uranium block as a function of the incident proton energy.

3.5.2 Hadron Shower Dimensions

Longitudinal Development of Hadron Showers

For the longitudinal and transverse development of hadron showers the material independent measure is the nuclear interaction length λ. It is defined by:

$$\lambda = \frac{A}{N_A \cdot \sigma_i} \left[\frac{g}{cm^2}\right] ,$$

where A = mass number of the absorber, N_A = Avogadro number and σ_i = inelastic cross section.

A good approximation for λ is given by:

$$\lambda = 35 \, \frac{A^{1/3}}{\rho} \, [\mathrm{cm}] ,$$

where ρ = the specific density [g/cm^3].

For a few materials the values of λ are summarized in Table 3.1. These values are significantly larger than the radiation lengths X_0 for high A materials and indicate already, that hadron calorimeters have to be much more massive than electromagnetic calorimeters. Showers of 300GeV pions are for example contained at the 95% level in about 80cm uranium, while for 300GeV electrons a depth of 10cm uranium is sufficient (chapter 4.2), [KRÜ86b,90e], [FAB89]. Typical dimensions of iron hadron calorimeters at 300GeV are e.g. 2m length and 1m transverse, while for em iron calorimeters a total length of only 0.5m and about 0.15m transverse are necessary.

The longitudinal profiles of hadron showers starting from the interaction point with momenta from 5GeV/c to 210GeV/c are presented in Fig. 3.9. They have been measured at CERN with the longitudinally fine segmented WA78–H1–ZEUS sampling calorimeter with a length of 13λ (5.4λ U/Scint plus 8λ Fe/Scint) built of 10mm U (25mmFe) absober plates interleaved with 5mm scintillator layers and read out by associated photomultipliers [KRÜ86], [CAT87].

A phenomenological function has been fitted to the data. The parametrization of the energy deposit dE/dx(x) as a function of the distance x in interaction lengths from the shower vertex is:

$$\frac{dE}{dx}(x) = E \cdot \left\{ \alpha \, \frac{b^{a+1}}{\Gamma(a+1)} \, x^a \, exp\,(-bx) \; + \; (1-\alpha)\, c \, exp\,(-cx) \right\},$$

where E is the incident energy, a=3, $b[\lambda^{-1}]$=19.5, α=0.13±0.02 and $c[\lambda^{-1}]$=(0.67±0.03)-(0.166±0.003) ln(E[GeV]/50). This parametrization was adjusted, starting from [BÖC81], for the longitudinal segmentation in steps of 0.45λ in the uranium and 0.62λ in the iron part of the WA78 calorimeter. The function describes well the data for energies above 10GeV. Further results of this test, in particular studies on shower containment and calorimeter length are discussed in full detail in chapter 4.2.

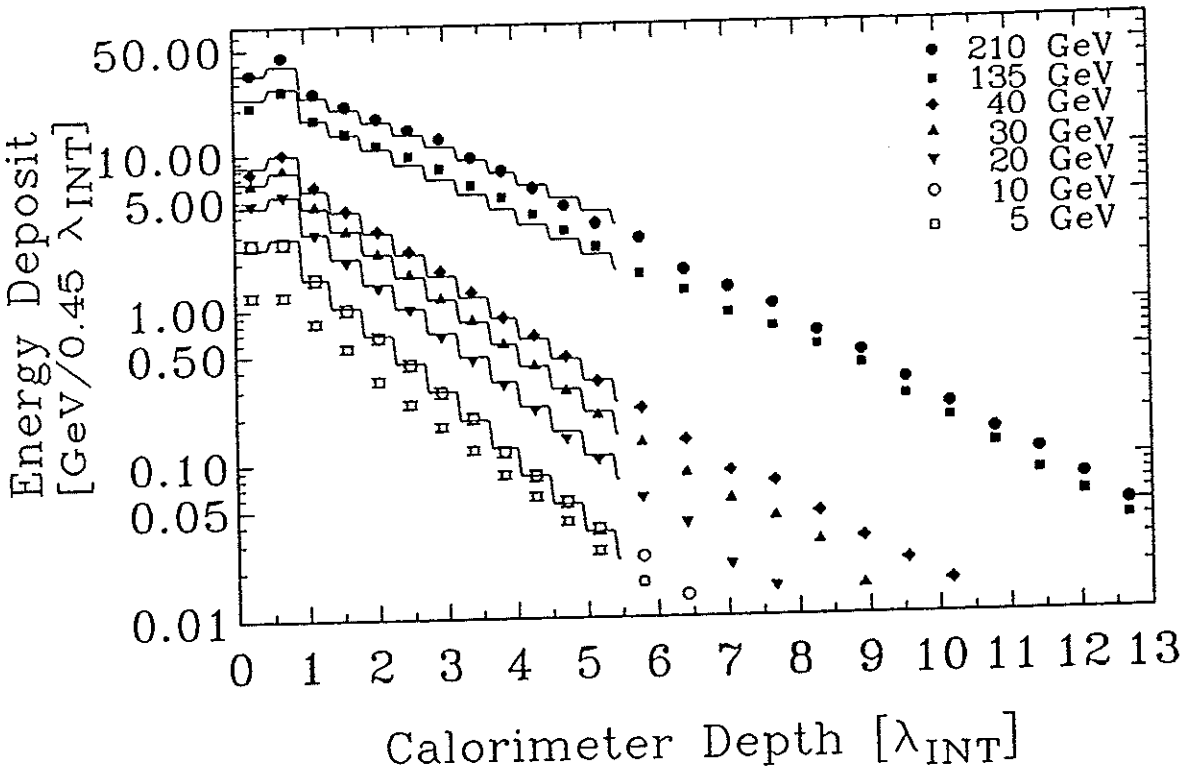

Fig. 3.9 Longitudinal shower profiles for hadrons between 5 to 210 GeV for events with shower vertices in the first 0.45λ.

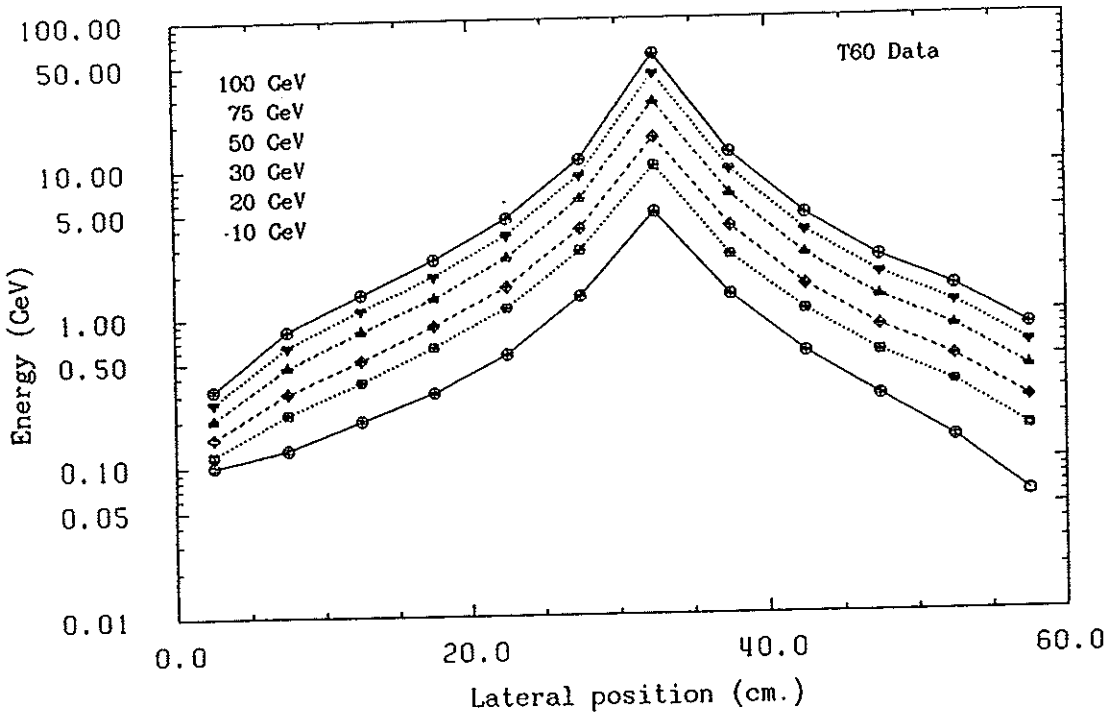

Fig. 3.10 Transverse projections of shower profiles, integrated over the whole calorimeter depth, for hadrons between 10 to 100GeV. The lines are meant to guide the eye.

The length L of a calorimeter, after which 95% of the energy of a hadron shower is contained can be described by the parametrization [FAB85]:

$$L(95\%) \approx t_{max} + 2.5 \cdot \lambda_{att} ,$$

where $t_{max}[\lambda] \approx 0.2 \cdot \ln E[GeV] + 0.7$ is the position of the shower maximum measured from the entrance face of the calorimeter and $\lambda_{att} \approx \lambda(E[GeV])^{0.13}$ describes the exponential decrease after t_{max}. For high Z materials the energy dependence of λ_{att} becomes a little bit weaker.

Transverse Development of Hadron Showers

Hadron showers have highly energetic narrow cores with widths of about 0.1 to 0.5λ (FWHM), which increase with shower depth. For 95% radial containment of a hadron shower a cylinder with a radius of R is necessary [FAB85]:

$$R(95\%) \lesssim \lambda .$$

R does not really scale with λ and decreases for high Z materials.

The lateral spread of 30GeV/c hadron showers in the ZEUS FCAL prototype calorimeter is presented in Fig. 5.40 [BEH89].

The transverse hadron shower profile $dE/dx(x)$, where x describes the transverse horizontal coordinate of the calorimeter in cm from the shower maximum, can be parametrized like electromagnetic ones by a combination of two exponential functions:

$$\frac{dE}{dx}(x) = A_1 e^{-|x|/B_1} + A_2 e^{-|x|/B_2} ,$$

with the parameters A_1, A_2 for the contributions and B_1, B_2 for the slopes of the two exponential functions. The spatial energy deposition $f(x,y,z)$ in the calorimeter is integrated over the whole calorimeter depth $dE/dx(x) = \int f(x,y,z)dydz$, with y [cm] and z [cm] the vertical and longitudinal coordinates. The first exponential describes the high energetic core of the hadron shower and the second one the low energetic halo [BAR89].

Figure 3.10 shows the transverse shower profiles of hadrons with energies from 10GeV to 100GeV measured with the ZEUS T60 uranium scintillator test calorimeter [AGO89]. The fits with the indicated parametrization are in good agreement with the measured data [BAR89]. Further results of the T60 calorimeter test are presented in chapter 4.5.

3.6 Monte Carlo Shower Simulations

Monte Carlo simulations are very helpful in optimizing the calorimeter design. The simulation of electromagnetic and hadronic showers provide important information on the physical properties of this calorimeter, e.g. the ratios of e/mip, e/h, etc ... on the energy resolution.

There exist various Monte Carlo simulation packages. The EGS [NEL85] program package provides an excellent simulation of electromagnetic showers. It represents the world standard for electron and photon shower simulations. For hadronic showers various elaborate simulation packages exist, e.g. CALOR, HERMES, NEUKA, GHEISHA etc ...

In order to analyse and compare the results of the various ZEUS calorimeter tests carried out to determine the best design for the ZEUS calorimeter, hadron shower simulations were performed [ZEU89], in particular with the simulation package HERMES. HERMES was derived from CALOR [GAB85], developed at ORNL (Oak Ridge National Laboratory).

HERMES (High Energy Radiation Monte–Carlo Elaborate System) [CLO87] simulates all known individual physical processes of photons, electrons and hadrons in the absorber plates and active layers down to very low energies ($\approx$ 10keV), using measured cross sections and the precise calorimeter configuration. As a consequence of such detailed event–by–event simulation a large amount of computing time is necessary; thus HERMES has been applied for selected questions of calorimetry.

Figure 3.11 describes as an example the organization of HERMES. HERMES represents a collection of various Monte Carlo codes, which have been selected, improved and completed for the simulation of high energy hadron showers in calorimeters.

HETC–KFA simulates the high energy hadron processes, MORSE–KFA the low energy particle transport of neutrons and gammas and EGS–KFA the electromagnetic shower component. SIM and STATIST provide detailed information on the shower properties and the calorimeter response.

The standard input/output coupling system between the different HERMES Monte Carlo codes is presented in Fig. 3.12. Each MC code can run independently of the other ones.

The computing times necessary for the most important codes of HERMES are summarized in Table 3.4 per GeV incident energy for an IBM 3081 (calorimeter test T35). About 3.1 seconds CPU time are overall needed per GeV. The simulation can be sped up by code vectorization [ZEU89].

Monte Carlo Codes in HERMES		CPU time [s]/GeV
HET/SIM	(hadron cascade)	0.4
EGS	(electromagnetic cascade)	0.6
MORSE	(neutron and gamma transport)	2.1
in total		3.1

Table 3.4 Computing time for hadron shower simulation with HERMES for the T35 calorimeter test in seconds per GeV incident energy (CPU time on an IBM 3081).

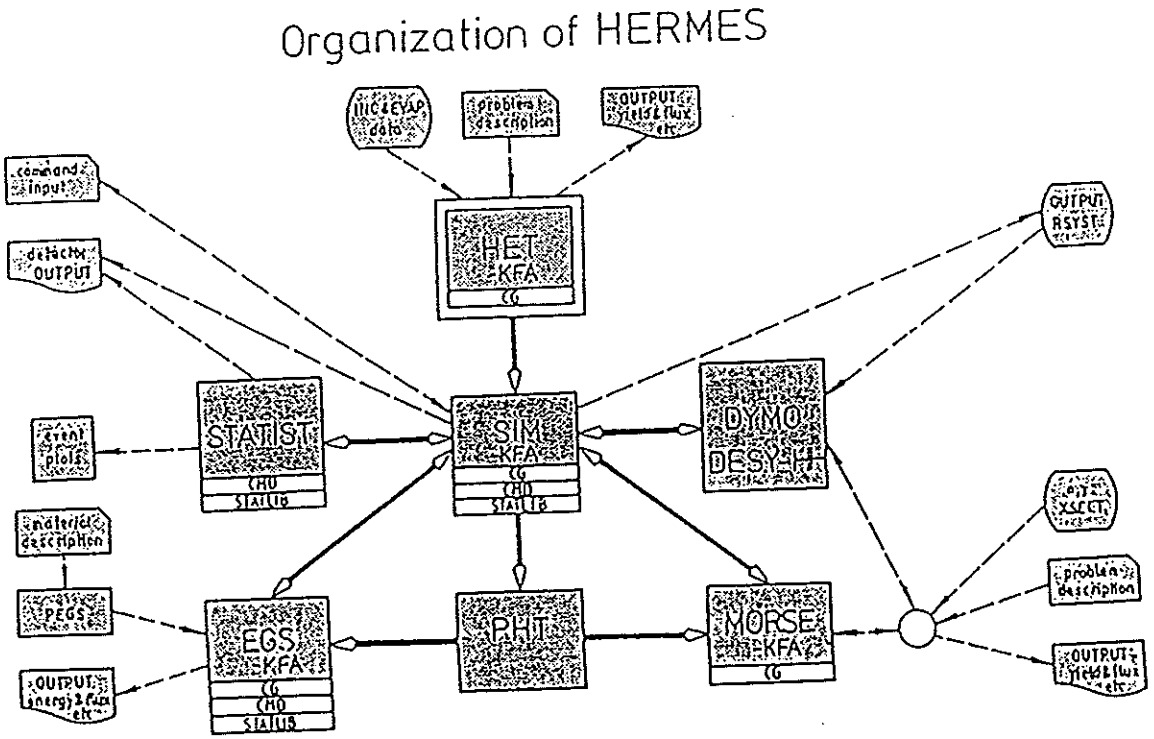

Fig. 3.11 Organization of HERMES.

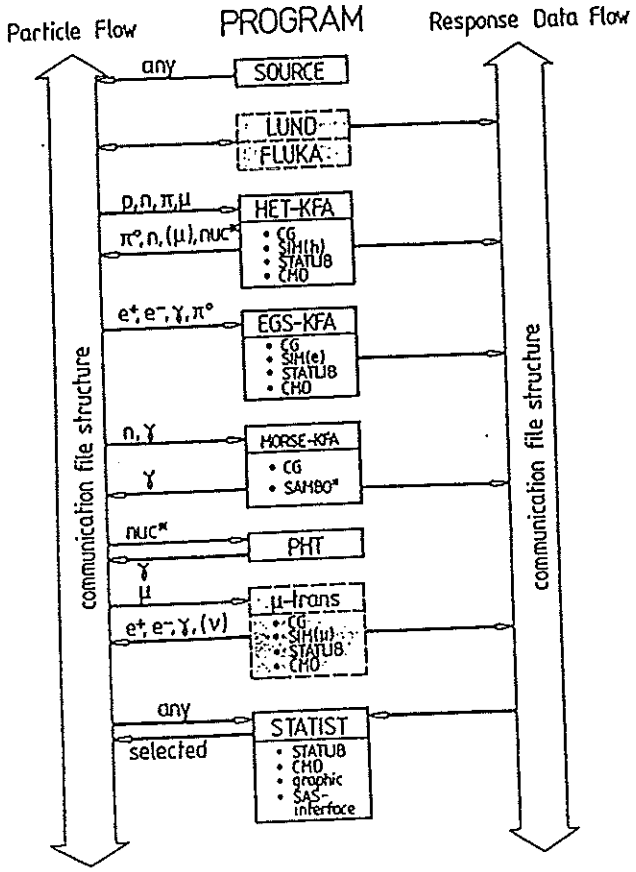

Fig. 3.12 Scheme of the HERMES Monte Carlo programs for calorimeter simulations.

3.7 Energy Resolution and Compensation in Hadron Sampling Calorimeters

The energy resolution of hadron sampling calorimeters is significantly worse in comparison to electromagnetic (em) sampling calorimeters. This is the result of the different physical contributions to a hadron shower, giving different measurable signals for the same amount of deposited energy. Furthermore the relative fractions of these different contributions fluctuate from event to event.

Fabjan and Willis realized that for hadron calorimeters the energy resolution is strongly affected by the loss of binding energy [FAB77]. For 10GeV incoming $\pi^{\pm}$ about 20% of the energy is spent on binding energy. However, in the nuclear breakup neutrons (n) are produced, $N_n \sim E_{Bind}$. Hence if one is able to detect the neutrons with a certain response it should be possible to compensate for E_{Bind} loss. A prototype was built and verified this [BOT81]. Tuning of the neutron signal by changing the scintillator thickness of a uranium scintillator calorimeter was proposed by Brückmann [BRÜ86] and has lead to a compensating calorimeter yielding equal response to electrons and hadrons.

The energy resolution σ/E for conventional hadron calorimeters scales as $1/\sqrt{E}$ + const. Typical values of σ/E for sampling sandwich calorimeters with 1–2X_0 thick absorber plates of Fe or Pb, are in the order of $0.5/\sqrt{E}$ to $0.9/\sqrt{E}$ (E in GeV) plus an additional term of a few %. A significant improvement was reported by Fabjan and Willis for uranium liquid argon sampling calorimeters [FAB77]. A reanalysis of the data showed only a marginal improvement [REH85]. However a uranium calorimeter with scintillator readout (2mm/3mm U, 2.5mm Scint) showed an energy resolution as good as $0.33/\sqrt{E}$ [BOT81] and [AKE87]. On the other hand a uranium scintillator calorimeter with 10mm U and 2.5mm Scint showed an energy resolution of $0.5/\sqrt{E}$ [CAT87] (chapter 4.2) similar to that of conventional calorimeters.

These results show, that the energy resolutions for hadrons depend not only on the choice of active and passive material, but also on correct thicknesses of the passive and active layers.

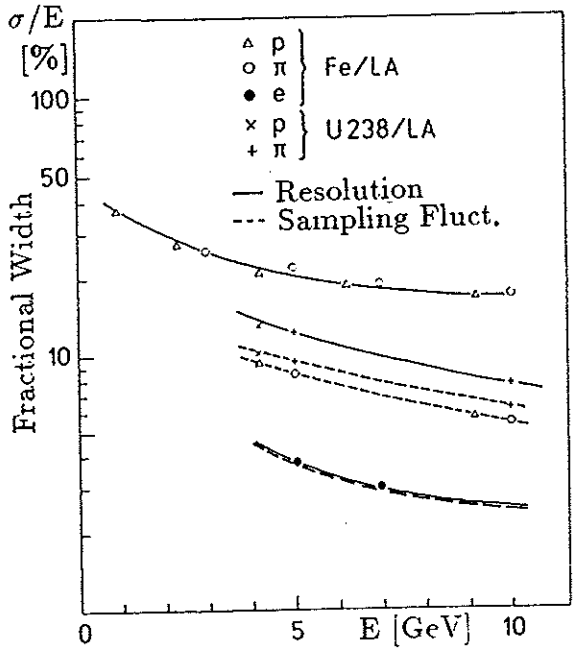

Figure 3.13
Energy resolution and contribution from sampling fluctuations for electromagnetic and hadron showers.

Figure 3.13 presents for comparison the contribution of sampling fluctuations to the energy resolution of em and hadron showers in sampling calorimeters (Fe/LAr, U/LAr). The electromagnetic energy resolution is completely dominated by sampling fluctuations. The hadronic energy resolution has in addition strong contributions from other effects [FAB77], [TIE89], [DRE90]. How sampling fluctuations can be measured is presented in detail in chapter 4.5.3.

For hadron showers in sampling calorimeters the following relation is valid [DRE90]:

$$E_{vis} = hE \ ,$$

with the hadronic sampling fraction h.

The energy E of the hadron shower consists of the following components:

$$E = E_{em} + E_{\pi} + E_p + E_n + E_{Nucl} \ ,$$

where E_{em} is the energy of the electromagnetic component (mainly from π^0s), E_{π} that of the charged pion component, E_p that of the proton component, E_n that of the neutron component and E_{Nucl} is the energy lost to nuclear binding energy (sometimes called "invisible energy") or taken by nuclear fragments. Each component has its own sampling fraction. The detection efficiency of the readout medium for the different components plays an important role and is included in the sampling fractions.

The visible energy of a hadron shower in a sampling calorimeter is then given by:

$$E_{vis} = eE_{em} + \pi E_{\pi} + pE_p + nE_n + NE_{Nucl} \ ,$$

where e, π, p, n and N represent the sampling fractions of the different shower components.

In hadron showers the fluctuations of the visible energy have two different origins:

- Fluctuations of the sampling fractions, denoted by Δe, $\Delta \pi$, etc. for the different sampling fractions e (:=R_e), π (:=R_{π}) etc. , produce the so-called "sampling fluctuations" (σ_{samp}). They can be reduced by increasing the sampling frequency.
- Fluctuations of the energy fractions of the different shower components, ΔE_{em}, ΔE_{π}, etc., through the different sampling fractions, produce the so-called "intrinsic fluctuations" (σ_{intr}).

The fractional energy resolution of hadron sampling calorimeters can then be expressed by the following empirical formula:

$$\frac{\Delta E_{vis}}{E_{vis}} = \frac{\Delta h}{h} = \sigma_{samp} \oplus \sigma_{intr} \ ,$$

where σ_{samp} is a function of $\sqrt{t}$ and σ_{intr} is a function of R (=t/s, t thickness of an absorber plate and s of a readout layer).

A parametrization of σ_{samp} for experimental data is given by [FAB85]:

$$\sigma_{samp} = \frac{a}{\sqrt{E}} \qquad (E \text{ in GeV})$$

with $a = 9.0\%\sqrt{\Delta\epsilon[MeV]}$.

A parametrization of σ_{intr} for experimental data and Monte Carlo calculations has the following form [WIG87]:

$$\sigma_{intr} = \frac{b}{\sqrt{E}} + c \ ,$$

where c depends on the e/h ratio and vanishes for compensating calorimeters.

These results show, that for compensating hadron calorimeters both σ_{samp} and σ_{intr} scale with $\sqrt{E}$ and therefore the hadron energy resolution does so as well.

Frequently sampling fluctuations σ_{samp} dominate the total hadronic energy resolution. They have a purely statistical nature due to the sampling of the showers and contribute as $a/\sqrt{E}$ to the energy resolution. In sampling sandwich calorimeters with fixed thicknesses of passive (t) and active (s) planes the contribution of sampling fluctuations to the energy resolution tends to scale as $\sqrt{t}/\sqrt{E}$ [FAB89].

Sampling fluctuations of hadronic showers are significantly larger compared to those of electromagnetic showers. The number of different shower particles contributing to the hadronic signal is smaller. Individual hadronic shower particles such as protons may traverse many sampling layers and deposit on average more energy in the active layers with a much larger spread in the dE/dx loss than electrons.

Intrinsic fluctuations σ_{intr} are created for example by fluctuations in the fraction of the initial energy transformed into ionizing shower particles. The main factors which drive the intrinsic fluctuations of hadron sampling calorimeters are: 1) the binding energy needed for nuclear break up and 2) the difference between e/mip and h/mip. Intrinsic fluctuations set the limit for the energy resolution achievable for a hadron calorimeter. For instance, the electromagnetic contributions in hadron showers created from π^0–decays yield non–Gaussian fluctuations and an additional constant term to the energy resolution. This term only vanishes if compensation (e/h=1) is achieved.

The energy resolution for well designed hadron calorimeters, neglecting instrumental effects such as shower leakage, calibration nonuniformities, etc., can be described by [FAB89]:

$$\frac{\sigma_{had}}{E} = \sqrt{\frac{c_{intr}^2 + c_{samp}^2}{E}} + C \ .$$

The energy resolution improves with increasing energy and is dominated at high energies by the constant term C. The value of C depends in first approximation on the degree of compensation and vanishes if compensation is achieved. In addition this formula indicates, that an increase of the sampling frequency doesn't make sense if intrinsic fluctuations dominate.

The contributions of sampling fluctuations and intrinsic fluctuations to the energy resolution for hadrons can be determined by comparing the energy resolutions measured with different fractions of the calorimeter readout layers (chapter 4.5.3) [FAB77], [TIE89], [DRE90].

In order to find the optimum parameters for a calorimeter configuration with the best possible energy resolution for hadrons, the relevant quantities, which create the different fluctuations, in particular the intrinsic fluctuations, have to be known and understood. These quantities are presented and discussed in the following section. Methods are presented of how to minimize the effects of fluctuations in hadronic showers. This is demonstrated using the ZEUS uranium scintillator calorimeter as example.

The relative sampling fraction (relative measurable signal) of electrons is given by the response ratio e/mip (chapter 3.2). The corresponding sampling fraction of the pure hadronic (intrinsic) part of the hadron shower, without electromagnetic contributions from π^0 decays, is described by the experimentally not measurable response ratio h_i/mip of a calorimeter. The signals measured for electrons S(e) and hadrons S(h) can be expressed by:

$$S(e) = kE \cdot \frac{e}{mip}$$

and

$$S(h) = kE \cdot [f_{em}\frac{e}{mip} + (1 - f_{em})\frac{h_i}{mip}] ,$$

where k represents the calibration constant for a specific calorimeter configuration and f_{em} describes the electromagnetic energy fraction in a hadron shower, which grows logarithmically with the energy E of the primary hadron (Fig. 3.8); $f_{h_i} = (1 - f_{em})$ is the hadronic fraction.

The signal ratio for electrons and hadrons (e/h) is then:

$$\frac{S(e)}{S(h)} = \frac{e/mip}{f_{em} \cdot e/mip + (1 - f_{em}) \cdot h_i/mip} .$$

If the ratio e/h does not equal 1, then the electromagnetic fraction, which is strongly fluctuating from event to event, yields a significant contribution to the width of the hadron pulse height distribution.

A simplified but illustrative consideration of a conventional calorimeter with e/h=1.4 shows clearly the degradation of the energy resolution [WOL86]. The assumptions are:

- the shower consists only of $\pi^{\pm}$ and π^0 (electromagnetic fraction),
- on average the contribution to the energy of $E(\pi^{\pm}) : E(\pi^0)$ is 2 : 1 ,
- large fluctuations of $E(\pi^{\pm}) : E(\pi^0)$ from event to event.

For example:

$E_{\pi^{\pm}}$	:	E_{π^0}		relative Signal S(h)
3	:	0	→	1.0
2	:	1	→	1.13
1	:	2	→	1.27
0	:	3	→	1.4

This simple example illustrates, that the distribution of hadron pulse heights becomes very broad and the energy resolution is degraded if e/h $\neq$ 1.

Figure 3.14 shows experimental results of the ZEUS calorimeter test T60 [AGO89] (chapter 4.5) on the influence of the e/h–ratio on the hadronic energy resolution. For comparison the pulse height distributions of 5GeV electrons, hadrons and muons are presented for a non–compensating lead scintillator calorimeter (5mm Pb, 5mm Scint) with e/h=1.3 (a) and a depleted–uranium scintillator calorimeter (3.2mm DU, 5mm Scint (not yet optimized for compensation)) with e/h=1.07 (b). This result illustrates, that with an e/h–ratio closer to 1, the width of the hadron pulse height distribution is significantly reduced and the energy resolution is strongly improved.

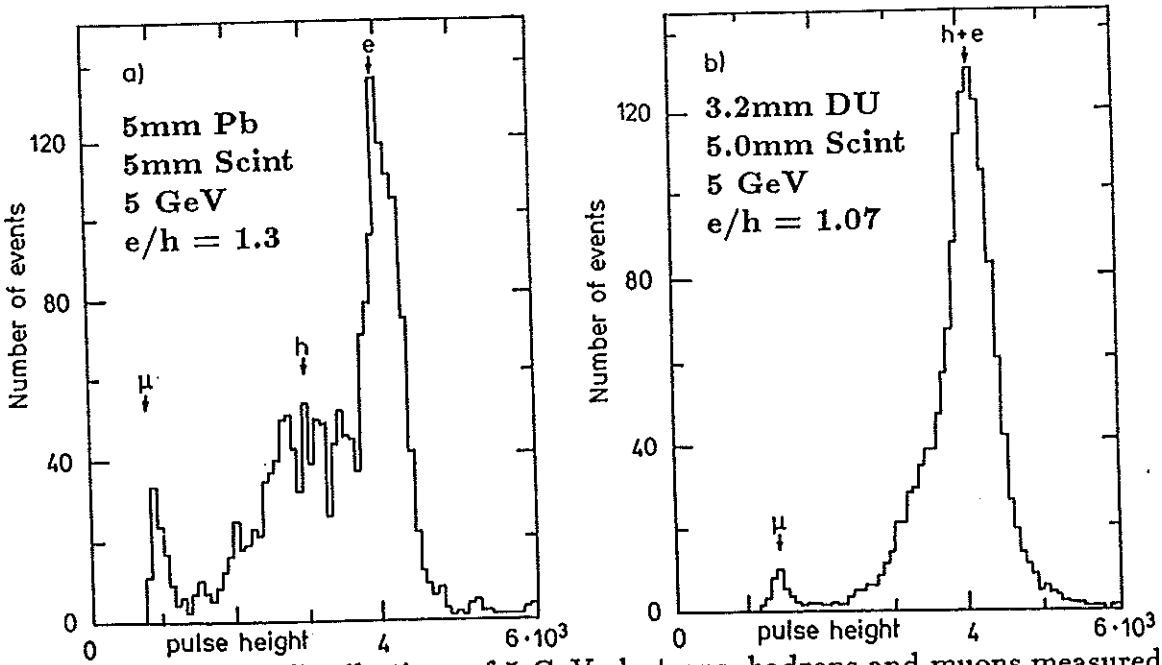

Fig. 3.14 Pulse height distributions of 5 GeV electrons, hadrons and muons measured with a lead scintillator (5mm Pb, 5mm Scint) calorimeter (a), and a depleted–uranium scintillator (3.2mm DU, 5mm Scint) calorimeter (b) (ZEUS).

Methods to Minimize the Effects of Fluctuations on the Hadron Response

In order to achieve compensation (e/h=1), to get the best possible energy resolution for hadrons, in principle two ways are possible: either by a reduction of the e/mip–ratio (by software) or by an increase of the h_i/mip–ratio (by hardware).

The different shower components and their influence on the e/h–ratio and the hadron response will be discussed in the following.

By Software – Weighting of the Local Electromagnetic Energy Depositions

If the spatial information in a noncompensating calorimeter is sufficient to recognize highly localized depositions of electromagnetic energy from $\pi^0 \rightarrow \gamma\gamma$ decays, then the electromagnetic contribution to the hadron signal can be reduced by weighting so that e/h=1. Thus fluctuations in the hadron response due to the electromagnetic content will be reduced and the energy resolution will improve. Suitable weighting algorithms have been developed and successfully introduced by the CDHS [HOL78], [ABR81] and H1 collaborations [BRA88].

Figure 3.15 shows the energy resolution of the 2.5cm iron/scintillator sampling calorimeter of the CDHS collaboration as a function of the incident particle energy [ABR81]. Every 5 layers were read out by a separate photomultiplier. The energy resolution without weighting increases from about $60\%/\sqrt{E}$ at 10GeV to about $100\%/\sqrt{E}$ at 160GeV pion energy. After weighting the energy resolution improves to about $58\%/\sqrt{E}$ over the full energy range.

Figure 3.16 and 3.17 present results from a lead–copper/liquid argon test calorimeter (1st part: 1.1λ (2.4mm Pb), 2nd part: 6.1λ (5mm Cu)) of the H1 collaboration [BRA88]. The hadronic section was read out longitudinally by 57 readout boards. The weighting method relies on the frequent longitudinal sampling.

Figure 3.16 shows the calorimeter response of 50GeV pions and electrons before (a) and after (b) software weighting. The weighting equalizes the response of pions and electrons, thus the energy resolution of pions is improved by removing "tails" due to fluctuations in the em content of the hadron shower [BRA88], [KÜS91]. Figure 3.17 presents the energy resolution without and with weighting as a function of the pion energy from 30GeV to 230GeV. After weighting a hadronic energy resolution of about $50\%/\sqrt{E}$ was obtained [BRA88].

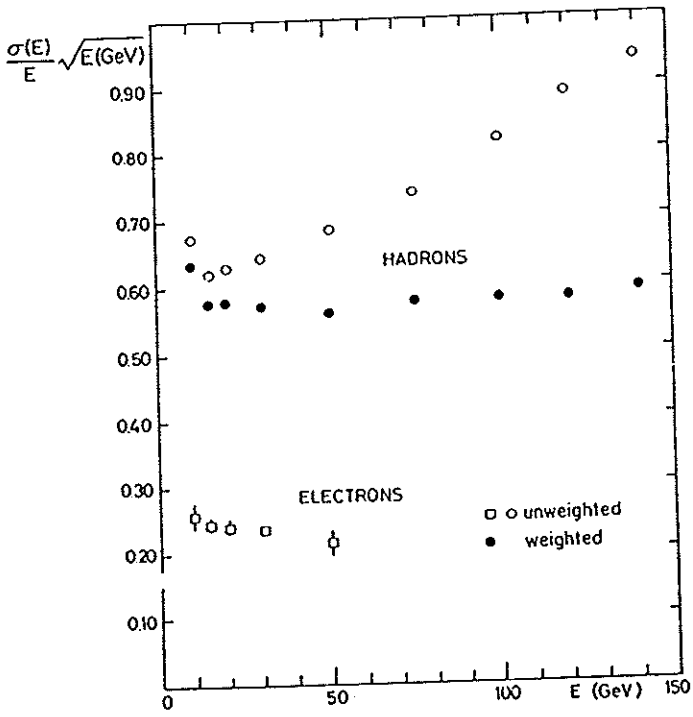

Figure 3.15
Energy resolution of the 2.5cm iron/scintillator calorimeter of the CDHS collaboration as a function of the incident particle energy, without and with weighting.

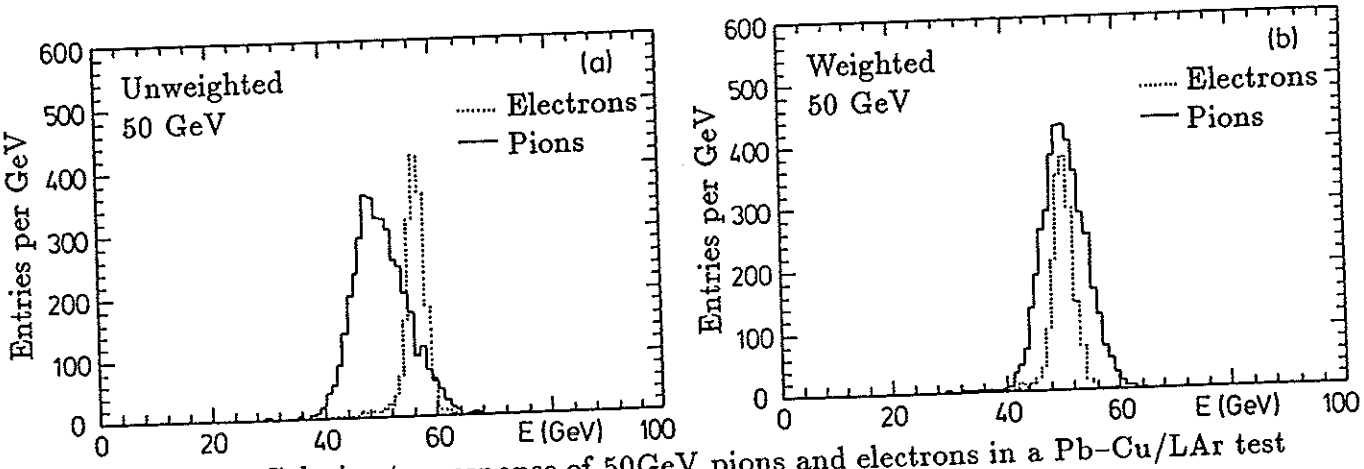

Fig. 3.16 Calorimeter response of 50GeV pions and electrons in a Pb–Cu/LAr test calorimeter of the H1 collaboration, without (a) and with (b) weighting.

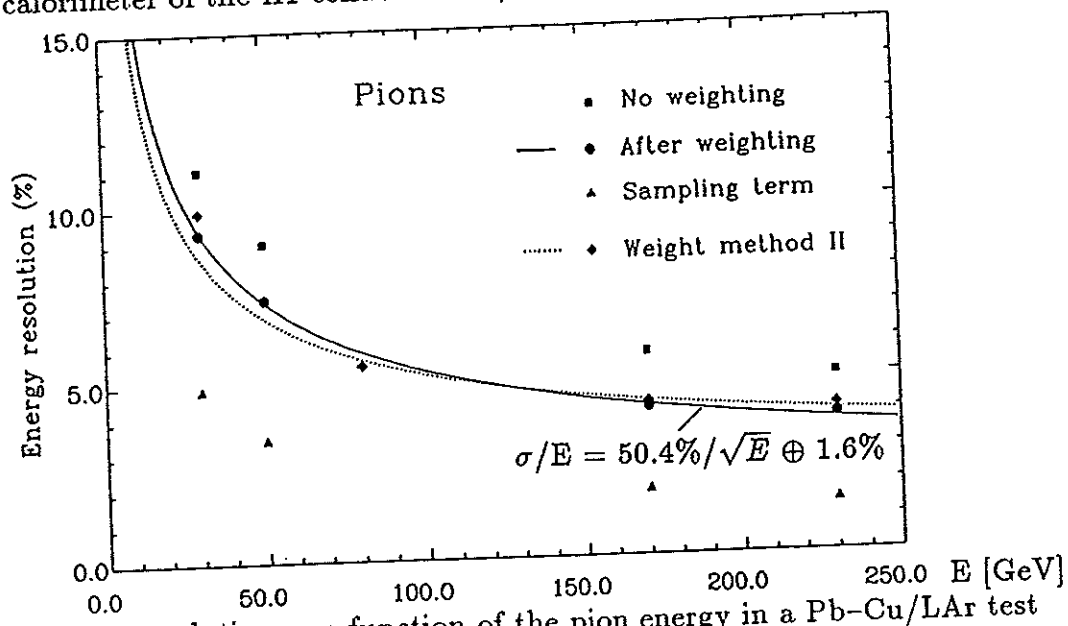

Fig. 3.17 Energy resolution as a function of the pion energy in a Pb–Cu/LAr test calorimeter of the H1 collaboration, without and with weighting.

By Hardware – Lost Nuclear Binding Energy Compensated by Neutrons (γ's)

The different contributions to the h_i/mip–ratio can be written as

$$\frac{h_i}{mip} = f_{ion}\frac{ion}{mip} + f_n\frac{n}{mip} + f_\gamma\frac{\gamma}{mip} + f_B\frac{B}{mip} + f_\nu\frac{\nu}{mip} ,$$

where $f_{ion} + f_n + f_\gamma + f_B + f_\nu = 1$ and

f_i $(i = ion, n, \gamma, B, \nu)$	describes the average fraction of the hadronic energy excluding the electromagnetic fraction, f_{em}, of hadron showers in sampling calorimeters, in form of
f_{ion}	– charged hadrons and muons (p, $\pi^\pm$, $\mu^\pm$, ...) (ionization)
$f_{n(\gamma)}$	– neutrons (γ)
f_B	– nuclear binding energy B lost in nuclear break up
f_ν	– neutrinos (which leave the calorimeter undetected) and
i/mip	describes the relative sampling fractions.

$B/mip = 0$, because the nuclear binding energy B is lost in the nuclear break up and therefore does not contribute to the signal.

An improvement of the energy resolution is possible via compensation due to the fact that the fraction of nuclear binding energy (f_B) lost for a measurable signal is strongly correlated with the fraction of neutrons and γ's (f_n, f_γ) emitted in nuclear break up or deexitation. f_B is relatively large e.g. 20% for 10GeV pions. However, in ordinary calorimeters neutrons do not contribute appreciably to the signal.

In order to get a signal from the neutrons plastic or organic scintillator represents the favoured choice as active detector medium because of its high hydrogen content, by which the neutrons are moderated. The recoil protons produce visible light in the scintillator by ionization and create a signal which is correlated with f_B.

For elastic scattering a fraction of $1/(A + 1)$ of the neutron energy is transferred to the target recoil, where A denotes the mass number of the target nucleus. Hence, maximum energy transfer is obtained for a hydrogen nucleus ($A = 1$).

Comprehensive Monte Carlo (MC) simulation programs have been developed and qualitative and quantitative understanding of the different physics processes has been achieved to a reasonable extent (chapter 3.6).

Results of such MC simulations e.g. with HETC [CHA72] on the relative energy fractions (f_i) for 5GeV protons are presented in Table 3.5 for different sampling calorimeters [GAB85]. The results of these simulations show, that uranium yields the largest fraction of neutrons and nuclear γ's and in particular the smallest amount of lost energy.

Typical values of the relative sampling fractions (i/mip) are given in Table 3.6 [WIG87], [WEG89]. i/mip–ratios for $1X_0$ thick absorber/2.5mm scintillator plates (LAr gaps) are bold–faced.

Calorimeter:	**U/Scint**	**Pb/Scint**	**Fe/Scint**	**U/LAr**
Energy fraction (f_i) in form of:	[%]	[%]	[%]	[%]
ionization (f_{ion})	**41.8**	**46.7**	**57.0**	**41.6**
primary proton	4.9	5.0	4.6	5.2
secondary protons	29.4	33.4	42.4	28.8
secondary $\pi^{\pm}$'s	7.4	8.1	9.8	7.4
secondary $\mu^{\pm}$'s	0.1	0.2	0.2	0.2
neutrons (f_n)	**19.5**	**12.1**	**7.8**	**20.2**
low energy (<20MeV) neutrons	14.7	12.1	7.8	14.3
(not from fission by n's<20MeV) fission neutrons (from fission by n's<20MeV)	4.8	–	–	5.9
nuclear γ's (f_γ)	**21.6**	**7.3**	**8.3**	**24.1**
excitation γ's	2.0	2.5	3.4	2.4
fission γ's (from all charged particles plus neutrons >20MeV)	2.7	0.0	0.0	2.6
γ's from neutrons <20MeV (fission, in–, non elastic and n–capture)	16.9	4.8	4.9	19.1
'lost' energy ('$f_{B,\nu}$')	**17.1**	**33.8**	**27.0**	**14.1**
electromagnetic energy (f_{em}) from π^0–decays (E_{em}/E [%])	**12.1**	**15.3**	**17.4**	**12.6**

U/Scint: 72 cells of 2mm U, 3mm Scint and 275 cells of 3mm U, 3mm Scint;
Pb/Scint: 1.2mm Al, 3.6mm Pb, 1.2mm Al, 3mm Scint; Fe/Scint: 6mm Fe, 3mm Scint;
U/LAr: 30 cells of 2mm U, 1.6mm LAr, 1.6mm G10, 1.6mm LAr and
112 unit cells of 4mm U, 1.6mm LAr, 1.6mm G10, 1.6mm LAr

Table 3.5 Energy available from 5GeV protons incident in U/Scint[a], Pb/Scint[a], Fe/Scint[a] and U/LAr[b] calorimeters as calculated with CALOR [GAB85] with 50ns (*a*) or 100ns (*b*) integration time. The numbers denote the average fractions of the pure hadronic energy available from the different hadron shower components. The numbers for the em fraction are related to the primary proton energy E.

Calorimeter:	**U/Scint**	**Pb/Scint**	**Fe/Scint**	**U/LAr**	**Pb/LAr**	**Fe/LAr**
ion/mip	0.93		0.83	1.0		0.88
p/mip	**0.96**	**0.94**	0.83	**0.99**	**0.97**	0.88
n/mip	0.8 – 2.5	0.8 – 2	0.5 – 2	0	0	0
γ/mip (low E)	**0.36**	**0.41**	**0.73**	**0.4**	**0.45**	**0.94**
e/mip	**0.58**	**0.6**	**0.83**	**0.63**	**0.66**	**0.92**

Table 3.6 Typical values of relative sampling fractions (i/mip) for different sampling calorimeters. The i/mip–ratios for $1X_0$ thick absorber/2.5mm scintillator (PMMA) or liquid argon readout are bold–faced.

Energy Fractions f_i

The different fractions of deposited energy in a uranium block as a function of the primary hadron energy have been presented already in Fig. 3.8 [GAB89]. Detailed information from Monte Carlo simulations for 5GeV protons incident on different calorimeter configurations are summarized in Table 3.5. The most important characteristics of f_i are discussed in the following:

f_{ion}, f_n, f_γ, $f_{B,\nu}$

are approximately independent of the primary particle energy (with $f_{ion}+f_n+f_\gamma+f_{B,\nu}=1$; see Fig. 3.8), but depend on the absorber material.

f_{ion}

decreases with increasing Z_{pas}. It is essentially determined by the number of secondary protons from spallation ($\approx$70%) (Table 3.5). The fraction of secondary protons decreases with decreasing Z_{pas}/A_{pas} of the (passive) absorber.

f_n

increases with Z_{pas}. f_n is particularly large for uranium, because in addition to spallation, nuclear fission contributes to the creation of neutrons. The signal of this contribution depends on the integration time because the neutrons have to transfer their energy to the protons of the active medium.

f_γ

depends on Z_{pas} (Table 3.5). For uranium a large contribution (17%) comes from slow neutrons (<20MeV) and about 3% from fission γ's induced by particles faster than 20MeV.

Relative Sampling Fractions i/mip

The relative sampling fractions i/mip of the different shower components (i = e, ion, n, γ) are discussed in the following [BRÜ86], [WOL86], [WIG87], [KRÜ87], [WEG89]:

e/mip

The e/mip–ratio is smaller than 1 in sampling calorimeters with $Z_{pas} > Z_{act}$ and decreases with increasing Z_{pas} [FLA85], [PES89]. This is essentially the result of the different Z–dependences of the various cross sections:

- ionization ($\approx Z^1$)
- bremsstrahlung ($\approx Z^2$)
- Compton effect ($\approx Z^1$)
- pair production ($\approx Z^2$)
- photo effect ($\approx Z^4$–Z^5)

The e/mip–ratio decreases with increasing passive absorber thickness d_{pas} at fixed (active) detector layer thickness d_{act} and becomes independent for large absorber thicknesses, e.g. for uranium absorber plates with $d_U \gtrsim 3$mm [BRÜ86], [WIG87] and for lead with $d_{Pb} \gtrsim 5$mm [HOF82].

This behaviour is expected due to the photo effect, where most of the energy of the low energy photons ($\lesssim$1MeV) is lost in the high Z absorber. Only electrons produced close to the absorber surface can contribute to the signal. For the ZEUS uranium scintillator calorimeter the sampling fraction for mip's is about 6.6% and the e/mip–ratio has a value of about 0.62 for 3.3mm thick DU plates with 2 x 0.2mm thick stainless steel cladding interleaved with 2.6mm thick scintillator plates.

ion/mip

The ion/mip–ratio is in the order of 0.8 – 1.1 . The largest fraction of ionization loss results from secondary protons ($\approx$70%) mainly released from spallation (Table 3.5, 3.6 and Fig. 3.7, 3.8) and dominates therefore the ion/mip–ratio. It depends on the energy spectrum of the spallation protons and recombination effects.

The number of released protons and hence the ionization loss decreases with decreasing Z_{pas}/A_{pas}; e.g. the ionization loss due to secondary protons is about 2.4% smaller for $^{238}_{92}$U than for $^{207}_{82}$Pb.

The ion/mip–ratio may be varied by the choice of the material thickness. For a fixed thickness d_U of uranium plates the p/mip–ratio decreases with decreasing thickness d_{Scint} of the scintillator plate.

For a uranium scintillator calorimeter the p/mip–ratio is in the order of 0.9. The contribution of pions from spallation is with about 7% – 8% relatively small.

n/mip

The n/mip–ratio depends strongly on the efficiency with which the neutrons are measured in the active medium. Organic scintillator represents the favoured medium due to its hydrogen content, in which a high energy transfer is possible between the neutrons created in the absorber material and light nuclei (free protons) of the scintillator. This is not the case for uranium liquid argon calorimeters (U/LAr) for which n/mip=0 (Table 3.6). The large fraction of neutrons (f_n) produced in the uranium (Table 3.5) does not create a measurable signal in the liquid argon and is lost for compensation. Tests performed with admixtures of several % of CH_4 to the liquid argon or organic substances at the surface of the readout boards have not yielded larger n/mip–ratios. In recent test measurements with α and β particles in liquid argon doped with ethylene (C_2H_4) an increase in the collected charge of the α particles was observed at low concentrations (200ppm). This would correspond to better compensation between electron and hadron energy measurements in a hadron calorimeter [FAB91].

The cross sections for neutron induced reactions on uranium and hydrogen are shown in Fig. 3.18 [BRÜ86]; for the individual physical processes see Fig. 3.7. In organic scintillator, with its large hydrogen content, almost all the kinetic energy of the neutrons is transformed into measurable proton recoil energy. This offers the possibility to increase significantly the pure hadron signal and plays an important role for compensation.

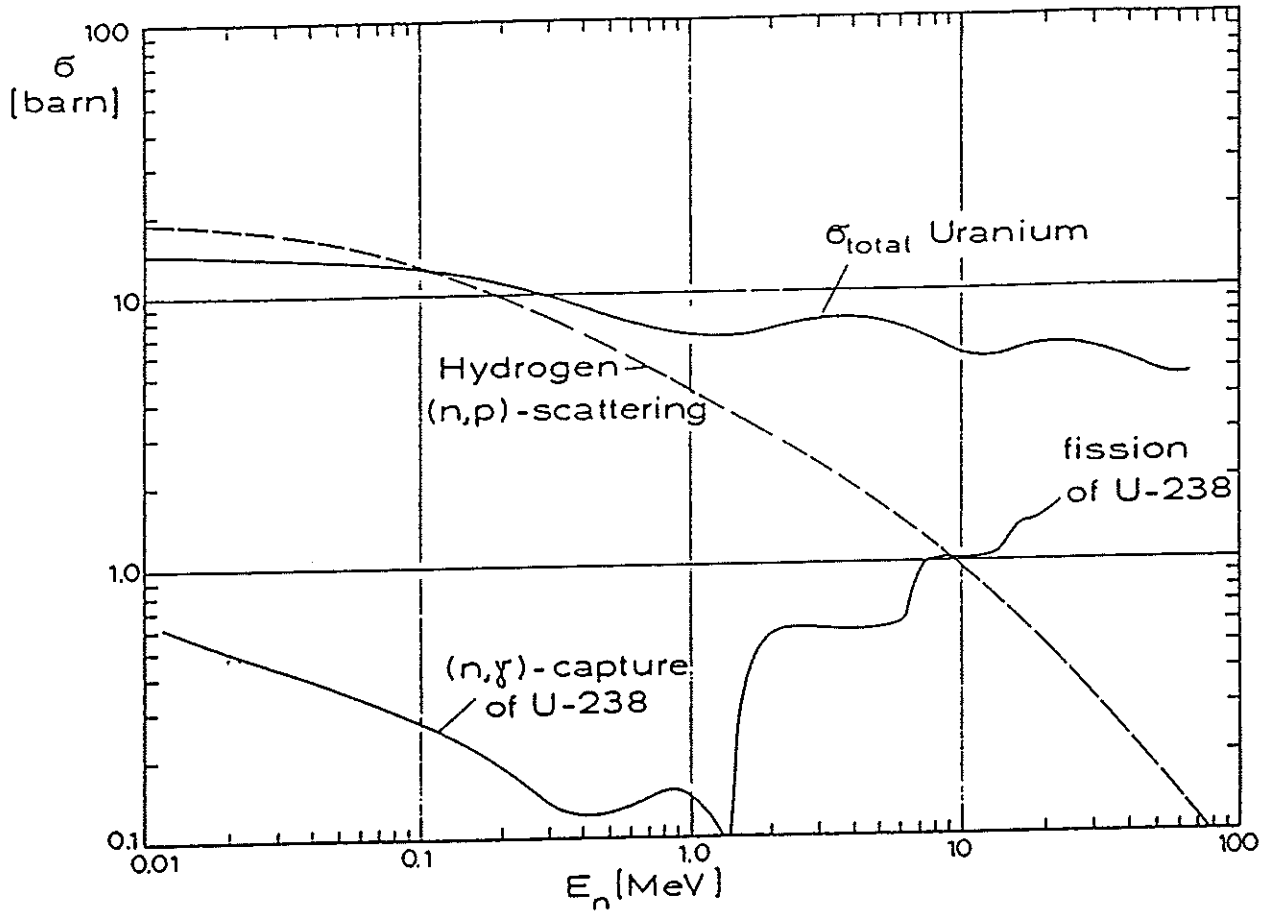

Fig. 3.18 Cross sections for neutron induced reactions on uranium and hydrogen.

Low energetic neutrons in the MeV range loose most of their kinetic energy to protons in elastic np collisions with the hydrogen of the scintillator. At very low neutron energies n–capture dominates, which yields a related γ–emission and therefore a related contribution to the hadron signal.

An incoming hadron with an energy of E=10GeV produces on average about 450 neutrons with an energy of $<E_n> \approx 3$MeV; most of the neutrons stem from spallation. In fissionable material like uranium, neutrons are created also by fission.

For low energy protons passing through scintillator yet another effect has to be taken into account: saturation of the scintillator light output. For $<E_n> \approx 3$MeV it follows that $<E_p> \approx 1.5$MeV, for which β is about 0.08. The result is a very high ionization density because $dE/dx \sim 1/\beta^2$. The saturation can be parametrized by (Birk's law [BIR60])

$$\frac{dL}{dx} = \frac{S \cdot dE/dx}{1 + kB \cdot dE/dx} ,$$

where L = light yield, S = absolute signal efficiency, kB = product of quenching parameter k and the ionization density along the track B. The kB factor of the scintillator material SCSN–38 used for the ZEUS calorimeter is 0.00835[g/MeVcm^2].

The n/mip–ratio depends strongly on the readout medium. If the readout layers contain hydrogen, the neutrons will essentially travel until they hit the hydrogen and their sampling fraction is approximately independent of the ratio d_{act}/d_{pas}, while the sampling fraction of mip's increases with d_{act}/d_{pas} [BRÜ86,87]. Therefore the n/mip–ratio increases with decreasing d_{act}/d_{pas}. The n/mip–ratio can be tuned in the range of about 0.5 – 2.5 .

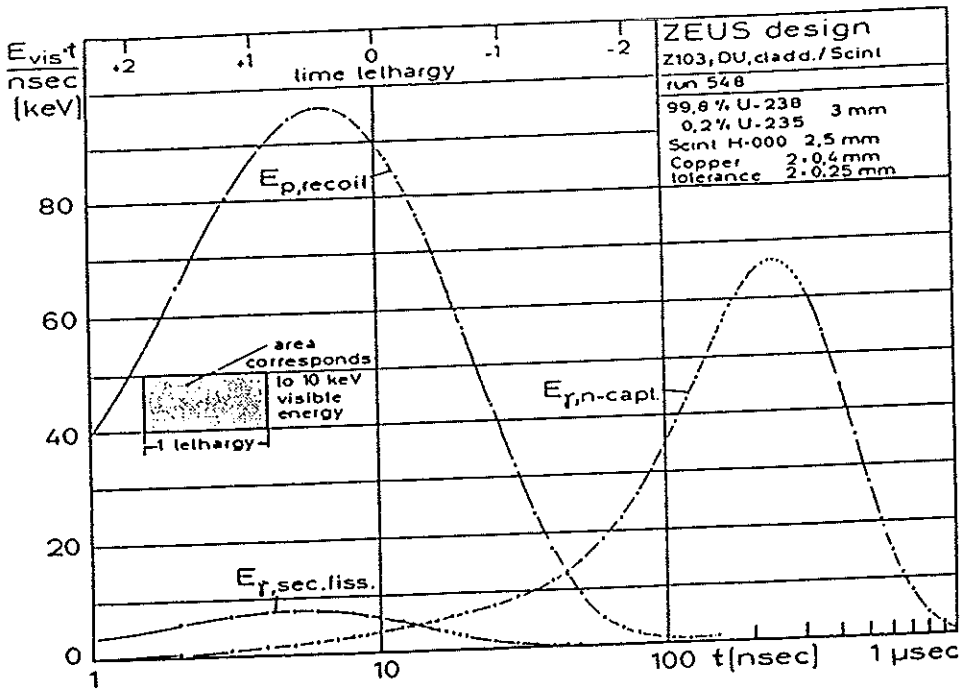

Fig. 3.19 Contributions to 'visible' (measurable) energy from proton recoils and from nuclear processes in a uranium scintillator calorimeter (3mm DU, 2.5mm Scint) calculated from HERMES Monte Carlo simulations.

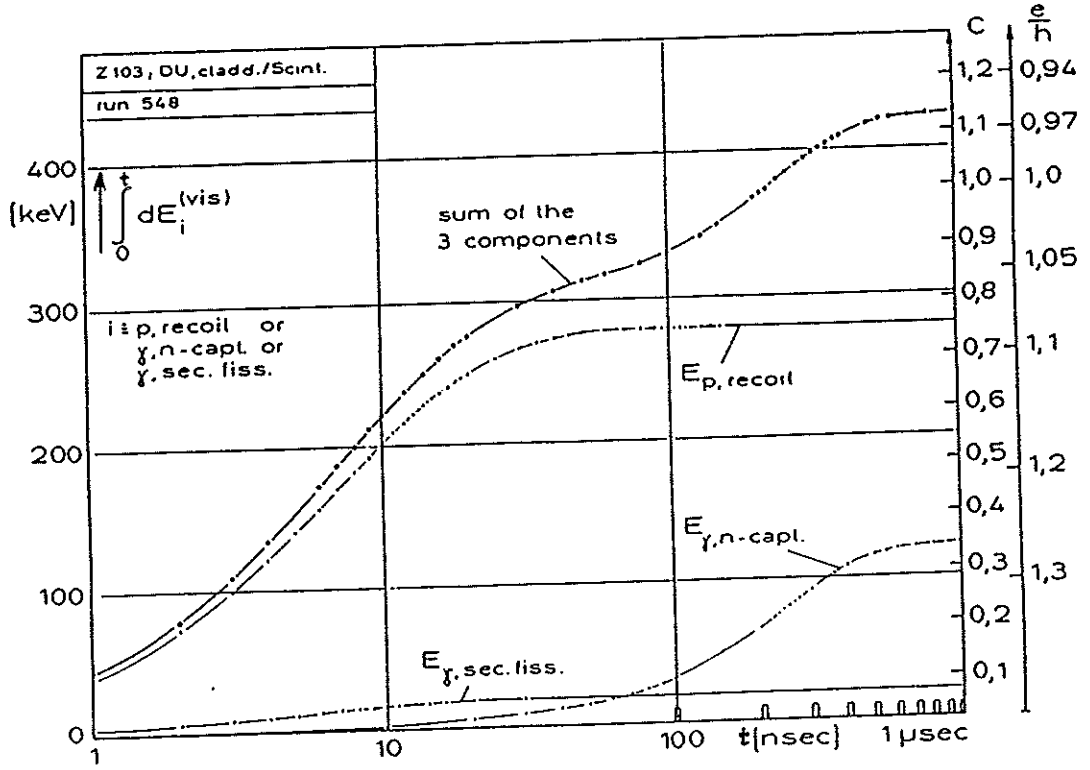

Fig. 3.20 The visible energies from Fig. 3.19 integrated over time. The contributions to compensation can be read at the right ordinate versus gate time [BRÜ86]. An e/mip = 0.6 was taken from an EGS calculation including the cladding.

γ/mip

Photons are produced by many different physical processes: spallation, inelastic reactions, fission and neutron capture. A large fraction of photons are low energetic, $E_\gamma < 20MeV$, and are absorbed in the high Z_{pas} material, thus γ/mip decreases with increasing Z_{pas}.

Prompt γ's produced in fission processes give a measurable signal. Photons from neutron capture yield also a measurable contribution, which is delayed by a few 100ns up to $1\mu s$ because neutrons have to be slowed down before they can be captured. For low energetic γ's the γ/mip–ratio is of the order of 0.36 for a uranium scintillator calorimeter (Table 3.6).

—

Figure 3.19 shows the contributions to 'visible' (measurable) energy from proton recoils and from nuclear processes as a function of time for a uranium scintillator calorimeter (3mm DU, 2.5mm Scint). The proton recoil produces the dominating contribution within the first 100ns. Later an additional contribution arises from (n,γ)–capture in ^{238}U [BRÜ86].

Figure 3.20 shows the contributions to the measurable signal of Fig. 3.19 integrated over time. The additional scale at the right ordinate of Fig. 3.20 indicates the e/h–ratio and points out, that a fine adjustment of the e/h–ratio is possible also by varying the integration time.

The measurable signals from the intranuclear cascade process (without em) contributing to compensation are summarized in Fig. 3.21.

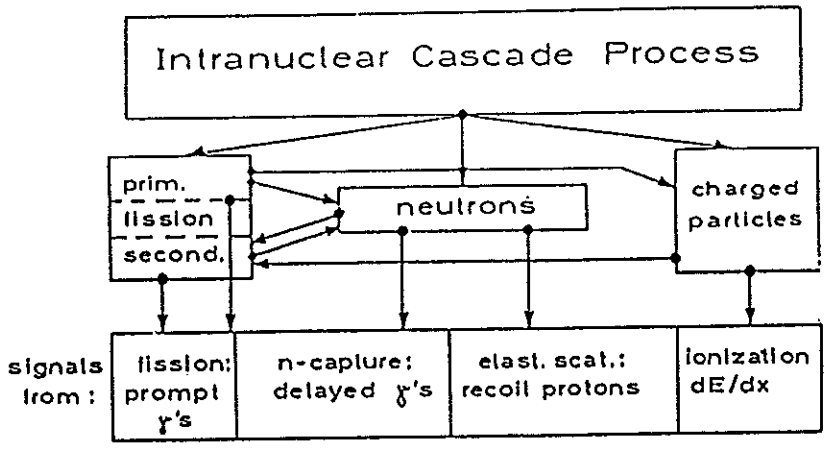

Fig. 3.21 Measurable signals from the different components of an intranuclear cascade (without electromagnetic contribution).

Hadron Energy Resolution

The study of the two sets of parameters, the energy fractions f_i and the relative sampling fractions i/mip, has shown, which factors dominate the h_i/mip–ratio and have to be tuned to achieve compensation (e/h=1). The most important result is, that passive absorbers with high Z_{pas} reduce the e/mip–ratio and yield a sizeable neutron contribution (f_n), which is correlated with the energy (f_B) lost to nuclear break up. The neutron yield can be measured with a relatively large n/mip–ratio by using active layers with a high hydrogen content, e.g. scintillator; as a result the hadronic signal will increase on an event–by–event basis and correlate with the energy lost for nuclear break–up (E_B).

The parameters of a calorimeter configuration which dominate the e/h–ratio can be summarized as follows:

- atomic number Z_{pas} and thickness d_{pas} of the absorber material
- properties and thickness d_{act} of the detector material, e.g. density fraction of hydrogeneous material
- thickness ratio $R_d = d_{pas}/d_{act} = \frac{thickness\ of\ passive\ absorber\ plates}{thickness\ of\ active\ detector\ layers}$
- signal integration time.

Comprehensive Monte Carlo simulations have been performed to determine the best choice of Z_{pas}, d_{pas}, d_{act}, ... and have predicted compensation for a uranium scintillator calorimeter [BRA85], [BRÜ86], [WIG87].

The most important parameter to achieve compensation is the ratio of absorber plate thickness to active layer thickness ($R_d = d_{pas}/d_{act}$). This ratio has been tuned by calculations and experimentally verified and/or optimized.

Figure 3.22 presents the prediction for the e/h–ratio calculated as a function of the uranium to scintillator plate thickness R_d [BRÜ86]. The e/h–ratio scales as $1/R_d$ and compensation is predicted for a uranium scintillator calorimeter with $R_d = d_U/d_{Scint}$ of about 1.3 , d_U and d_{Scint} measured in mm.

Figure 3.23 shows good agreement between HERMES Monte Carlo predictions and experimental results for 10GeV pions [BRÜ86], [ZEU89].

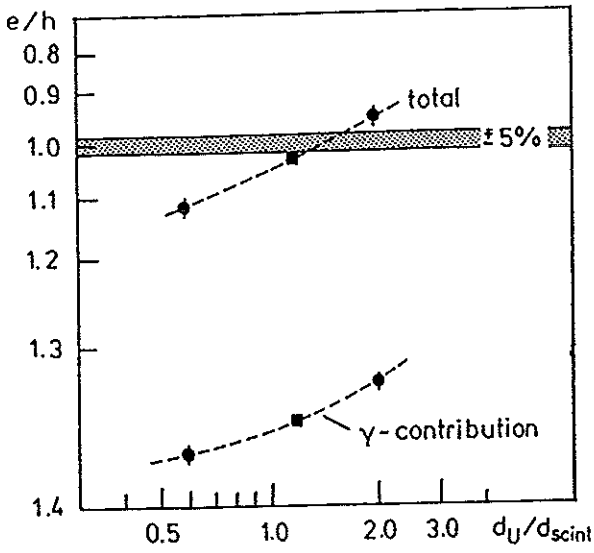

Figure 3.22
The e/h–ratio as a function of the ratio of uranium to scintillator plate thickness $R_d = d_U/d_{Scint}$.

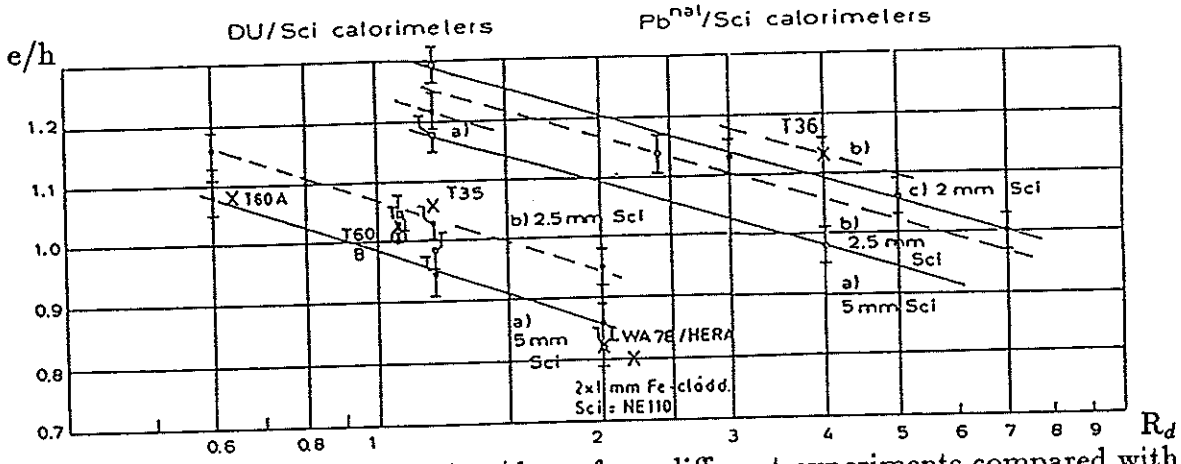

Fig. 3.23 e/h–ratios versus $R_d = d_{pas}/d_{Scint}$ from different experiments compared with predictions from HERMES Monte Carlo simulations for 10GeV pions.

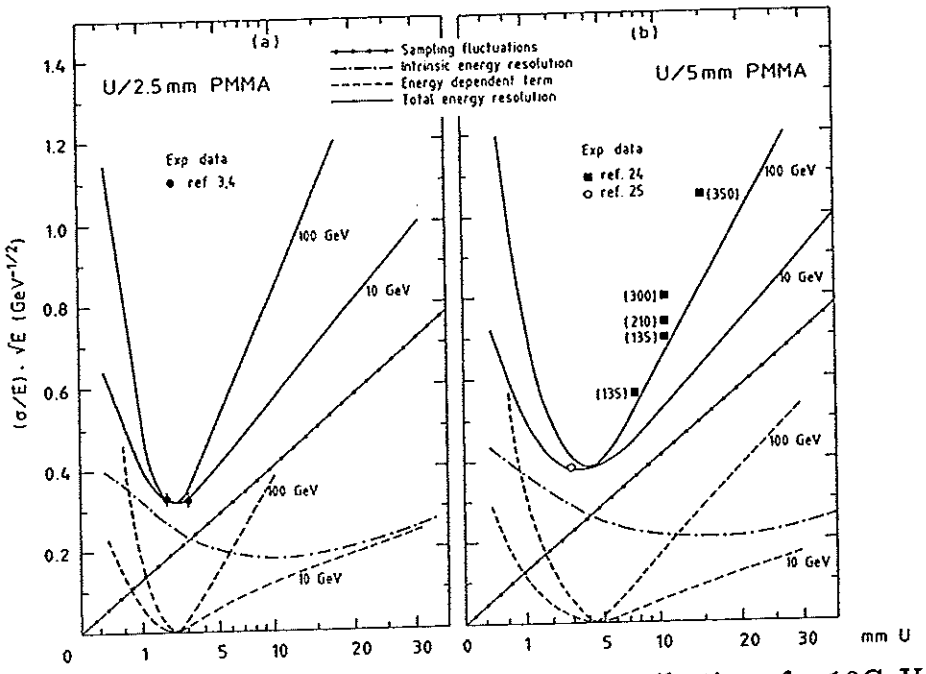

Fig. 3.24 The total energy resolution and the various contributions for 10GeV and 100GeV hadrons in uranium scintillator calorimeters as a function of the uranium plate thickness for 2.5mm (a) and 5mm (b) thick scintillator layers. The numbers in brackets denote the energies at which the experimental results were reported from Wigmans.

For well designed uranium scintillator calorimeters f_n is relatively large and correlated with f_B, thus losses in nuclear binding energy can be compensated event–by–event.

The contributions to the hadron energy resolution such as intrinsic fluctuations, sampling fluctuations, photoelectron statistics due to optical readout etc ... have been measured for several ZEUS test calorimeters and will be discussed in detail in chapter 4.5.3. The most important results of the compensating ZEUS uranium scintillator test calorimeter T60B (3.2mm DU, 3mm Scint.) are briefly reported here.

The contribution of intrinsic fluctuations to the hadron energy resolution is

$$\frac{\sigma_{had}^{intr}}{E} = \frac{20\%}{\sqrt{E[GeV]}} .$$

Without neutron and γ detection it is in the order of $30\% - 35\%/\sqrt{E[GeV]}$.

The contribution of sampling fluctuations to the hadron energy resolution is larger. It is

$$\frac{\sigma_{had}^{samp}}{E} = \frac{31\%}{\sqrt{E[GeV]}} \quad \text{or} \quad \frac{\sigma_{had}^{samp}}{E} = \frac{11.5\%\sqrt{\Delta\epsilon}}{\sqrt{E[GeV]}} ,$$

where $\Delta\epsilon$ is the average energy loss of a minimum ionizing particle in one calorimeter layer.

The hadron energy resolution of the compensating ZEUS calorimeter, taking into account all known instrumental calorimeter imperfections such as nonuniformities, leakage etc ..., can be described by:

$$\frac{\sigma_{had}}{E} = \frac{35\%}{\sqrt{E[GeV]}} \oplus 2\% .$$

Frequently the energy resolution of hadron calorimeters, neglecting instrumental effects, is parametrized by [FAB89]:

$$\frac{\sigma_{had}}{E} = \frac{A}{\sqrt{E[GeV]}} + C ,$$

where A is a constant and C is essentially a function of the deviation from compensation (C:= f(e/h – 1)). C vanishes for compensating calorimeters.

Figure 3.24 presents Monte Carlo simulations for 10GeV and 100GeV hadrons on the energy resolution as a function of the uranium absorber thickness for fixed scintillator plate thicknesses of 2.5mm and 5mm [WIG87]. The contributions to the total energy resolution from sampling fluctuations, intrinsic energy resolution and an additional energy dependent term are indicated. The curves of the total hadronic energy resolution favour for both uranium scintillator calorimeters configurations with a ratio $R_d = d_U/d_{Scint}$ of about 1 .

The thicknesses of the uranium and scintillator plates for the ZEUS calorimeter have been calculated by detailed Monte Carlo simulations [BRÜ86], [BRÜ87], [ZEU87] and have been checked and finally optimized by various systematic calorimeter tests described in chapter 4.

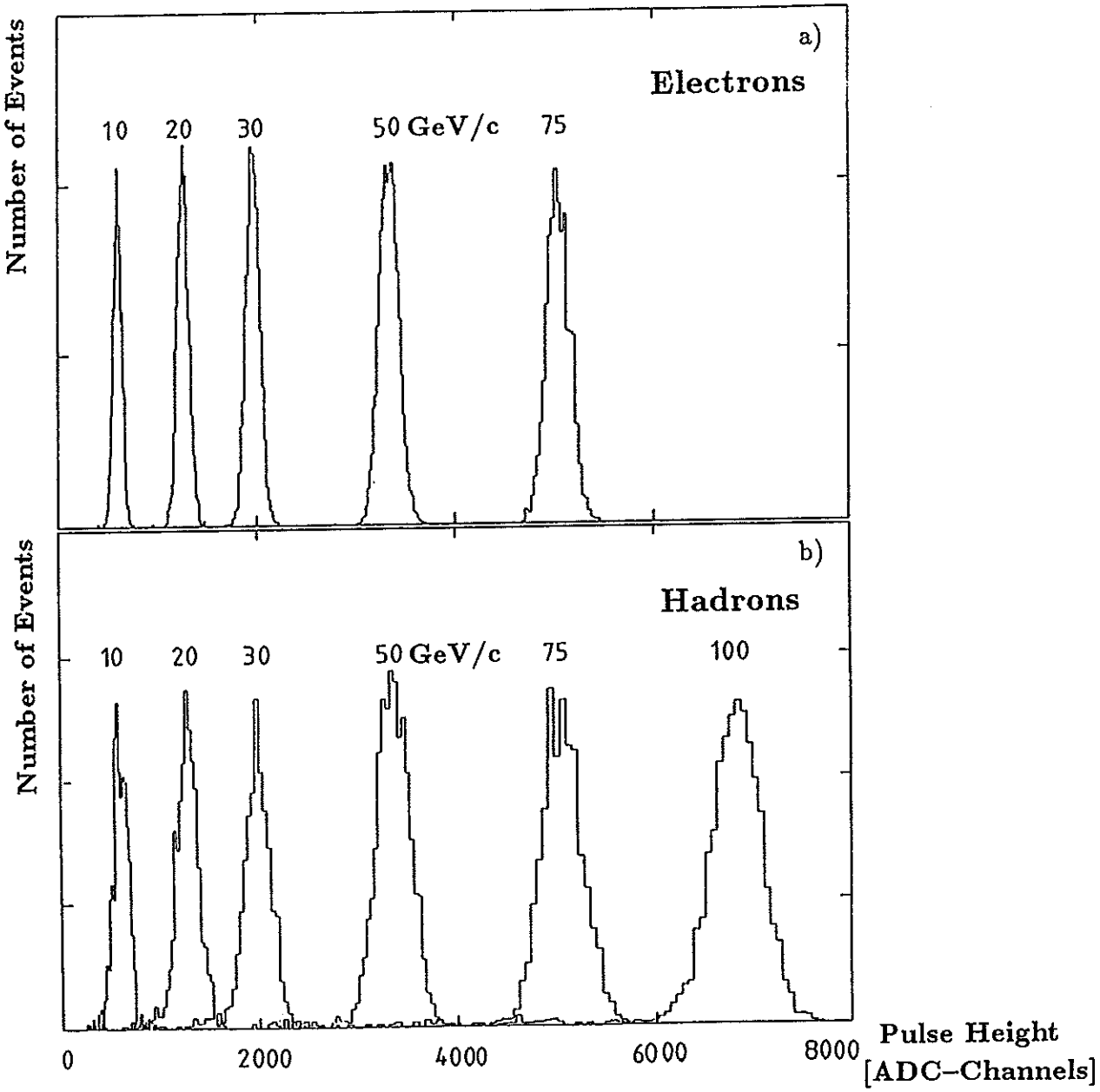

Fig. 3.25 Pulse height distributions for electrons (a) and hadrons (b) measured with the ZEUS forward prototype calorimeter at CERN SPS in the momentum range from 10GeV/c to 100GeV/c.

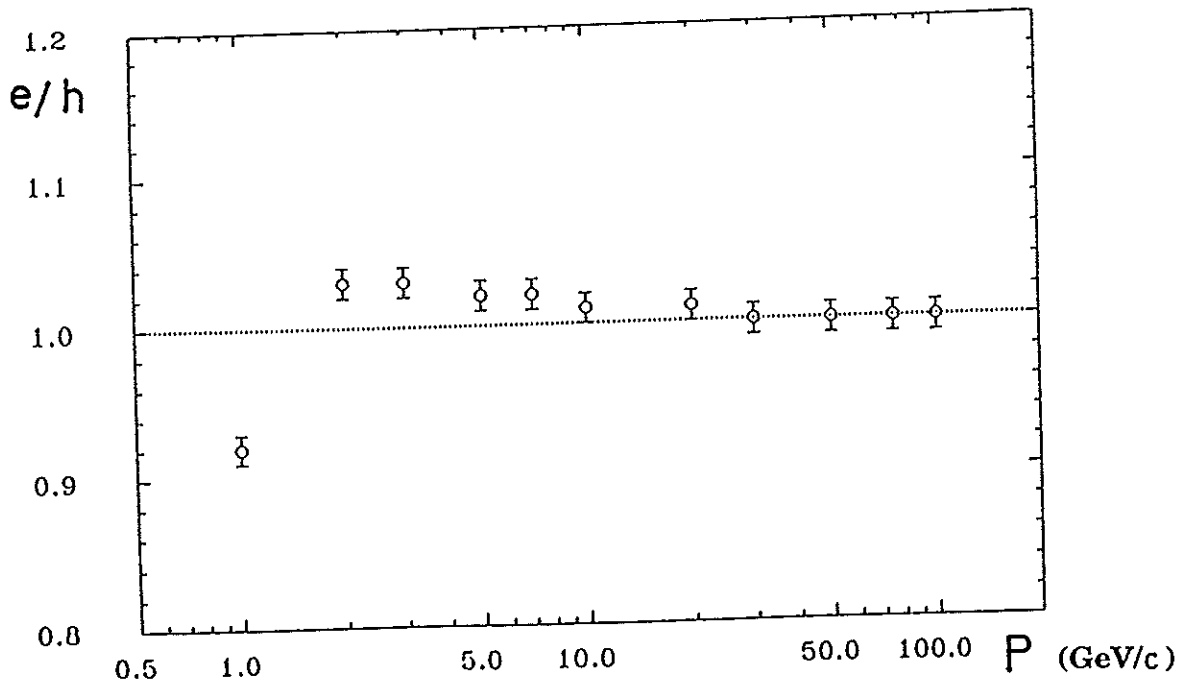

Fig. 3.26 The e/h–ratio versus beam momentum measured with the ZEUS prototype calorimeter at CERN.

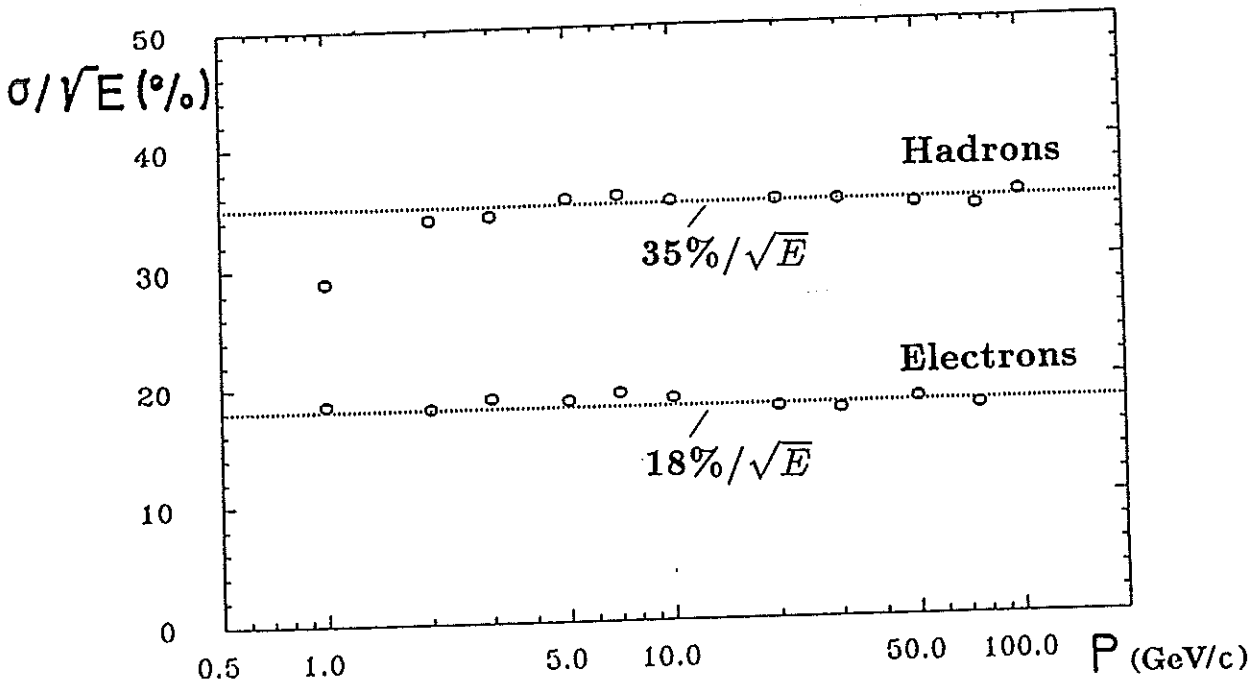

Fig. 3.27 The energy resolution versus beam momentum for electrons and hadrons measured with the ZEUS prototype calorimeter at CERN.

Final results from the ZEUS prototype calorimeter (3.3mm DU, 2.6mm Scint) are given in Fig. 3.25, 3.26 and 3.27 [BEH89].

Figure 3.25 presents the pulse height distributions of electrons (a) and hadrons (b) measured at CERN in the momentum range from 10GeV/c to 100GeV/c. The distributions for electrons and hadrons show the same mean values within 2%. This clearly illustrates, that compensation (e/h=1.0) has been achieved.

The e/h–ratio is shown in Fig. 3.26 as a function of the particle momentum. Above 5GeV electrons and hadrons yield the same pulse heights to better than 2%.

Figure 3.27 presents the energy resolution of hadrons and electrons measured in the momentum range from 1GeV/c to 100GeV/c. The relative energy resolution for electrons and hadrons improves with increasing energy proportional to $1/\sqrt{E}$. For electrons the energy resolution is $18\%/\sqrt{E}$ and for hadrons $35\%/\sqrt{E}$ above 2GeV/c. Further results of the ZEUS prototype calorimeter tests are presented and discussed in detail in chapter 5.

Compensating Lead Scintillator Calorimeters

After studying uranium scintillator calorimeters and understanding the tuning required to achieve compensation and high energy resolution for hadrons, Brückmann suggested that also lead scintillator calorimeters might be able to compensate [BRÜ86], [AND87]. Wigmans had come to the same conclusion [WIG87]. Since lead as absorber yields less neutrons and its e/mip–ratio is larger, a higher n/mip–ratio is needed e.g. by using smaller scintillator thicknesses d_{Scint}.

Monte Carlo simulations have been performed for Pb as absorber material and scintillator as active medium. These calculations predict, that compensation is possible for a lead scintillator calorimeter with a thickness ratio $R_d = d_{Pb}/d_{Scint}$ of about 4 [WIG87]. The larger ratio R_d is expected due to the lower neutron yield and the lower density of Pb as absorber.

The sampling fraction of a compensating lead scintillator calorimeter is about 0.4 times the sampling fraction of a compensating uranium scintillator calorimeter. The higher sampling fluctuation of the Pb calorimeter will of course degrade the energy resolution for electrons and hadrons.

Part of the ZEUS calorimeter group set out to test the idea of a compensating lead scintillator calorimeter experimentally and has built the first lead scintillator calorimeter which was almost compensating [BER87]. The results of this calorimeter test (TEST 36) will be discussed in detail in chapter 4.4.

Chapter 4

Development and Optimization of the High Resolution Uranium Scintillator Hadron Calorimeter for ZEUS

4.1 Overview of the ZEUS Calorimeter Tests

Much research and measurements of different calorimeter configurations and detailed simulation calculations have been done to determine the best parameters and dimensions for the ZEUS calorimeter. The most important calorimeter tests were performed with particle beams at CERN (PS, SPS) where different kinds of particles (e, h, μ) were available at momenta between 0.5 and 210GeV/c. A list of the relevant ZEUS calorimeter tests and the main parameters of the calorimeters are summarized in Tables 4.1a,b [ZEU89], [KRÜ90b].

The WA78–H1–ZEUS calorimeter test allowed a detailed study of the longitudinal development of hadronic showers and the determination of the optimum calorimeter depth.

TEST 35 confirmed that the excellent energy resolution of $35\%/\sqrt{E}$ for hadrons can be achieved with a uranium scintillator calorimeter.

With TEST 36 ZEUS showed for the first time that compensation can also be achieved with a lead scintillator calorimeter.

TEST 60 represents a comprehensive experimental study of various uranium and lead scintillator calorimeters (T60A, T60B, T60C) with particle momenta up to 100 GeV/c. The spatial distribution of showers, the spatial and time resolution, and many other fundamental calorimeter characteristics have been studied.

After having determined the optimum parameters for a uranium scintillator calorimeter, a prototype of the forward calorimeter FCAL has been built. The four FCAL prototype modules were identical to the planned ZEUS modules apart from their height of only 80cm. The FCAL prototype was extensively tested at the PS and the SPS to verify and where necessary to fine tune the parameters and dimensions for the ZEUS calorimeter. The FCAL prototype tests and results are presented and discussed in detail in chapter 5.

Parameters	ZEUS Calorimeter Tests				
	WA78–H1–ZEUS	**TEST 35**	**T60A**	**T60B**	**FCAL Prototype**
DU Thickness	10 mm	3.0 mm	3.2 mm	3.2 mm	3.3 mm
Scint. Thickness	5 mm	2.5 mm	5.0 mm	3.0 mm	2.6 mm
Depth	5.5λ + back	4.2λ	4.4λ	6.0λ + back	7.1λ + back
Area	60 × 60 cm^2	60 × 60 cm^2	60 × 60 cm^2	60 × 60 cm^2	80 × 80 cm^2
Effective λ	19.1cm	18.2cm	33.3cm	25.7cm	19.5cm
Trans. Segmentation	60 × 60 cm^2	20 × 20 cm^2	5 × 60 cm^2	5 × 60 cm^2	5 × 20 cm^2
Long. Segmentation	0.45λ	4.2λ	1.1λ	1.5λ	1.0, 3.1, 3.1λ
Momentum [GeV/c]	5 – 210	3 – 9	3 – 9	1 – 100	0.5 – 100
References	[CAT87], [KRÜ86b], [KRÜ90e]	[AND86], [KRÜ87c], [BEH90a]	[ENG86], [AGO89], [KRÜ87b]	[BER87], [KRÜ88a], [DRE90]	[BEH90], [AND90], [KRÜ89c,90a]

Table 4.1a List of ZEUS uranium scintillator test calorimeters.

Parameters	ZEUS Calorimeter Tests	
	T60C	**TEST 36**
Pb Thickness	5 mm	10 mm
Scint. Thickness	5 mm SCSN-38	2.5 mm SCSN-38
Depth	4.0λ	5.0λ + back
Area	60 × 60 cm^2	68.4 × 66 cm^2
Effective λ	37.1cm	22.1cm
Trans. Readout Segmentation	5 × 60 cm^2	22.8 × 22 cm^2
Long. Readout Segmentation	1.0λ	1.0λ + 4.0λ
Momentum [GeV/c]	3 – 9	3 – 75
References	[ENG86], [AGO89] [BER87], [KRÜ88a]	[BER87a], [DRE90] [KRÜ88a]

Table 4.1b List of ZEUS lead scintillator test calorimeters.

4.2 Hadron Shower Development in a Uranium Scintillator Calorimeter and Determination of the Optimal Depth for the ZEUS Calorimeter — WA78–H1–ZEUS Calorimeter Test

4.2.1 Introductory Remarks

Many experimental data have been taken with sampling hadron calorimeters of different configurations (materials, design etc...). But up to now it has been impossible to formulate a comprehensive theory to describe all significant effects. Thus it is impossible to predict precisely the behaviour of a particular hadron calorimeter design. Monte Carlo programs developed so far are still too uncertain to give sufficiently reliable predictions.

The only possible way to be sure about the behaviour of a particular calorimeter is to test an experimental set up which is as close as possible to the designed calorimeter layout.

A combined electromagnetic/hadron calorimeter (hadronic part: 5.4λ depleted uranium/ scintillator plus 8λ iron/scintillator) has been tested by a collaboration of the WA78, H1 and ZEUS groups in a hadron beam at CERN. One of the primary goals of this test was a study of the longitudinal shower development and the necessary depth of a calorimeter.

Data have been taken in the H3 beamline at the CERN–SPS yielding results in the momentum range from 5GeV/c to 210GeV/c.

After a short description of the experimental set up of the WA78–H1–ZEUS calorimeter, the particle identification and the calibration of the hadron calorimeter are discussed and results of general interest are presented. Since this kind of data analysis is typical for the field of calorimetry it is described here in some detail. The longitudinal shower development for hadrons is presented and the main features and requirements of the hadron calorimeter system of the ZEUS detector are described. This is followed by a discussion of the optimization of the calorimeter depth based on containment studies and the shower leakage due to inactive regions such as photomultiplier boxes (PMs, iron shielding, I-beams etc...). Finally, the data on longitudinal shower development are extrapolated into the TeV range which will be the playground of LHC and SSC detectors.

4.2.2 The Experimental Set Up of the WA78–H1–ZEUS Test

The experimental set up of the WA78–H1–ZEUS calorimeter test is shown in Fig. 4.1. It consists of a set of scintillation counters defining the beam ($BEAM = B1 \cdot B2 \cdot \overline{H1} \cdot \overline{H2} \cdot \overline{A}$), an 11m long threshold Cherenkov counter filled with He for particle identification and the electromagnetic and hadronic calorimeters. For the following analysis only the hadronic calorimeter was used while the electromagnetic calorimeter was removed. The hadronic calorimeter (HAD) consisted of two parts with different absorber materials. The front part was equipped with uranium layers (60 x 60 x 1 cm^3), the rear part with iron layers (60 x 60 x 2.5 cm^3). The first part was operated with 12 modules, the second part with 13 modules. Each module was built of 4 layers of absorber plates (U/Fe) and scintillator plates plus readout fibres viewed by one photomultiplier (Fig. 4.2). For reasons of safety and easier handling the uranium plates were enclosed in 1 mm steel.

The relevant values of the layer structure are given in Table 4.1c. The main parameters of the hadronic calorimeter are summarized here:

1st part ($\approx$5.4λ): 12 modules x 4 layers	absorber: 10 mm U + 2 x 1 mm Fe scintillator: 5 mm NE 110
2nd part ($\approx$8λ): 13 modules x 4 layers	absorber: 25 mm Fe scintillator: 5 mm NE 110

A detailed description of the set up can be found in [VIN86a], [VIN86b], [CAT87]. The electromagnetic calorimeter is described in [PET86], [GEN87].

In order to achieve good particle identification for electrons, muons and hadrons contained in the beam a He gas Cherenkov counter was placed in front of the calorimeter set up. The method by which the particles were identified and how the beam content was determined for all momenta is presented in section 4.2.3 .

	EM-Calorimeter	**HAD-Calorimeter**	
		Uranium Part	*Iron Part*
Sampling Layer	0.5 mm Fe 1.57 mm U 0.5 mm Fe 4.0 mm SCSN 38	1 mm Fe 10 mm U 1 mm Fe 5 mm NE 110	25 mm Fe 5 mm NE 110
Readout Module	4.0 mm Al 4.0 mm SCSN 38 8 Sampl. Layers 4.0 mm Al	4 Sampling Layers $\approx$ 0.45 λ_{int} $\approx$ 13.5 X_0	4 Sampling Layers $\approx$ 0.62 λ_{int}
Total Calorimeter	6 Readout Modules	12 Readout Modules $\approx$ 5.4 λ_{int}	13 Readout Modules $\approx$ 8 λ_{int}

Table 4.1c Layer structure of the WA78–H1–ZEUS calorimeter set up.

The relative calibration of individual modules against each other was performed by using hadron showers. The intercalibration between the two different parts of the calorimeter (U/Fe) was achieved by comparing the energy depositions in both parts. The calibration and the intercalibration are discussed in more detail in section 4.2.4 .

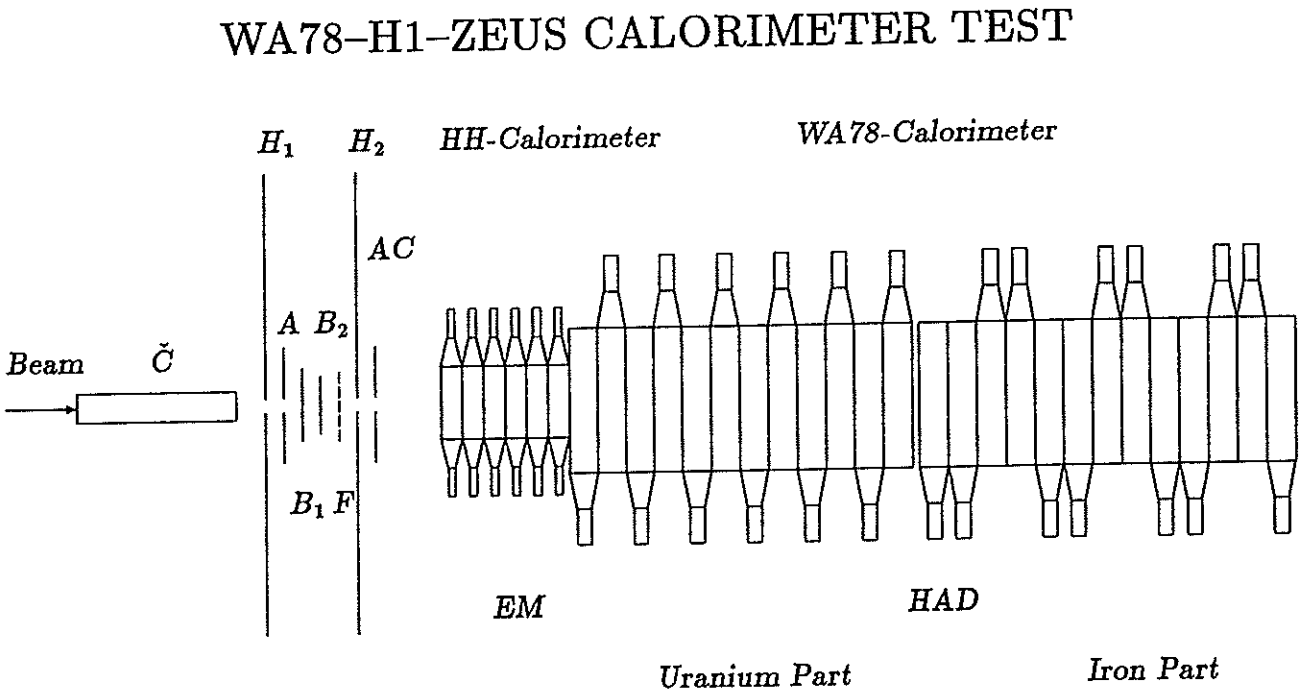

Č	Cherenkov Counter	B_1	Beam Trigger 1
A	Anticounter	B_2	Beam Trigger 2
F	Finger Hodoscope	H_1	Veto Wall 1
AC	Albedo Counter	H_2	Veto Wall 2
EM	Electromagnetic Calorimeter	*HAD*	Hadronic Calorimeter

Fig. 4.1 The experimental set up of the WA78–H1–ZEUS calorimeter test.

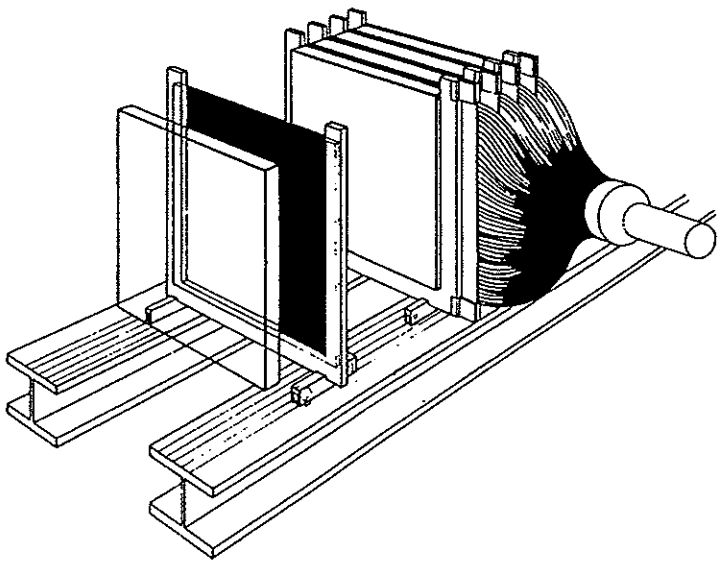

Fig. 4.2 Construction of one module of the WA78 hadron calorimeter.

4.2.3 Particle Identification (WA78–H1–ZEUS)

For particle identification an 11 m long threshold Cherenkov counter ($\phi \approx 15$cm) filled with He gas was placed in front of the experimental set up. It was possible to vary the refractive index n as a function of the gas pressure (individually for each energy):

$$(n - 1) = (n_o - 1) \cdot p \text{ [atm]},$$

where $n_o \approx 3.3\ 10^{-5}$ for He at 20°C.

The different particles (electrons, muons and hadrons) contained in the beam were identified by the Cherenkov counter and/or the WA78 hadron calorimeter.

Muons were separated by means of the calorimeter. Electron/hadron identification was performed in the following way:

1. clean electron and clean hadron samples were determined for each energy by means of the calorimeter,
2. the ADC spectra and efficiencies of the Cherenkov counter were calculated for these two samples,
3. the absolute electron and hadron fractions contained in the beam were extracted from the Cherenkov spectra.

As an example the particle identification performed for the 30GeV/c data (electromagnetic calorimeter out) is presented in the following figures.

Figure 4.3 shows the sum of ADC signals of the calorimeter modules 3 to 24 (PH3–24) without any cuts on the particle types. It shows a structure that is characteristic for the different longitudinal energy deposits of the particle types contained in the beam.

Electrons deposit almost their whole energy in the first two modules (one U/Scin module corresponds to ≈13.5 radiation lengths (X_0) or 0.45 interaction lengths (λ_{int})). They are therefore found in this plot near 0.

The energy deposited by muons is on the average about the same in each module, depending of course on whether the material is U/Scin or Fe/Scin. Muons are found, for the 30GeV/c data, at about ADC channel 120 and their shape is essentially described by a Landau distribution (convoluted by a Gaussian distribution). Hadrons show the widest spread and reach the largest pulse heights. The smaller maximum in the hadron spectrum at ADC channel 450 arises from events which have deposited a large fraction of energy in module 1 and 2.

The clean separation between muons and hadrons can be seen in Fig. 4.4, where the ADC sum spectra of modules 1 to 12 (PH1–12) is shown. Electrons are excluded from this plot by a cut on PH3–24 < 30 (see Fig. 4.3).

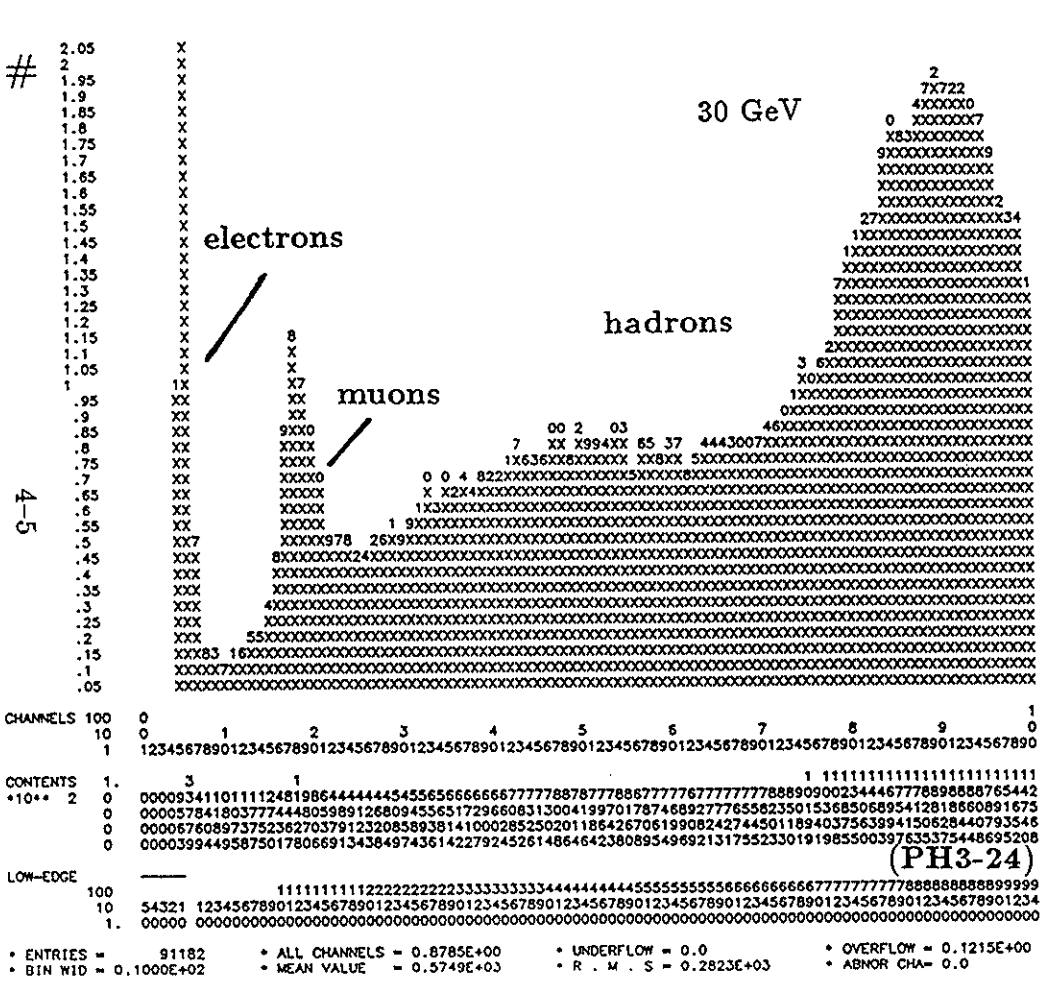

Fig. 4.3 Sum of the ADC Signals of the Calorimeter Modules 3 to 24 (PH3-24).

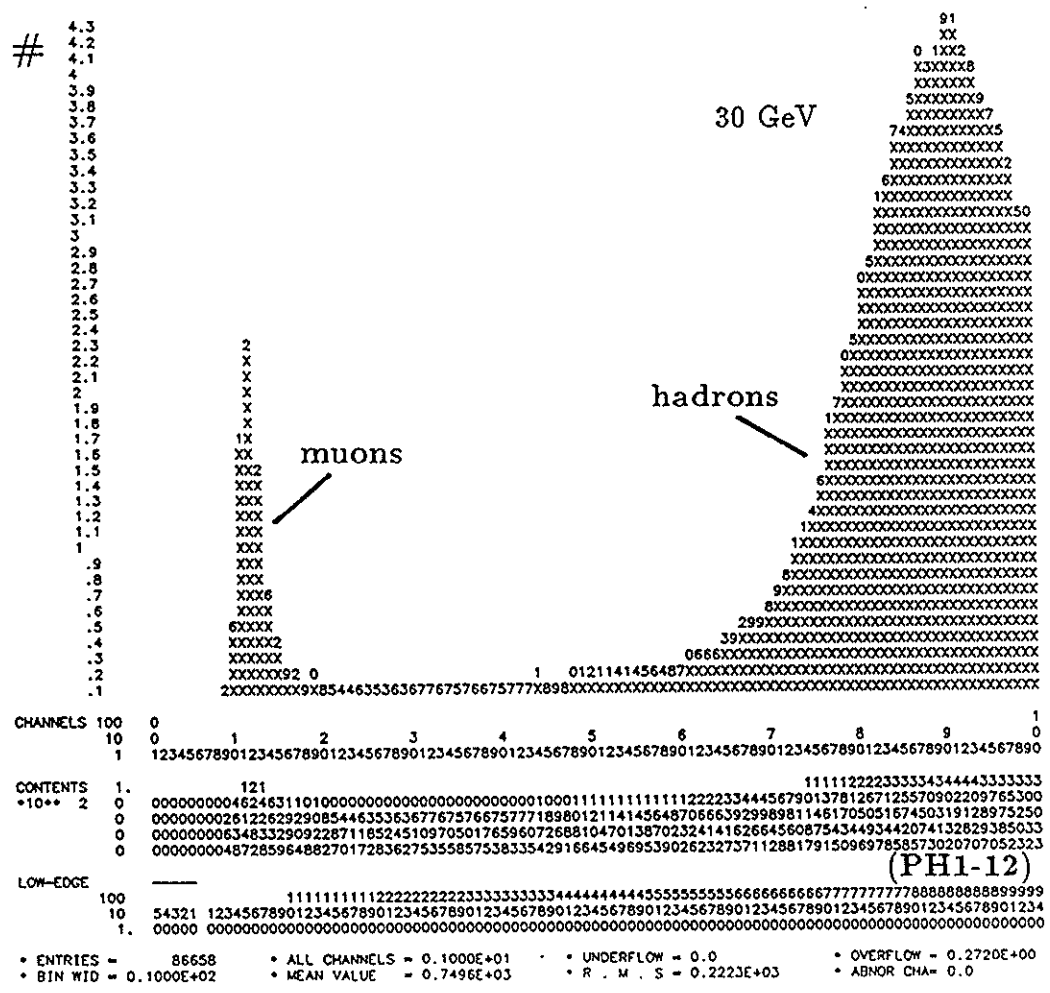

Fig. 4.4 Sum of the ADC Signals of the Calorimeter Modules 1 to 12 (PH1-12).

An even cleaner separation between the different particle types was achieved by studying the distribution of RATIO=(PH13–24)/(PH1–12) versus (PH3–24) in Fig. 4.5 . Figure 4.3 is the one-dimensional projection of this plot. For electrons both PH3–24 and PH13–24 are close to zero. Muons are easily separated since they deposit about the same energy in the first and the second part of the calorimeter.

The hadron signal is found essentially on the right lower side of the plot. Hadron showers start with an exponential decrease from the beginning of the calorimeter, thus their RATIO is preferentially found near 0.

The separated muon signal is shown in Fig. 4.6 and the distribution without muons PH3–24 is shown in Fig. 4.7 .

After a successful separation of muons from the data sample, by the calorimeter itself, the Cherenkov counter was used for a further separation of electrons and hadrons.

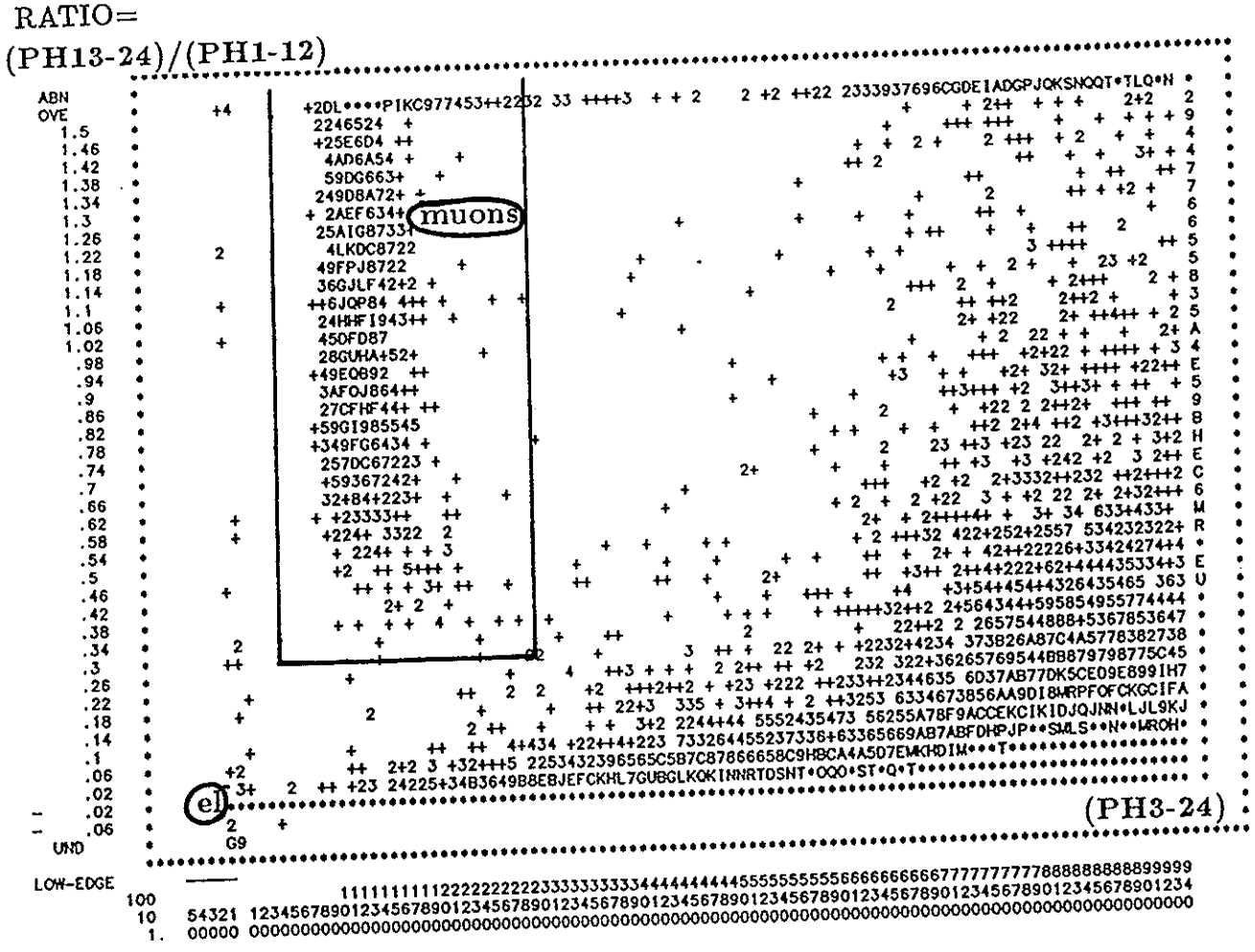

Fig. 4.5 Calorimeter Signals: (PH13-24)/(PH1-12) versus (PH3-24).

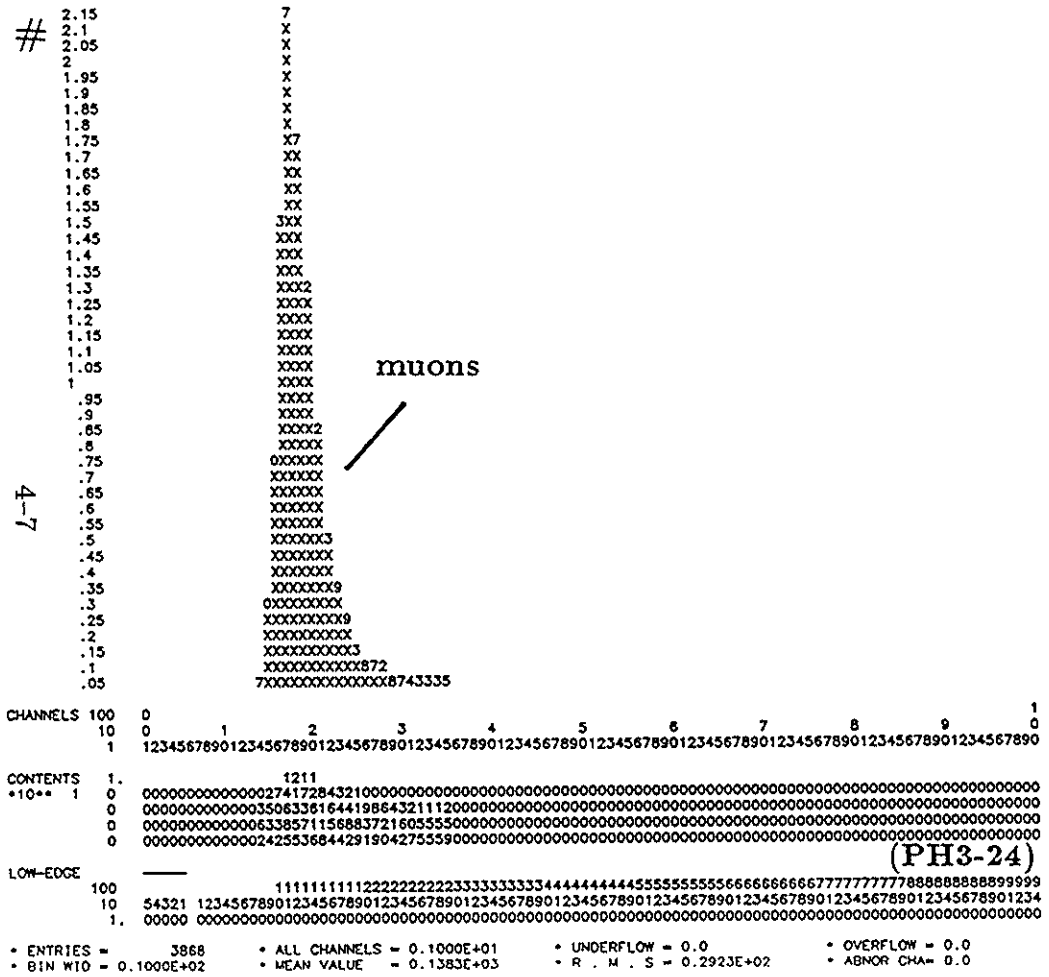

Fig. 4.6 Muon Sample Identified by the Calorimeter as Function of PH3-24.

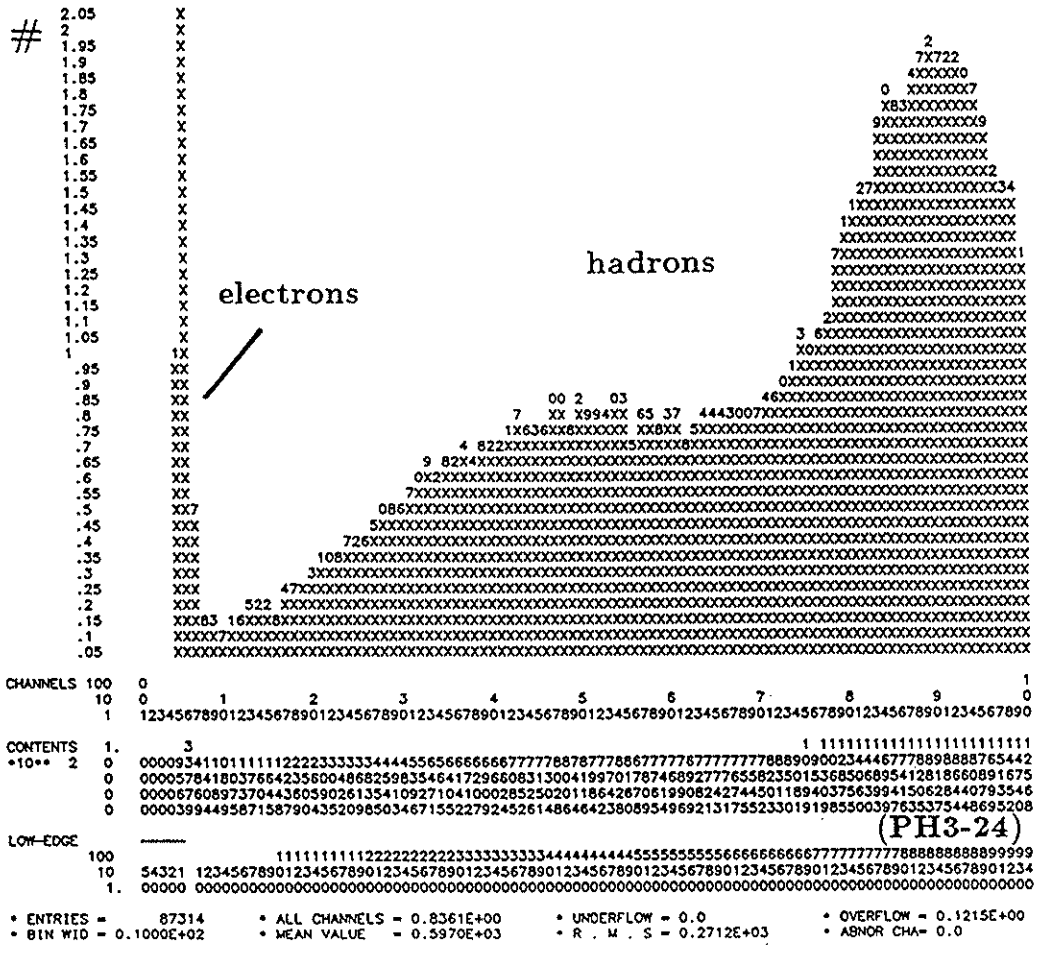

Fig. 4.7 Electrons and Hadrons as Function of PH3-24, with Cut on Muons by the Calorimeter.

In order to determine the Cherenkov ADC spectrum and the efficiency for electrons, first a clean sample of electrons using the calorimeter information was selected. Figure 4.8 shows PH2 versus PH1. The electrons are expected in the right corner of this plot and a cut of PH1 > 530 and PH2 < 150 was found to determine a clean electron sample.

The Cherenkov ADC spectrum for the electron sample determined in this manner is shown in Fig. 4.9 . The spectrum shows a photoelectron number of $< n > \approx 1.2$ ph_{el} and is in good agreement with the expected photoelectron statistics:

$$\frac{e^{-<n>}<n>^i}{i!} \text{ for i = 0, 1, 2, 3 ... , e.g. i=0: } e^{-1.2} \approx 0.30 .$$

The efficiency for electrons determined by the Cherenkov is presented in Fig. 4.10 . The Cherenkov spectrum and the efficiency for hadrons are presented in Figs 4.11, 12 . The hadron sample was selected by the two-dimensional calorimeter information in Fig. 4.5, where muons can be clearly excluded, and hadrons have to fulfil the cut PH3–24 > 250.

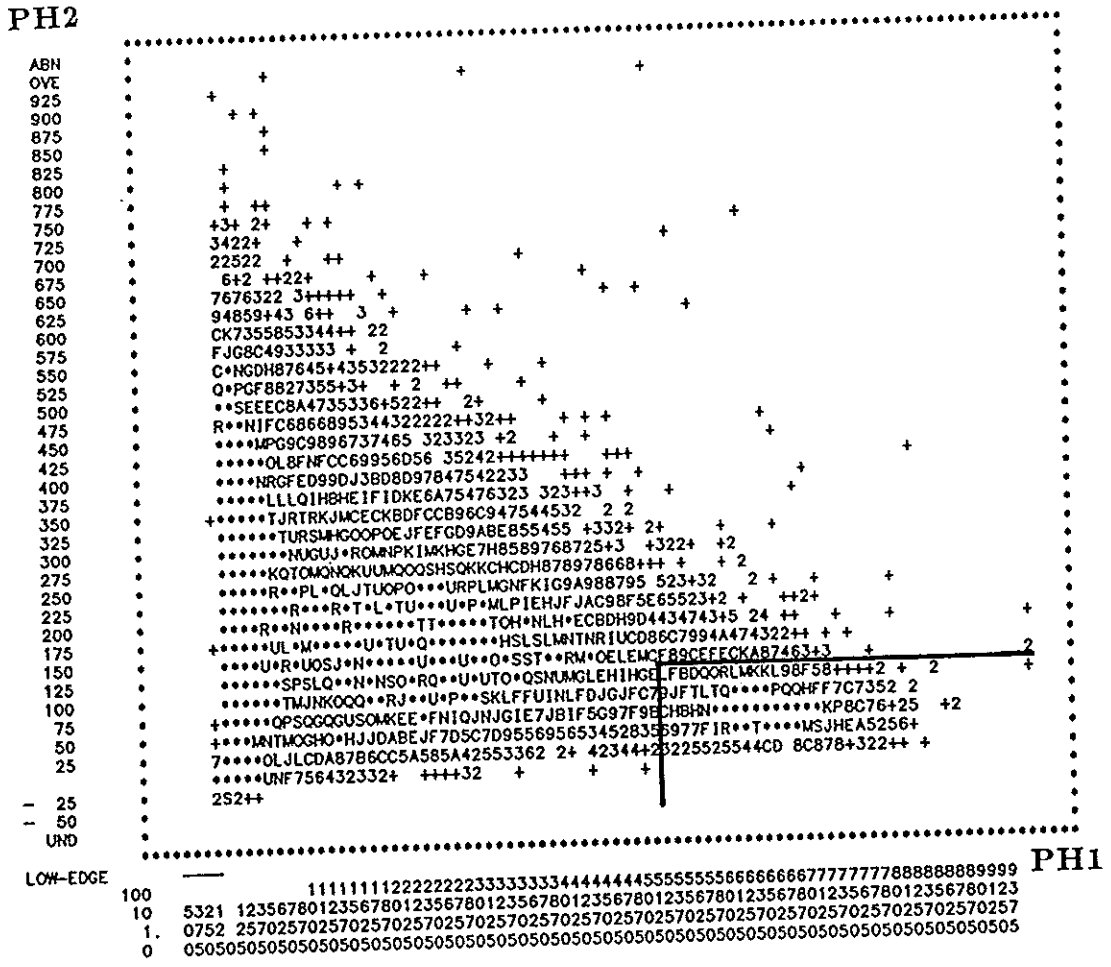

Fig. 4.8 Calorimeter ADC Signal of Module 2 versus Module 1 (PH2 .vs. PH1).

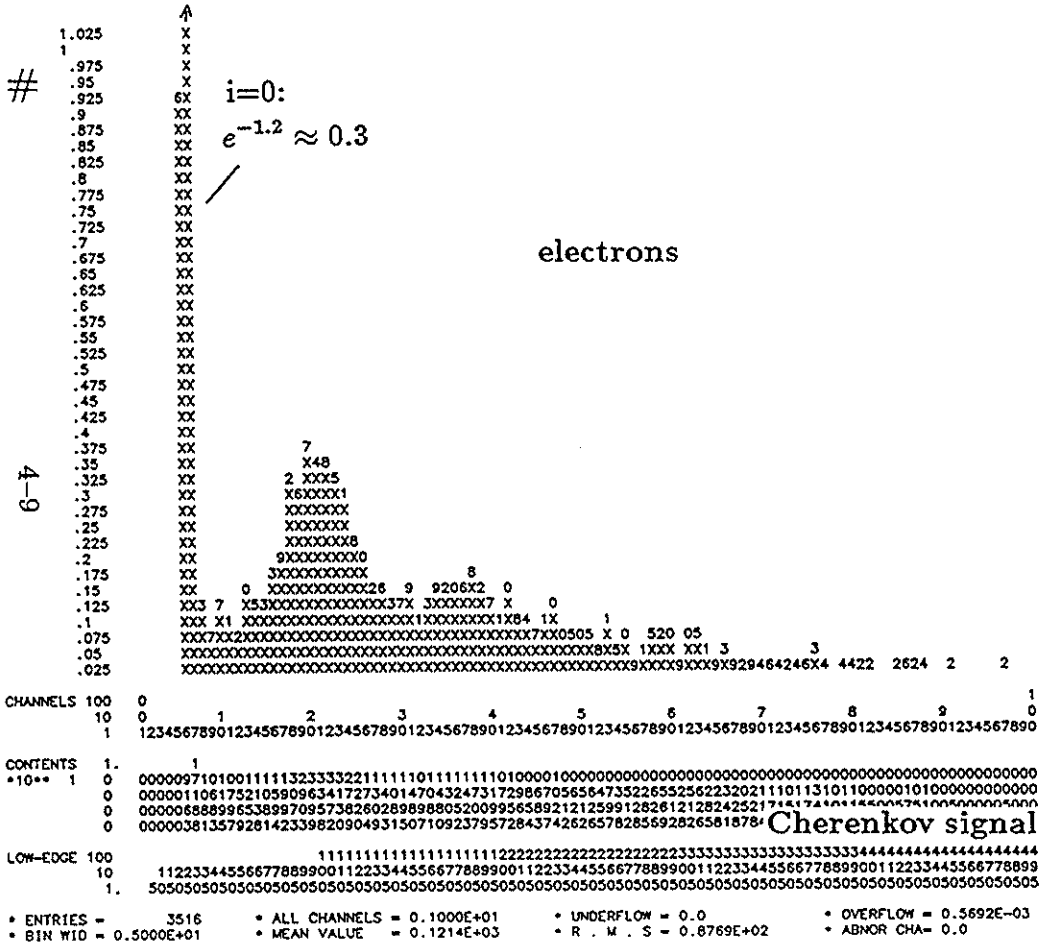

Fig. 4.9 Cherenkov ADC Spectrum for an Electron Sample Identified by the Calorimeter.

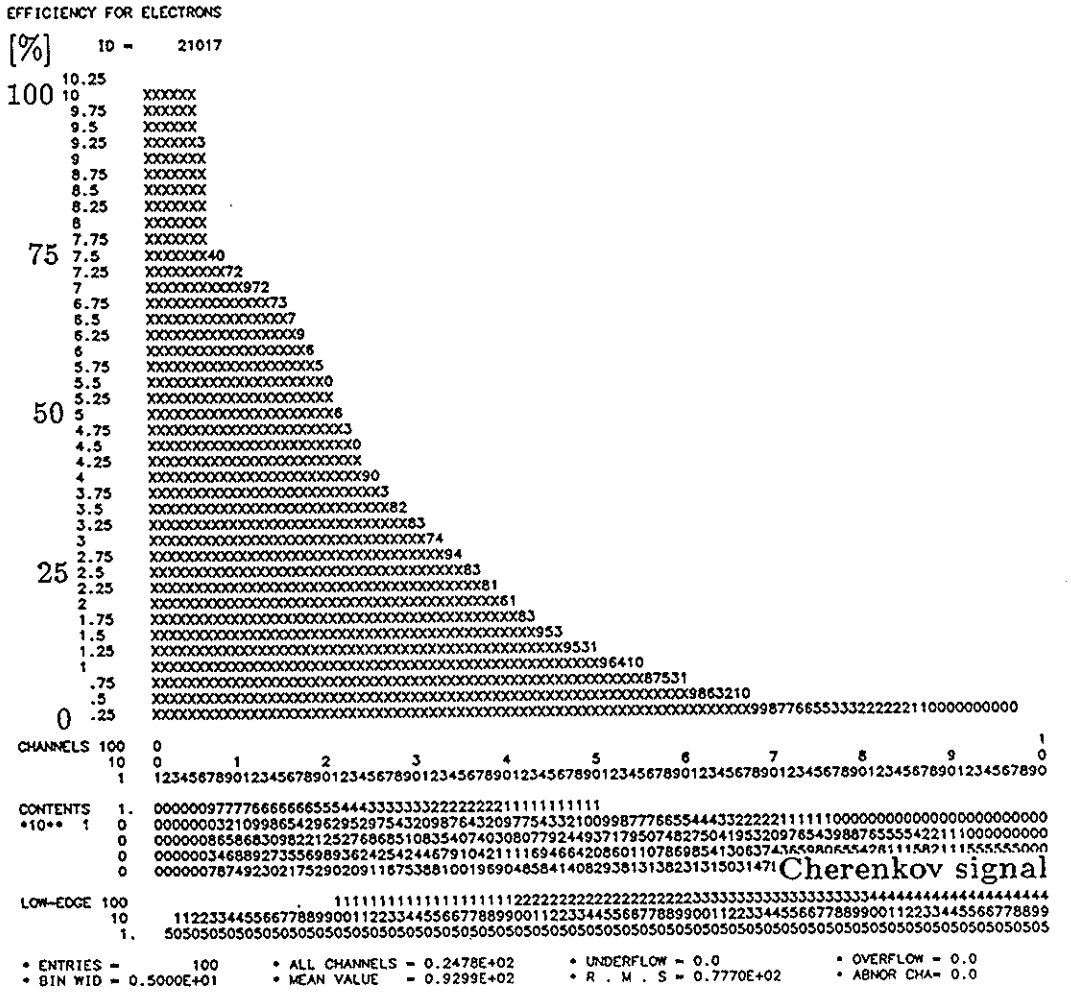

Fig. 4.10 Efficiency for Electrons as Function of the Cherenkov Signal (Fig. 4.9 cumulated).

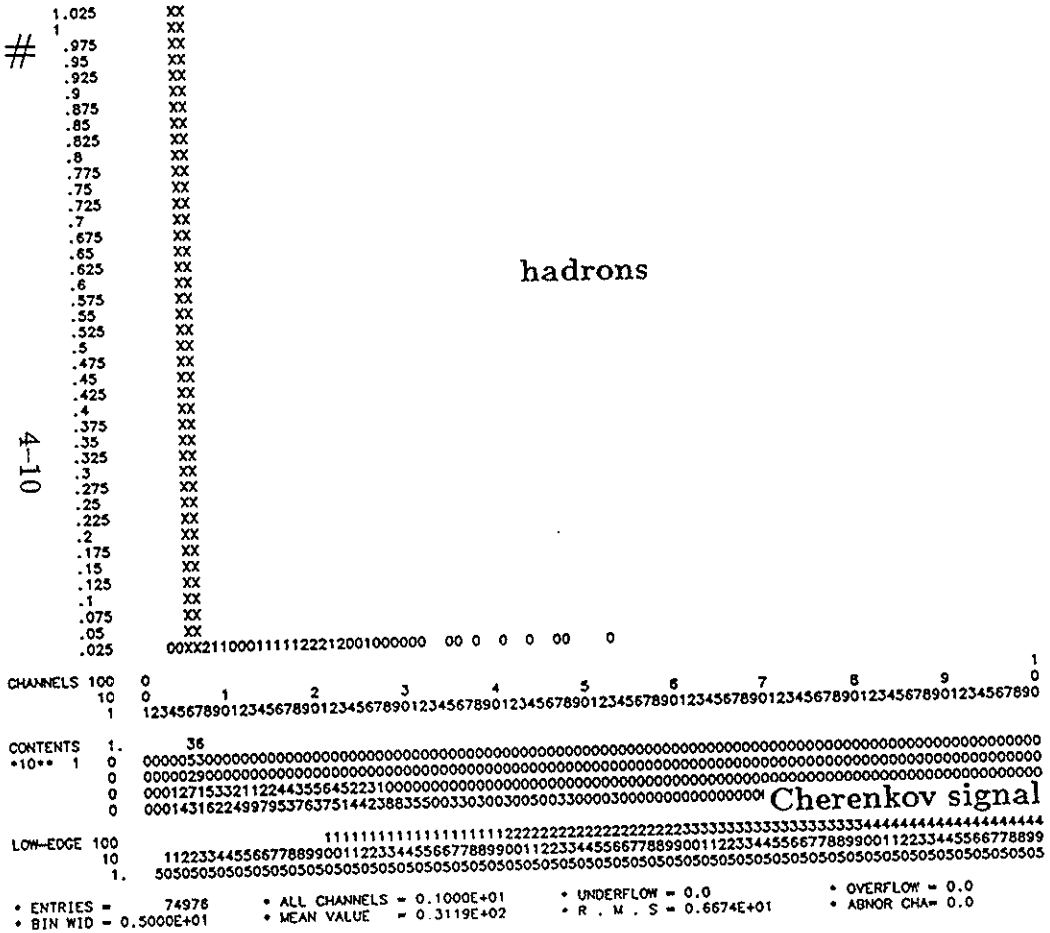

Fig. 4.11 Cherenkov ADC Spectrum for a Hadron Sample Identified by the Calorimeter.

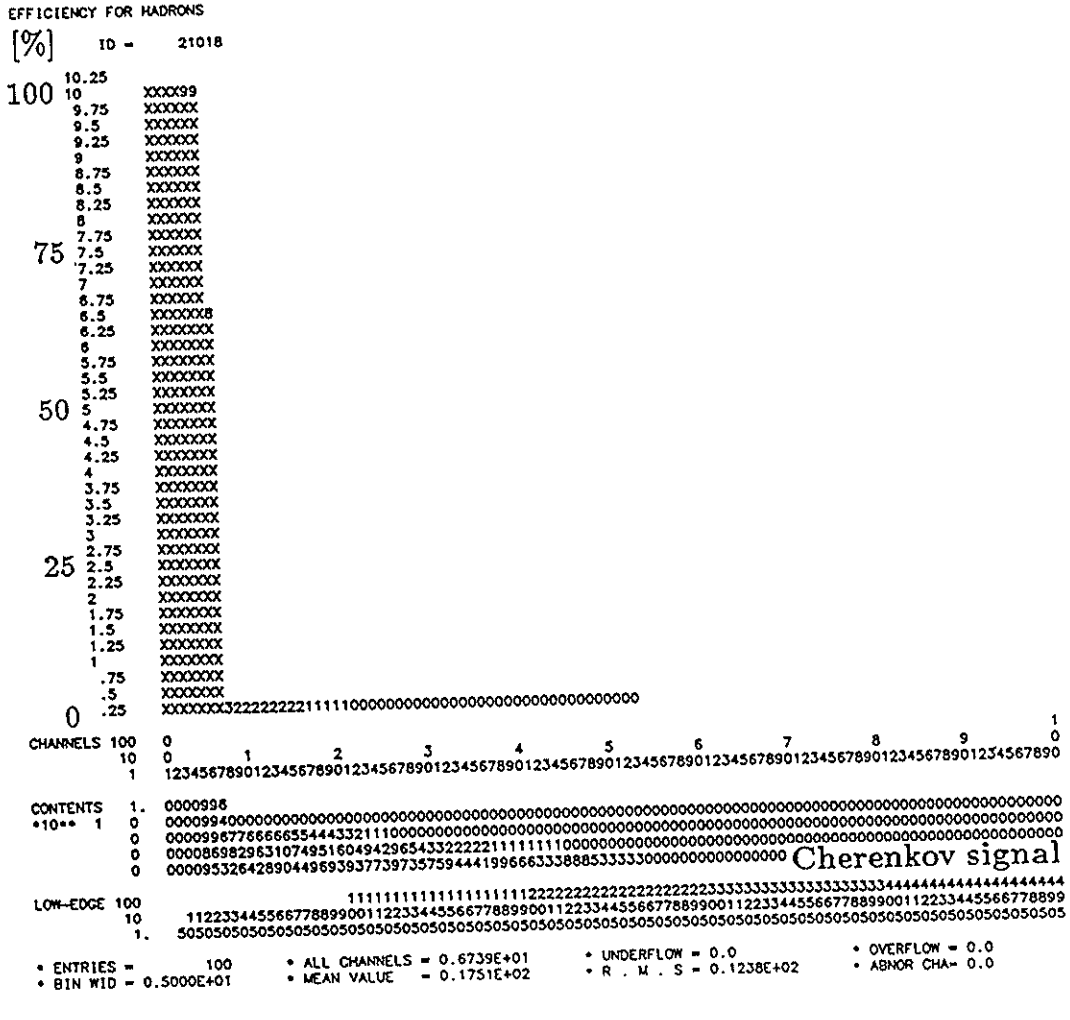

Fig. 4.12 Efficiency for Hadrons as Function of the Cherenkov Signal (Fig. 4.11 cumulated).

A cut on the Cherenkov pulse height at 50 channels yields an efficiency of $\approx$ 70% for electrons and a contribution of $\approx$17% hadrons to this sample. A cut on the Cherenkov signal at 150 channels yields an efficiency of $\approx$31% for electrons and a contribution of only $\approx$2.4% hadrons to the electron sample. The information for different Cherenkov signal cuts for the 30 GeV/c data is given in Table 4.2 . A more severe cut on the Cherenkov pulse height decreases significantly the contribution of hadrons to the electron sample, but it reduces also the statistics of the electron sample. For each beam energy the cuts were individually optimized.

Cherenkov ADC Channels $\geq$:	50	100	150	200	250	300
Electron Efficiency [%]	70.7	52.6	30.8	17.8	9.8	4.8
Hadron Efficiency [%]	0.604	0.283	0.032	0.015	0.003	0.0
Hadrons in e^-–Sample [%]	16.6	11.1	2.4	1.9	0.007	0.0

Table 4.2 Efficiencies of electrons and hadrons for different Cherenkov cuts (30GeV/c).

For the final particle identification the combined information of the Cherenkov counter and the calorimeter was used.

In order to determine the fraction of different particle types contained in the beam the following procedure was used. First the muon fraction was isolated from Fig. 4.5, then the electron fraction (a_{el}) and the hadron fraction (b_{hd}), where $b_{hd} = (1 - a_{el})$ were determined by means of the normalized Cherenkov spectra for electrons (f_{el}), hadrons (f_{hd}) and the measured sum spectrum of both (f_{sum}):

$$a_{el} \cdot f_{el} + b_{hd} \cdot f_{hd} = f_{sum}$$

The beam content of muons, electrons and hadrons for different energies is summarized in Table 4.3 .

Momentum [GeV/c]	Beam Content [%]		
	Muons	Electrons	Hadrons
5	3.5	52.6	43.9
10	3.7	22.4	73.9
20	3.9	7.2	88.9
30	4.3	4.5	91.2
40	3.5	2.7	93.8

Table 4.3 Particle types contained in the beam for 5, 10, 20, 30 and 40 GeV/c.

The fraction of electrons contained in the beam decreased rapidly with increasing momentum while the muon content is almost momentum independent.

4.2.4 Calibration and Intercalibration of the WA78 Calorimeter

The calibration of different modules was performed separately for each calorimeter part (U/Scin, Fe/Scin) in a way similar to that described in [VIN86a,b]. It was assumed that the longitudinal energy deposition of hadronic showers on average is independent of the position of the shower vertex. Therefore events were selected with shower start vertex in module n. The energy deposit in module n + 1, n + 2, ... must be the same for all n. Five samples of events were selected with shower start vertex in module n = 1,...,5. Thus, calibration constants could be determined from a system of five equations that was overdetermined. Except for the first module, which showed a different energy deposit e.g. due to upstream interactions and back-scattering, the calibration constants were actually averaged over the five equations and related arbitrarily to the fourth module. To correct for the different physical conditions of the first module, the latter was also tuned using muons. The threshold defining the position of the start vertex was determined for each module in such a way that the best exponential decrease for an interaction as function of the calorimeter depth with minimal fluctuations was determined. The number of interactions as function of the module number is shown for the 30 GeV/c data in Fig. 4.13 . It clearly shows an exponential decrease and the slope is in agreement with λ_{int}.

This calibration method, using hadronic showers, is then checked by comparing the average energy deposit of muons in each module with each other. The result of this comparison is presented in Fig. 4.14, where the average energy deposited by muons in each module is shown as a function of the module number. The energy deposited by muons is the same within errors for all modules in the U/Scin (Fe/Scin) part.

The calibration factors of all modules normalized arbitrarily to the fourth module of each part of the calorimeter represent a set of intermediate factors at this stage.

The final intercalibration of both calorimeter parts was then performed in a way different from that applied in [VIN86a,b], which uses the formula:

$$E_i = A_i \{[(dE/dx)_{abs}\Delta x_{abs} + (dE/dx)_{scin}\,\Delta x_{scin}]_i \,/\, [(dE/dx)_{Fe}\Delta x_{Fe} + (dE/dx)_{scin}\Delta x_{scin}]\},$$

where A_i are the ADC outputs after calibration and the values for $(dE/dx)_{mat}$ were taken from the tables of the Particle Data Group.

The intercalibration method applied in this calorimeter test uses the measured data itself. It requires, that on average the energies measured for particles completely contained in either the U/Scin or in the Fe/Scin part of the calorimeter have to give the same value. Thus the intercalibration factor between the two calorimeter parts was adjusted in such a way that the sums of the measured energies of the U/Scin and the Fe/Scin part lie on average on a straight line intersecting the two axis at the same values. This behaviour is shown in Fig. 4.15 after the intercalibration factor has been determined. Most showers start at the beginning of the U/Scin calorimeter, thus most of the entries are found in the lower right corner of this plot. The wide spread around the straight line reflects directly the resolution of the calorimeter.

The absolute energy calibration of the whole calorimeter was achieved by setting the area below the shower profiles for each individual energy equal to the nominal beam energy.

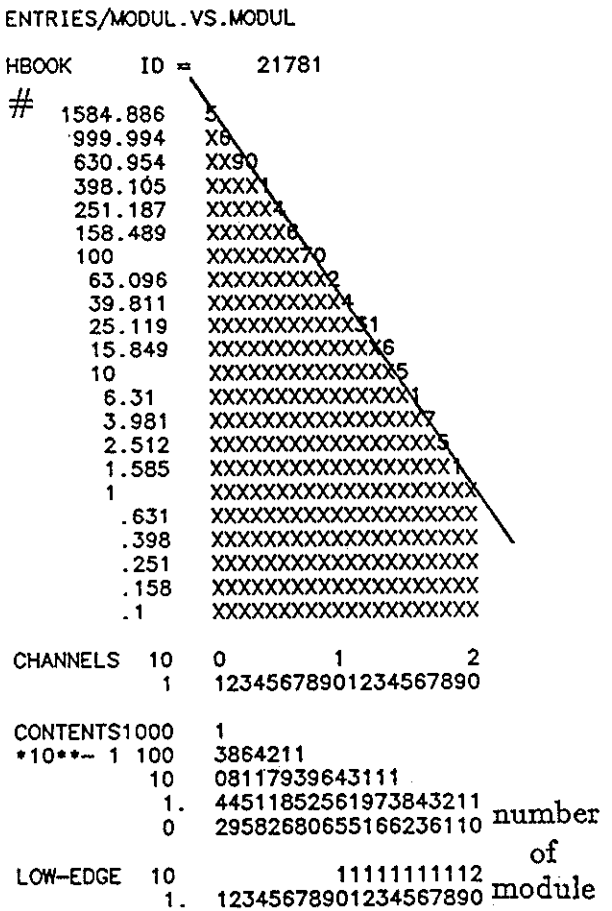

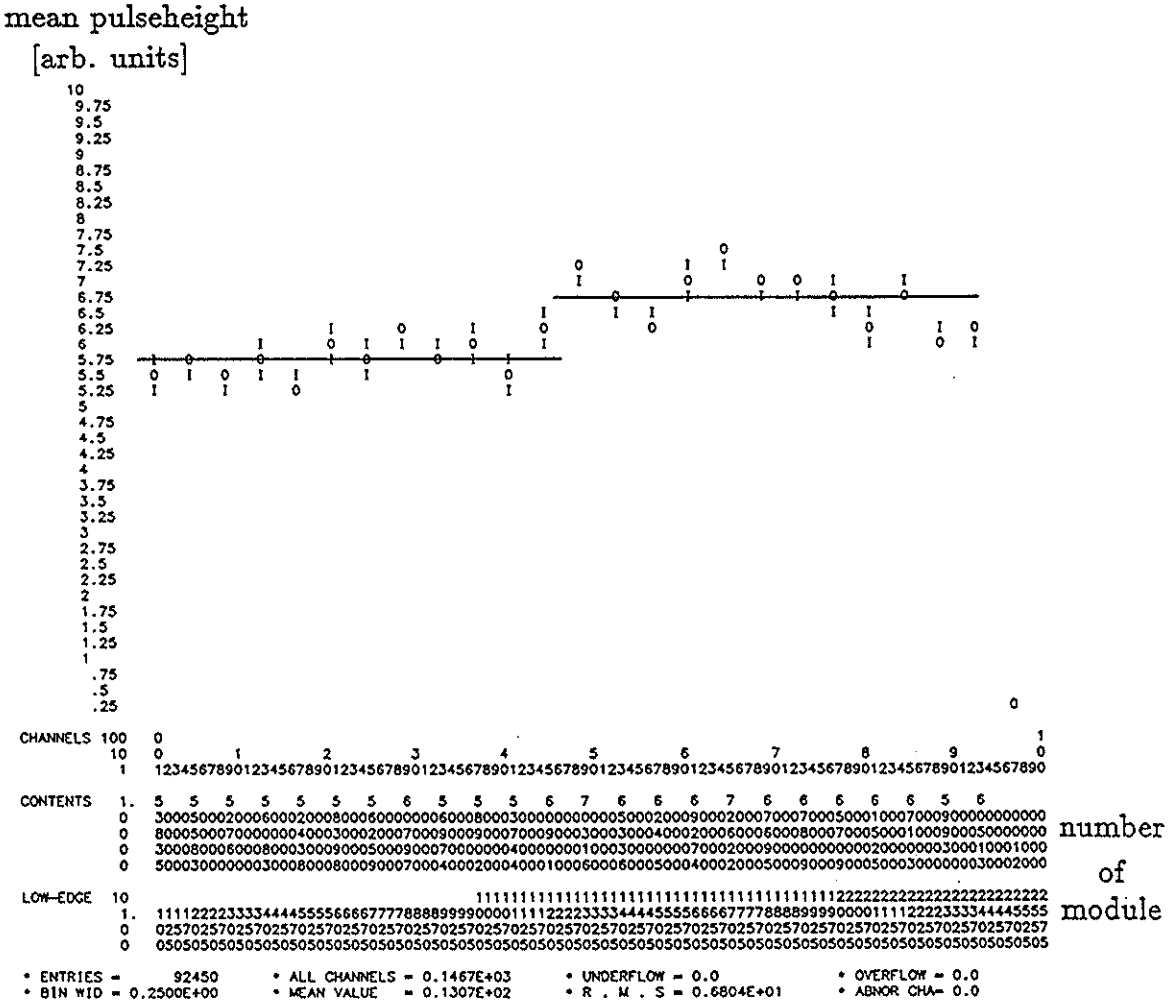

Fig. 4.13 Distribution of the Shower Vertex Position for 30 GeV.

Fig. 4.14 Average Energy Deposit of Muons as Function of the Module Number.

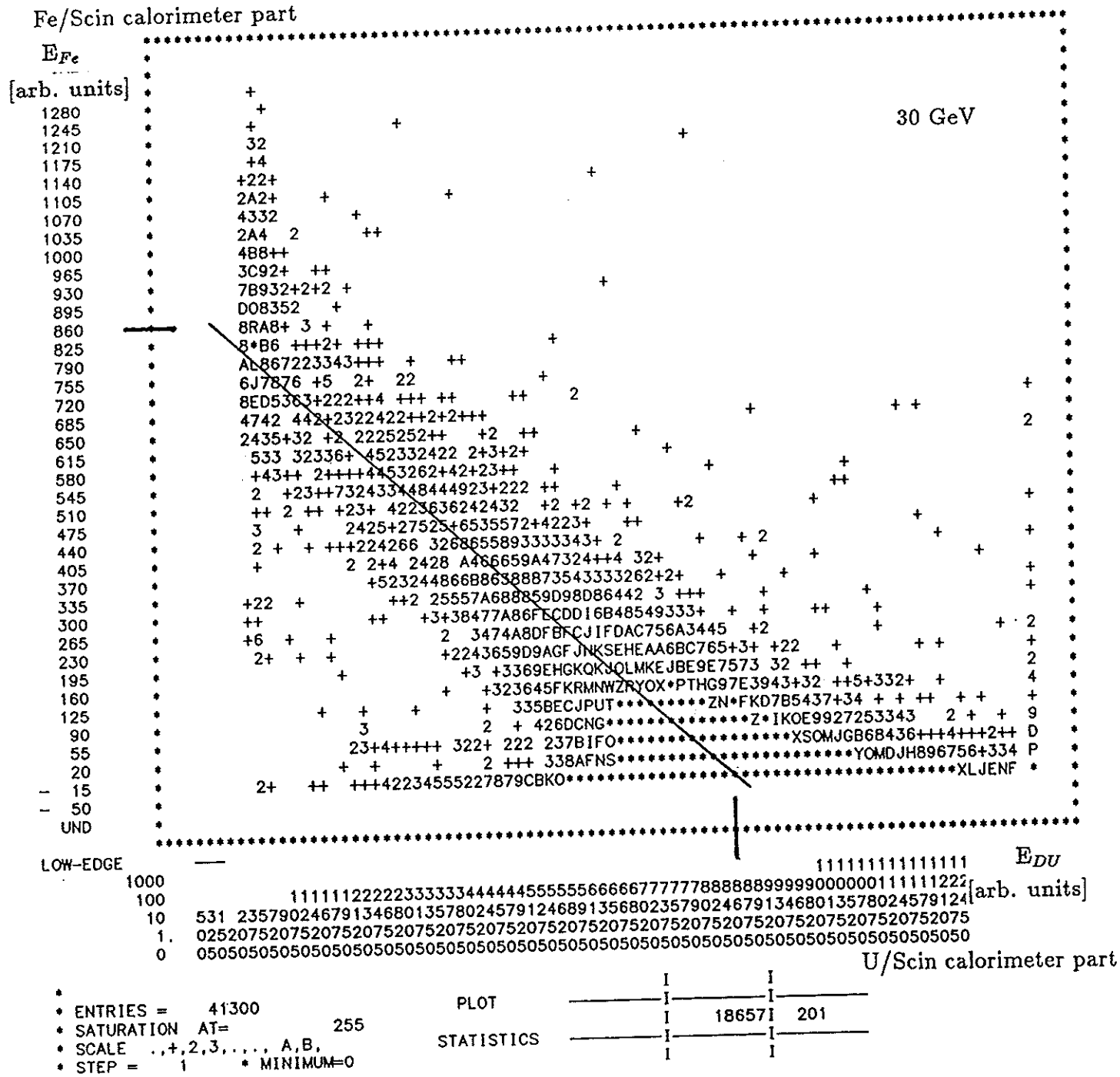

Fig. 4.15 Energy measured in the iron scintillator calorimeter part versus the energy measured in the uranium scintillator calorimeter part after intercalibration.

4.2.5 General Experimental Results from the WA78–H1–ZEUS Test

This section summarizes general results of the WA78–H1–ZEUS experiment [CAT87]. Figure 4.16 shows the pulse height spectra for 30GeV hadrons, electrons and muons. The hadron spectrum has a larger mean value in comparison with the electron spectrum. This is true for all measurements from 5GeV to 40GeV as shown in Fig. 4.17 and means that the WA78 calorimeter is overcompensating (e/h<1). The origin of this property is the ratio of the uranium plate to the scintillator plate thicknesses as predicted by Brückmann [BRÜ86]. The mean values and standard deviations of the distributions were determined for hadrons and electrons from Gaussian fits and are given in Table 4.4. The transverse size of the calorimeter is not sufficient to fully contain hadronic showers. This causes some deviations from Gaussian fits to lower pulse heights.

The increased response for hadron showers in uranium scintillator calorimeters results mainly from slow neutrons produced by spallation and fission, which scatter elastically off the free protons in the plastic scintillator [BRA85], [WIG87], [BRÜ86]. In this scattering process the neutrons deposit their energy in several successive interactions. The signal from neutrons is therefore delayed compared to the prompt signal from relativistic particles. This can be seen in Fig. 4.18, where the e/π–ratio at 30 GeV is plotted as a function of the ADC gating time. The value of the e/h–ratio depends on the signal collection time. It is about 0.8 for 80ns. Side leakage of slow neutrons accounts for a reduction of e/h by about 0.05.

The measured energy resolution for hadrons can be parametrized by:

$$\sigma_E(\pi)/\mathrm{E} = 51\%/\sqrt{E} \oplus 7\% \quad .$$

It includes the momentum uncertainty of the beam ($\sigma_p/\mathrm{p} = 14\%/\sqrt{p} \oplus 7\%$), which gives a significant contribution in particular at high energies.

The measurement of muons and electrons allows the determination of the electromagnetic sampling fraction "e". The measured values for muons are summarized in Table 4.5. The mean energy $\Delta E(\mu)|_{SCI}$ in MeV detected in the scintillator is calculated by two methods giving a lower (1) and an upper (2) estimate for the true value.

- In method 1 the energy loss by ionization (Ion), bremsstrahlung (Brems) and pair production (Pair) in the scintillator is taken from experimental data [STE71], [STE84], [LOH85] and listed in Table 4.5. Hadronic interactions of muons are not considered since these events are removed by cuts in the analysis:

$$\Delta E(\mu)|_{SCI}^{meth.1} = \left(\frac{dE}{dx}(\mu)\Big|_{SCI}^{Ion} + \frac{dE}{dx}(\mu)\Big|_{SCI}^{Brems} + \frac{dE}{dx}(\mu)\Big|_{SCI}^{Pair} \right) \cdot \Delta x_{SCI}$$

- In method 2 the ionization loss in the scintillator plus the energy lost by bremsstrahlung and pair production in the entire calorimeter (uranium plus scintillator) multiplied by "e" are taken into account:

$$\Delta E(\mu)|_{SCI}^{meth.2} = \left.\frac{dE}{dx}(\mu)\right|_{SCI}^{Ion} \cdot \Delta x_{SCI} + "e" \cdot \left\{ \Delta E(\mu)|_{CAL}^{Brems} + \Delta E(\mu)|_{CAL}^{Pair} \right\}$$

with:

$$\Delta E(\mu)|_{CAL}^{i} = \left.\frac{dE}{dx}(\mu)\right|_{SCI}^{i} \cdot \Delta x_{SCI} + \sum_{ABS} \left.\frac{dE}{dx}(\mu)\right|_{ABS}^{i} \cdot \Delta x_{ABS}$$

With the measured pulse heights $PH(e)$ and $PH(\mu)$ and the calculated energy loss $\Delta E(\mu)|_{SCI}$ the sampling fraction "e" is:

- Method 1:

$$"e" = \frac{\Delta E(\mu)|_{SCI}^{meth.1}}{PH(\mu)} \cdot \frac{PH(e)}{E}$$

- Method 2:

$$"e" = \frac{\Delta E(\mu)|_{SCI}^{Ion}}{PH(\mu) \cdot \left\{ 1 - \left(\Delta E(\mu)|_{CAL}^{Brems} + \Delta E(\mu)|_{CAL}^{Pair} \right) \cdot \frac{PH(e)}{E \cdot PH(\mu)} \right\}} \cdot \frac{PH(e)}{E}$$

The estimate of "e" is about 2.5 % (Table 4.5) with a relative systematic error of about 7% (for calibration constants (2%), absorber and scintillator thicknesses (4% for the EM and 1% for the HAD calorimeter), beam energy (2%) and ADC non–linearities (5%)).

For comparison EGS4 shower simulations yield for the sampling fraction "e" a value of 2.28% at 10 GeV.

The electron sampling fraction is often quoted relative to the sampling fraction of a hypothetical minimum ionizing particle (mip). The e/mip ratio is about 0.6 for the WA78 calorimeter. The constants needed for the calculation and the results are listed in Table 4.6. This ratio offers the possibility for comparisons between different calorimeter configurations. It is smaller than 1 because the different electromagnetic processes have different Z – dependences (Z^1 for ionization loss, Z^2 for pair production and $\approx Z^4$–Z^5 for the photo effect) and the low energetic component of the electromagnetic showers is only poorly sampled in the scintillator because of its small range in the uranium.

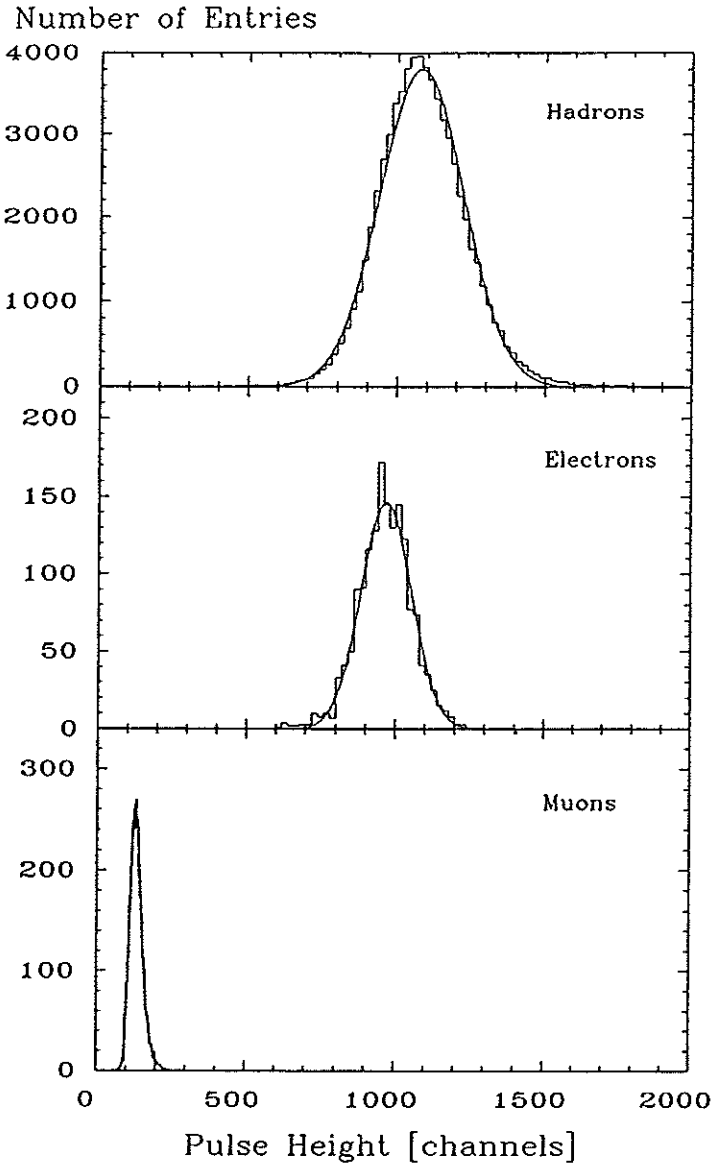

Fig. 4.16 Hadron, Electron and Muon Response in the Uranium Part at 30 GeV.

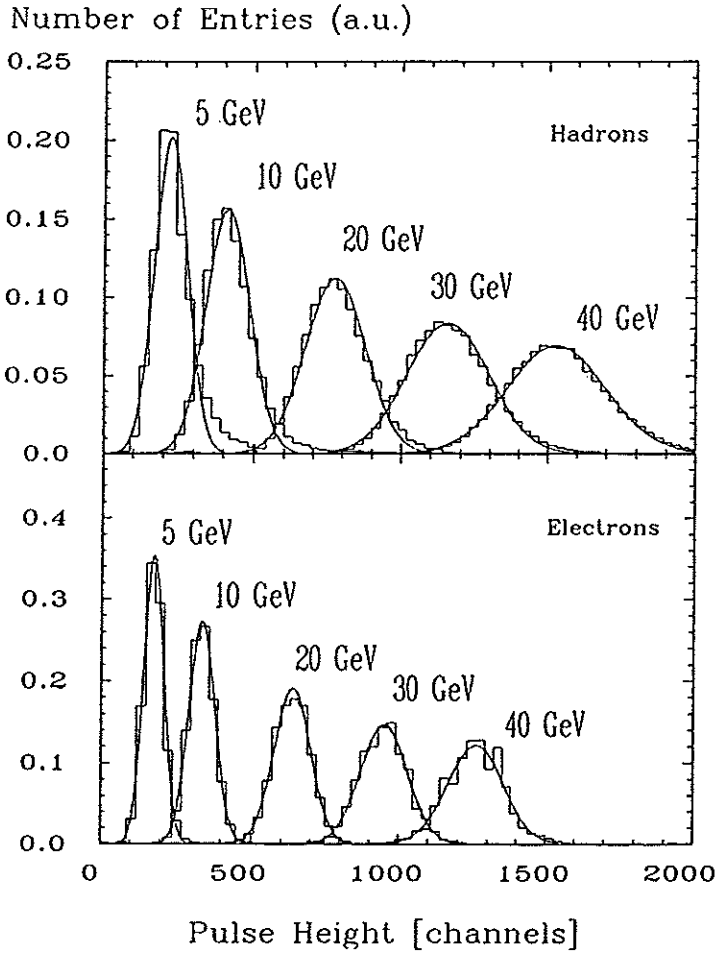

Fig. 4.17 Hadron and Electron Response in the Uranium Part for Various Beam Energies.

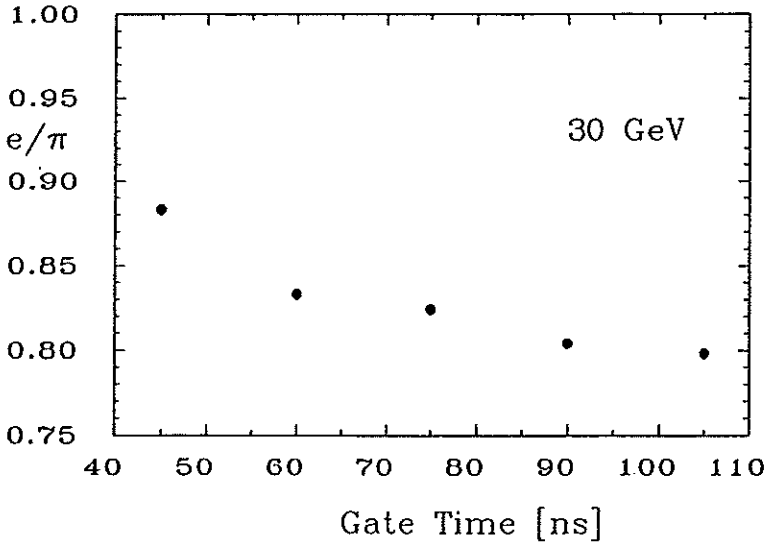

Fig. 4.18 e/π–Ratio at 30 GeV as a Function of the ADC Gating Time.

Energy [GeV]	EM–Calorimeter $PH(\mu)$ [ch]	$PH(e)$ [ch]	$\frac{\sigma_E}{E}(e)$ [%]	HAD–Calorimeter $PH(\mu)$ [ch]	$PH(e)$ [ch]	$\frac{\sigma_E}{E}(e)$ [%]	$PH(\pi)$ [ch]	$\frac{\sigma_E}{E}(\pi)$ [%]	e/π
5.1	56	576	12.2	79.2	176	18.2	226	23.7	0.78
10.1	53	1200	10.0	80.4	337	12.5	414	17.5	0.81
20.2	–	–	–	81.5	639	9.7	780	13.7	0.82
30.3	55	3300	6.7	84.1	955	8.4	1163	12.1	0.82
40.3	56	4415	6.3	86.5	1263	7.7	1533	11.2	0.82

Table 4.4 Response to different particles measured with the WA78–H1–ZEUS calorimeter.

Energy [GeV]	$\frac{dE}{dx}(\mu)\Big\vert_{SCI}$ $[\frac{MeV cm^2}{g}]$	EM–Calorimeter $\Delta E(\mu)\vert_{SCI}^{meth.1}$ [MeV]	e [%] Meth.1	Meth.2	HAD–Cal.: Uranium Part $\Delta E(\mu)\vert_{SCI}^{meth.1}$ [MeV]	e [%] Meth.1	Meth.2
5.1	2.30	52.7	10.6	10.7	57.0	2.48	2.48
10.1	2.41	55.2	12.4	12.8	59.7	2.48	2.56
20.2	2.51	57.5	–	–	62.2	2.41	2.59
30.3	2.58	59.1	11.6	12.8	63.9	2.39	2.67
40.3	2.63	60.2	11.7	13.4	65.1	2.37	2.75
Mean			11.6	12.4		2.43	2.61

Table 4.5 Calculated electron sampling fraction.

Material	Density $[\frac{g}{cm^3}]$	Energy Loss mip $[\frac{MeV cm^2}{g}]$	Total Thickness [cm] EM-Calorimeter (H1)	HAD-Calorimeter Uranium Part
Aluminium	2.70	1.62	4.8	–
Uranium	18.50	1.09	7.5	48.0
Iron	7.87	1.48	4.8	9.6
SCSN 38	1.06	1.95	21.6	–
NE 110	1.032	1.95	–	24.0
Average e/mip		Method 1	0.71	0.57
Average e/mip		Method 2	0.76	0.61

Table 4.6 Materials in the WA78–H1 calorimeter and energy loss for minimum ionizing particles (mip).

4.2.6 Longitudinal Hadron Shower Development in Uranium Scintillator

In the following, longitudinal distributions of hadron showers are presented for different incident particle energies from 5 GeV to 210 GeV [KRÜ86a], [KRÜ86b], [CAT87].

Figure 4.19 shows the longitudinal energy deposit as a function of the longitudinal depth in units of the interaction length λ. The interaction length λ is calculated as given in the tables of the Particle Data Group. Longitudinal distributions scale to first approximation in units of the interaction length. This can also be seen in the region where the different parts of the calorimeter (U/Scin (5.4λ) and Fe/Scin (8λ)) come together.

The shower maxima, measured from the face of the calorimeter, occur almost at the same depth of about 1 λ for all energies. In comparison to the general approximation for hadronic shower maxima [FAB85] given by

$$t_{max} \approx 0.2 \ln \cdot \mathrm{E\ (GeV)} + 0.7$$

the maxima are found at a somewhat smaller depth as expected for materials with high Z due to the smaller ratio of X_o/λ.
After the first few interaction lengths the distributions essentially show an exponential behaviour.

Figure 4.20 represents the longitudinal energy deposit of hadron showers starting in the first module ($\approx 0.45\ \lambda$) of the calorimeter as function of the longitudinal depth. A shower is defined to have started in the first module, if at least 4 times the deposited energy of a muon has been seen in the 1st module for energies from 5 GeV to 40 GeV or at least 8 times the deposited energy of a muon for energies of 135 GeV or 210 GeV.
This kind of longitudinal shower distribution is thought to describe the behaviour of a jet-like object, the complete energy of which is not carried by a single particle, but distributed over a whole jet of particles hitting the calorimeter. Therefore for hadron showers starting in the first module (Fig. 4.20) the name 'jet' is used in the following.

For 'jets' the shower maxima are shifted to smaller depths of about 0.7 λ and their positions are almost independent of the particle ('jet') energies. The absolute heights of the maxima strongly increase while the total lengths of the showers decrease compared to the single particle results.

The corresponding cumulative distributions are shown in Fig. 4.21 for all events and in Fig. 4.22 for events with shower vertex in the 1st module.

A phenomenological function has been fitted to the data. The fits are overlayed in Fig. 4.19 and Fig. 4.20 and describe the experimental results reasonably well. This function allows also an extrapolation to energies other than the measured ones.

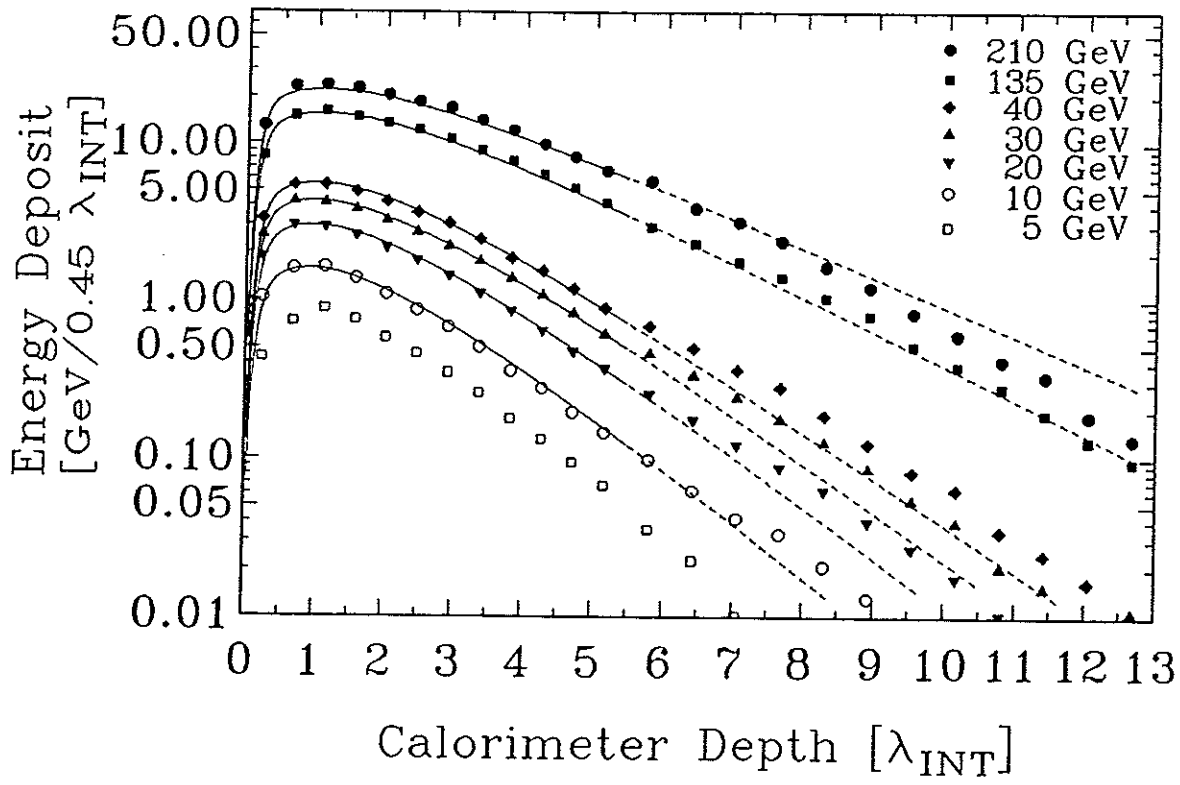

Fig. 4.19 Longitudinal Shower Profiles for Beam Momenta of 5 to 210 GeV for all Events.

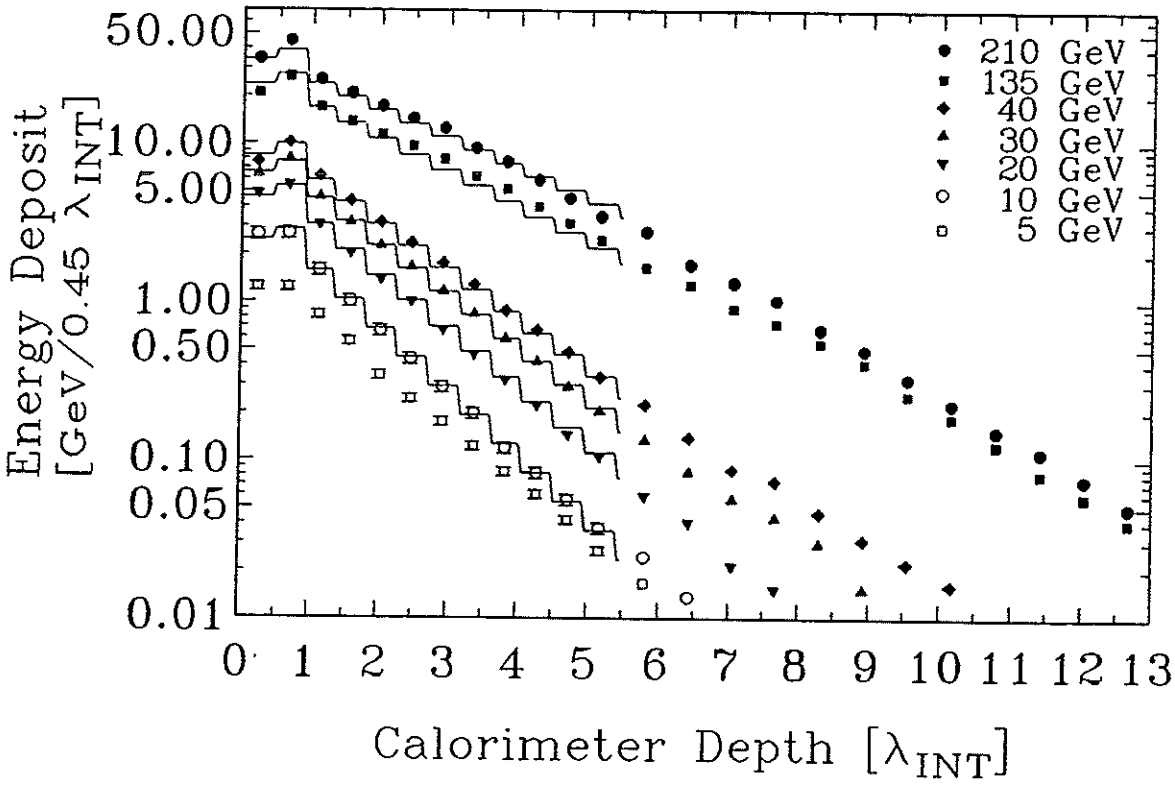

Fig. 4.20 Longitudinal Shower Profiles for Beam Momenta of 5 to 210 GeV for Events with Shower Vertices in the First Module.

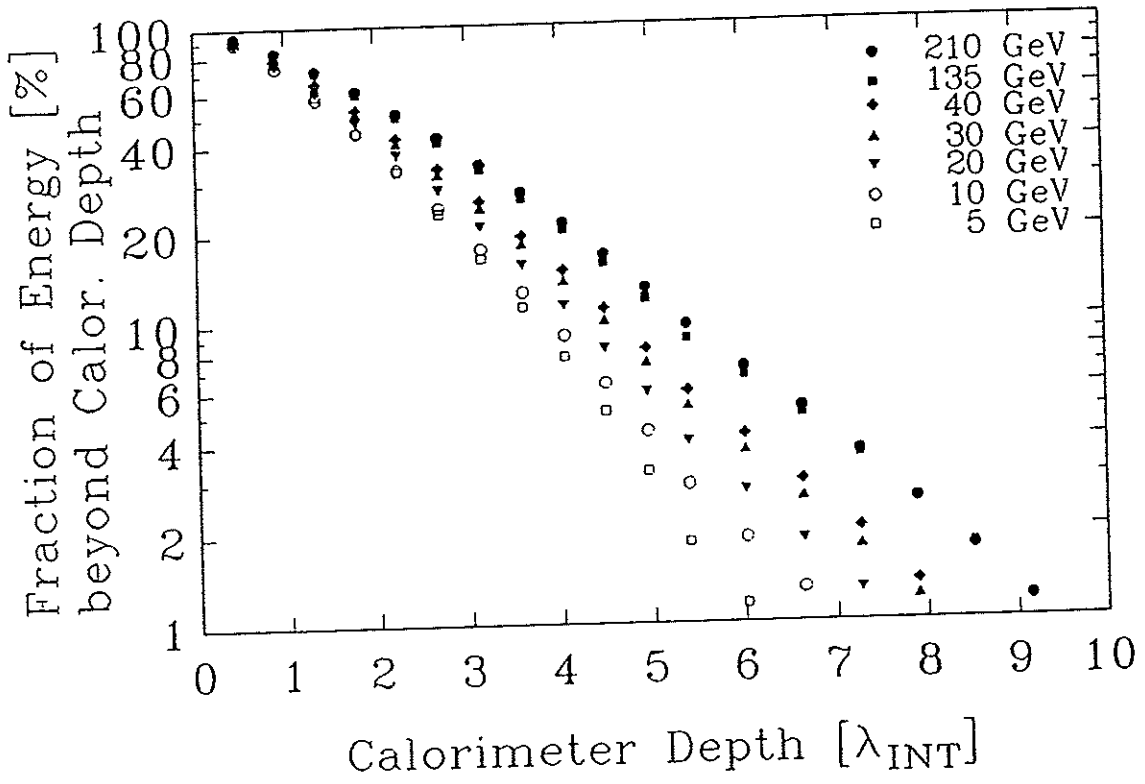

Fig. 4.21 Cumulative Distributions of Longitudinal Shower Profiles for All Events.

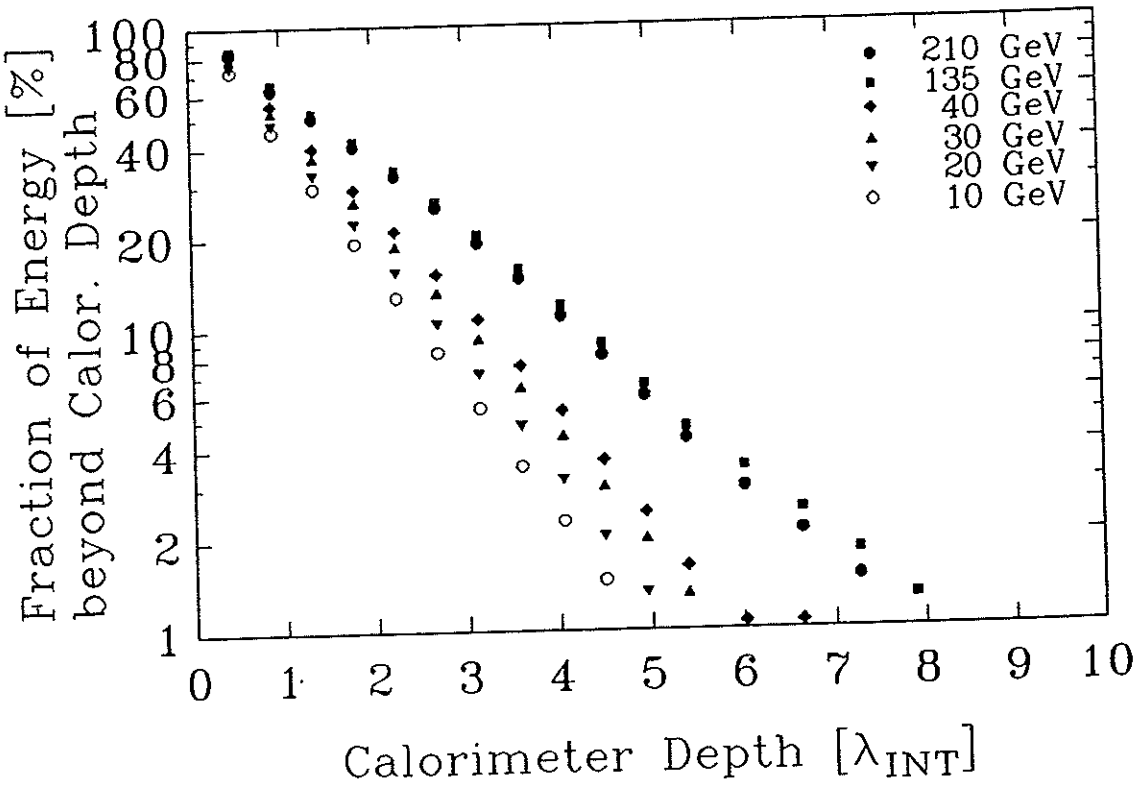

Fig. 4.22 Cumulative Distributions of Longitudinal Shower Profiles for Events with Shower Vertex in the First Module.

The energy deposit dE/dx as a function of the distance x from the shower vertex can be parametrized by:

$$\frac{dE}{dx}(x) = E\left\{ \alpha \frac{b^{a+1}}{\Gamma(a+1)} x^a \, exp\,(-bx) \; + \; (1-\alpha)\, c \, exp\,(-cx) \right\}$$

The first term has the shape used to parametrize electromagnetic showers [BÖC81], [AMA81]. It describes essentially the electromagnetic component of the shower close to the shower vertex. The second term reproduces the exponential dependence for large distances from the shower vertex and represents essentially the hadronic development of the "jet". The values of the parameters a and b are chosen to describe approximately the electromagnetic showers at 20 GeV:

$$\begin{aligned} a &= 3 \\ b\,[\lambda_{INT}^{-1}] &= 19.5 \end{aligned}$$

The parameters α and c have been obtained from fits to the data presented in Fig. 4.20 ('jets') by minimizing the correlations between the errors of the parameters. The function yields reasonable fits for energies above 5 GeV for:

$$\begin{aligned} \alpha &= 0.13 \pm 0.02 \\ c\,[\lambda_{INT}^{-1}] &= (0.67 \pm 0.03) - (0.166 \pm 0.003) \cdot \ln \frac{E\,[GeV]}{50} \end{aligned}$$

A description of the shower distributions measured from the front end of the calorimeter (t) for all events without selection on particles with shower vertex in the 1st module can be determined by the convolution of $dE/dx(x)$ with the interaction probability of the incoming particle:

$$\frac{dE}{dt} = \frac{1}{\lambda_\pi} \int_0^t exp\,(-\frac{x}{\lambda_\pi}) \, \frac{dE}{dx}\,(t-x)\,dx$$

where $\lambda_\pi = 1.11$ represents the interaction length of the incoming hadrons in units of the nominal interaction length as given in the tables of the Particle Data Group. The corresponding curves of dE/dt are overlayed for the different energies in Fig. 4.19 for single particles.

So far only average distributions of the shower development have been presented. But also the fluctuations of the energy deposit in the different modules are of interest for calorimetry. Figures 4.23, 4.24a and 4.25 show the energy deposits in module 1 to module 12 for 20 GeV, 40 GeV and 135 GeV 'jets'. The mean pulse heights and standard deviations are indicated in GeV for each module (0.45 λ) and summarized in Table 4.7a . For 40 GeV jets the maximum is for example found in module 2 with a mean value of 10.2 GeV and a standard deviation of 5.9 GeV. The corresponding energy deposits for 135 GeV 'jets' are presented in Fig. 4.25 with a maximum mean value of 28.4 GeV and a standard deviation of 16.7 GeV in module 2. Figure 4.24b shows for comparison the energy deposits for 40 GeV 'jets' where the signals of two modules (0.9 λ) are summed up per event (see Table 4.7b).

Energy Deposit [GeV] in one Module [0.45λ_{int}]												
Module:		1	2	3	4	5	6	7	8	9	10	11	12
20 GeV Jets	Mean:	4.9	5.5	3.1	2.1	1.4	1.0	0.7	0.5	0.32	0.2	0.12	0.07
	RMS:	3.4	3.2	2.1	1.7	1.4	1.2	1.0	0.9	0.7	0.6	0.5	0.4
40 GeV Jets	Mean:	7.7	10.2	6.2	4.4	3.2	2.4	1.8	1.3	0.88	0.7	0.52	0.3
	RMS:	6.4	5.9	4.0	3.1	2.6	2.3	2.0	1.7	1.5	1.3	1.1	0.9
135 GeV Jets	Mean:	17.1	28.4	17.7	14.5	12.0	10.1	8.3	6.4	5.3	4.1	3.2	2.5
	RMS:	11.4	16.7	11.0	9.5	8.7	7.2	7.1	5.8	5.6	4.9	4.4	4.0

Table 4.7a Energy deposit in an individual module of the WA78 calorimeter. Note: since the distributions are strongly nongaussian "RMS" can only give a very qualitative measure of the spread.

Energy Deposit [GeV] in two Modules [0.9λ_{int}]							
Module:		1 + 2	2 + 3	3 + 4	4 + 5	5 + 6	6 + 7
40 GeV Jets	Mean:	17.9	16.4	10.6	7.5	5.5	4.1
	RMS:	7.9	7.4	5.8	4.8	4.1	3.6
Module:		7 + 8	8 + 9	9 + 10	10 + 11	11 + 12	12 + 13
40 GeV Jets	Mean:	3.0	2.2	1.5	1.1	0.8	0.6
	RMS:	3.2	2.8	2.3	2.1	1.7	1.4

Table 4.7b Energy deposit in two individual modules of the WA78 calorimeter.

An important parameter when designing a calorimeter is the depth of the calorimeter necessary to contain a certain fraction of the hadron shower energy for a desired percentage of events. This problem is related to the longitudinal development of the showers and will be discussed in detail in section 4.2.8 .

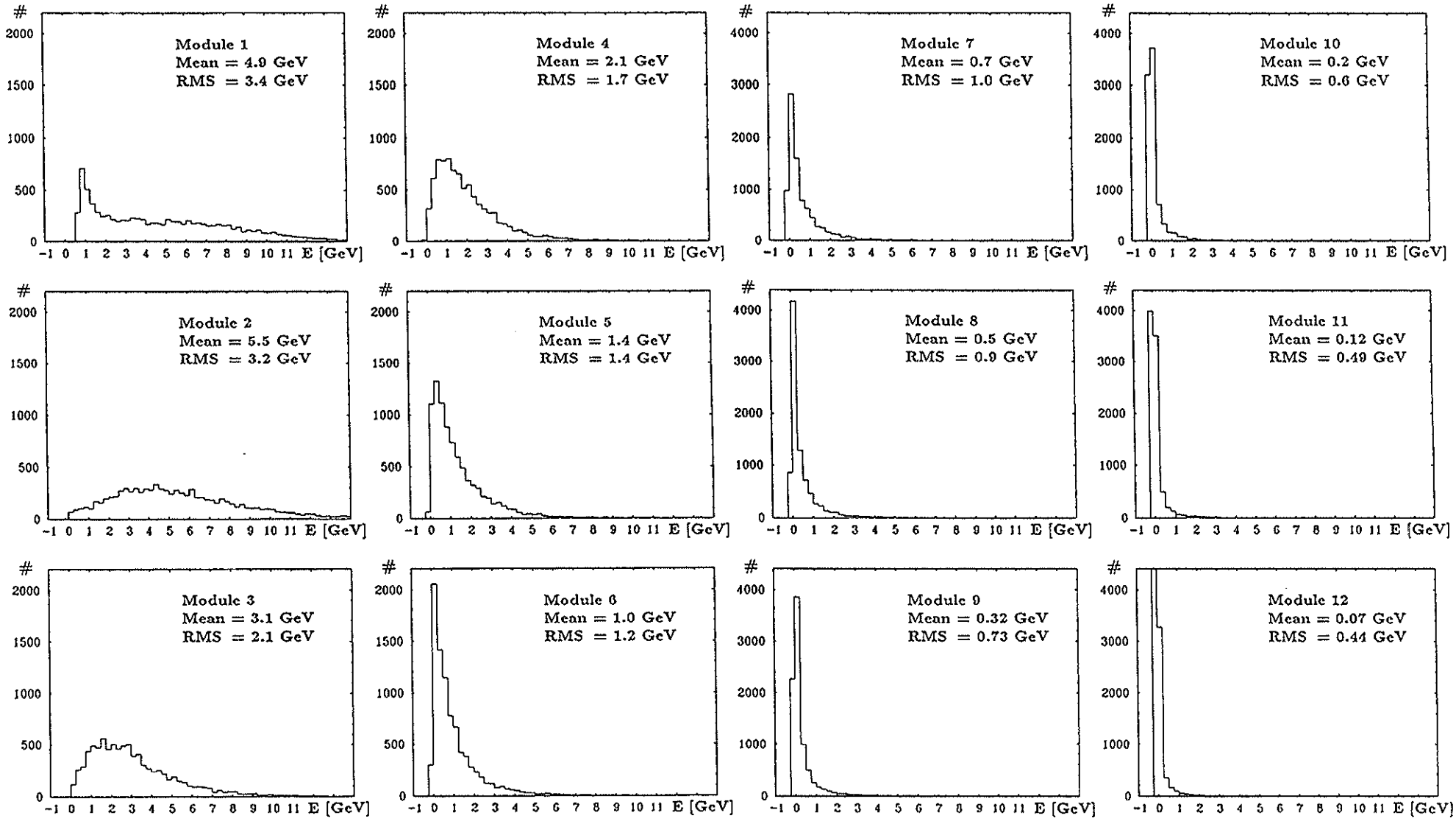

Fig. 4.23 Energy Deposit in Individual Modules [$0.45\lambda_{int}$] for 20 GeV Jets.

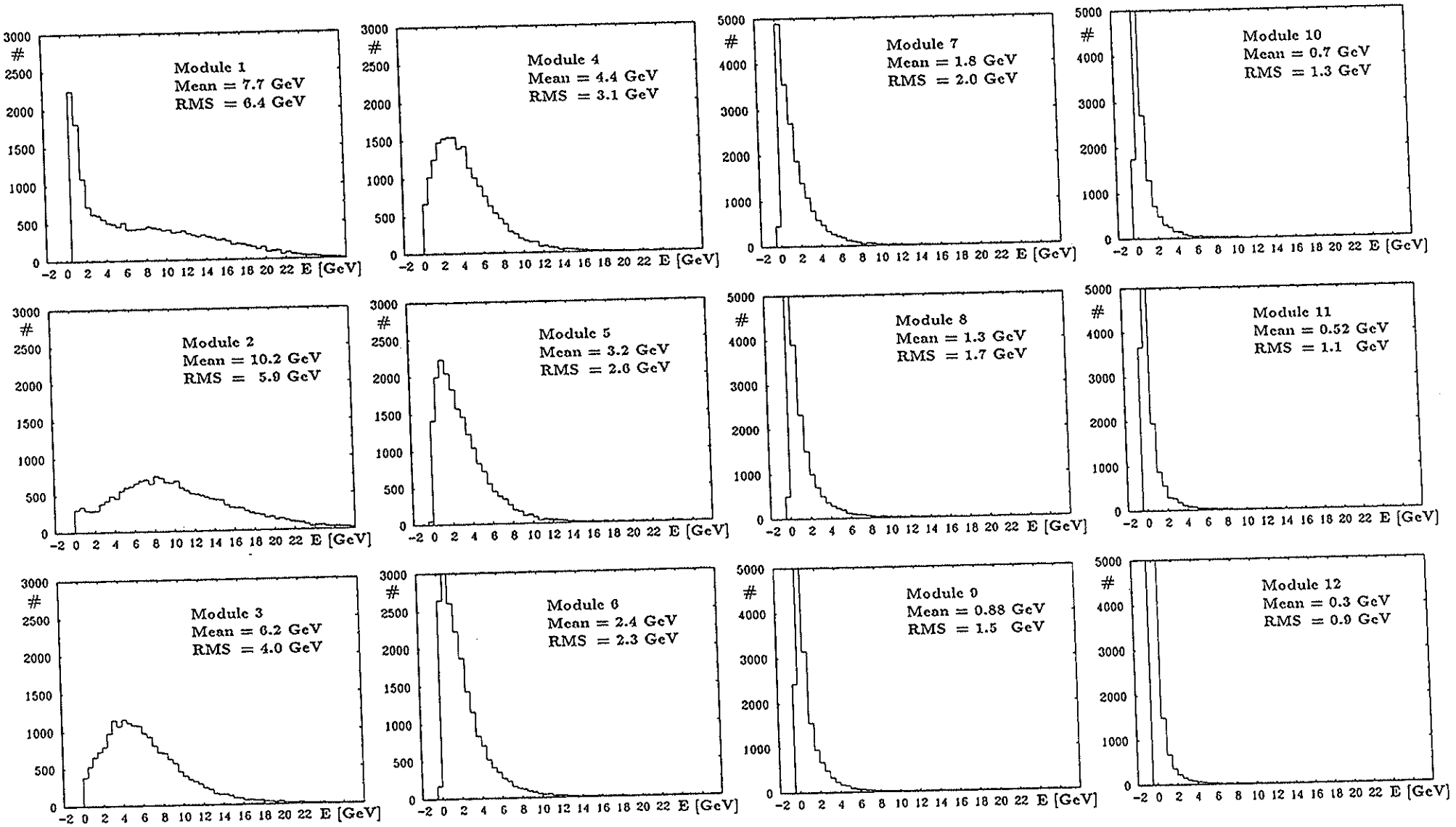

Fig. 4.24a Energy Deposit in Individual Modules [$0.45\lambda_{int}$] for 40 GeV Jets.

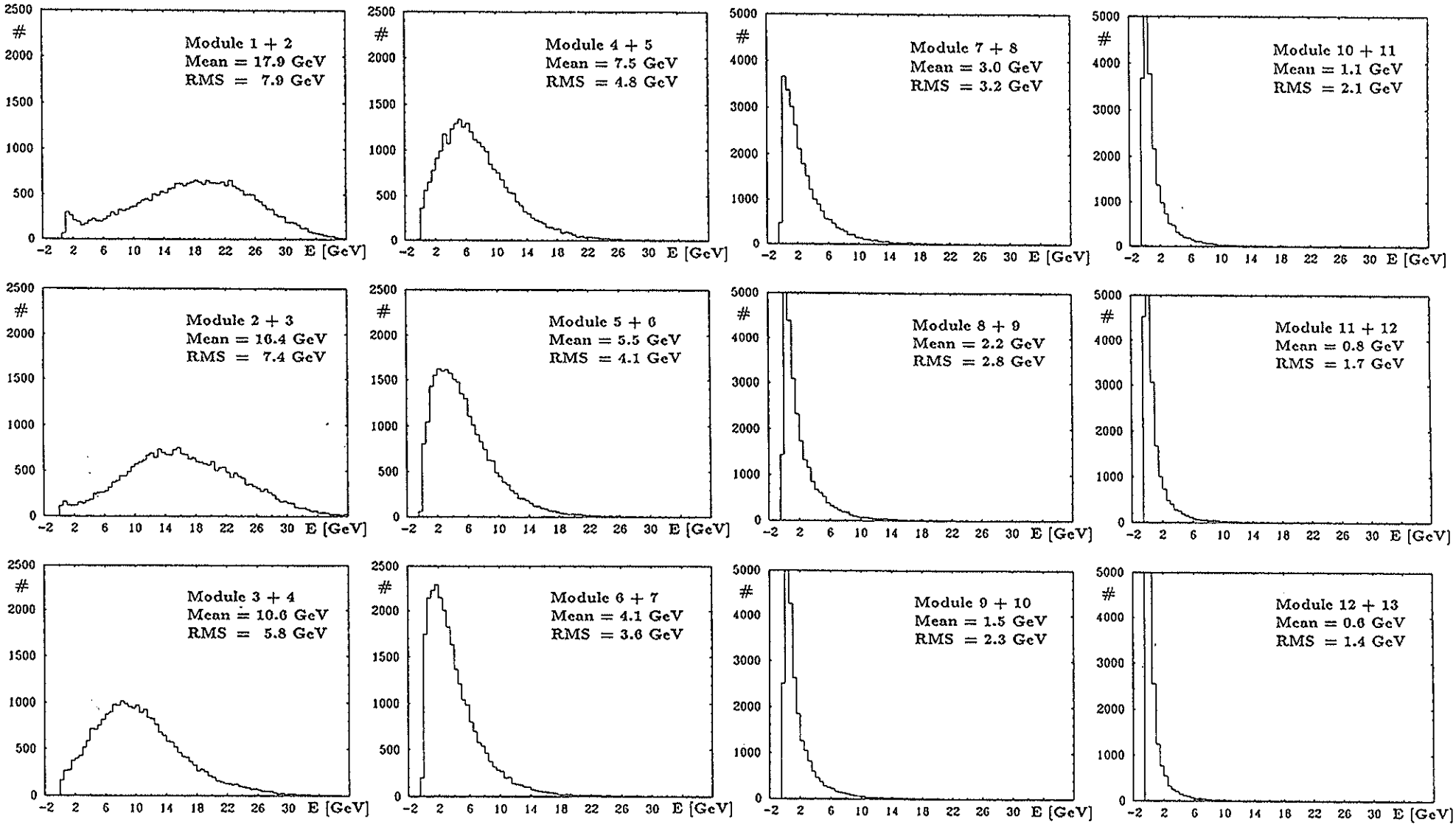

Fig. 4.24b Energy Deposit in two Individual Modules [$0.9\lambda_{int}$] for 40 GeV Jets.

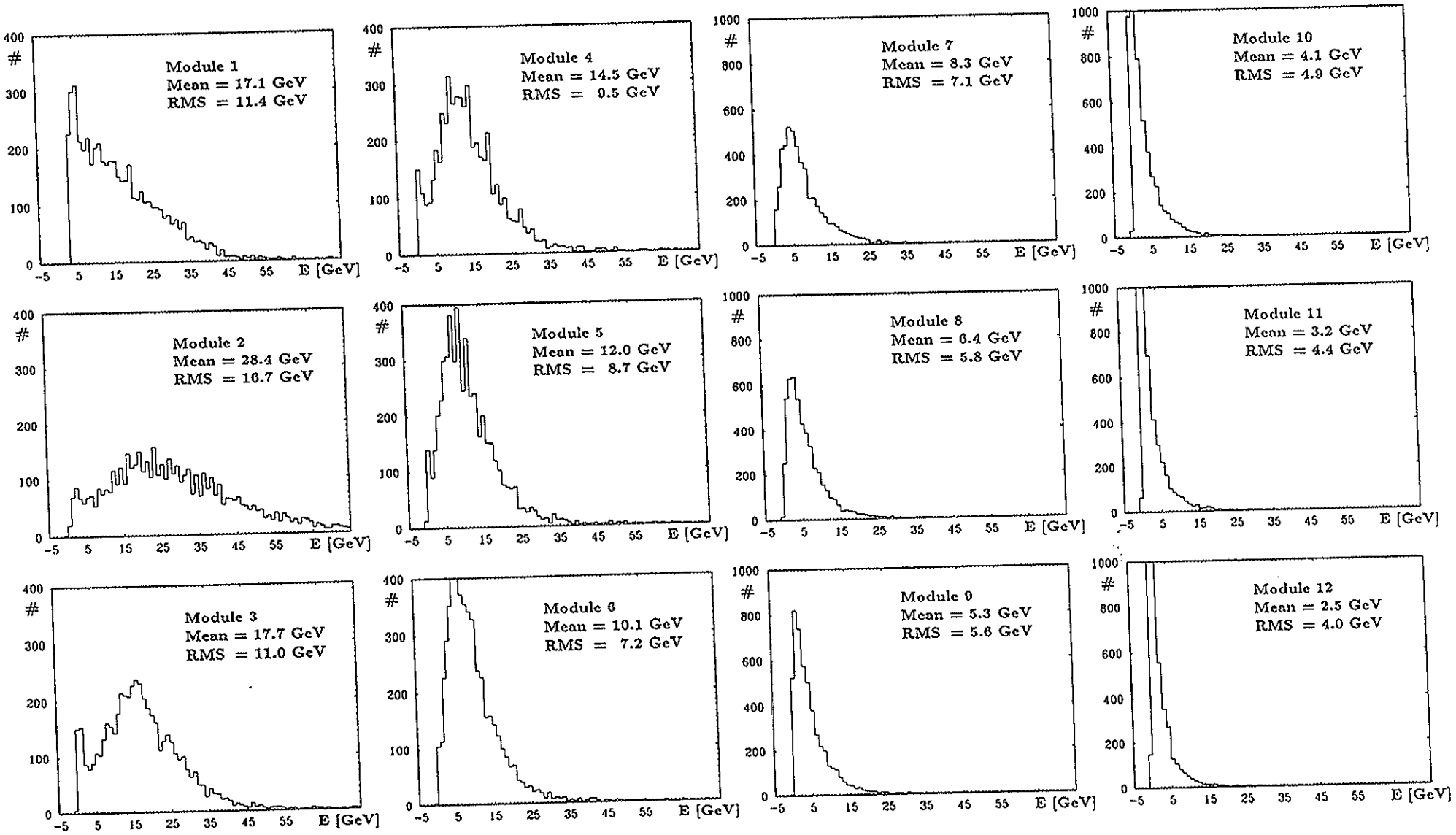

Fig. 4.25 Energy Deposit in Individual Modules [$0.45\lambda_{int}$] for 135 GeV Jets.

Longitudinal Shower Development Created from LUND Jets

A different way to study the longitudinal shower development of jets is to use Monte Carlo techniques for specifying the number and energies of particles in jets and using the longitudinal energy deposition distributions measured for single particles. In comparison to jets defined by hadron showers starting in the first module of the calorimeter (depending of course on a chosen threshold), Monte Carlo (MC) simulated jets are expected to describe well the behaviour of real jets as expected at HERA, in the sense that they take into account the distributions of particle momenta, multiplicities, angles etc... of measured jets.
The longitudinal shower development of LUND MC jets is determined in the following way:

1. Events are generated by means of the LUND MC program [LUN52] via weak charge exchange ep$\rightarrow \nu$X in the kinematical region of HERA (e.g. x>0.1 and y>0.6) [LOH83].

2. Jets with the desired energy are selected from this event sample. For all single particles (γ's, e's or hadrons) contained in a jet the measured longitudinal em or hadronic showers for single particles (scaled from the measured energies 5, 10, 20, 30, 40, 135 or 210 GeV) are used and added up to create the longitudinal shower profile of the jet.

This generation of longitudinal showers of jets obviously has the following advantages:
The LUND MC jets generated in the first step are based on momentum and multiplicity distributions, that have been tuned and adjusted to real data and should therefore resemble the behaviour of true jets.

The electromagnetic and hadronic showers used for the single particles are measured and therefore don't contain Monte Carlo uncertainties. In addition this method has the advantage that it is very fast, consuming only a relatively small amount of computer time. For each generated particle only one measured shower with an energy next to that of the generated particle has to be read in and its energy simply has to be scaled.

The jets were generated in the kinematical region of $x > 0.1$ and $y > 0.6$ and cover essentially the energy range from 20 GeV to 160 GeV. The longitudinal shower development of these jets is presented in Fig. 4.26, the electromagnetic and hadronic parts contributing to this profile are also shown. About half of the generated particles interact electromagnetically (γ, e, π^o) and produce a strong contribution to the showers in the first module.

For comparison with the jets of Fig. 4.20 (WA78 hadron showers starting in the first module) two sets of LUND jets are selected with an energy of $\approx$ 40 GeV ($\pm$5 GeV) and $\approx$ 135 GeV ($\pm$15 GeV) and are presented in Fig. 4.27 .

The longitudinal shower profiles of LUND jets have their maximum already in the 1st module instead of the 2nd module as the WA78 'jets' do. For LUND jets this is due to the electromagnetically interacting particles which deposit their energy already at the front face of the calorimeter (see Fig. 4.26). But uncertainties in a single point are of less importance for the study of calorimeter lengths, for which cumulated distributions of the longitudinal shower profiles are studied. In the central region of the shower profiles of LUND jets the shape is similar to that of WA78 'jets', but there are some deviations for calorimeter depths above 4λ. Particle multiplicities, momentum distributions etc ... of LUND jets depend of course on various physical processes and on the selected kinematical region thus deviations from the longitudinal development of WA78 'jets' may be expected. The shape of the shower profiles of WA78 'jets' could be tuned of course to some extent by varying the threshold used for the definition of the start vertex. But in general both kinds of jets show a rather similar structure to their longitudinal shower development.

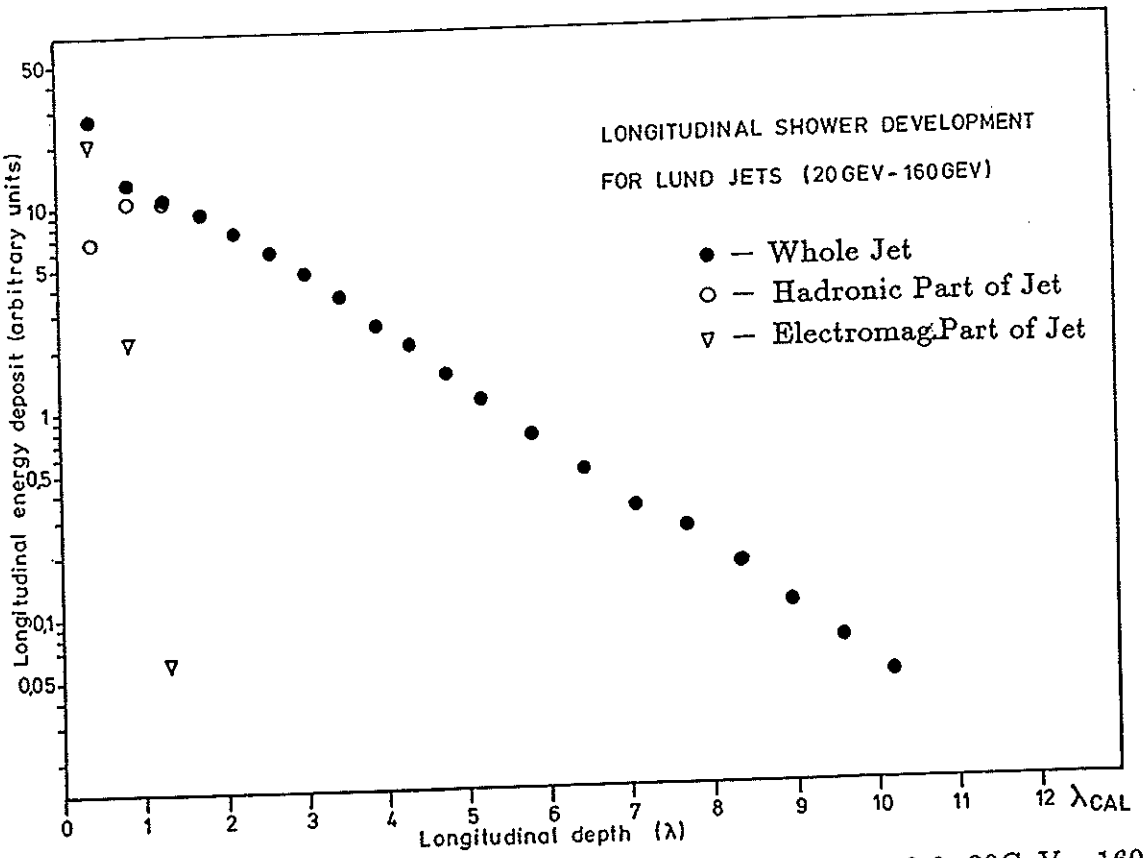

Fig. 4.26 Longitudinal shower profiles of LUND jets ($x > 0.1$, $y > 0.6$; 20GeV - 160GeV jets) plus electromagnetic and hadronic parts as function of the calorimeter depth λ_{CAL} using the shower development measured for single particles.

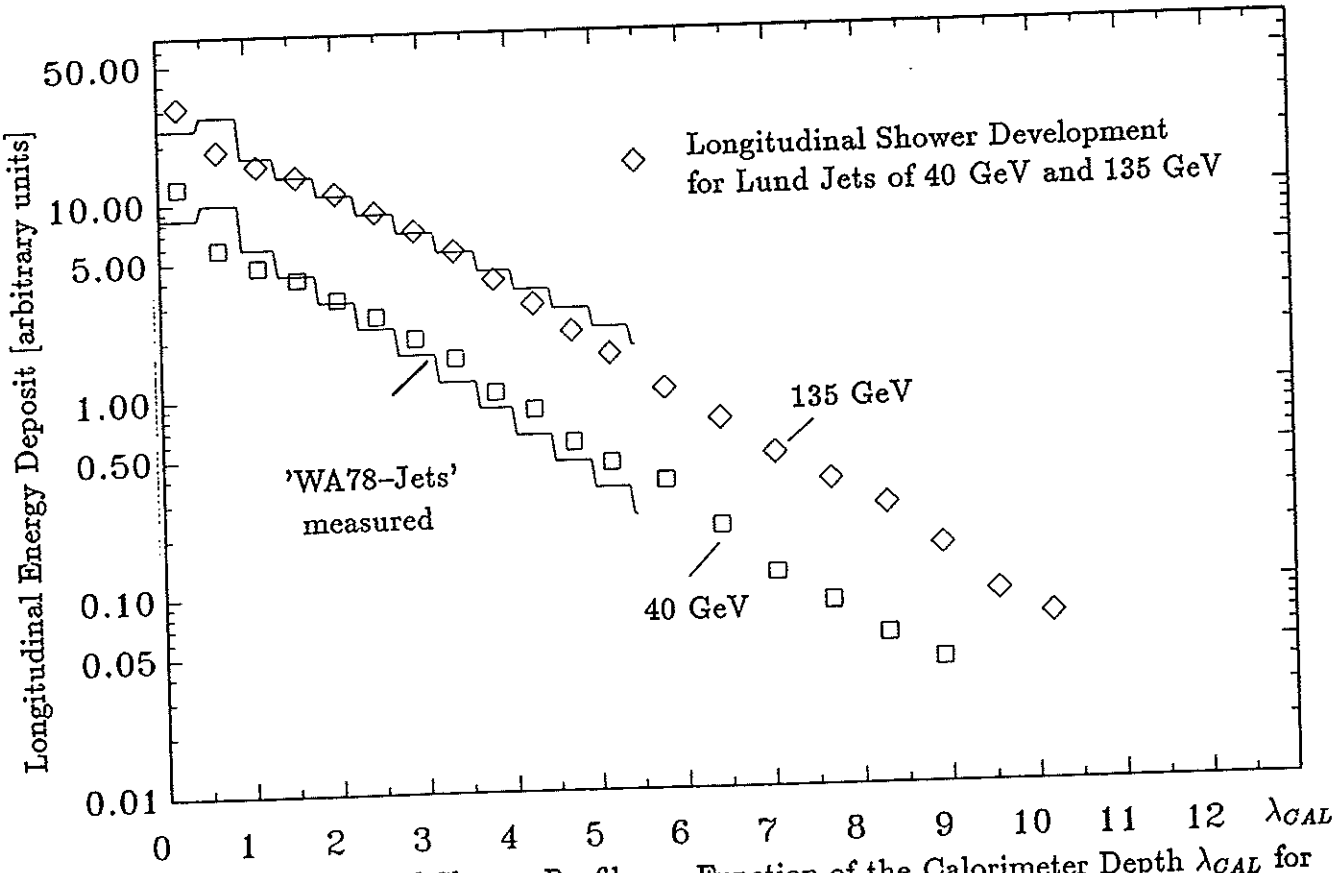

Fig. 4.27 Longitudinal Shower Profiles as Function of the Calorimeter Depth λ_{CAL} for 40 GeV and 135 GeV LUND Jets.

4.2.7 The Hadron Calorimeter System for the ZEUS Detector

The hadron calorimeter for the ZEUS detector surrounds hermetically the interaction region with an acceptance of about 99.8% of 4π detecting all single particles and jets produced as described in detail in section 2.3 and in [ZEU85],..., [ZEU91].

The calorimeter system consists of an inner high resolution depleted Uranium/Scintillator (DU/Scin) calorimeter with a depth of $\approx 7\lambda$ for the forward (FCAL), $\approx 5\lambda$ for the barrel (BCAL) and $\approx 4\lambda$ for the rear calorimeter (RCAL). The high resolution calorimeter is fully contained in the coarser iron sandwich backing calorimeter (BAC) with a depth of 6 to 4λ (see Fig. 4.28). The BAC uses the Fe plates of the iron yoke as absorber plates and is equipped with multiwire proportional tube chambers.

The depth of the DU/Scin calorimeter is determined by requiring that 95% of the shower energy is contained for 90% of the jets of maximum energy from the HERA kinematics. The leaking energy can be measured in the backing calorimeter thus a high resolution data sample can be selected by using the BAC as a veto counter ($E_{BAC} < E_{min}$).

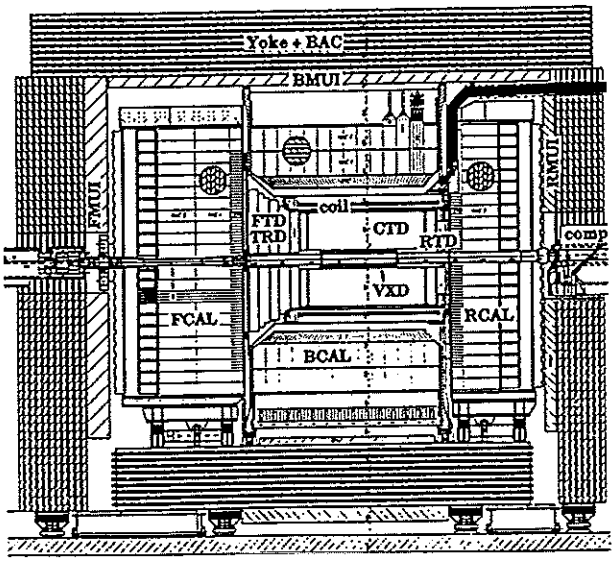

Fig. 4.28 Section of the ZEUS Calorimeter System along the Beam.

The maximum jet energy and therefore the required calorimeter depth is determined by the HERA kinematics and is presented as a function of the polar angle θ with respect to the proton direction in Fig. 4.29 . It falls from 800 GeV near the forward proton direction ($\theta = 0°$) to about 300 GeV at $\theta = 30°$, 100 GeV at $\theta = 60°$ and < 50 GeV for θ greater than 90°.

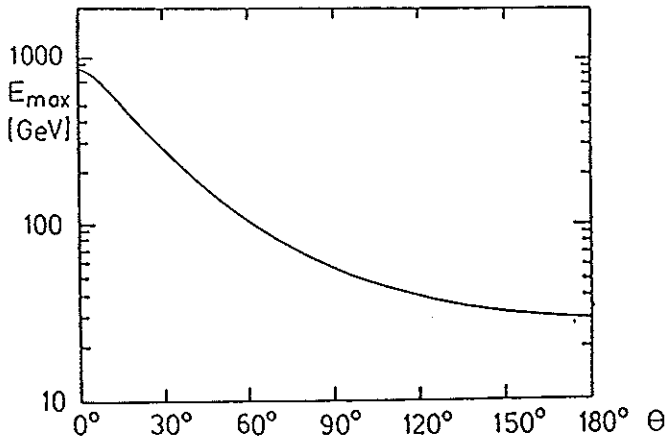

Fig. 4.29 Maximum Jet Energy as a Function of the Polar Angle θ with Respect to the Proton Direction at HERA.

The depth required for the high resolution DU/Scin calorimeter as a function of the particle or jet energy (θ) is discussed in the following with the data obtained from the WA78-H1-ZEUS calorimeter test measurements.

4.2.8 Shower Containment and Optimization of the Depth for the High Resolution ZEUS Calorimeter

The shower containment as function of the calorimeter depth λ_{CAL} is studied to optimize the depth of the calorimeter. The percentage of single particles with a fraction x_{con} [%] of their shower energy contained in a calorimeter of λ_{CAL} depth is shown for different energies in Fig. 4.30a – 4.35a. The analysis is performed for fixed shower containments of x_{con} = 90%, 92.5%, 95% and 97.5%.

The results of an equivalent analysis for 'jets', defined by hadron showers starting directly in the first module of the calorimeter are shown in Fig. 4.30b – 4.35b. The shower containment for LUND jets of 135 GeV is presented in Fig. 4.36. The fraction of events with 95% shower containment in the calorimeter as a function of the calorimeter depth is shown for different energies in Fig. 4.37 for all events and in Fig. 4.38 for WA78 'jets'.

The calorimeter depth λ_{CAL} required to measure a shower containment of 95% for 90% of the single particles and the WA78 'jets' is summarized as a function of the polar angle θ in Fig. 4.39 . This information is also given in Table 4.8. To achieve a shower containment of 95% for 90% of the jets requires a calorimeter depth, that is on average about 1.5λ shorter than for single particles. In the forward direction at about $\theta = 40°$ ($\hat{=}$ 210 GeV) a depth of about 6.6 λ is required that goes down to about 4.9λ at $\theta = 180°$ ($\hat{=}$ 30 GeV). For LUND jets the depth required in forward direction is somewhat shorter while in backward direction it is larger.

Comparing the depth of the U/Scin hadron calorimeter designed for the ZEUS detector with the required depth determined by the containment studies above as function of the polar angle θ shows reasonable agreement (Fig. 4.40).

Fraction of All Events or Jets	**Shower Containment of 95% of the Energy Calorimeter Depth in λ_{int} for**					
	10 GeV	20 GeV	30 GeV	40 GeV	135 GeV	210 GeV
85% of all Events	4.8	5.3	5.8	6.0	7.2	7.4
85% of the Jets	3.7	4.1	4.5	4.7	5.9	6.0
90% of all Events	5.3	5.9	6.5	6.8	7.9	8.1
90% of the Jets	4.1	4.5	4.9	5.1	6.5	6.6
92.5% of all Events	5.6	6.4	7.0	7.3	8.4	8.6
92.5% of the Jets	4.4	4.8	5.2	5.5	7.0	7.1

Table 4.8 Calorimeter depth required for a shower containment of 95% for various fractions of all events and jets.

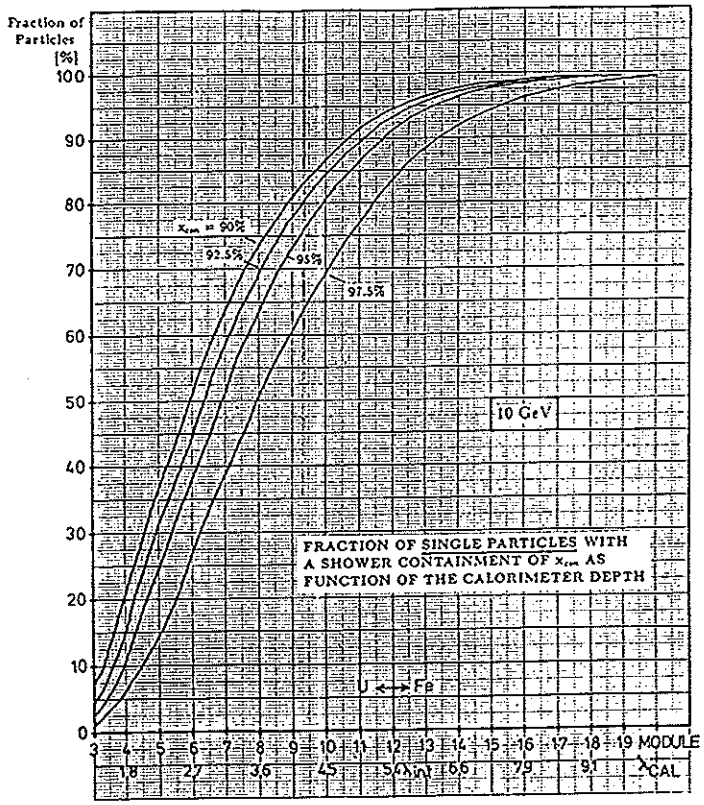

Fig. 4.30a Fraction of single particles with a shower containment of x_{con} as function of the calorimeter depth λ_{CAL} for 10 GeV.

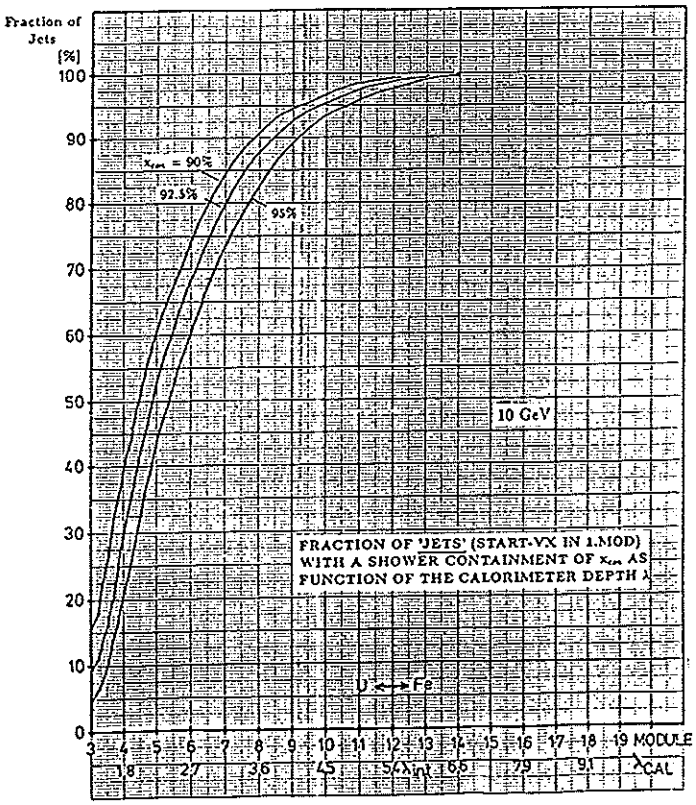

Fig. 4.30b Fraction of 'jets' with a shower containment of x_{con} as function of the calorimeter depth λ_{CAL} for 10 GeV.

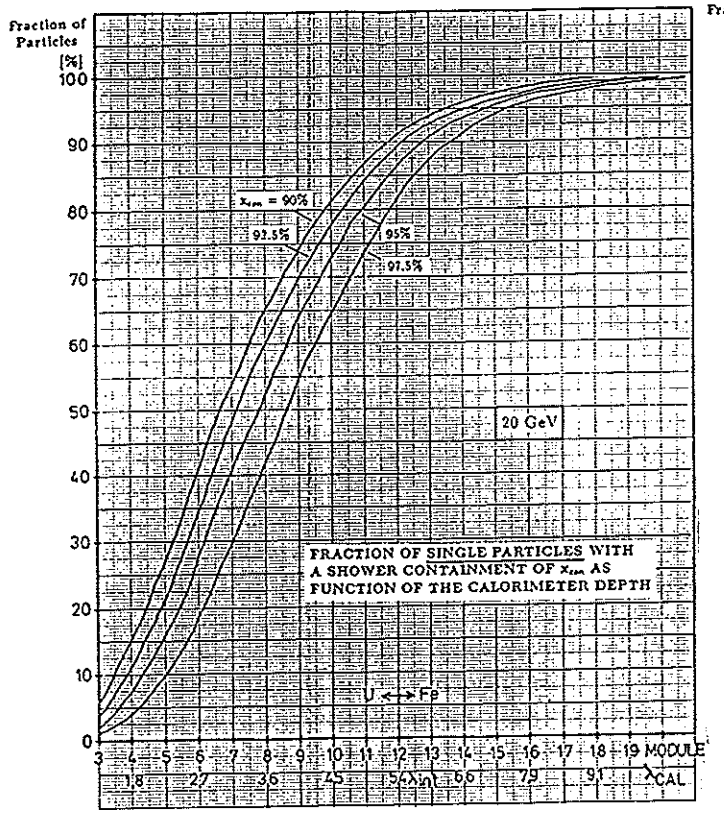

Fig. 4.31a Fraction of single particles with a shower containment of x_{con} as function of the calorimeter depth λ_{CAL} for 20 GeV.

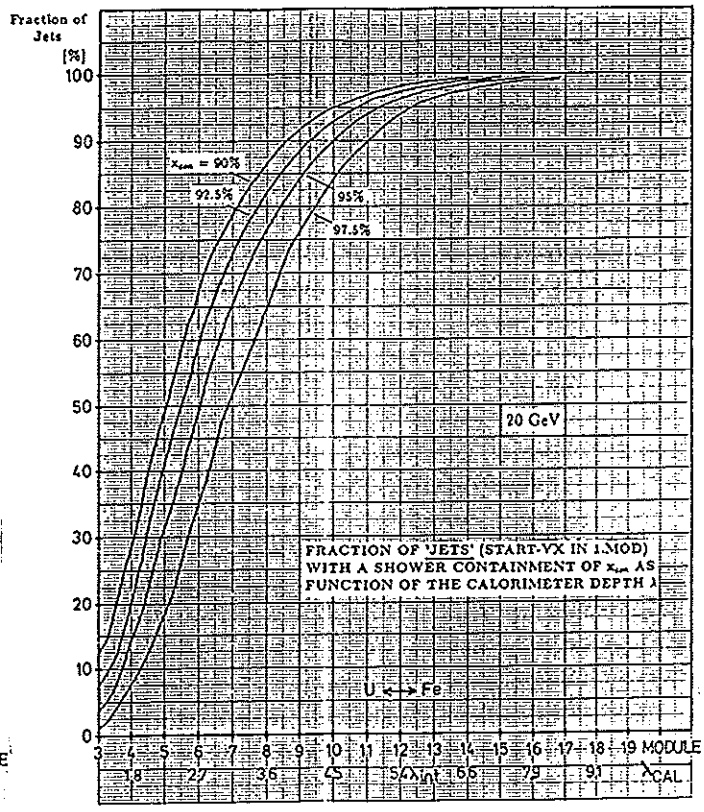

Fig. 4.31b Fraction of 'jets' with a shower containment of x_{con} as function of the calorimeter depth λ_{CAL} for 20 GeV.

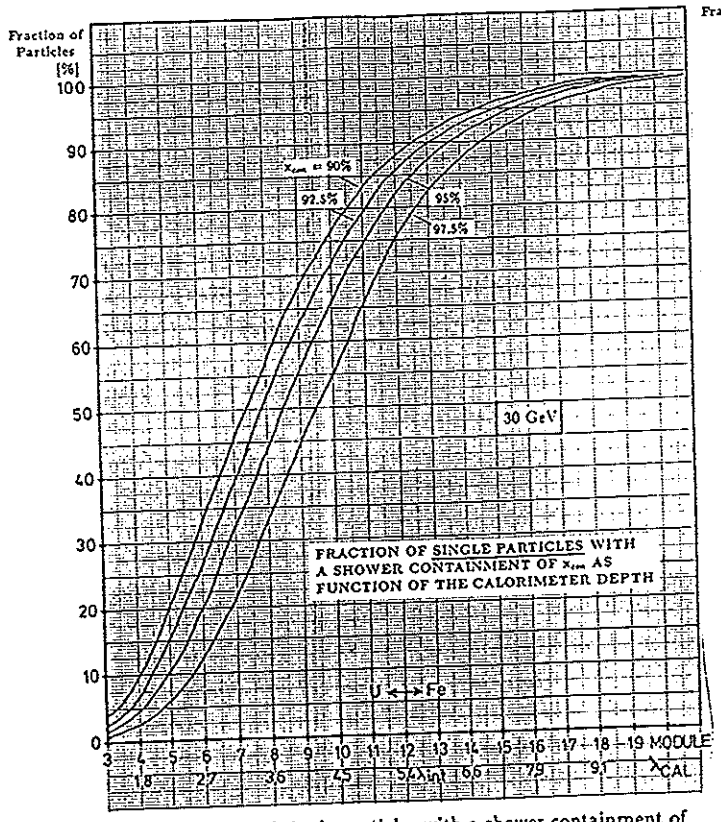

Fig. 4.32a Fraction of single particles with a shower containment of x_{con} as function of the calorimeter depth λ_{CAL} for 30 GeV.

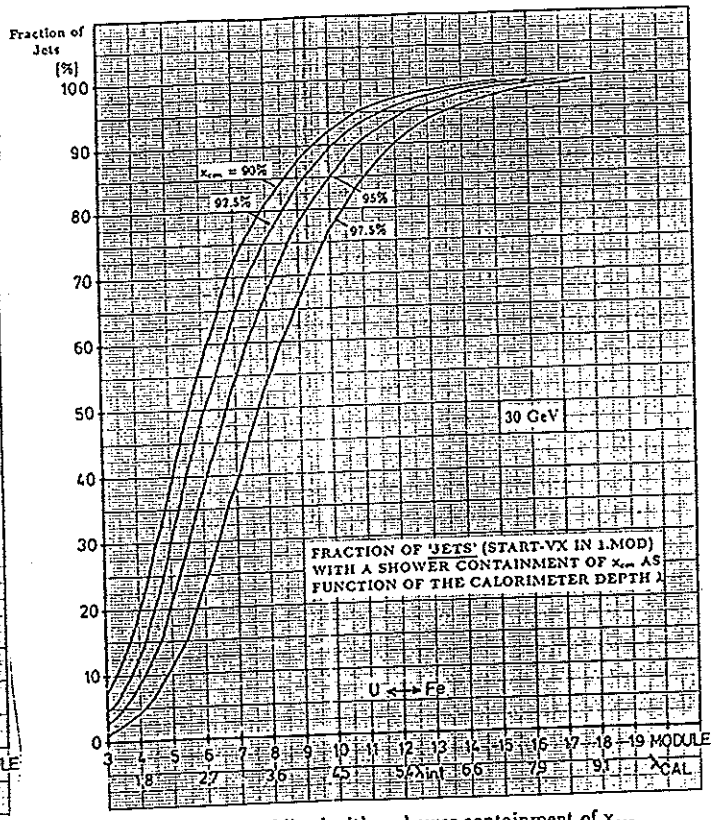

Fig. 4.32b Fraction of 'jets' with a shower containment of x_{con} as function of the calorimeter depth λ_{CAL} for 30 GeV.

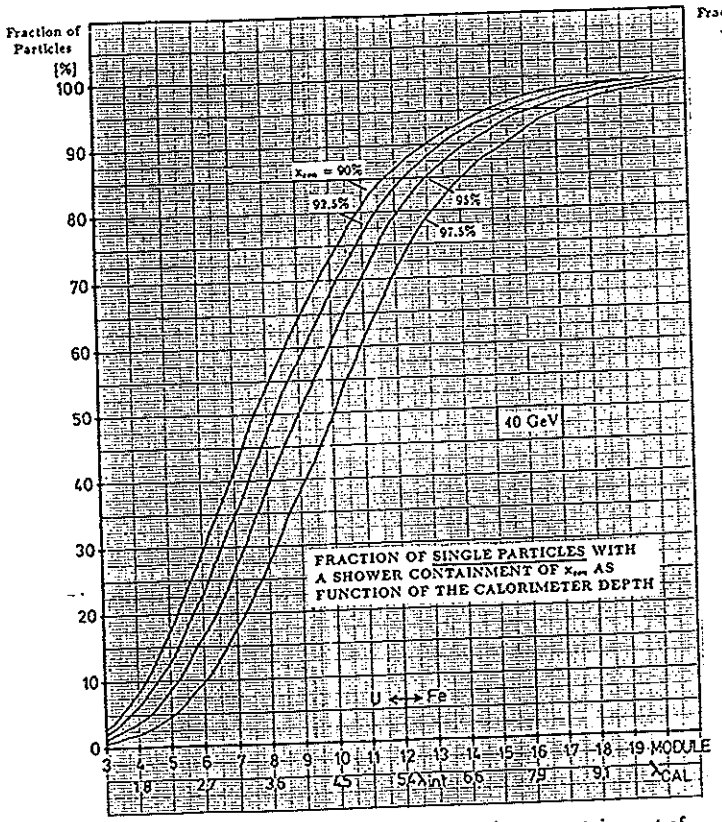

Fig. 4.33a Fraction of single particles with a shower containment of x_{con} as function of the calorimeter depth λ_{CAL} for 40 GeV.

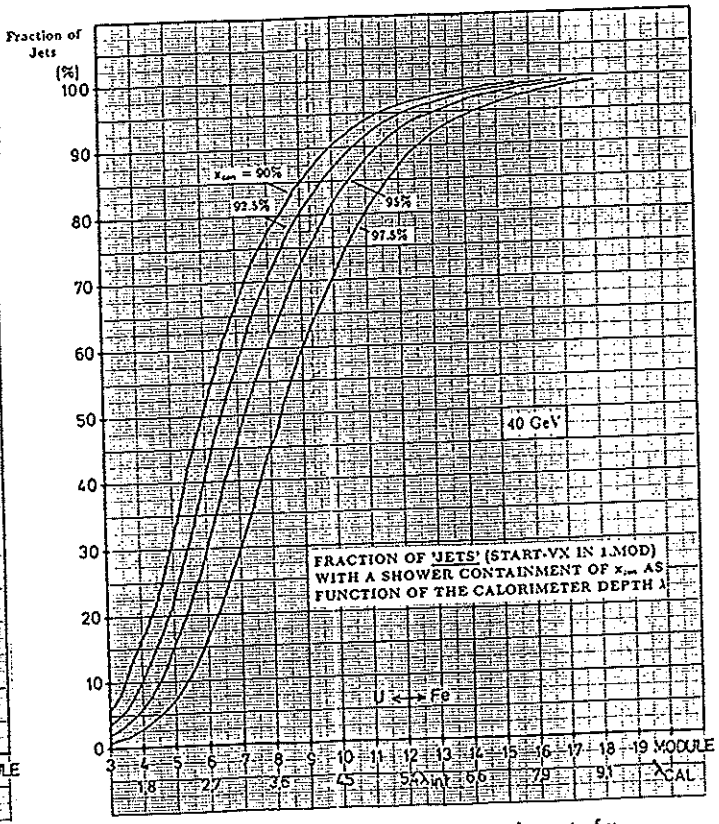

Fig. 4.33b Fraction of 'jets' with a shower containment of x_{con} as function of the calorimeter depth λ_{CAL} for 40 GeV.

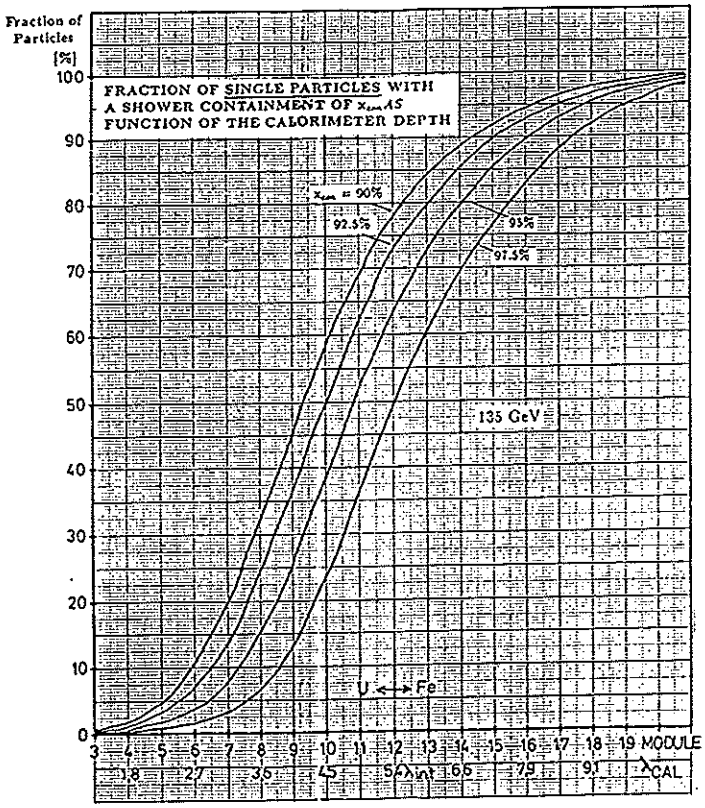

Fig. 4.34a Fraction of single particles with a shower containment of x_{con} as function of the calorimeter depth λ_{CAL} for 135 GeV.

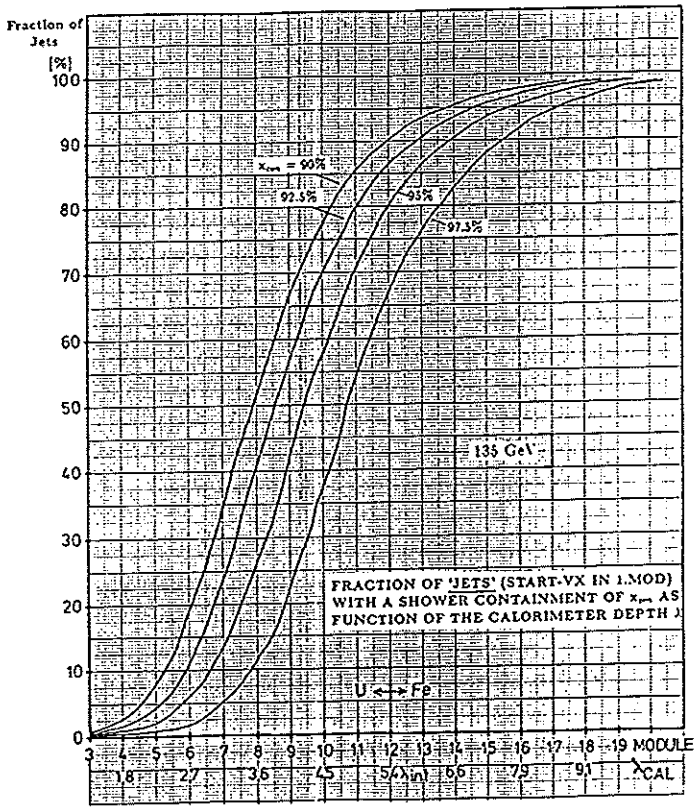

Fig. 4.34b Fraction of 'jets' with a shower containment of x_{con} as function of the calorimeter depth λ_{CAL} for 135 GeV.

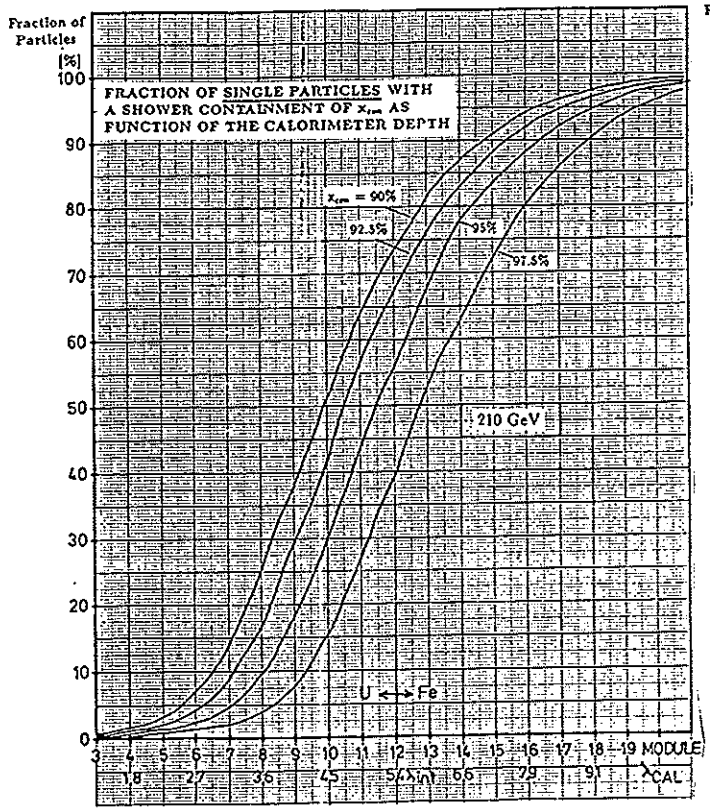

Fig. 4.35a Fraction of single particles with a shower containment of x_{con} as function of the calorimeter depth λ_{CAL} for 210 GeV.

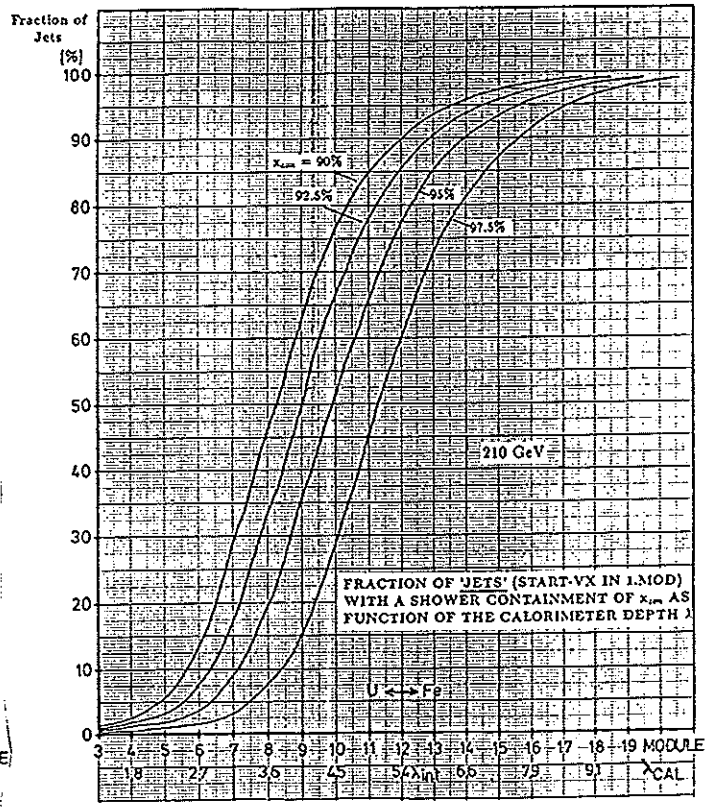

Fig. 4.35b Fraction of 'jets' with a shower containment of x_{con} as function of the calorimeter depth λ_{CAL} for 210 GeV.

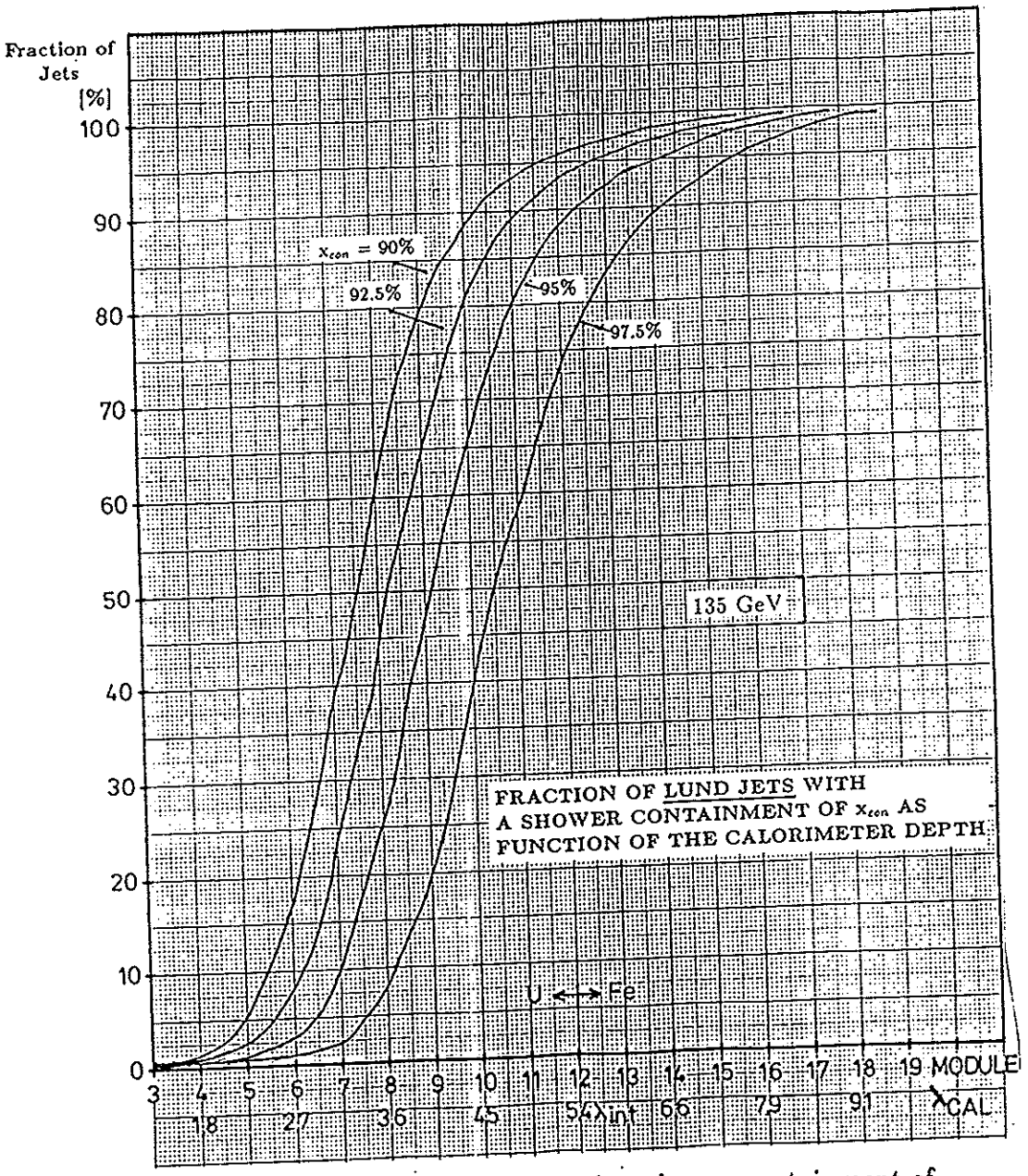

Fig. 4.36 Fraction of LUND jets with a shower containment of x_{con} as function of the calorimeter depth λ_{CAL} for 135 GeV.

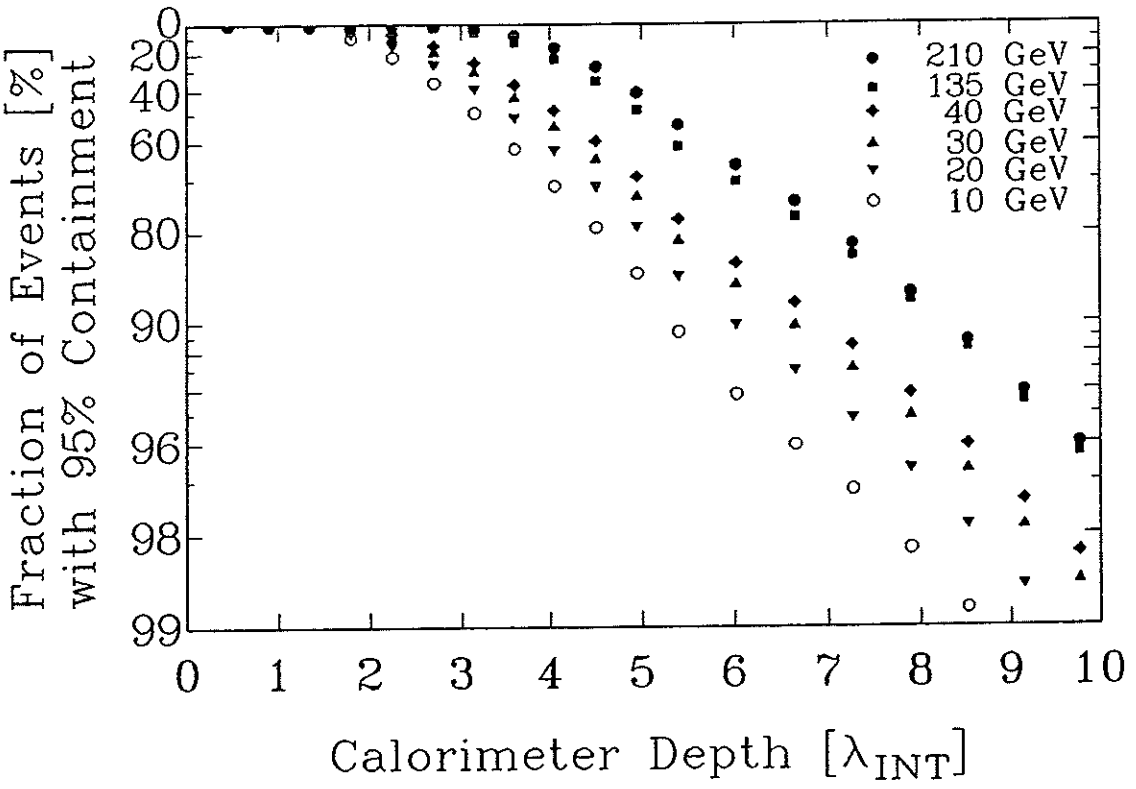

Fig. 4.37 Fraction of Events with 95% Containment in the Calorimeter for all Events.

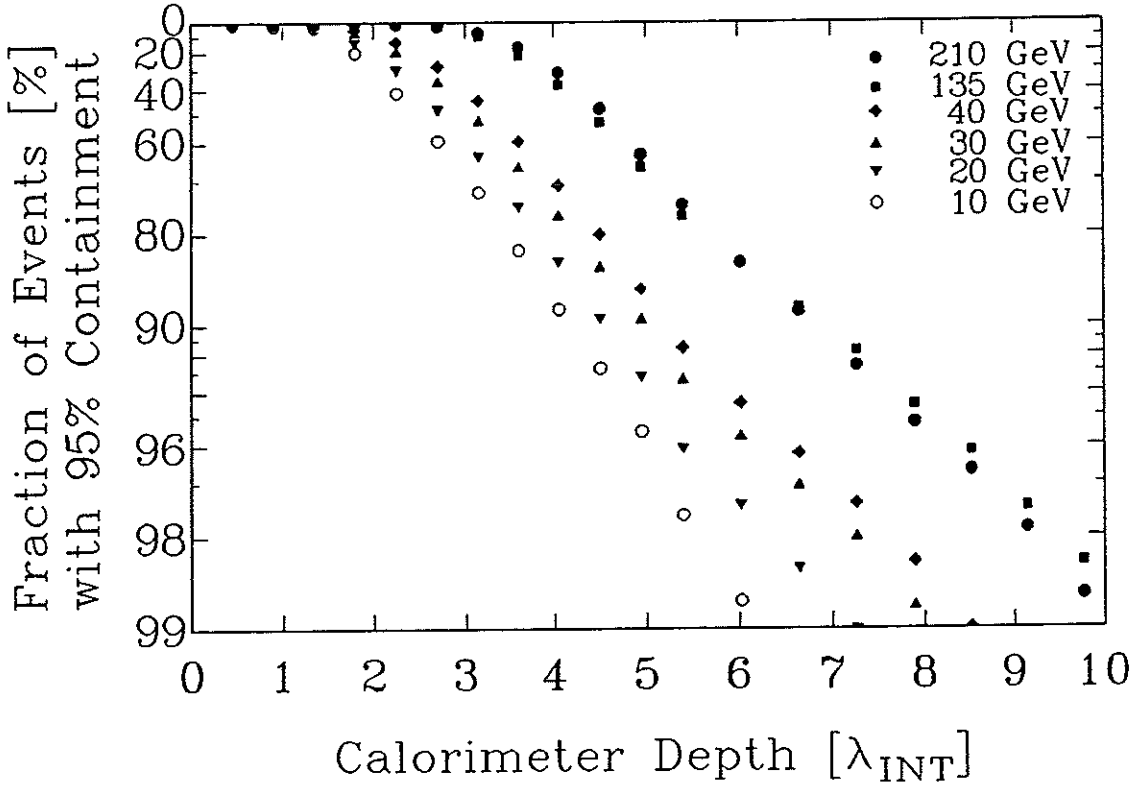

Fig. 4.38 Fraction of Events with 95% Containment in the Calorimeter for Events with Shower Vertex in the First Module.

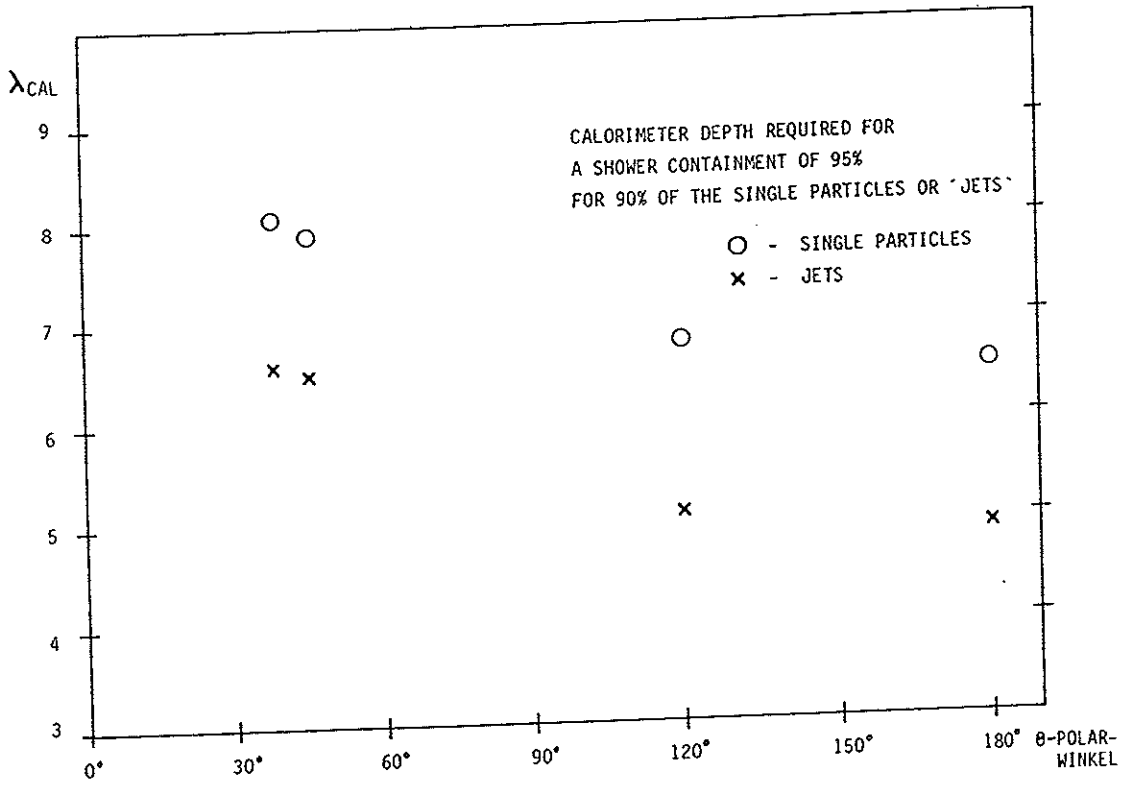

Fig. 4.39a Calorimeter depth (U/Scin) as a function of the polar angle θ required for a shower containment of 95% for 90% of single particles and WA78 'jets'.

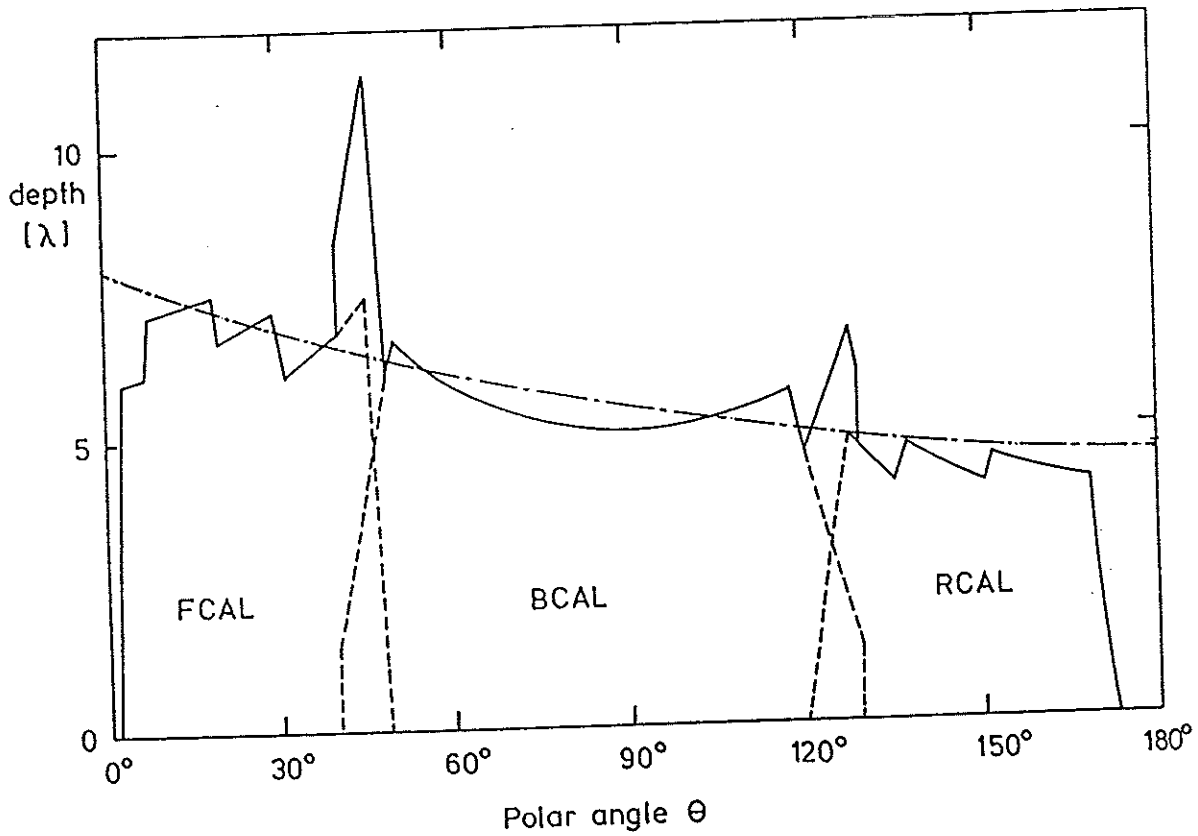

Fig. 4.39b Depth in absorption length of the high resolution calorimeter as a function of the polar angle θ in the vertical plane. The dotted line indicates the length needed to contain 95% of the energy for 90% of the jets with the maximum energy allowed by HERA kinematics.

4.2.9 Leakage due to Inactive Material (PM–Boxes) in the Calorimeter

As mentioned already, the WA78–H1–ZEUS data offers the possibility to investigate the influence of inactive material at various places inside the calorimeter system [KRÜ86b].

A relatively large amount of inactive material like the shielding for the photomultipliers and I-beams as structural elements of the calorimeter, is present between the high resolution sampling DU/Scin calorimeter and the iron backing calorimeter. The average absorption length of this inactive area is about 1.16λ in FCAL (FEMC), 1.17λ in RCAL (REMC) and 0.57λ in BCAL, see Table 4.9 [MUS92], [TIE92], [ZEU91]. Its position is at a depth of 5.4λ in the barrel region and at 7.2λ in the forward region (see Fig. 4.40) .

FCAL		RCAL	BCAL
EMC	HAC		
PM: XP1911 1) μ–metal ϕ=20–24mm l = 100mm 2) shrink tube (plastic, isol.) 3) iron tube ϕ=28.5–33.7mm l = 250mm	PM: R580 1) μ–metal ϕ=40–43.7mm l = 130mm 2) shrink tube (plastic, isol.) 3) iron tube ϕ=48–56mm l = 250mm	PM: R580 1) μ–metal ϕ=40–43.7mm l = 130mm 2) shrink tube (plastic, isol.) 3) Ferroperm ϕ=48–62mm l = 250mm	PM: R580 1) shrink tube (plastic, isol.) 2) μ–metal ϕ=40–42mm l = 171mm 3) iron tube ϕ=47–53mm l = 262mm
Magn. field:	$\approx$ 100 Gauss	$\approx$ 400 Gauss	$\approx$ 100 Gauss
PM–boxes:	$\approx 0.52\ \lambda_{int}$	$\approx 0.62\ \lambda_{int}$	$\approx 0.11\ \lambda_{int}$
I–beam etc...:	$\approx 0.64\ \lambda_{int}$	$\approx 0.55\ \lambda_{int}$	$\approx 0.46\ \lambda_{int}$
Total:	$\approx 1.16\ \lambda_{int}$	$\approx 1.17\ \lambda_{int}$	$\approx 0.57\ \lambda_{int}$

Table 4.9 Inactive material due to PM–boxes etc ... between the high resolution calorimeter CAL and the backing calorimeter BAC.

The inactive material of 0.6λ corresponds to about one module of the Fe/Scin part of the WA78 calorimeter. The influence on the resolution of the inactive material of 0.6λ behind 5.4λ is studied for 40 GeV "WA78–jets" and behind 7.2λ for 135 GeV "WA78–jets". Similar studies can be performed with inactive material of 1.2λ corresponding to two modules. Figure 4.40a shows for 40GeV 'jets' the fraction of energy deposited in the DU/Scint. (E_{CAL}) + BAC (E_{BAC}) calorimeters without the energy lost in the PM–boxes (E_{PM}), ($1 - \frac{E_{PM}}{E_{TOT}} = \frac{E_{CAL}+E_{BAC}}{E_{CAL}+E_{PM}+E_{BAC}}$), with an energy deposition of 4% – 5% in the BAC. About 1% of the 40GeV jets deposit 4% – 5% in the BAC. The fraction of events which move outside 1, 2 and 3 standard deviations of the hadronic energy resolution of $35\%/\sqrt{E}$ due to the energy lost in the PM–boxes are also indicated in Fig. 4.40a. About 34% of the events loose more than 1 standard deviation energy in the inactive material, about 11% loose more than 2 standard deviations energy.

Figures 4.41 and 4.42 present the fractions of 40GeV 'jets' which have x% of their energy deposited in the DU/Scint. + BAC calorimeters ($1 - \frac{E_{PM}}{E_{TOT}}$) with a given energy deposition of $< 2\%$ and $4\% - 5\%$ in the BAC.

The fraction of events contributing to nongaussian tails due to the energy lost in the inactive PM region can be displayed in units of the calorimeter resolution σ/E. For this resolution the nominal value of $35\%/\sqrt{E}$ is chosen as the scale (σ_{35}). About 89.8% of all jets deposit less than $< 2\%$ of their shower energy in the BAC ($E_{BAC} < 2\%$). The percentage of 40 GeV jets having an energy deposit outside $1\sigma_{35}$, $2\sigma_{35}$ and $3\sigma_{35}$ as function of the calorimeter depth λ_{CAL} is shown in Fig. 4.43. With a calorimeter depth of 5.4λ about 2.6% of the jets are outside $1\sigma_{35}$, $\approx$0.6% are outside $2\sigma_{35}$ and less than 0.15% are outside $3\sigma_{35}$. The corresponding results for the forward calorimeter with a length of 7.2λ and 135 GeV jets about 3% of the jets are additionally outside 1σ, only $\approx$0.6% are outside $2\sigma_{35}$ and less than 0.1% are outside $3\sigma_{35}$ (Fig. 4.44).

The fraction of events outside $i\cdot\sigma_{35}$ as function of the shower energy deposited in the backing calorimeter is shown for both energies in Fig. 4.45 and Fig. 4.46. This is also summarized in Table 4.10. It offers a quantitative measure for the effect of the inactive material inside the calorimeter on the calorimeter resolution.

Further studies on the influence of different inactive materials on the resolution of the ZEUS hadron calorimeter were performed. Iron and aluminium plates of various thicknesses (1cm, 2cm etc ...) were placed at various positions inside the ZEUS test calorimeter TEST 60.

Jet Energy	Calori-meter depth	$E_{BAC} < 2\%$ No of Jets	outside $1,2,3\sigma_{35}$	$E_{BAC} = 2\%$–3% No of Jets	outside $1,2,3\sigma_{35}$	$E_{BAC} = 3\%$–4% No of Jets	outside $1,2,3\sigma_{35}$	$E_{BAC} = 4\%$–5% No of Jets	outside $1,2,3\sigma_{35}$
40 GeV	$5.4\lambda_{int}$	89.9%	3.0% 0.6% 0.15%	2.2%	27% 10% 4%	1.5%	30% 12% 5%	1%	34% 11% 4%
135 GeV	$7.2\lambda_{int}$	89%	3.3% 0.6% 0.1%	3%	35% 11% 3%	2%	44% 16% 6%	1.3%	46% 25% 15%

Table 4.10 Influence of inactive material ($0.6\lambda_{int}$) at $5.4\lambda_{int}$ and at $7.2\lambda_{int}$ on the resolution of the ZEUS calorimeter.

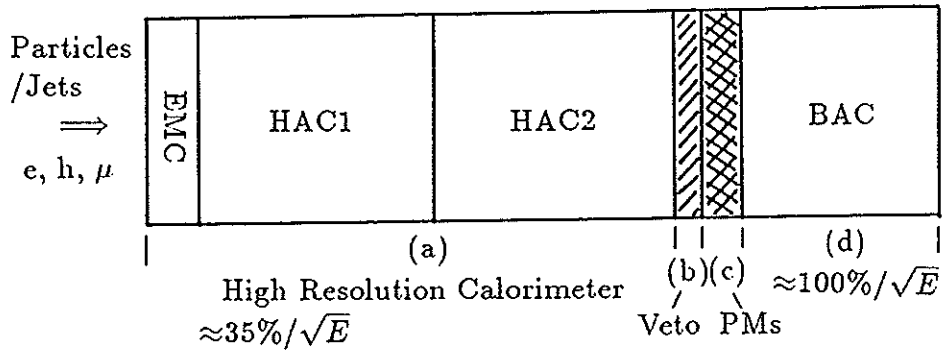

Fig. 4.40 Calorimeter Design of a High Resolution Calorimeter (a), (Veto Readout Section (b),) PM Boxes (c) and Backing Calorimeter (d).

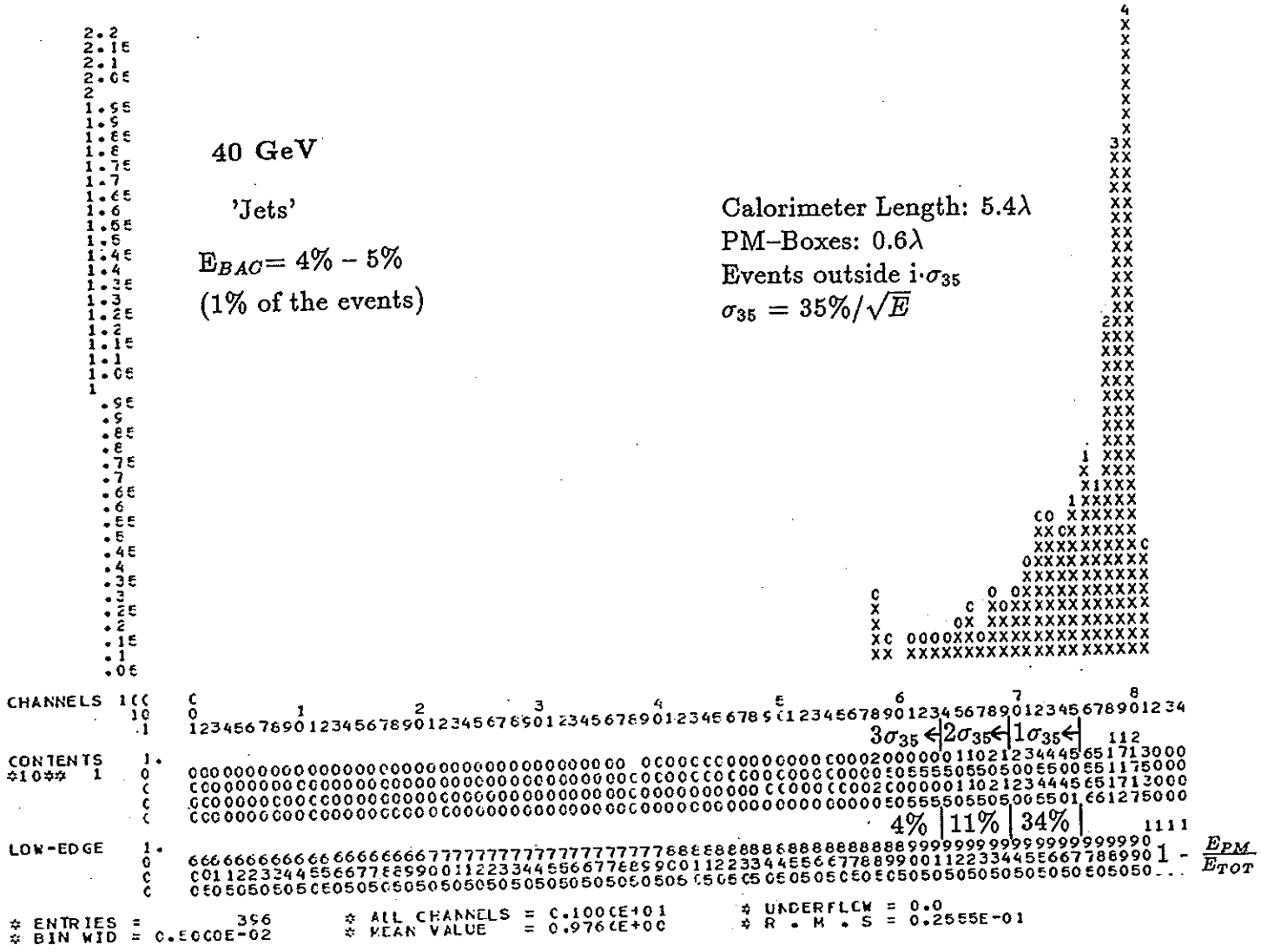

Fig. 4.40a Fraction of energy deposition in the DU/Scint. + BAC calorimeters ($1 - \frac{E_{PM}}{E_{TOT}}$) for 40GeV jets with $E_{BAC} = 4\% - 5\%$; $\lambda_{CAL} = 5.4\lambda$.

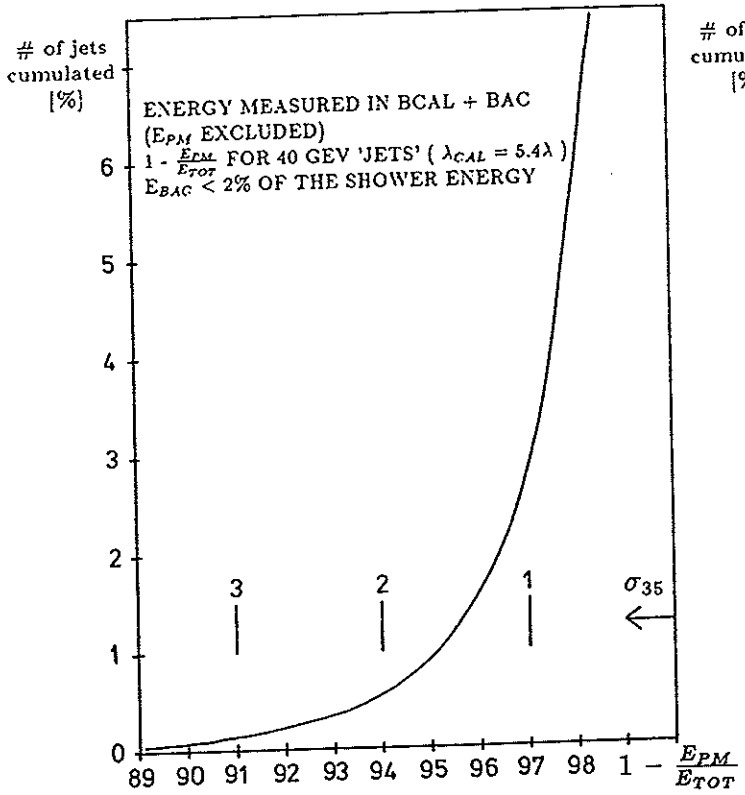

Fig. 4.41 Fraction of 40 GeV 'Jets' as Function of $1 - \frac{E_{PM}}{E_{TOT}}$ for $E_{BAC} < 2\%$ of the Shower Energy; $\lambda_{CAL} = 5.4\lambda$.

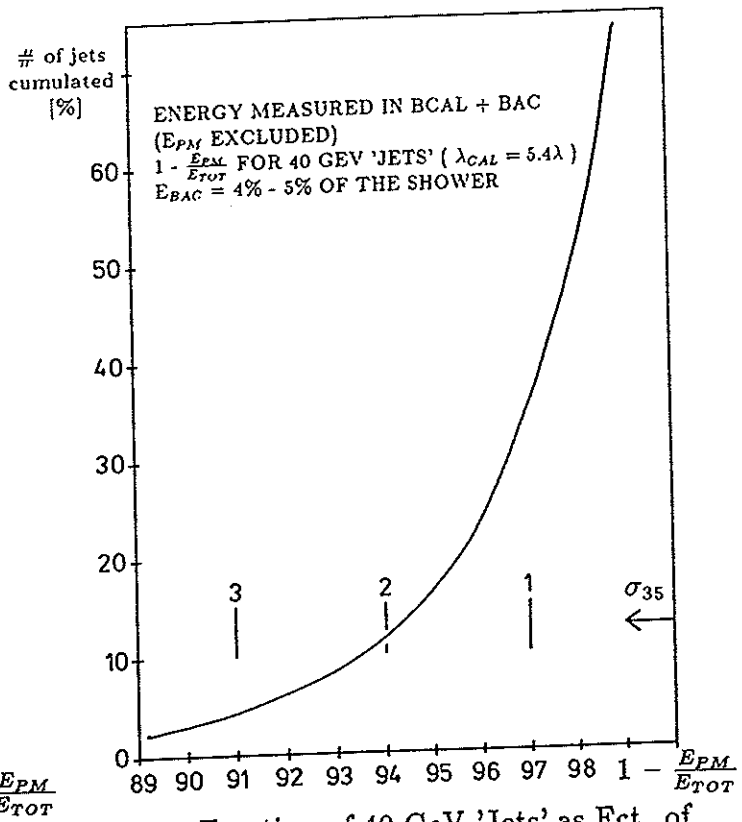

Fig. 4.42 Fraction of 40 GeV 'Jets' as Fct. of $1 - \frac{E_{PM}}{E_{TOT}}$ for $E_{BAC} = 4\% - 5\%$ of the Shower Energy; $\lambda_{CAL} = 5.4\lambda$.

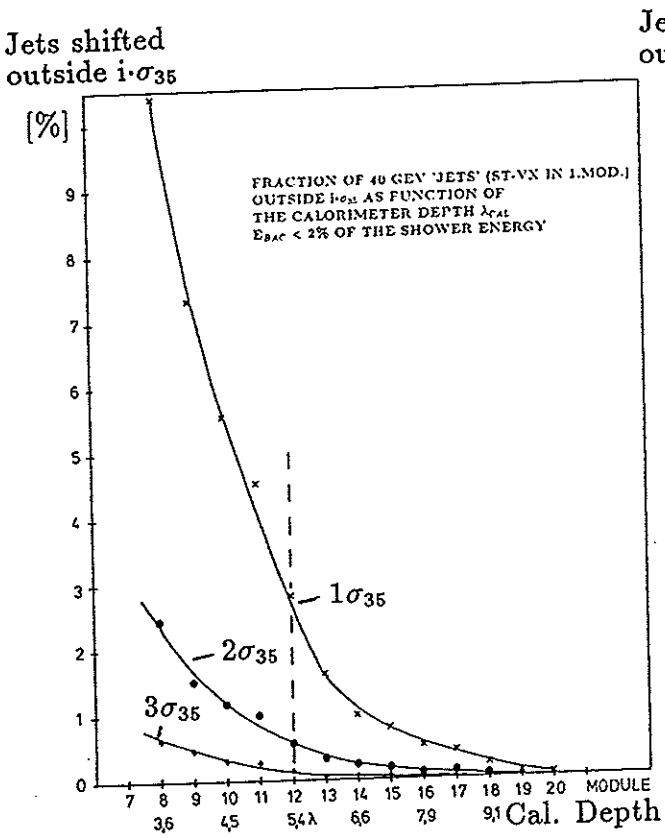

Fig. 4.43 Fraction of 40 GeV 'Jets' additionally outside i·σ_{35} as Function of the Calorimeter Depth for $E_{BAC} < 2\%$ of the Shower Energy.

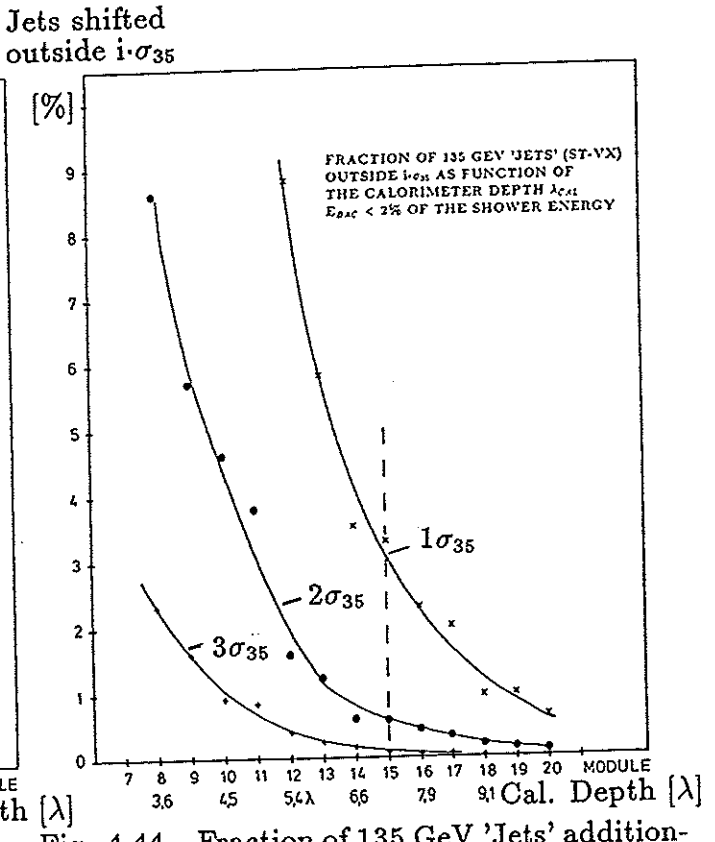

Fig. 4.44 Fraction of 135 GeV 'Jets' additionally outside i·σ_{35} as Function of the Calorimeter Depth for $E_{BAC} < 2\%$ of the Shower Energy.

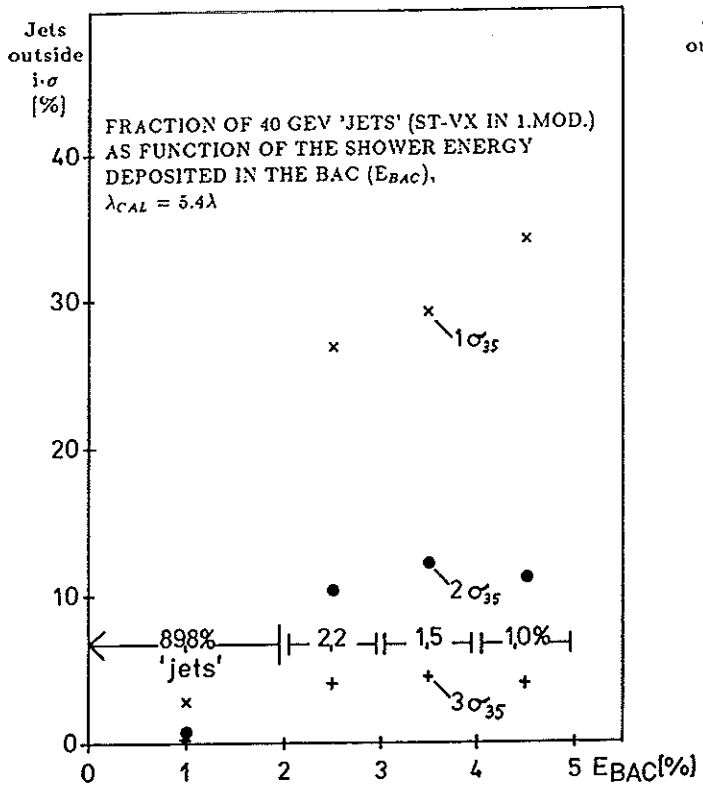

Fig. 4.45 Fraction of 40 GeV 'Jets' as Function of the Shower Energy in the BAC (E_{BAC}); $\lambda_{CAL} = 5.4\lambda$.

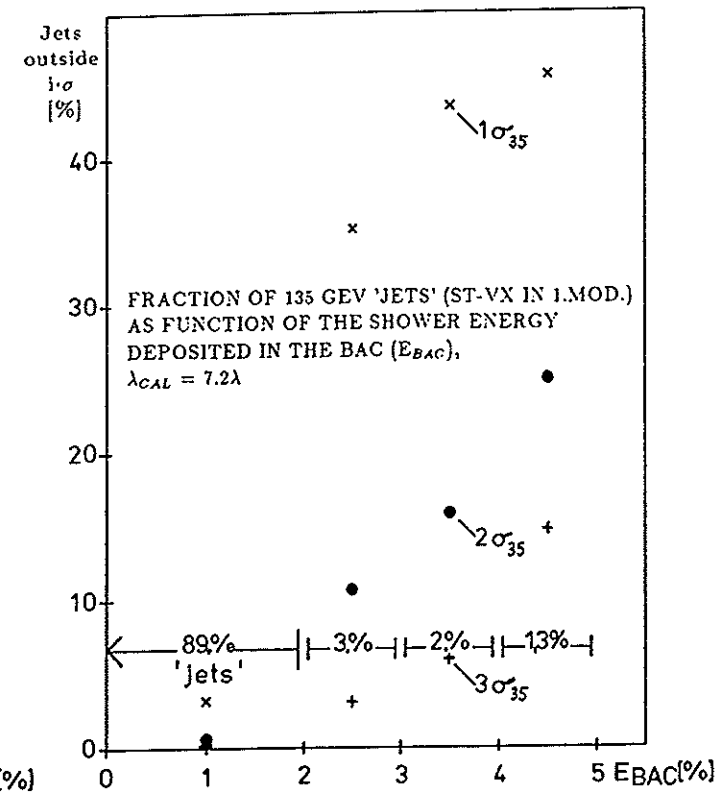

Fig. 4.46 Fraction of 135 GeV 'Jets' as Function of the Shower Energy in the BAC (E_{BAC}); $\lambda_{CAL} = 7.2\lambda$.

4.2.10 Final Conclusions on the Chosen Depth of the ZEUS Calorimeter

The longitudinal shower development in the WA78 hadron calorimeter measured for single particles with energies of 5, 10, 20, 30, 40, 135 and 210 GeV show a shower maximum at about 1 λ for all energies.

The longitudinal shower development of jets, defined by hadrons interacting in the first module, have their shower maxima shifted to smaller depths by about 0.3λ. The structure of their shower profiles is similar to that created from LUND jets apart from some deviations in the first two modules and at calorimeter depths above 4λ.

The studies of the shower containment as a function of the calorimeter depth yield a required minimum depth of about 6.6λ in the forward region and about 4.9λ in the barrel region (using a shower containment of 95% for 90% of the jets). It shows that the ZEUS calorimeter fulfils these requirements.

The shower leakage due to inactive material between the high resolution and the backing calorimeter and the influence on the calorimeter resolution has also been investigated. The inactive material results mainly from the shielding of the photomultipliers and the I-beam necessary for the construction of the calorimeter. A study was performed with inactive material of 0.6λ corresponding to one Fe/Scin module. About 90% of the 'jets' (40 GeV, 135 GeV) deposit less than 2% of their shower energy in the backing calorimeter. For less than 1% of these 'jets' lower energies are measured, outside $2\sigma_{35}$ of the nominal energy resolution of $35\%/\sqrt{E}$, due to the energy lost in the inactive material of the PM–boxes at 5.4λ for 40 GeV and at 7.2λ for 135 GeV.

The WA78–H1–ZEUS measurements have permitted developing for ZEUS an optimum calorimeter. It combines a high resolution calorimeter of optimized depth with a coarser backing calorimeter acting as veto counter or as tail catcher. This presents an excellent solution to determine with high precision the energy of particles and jets expected at HERA.

4.2.11 Extrapolation of the Calorimeter Depth Requirements to Particles and Jets in the TeV Range

For future accelerators such as LHC at CERN or SSC in Dallas the development of high resolution calorimeters should be one of the most important tasks.

The depth of the calorimeters has to be large enough to fulfil the physics requirements at acceptable cost. The data from WA78–H1–ZEUS and the analysis performed for the ZEUS calorimeter can be used to extrapolate to the TeV region [KRÜ90c], [KRÜ90e,d].

Figure 4.47a and 4.47b show the required calorimeter depth for 80% of single hadrons and WA78 'jets' as a function of the incident particle and 'jet' energy for shower containments of 90%, 92.5%, 95% and 97.5%. The increase of the necessary calorimeter depth as a function of the energy shows in first approximation a logarithmic dependence. Straight lines are overlayed to guide the eye and extrapolations are indicated up to 1 TeV. The corresponding plots for 85%, 90% and 95% of single hadrons and 'jets' are shown in Fig. 4.48a,b, 4.49a,b and 4.50a,b. Extrapolations up to 10TeV are shown in Fig. 4.49c,d. Limitations of the data are due to transverse leakage and limited accuracy, in particular at high energies (135GeV, 210GeV) due to some photomultiplier and pedestal problems.

Figure 4.51a and 4.51b represent the calorimeter depth necessary for 1 TeV single hadrons and jets (extrapolations) as a function of the shower containment for 80%, 85%, 90% and 95% of single hadrons and jets. This representation allows also an extrapolation to even higher shower containments by an exponential fit to the extrapolated data points.

Figure 4.52a and 4.52b show the calorimeter depth necessary for 1 TeV single hadrons and jets (extrapolations) as a function of the fraction of single hadrons and jets with a shower containment of 90%, 92.5%, 95%, 97.5% and 98.75%.

For 85% – 90% of the 1 TeV jets with a shower containment of 98.75% a calorimeter depth of $10\lambda - 10.5\lambda$ is needed; for 95% of the 1 TeV jets with a shower containment of 95% a calorimeter depth of $9.5\lambda - 10\lambda$ is necessary.

At 1 TeV the relative energy resolution of a high resolution hadron calorimeter with $\sigma_h/\mathrm{E} \approx 35\%/\sqrt{E}$ approaches 1% .

In order not to lose this excellent energy resolution at very high energies e.g. due to energy leakage one can read out separately the last $\approx 1\lambda$ deep section of the calorimeter and use it as a veto counter to select events fully contained in the high resolution calorimeter as indicated in Fig. 4.40.

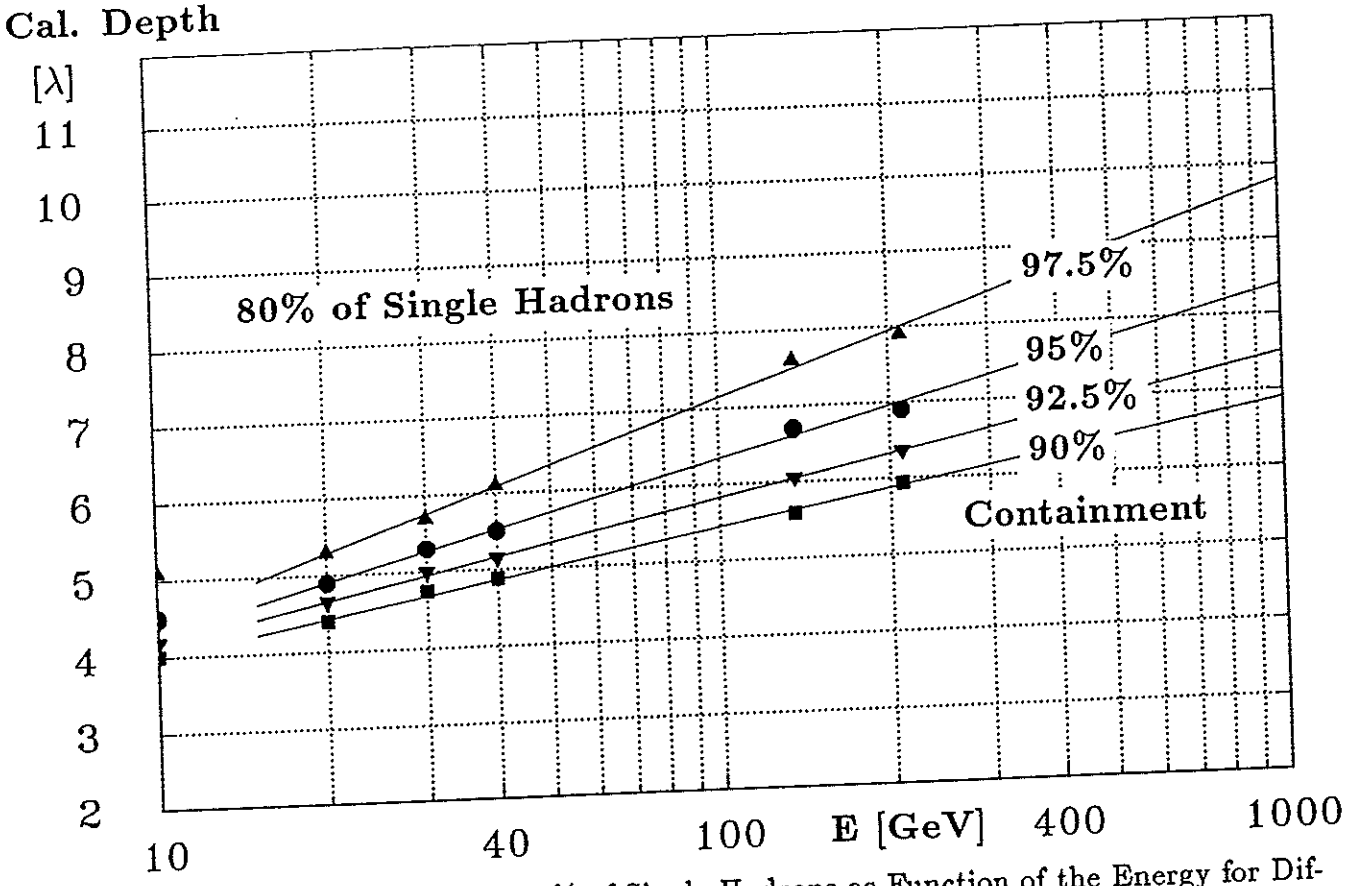

Fig. 4.47a Calorimeter Depth for 80% of Single Hadrons as Function of the Energy for Different Fractions of Shower Containment.

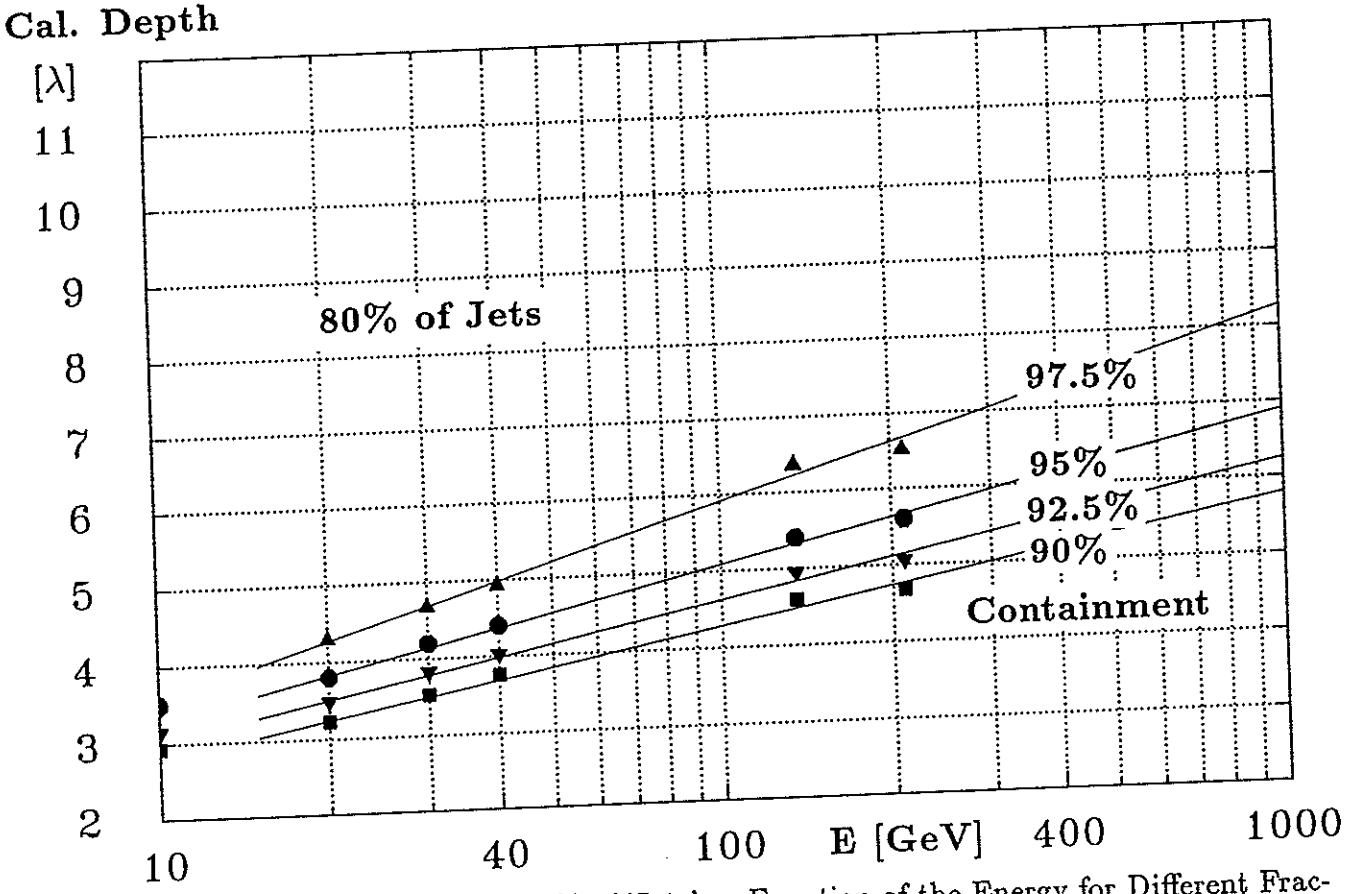

Fig. 4.47b Calorimeter Depth for 80% of 'Jets' as Function of the Energy for Different Fractions of Shower Containment.

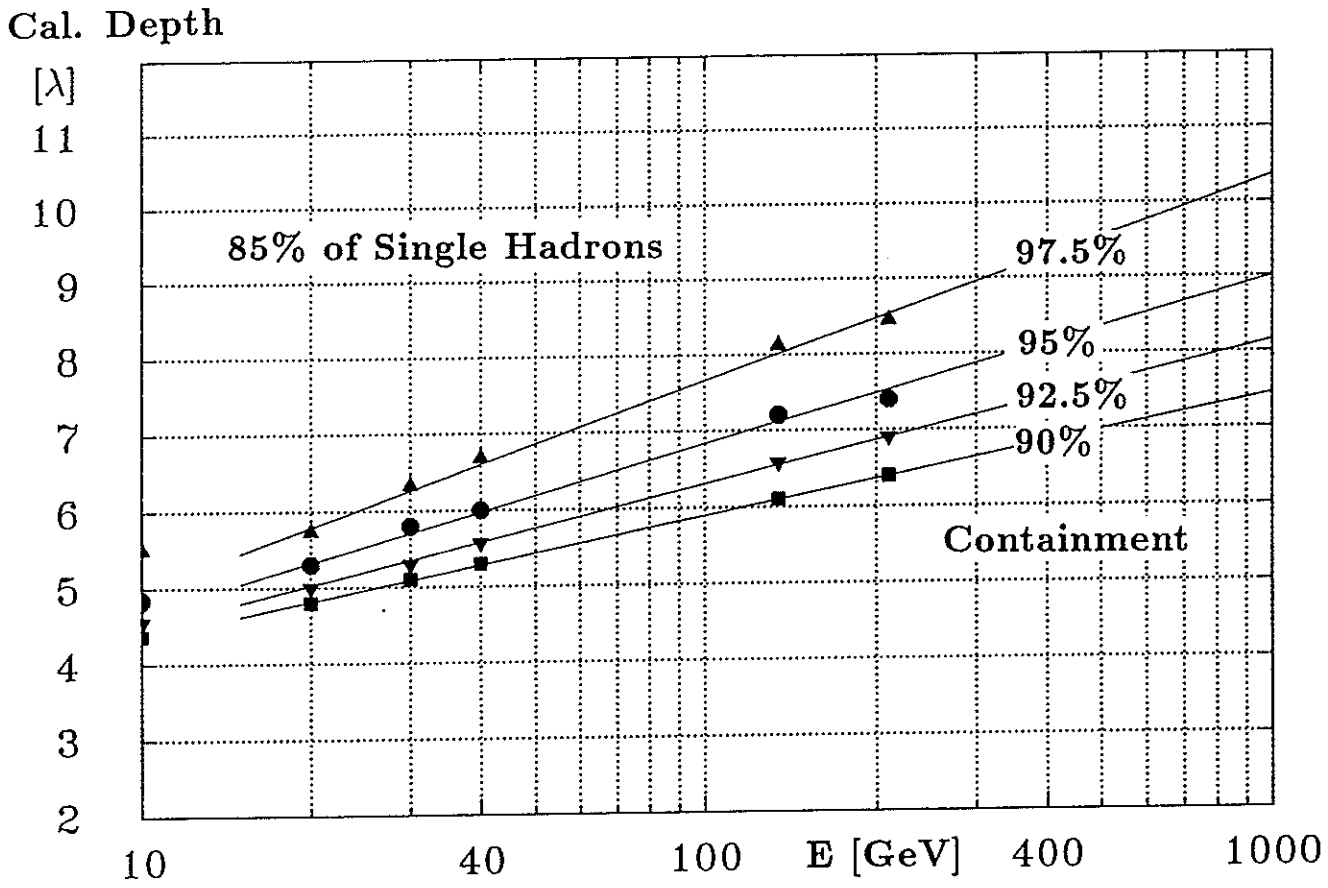

Fig. 4.48a Calorimeter Depth for 85% of Single Hadrons as Function of the Energy for Different Fractions of Shower Containment.

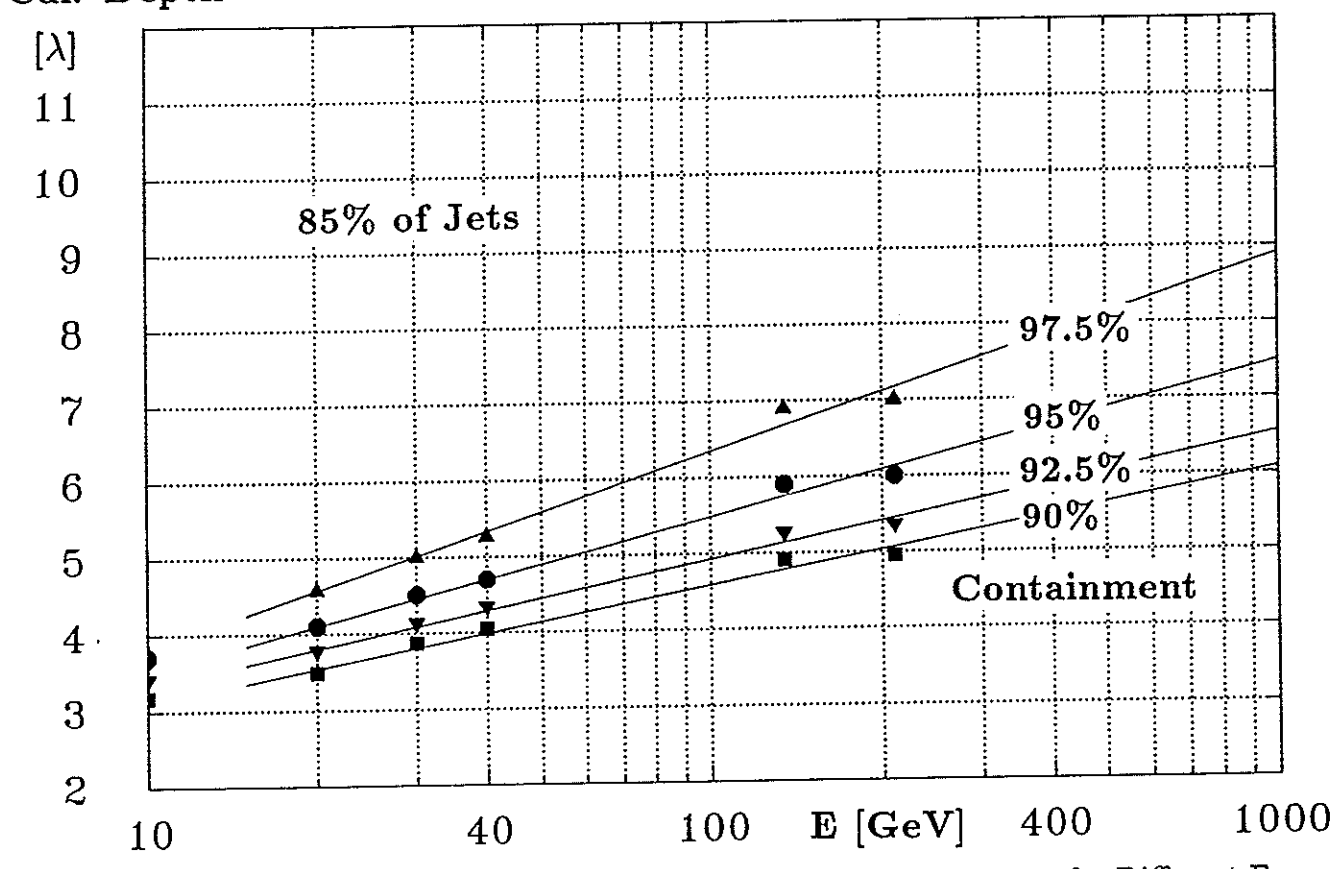

Fig. 4.48b Calorimeter Depth for 85% of 'Jets' as Function of the Energy for Different Fractions of Shower Containment.

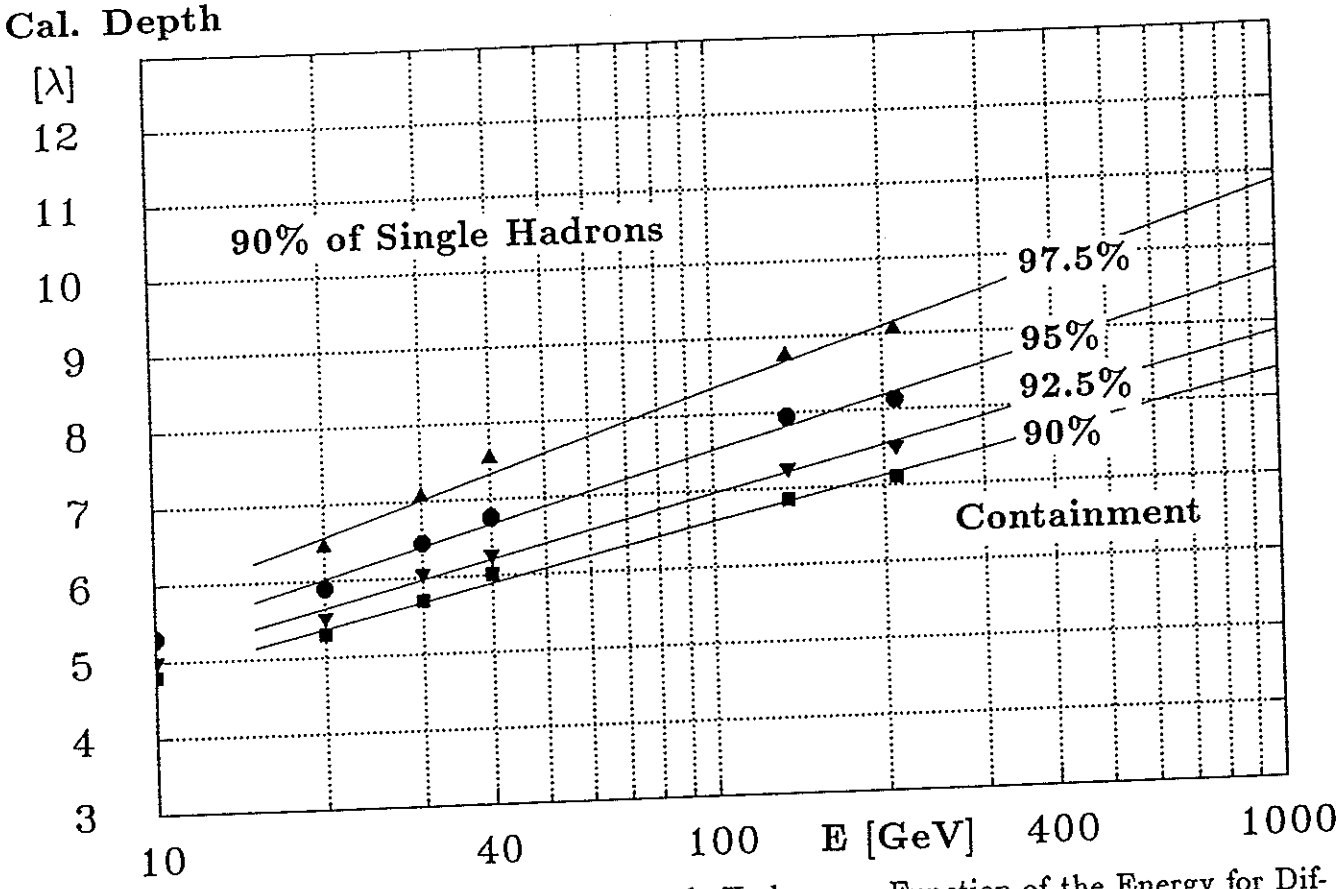

Fig. 4.49a Calorimeter Depth for 90% of Single Hadrons as Function of the Energy for Different Fractions of Shower Containment.

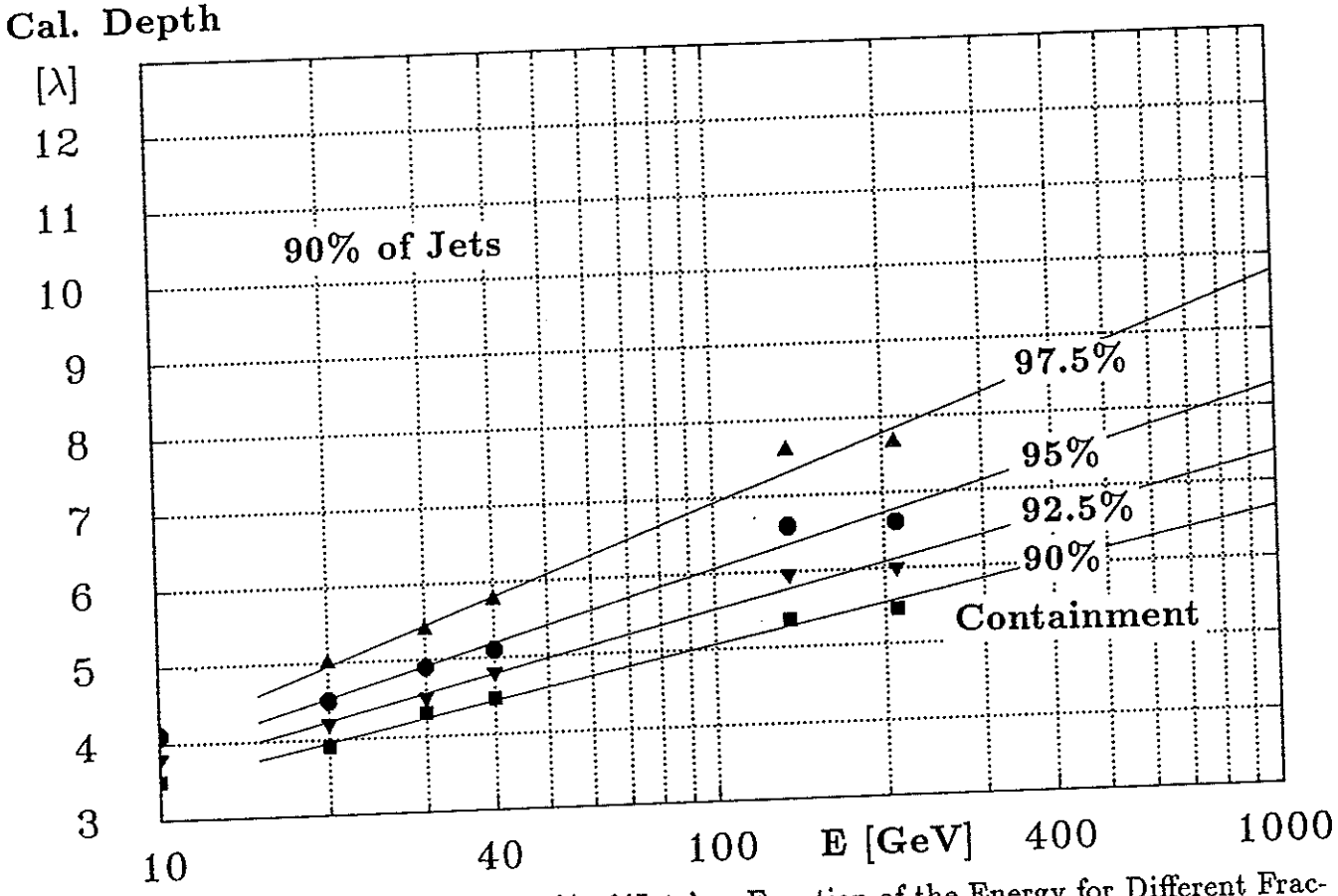

Fig. 4.49b Calorimeter Depth for 90% of 'Jets' as Function of the Energy for Different Fractions of Shower Containment.

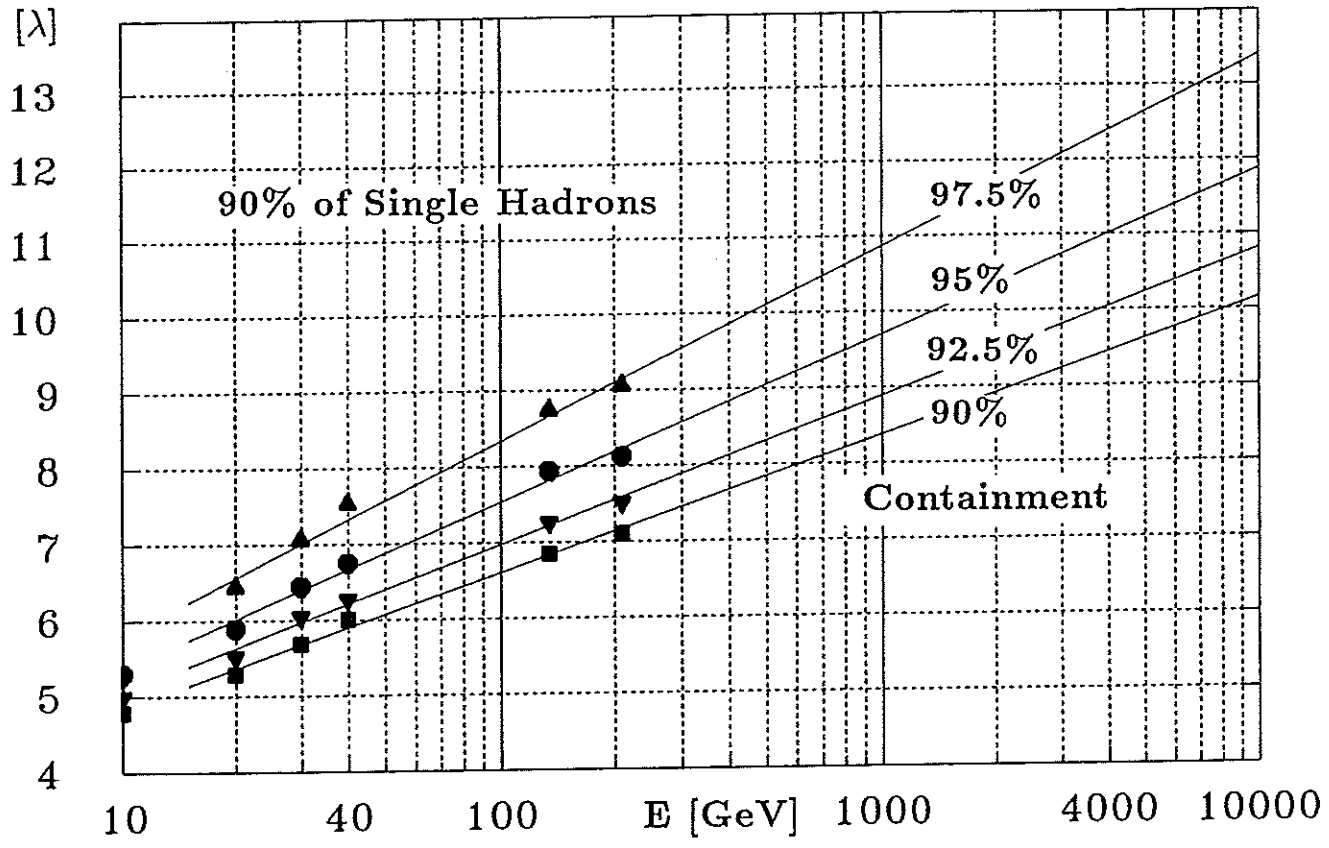

Fig. 4.49c Calorimeter depth for 90% of single hadrons as function of the energy for different fractions of shower containment (extrapolation up to 10 TeV).

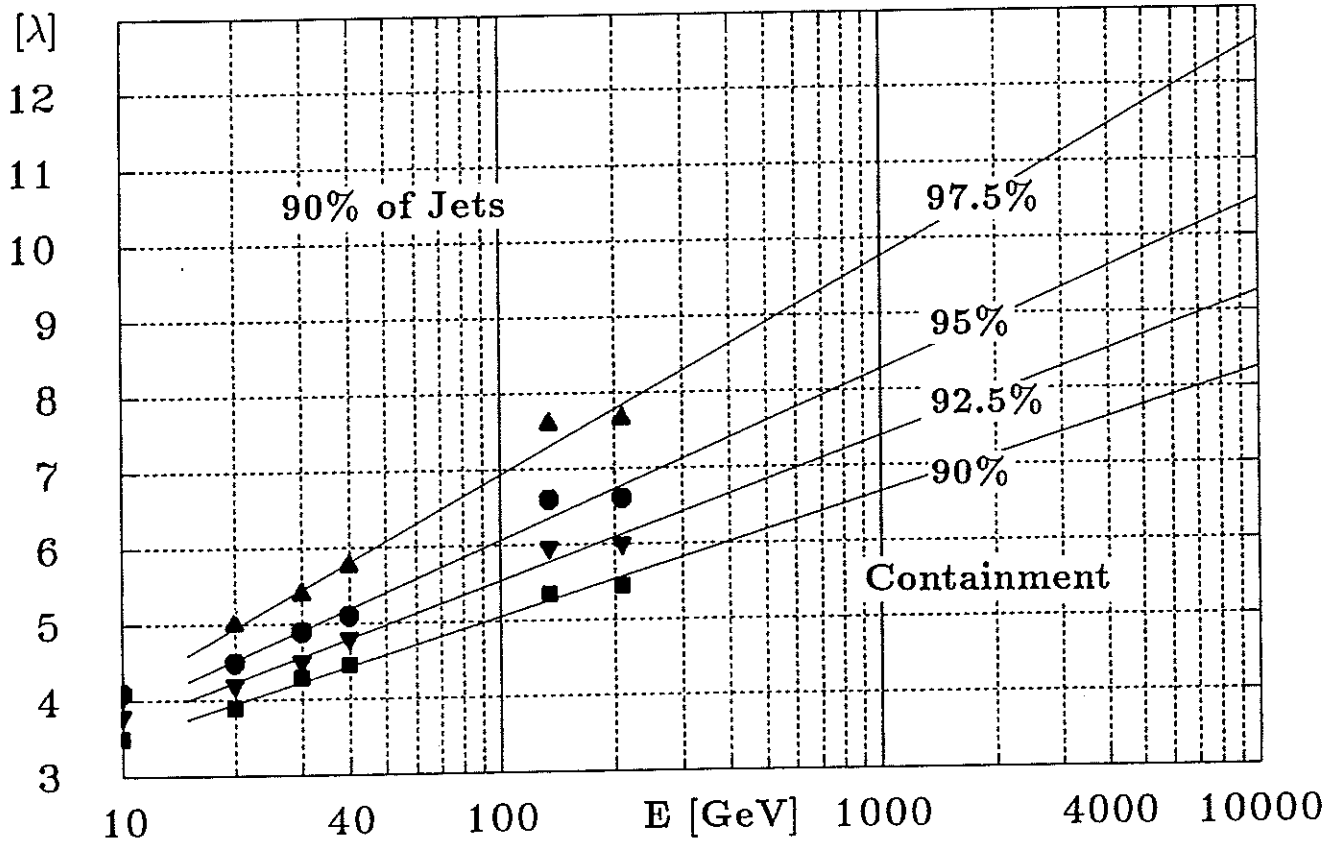

Fig. 4.49d Calorimeter depth for 90% of 'jets' as function of the energy for different fractions of shower containment (extrapolation up to 10 TeV).

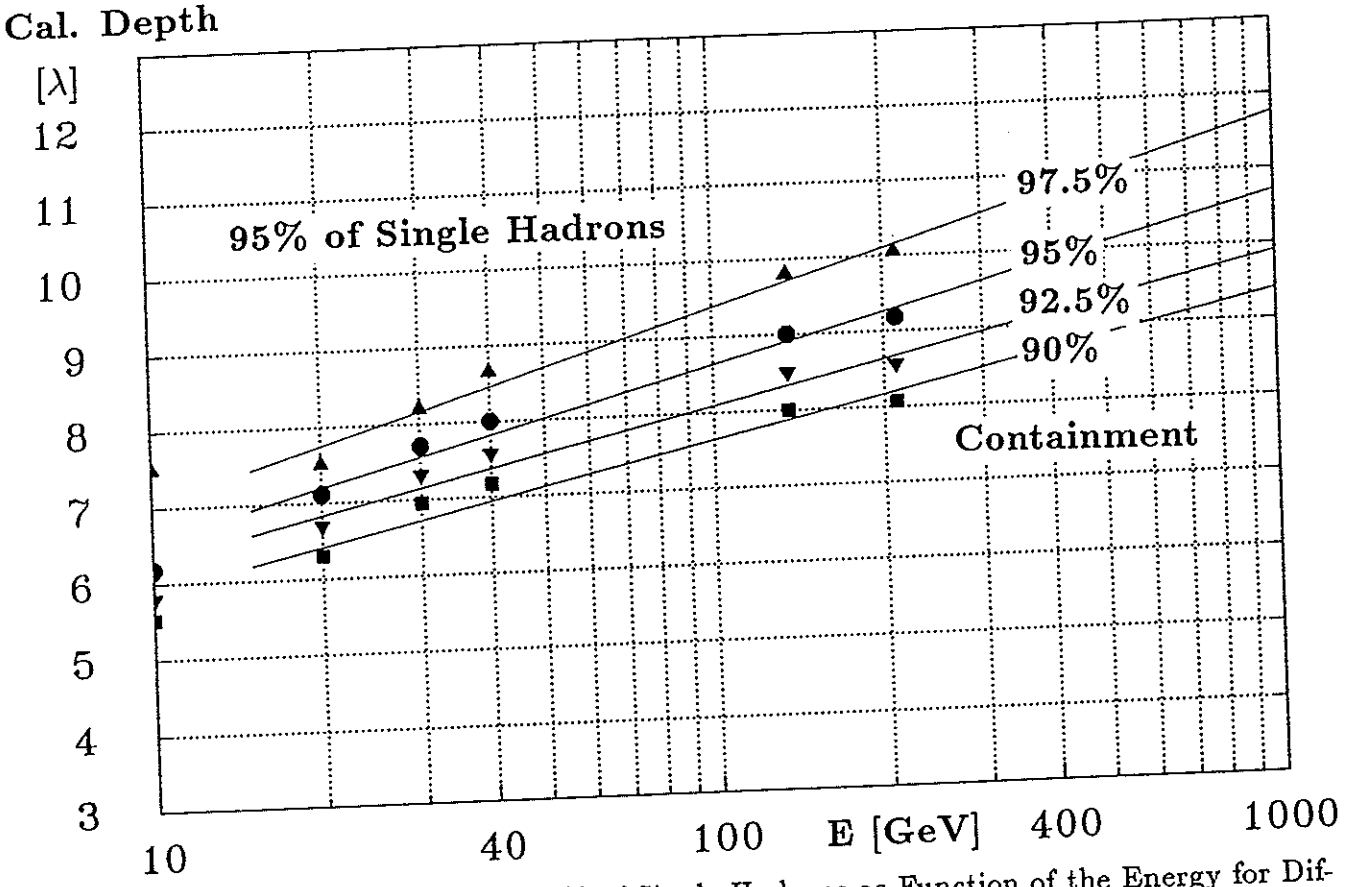

Fig. 4.50a Calorimeter Depth for 95% of Single Hadrons as Function of the Energy for Different Fractions of Shower Containment.

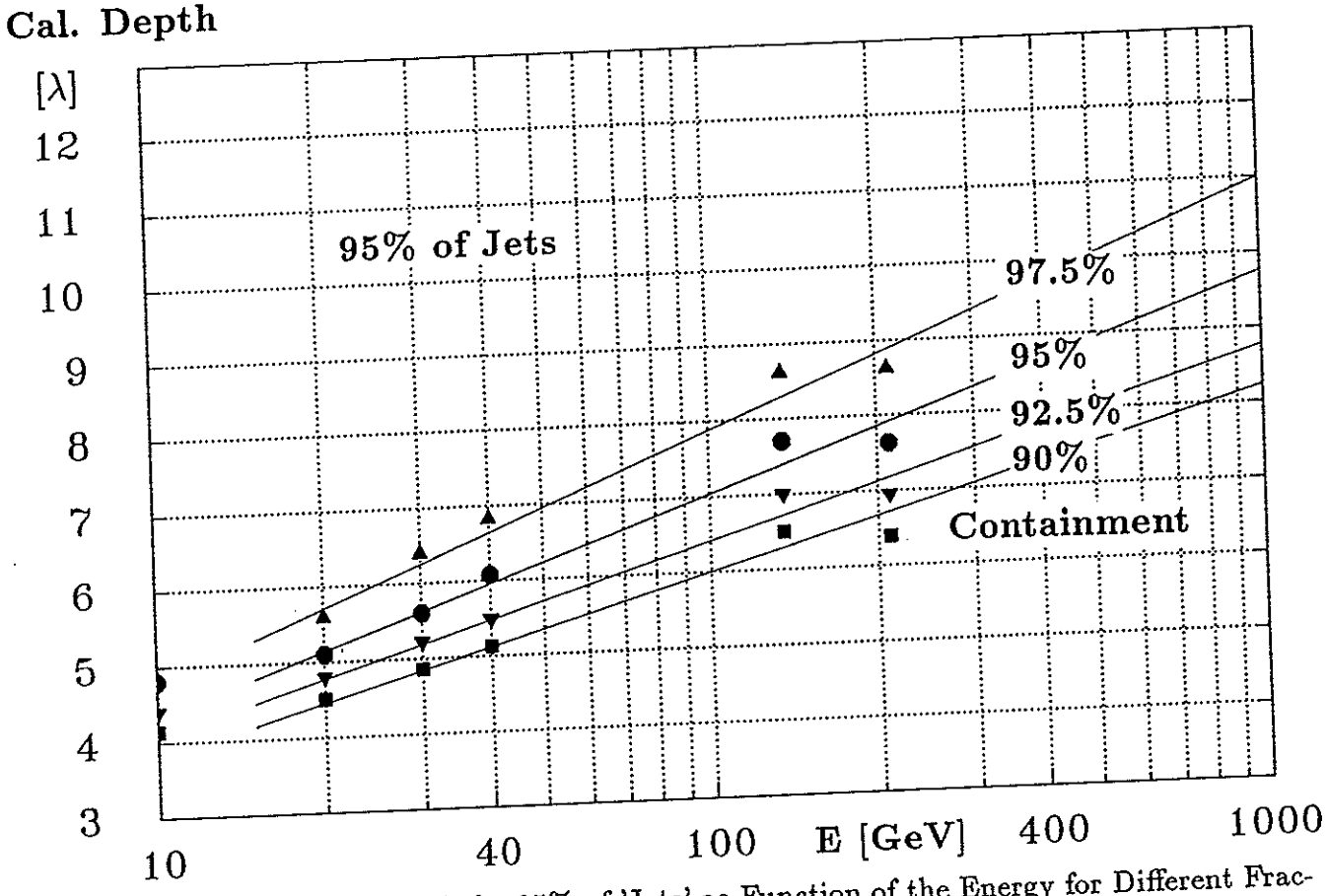

Fig. 4.50b Calorimeter Depth for 95% of 'Jets' as Function of the Energy for Different Fractions of Shower Containment.

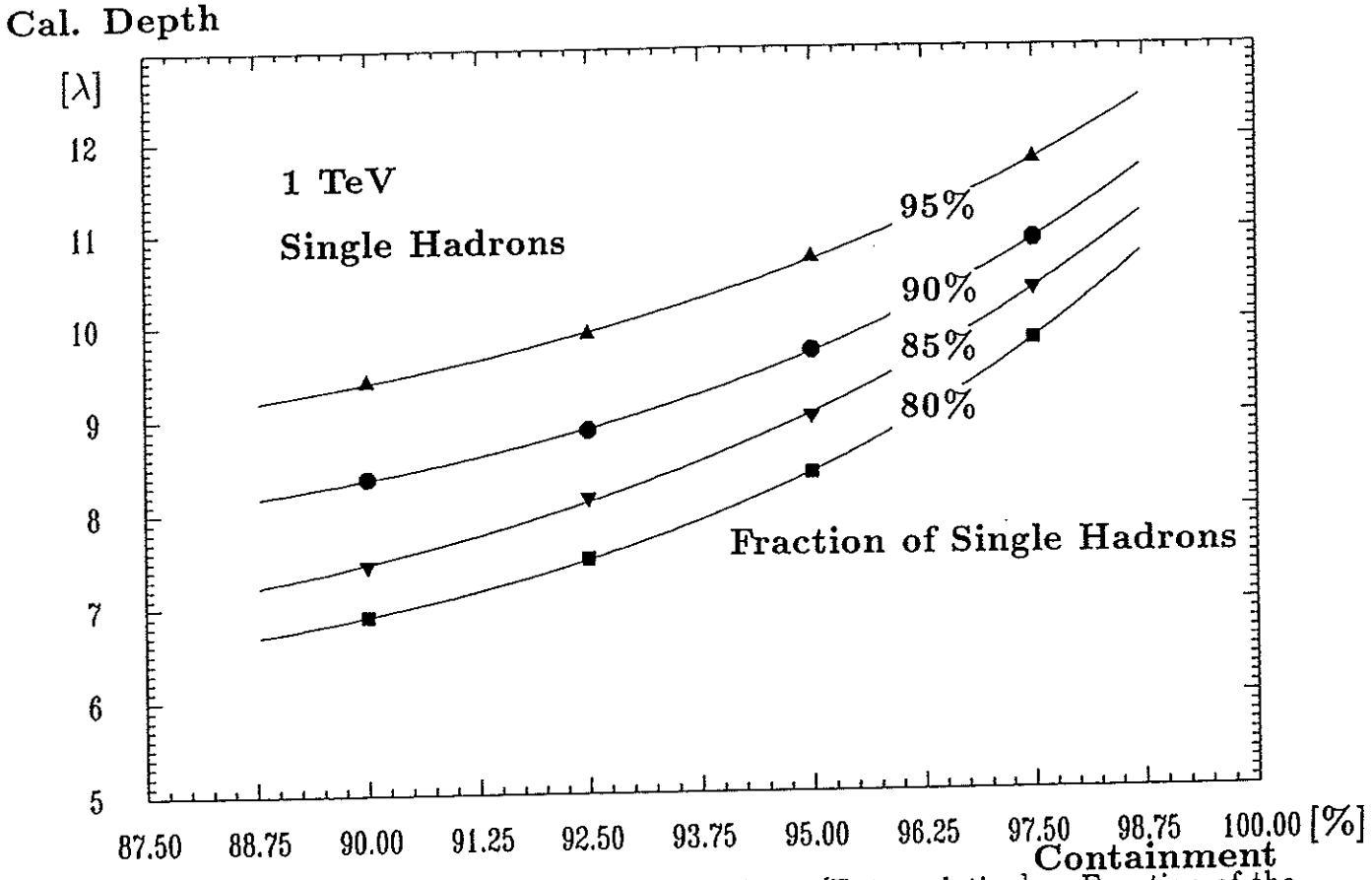

Fig. 4.51a Calorimeter Depth for 1 TeV Single Hadrons [Extrapolation] as Function of the Shower Containment for Different Fractions of Single Hadrons.

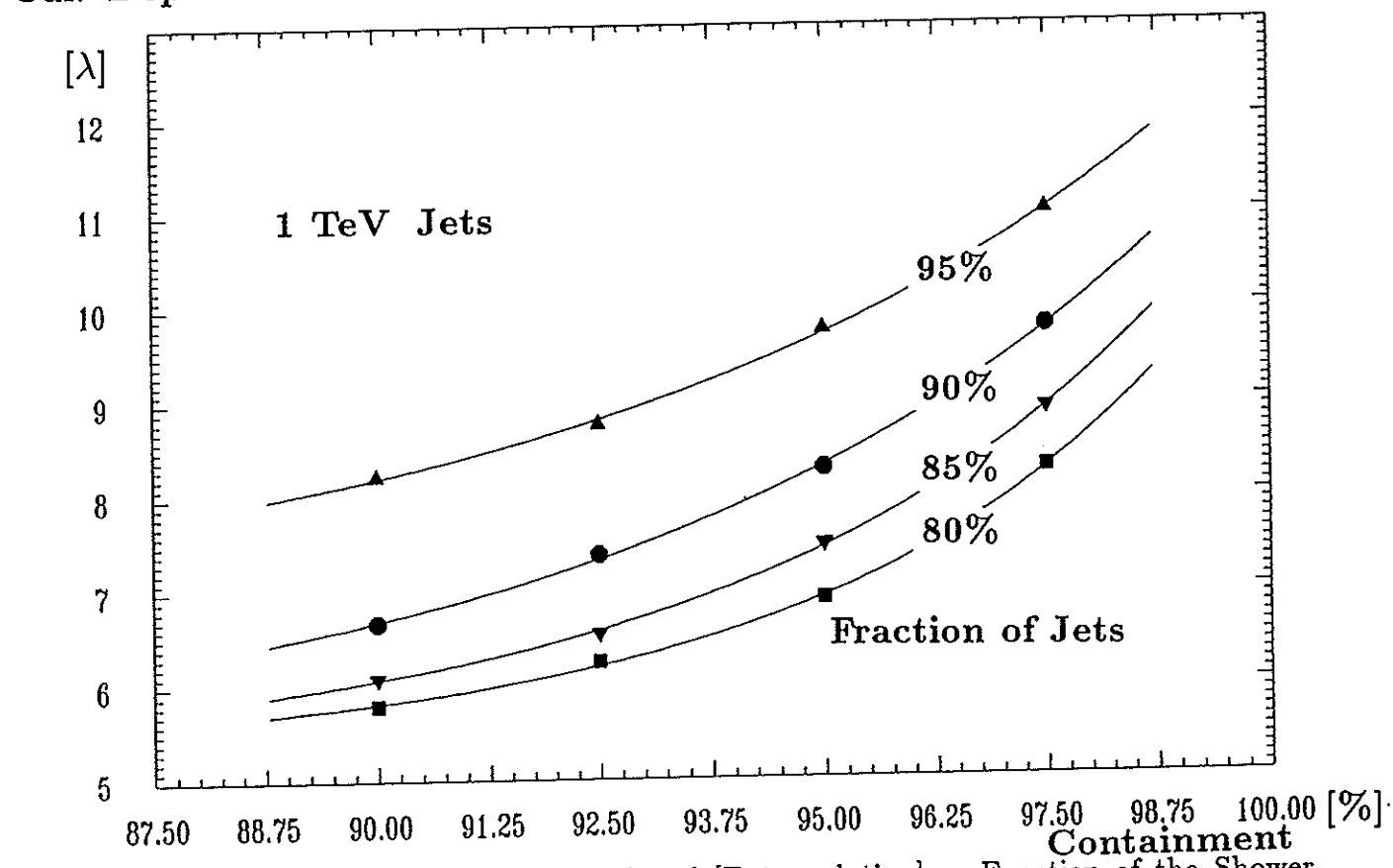

Fig. 4.51b Calorimeter Depth for 1 TeV 'Jets' [Extrapolation] as Function of the Shower Containment for Different Fractions of 'Jets'.

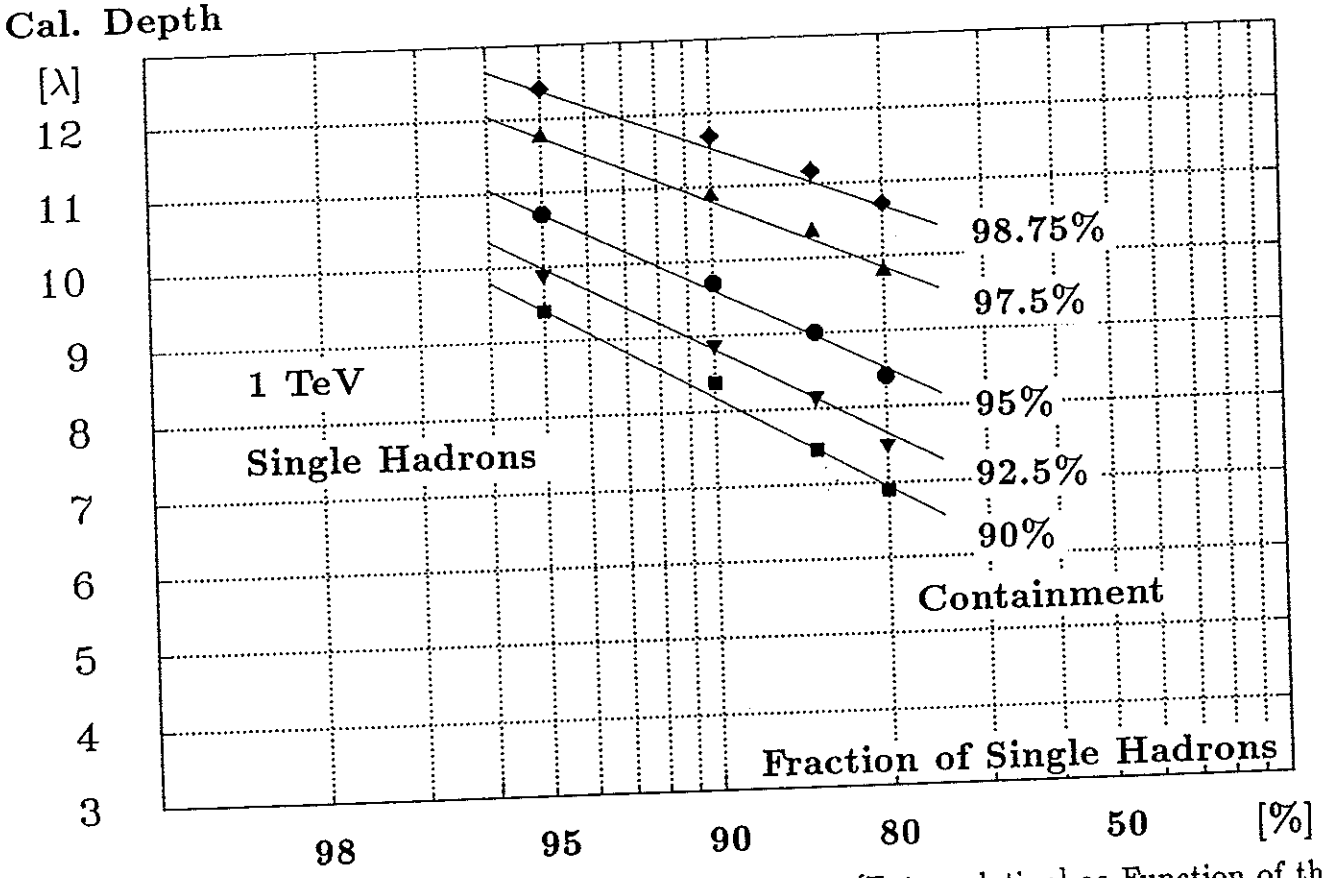

Fig. 4.52a Calorimeter Depth for 1 TeV Single Hadrons [Extrapolation] as Function of the Fraction of Single Hadrons for Different Fractions of Shower Containment.

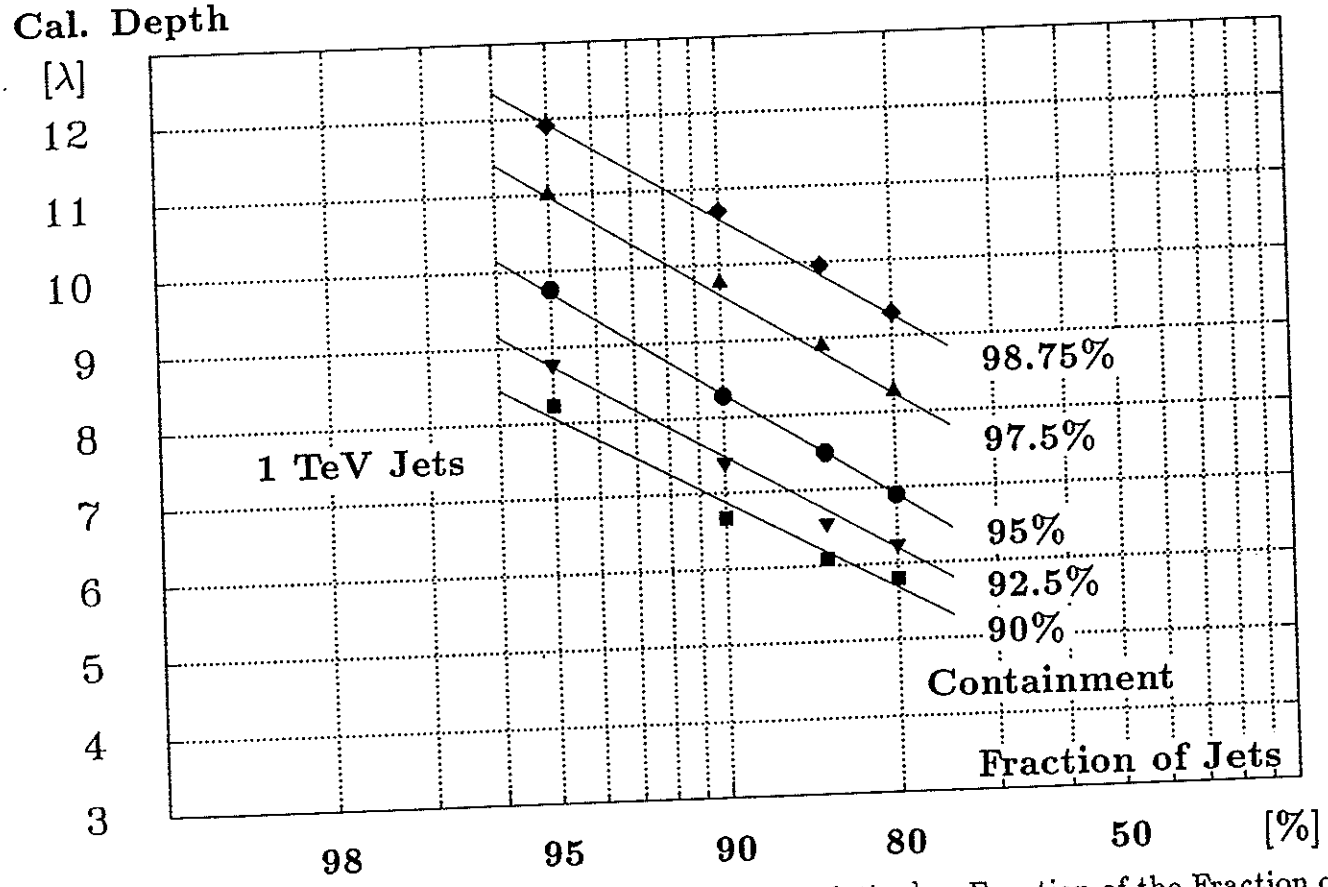

Fig. 4.52b Calorimeter Depth for 1 TeV 'Jets' [Extrapolation] as Function of the Fraction of 'Jets' for Different Fractions of Shower Containment.

4.3 A Uranium Scintillator Test Calorimeter with Compensation and High Energy Resolution for Hadrons — Calorimeter TEST 35

4.3.1 The Experimental Set Up of Calorimeter TEST 35

The main aim of calorimeter TEST 35 was to verify, that a modular uranium scintillator calorimeter with wavelength shifter readout and a tower structure as planned for the ZEUS calorimeter can be built, which achieves compensation and an energy resolution of $35\%/\sqrt{E}$ for hadrons ($\Rightarrow$ name TEST 35) [AND86], [ZEU87], [KRÜ88b], [BEH90a].

Three uranium modules, on loan from the HELIOS experiment at CERN [AKE85], were restacked with new scintillator plates and test measurements were performed during June and July 1986 in the T7 beam line (East Hall) at the CERN PS.

Figure 4.53 shows a sketch of the TEST 35 calorimeter. It consisted of 3 modules, each with a width of 20cm, a height of 120cm and a total depth of 125 radiation lengths (X_0) or 4.2 interaction lengths (λ_{int}).

The modules had an internal sandwich sampling structure of 3mm thick depleted uranium plates interleaved with 2.5mm thick scintillator plates. The 20cm x 20cm towers were read out on two opposite sides by wavelength shifter bars of 20cm x 80cm followed by light guides and photomultipliers. The uniform readout along the wavelength shifters was achieved by back reflectors of aluminium foils with black printed "backgammon" patterns to compensate the light attenuation in the wavelength shifters. The upper half of the calorimeter with an entrance area of 60cm x 60cm was equipped with SCSN–38 scintillator tiles and consisted of 9 towers without longitudinal segmentation. The SCSN–38 scintillator tiles with dimensions of 60cm x 20cm were optically separated into 20cm x 20cm units by a sawing method. The main parameters of the TEST 35 calorimeter are summarized in Table 4.11.

The relative calibration of the photomultipliers was performed using the radioactivity of the uranium. The high voltages of the photomultipliers were adjusted in such a way, that they gave the same mean signals created in the scintillator tiles by the radioactivity of the uranium integrated over $10\mu s$. The calibration was continuously monitored during the data taking in between spills. By adjusting the high voltages of the photomultipliers every 3 to 4 hours the variation of the uranium signal from photomultiplier to photomultiplier was less than 0.5%.

The beam set up is presented in Fig. 4.54. It consisted of two threshold Cherenkov counters for the separation between electrons and hadrons, a set of scintillation counters defining the beam and the TEST 35 calorimeter itself. Muons were identified by a signal in the scintillation counter B6 positioned behind the calorimeter.

The calorimeter was aligned such, that the beam particles were incident on the centre of the upper half of the calorimeter. Measurements with this calorimeter configuration were performed with electrons, muons and hadrons at momenta of 3, 5, 7 and 9GeV/c.

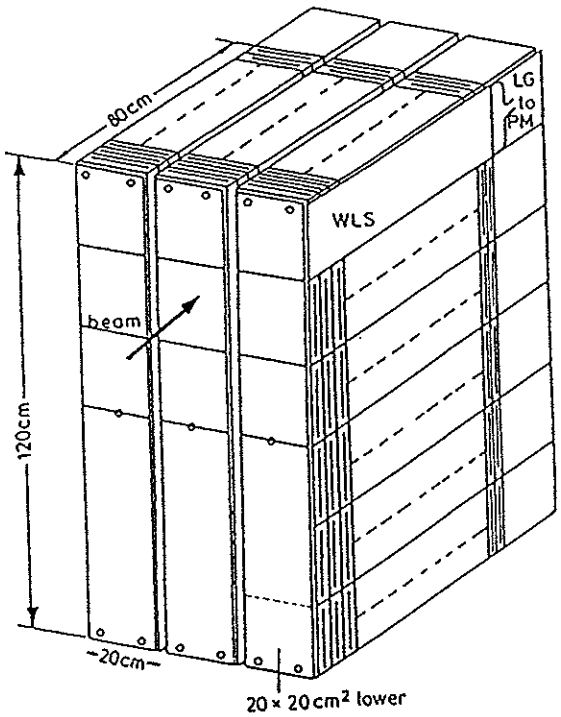

Fig. 4.53 Sketch of the TEST 35 calorimeter.

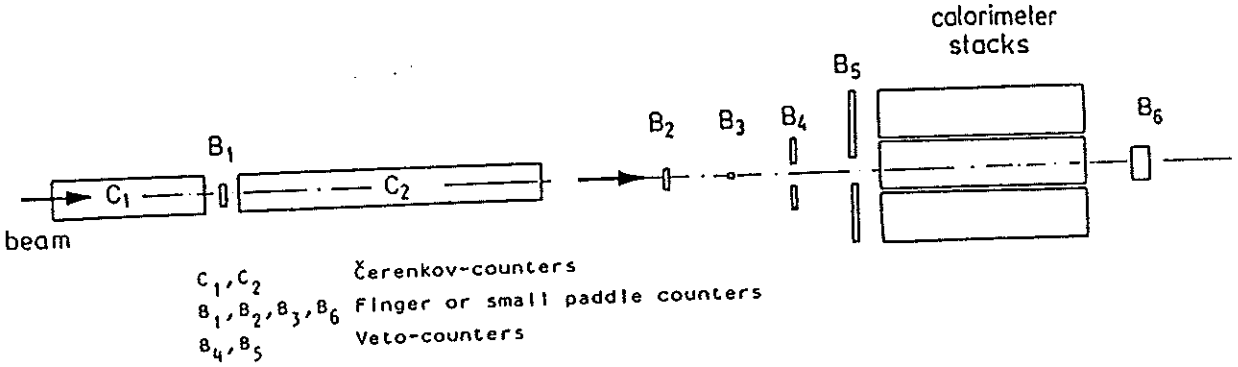

Fig. 4.54 The experimental set up of calorimeter TEST 35 at the CERN PS.

Sampling structure: DU / SCI	3mm / 2.5mm
Number of DU plates	133
Size of DU plate	1200 × 199 × 3 mm^3
Number of SCI plates	134
Size of SCI plates:	
in the upper half – SCSN–38	3× [200×200×2.5 mm^3]
in the lower half – Altustipe	600×200×2.5 mm^3
Number of optical channels	
to readout the SCSN–38	18
Doping of K–27 WLS	100 mg/l
Photomultipliers	XP2011
Average density	9.9 g/cm^3
Total depth of the stack	806.5 mm = 125 r.l. = 4.2λ_{int}

Table 4.11 Main parameters of the TEST 35 calorimeter.

4.3.2 Experimental Results of Calorimeter TEST 35

Figures 4.55, 4.56 and 4.57 show the pulse height spectra of 5GeV/c muons, electrons and hadrons (pions) with a gate width of 100ns. Gaussian distributions were fit to the pulse height spectra of electrons and hadrons within ± 2 standard deviations around the most probable values. An energy resolution of $33.7\%/\sqrt{E}$ was achieved for hadrons and of $16.3\%/\sqrt{E}$ for electrons with an e/h–ratio of 1.04 ± 0.03, here calculated as the ratio of the pulse heights for hadrons to the pulse heights for electrons measured in the central tower. The hadron distribution shows a tail to lower pulse heights due to leakage.

The transverse leakage of hadron showers was determined by scanning the calorimeter in horizontal direction. The transverse energy distribution for 5GeV/c hadron showers is plotted in Fig. 4.58 indicating the average pulse heights measured by the upper 18 photomultipliers. About 80% of the shower energy is deposited in the central tower. The distribution indicates that the transverse leakage is at the few % level.

Monte Carlo calculations [CLO87a] simulating a hermetic TEST 35 calorimeter with uniform readout yield an e/h–ratio of 1.00 ± 0.02 and an energy resolution of $30\%/\sqrt{E}$ for hadrons. These predictions are compatible with the measured values if inhomogenities in the readout and energy leakage are taken into account.

Figure 4.59 presents the e/h–ratio as a function of the gate width (Δt). It decreases with the gate width from e/h = 1.11 at Δt = 70ns to e/h = 1.04 at Δt = 600ns. This is due to the delayed contribution of low energy neutrons to the hadron signal. But the higher degree of compensation due to the larger gate width does not lead to an improved energy resolution (Fig. 4.60) because of an increase of the contribution from the uranium noise. Corrections for transverse and longitudinal leakage of the hadron showers, estimated to be about 5% to 10%, and for nonuniformities in the wavelength shifter readout will bring the e/h–ratio close to 1.

Similar results were also obtained for 3, 7 and 9GeV/c. The deviation of the average hadron signal from linearity is less than 1.5%. Figure 4.61 shows the energy resolution for hadrons with a gate width of 200ns as a function of the hadron momentum. The energy resolution achieved for hadrons is about $33.7\%/\sqrt{E}$ in the momentum range from 3GeV/c to 9GeV/c and scales with $1/\sqrt{E}$.

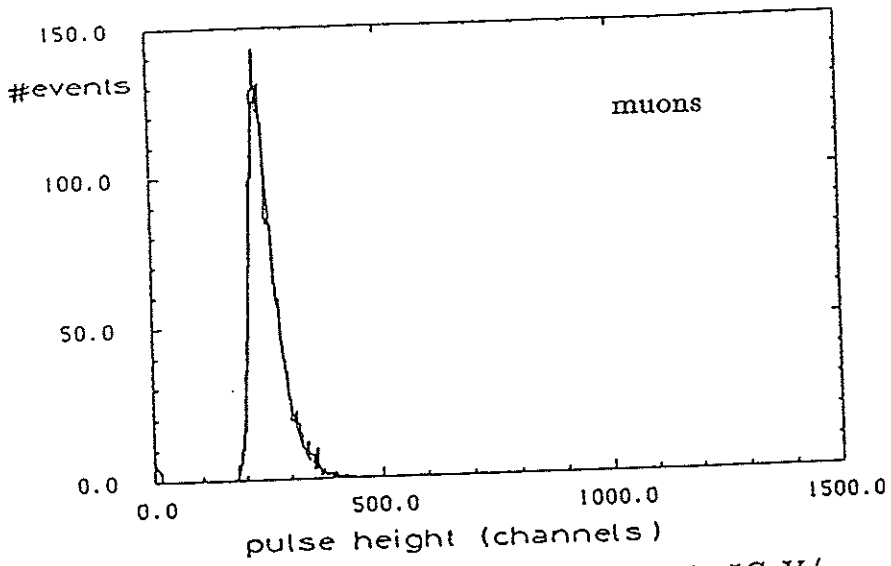

Fig. 4.55 Response of the TEST 35 calorimeter to 5GeV/c muons.

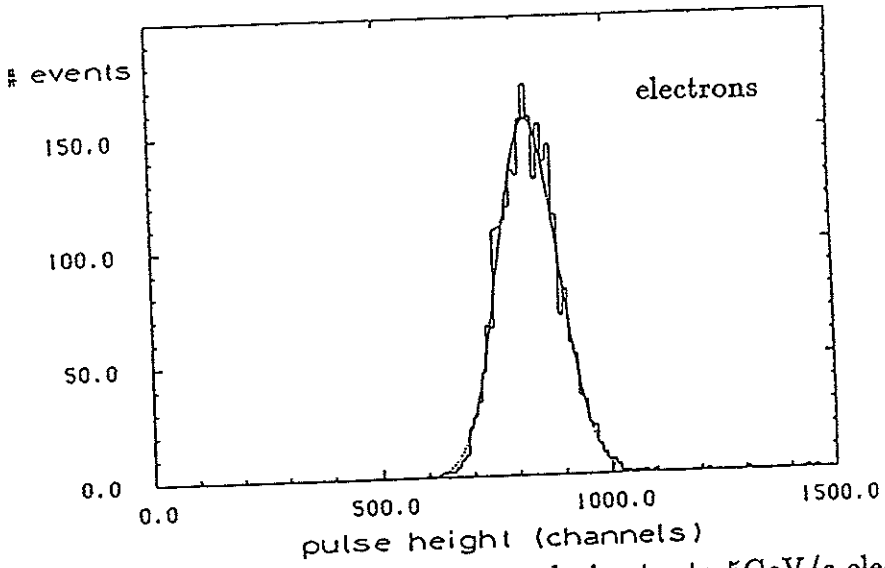

Fig. 4.56 Response of the TEST 35 calorimeter to 5GeV/c electrons.

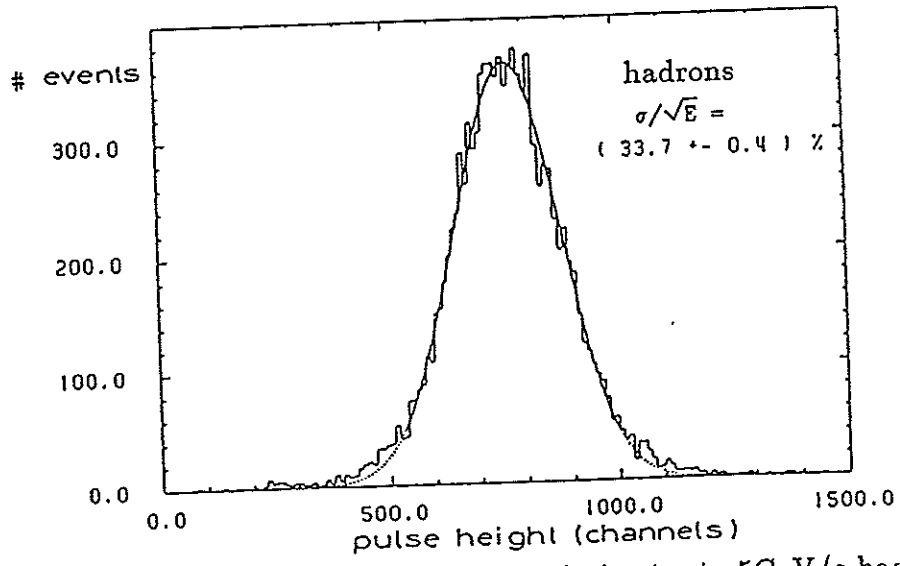

Fig. 4.57 Response of the TEST 35 calorimeter to 5GeV/c hadrons.

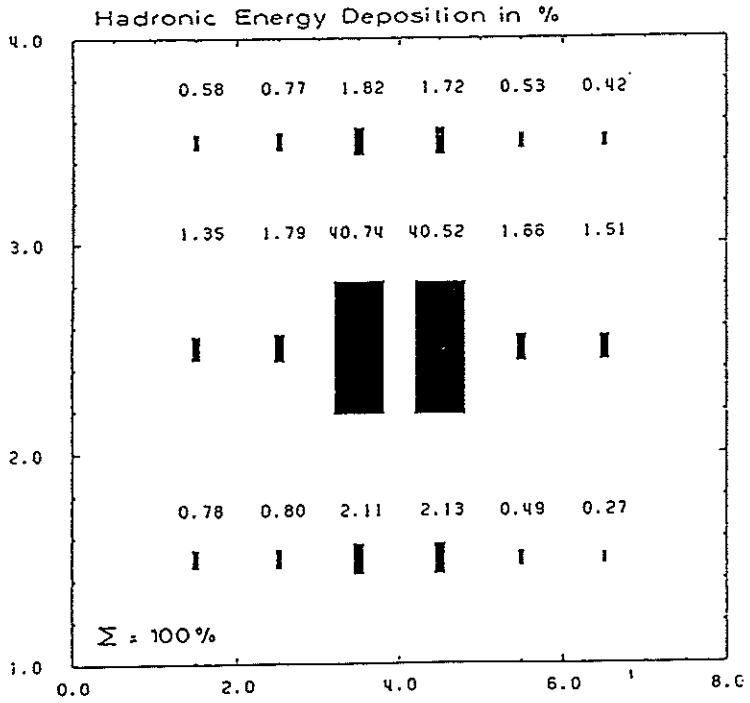

Fig. 4.58 Transverse energy distribution of 5GeV/c hadrons in the TEST 35 calorimeter.

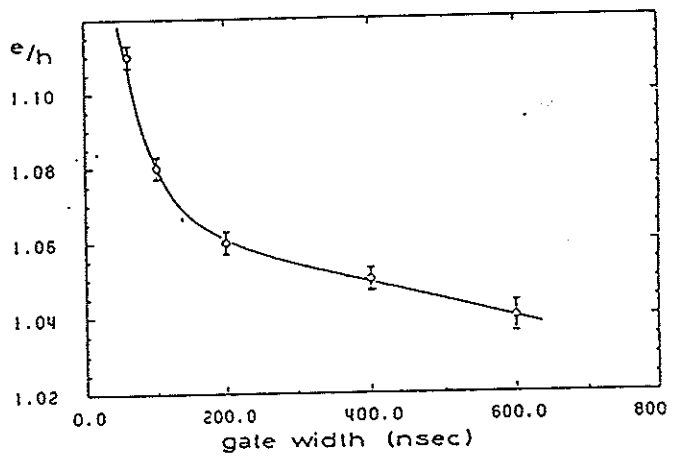

Figure 4.59
e/h–ratio vs. integration time in TEST 35.

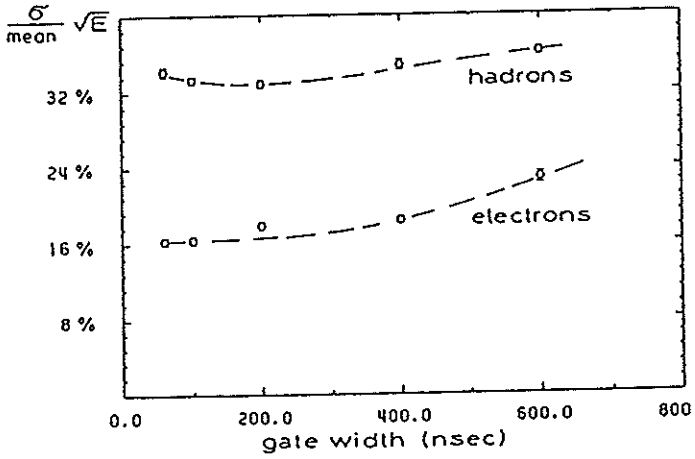

Figure 4.60
Energy resolution for hadrons and electrons vs. integration time in TEST 35.

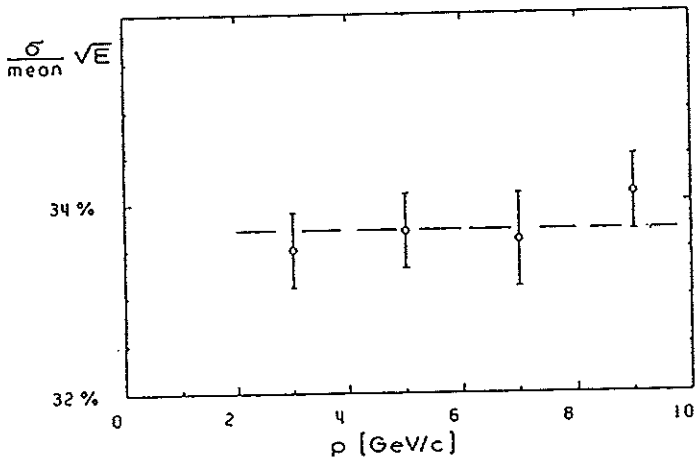

Fig. 4.61 Energy resolution for hadrons vs. beam momentum in TEST 35.

4.4 A Lead Scintillator Test Calorimeter with Compensation and High Energy Resolution for Hadrons — Calorimeter TEST 36

4.4.1 The Experimental Set Up of Calorimeter TEST 36

The aim of TEST 36 was to find out, if compensation can be achieved also with a lead scintillator calorimeter. Following a proposal by H. Brückmann [AND87] a sandwich sampling calorimeter has been built of 10mm thick lead plates interleaved with 2.5mm thick SCSN–38 scintillator tiles [BER87a], [ZEU87], [BER87], [KRÜ88a]. The unusual high ratio of about 4 for the thicknesses between the lead and scintillator plates was predicted as the optimum one [WIG87]. For this configuration the contributions of neutrons to the hadronic signal was expected to be large enough to obtain compensation.

Figure 4.62 shows the lead scintillator calorimeter of TEST 36 with a total entrance area of about 66cm x 68cm. It consisted of 9 towers, with wavelength shifter readout on two opposite sides, plexiglass light guides and photomultipliers (XP2011). Each tower had transverse dimensions of about 20cm x 20cm and a longitudinal segmentation into one electromagnetic (1λ or $29X_0$ deep) and one hadronic section (4λ deep). The uniformity along the wavelength shifter bars, made from PMMA and doped with K–27, was achieved by graded light filters, which were optimized in bench tests. The main parameters of the TEST 36 lead scintillator calorimeter are summarized in Table 4.12.

The experimental set up of TEST 36 in the X5 beam line at the CERN SPS is presented in Fig. 4.63. It consisted of two Cherenkov counters and one muon tagger for particle identification, scintillation beam counters and the TEST 36 calorimeter itself.

The online calibration of the calorimeter was performed with a ^{60}Co–source (3mCi), which could be inserted in the middle of a lead plate between the EM and HAD towers. An offline calibration was done with electrons, hadrons and muons incident on the centre of each tower [BER87a]. The mean signals of the photomultipliers in the EM section were equalized for 10GeV electrons and in the HAD section for 10GeV hadrons. The electron and hadron calibration agreed within $\pm 1\%$ in the EM section.

The intercalibration between the EM and HAD sections was performed by multiplying the gain of the HAD photomultiplier signals by a factor α and demanding that the fractional energy resolution for hadrons be optimum.

Measurements have been performed with electrons, hadrons (pions) and muons at the CERN PS (T7 beam, East Hall) in the momentum range from 3GeV/c to 10GeV/c and at the CERN SPS (X5 beam, West Hall) from 10GeV/c to 75GeV/c.

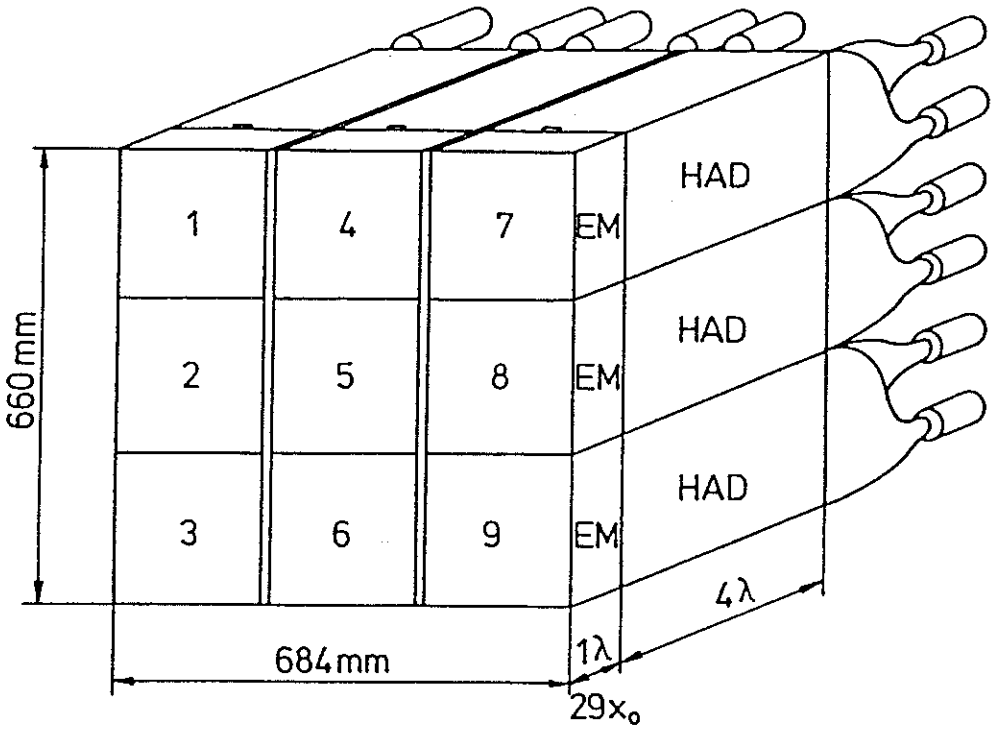

Fig. 4.62 Sketch of the TEST 36 calorimeter.

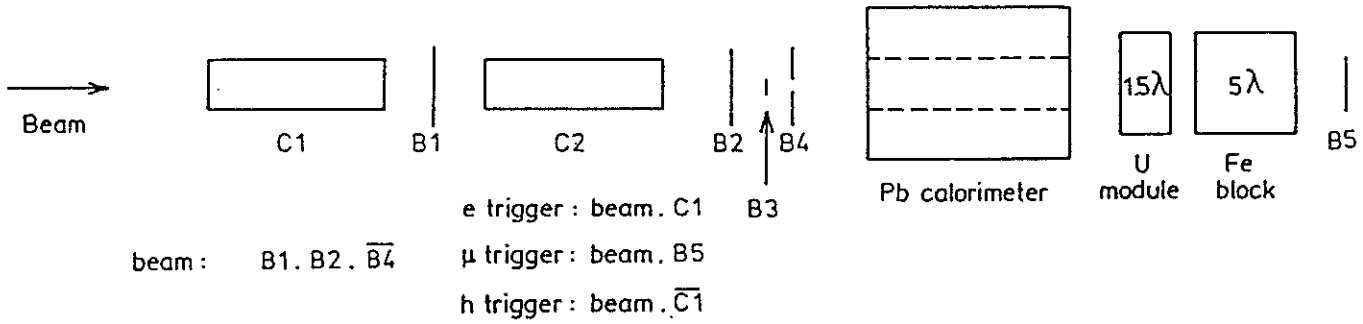

Fig. 4.63 The experimental set up of calorimeter TEST 36 at the CERN SPS.

TEST 36	EM section	HAD section
Sampling structure: Pb / Scint.	10mm / 2.5mm	10mm / 2.5mm
Number of Pb plates	16	65
Number of Scint. plates	16	65
Size of Pb plates	700 x 218 x 10mm^3	700 x 211 x 10mm^3
Size of Scint. plates	218 x 218 x 2.5mm^3	211 x 218 x 2.5mm^3
Size of WLS bars	218 x 310 x 2.0mm^3	218 x 918 x 2.0mm^3
Photomultipliers per module	6	6
Material of the Pb plates	96%Pb + 4%Sb	
Material of the Scint. plates	SCSN–38	
Material of the WLS bars	PMMA UV absorbant	
Doping of the WLS	125mg/l of K–27	
Photomultipliers	Philips XP2011	

Table 4.12 Main parameters of the TEST 36 lead scintillator calorimeter.

4.4.2 Experimental Results of Calorimeter TEST 36

Figures 4.64, 4.65 and 4.66 show the pulse height spectra of 10GeV/c muons and 10GeV/c to 75GeV/c electrons and hadrons. Gaussian distributions were fit to the pulse height spectra of the electrons and hadrons within ± 3 standard deviations around the most probable values.

Figure 4.67 presents the energy resolution for electrons and hadrons as a function of the particle energy.

The energy resolution for electrons can be parametrized by

$$\frac{\sigma_e}{< E_e >} = \frac{(23.5 \pm 0.2)\%}{\sqrt{E}} \oplus (1.2 \pm 0.2)\% \ ,$$

where the first term is in agreement with EGS4 Monte Carlo simulations with a contribution of 6.6% from photoelectron statistics and the constant term is compatible with the beam momentum spread.

The hadrons were incident on the centre of tower 5 with an energy deposition of about 80% in the central tower for energies from 3GeV to 75GeV. The energy deposited in the EM section decreases from 50% at 3GeV to 30% at 75GeV.

The energy resolution for hadrons with negligible transverse and longitudinal leakage can be parametrized by

$$\frac{\sigma_h}{< E_h >} = \frac{(44.2 \pm 1.3)\%}{\sqrt{E}} \ .$$

Although 10mm thick Pb absorber plates are quite coarse an excellent energy resolution is achieved, in particular at high momenta and no constant term is necessary for the parametrization. This result demonstrates that for optimization of the compensation at high momenta, the minimization of intrinsic fluctuations is more important than that of sampling fluctuations.

Figure 4.68 shows the e/h–ratio as a function of the energy and in addition the contribution from photostatistics. The e/h–ratio varies from 1.19 at 3GeV/c to 1.09 at 75GeV/c. After correcting for an estimated leakage of about 5%, an e/h–ratio was found of

$$\frac{e}{h} = 1.05 \pm 0.04 \ \ for \ \ p > 10 GeV/c \ .$$

The e/mip–ratio has also been determined [BER87a] to

$$\frac{e}{mip} = 0.67 \pm 0.03 \ ,$$

which is in agreement with a value of e/mip=0.65 from Monte Carlo calculations using EGS4 [NEL85].

TEST 36 for the first time has shown, that compensation can be achieved also with lead as absorber. Using scintillator for readout a ratio of about 4 for the thicknesses of lead to scintillator plates is necessary. The equalization of the electron and hadron signals yields a significant improvement of the energy resolution for hadrons.

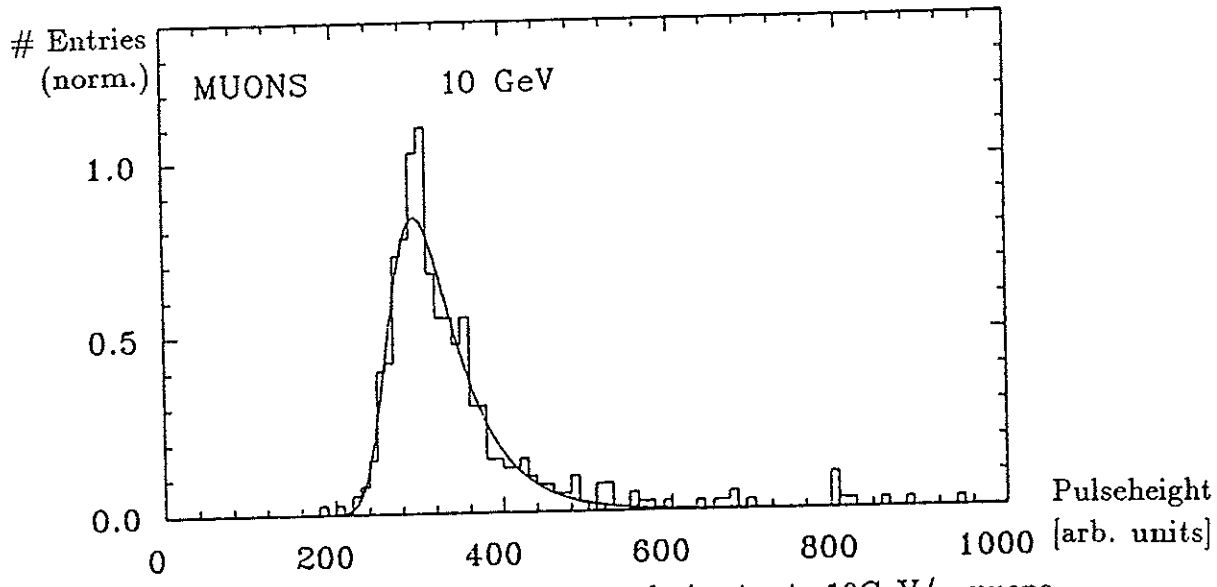

Fig. 4.64 Response of the TEST 36 calorimeter to 10GeV/c muons.

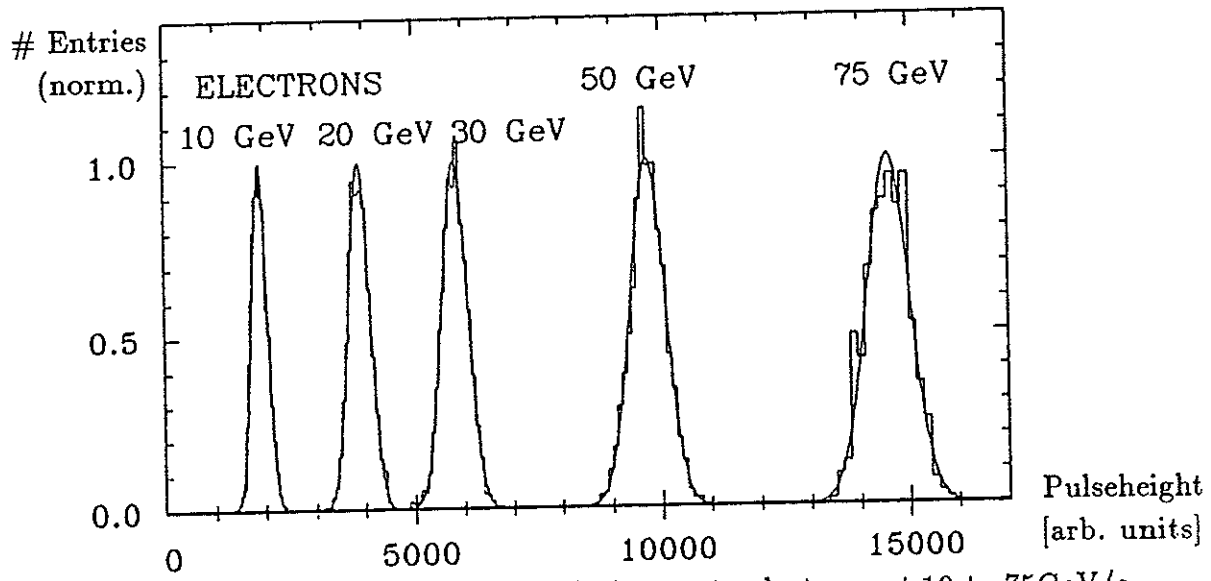

Fig. 4.65 Response of the TEST 36 calorimeter to electrons at 10 to 75GeV/c.

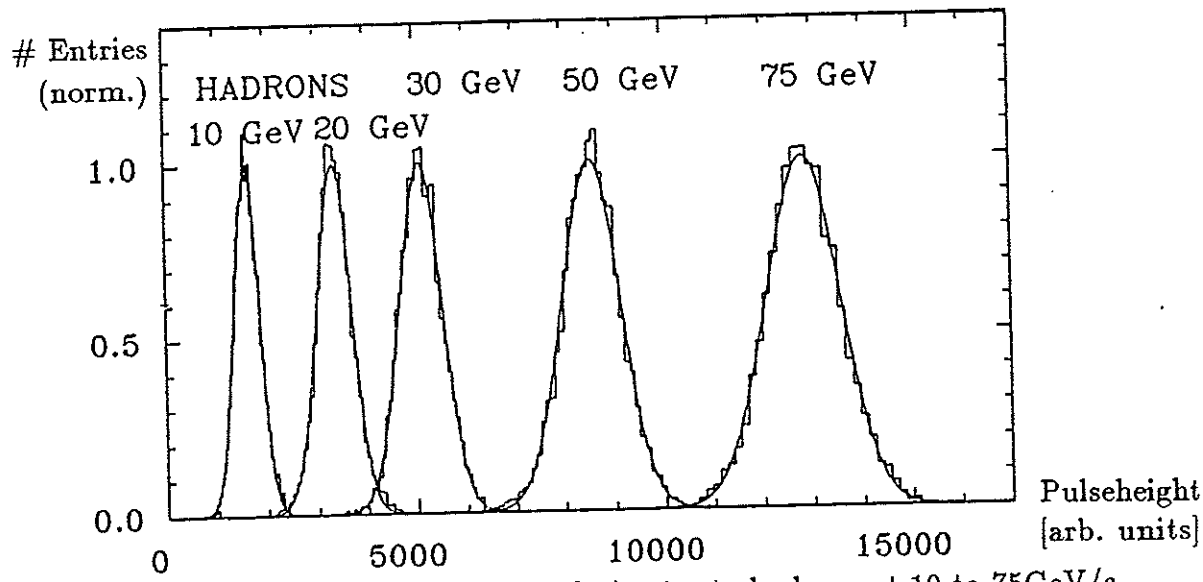

Fig. 4.66 Response of the TEST 36 calorimeter to hadrons at 10 to 75GeV/c.

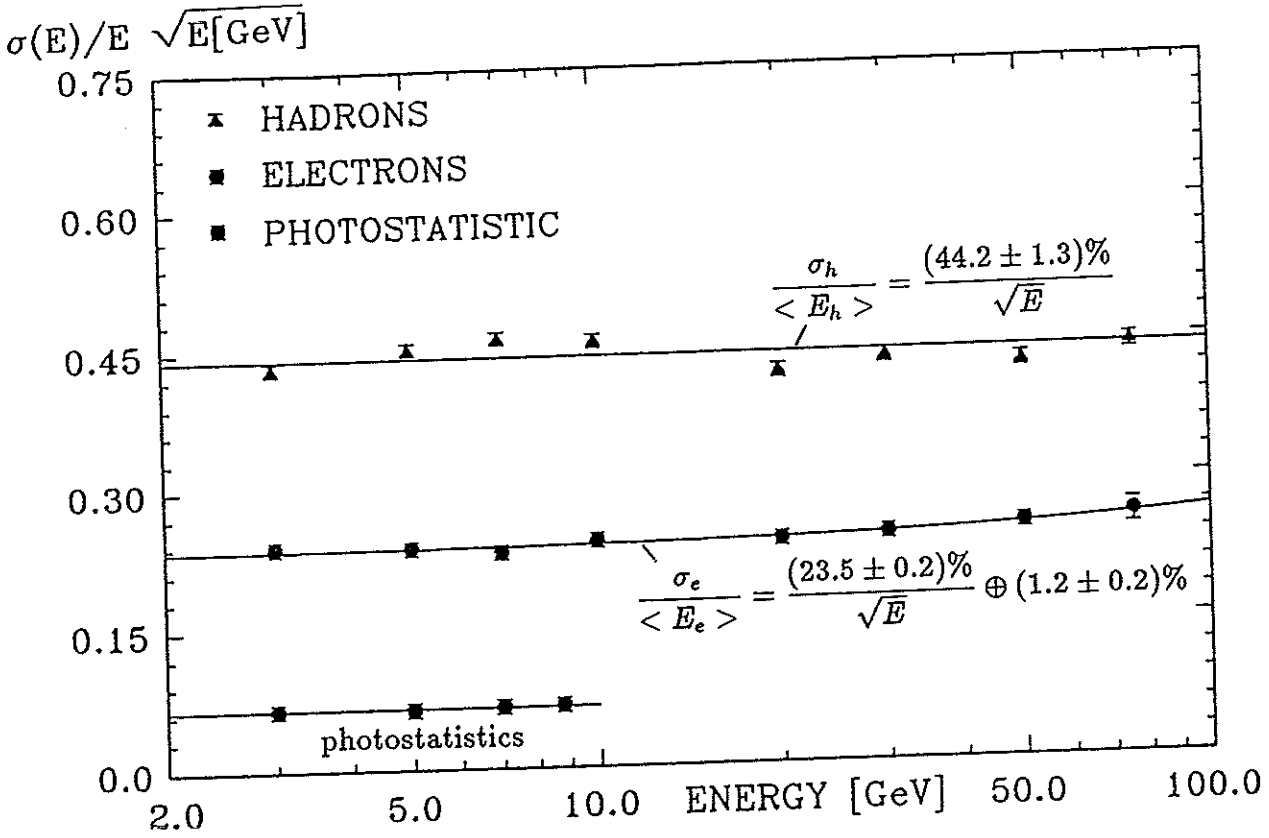

Fig. 4.67 Energy resolution for hadrons and electrons vs. energy in TEST 36.

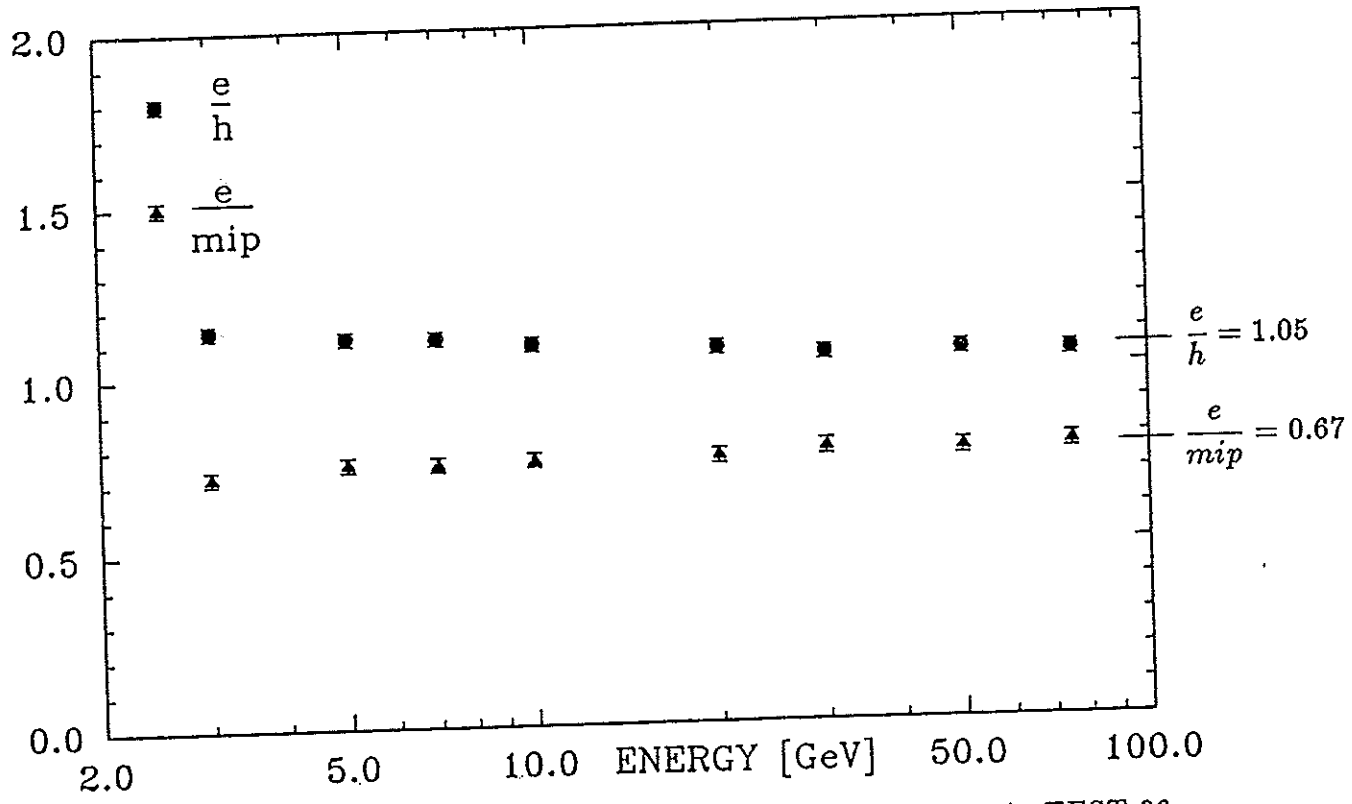

Fig. 4.68 The e/h- and e/mip-ratio as a function of the energy in TEST 36.

4.5 Optimization of the Calorimeter Configuration — Calorimeter TEST 60

4.5.1 The Experimental Set Up of Calorimeter TEST 60

TEST 60 had a modular structure and consisted of a set of different sampling calorimeter configurations in which materials could easily be exchanged. It had good uniformity, no spacers or dead spaces, fine transverse segmentation and longitudinal segmentation. The aim of TEST 60 was to study the energy resolution and e/h–ratio versus material composition, transverse and longitudinal leakage, transverse and longitudinal shower profiles, position resolution and to learn how to calibrate the calorimeter. In addition many important effects on the energy resolution and the uniformity, e.g. of the optical readout were studied [ENG86], [KRÜ87b], [ZEU87], [BER87], [KRÜ88a], [AGO89].

Calorimeter TEST 60 consisted of separate modules positioned closely behind each other. Figure 4.69 shows the layout and mechanical structure of one TEST 60 calorimeter module. The entrance area of each module was 60cm x 60cm ($\Rightarrow$ name TEST 60). The scintillator plane was segmented in the vertical direction into twelve 50mm high SCSN–38 scintillator strips, each wrapped in white paper to increase the light output and in addition in one layer of aluminized mylar foil to decouple the strips optically from each other. The scintillator strips were read out by 3mm thick PMMA wavelength shifter bars glued to bent plexiglass lightguides with associated photomultipliers (XP2011). The absorber plates could be exchanged up to certain thickness limits without disturbing the readout configuration. The main parameters of the TEST 60 calorimeter modules are summarized in Table 4.13.

In total nine TEST 60 calorimeter modules were built at NIKHEF. The modules #1–5 were constructed of 30 layers of 5mm thick scintillator plates and the modules #6–9 of 45 layers of 3mm thick scintillator plates. First the modules #1–5 were equipped with 4mm thick lead absorber plates. In the final configuration for all modules 3.2mm DU plates were used apart from module #8, which was equipped with 3mm thick DU plates.

Tests were performed with DU absorber plates interleaved with 5mm scintillator plates in modules #1–5 (T60A) and with 3mm scintillator plates in modules #6–9 (T60B1).

Measurements were then also done with graded light filters installed between the scintillator strips and the wavelength shifters to correct for the light attenuation in the WLS (T60B2).

In the following test the DU plates were clad in addition with 0.2mm thick stainless steel foils to reduce the dark current in the photomultipliers due to the radioactivity of the uranium and to check its influence on the calorimeter performance (T60B3).

There were two different experimental set ups of TEST 60: T60A consisted of 4 modules #1–4 with a total depth of 4.4λ and T60B consisted of 4 modules #6–9 with a depth of 6λ, which in addition uses module #1 (1.1λ) as a backing calorimeter (Fig. 4.70). T60A was tested in the T7 beam at the CERN PS with particles up to 9GeV/c and T60B in the X5 beam at the CERN SPS with particles from 10GeV/c to 100GeV/c.

The beam setup is shown in Fig. 4.70. Electrons were identified by two Cherenkov counters and also by the transverse and longitudinal shower deposition in the calorimeter.

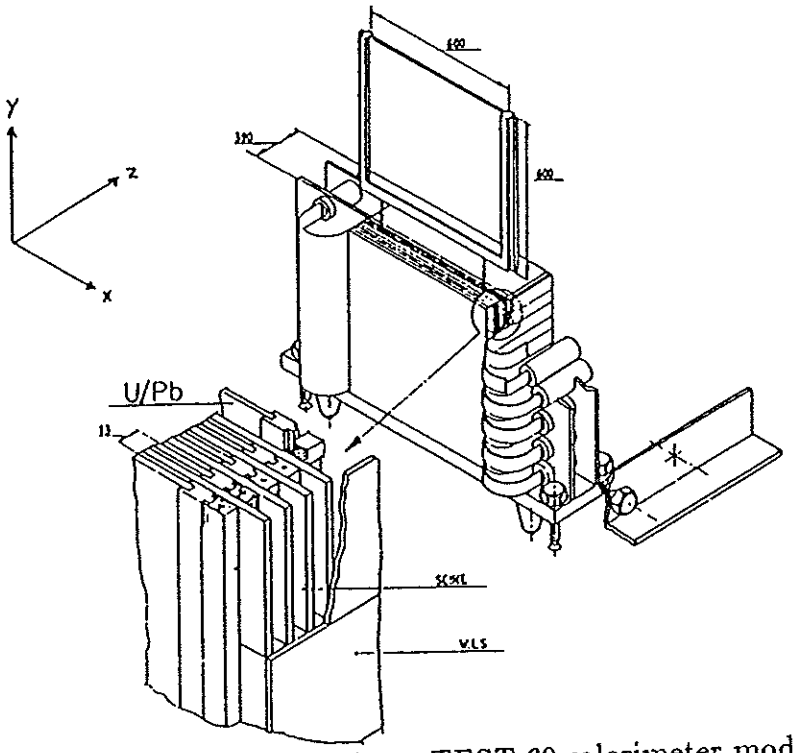

Fig. 4.69 Construction of one TEST 60 calorimeter module.

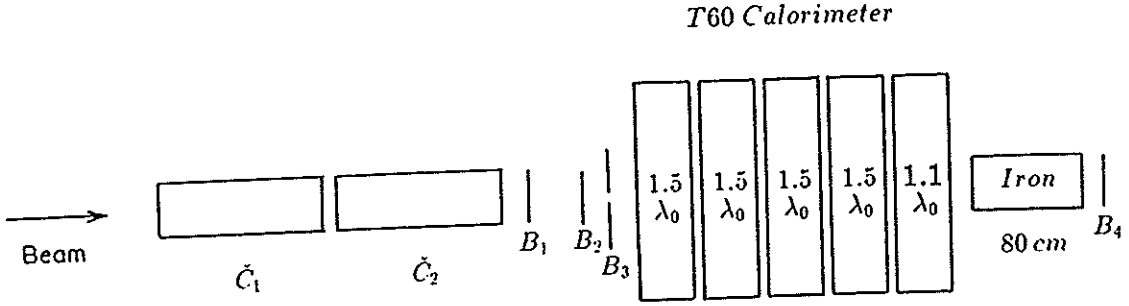

Fig. 4.70 The experimental set up of calorimeter TEST 60 at the CERN SPS.

TEST 60	Module #1–5	Module #6–9
Lateral dimension	60cm x 60cm	60cm x 60cm
#Absorber layers	30	45
Space per layer	7 mm	5 mm
Absorber material	depleted uranium (lead)	depleted uranium
Absorber thickness	3.2mm (4mm)	3.2mm (3mm for mod #8)
# Scintillator layers	30	45
Space per layer	6 mm	4 mm
Scintillator material	SCSN–38	SCSN–38
Dimension	$600 \times 50 \times 5$ mm^3	$600 \times 50 \times 3$ mm^3
#Strips/layer	12	12
Total thickness	390 mm	405 mm
Depth [r.l.], [λ_{int}]	$30X_0$, $1.1\lambda_{int}$	$45X_0$, $1.5\lambda_{int}$
WLS material	PMMA UV absorbant ..	... with K–27(120 mg/l)
WLS dimension	$388 \times 50 \times 3$ mm^3	$405 \times 50 \times 3$ mm^3
# Strips (PMs)	2×12 (XP2011)	2×12 (XP2011)

Table 4.13 Parameters of the calorimeter modules of TEST 60.

4.5.2 Experimental Results of Calorimeter TEST 60

The results of four different data samples taken with the TEST 60 calorimeter are presented in the following. The characteristics of these data samples, called T60A, T60B1, T60B2 and T60B3 are described in Table 4.14.

Data Sample	Sampling Structure	Momentum [GeV/c]	Comments
T60A	3.2mm DU 5mm Scint.	3 – 8.75	
T60B1	3.2mm DU 3mm Scint.	10 – 100	attenuation length of the WLS: 1.3m, no light filters between Scint./WLS
T60B2	3.2mm DU 3mm Scint.	10 – 100	with graded light filters between Scint./WLS for linear readout along the WLS
T60B3	3.2mm DU 3mm Scint.	10 – 100	with graded light filters between Scint./WLS; DU plates wrapped in a 0.2mm steel foil

Table 4.14 Data samples of four different TEST 60 configurations.

The transverse leakage of the hadron showers were determined by scanning over the vertical segmentation of the calorimeter. It was about 3% to 4% and in first approximation independent of the particle energy.

In order to remove events, which have a significant longitudinal leakage cuts were applied.

For T60A about 15% of the events are removed from the data sample at 7GeV/c if more than 10% of the total measured particle energy is deposited after 3.3λ in module 4.

For T60B about 10% of the events are removed at 10GeV/c and about 30% at 75GeV/c if more than 2% of the total measured particle energy is deposited after 6λ in the backing calorimeter.

Figures 4.71, 4.72a and 4.72b show the pulse height spectra of muons at 50GeV/c, electrons from 10GeV/c to 50GeV/c and hadrons from 10GeV/c to 100GeV/c.

Electromagnetic showers are completely contained in the first module ($30X_0$ or $45X_0$ deep). Therefore only the response of the first module is plotted in Fig. 4.72a. The response is linear within $\pm 1\%$ and the energy resolutions with 3σ–cuts are summarized in Table 4.15. A fit to the data points yields a parametrization of the energy resolution for electrons of

$$\sigma/E = \frac{17.2\%}{\sqrt{E}} \oplus 0.8\% \quad for \ T60B2 \ .$$

The contribution of photoelectron statistics is about $7\%/\sqrt{E}$ (quadratically added) to the first term. The constant term is compatible with the beam momentum spread of $\approx 1\%$. The electron energy resolution for T60A is better than for T60B1, 2 or 3 due to the smaller contribution from photoelectron statistics and a smaller spread in the beam momentum.

The energy resolution for hadrons after the longitudinal leakage cut is given in Table 4.16. It improves with the change from 5mm (T60A) to 3mm thick scintillator plates (T60B) and improves in addition with the implementation of the graded light filters between the scintillator tiles and the wavelength shifter bars.

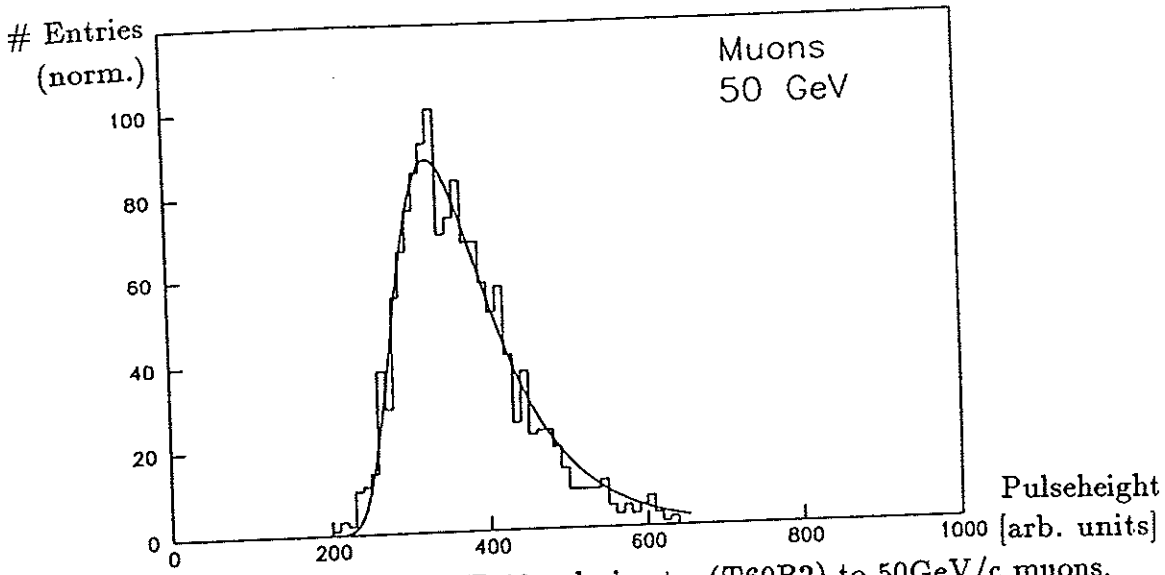

Fig. 4.71 Response of the TEST 60 calorimeter (T60B2) to 50GeV/c muons.

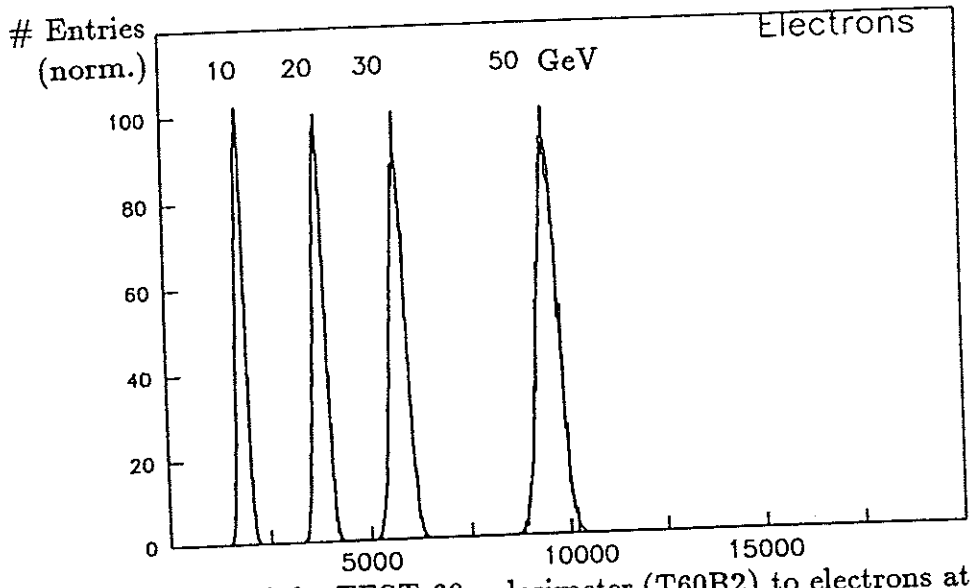

Fig. 4.72a Response of the TEST 60 calorimeter (T60B2) to electrons at 10 to 50GeV/c.

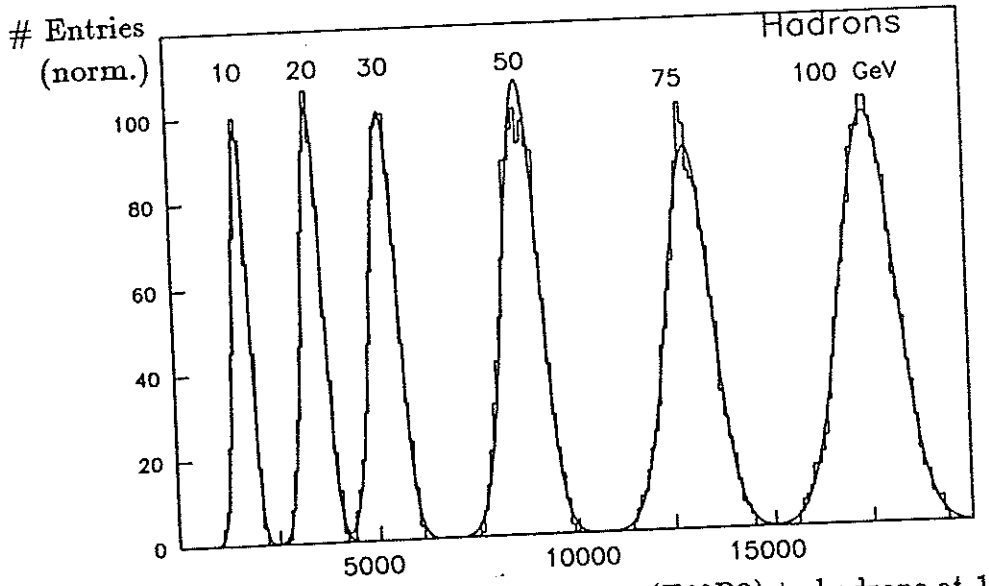

Fig. 4.72b Response of the TEST 60 calorimeter (T60B2) to hadrons at 10 to 100GeV/c.

	T60A	T60B1		T60B2		T60B3	
p [GeV/c]	$\sigma/\sqrt{E}$ [%]	$\sigma/\sqrt{E}$ [%]	σ/E (fit)	$\sigma/\sqrt{E}$ [%]	σ/E (fit)	$\sigma/\sqrt{E}$ [%]	σ/E (fit)
3	15.7						
5	15.5						
7	15.5						
8.75	15.7						
10		17.3		17.3		17.6	
20		17.9	$17.8\%/\sqrt{E}$	17.3	$17.2\%/\sqrt{E}$	17.3	$17.6\%/\sqrt{E}$
30		18.6	$\oplus 0.7\%$	18.1	$\oplus 0.8\%$	17.9	$\oplus 0.4\%$
50		19.7		18.9		18.6	

Table 4.15 Energy resolution of electrons for different TEST 60 configurations.

	T60A	T60B1		T60B2		T60B3	
p [GeV/c]	$\sigma/\sqrt{E}$ [%]	$\sigma/\sqrt{E}$ [%]	σ/E (fit)	$\sigma/\sqrt{E}$ [%]	σ/E (fit)	$\sigma/\sqrt{E}$ [%]	σ/E (fit)
3	40.1						
5	41.6						
7	41.4						
8.75	41.8						
10		38.4		36.8		35.1	
20		36.9		34.9		33.4	
30		39.1	$37.6\%/\sqrt{E}$	35.3	$36.0\%/\sqrt{E}$	34.2	$34.5\%/\sqrt{E}$
50		41.4	$\oplus 1.8\%$	36.8	$\oplus 1.0\%$	35.3	$\oplus 1.0\%$
75		41.0		38.1		36.3	
100		40.0		38.9		37.3	

Table 4.16 Energy resolution of hadrons for different TEST 60 configurations.

p [GeV/c]	T60A	T60B1	T60B2	T60B3
3	1.13±0.05			
5	1.12±0.05			
7	1.12±0.05			
8.75	1.10±0.05			
10		1.00±0.05	1.01±0.05	0.95±0.05
20		0.99±0.05	1.00±0.05	0.95±0.05
30		1.00±0.05	1.01±0.05	0.96±0.05
50		1.01±0.05	1.02±0.05	0.96±0.05

Table 4.17 e/h–ratios for different TEST 60 configurations.

The hadron energy resolution can be parametrized by

$$\sigma/E = \frac{36.0\%}{\sqrt{E}} \oplus 1.0\% \quad for \ T60B2.$$

The best energy resolution of $34.5\%/\sqrt{E} \oplus 1.0\%$ was achieved for T60B3, where the DU plates were in addition clad with 0.2mm thick stainless steel foils and module 8 with 3mm thick DU plates was moved from the last (T60B2) to the first calorimeter module position.

Table 4.17 presents the e/h–ratios for the different calorimeter configurations. The results were corrected for longitudinal nonuniformities and leakage.

For T60A the thickness ratio of DU to scintillator was $d_{DU}/d_{Scint} = 0.64$ and an e/h–ratio of 1.12 was determined, while for T60B2 with $d_{DU}/d_{Scint} = 1.07$ an e/h–ratio of 1.0 was determined in agreement with theoretical predictions described in chapter 3 [ZEU86]. The decrease of the e/h–ratio by about 5% for T60B3 is due to the cladding as predicted by EGS shower simulations [BRÜ86], [WIG87a]. The e/mip–ratio is reduced because of the low energy electrons produced by photoeffect and Compton scattering ($\sim Z^{3-5}$), which normally leak from the absorber plates into the scintillator. But in T60B3 these electrons are partially absorbed in the cladding.

The position resolution in x and y was measured with T60B3 for 30GeV electrons and hadrons and is presented in Fig. 4.73. The vertical position (y) is obtained from the charge sharing between the scintillator strips and the horizontal position (x) from the right and left photomultiplier signals. The spatial resolution for 30GeV electrons is σ_x=12.4mm and σ_y=2.7mm and for 30GeV hadrons σ_x=22.7mm and σ_y=13.0mm. The position resolution as a function of the energy can be parametrized as $\sigma = a/\sqrt{E} \oplus b$ with a_x=82, b_x=0.6 and a_y=12.9, b_y=1.3 for electrons and a_x=123.2, b_x=10.9 and a_y=74.2, b_y=0 for hadrons.

Various other test measurements were performed with calorimeter TEST 60. For example in BCAL a 17mm thick iron plate is forseen after $1\lambda_{int}$ for mechanical stability. The effect of iron plates with various thicknesses of up to 20mm after about $1\lambda_{int}$ was studied for hadrons at 20, 30 and 50GeV/c. At 50GeV/c the energy resolution degrades by about 2% for a 20mm thick iron plate installed after $1\lambda_{int}$. The effect on the energy resolution of a 20mm iron plate at 20GeV/c and 30GeV/c and a plate up to 15mm at 50GeV/c is below 1% [KRÜ87b].

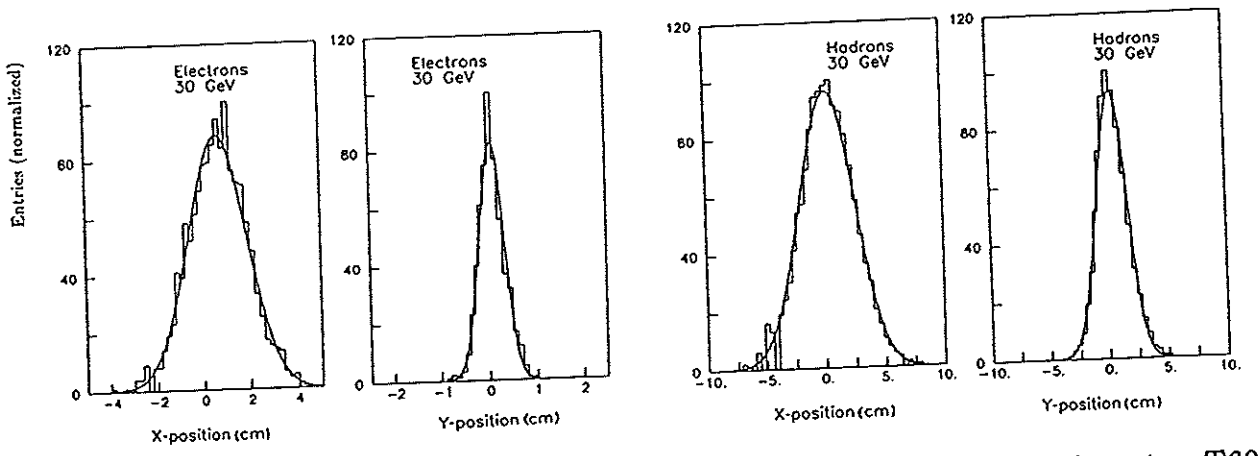

Fig. 4.73 Spatial resolution in x and y for 30GeV/c electrons and hadrons for setup T60B3.

4.5.3 Experimental Determination of Intrinsic and Sampling Fluctuations in Uranium and Lead Scintillator Calorimeters

In order to determine the contributions of intrinsic and sampling fluctuations to the total energy resolution, the readout of the compensating ZEUS uranium and lead scintillator calorimeters, TEST 60 and TEST 36, has been modified and test measurements have been performed [TIE89], [DRE90].

The fractional energy resolution of hadron sampling calorimeters can be described by

$$\frac{\Delta h}{h} = \sigma_{samp} \oplus \sigma_{intr} \ ,$$

the quadratic sum ($\oplus$) of sampling fluctuations σ_{samp} and intrinsic fluctuations σ_{intr}.

The fluctuations of sampling fractions (Δe, $\Delta\pi$, etc...), which produce "sampling fluctuations" can be reduced by increasing the sampling frequency. The fluctuations of shower components (ΔE_{em}, ΔE_{π}, etc...) produce through the different sampling fractions the so–called "intrinsic fluctuations".

Sampling fluctuations are approximately proportional to $\sqrt{t}$, t = thickness of the absorber. The thickness of the active medium is called s and the sampling ratio R = t/s.

Sampling fluctuations have been parametrized [FAB85] by

$$\sigma_{samp} = \frac{a'}{\sqrt{E}} \text{ (E in GeV)} \quad \text{with} \quad a' = 9\%\sqrt{\Delta\epsilon[MeV]}$$

and $\Delta\epsilon = \text{t}(\frac{dE}{dx})_t + \text{s}(\frac{dE}{dx})_s$ the energy loss per unit sampling cell for minimum ionizing particles in MeV.

Intrinsic fluctuations are a function of R and depend on the sampling fractions, possibly also on the sampling ratio R. They can be described [WIG87] by

$$\sigma_{intr} = \frac{b'}{\sqrt{E}} + \text{c} \ ,$$

where c depends on the e/h–ratio and vanishes if compensation is achieved. For compensating calorimeters, both σ_{samp} and σ_{intr} scale with $1/\sqrt{E}$.

In order to determine the sampling fluctuations the technique of the "two interleaved calorimeters" was applied [FAB77]. Figure 4.74 shows the two interleaved calorimeters. For calorimeter a the readout layers with odd–numbers and for calorimeter b the readout layers with even–numbers are summed up.

The relative fluctuations are defined as

$$\sigma_a = \frac{\Delta E_a}{< E_a >}, \qquad \sigma_b = \frac{\Delta E_b}{< E_b >}, \qquad \sigma_{sum} = \frac{\Delta E_{sum}}{< E_{sum} >}, \qquad \sigma_{dif} = \frac{\Delta E_{dif}}{< E_{sum} >},$$

with the average energy sums $< E_a >$ and $< E_b >$ of the two calorimeters a and b, and $< E_{sum} > = < E_a + E_b >$, $< E_{dif} > = < E_a - E_b >$ their sum and difference, and ΔE_a, ΔE_b, ΔE_{sum} and ΔE_{dif} the corresponding fluctuations.

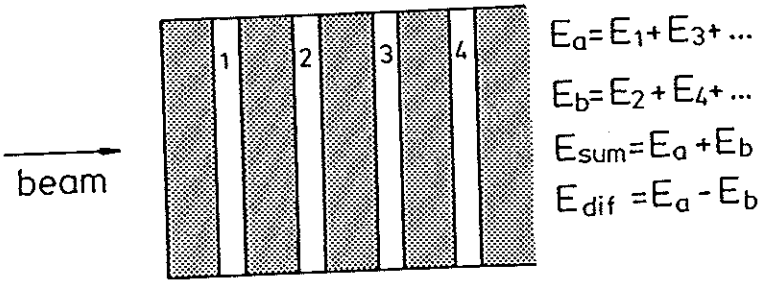

Fig. 4.74 The two interleaved calorimeters with the definitions of E_a, E_b (partial energy sums), E_{sum} (total energy) and E_{dif} (energy difference).

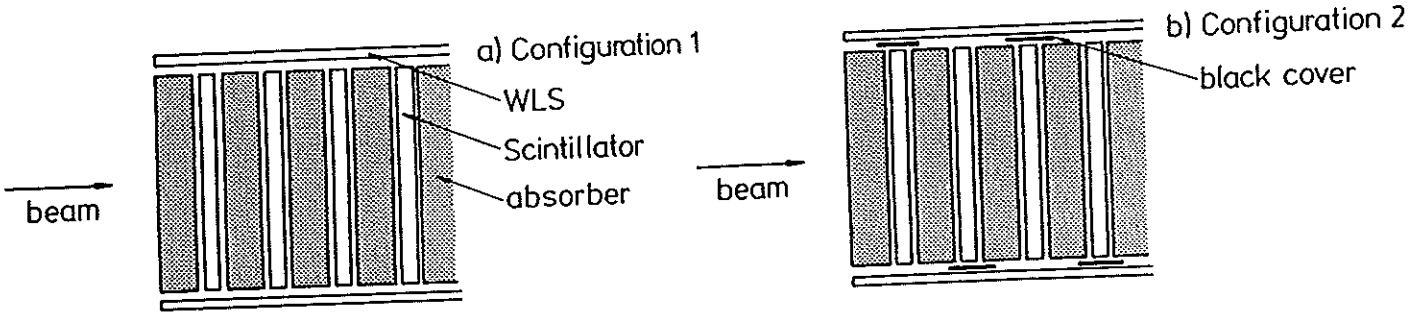

Fig. 4.75 Calorimeter setups used in the test: (a) all plates are read out on both sides (configuration 1); (b) each plate is read out only on one side (configuration 2).

For electromagnetic showers only sampling fluctuations are present. With the absorber thickness 2t of the interleaved calorimeters

$$\sigma_{sum} = \sigma_{samp} \qquad \text{and} \qquad \sigma_a = \sigma_b = \sqrt{2} \cdot \sigma_{samp} \ ,$$

with σ_{samp} for the complete calorimeter consisting of calorimeter a and b.

Since the sampling fluctuations for the calorimeters a and b are independent:

$$\sigma_{dif} = \sigma_{sum} \ .$$

For hadron showers intrinsic fluctuations are the same for calorimeters a and b and also for the complete calorimeter. From this it follows, that intrinsic fluctuations contribute in the same way to σ_a, σ_b and σ_{sum}, but cancel in σ_{dif}.

The sampling fluctuations are independent in the calorimeters a and b, as for electromagnetic showers. Therefore for hadronic calorimeters the following relations are valid:

$$\sigma_{sum} = \sigma_{intr} \oplus \sigma_{samp}, \qquad \sigma_a = \sigma_b = \sigma_{intr} \oplus \sqrt{2} \cdot \sigma_{samp}, \qquad \sigma_{dif} = \sigma_{samp} \ .$$

Two different readout configurations (Fig. 4.75) have been prepared for the compensating lead scintillator calorimeter TEST 36 (10mm Pb, 2.5mm Scint.) and the compensating uranium scintillator calorimeter TEST 60 (3.2mm DU, 3mm Scint. (T60B)).

Both calorimeters were tested with electrons and hadrons at momenta of 10, 20, 30 and 50GeV/c for configuration 1 (standard readout) and 2 (interleaved calorimeters). The measurement results averaged for 10 to 50GeV/c are summarized in Table 4.18.

Cal.	Conf.	Hadrons			Electrons			e/h
		$\sigma_{sum}\sqrt{E}$ [%]	$\sigma_{dif}\sqrt{E}$ [%]	$\sigma_{side}\sqrt{E}$ [%]	$\sigma_{sum}\sqrt{E}$ [%]	$\sigma_{dif}\sqrt{E}$ [%]	$\sigma_{side}\sqrt{E}$ [%]	
Pb/ Scint.	Conf. 1	43.5	10.3	44.8	24.4	8.6	25.8	1.11±0.01
	Conf. 2	43.5	42.3	60.5	24.5	25.8	36.0	1.11±0.01
DU/ Scint.	Conf. 1	35.8	11.7	37.7	17.1	8.2	18.9	1.01±0.01
	Conf. 2	37.3	32.6	49.5	18.5	19.2	26.8	1.00±0.01

Table 4.18 Results from the lead and uranium calorimeters for configuration 1 and 2. The estimated total errors are about ±1.0% for the individual fluctuations.

The readout was available on left and right sides and the quantity $\sigma_{side} = \frac{1}{2}(\sigma_R + \sigma_L)$ was defined, where σ_R and σ_L are the fractional energy fluctuations measured by summing the left and right readout. For configuration 2 these left and right readout calorimeters are the two interleaved calorimeters.

The measurements have shown that all fluctuations scale with $1/\sqrt{E}$. A first estimation of intrinsic and sampling fluctuations yields:

$\sigma_{samp} = \sigma_{side} \ominus \sigma_{sum} = 42.0\%/\sqrt{E}$ for the lead and $32.5\%/\sqrt{E}$ for the uranium calorimeter,
$\sigma_{intr} = \sigma_{sum} \ominus \sigma_{samp} = 11.3\%/\sqrt{E}$ for the lead and $18.3\%/\sqrt{E}$ for the uranium calorimeter.

In addition instrumental effects such as photoelectron statistics σ_{pe}, finite beam size σ_{beam} and light attenuation in the scintillator σ_λ contribute to the fluctuations of the total energy resolution. These fluctuations have been investigated [DRE90] and are given in Table 4.19.

Cal.	Conf.	$\sigma_{pe}\sqrt{E}$ [%]	$\sigma_{beam}\sqrt{E}$ [%]	$\sigma_\lambda\sqrt{E}$ [%]
Pb/ Scint.	Conf. 1	6.5	5.6	6.0
	Conf. 2	7.0	5.6	6.6
DU/ Scint.	Conf. 1	7.5	5.6	7.0
	Conf. 2	10.5	5.6	7.4

Table 4.19 Instrumental effects on the lead and uranium calorimeters for configuration 1 and 2.

Taking into account the instrumental effects, the following three equations with two unknowns, σ_{intr} and σ_{samp}, are valid for configuration 2:

$$\begin{aligned} \sigma_{sum} &= \sigma_{intr} \oplus \sigma_{samp} \oplus \sigma_{pe}, \\ \sigma_{side} &= \sigma_{intr} \oplus \sqrt{2}\cdot\sigma_{samp} \oplus \sqrt{2}\cdot\sigma_{pe} \oplus \sigma_{beam} \oplus \sigma_\lambda, \\ \sigma_{dif} &= \sigma_{samp} \oplus \sigma_{pe} \oplus \sigma_{beam} \oplus \sigma_\lambda, \end{aligned}$$

and in addition $\sigma_{sum} \oplus \sigma_{dif} = \sigma_{side}$.

The experimental results, including instrumental effects, of the contributions of intrinsic and sampling fluctuations to the total energy resolution of electrons and hadrons for the two compensating uranium and lead scintillator calorimeters are summarized in Table 4.20.

Cal.	Particles	$\sigma_{intr}\sqrt{E}$ [%]	$\sigma_{samp}\sqrt{E}$ [%]	$\sigma_{samp}\sqrt{E}/\sqrt{\Delta\epsilon}$ [%]
Pb/ Scint.	Hadrons	13.4±4.7	41.2±0.9	11.3±0.3
	Electrons	0.3±5.1	23.5±0.5	6.4±0.2
DU/ Scint.	Hadrons	20.4±2.4	31.1±0.9	11.6±0.4
	Electrons	2.2±4.8	16.5±0.5	6.1±0.2

Table 4.20 Intrinsic and sampling fluctuations of the compensating lead and uranium calorimeters with $\Delta\epsilon^{Pb} = 13.3\text{MeV}$ and $\Delta\epsilon^{DU} = 7.2\text{MeV}$.

The instrumental effects have no significant effect on the final results. The measured sampling fluctuations dominate the hadronic energy resolution of both calorimeters and are

$$\sigma_{samp} \approx 11.5\%\sqrt{\Delta\epsilon[MeV]}/\sqrt{E[GeV]}\ ,$$

slightly larger compared to a value of $a' \approx 9\%\sqrt{\Delta\epsilon[MeV]}$ mentioned already before [FAB85]. They are by a factor 2 larger for hadrons than for electrons.

The intrinsic fluctuations are smaller for lead ($\sigma^{Pb}_{intr} \approx 13.4\%/\sqrt{E}$) than for uranium ($\sigma^{DU}_{intr} \approx 20.4\%/\sqrt{E}$). One possible explanation is, that the neutrons from nuclear reactions, which are necessary to achieve compensation in the scintillator, are more strongly correlated with the lost nuclear binding energy in lead than in uranium, for which fission may deliver in addition an uncorrelated contribution (fluctuations). One has also to keep in mind, that intrinsic fluctuations depend possibly also on the sampling ratio R, which is much larger for the lead scintillator calorimeter ($R^{Pb} \approx 4$) than for the uranium scintillator calorimeter ($R^{DU} \approx 1$).

Apart from the unique possibility with high resolution compensating uranium scintillator calorimeters of calibrating the calorimeter using the radioactivity of the uranium with high accuracy to better than about 1%, as achieved for the ZEUS calorimeter (chapter 6), compensating lead scintillator calorimeters (as demonstrated by TEST 36) offer also an excellent energy resolution for hadrons, in particular at high energies.

The hadronic energy resolution of compensating lead scintillator calorimeters with a sampling ratio R of about 4 is practically limited by the sampling fluctuations due to the presently achievable mechanical tolerances in the thicknesses of the scintillator (2.5mm) and lead (10mm) plates. For a same sampling ratio of 4 but smaller thicknesses of the sampling layers and improved thickness tolerances, the energy resolution for hadrons is in principle only limited by the small contribution of intrinsic fluctuations for lead scintillator calorimeters. Provided that thinner scintillator plates are feasible and give sufficient light and mechanical tolerances can be controlled lead could give a better energy resolution than DU. But: DU calorimeters are self calibrating while Pb calorimeters are not.

Promising projects in research and development of lead scintillator (fiber) calorimeters are in progress [WIG88], [WIG89], [ACO90], [WIG91].

Chapter 5

Construction and Test of the ZEUS FCAL Prototype Calorimeter

5.1 Description of the Calorimeter

5.1.1 Introduction

Several test calorimeters have been constructed and many beam studies have been performed in order to optimize the parameters of the ZEUS calorimeter (chapter 4). The FCAL prototype calorimeter was then built to verify and optimize the final parameters [BEH89], [AND89], [KRÜ89c], [KRÜ90b]. The prototype modules follow the same design as the final ZEUS forward calorimeter modules (chapter 2.3.3).

Figure 5.1 shows a three dimensional view of the FCAL prototype with its module, tower and longitudinal structure. It consists of four modules with a front area of 80cm x 80cm (4 x (20cm x 80cm)), a depth of 1.55m (7λ) and 192 PMs (EMC: 128 Valvo XP2972, HAC: 64 Valvo XP2081). The sampling structure is 3.3mm depleted uranium plates interleaved with 2.6mm scintillator plates. The scintillator plates were wrapped in white Tyvek paper which had a black printed pattern to obtain a uniform response independent of position. The main parameters are summarized in Table 5.1.

The thicknesses and mechanical tolerances achieved for the various components are: 3.3±0.15mm for the uranium plates, 0.2±0.01mm (EMC) and 0.4±0.02mm (HAC) for the steel cladding, 2.6±0.30mm for the scintillator plates, 2.0±0.2.mm for the WLS plates and typical tolerances of 0.5mm for the stacking.

The four prototype modules were assembled at York University (Canada) (Fig. 2.45).

5.1.2 The Experimental Set Up

An extensive test programme has been carried out at CERN. The experimental set up used at the PS (East Hall, T7 beam line) is described in Fig. 5.2. It consisted of the scintillation beam counters B1, B2, B3 and B4 defining the beam, two Cherenkov counters C1 and C2 and the FCAL prototype calorimeter itself.

The beam position at the entrance of the calorimeter could be located with a precision of 2mm in horizontal and 1mm in vertical direction.

The particle identification of pions, protons and electrons was performed by the Cherenkov counters and for low momenta by a time of flight measurement between B1 and B2.

A similar experimental set up was used at the SPS to study the behaviour at high energies.

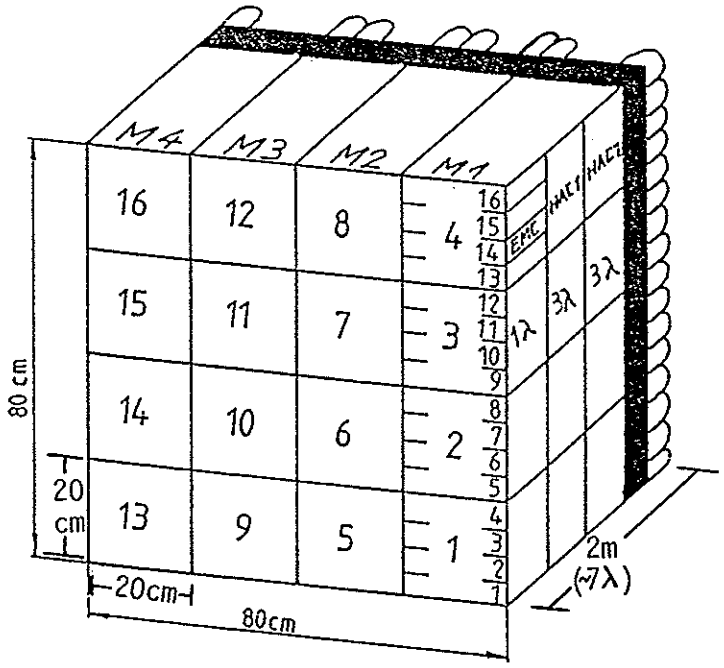

Fig. 5.1 The module, tower and longitudinal structure of the FCAL prototype.

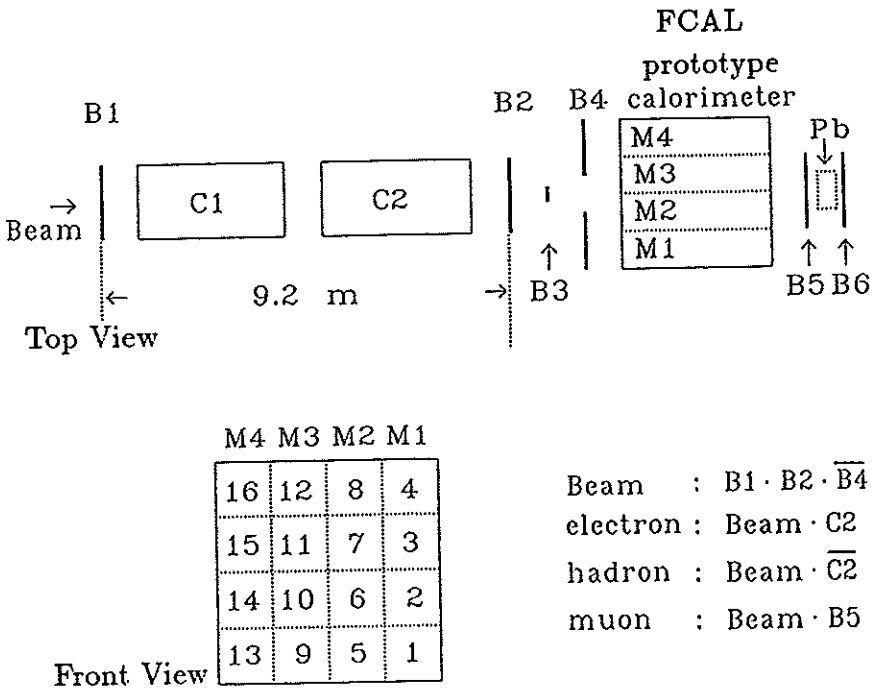

Fig. 5.2 The experimental set up with the FCAL prototype at CERN.

	EMC	HAC
Absorber material Absorber cladding Readout material	Depleted Uranium (DU) stainless steel SCSN–38 Scintillator (SCI)	
Layer structure: Steel DU Steel Paper SCI Paper Contingency	 0.2 mm 3.3 mm 0.2 mm 0.2 mm 2.6 mm 0.2 mm 0.9 mm	 0.4 mm 3.3 mm 0.4 mm 0.2 mm 2.6 mm 0.2 mm 0.9 mm
Effective X_0 Effective λ Effective R_M Effective density	7.4 mm 210 mm 20.2 mm 8.7 g/cm^3	7.6 mm 207 mm 20.0 mm 8.7 g/cm^3
Transverse segmentation	5cm × 20cm	20cm × 20cm
Longitudinal segmentation	$25.9X_0$ (0.96λ)	HAC1 (3.09λ) HAC2 (3.09λ)
Number of layers Total length Total cross–section	(1Al–SCI) 25DU–SCI 24.1 cm 80cm × 80cm	2 × 80DU–SCI 128.0 cm 80cm × 80cm
Optical readout	2mm thick WLS plates + light guides	
WLS material	PMMA + Y7(45ppm)	PMMA + Y7(30ppm)
Photomultipliers	XP2972 (Valvo)	XP2081 (Valvo)
Readout channels	128	64

Table 5.1 Main parameters of the FCAL prototype calorimeter.

Figure 5.3 presents a picture of the first FCAL prototype module, which has been stacked and assembled at York (Canada) and has just arrived at CERN.

A picture of the experimental area with the complete FCAL prototype test stand at the CERN SPS (West Hall, X5 beam line) is shown in Fig. 5.4. From the left the particle beam containing hadrons, electrons and muons is entering the experimental area through a vacuum beam pipe.

First the beam particles pass the scintillation beam counters installed on a movable table. Then they enter the FCAL prototype calorimeter which is placed in an iron frame and is completely covered with black plastic foil for light tightness. The iron frame is movable in the horizontal and vertical direction and can be rotated in the horizontal plane in order to vary the angle of beam incidence. The complete entrance face of the prototype can be scanned with beam particles under various angles of particle incidence.

The FCAL prototype test stand seen on the picture has been rotated by an angle of about 20°, and the backing calorimeter (BCAL) prototype positioned just behind the FCAL prototype is visible at the right side of the picture.

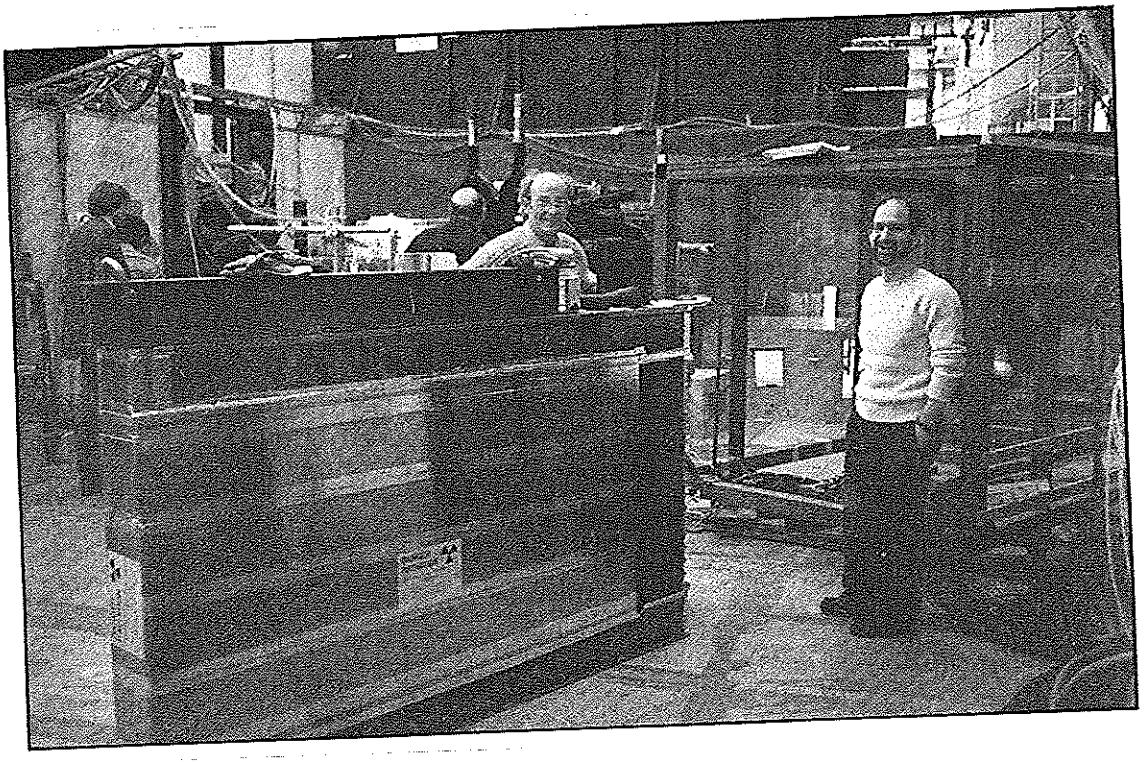

Fig. 5.3 The first FCAL prototype module arrived at CERN.

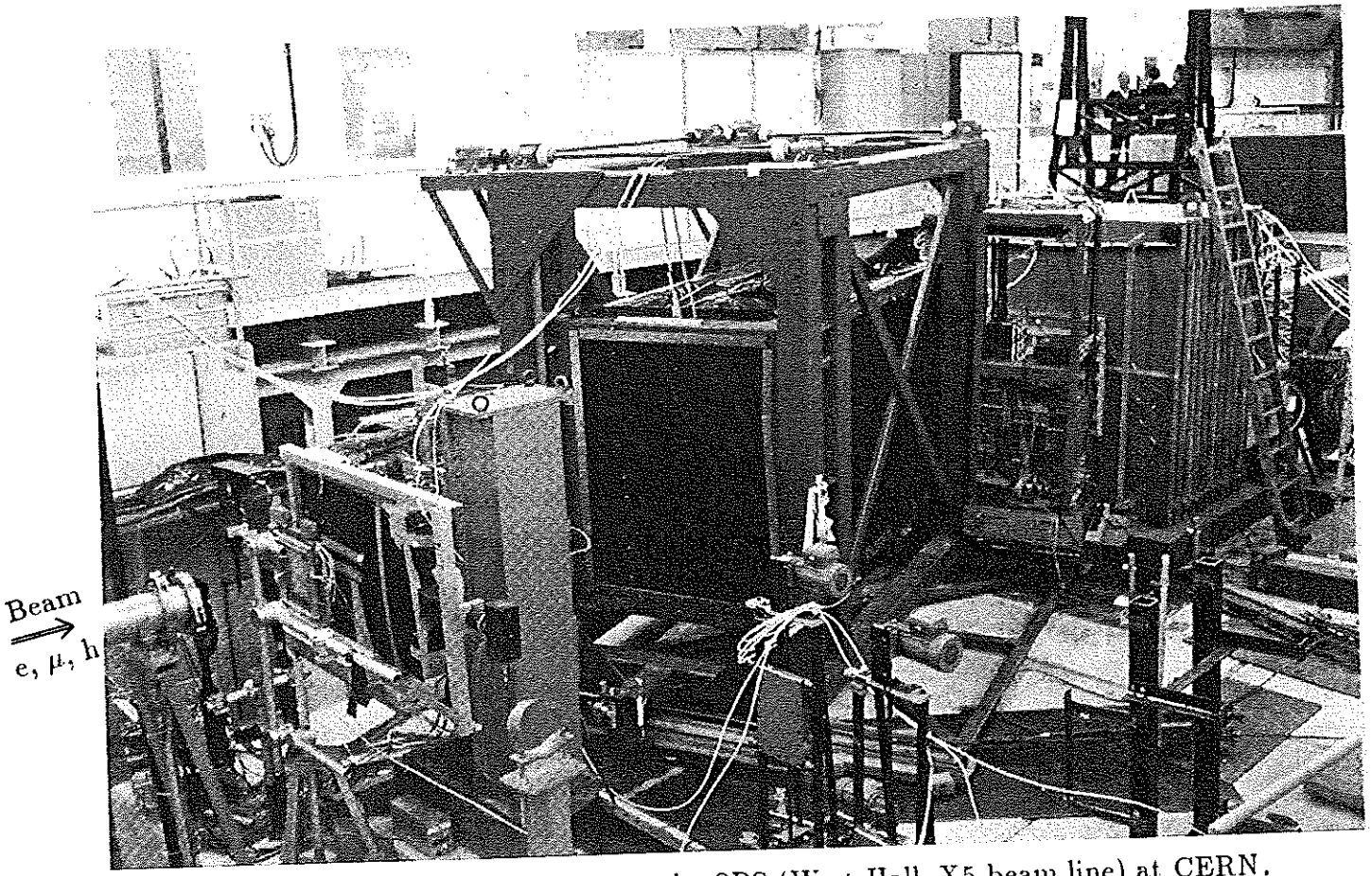

Fig. 5.4 The FCAL prototype at the SPS (West Hall, X5 beam line) at CERN.

5.1.3 Calibration of the FCAL Prototype

Different methods of calibrating the ZEUS calorimeter were tested at CERN. The techniques use: the radioactivity of the uranium, pointlike radioactive gamma sources, LEDs and laser light pulses.

An important advantage of uranium calorimeters is the possibility of using the signal from the radioactivity of the uranium for the calibration [AKE85], [AND86], [AKE87], [AGO89], [BEH89]. This calibration method is in particular discussed in this section, the other ones are explained in more detail in chapter 6.

It became very clear during the prototype tests, that the calibration of the ZEUS calorimeter modules by means of the radioactivity of the uranium represents a particularly simple and efficient method which can be carried out during data–taking.

At the PS the HV of the photomultipliers was tuned in such a way, that the signal from 5GeV/c electrons corresponded to 125pC ($\hat{=}$ 500 ADC channels). The current induced by the radioactivity of the uranium was then 0.6μA for the EMC tubes [BEH89]. The signal from the uranium radioactivity (UNO) was used to study and correct the photomultiplier gain variations as a function of time. Figure 5.5 shows the UNO signal for a well–behaved tube as a function of time. A measurement was performed every 2 hours during a period of 30 days. The short term variation of this channel (tube 1), defined as the difference of the UNO signals between 2 consecutive runs (δ), is on average $< \delta > = 0.2\%$; the long term variation, defined as the maximum UNO variation during the total measurement period (Δ), is $\Delta = 3\%$. The variations differ from channel to channel; short term variations are typically below 1%, long term variations are about 10%.

Short term variations depend on the frequency of the measurements. The experimental results show, that measurements done every 8 hours are sufficient to monitor the UNO signal with an accuracy of 1% (0.7% for EMC and 0.2% for HAC tubes) [BEH89].

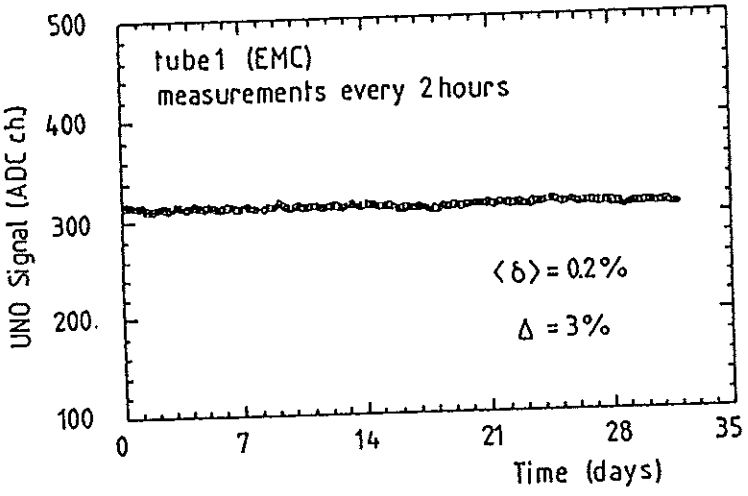

Fig. 5.5 The UNO signal variations for a well behaved channel as a function of time. Measurements were taken every 2 hours during a period of 30 days.

In order to study the ability of the UNO signal to detect real PM gain variations the whole calorimeter was scanned 5 times with 5GeV/c electrons and muons. The average spread of the e/UNO ratios for the EMC tubes is 1.1% and of the μ/UNO ratios for the HAC tubes about 0.5%, including small effects like e.g. statistical errors and shifts due to the calorimeter positioning. The PM gain variations can be traced by the UNO signal with an accuracy of better than 1%.

The intercalibration between the same calorimeter sections (EMC, HAC1, HAC2) with the UNO signal was studied in comparison with beam particles.

For the FCAL prototype an intercalibration between the PM gains of the same type of sections with the UNO signal was possible with an accuracy of 2% to 3%, with beam particles within 1%.

An intercalibration between EMC and HAC sections is possible with beam particles by tuning the intercalibration parameter α in the formula: $E = E_{EMC} + \alpha \cdot E_{HAC}$, where E_{EMC} and E_{HAC} are the energies deposited in EMC and HAC. The α parameter can be determined by various methods, which are expected to be equivalent for a compensating calorimeter [BEH89], [KÖL89], for example by requiring

1) optimum hadron energy resolution,
2) equal response for electrons and hadrons,
3) the muon response to be proportional to the number of scintillator layers.

Figure 5.6 shows the fractional energy resolution (σ/E) as a function of the intercalibration parameter α for 10GeV/c and 100GeV/c hadrons (method 1). The minimum of σ/E is more pronounced at higher momenta and is slightly shifted to lower values of α with decreasing momenta. This shift to lower α values is in particular seen in Fig. 5.7, where α(p)/α(30GeV/c) is plotted as a function of the beam momentum. It can be understood as a result of the change in shower development for hadrons below 2GeV which is presented in chapter 5.2.2 (Fig. 5.19). There is no significant increase of α observed above 30GeV/c. The value of α (=1) at p = 30GeV/c was then used for the final calibration. This α value is also in reasonable agreement with the requirement of an optimum e/h–ratio (method 2) (Fig. 5.8).

The final UNO ratio between HAC and EMC sections obtained from the intercalibration with beam particles was then 5.40 in comparison to an estimated value of about 5.

For 5GeV/c muons a signal ratio of the HAC to EMC sections of 3.14 was measured. This is compatible with the ratio of the number of scintillator layers of 80(HAC)/26(EMC) = 3.08. However corrections taking into account the multiple scattering of muons and the different cladding in EMC and HAC are needed.

A typical calibration cycle used for the FCAL prototype tests had then the following form:

1) electron calibration for each EMC tower at the beginning of the test,
2) charge injection measurement every 24 hours to calibrate the readout electronics,
3) uranium radioactivity measurements every 8 hours.

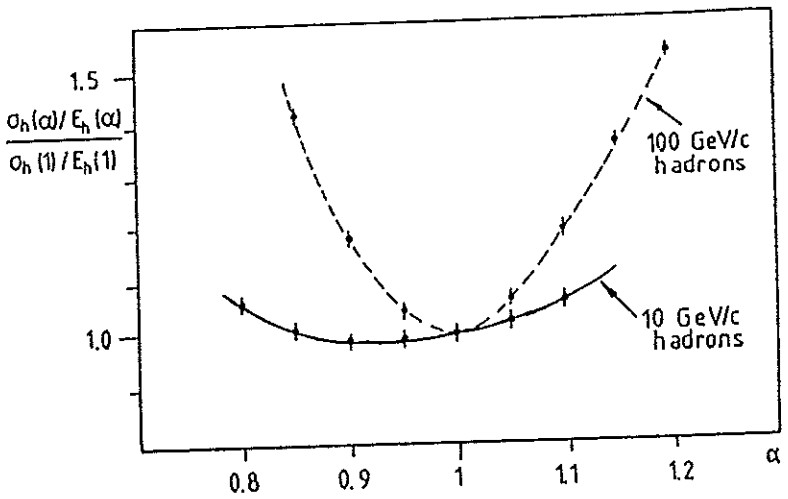

Fig. 5.6 The energy resolution normalized to a value at $\alpha = 1$ as a function of the intercalibration parameter α for 10GeV/c and 100GeV/c hadrons.

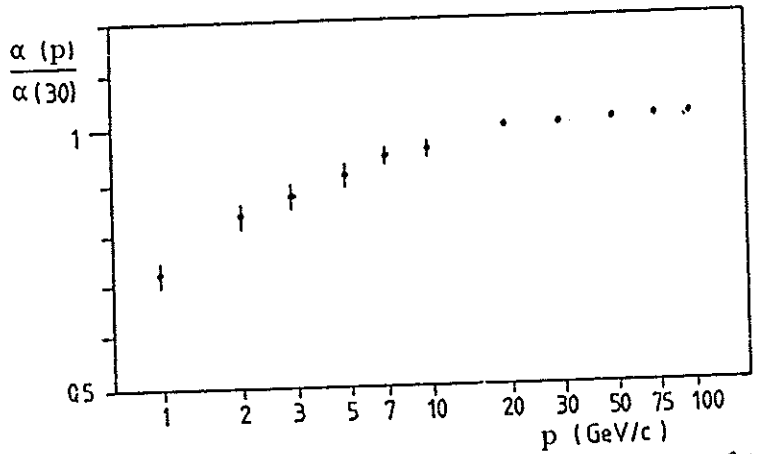

Fig. 5.7 Intercalibration parameter α obtained by minimization of the hadronic energy resolution as a function of the momentum (α normalized to α at 30GeV/c).

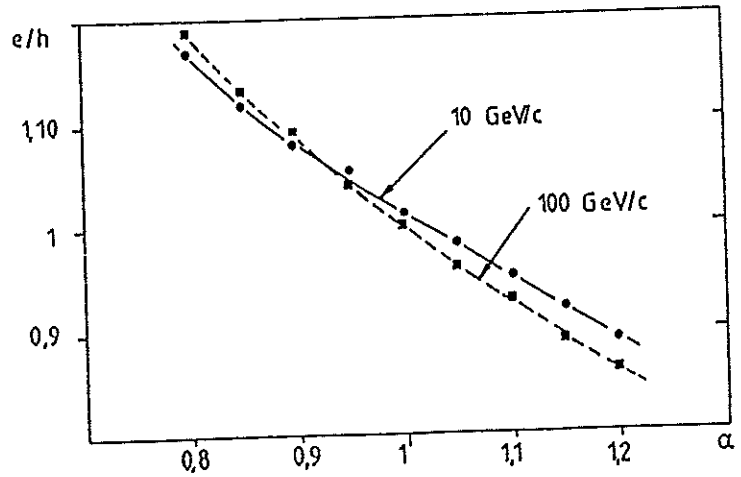

Fig. 5.8 e/h as a fct. of the intercalibration parameter α for 10 and 100GeV/c particles.

5.2 Energy Resolution and e/h–Ratio at High and Low Energies

5.2.1 Response to Hadrons and Electrons with Momenta up to 100GeV/c

The response to hadrons and electrons was studied in the momentum range from 1GeV/c to 10GeV/c at the PS and from 10GeV/c to 100GeV/c at the SPS [BEH89].

Figure 5.9 shows the pulse height distributions for electrons and hadrons measured at the PS, summing up all calorimeter channels. The distributions are normalized to the same number of events. The linearity of the electron response is plotted in Fig. 5.10. Deviations from linearity are at the ±1% level. The most important experimental results on the e/h–ratio and the energy resolution have been presented already in chapter 3.7 (Fig. 3.25, 3.26 and 3.27). The mean values of the distributions for hadrons and electrons are equal within ≈2%. An energy resolution of $35\%/\sqrt{E}$ for hadrons and $18\%/\sqrt{E}$ for electrons was measured.

The Overall Energy Resolution

The overall energy resolution of the FCAL can be described by the following expression:

$$\frac{\sigma_E}{E} = \frac{\sigma_{noise}}{E} \oplus \frac{a}{\sqrt{E}} \oplus \mathrm{b} \qquad \text{(E in GeV)},$$

where the first term describes the contribution from noise of the electronics and the uranium radioactivity (1), the second term the contribution of intrinsic, sampling and photoelectron fluctuations (2) and the third term the contribution of calibration errors and non–uniformities (3).

The value of a is, as already mentioned, about 35% for hadrons and 18% for electrons. The contribution to the parameter a from photoelectron statistics, governing the light yield, could be tested by a LED system installed in each prototype module. The number of photoelectrons (p.e.) for a 1GeV electron equivalent signal (E_0) can be determined by the formula:

$$\mathrm{N} = (\frac{E_{led}}{\sigma_{led}})^2 \cdot (\frac{E_0}{E_{led}}) \ ,$$

where E_{led} and σ_{led} are the average response and r.m.s. fluctuation for a given PM. The number of photoelectrons is on average N = 41.3 p.e./GeV for EMC tubes and N = 101 p.e./GeV for HAC tubes [BEH89], [KRÜ89b]. The difference in light yield between EMC and HAC sections depends strongly on the quality of the wave length shifter pieces. The non–negligible contribution of the photoelectron statistic to the energy resolution of $18\%/\sqrt{E}$ for electrons is $10\%/\sqrt{E}$, the sampling fluctuations alone are about $15\%/\sqrt{E}$. The quality of the wave length shifters, in particular that of the EMC wave length shifters, was significantly improved for the final modules by polishing the edges (chapter 6.6.2).

The noise from the electronics and the uranium radioactivity (1) is plotted in Fig. 5.11. The uranium noise dominates in the measurements at the PS, but not at the SPS due to reduced PM gains.

It is in the order of 25MeV per 20cm x 20cm tower (EMC+HAC1+HAC2) and 100MeV for all channels in the 4 modules. $\sigma_{noise} = 2.5\%\sqrt{N_t}$, where N_t is the number of towers necessary to sum up the total signal, with $N_t \approx 1$ for electrons and $N_t \approx 16$ for hadrons. For all 460 towers of the FCAL the maximum value of σ_{noise} will be 0.5GeV, still relatively small compared to typical energies deposited in the FCAL.

The value of b is in the order of 2%. This is essentially the result of the accuracy (≈1%) and stability (≈1%) of the UNO signal measured every 8 hours and non–uniformities from particles incident at the boundaries between modules (≈1%) and between EMC sections or close to spacers (≈1%).

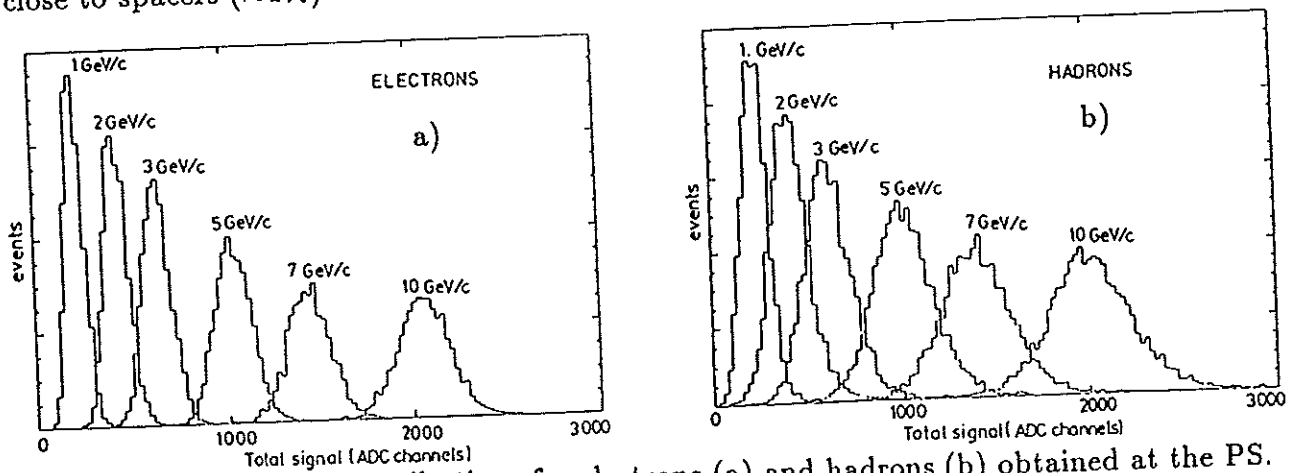

Fig. 5.9 Pulseheight distributions for electrons (a) and hadrons (b) obtained at the PS.

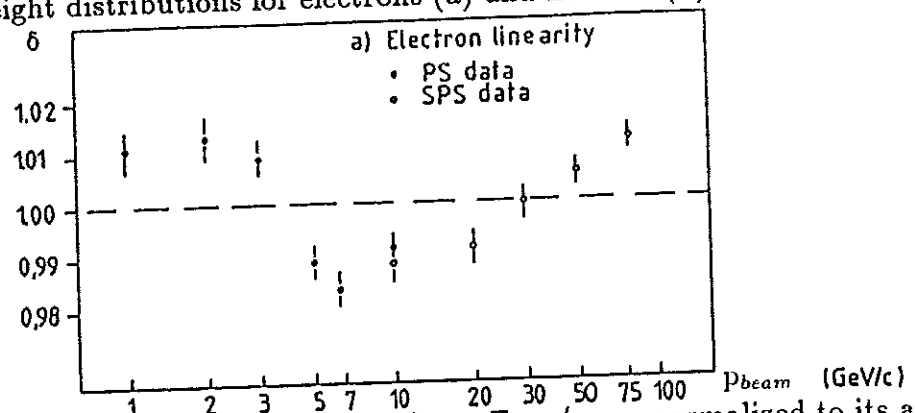

Fig. 5.10 Electron linearity. The parameter $\delta = <E_e>/p_{beam}$ normalized to its average value (PS, SPS independent) is plotted versus the beam momentum.

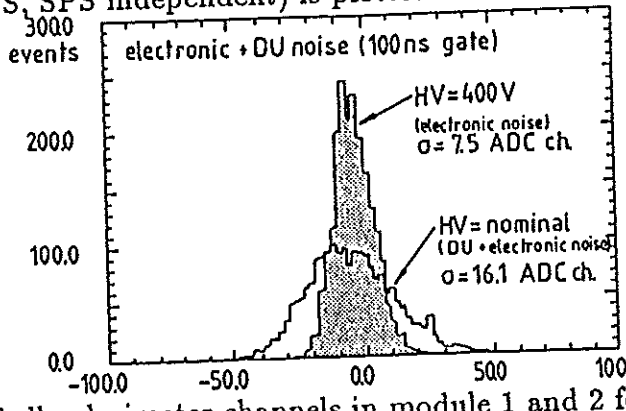

Fig. 5.11 Sum of all calorimeter channels in module 1 and 2 for random trigger events (only calorimeter noise) for the two following cases: HV for PM at nominal value (showing electronic and uranium noise) and reduced to 400 V (showing only electronic noise) at the PS with nominal PM electronic gains.

5.2.2 Response to Pions, Protons and Electrons with Momenta between 0.5 and 10GeV/c

In our test measurements at the PS in April to June 1989 we have studied in detail the response to pions, protons and electrons in the low momentum range from 0.5 GeV/c to 10 GeV/c [AND89], [KRÜ89c], [FÜR90].

Particle Identification

For low momenta the particle identification was achieved by a time of flight (TOF) measurement between the scintillation beam counters B1 and B2 separated by a distance L of 9.2m. The TOF difference between hadrons and pions can be calculated by the formula:

$$\Delta t = \frac{L}{c}\left(\sqrt{1+\frac{m_h^2}{p^2}} - \sqrt{1+\frac{m_\pi^2}{p^2}}\right) ,$$

where m_h, m_π and p are the hadron mass, the pion mass and the beam momentum.

A clean separation between pions of positive charge and protons was possible by a TOF measurement for momenta up to 2GeV/c (Fig. 5.12).

For all momenta up to 10GeV/c pure samples of electrons, pions and protons were separated by combining the information from TOF, Cherenkov counters and the calorimeter itself.

Readout Electronics

Before this test the readout electronics of the FCAL prototype had been changed to a state almost identical to that of the final ZEUS calorimeter electronics (Fig. 5.13) [ZEU85...89], [CAL89], [AND89]. The PM signals were connected to a DC coupled integrator used to measure the current induced by the radioactivity of the uranium (UNO signal) and an AC coupled shaper whose output was sampled 5 times in 96ns steps, corresponding to the time difference between consecutive HERA bunch crossings (Fig. 5.14). In contrast to the final hardware the samples were pipelined by Le Croy MVV200 CCDs and used for charge reconstruction.

Calibration

The calibration was performed in the same way as descibed in chapter 5.1. The intercalibration parameter α with a value of 1 yields the best energy resolution (method 1) and also an e/π–ratio of 1 (method 2) for p = 10GeV/c (Fig. 5.15).

Experimental Results

The electron response is linear within 1%; no difference is seen between e^+ and e^- and the energy resolution for electrons is $18\%/\sqrt{E}$. A significant difference in the response to the different particle types is found at momenta below 2 GeV/c. The pulse height distributions of 0.5 GeV/c pions, protons and electrons are displayed in Fig. 5.16.

Figure 5.17 shows the e/h–ratios at equal momenta for π^+, π^- and p. There is obviously no significant difference between pions of opposite charge but a strong difference between pions and protons which increases towards low momenta.

However, a different picture emerges if the e/h–ratios for π^+, π^- and p are plotted at equal kinetic energies E_K. This presentation shows, that e/h is the same for π^+, π^- and p and depends in first approximation only on the kinetic energy E_K, the energy available for particle production and energy deposit in the calorimeter. At low energies hadrons loose more and more of their energy via dE/dx of a single particle, hence they give the sampling fraction as a minimum ionizing particle (mip). Thus e/h approaches e/mip, which is 0.62 in the present calorimeter. The value of e/mip = 0.62 has been calculated according to EGS4 [NEL85] and was experimentally determined from e/μ.

The energy resolution as a function of the kinetic energy is equal for pions and protons and is about $34\%/\sqrt{E_K}$ above 2 GeV and approaches $22\%/\sqrt{E_K}$ at 0.2 GeV (Fig. 5.19). Below 0.2GeV the total calorimeter noise starts to dominate the energy resolution for hadrons.

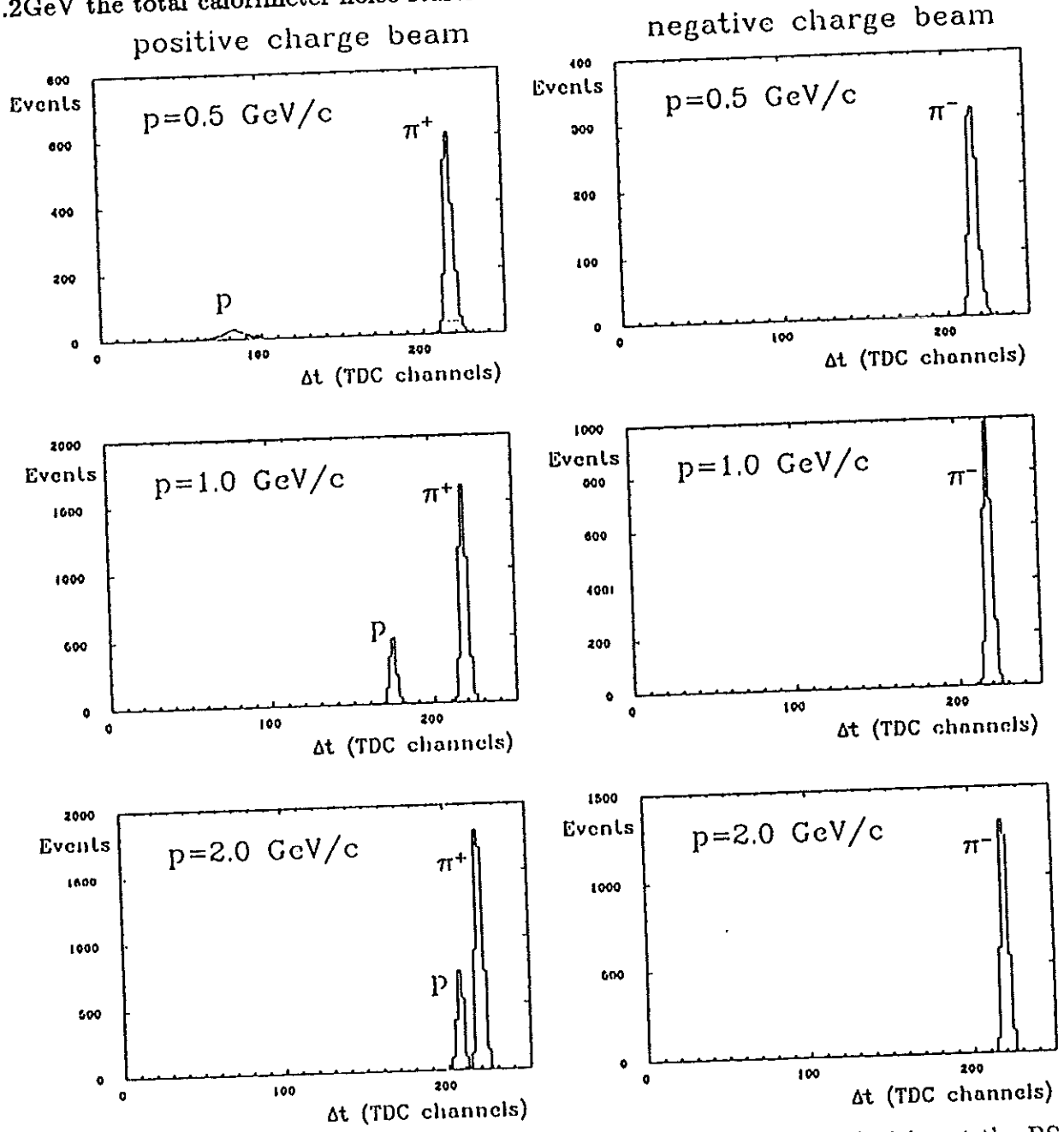

Fig. 5.12 TOF spectra for various beam momenta and both polarities at the PS.

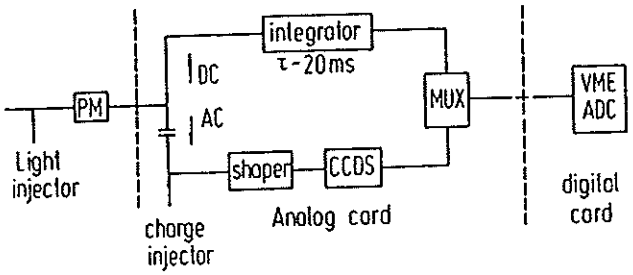

Fig. 5.13 Readout electronics.

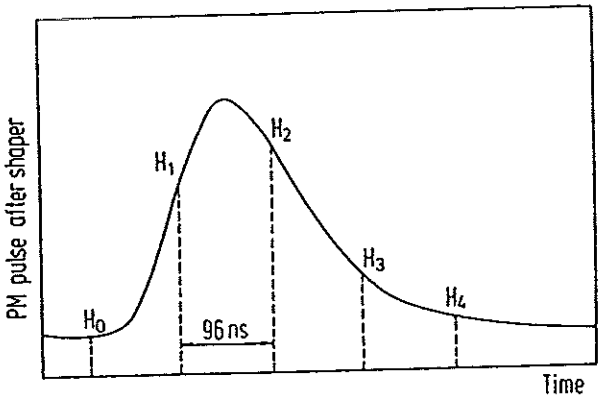

Fig. 5.14 PM pulse after shaper with 5 samples.

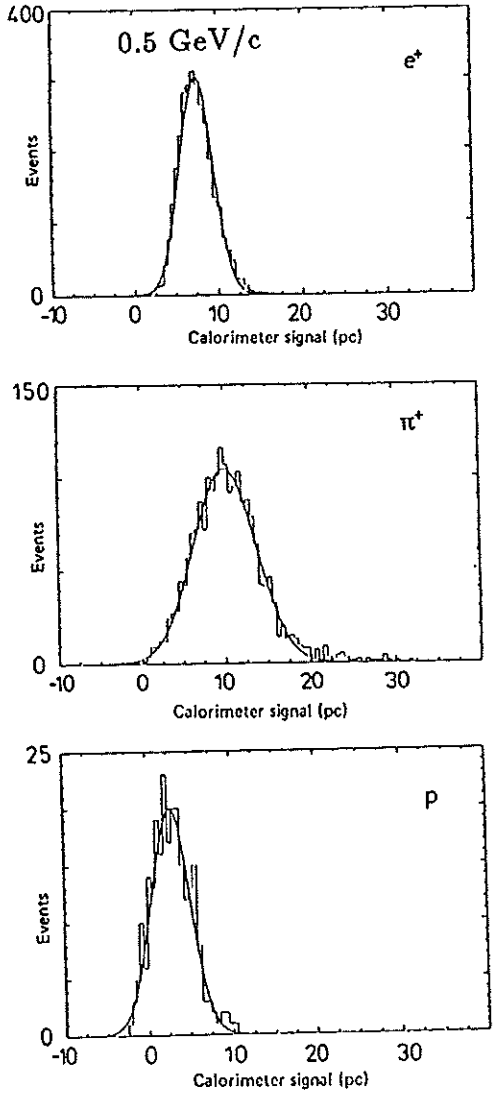

Figure 5.16
Pulseheight distributions for e^+, π^+ and p with a momentum of 0.5 GeV/c. Gaussian fits are overlayed.

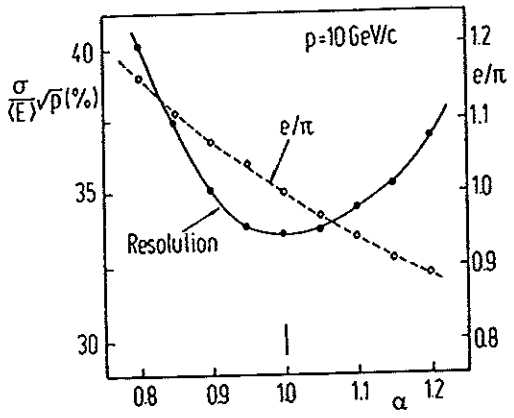

Figure 5.15
Energy resolution and e/h–ratio for 10 GeV/c pions as a function of the inter-calibration parameter α.

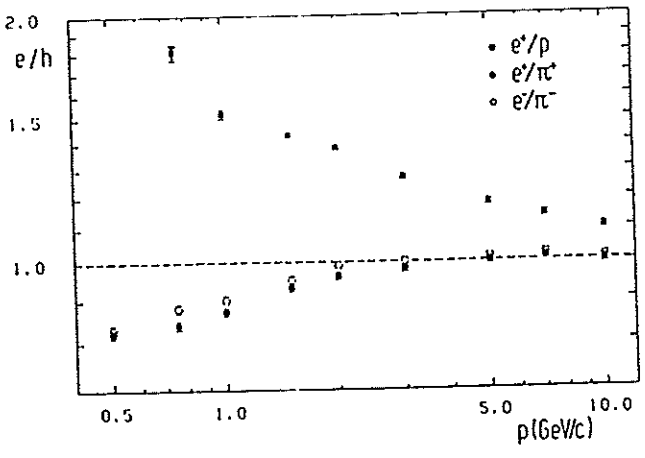

Figure 5.17
e/h–ratio as a function of the momentum for π^+, π^- and p.

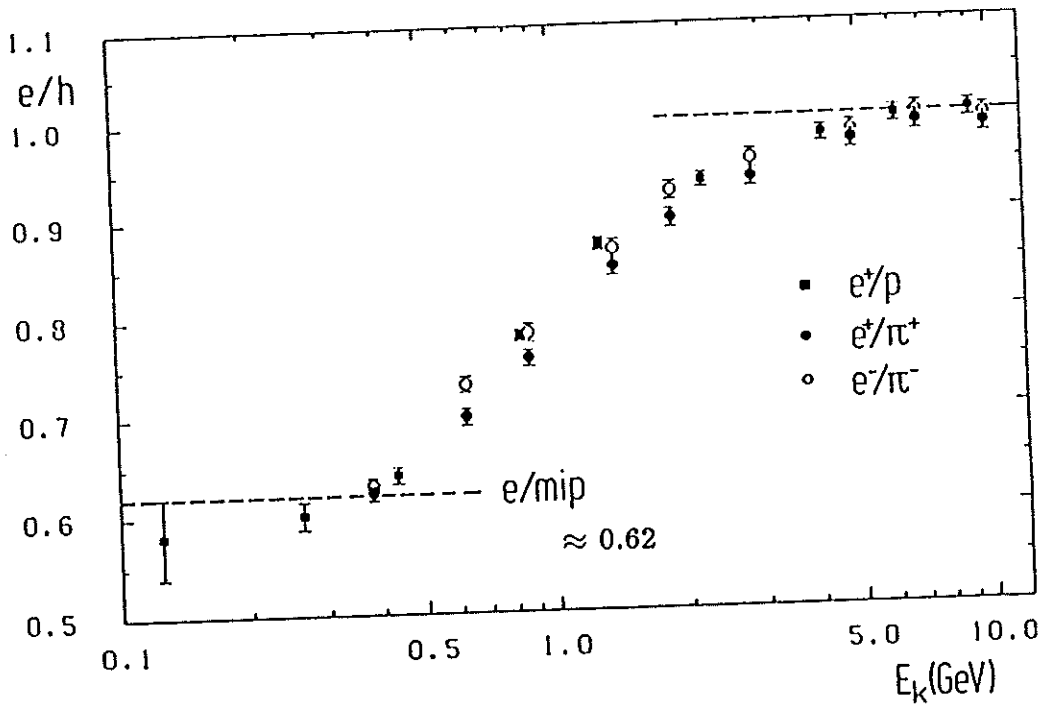

Fig. 5.18 e/h–ratio as a function of the kinetic energy for π^+, π^- and p.

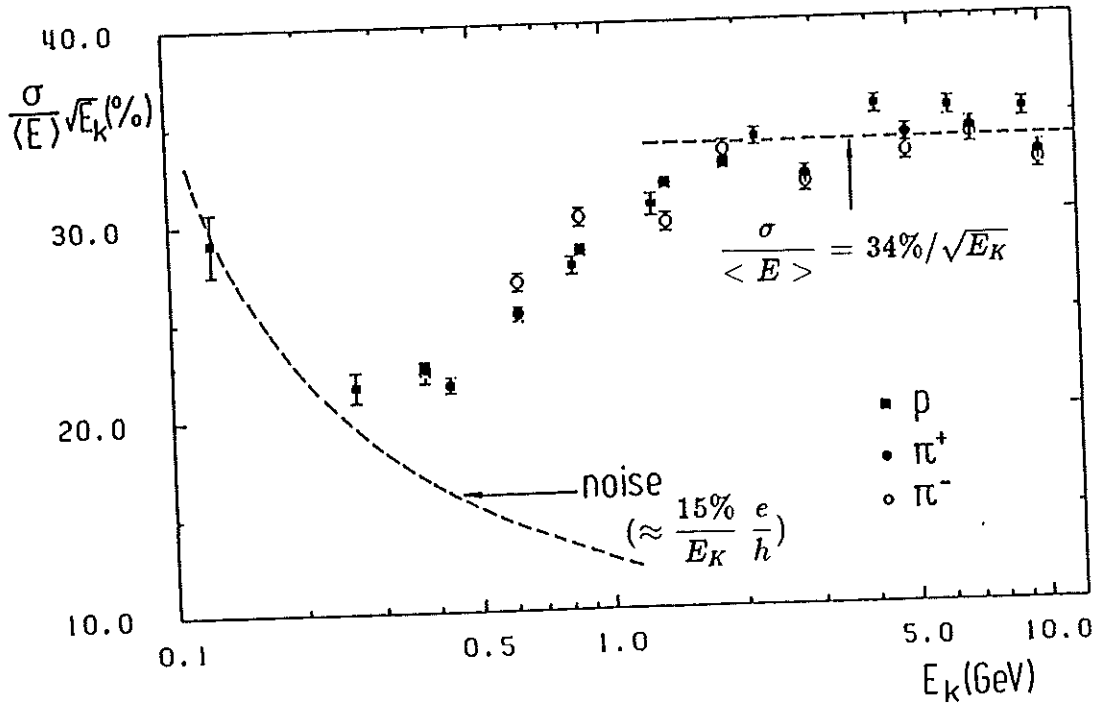

Fig. 5.19 The energy resolution for π^+, π^- and p as a function of the kinetic energy E_K.

5.3 Calorimeter Uniformity

5.3.1 Uniformity at the Boundary between Calorimeter Modules

The ZEUS FCAL calorimeter is nonprojective (chapter 2.3). The minimum angle of a boundary between two calorimeter modules seen by a high momentum particle is 40mrad. Boundaries in the ZEUS FCAL are at θ angles of (40 + (n − 1)·80)mrad where n is the 'crack number'.

Test measurements at the PS and the SPS have shown that the boundary between two modules has only a negligible effect on the response to hadrons even at very small angles of beam incidence. But the response to electrons at small angles is increased significantly in the region of the boundary [BEH89], [KRÜ89c].

Figure 5.20 presents the calorimeter response to 5GeV/c electrons (a) and 5GeV/c hadrons (b) for angles of particle incidence of 0mrad, 40mrad and 80mrad in a horizontal direction over the centre of two EMC sections of modules 2 and 3 in the central region of the FCAL prototype. An increase of the response is found for electrons at the boundary between two calorimeter modules, which is about 40% for the minimum incident angle of 40mrad and decreases with larger θ angles. Hadron showers are much less sensitive to mechanical details inside the calorimeter and only a negligible effect is seen for hadrons. The significant increase of the electron response is the result of part of the electromagnetic shower, passing along the wavelength shifters with a high local density of shower particles and producing a strong contribution of Cherenkov light. The region of the increase of the electron response is confined to a small area of less than 2cm width, to be compared to the tower size of 20cm.

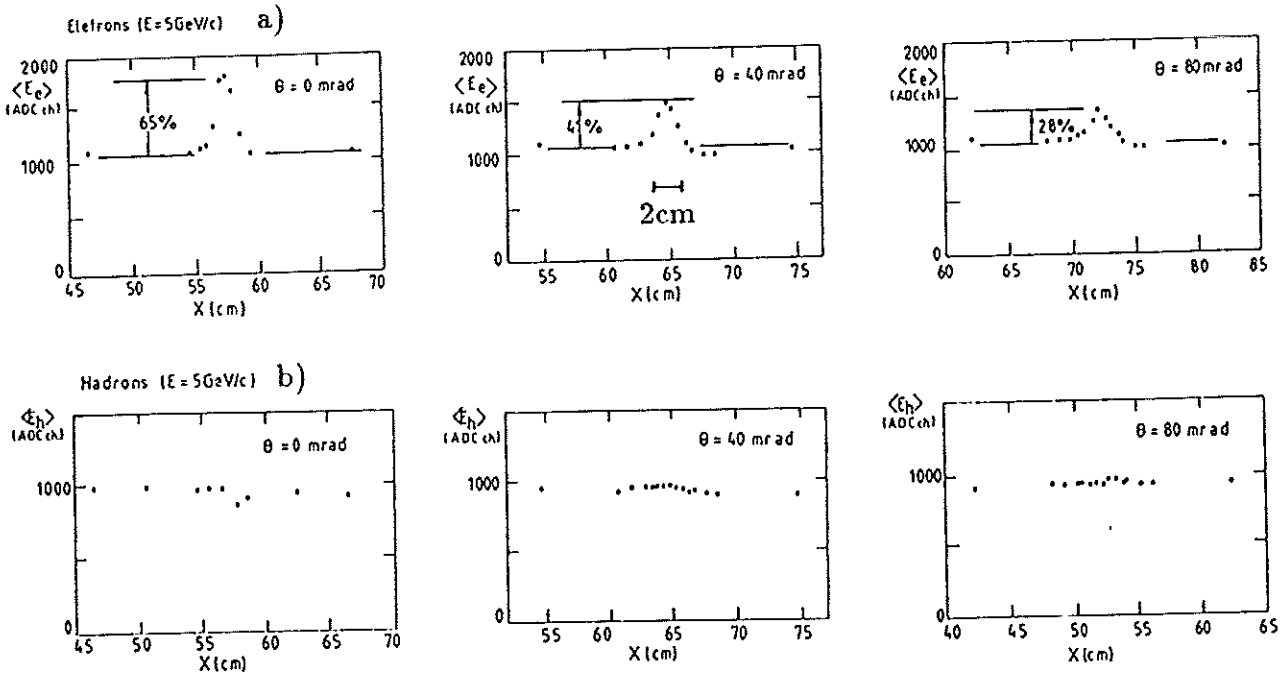

Fig. 5.20 Calorimeter response to 5GeV/c electrons (a) and 5GeV/c hadrons (b) as a function of the beam impact position at the boundary between two calorimeter modules for various angles of incidence (0mrad, 40mrad, 80mrad).

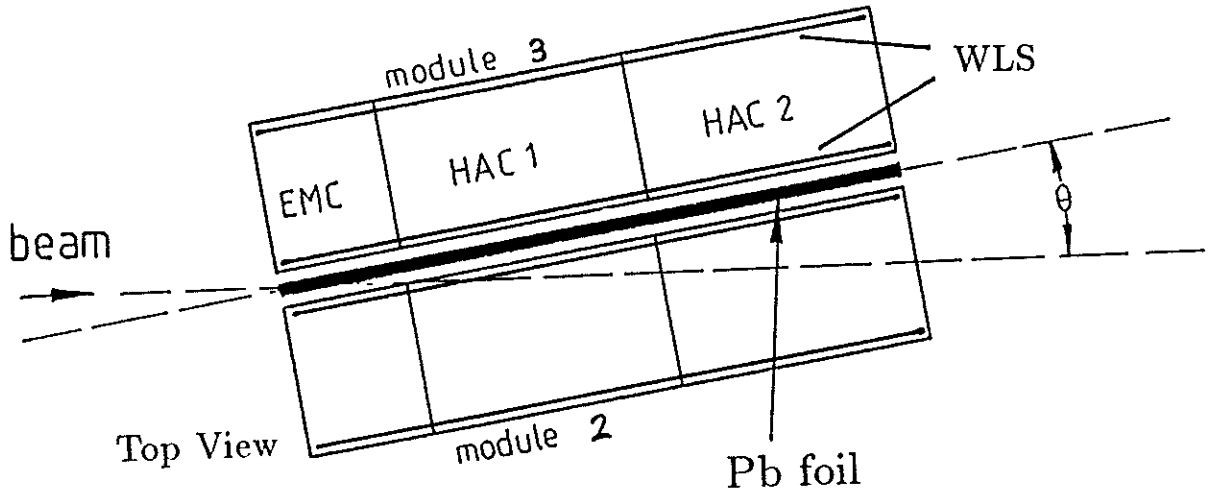

Fig. 5.21 Location of the Pb foil between modules 2 and 3 of the FCAL prototype.

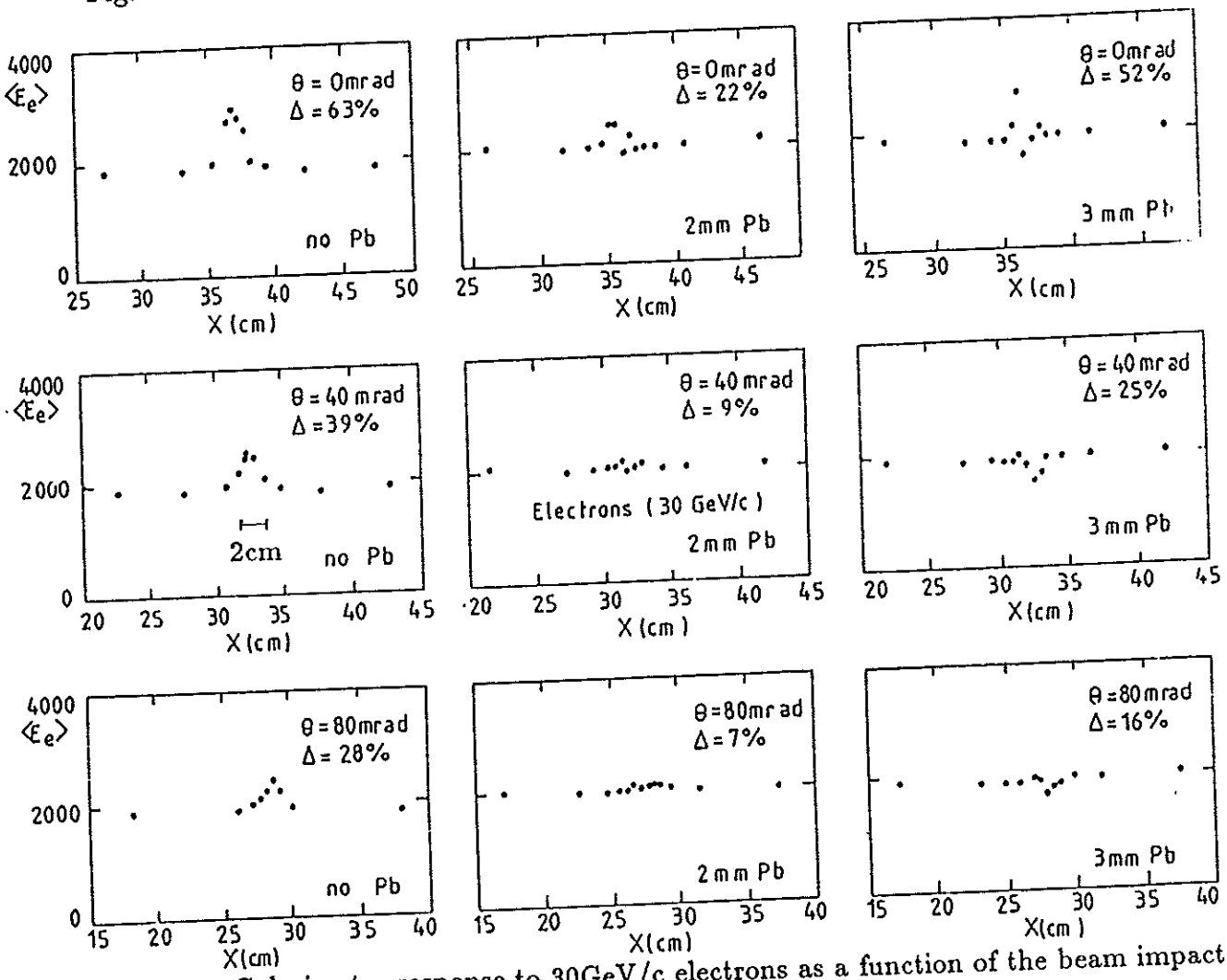

Fig. 5.22 Calorimeter response to 30GeV/c electrons as a function of the beam impact position for various angles of incidence and thicknesses of Pb foils between modules 2 and 3.

A Pb foil inserted between two calorimeter modules can absorb part of the electromagnetic shower and improve considerably the uniformity of the calorimeter. Figure 5.21 shows a schematic drawing of the location (top view) of the Pb foil between two modules.

In order to determine the optimum thickness for the Pb foil systematic scans over the entrance area of the calorimeter have been performed with electrons of 5GeV/c, 30GeV/c and 75GeV/c and in addition with hadrons for various angles of beam incidence and Pb foils with thicknesses of 0, 1, 2, 3 and 4mm between modules 2 and 3.

Figure 5.22 shows various scans with 30GeV/c electrons over the boundary between modules 2 and 3 under angles of 0mrad, 40mrad and 80mrad without and with 2mm and 3mm thick Pb foils. The maximum deviation from uniform response is indicated on each plot. At an angle of incidence of 80mrad the deviation is reduced to about +7% for a 2mm thick Pb foil and to -16% for a 3mm thick Pb foil. The plots illustrate, that 2mm and 3mm thick Pb foils reduce considerably the non-uniformity of the electron response at the boundary. The optimum thickness for the Pb foil is obviously between 2mm and 3mm. The Pb foil has only little impact on the hadron response (Fig. 5.20). It still improves the uniformity for hadrons.

Figure 5.23 indicates the contribution of the different calorimeter sections to the total signal of 30GeV/c electrons for a θ angle of 40mrad without and with a 2mm thick Pb foil. These measurements point out, that in particular the strong contribution from the HAC1 signal is significantly reduced by the Pb foil and the total signal becomes more uniform.

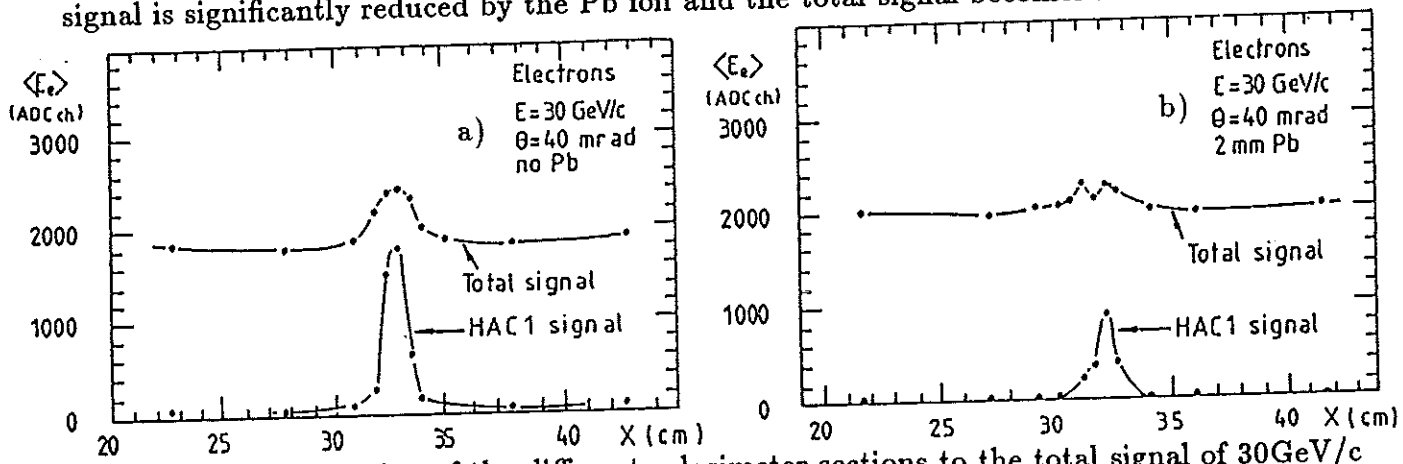

Fig. 5.23 Contribution of the different calorimeter sections to the total signal of 30GeV/c electrons for 40mrad beam incidence a) without and b) with a 2mm thick Pb foil between modules 2 and 3.

The average shift from uniform response, when averaged over one module, is presented for 5GeV/c electrons (a) and 30GeV/c electrons (b) in Fig. 5.24 for different thicknesses of Pb between two modules. Figure 5.25 shows the r.m.s. of the response distributions for the same conditions as in Fig. 5.24. The values of Fig. 5.25 give the direct contribution to the electron energy resolution. Both representations favour a 2mm to 3mm thick Pb foil.

The optimum thickness of the Pb foil was finally determined by averaging the experimental results of the 5GeV/c, 30GeV/c and 75GeV/c electron scans. The average shift from uniform response, the r.m.s. of the response distribution and the mean square deviations from uniform response have been taken into account. An optimum thickness of 2.6±0.2mm has been determined for the Pb foils [DAN90].

For the ZEUS calorimeter Pb foils with a thickness of 2.5mm, for stability glued on 0.2mm thick steel foils, have been finally installed between the modules of FCAL and RCAL.

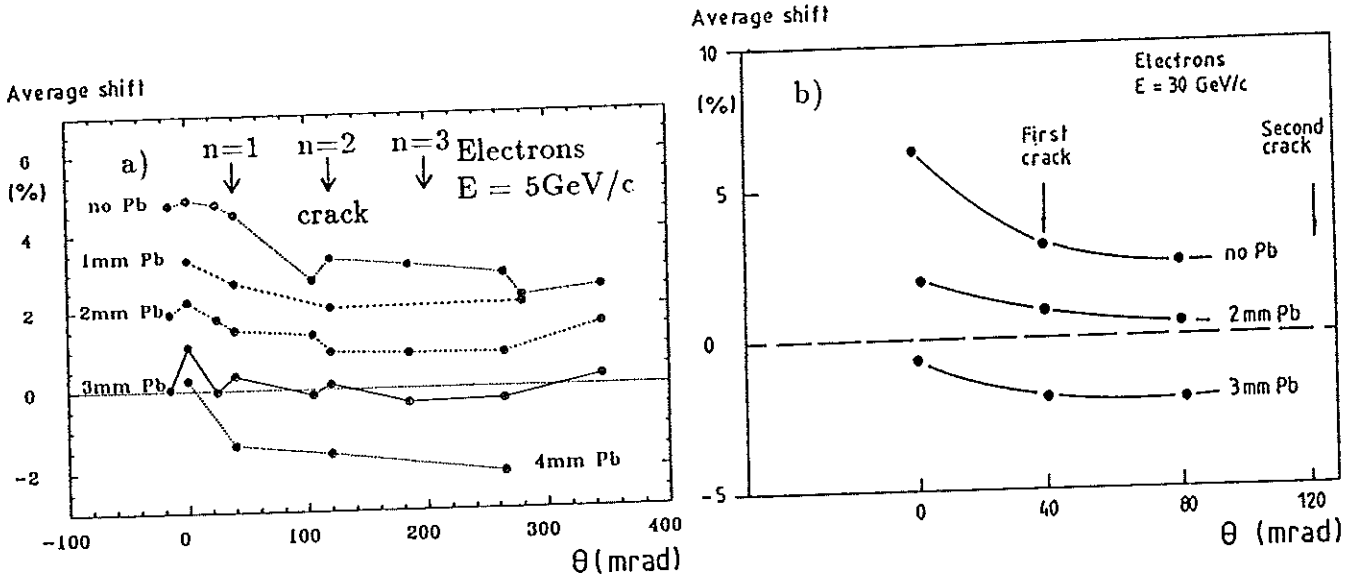

Fig. 5.24 Shift of the electron response for 5GeV/c (a) and 30GeV/c (b) due to the non-uniformity at the boundary between two calorimeter modules as a function of the angle of beam incidence for various thicknesses of Pb foils.

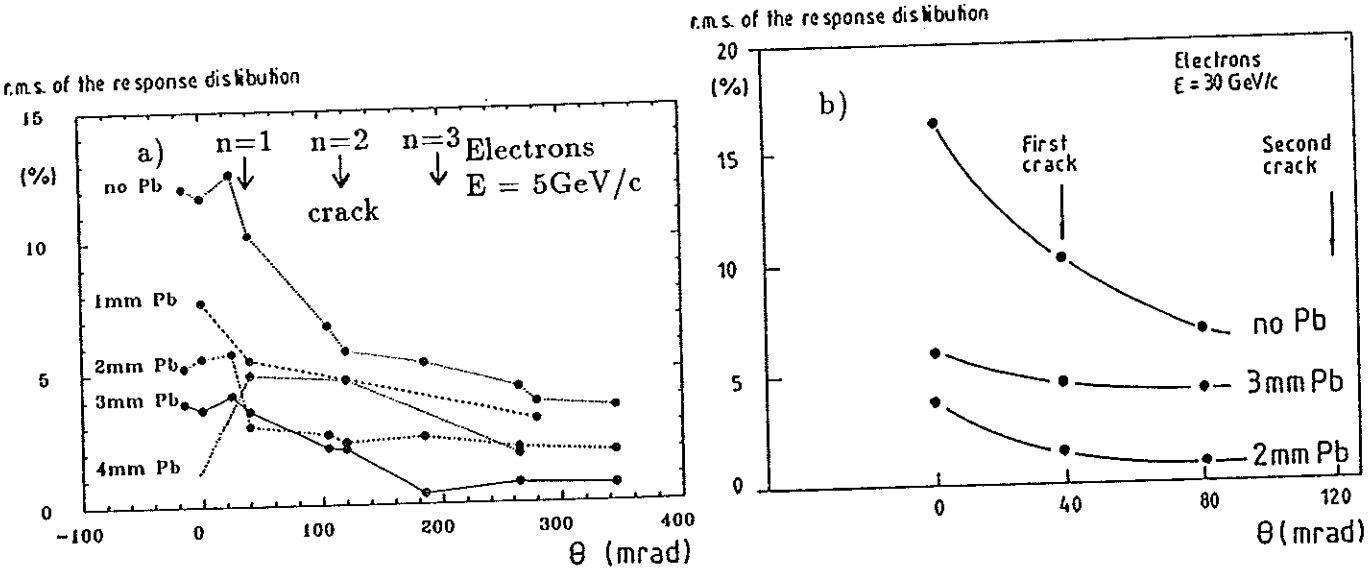

Fig. 5.25 R.m.s. of the response distribution for the same conditions as for Fig. 5.24. These values indicate the direct contribution to the electron energy resolution.

5.3.2 Uniformity at the Location of Spacers

Spacers made from tungsten-carbide with dimensions of 4 x 5 x 6mm^3 in the EMC are located between the uranium plates at the corners of each 20cm x 20cm tower. Their influence on the response of 5GeV/c electrons is plotted in Fig. 5.26 for an angle of incidence of 0mrad [BEH89]. The maximum size of the dip in the electron response is about 20%. This size is reduced for the final FCAL by spacers of lower Z material (titanium carbide). In the ZEUS detector particles always enter the calorimeter under angles bigger than 40mrad at the spacers thus the effect of spacers will be significantly reduced with increasing incidence angle.

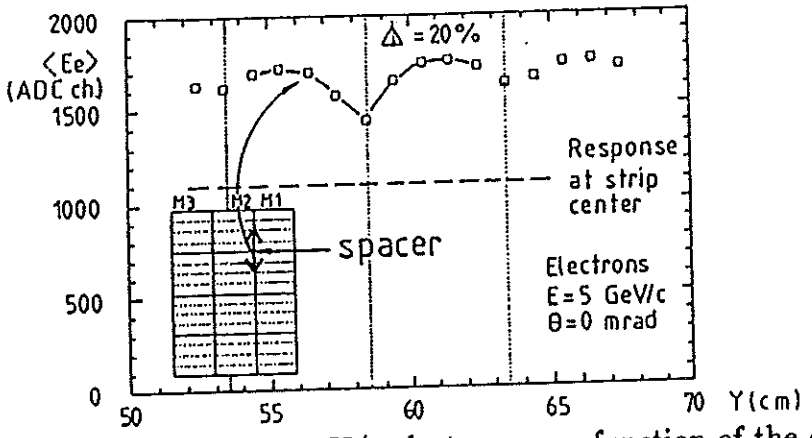

Fig. 5.26 Calorimeter response to 5GeV/c electrons as a function of the calorimeter position in vertical direction over the spacers at the module boundary.

5.3.3 Uniformity at the Boundary between EMC Sections

The influence of the 1mm gaps between the EMC sections of the FCAL prototype is shown in Fig. 5.27 [BEH89]. The maximum reduction of the electron response is 5% at an angle of incidence of 0mrad. For the final FCAL these gaps are reduced to 0.6mm and the maximum dip in the electron response is reduced to 3% according to Monte Carlo (EGS4) calculations. In the real detector particles will enter the calorimeter at the boundaries between EMC sections always under a certain incidence angle thus the effect of gaps between EMC sections will be essentially smeared out with increasing incidence angle.

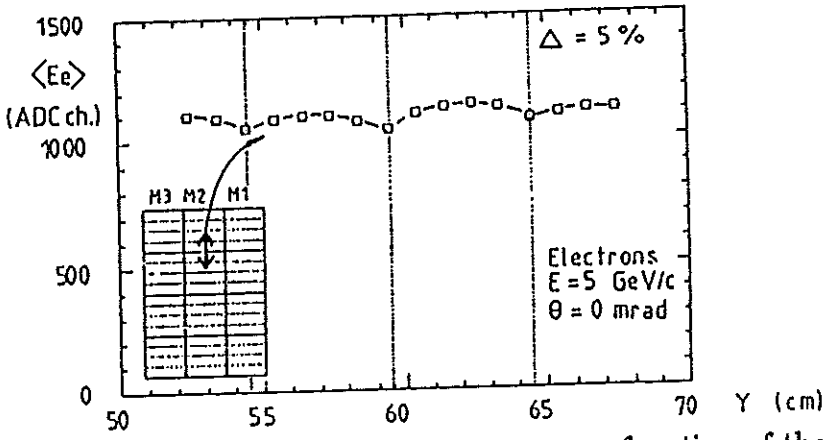

Fig. 5.27 Calorimeter response to 5GeV/c electrons as a function of the calorimeter position in vertical direction over the central region of the EMC sections.

5.4 Effect of Absorbers in Front of Calorimeters

5.4.1 Material in Front of the ZEUS Calorimeter

Tracking chambers, a magnet coil and various mechanical constructions are installed in front of the calorimeter. The material is presented in Fig. 5.28 in units of radiation lengths [X_0] as a function of the polar angle θ. For most of the θ range the thickness of the material is only 1 – 1.5 radiation lengths X_0. But there are also narrow peaks up to 4 X_0 at a few small regions where mechanical support structures are necessary. This material degrades the measured signal and the energy resolution of the calorimeter.

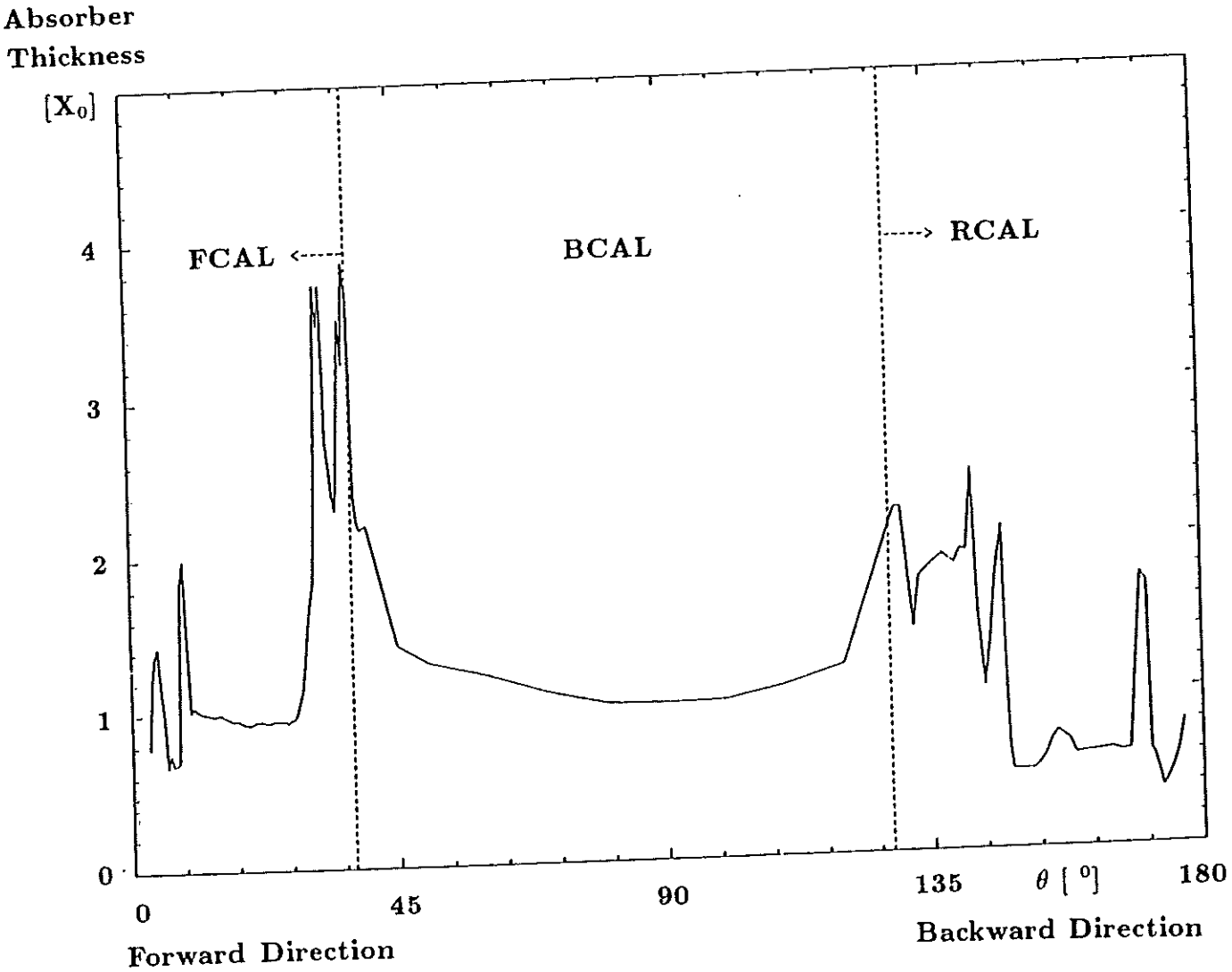

Fig. 5.28 Material in front of the high resolution ZEUS uranium scintillator calorimeter in units of radiation lengths [X_0] as a function of the polar angle θ (as estimated in ZEUS 88–52).

5.4.2 Studies of Absorbers in Front of the FCAL Prototype

Systematic studies with various thicknesses of absorber (Al) directly in front of the ZEUS forward calorimeter (FCAL) prototype have been performed at CERN in the momentum range from 0.5 to 100GeV/c to determine quantitatively the effect of absorbers [FÜR90], [KRÜ90a], [KRÜ90e].

The experimental set up used at CERN was already described in Fig. 5.2. It consists of scintillation counters defining the beam, two Cherenkov counters C1 and C2, the FCAL prototype calorimeter and the absorber in form of aluminum plates placed in the central region directly in front of the prototype.

The most important parameters of the measurement program with absorbers in front of the FCAL prototype are listed in the following:

Hadrons and Electrons (Chapter 5.4.3)

Absorber: aluminum	Thickness:	0cm, 9cm, 18cm, 27cm ($\hat{=}$ 0, 1, 2, 3 X_0)
Momentum:	at CERN PS:	0.5, 1, 2, 3, 5 GeV/c
	at CERN SPS:	10, 20, 30, 75 GeV/c

Hadrons and Particle – Jets (Chapter 5.4.4)

Absorber: aluminum	Thickness:	0cm, 4cm, 10cm
Momentum:	at CERN SPS:	50, 100 GeV/c

5.4.3 Effect of Absorbers on Hadrons and Electrons

Figure 5.29 and 5.30 show the pulse height spectra for electrons and pions at 5GeV/c and 30GeV/c with different thicknesses of aluminum absorber directly in front of the FCAL prototype. With absorber in front, the mean values of the spectra are significantly shifted to lower values and the widths of the distributions increase. Whereas for electrons the shape remains approximately Gaussian, it becomes strongly asymmetric for hadrons with a tail to small pulse heights. The influence of the absorber is considerably stronger for particles at 5GeV/c than at 30GeV/c, in particular for hadrons, and decreases with increasing momentum.

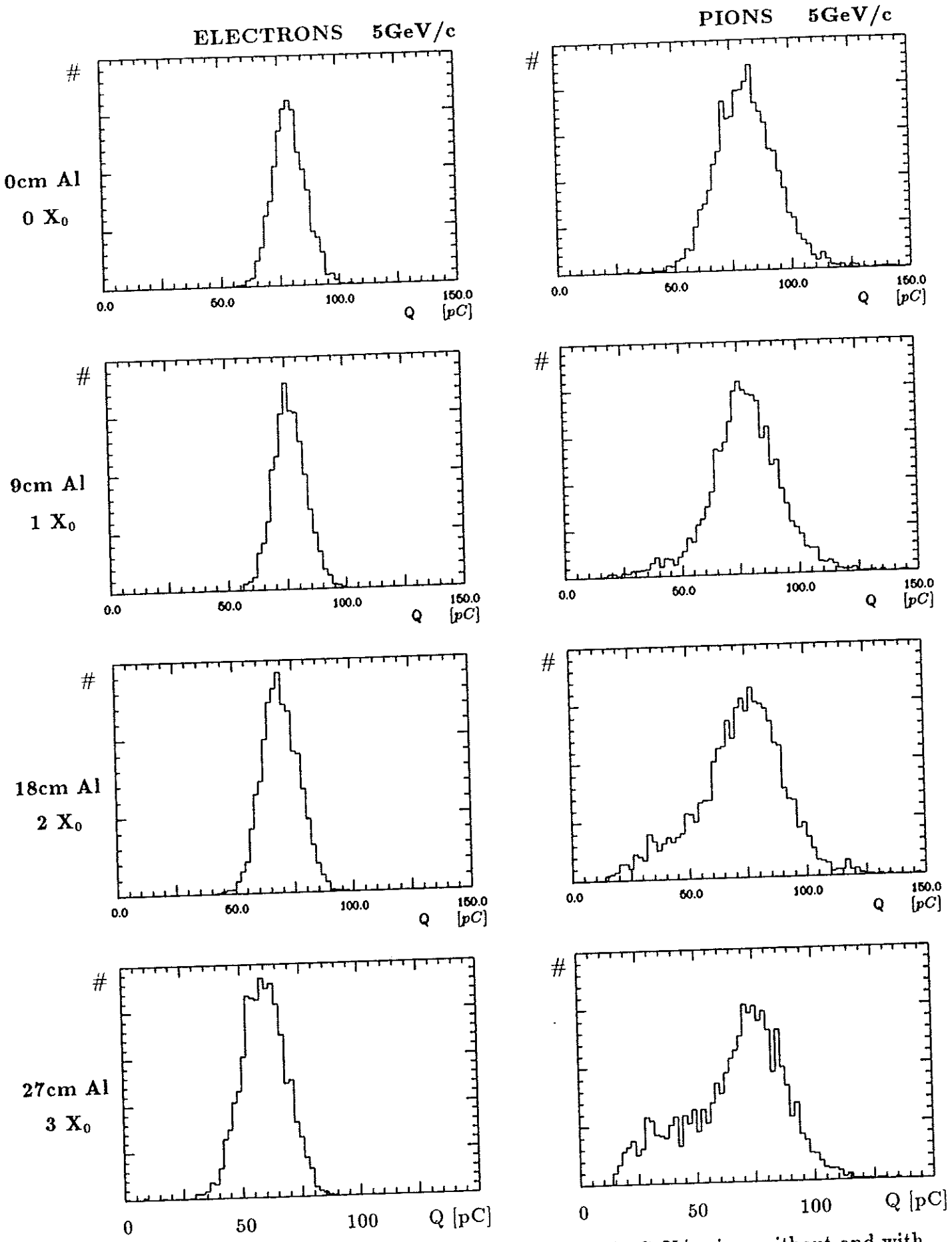

Fig. 5.29 Pulseheight spectra of 5GeV/c electrons and 5GeV/c pions without and with 9cm, 18cm and 27cm Al absorber in front of the FCAL prototype (# = number of events [arbitrary units]).

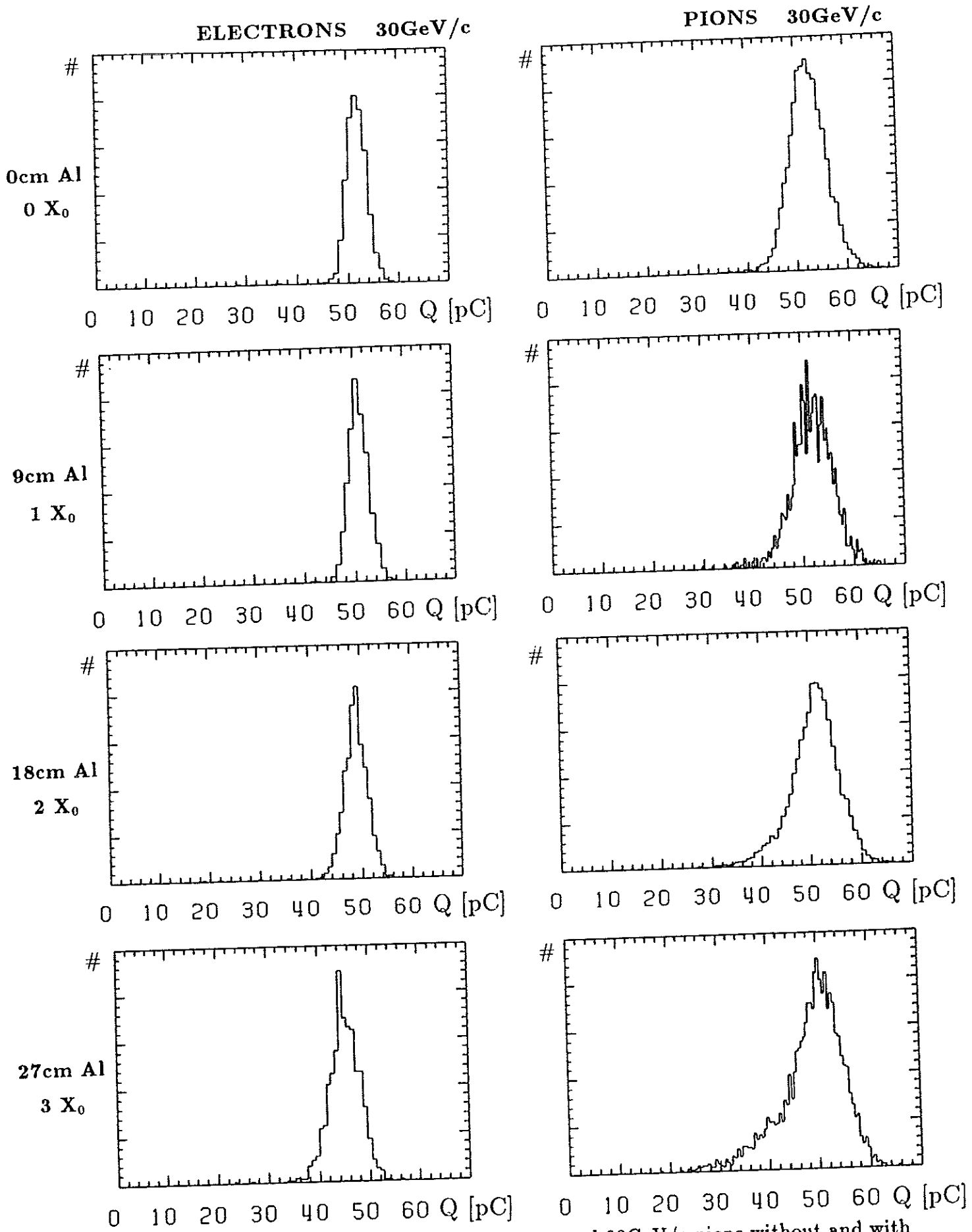

Fig. 5.30 Pulseheight spectra of 30GeV/c electrons and 30GeV/c pions without and with 9cm, 18cm and 27cm Al absorber in front of the FCAL prototype (# = number of events [arbitrary units]).

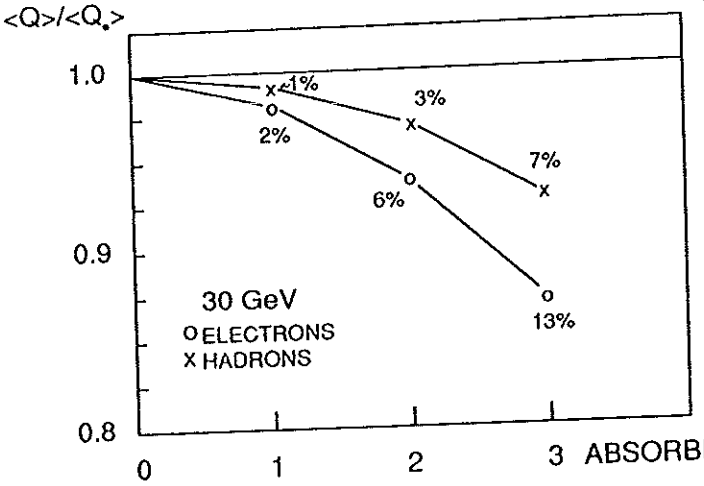

Fig. 5.31 Ratio of the mean signal height with absorber (<Q>) and without absorber (<Q_0>) as function of the absorber thickness.

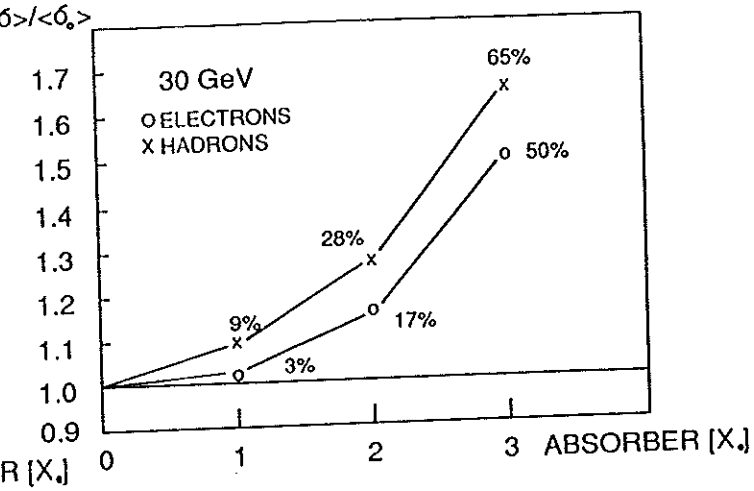

Fig. 5.32 Ratio of the standard deviation with absorber (< σ >) and without absorber (< σ_0 >) as function of the absorber thickness.

Figure 5.31 and 5.32 show for electrons and hadrons at 30GeV the ratio of the mean signal height and the standard deviation (3σ cut used) with and without material as a function of the absorber thickness in front of the calorimeter [KRÜ90e]. For 1 X_0 material in front the mean value is reduced by about 1% for hadrons and 2% for electrons and decreases significantly in particular for electrons with increasing absorber thickness. The widths increase with absorber material in front and are for 1 X_0 by about 3% larger for electrons and 9% larger for hadrons.

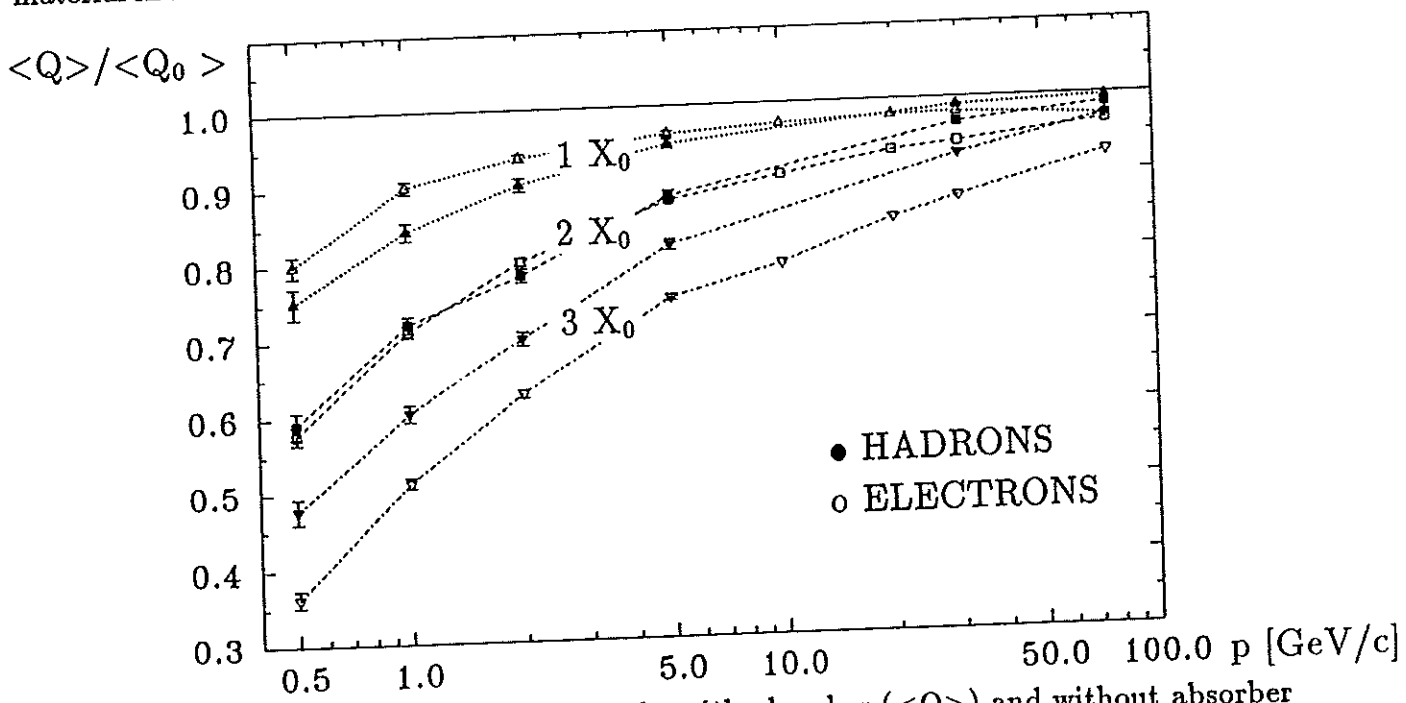

Fig. 5.33 Ratio of the mean signal height with absorber (<Q>) and without absorber (<Q_0 >) as a function of the momentum for various thicknesses of absorber in front of the FCAL prototype.

The ratio <Q>/<Q_0 > for 9cm, 18cm and 27cm aluminum absorber as a function of the particle momentum is shown in Fig. 5.33. The deviation from 1.0 is large at low momenta and is decreasing with increasing momentum. Monte Carlo simulations have been performed and a similar behaviour has been found [KAW91].

As already discussed in chapter 5.2, Fig. 5.18 shows the e/h–ratios at equal kinetic energies E_K for π^+, π^- and p. The e/h–ratio is the same for π^+, π^- and p and depends in first approximation only on the kinetic energy E_K, the energy available for particle production and energy deposit in the calorimeter. At low energies hadrons lose more and more of their energy via dE/dx of single particles and approach the sampling fraction of a minimum ionizing particle (mip). Thus e/h approaches e/mip, which is 0.62 in the present calorimeter. In addition the energy resolution for hadrons improves to $22\%/\sqrt{E}$. As the electron response e is linear with kinetic energy, the ratio $<Q>/E_K$ normalized to $<Q_0>/E_K$ at 75GeV ($(<Q_0>/E_K)\,|_{75GeV}$) with absorber in front shows smaller deviations from 1 (see Fig. 5.34).

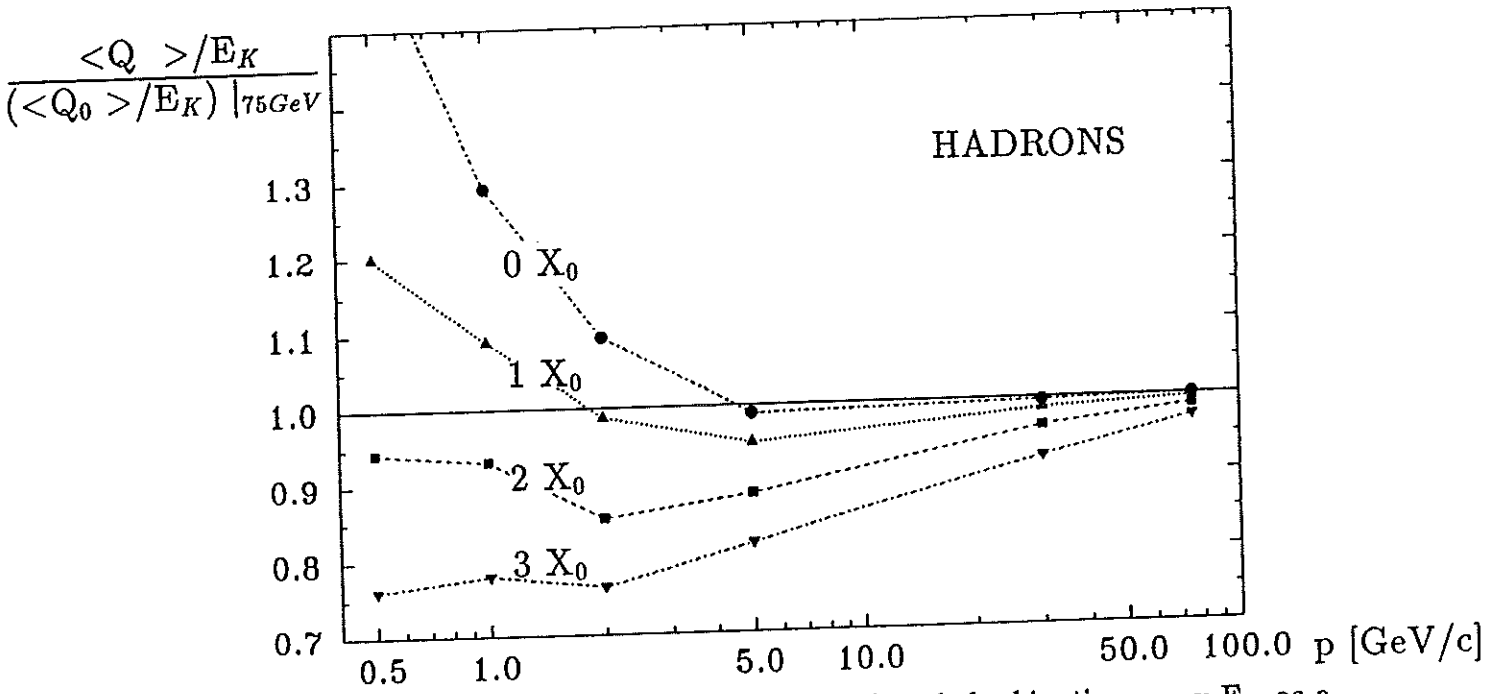

Fig. 5.34 Ratio of the mean signal height (<Q>) and the kinetic energy E_K as a function of the momentum for various thicknesses of absorber in front of the FCAL prototype.

The normalized ratio of $<Q>/E_K$ is shown in Fig. 5.34 for hadrons as a function of the momentum. The different curves show the dependence on the absorber thickness. The deviation from 1 is significantly reduced compared to $<Q>/<Q_0>$, in particular at low momenta with absorber in front.

This result is in particular important for the response of particle jets. Jets consist to a large extent of low energetic hadrons in the GeV range. The increase of the hadron response for momenta below 5GeV/c and the decrease of the response due to absorber (1–3X_0) infront of the calorimeter partially compensate each other (Fig. 5.34).

5.4.4 Effect of Absorbers on Particle Jets – Interaction Trigger

The analysis of the data taken with the interaction trigger installed to simulate particle jet production in front of the FCAL prototype and the study of methods to correct experimentally for energy lost in the absorber in front of the calorimeter via pulse height measurement are discussed in this section.

In order to study the effect of absorbers on the response and the energy resolution of particle jets, an interaction trigger has been built and installed in front of the FCAL prototype [KRÖ92].

Figure 5.35 shows the experimental set up at the CERN SPS with the interaction trigger. The interaction trigger consists of a thin 13mm Beryllium target (0.03λ) for single nuclear interactions, a leadglass veto system (L1,...,L8) and a scintillator trigger system (T1,...,T5). An aluminum absorber is placed behind the trigger system followed by a scintillation counter. This scintillation counter acts as presampler and is installed directly in front of the prototype. Data have been taken at beam momenta of 50GeV/c and 100GeV/c with 0cm, 4cm and 10cm thick Al absorbers.

The particle multiplicities created by interactions in the Be–target in comparison to single beam particles are presented in Fig. 5.36. Particle multiplicities in the order of 10 – 20 particles per interaction are created with a long tail to higher multiplicities [KRÖ91].

Without absorber in front of the prototype the average response to particle jets is somewhat reduced compared to single hadrons and the energy resolution is about the same. At 100GeV the average response to jets is reduced by about 1.7% and the energy resolution is 3.7% for jets which is about the same as for single hadrons.

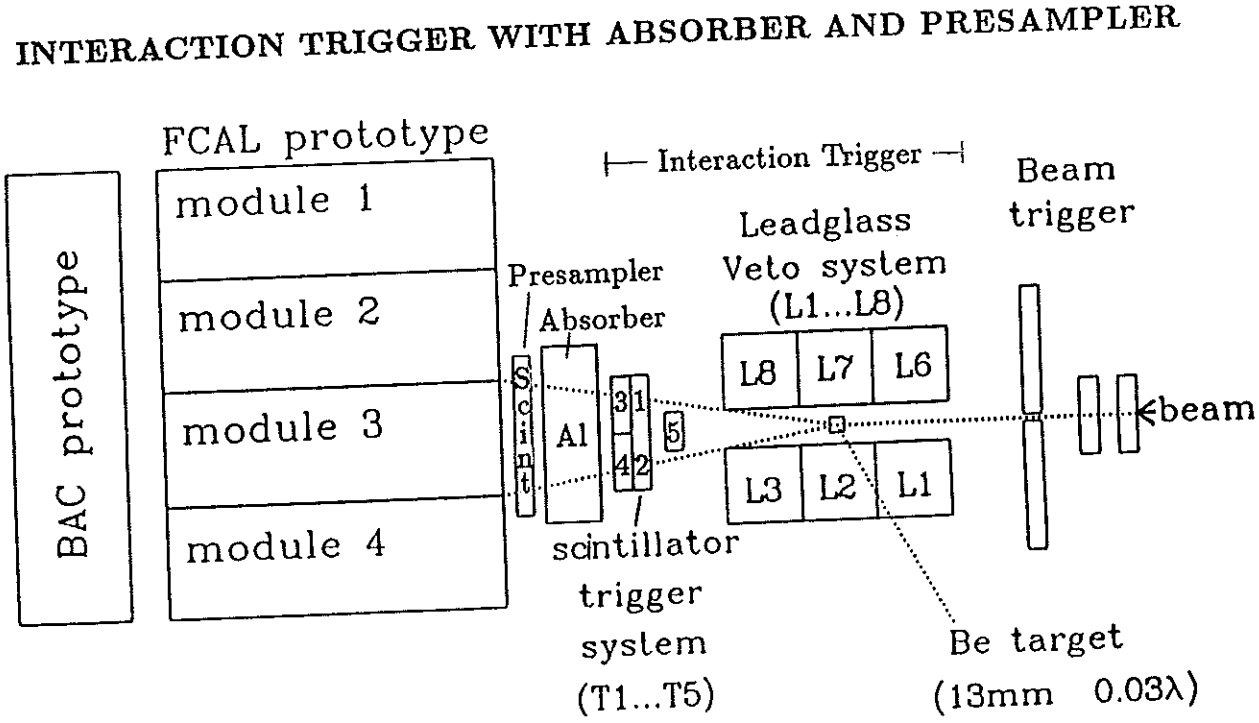

Fig. 5.35 Experimental set up of the interaction trigger, aluminum absorber and presampler in front of the FCAL prototype at the CERN SPS.

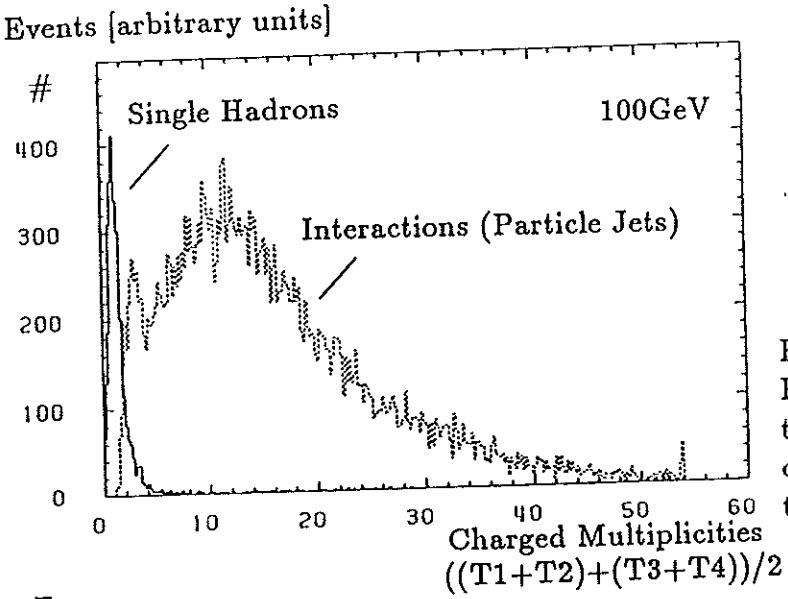

Figure 5.36
Particle multiplicities for interactions in the Be–target of the interaction trigger compared to single beam particles (Be–target removed).

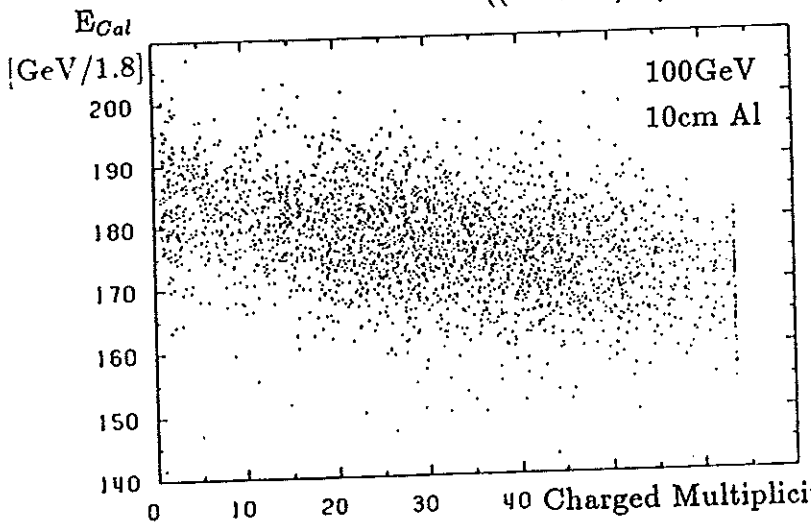

Figure 5.37
Correlation plot of the jet energy E_{Cal} measured in the FCAL prototype versus the charged particle multiplicity after 10cm Al absorber for 100GeV jets.

A correlation is seen between the jet energy measured in the calorimeter E_{Cal} and the multiplicities of charged particles measured in front of the Al absorber in the trigger system and after the Al absorber in the presampler. The correlation measured in the presampler is significantly stronger compared to that in the trigger system. For 100GeV jets and a 10cm thick Al absorber the correlation between E_{Cal} and the particle multiplicity measured in the presampler is presented in Fig. 5.37.

The effect of absorbers on the average response and the energy resolution for jets is presented in Fig. 5.38 and 5.39 as a function of the Al absorber thickness. For a 4cm thick Al absorber only a negligible effect on the average response is seen. For 10cm Al the response is reduced by about 4.5% for 50GeV and about 2% for 100GeV jets. In comparison to jets without absorber the energy resolution is degraded for 50GeV and 100GeV by about 5% for 4cm and 20% for 10cm Al absorber.

A significant improvement is achieved by a correction of the measured energy E_{Cal} with information on the particle multiplicities in front and behind the absorber. The degradation of the energy resolution of 20% is improved to less than 5% by this correction. A perfect correction of the average energy E_{Cal} to $(\frac{E_{Cal}(x)}{E_{Cal}(x=0)} - 1) = 0$ is possible with a negligible effect on the improved energy resolution.

In the ZEUS experiment the charged particle multiplicity will be measured by the tracking detectors in front of the magnet coil and mechanical support structures. Enough space is available for installation of a presampler between the inactive material and the calorimeter.

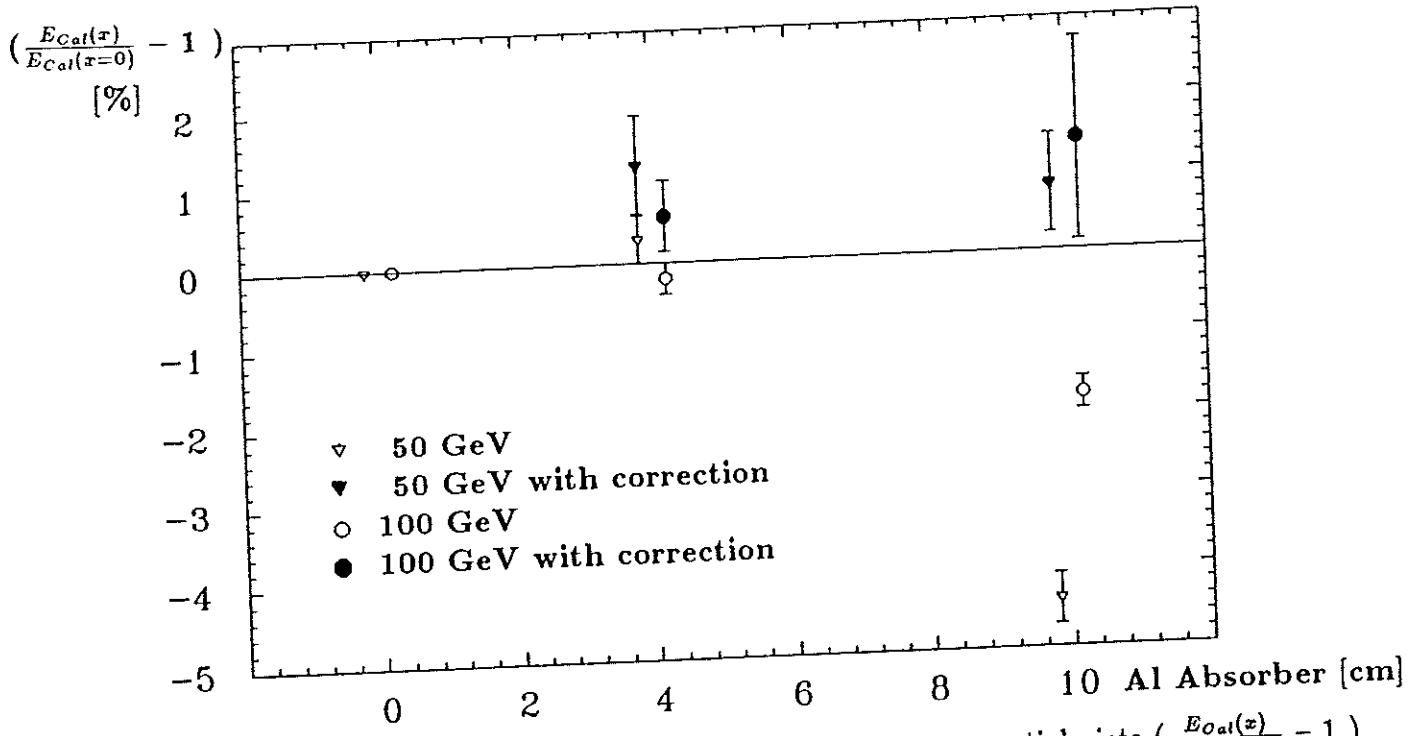

Fig. 5.38 Influence of an Al abs. on the average response to particle jets $(\frac{E_{Cal}(x)}{E_{Cal}(x=0)} - 1)$ as a function of the Al absorber thickness x[cm] for 50GeV and 100GeV jets without and with correction by the multiplicity measured with the trigger system and the presampler.

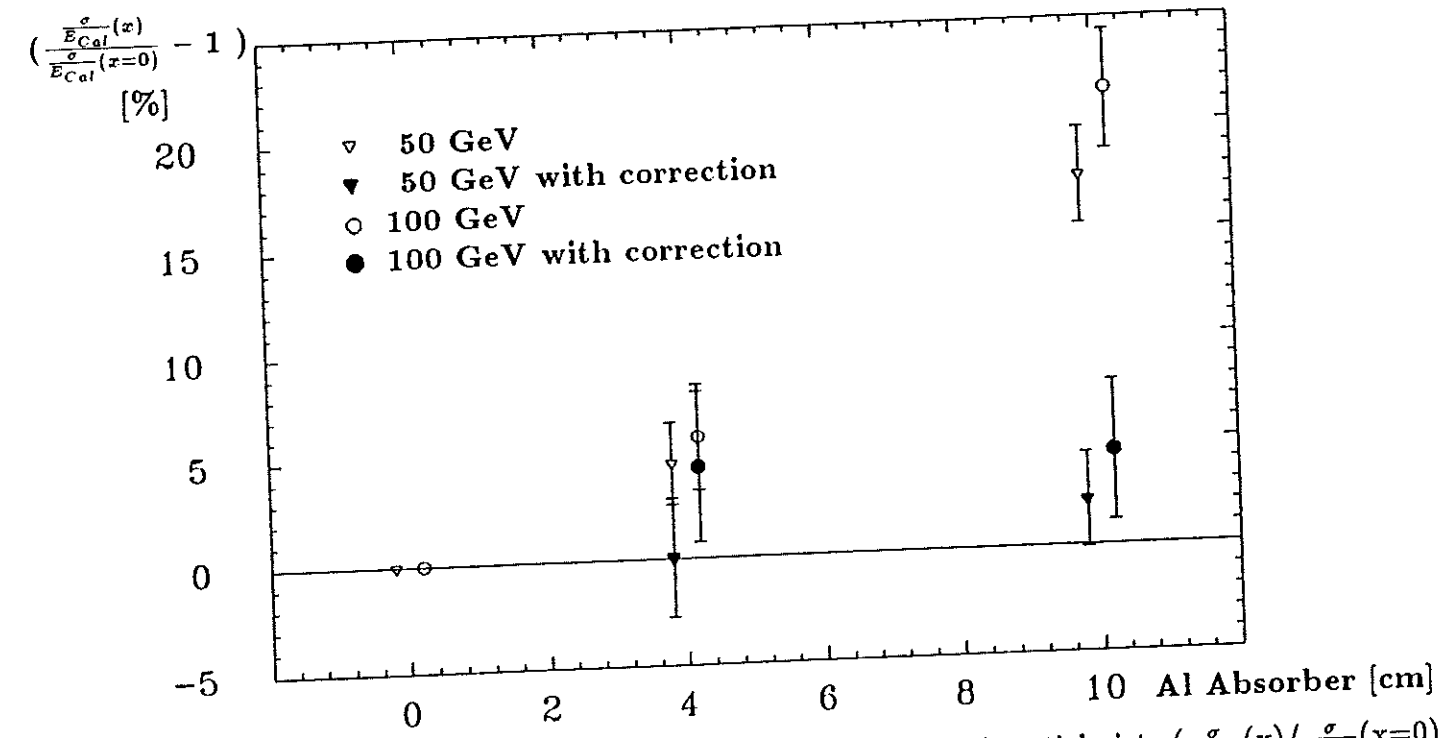

Fig. 5.39 Influence of an Al abs. on the energy resolution of particle jets $(\frac{\sigma}{E_{Cal}}(x)/\frac{\sigma}{E_{Cal}}(x=0) - 1)$ as a function of the Al absorber thickness x[cm] for 50GeV and 100GeV jets without and with correction by the multiplicity measured with the trigger system and the presampler.

5.5 Reconstruction of Position and Angle of the Axis of Particle Showers

5.5.1 Introductory Remarks

Besides excellent energy resolution for hadrons and jets, a precise determination of the angle of single electrons and hadrons (jets) to better than 10mrad with respect to the interaction point is required for the ZEUS calorimeter. As discussed already in detail in chapter 2.2.2 and 2.2.8 a precise energy and angular measurement of the scattered electron and the current jet are the basic conditions for determining x and Q^2 of the deep inelastic events with high precision.

Using the structure of the ZEUS calorimeter with a transverse segmentation of 5cm x 20cm in the EMC and 20cm x 20cm in the HAC sections and a longitudinal segmentation in one EMC ($25X_0$ and 1λ) and two HAC sections (each 3λ) for the FCAL, different methods have been studied to determine the positions and angles of the axis of electromagnetic and hadron showers.

Electromagnetic showers are fully contained in four EMC sections corresponding to a tower size of 20cm x 20cm. The position of the shower axis can be reconstructed in horizontal (x) and vertical (y) direction. The angle of the scattered electron can be determined in first approximation from the measurement of the position of the shower axis and the nominal or measured interaction point. This information can be used in the fast trigger.

Hadron showers are laterally spread over about four calorimeter modules ($\approx$ 80cm) and their energy is longitudinally deposited along the total depth of the calorimeter, in EMC, HAC1 and HAC2.

Figure 5.40 illustrates the lateral spread of 30GeV/c hadron showers measured with the FCAL prototype. Each cell represents a 20cm x 20cm calorimeter tower. The beam is incident in the middle of the central tower depositing a fraction of 75.5% of the incident energy in this tower. The numbers in the cells indicate the percentage of deposited energy [BEH89].

Figure 5.41 presents the fractions of deposited energy by hadron showers in the different longitudinal calorimeter sections (EMC, HAC1, HAC2) as a function of the beam momentum. With increasing momentum the average fraction of deposited energy increases logarithmically in HAC2, while it decreases in the EMC. For momenta above 20GeV/c to about 200GeV/c the energy deposited in HAC1 is almost constant at about 60%. At 200GeV/c the average fraction of deposited energy in EMC and HAC2 cross over and each section contains on average about 20% of the energy. The energies deposited in the different calorimeter sections fluctuate strongly from event to event.

The position of the hadron shower axis can be determined separately for each calorimeter section if enough energy is deposited in this section. This is clearly the case for EMC and HAC1; with increasing momentum this is also true for HAC2 providing an additional point on the shower axis.

In order to determine the angle of the hadron shower axis from the calorimeter alone the longitudinal centres of gravity of the shower have to be reconstructed in the different calorimeter sections. At least two centres of shower gravity have to be available for reconstruction of the hadron shower angle by the calorimeter alone. If the position of the interaction point can be used in addition, the precision is significantly improved.

Lateral Spread of 30GeV/c Hadron Showers

0.01	0.02	0.07	0.04	0.07	0.02	0.01	[%]
0.02	0.09	0.25	0.30	0.25	0.09	0.02	
0.07	0.25	1.3	3.7	1.3	0.25	0.07	
0.04	0.30	3.7	75.5	3.7	0.30	0.04	
0.07	0.25	1.3	3.7	1.3	0.25	0.07	
0.02	0.09	0.25	0.30	0.25	0.09	0.02	
0.01	0.02	0.07	0.04	0.07	0.02	0.01	20cm

Total sum = 100 — 20 cm

Fig. 5.40 Lateral spread of 30GeV/c hadron showers. Each cell represents a 20cm x 20cm tower. The beam is incident in the middle of the central tower.

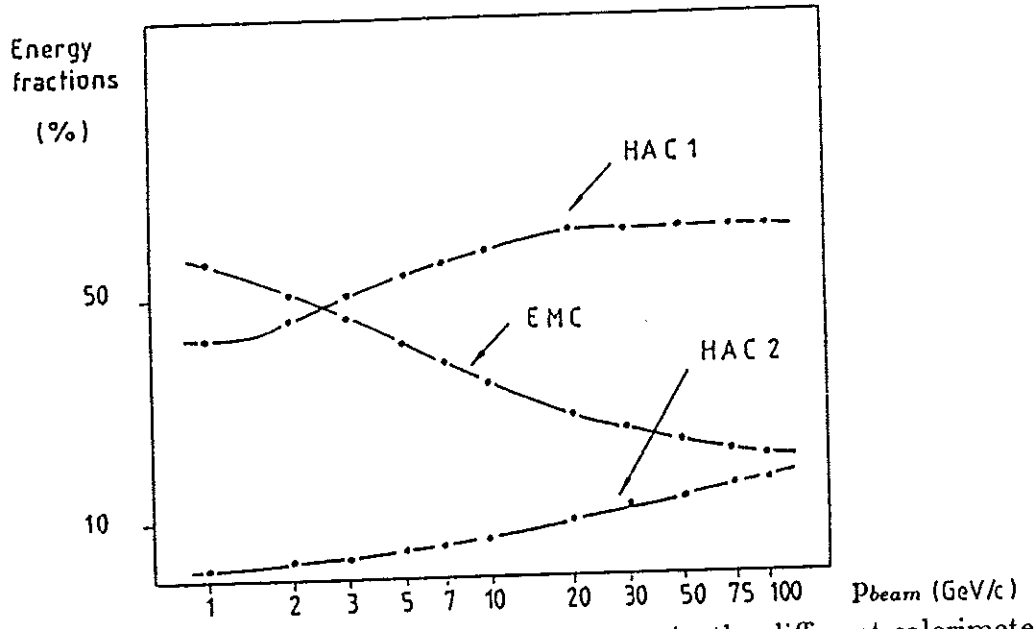

Fig. 5.41 Fraction of energy deposited by hadron showers in the different calorimeter sections as a function of the beam momentum.

5.5.2 Reconstruction of the Transverse Centres of Gravity of Particle Showers

In this section the reconstruction of the transverse positions of the axis of electromagnetic and hadron showers is described. The position resolution of the calorimeter has been studied for single electrons and hadrons at various angles of beam incidence up to momenta of 100GeV/c [BEH89], [AND90].

For each calorimeter section (cell) of EMC, HAC1 and HAC2 the transverse centre of gravity of the particle shower is determined from the ratio of the signals (energies) measured in the right E_R and left photomultiplier E_L.

Assuming an exponential light attenuation λ in x direction along the scintillator, the distance δx from the x- centre of the tower (Fig. 5.42) can be calculated by:

$$\delta x = \frac{\lambda}{2} ln(\frac{E_R}{E_L}) \; .$$

Figure 5.43 shows the ratio E_R/E_L as a function of δx for 5GeV/c electrons measured along the x axis at the middle of an EMC tower. It illustrates that δx has a logarithmic dependence of the ratio E_R/E_L except for the region close to the WLS (<2cm), which can be parametrized by a polynomial.

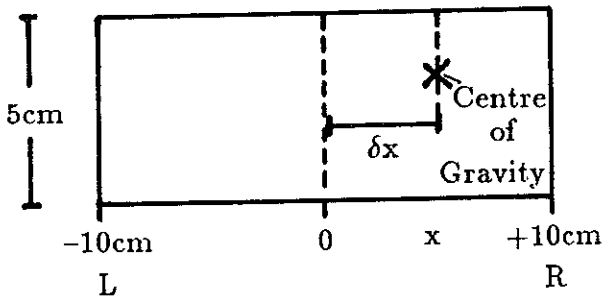

Figure 5.42
Distance δx between the centre of an EMC tower and the transverse centre of shower gravity.

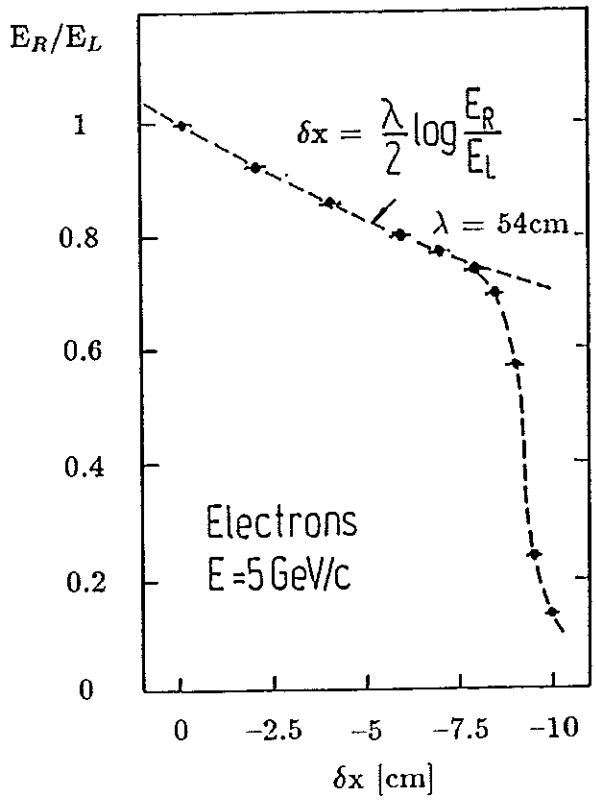

Figure 5.43
The signal ratio E_R/E_L of the right and left photomultipliers as a function of the distance δx to the centre of the tower.

The position of the incident particle can be determined by the transverse centre of gravity of the particle shower created in the calorimeter. The transverse centre of gravity of the particle shower can be calculated by summing up all towers weighted with their energy:

$$\mathrm{x} = \sum_i w_i x_i \quad \text{and} \quad \mathrm{y} = \sum_i w_i y_i \ ,$$

with $x_i = (x_o)_i + \delta x_i$ and $y_i = (y_o)_i + \delta y_i$ weighted by $\mathrm{w}_i = \mathrm{E}_i/\mathrm{E}$, where $(x_0)_i$, $(y_0)_i$ are the central x, y coordinates, E_i the energy deposited in the i^{th} calorimeter section and E the total energy.

The transverse centres of gravity can be calculated separately for EMC, HAC1 and HAC2. This is necessary if the angle of hadron incidence is determined from the calorimeter information alone, for which at least two points are required.

Figures 5.44 and 5.45 present for 5GeV/c electrons and hadrons the results of the horizontal (x) position reconstruction (a) and the horizontal position resolution (b) [BEH89]. The structures in the position reconstruction in particular at the boundaries between modules and strips are introduced by the simplicity of the reconstruction algorithms and can be corrected by more sophisticated ones.

Shifts in the reconstruction of the electron position are found close to the boundary between two calorimeter modules and are in the order of 5mm. The shifts of the hadron position reconstruction (Fig. 5.45a, 5.47a) are simply the result of energy leakage to the sides.

The position resolution at the centre of a section are expected to be about:

$$\sigma_x = \lambda \sigma_d \quad \text{with} \quad \sigma_d = \frac{\sigma(E_R - E_L)}{< E_R + E_L >}$$

For electrons σ_d represents essentially the photoelectron statistics of $10\%/\sqrt{E[GeV]}$ and for hadrons σ_d is about $12\%/\sqrt{E}$. The calculated position resolutions of $\sigma_x \approx 5.4/\sqrt{E}$cm for electrons and $\sigma_x \approx 6.6/\sqrt{E}$cm for hadrons are in good agreement with the measurements.

Figures 5.46 and 5.47 show the results of the vertical (y) position reconstruction of 5GeV/c electrons and hadrons. The vertical position resolution can be described by $\sigma_y \approx 1.4/\sqrt{E}$cm for electrons and $\sigma_y \approx 6.7/\sqrt{E}$cm for hadrons.

The simple algorithm used to reconstruct the particle position yields reasonable results. More sophisticated algorithms or parametrizations can reduce significantly the shifts in horizontal and vertical position reconstruction.

Systematic scans have been performed with hadrons and electrons also under various angles of beam incidence at momenta of 30, 75 and 100GeV/c [AND90], [AND90a], [AND91a].

The resolution of the transverse centres of gravity for hadrons with angles of beam incidence of 0mrad and 200mrad in the horizontal x,z– plane are presented in Fig. 5.48 as a function of the beam momentum for EMC, HAC1 and HAC2. The experimental results on position reconstruction and resolution are summarized in Table 5.2.

The transverse position resolution improves with increasing momentum for all three calorimeter sections; EMC, HAC1 and HAC2. At 30GeV/c and θ = 0mrad the position resolution in the x direction is σ_x = 1.6cm for the EMC and improves to σ_x = 1.2cm at 100GeV/c. The resolution becomes worse with the calorimeter depth, from EMC to HAC2, due to the increasing lateral shower spread and the decreasing energy deposition in each calorimeter section (cell).

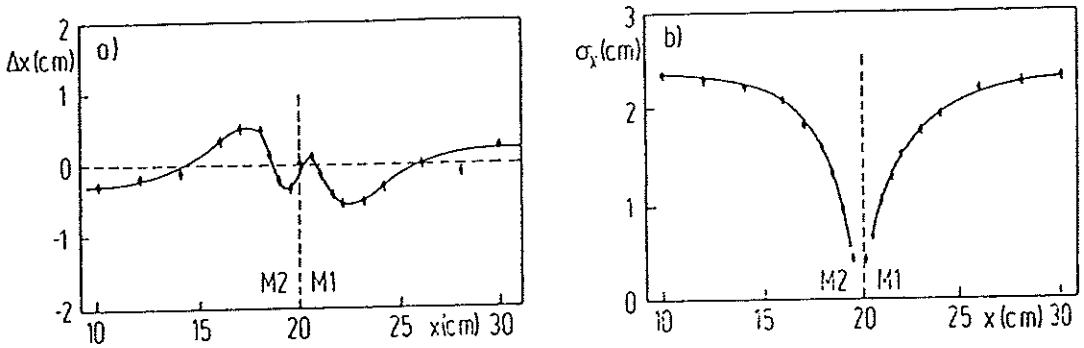

Fig. 5.44 Horizontal position reconstruction for 5GeV/c electrons under normal incidence showing a) the shift in the average position and b) the position resolution.

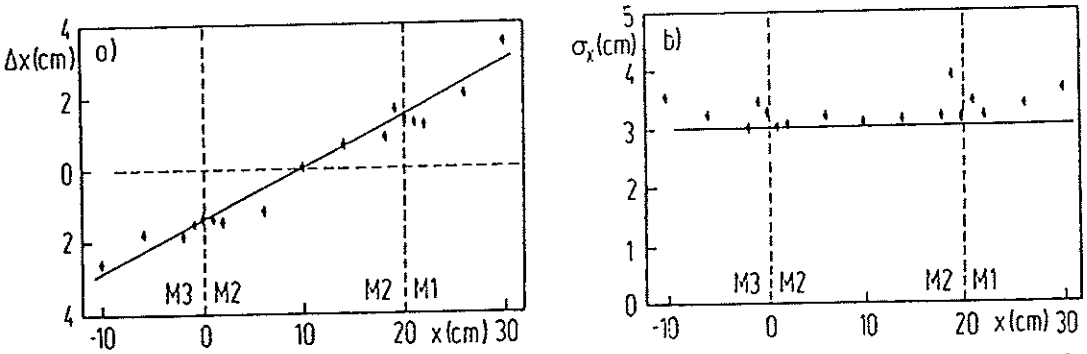

Fig. 5.45 Horizontal position reconstruction for 5GeV/c hadrons under normal incidence showing a) the shift in the average position and b) the position resolution.

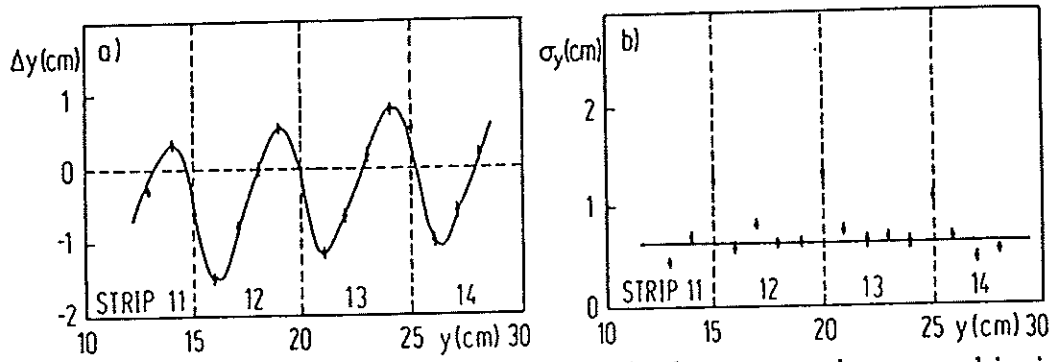

Fig. 5.46 Vertical position reconstruction for 5GeV/c electrons under normal incidence showing a) the shift in the average position and b) the position resolution.

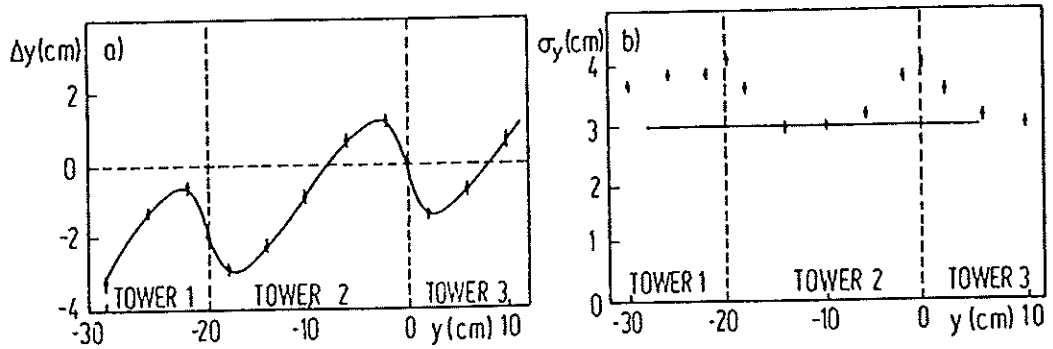

Fig. 5.47 Vertical position reconstruction for 5GeV/c hadrons under normal incidence showing a) the shift in the average position and b) the position resolution.

θ [mrad]	Energy [GeV]	x_{EMC} [cm]	σ_{XEMC} [cm]	x_{HAC1} [cm]	σ_{XHAC1} [cm]	x_{HAC2} [cm]	σ_{XHAC2} [cm]
0	30	-10.0 ± 0.05	1.6	-10.0 ± 0.04	1.9	-10.0 ± 0.16	5.3
	75	0.0 ± 0.04	1.0	0.0 ± 0.03	0.8	0.0 ± 0.09	2.4
	100	-10.0 ± 0.06	1.2	-10.0 ± 0.05	1.1	-10.0 ± 0.15	3.4
200	30	-9.5 ± 0.05	1.7	-2.2 ± 0.07	3.4	7.9 ± 0.16	4.8
	75	-9.5 ± 0.04	1.5	-2.9 ± 0.09	2.6	7.2 ± 0.15	4.0
	100	-9.8 ± 0.08	1.3	-3.1 ± 0.11	2.6	7.3 ± 0.15	3.3

Table 5.2 Position reconstruction and resolution of the transverse centres of shower gravity in EMC, HAC1 and HAC2 for 30GeV/c, 75GeV/c and 100GeV/c hadrons at θ angles of 0mrad and 200mrad (impact position in x at –10cm (0cm for 75GeV, 0mrad)).

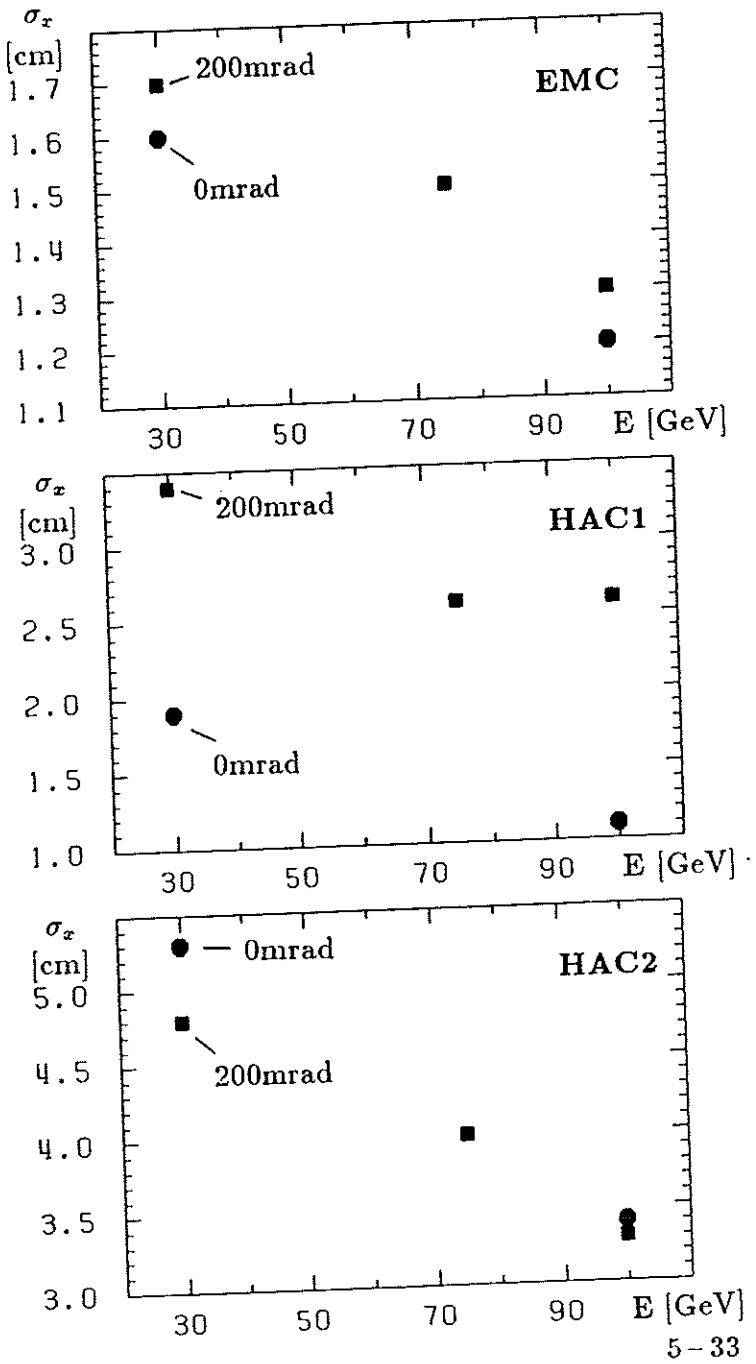

Figure 5.48
Position resolution of the transverse centres of gravity in EMC, HAC1 and HAC2 as a function of the hadron energy at θ angles of 0mrad and 200mrad with an impact position in the middle of tower 10 (see Fig. 5.50).

5.5.3 Reconstruction of the Longitudinal Centres of Gravity of Hadron Showers

Method 1 – Parametrization of the Longitudinal Centres of Gravity

In the first method the longitudinal centres of gravity of hadron showers z_i are parametrized separately for each calorimeter section (i = EMC, HAC1, HAC2) as a function of the energy E_i deposited in each section at a total energy E_0, thus $z_i = z_i(E_0, E_i)$.

Figure 5.49 illustrates the coordinate system used for this parametrization in one EMC section. The centres of gravity z_i ($\approx r_i$ for small angles) are determined at a fixed total energy E_0 by:

$$z_i(E_i) = \frac{x_i(E_i)}{tan\theta} \ ,$$

with the polar angle θ in the horizontal (x,z–) plane and $x_i(E_i)$ the transverse centre of shower gravity as a function of E_i. The θ angles were precisely adjusted by rotating the FCAL prototype (Fig. 5.4) and the x_i values were determined as described in the previous chapter 5.5.2.

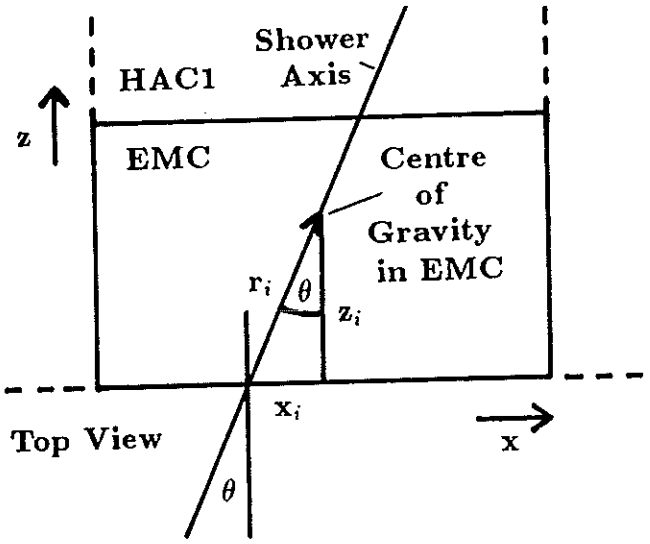

Figure 5.49
Description of the coordinate system used for the parametrization of the longitudinal centres of gravity in one EMC section.

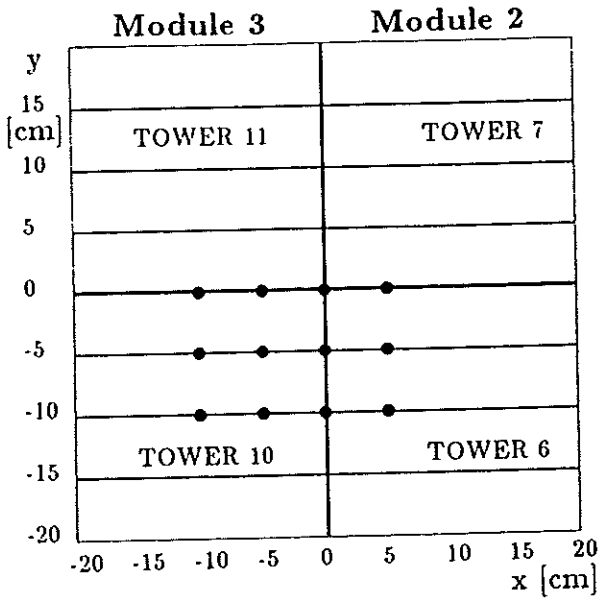

Figure 5.50
Matrix of impact positions over the central entrance face of the FCAL prototype calorimeter.

Momentum [GeV/c]	θ Angle in mrad					
	0	40	120	200	280	360
30	2150	2150	2150	2150	2150	2150
75	850	-	-	850	850	850
100	550	-	550	550	-	550

Table 5.3 Measurement program with numbers of hadron events taken at 30GeV/c, 75GeV/c and 100GeV/c at various angles of beam incidence.

This parametrization has been performed for hadrons with momenta of 30GeV/c, 75GeV/c and 100GeV/c with impact positions distributed over a matrix of points covering in a systematic way the central tower structure of the FCAL prototype for θ angles of beam incidence from 0mrad to 360mrad.

Figure 5.50 shows the matrix of impact positions over the central entrance face of the FCAL prototype calorimeter. The measurement program with the numbers of hadron events taken for 30GeV/c, 75GeV/c and 100GeV/c hadrons at various angles of beam incidence are summarized in Table 5.3.

Figure 5.51 illustrates the correlations measured between the energies deposited in EMC, HAC1 and HAC2 and the transverse centres of shower gravity for 75GeV/c hadron showers at an angle of beam incidence of 200mrad.

The average longitudinal centres of gravity z_{EMC}, z_{HAC1} and z_{HAC2} (z component) have been determined as functions of E_{EMC}, E_{HAC1} and E_{HAC2} at E_0:

$$z_{EMC} = z_{EMC}(E_0, E_{EMC}), \quad z_{HAC1} = z_{HAC1}(E_0, E_{HAC1}), \quad z_{HAC2} = z_{HAC2}(E_0, E_{HAC2}) \cdot$$

Figure 5.52 shows for 75GeV/c hadrons the parametrization of the longitudinal centres of shower gravity for EMC, HAC1 and HAC2 as a function of the energy E_i deposited in the corresponding calorimeter sections.

The strongest variation of the position of the longitudinal centre of shower gravity is found in the EMC. This is expected due to the longitudinal development of hadron showers with the maximum energy deposition on average at about 0.7λ after the start vertex (Fig. 4.20).

If the energy deposited in the EMC (or HAC1, HAC2) is below a certain value, a wrong z_i value could be calculated from a wrong transverse centre of gravity x_i dominated by noise, for example from the uranium radioactivity, the electronic readout (see Fig. 5.11) or the optical readout. The longitudinal centres of gravity are removed from the sample by a cut on E_i if the deposited energy is below a certain value (see Table 5.4).

This method represents a fast and reliable parametrization in both, determination and application of the average longitudinal centres of gravity of hadron showers in EMC, HAC1 and HAC2. A more sophisticated but also more time consuming algorithm has been developed which considers the longitudinal development of each single hadron shower and can therefore take at least partially into account the fluctuations on the average longitudinal centres of gravity presented by error bars in Fig. 5.52.

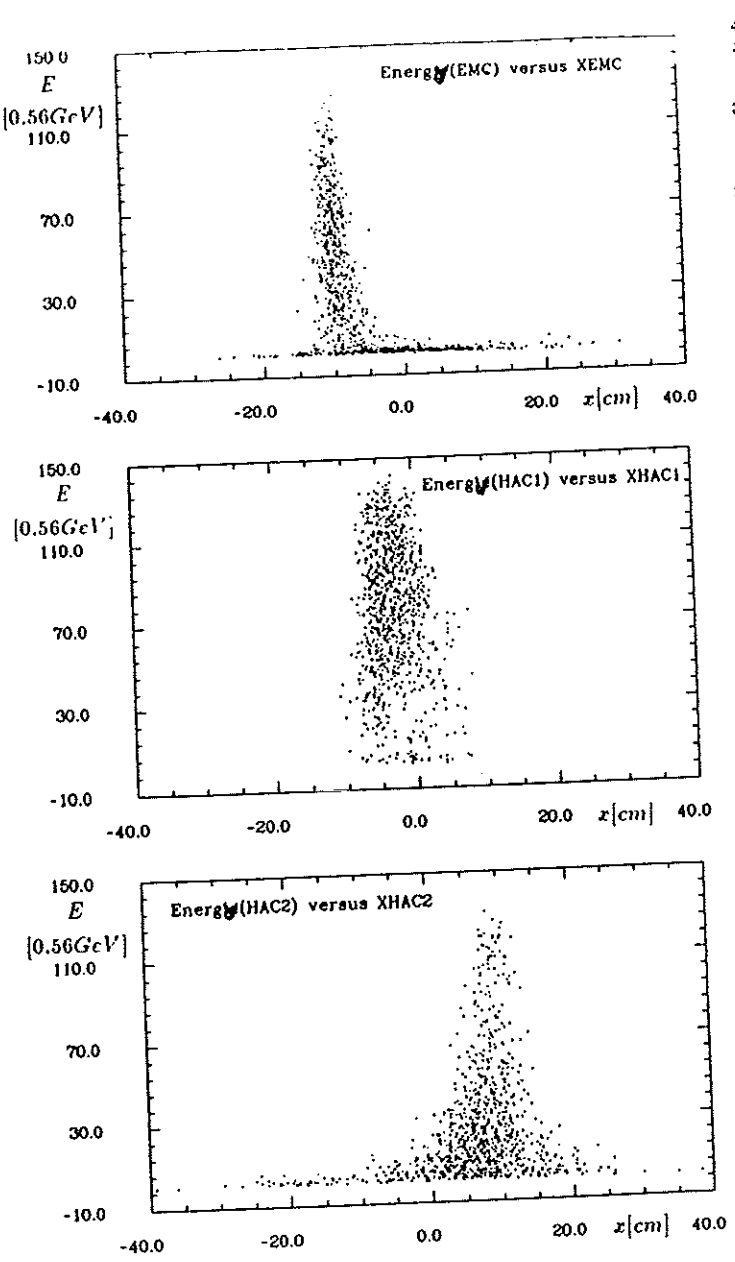

Figure 5.51
Correlation plots of the energies deposited in EMC, HAC1 and HAC2 and the transverse centres of shower gravity for 75GeV/c hadrons at θ = 200mrad.

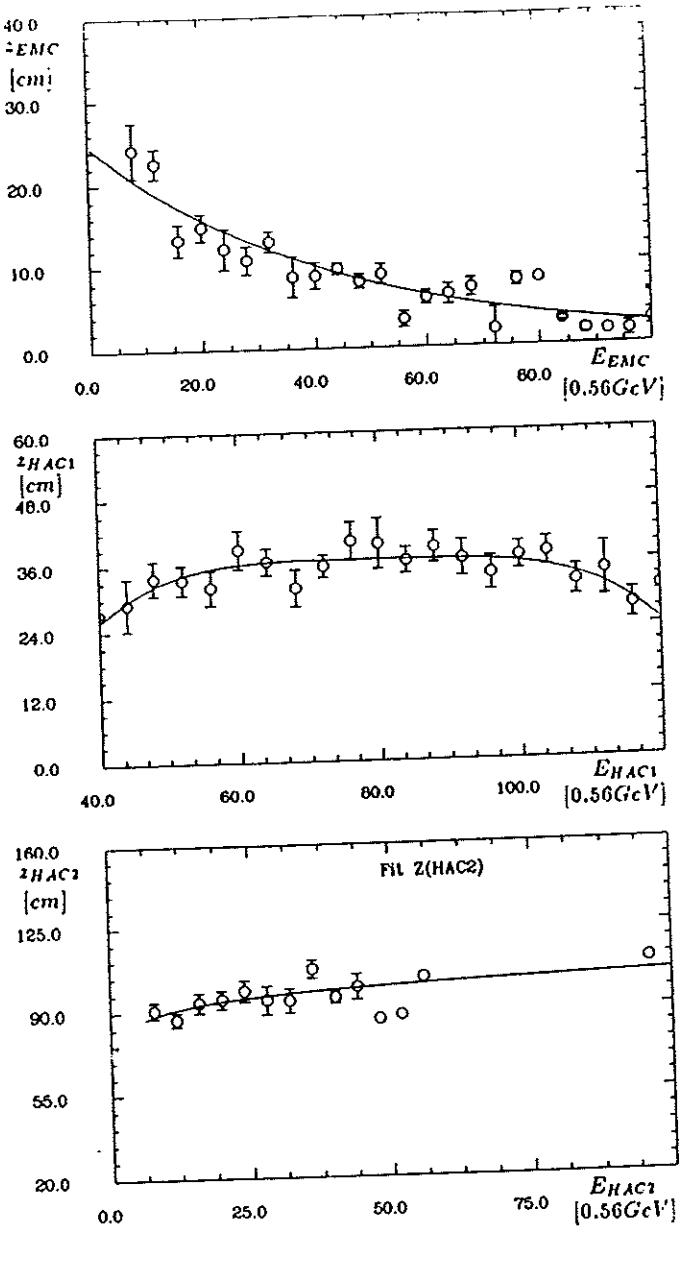

Figure 5.52
Parametrizations of the longitudinal centres of shower gravity for EMC, HAC1 and HAC2 for 75GeV/c hadrons at θ = 200mrad.

Method 2 – Parametrization of the Longitudinal Profile of Single Hadron Showers

This method starts from the parametrization developed for the average longitudinal hadron shower profiles already presented and discussed in detail in chapter 4.2.6 [KRÜ86b], [CAT87], [KRÜ90d]. This parametrization has been modified in order to be more flexible in describing the longitudinal profiles of single hadron showers with the information available from the calorimeter (PLSP–algorithm) [AND90a], [AND91a].

The parametrization of the energy deposition dE/dz of single hadron showers as a function of the distance z from the calorimeter entrance face has the following form:

$$\frac{dE}{dz}(z) = k \cdot E_0 \cdot \left\{ \alpha \, \frac{b^{a+1}}{\Gamma(a+1)} \, (z-s)^a \, e^{-b(z-s)} + (1-\alpha)\,(z-s)\,(e^{-c(z-s)} - e^{-2c(z-s)}) \right\},$$

where E_0 is the incident energy, k a normalization constant and s, b, c and α parameters, which have to be determined for each single hadron shower.

The parameter s describes the distance of the start vertex of the hadron shower to the entrance face of the calorimeter.

The first term has essentially the shape to reproduce the electromagnetic component of the hadron shower close to its start vertex.

The second term describes the exponential dependence for large distances from the shower start vertex and represents mainly the hadronic part of the shower.

The third exponential function in the parametrization allows for an increase of the energy deposition at the end of the shower profile, for example created by knock–on electrons.

For each single hadron shower the parameters are optimized in such a way, that:

$$\int_s^{L_{EMC}} \frac{dE}{dz} dz = \mathrm{E}_{EMC}, \qquad \int_{L_{EMC}}^{L_{HAC1}} \frac{dE}{dz} dz = \mathrm{E}_{HAC1}, \qquad \int_{L_{HAC1}}^{L_{HAC2}} \frac{dE}{dz} dz = \mathrm{E}_{HAC2},$$

with the integration limits $\mathrm{L}_{EMC} = 0.96\lambda$, $\mathrm{L}_{HAC1} = 4.05\lambda$ and $\mathrm{L}_{HAC2} = \mathrm{L}_{HAC1} + 0.377 \cdot (\mathrm{E}_{HAC2})^{0.73}\lambda$, where $\lambda = 25.1$cm for the EMC and 20.7cm for the HAC sections [ZEU89].

The parameters s, b, c and α determine completely the parametrization of the shower profile and the longitudinal centres of shower gravity:

$$z_{EMC}, \qquad z_{HAC1}, \qquad z_{HAC2}$$

can be calculated by integration from this parametrization.

This method can not reproduce the physical details of the longitudinal development of single hadron showers from the three calorimeter measurements available from EMC, HAC1 and HAC2. But it can take into account typical structures of the development of single hadron showers, in particular correlations between the energies deposited in EMC, HAC1 and HAC2, for example simply by energy conservation. Therefore it can handle partially the deviations from the average longitudinal centres of gravity presented in Fig. 5.52.

5.5.4 Determination of the Angle of the Axis of Hadron Showers

The FCAL prototype can be rotated in the horizontal x,z– plane. Figure 5.54 shows a top view of the FCAL prototype rotated in the horizontal plane. The position of the interaction point (IP) similar to that in the ZEUS detector is also indicated. The maximum number of centres of shower gravity (x_i, z_i) available from the calorimeter sections is three (EMC, HAC1, HAC2). At least two centres of gravity are necessary to determine the θ angle by the calorimeter information alone.

In the experiment, also the interaction point can be included in the analysis. The distance between the IP and the FCAL front face is 221cm in z.

The θ angle is determined by:

$$\theta = \arctan(\frac{\Delta x}{\Delta z}) ,$$

with $\Delta x = x_{i+1} - x_i$ and $\Delta z = z_{i+1} - z_i$. If more than two centres of gravity are available a straight line is calculated through the points by a least square fit.

Figure 5.55 illustrates the fractions of energy deposited by a hadron shower in the different towers of EMC, HAC1 and HAC2 created by a 100GeV/c hadron entering the FCAL prototype under a θ angle of 200mrad in the x,z– plane [AND90a].

The centre of gravity is shifted with increasing calorimeter depth, that means from EMC to HAC2, to larger x values.

In the EMC the energy is almost completely contained in one 20cm x 20cm tower, while the energy deposited in HAC1 and HAC2 is spread over at least five towers; a high fraction of energy is seen in the central core of the shower.

The cuts applied on the signals measured in EMC, HAC1 and HAC2 in order to remove statistical fluctuations and the fractions of events removed are summarized in Table 5.4.

The fractions of energy of 30GeV, 75GeV and 100GeV hadron showers deposited in the different calorimeter sections at θ = 0mrad are given in Table 5.5.

For all three energies the relative fractions of deposited energy are very similar: in EMC about 22%, in HAC1 about 62% and in HAC2 about 16%. Correspondingly, the absolute energies deposited for example in HAC2 increase linearly with the hadron energy and at higher energies information is no longer lost by a cut on the energy.

Figure 5.56 shows the fractions of θ angles reconstructed without interaction point from different combinations of calorimeter sections: EMC + HAC1, HAC1 + HAC2 and EMC + HAC1 + HAC2 as a function of the energy of the hadron shower.

For about 20% of the hadron showers at 30GeV the energy is almost completely deposited in the EMC and no θ angle can be determined from the calorimeter information alone. But for all events the θ angle can be determined by using the position of the interaction point.

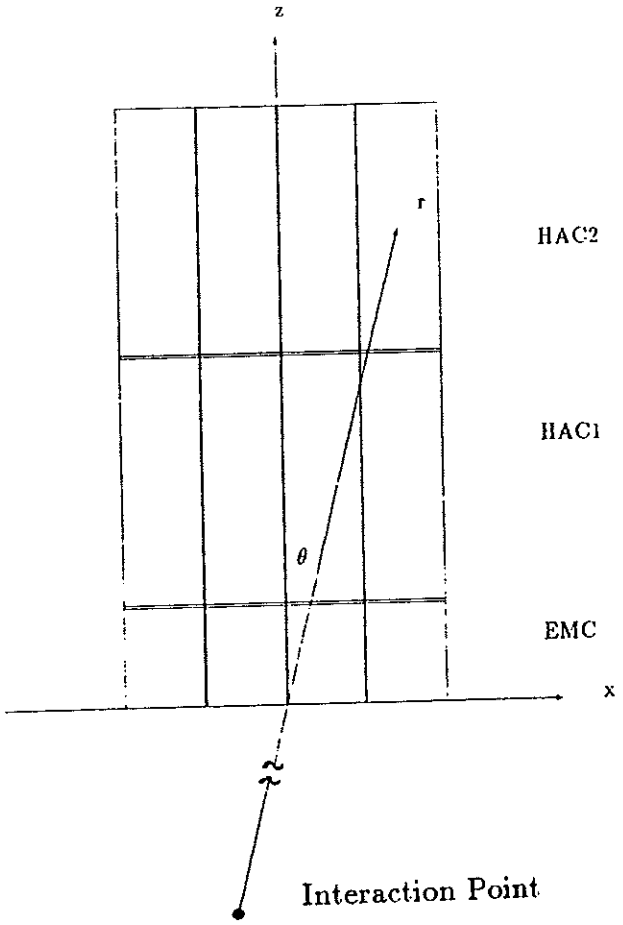

Figure 5.54
Determination of the θ angles of the axis of particle showers with the FCAL prototype at CERN SPS.

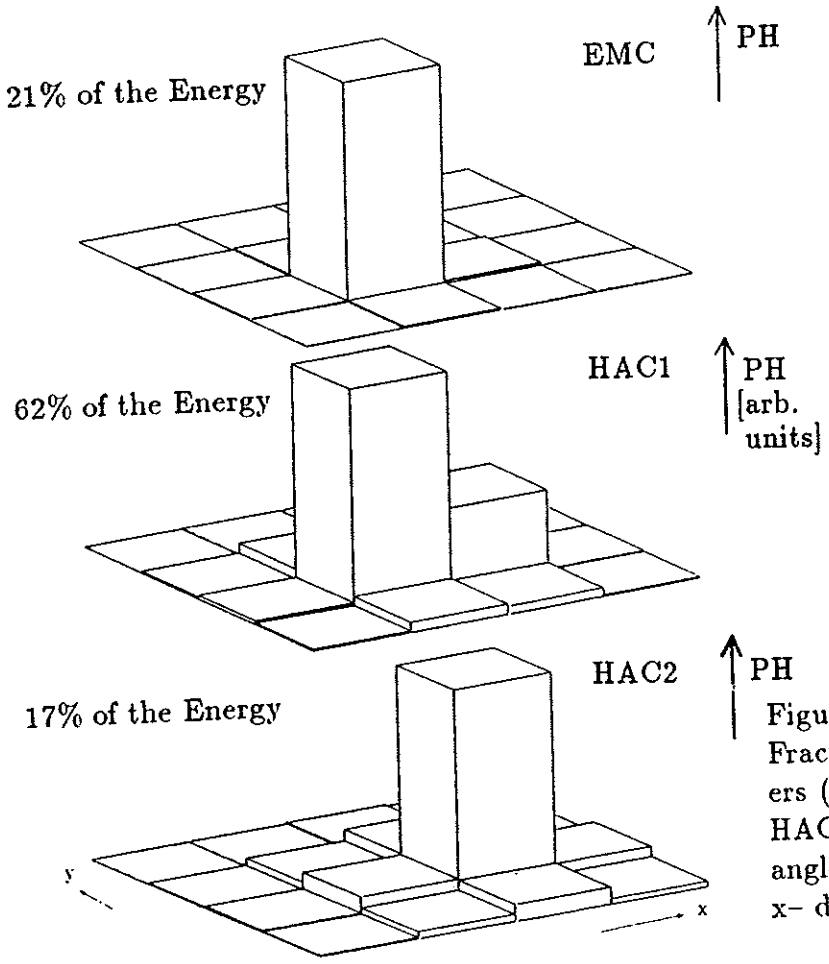

Figure 5.55
Fraction of energy deposited in the towers (20cm x 20cm) of EMC, HAC1 and HAC2 of a 100GeV/c hadron with a θ angle of beam incidence of 200mrad in x- direction.

The θ angles are reconstructed from the centres of shower gravity (x_i, z_i), that means from the transverse centres of gravity (chapter 5.5.2) and the longitudinal centres of gravity (chapter 5.5.3) determined either by method 1 (parametrization of $z_{EMC} = z_{EMC}(E_0, E_{EMC})$, etc...) or by method 2 (parametrization of the longitudinal profiles of single hadron showers, PLSP–algorithm).

Energy [GeV]	Cut_{EMC} [GeV]	Lost Events [%]	Cut_{HAC1} [GeV]	Lost Events [%]	Cut_{HAC2} [GeV]	Lost Events [%]
30	2.5	46.8	2.0	3.1	2.0	59.5
75	2.5	46.1	2.0	0.1	2.0	19.3
100	2.5	44.5	2.0	0.1	2.0	12.4

Table 5.4 Cuts applied on deposited energies and the fractions of events removed by these cuts in EMC, HAC1 and HAC2.

Energy [GeV]	E_{EMC} [%]	E_{EMC} [GeV]	E_{HAC1} [%]	E_{HAC1} [GeV]	E_{HAC2} [%]	E_{HAC2} [GeV]
30	25.8	7.7	61.2	18.4	13.0	3.90
75	21.5	16.1	62.1	46.6	16.5	12.4
100	21.1	21.1	62.0	62.0	16.9	16.9

Table 5.5 Fractions of energy of 30GeV, 75GeV and 100GeV hadron showers deposited in EMC, HAC1 and HAC2.

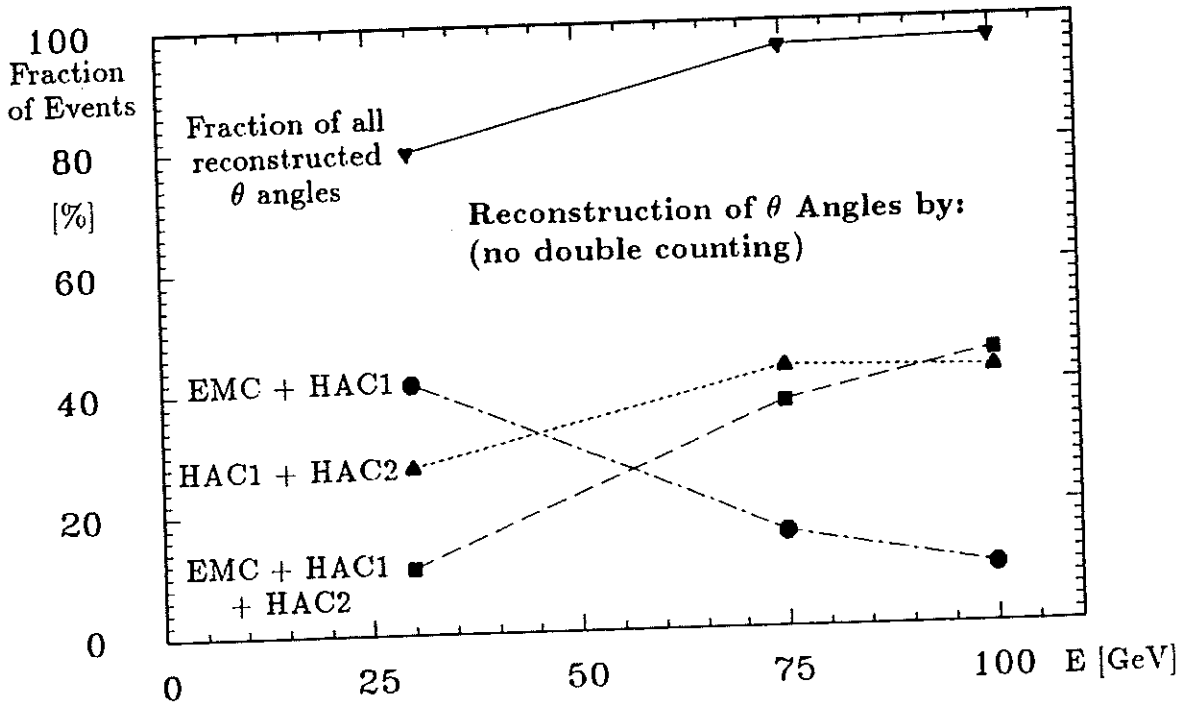

Fig. 5.56 Fractions of θ angles reconstructed from different calorimeter sections as a function of the energy of the hadron shower without interaction point. Each reconstructed θ angle is counted only once.

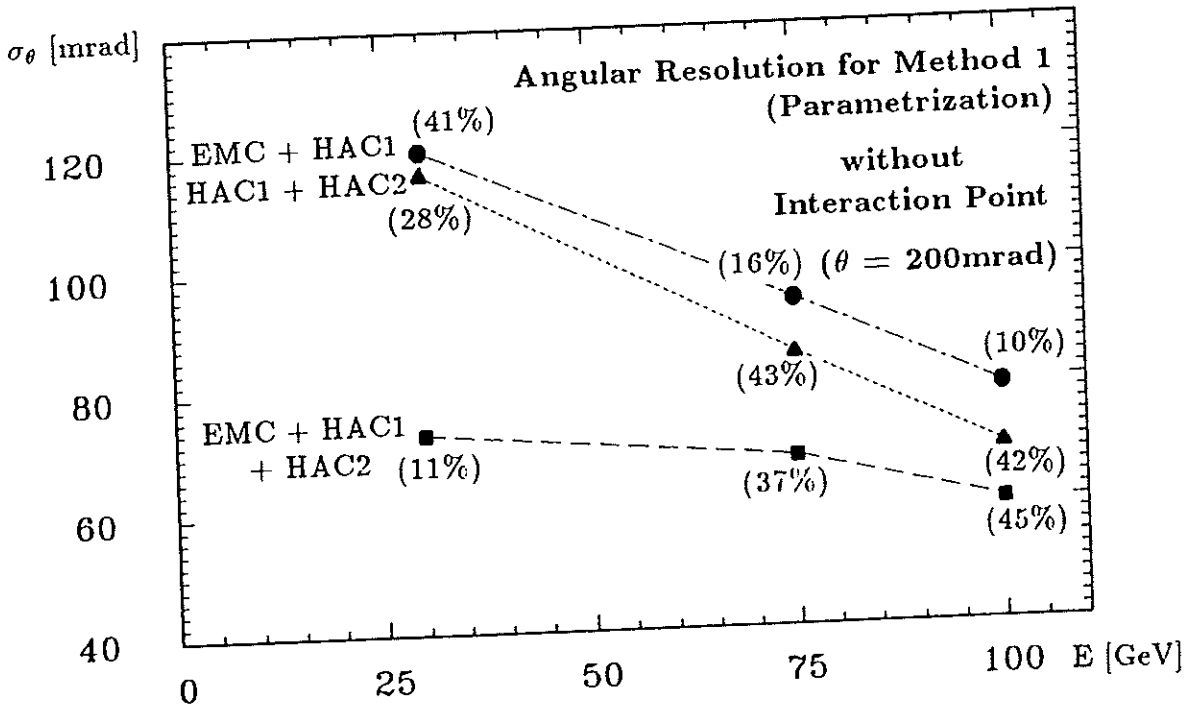

Fig. 5.57 Angular resolution as a function of the energy of the hadron shower determined by method 1 (parametrization) at θ = 200mrad without interaction point. The fractions of hadron showers are indicated in brackets.

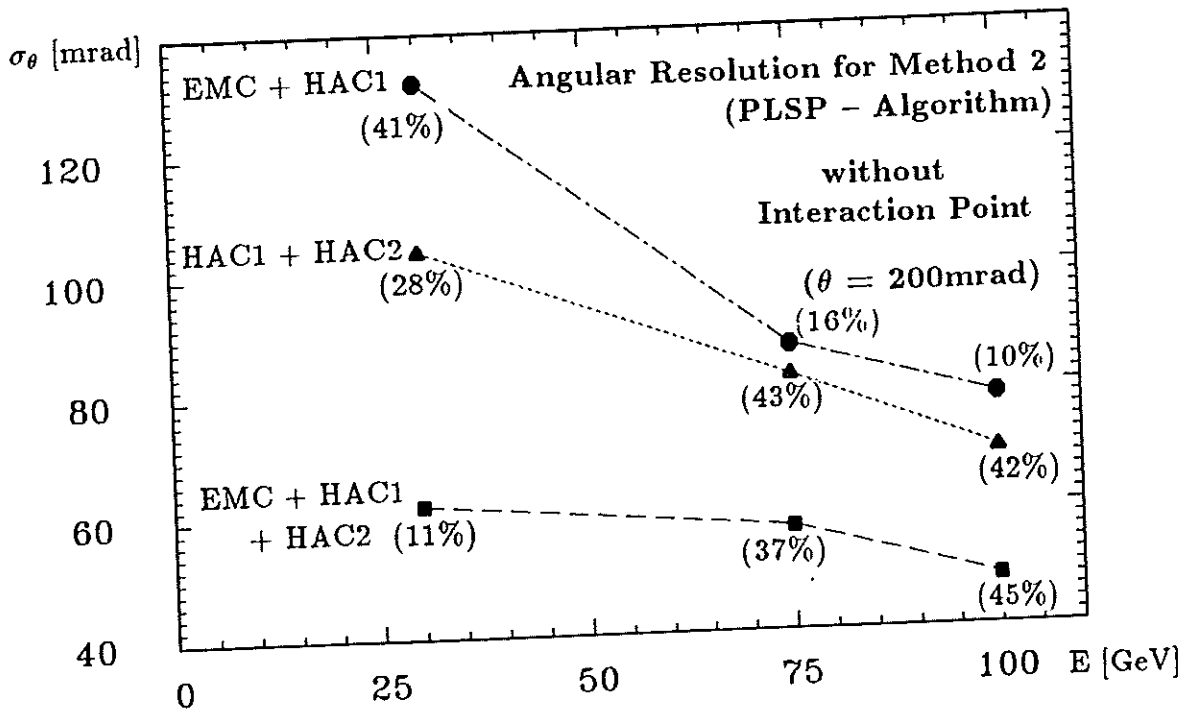

Fig. 5.58 Angular resolution as a function of the energy of the hadron shower determined by method 2 (PLSP–algorithm) at θ = 200mrad without interaction point. The fractions of hadron showers are indicated in brackets.

Figure 5.57 and 5.58 show for comparison the angular resolution at θ = 200mrad as a function of the energy for the longitudinal centres of gravity of showers determined by method 1 (parametrization) and by method 2 (PLSP–algorithm) without interaction point.

The angular resolution improves for both methods with increasing energy due to the fact that more energy is deposited in all three calorimeter sections and therefore statistical fluctuations play only a minor role.

The angular resolution determined by method 2 shows an improvement in comparison to method 1. This is in particular the case if all three centres of gravity are available. At 100GeV the improvement is in the order of 20% for 45% of the hadron showers.

The reconstruction of the particle shower axis by the calorimeter information alone can be very useful e.g. in the data analysis in order to remove particles or jets which don't belong to the primary interaction.

A considerable improvement of the angular resolution is achieved if the interaction point is taken into account to determine the θ angle. This is due to the large lever arm of more than 2m and the small errors on the position of the IP. For method 1 the reconstructed θ angles and the angular resolutions are summarized in Table 5.6 for a θ angle of beam incidence of 200mrad under various conditions. The measurements show very good results for the angular resolution in particular for the combination of EMC + IP. A further improvement of the angular resolution is expected for the combinations of EMC, HAC1 and HAC2 with the IP by a refined reconstruction algorithm aligning the different calorimeter sections against each other as a function of the θ angle.

Figure 5.59 presents the angular resolution of the θ angle reconstructed from EMC + IP, HAC1 + IP and HAC2 + IP as a function of the hadron shower energy at θ = 200mrad.

The angular resolution improves with increasing shower energy and yields the best results for a combination of EMC + IP. At 100GeV an angular resolution of 4.7mrad is achieved for 56% of the hadron showers by reconstruction with EMC + IP. A resolution of 9.8mrad is obtained for the remaining hadron showers by reconstruction with HAC1 + IP. We note that already at θ = 360mrad relatively large corrections have to be introduced due to side leakage of the hadron showers.

These results fulfil or even exceed the requirements on the angular resolution of the ZEUS uranium scintillator calorimeter. In addition an improvement of the position and angular reconstruction can be expected for the final ZEUS calorimeter due to the improved optical readout and better photomultiplier characteristics and an improved calibration in space and time of better than 1% (see chapter 6).

Energy	Reconstruction by	θ angle [mrad]	σ_θ [mrad]	Events [%]
30GeV	EMC + IP	200.0±0.21	6.9	52.3
	HAC1 + IP	200.0±0.27	12.0	95.6
	HAC2 + IP	199.7±0.49	15.1	44.1
	EMC + HAC1 + IP	200.2±0.22	7.1	50.4
	HAC1 + HAC2 + IP	201.1±0.40	11.7	41.5
	EMC + HAC1+2 + IP	200.0±0.67	9.8	10.9
75GeV	EMC + IP	200.3±0.25	5.5	55.2
	HAC1 + IP	201.1±0.37	10.7	99.0
	HAC2 + IP	199.3±0.46	12.1	80.9
	EMC + HAC1 + IP	199.3±0.26	5.6	50.4
	HAC1 + HAC2 + IP	200.7±0.40	10.2	78.9
	EMC + HAC1+2 + IP	200±0.36	6.4	37.3
100GeV	EMC + IP	199.2±0.27	4.7	55.5
	HAC1 + IP	202.0±0.42	9.8	99.1
	HAC2 + IP	198.4±0.46	10.1	87.7
	EMC + HAC1 + IP	199.1±0.27	4.7	54.0
	HAC1 + HAC2 + IP	202.2±0.45	9.9	86.8
	EMC + HAC1+2 + IP	199.2±0.39	6.3	45.1

Table 5.6 Angular resolution for 30GeV, 75GeV and 100GeV hadron showers at θ=200mrad for various combinations of calorimeter information plus interaction point.

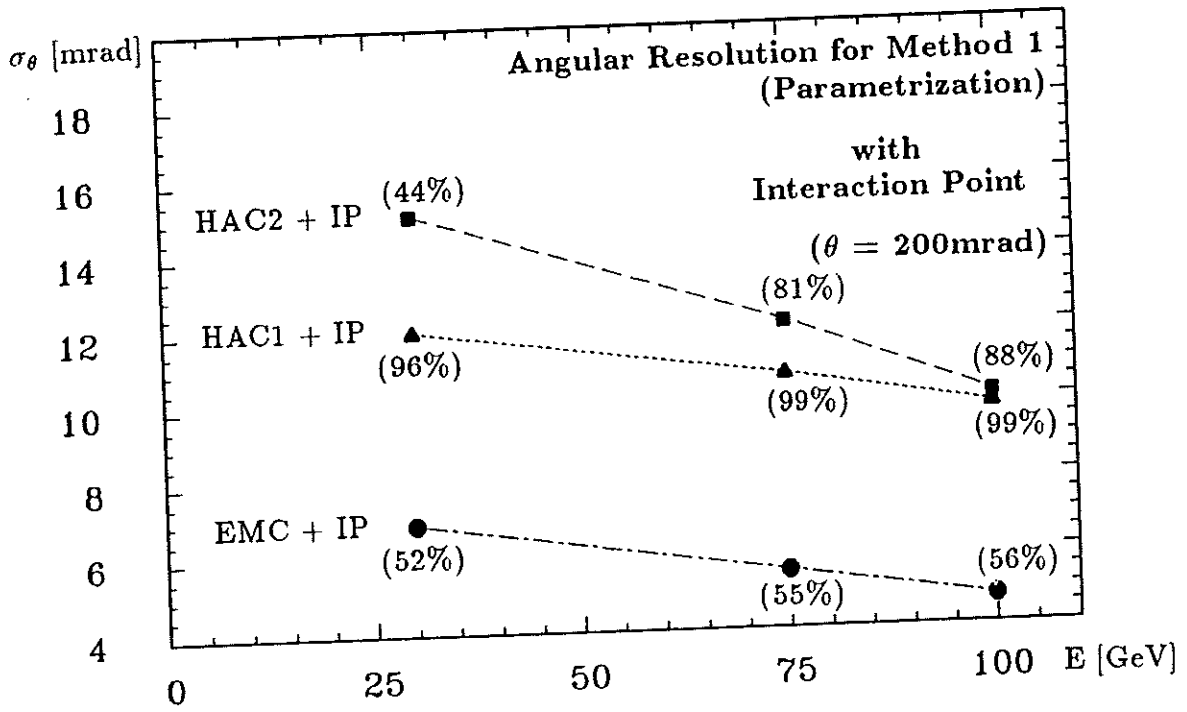

Fig. 5.59 Angular resolution as a function of the energy of the hadron shower at θ = 200mrad for combinations of EMC + IP, HAC1 + IP and HAC2 + IP. The fractions of hadron showers are indicated in brackets.

Chapter 6

Calibration of the ZEUS Uranium Scintillator Calorimeter

6.1 Motivation for a Precise Calibration ($\lesssim$1%) at HERA

Precise calibration is as important for HERA physics as is an excellent energy resolution for hadrons and jets. Figure 6.1 illustrates the difference between the true and the measured value. For the true physical quantity of a particle or jet, for example the energy E_0, a distribution is measured with a mean value <E> and an approximately Gaussian shape with a standard deviation σ_E. A perfect calibration is achieved if E_0 = <E>.

When measuring structure functions, calibration errors can fake interesting physics. Figure 2.26c shows the influence of a contact interaction, created by a quark substructure, with $\Lambda_H = 1$ TeV on the structure function [CAS83]. Unfortunately, similar deviations from the standard model can be faked by calibration errors. Figure 6.2 presents the influence of calibration errors on the cross section as a function of Q^2. It demonstrates that an absolute calibration of the calorimeter at the 1% level is required [ZEU85].

6.2 Concept of the Calorimeter Calibration

The design and production of the calorimeter were aimed at ensuring that the ratio $\frac{(Measured\ Signal)}{(Deposited\ Particle\ Energy)}$ is independent of position and time at the level of 1% [AND91], [KLA91], [KRÜ91].

To achieve this aim the calorimeter has to fulfil the following characteristics: uniform response as a function of the position in each calorimeter module from tower to tower, uniformity from module to module, signal stability in time and linearity of the signal with the particle energy.

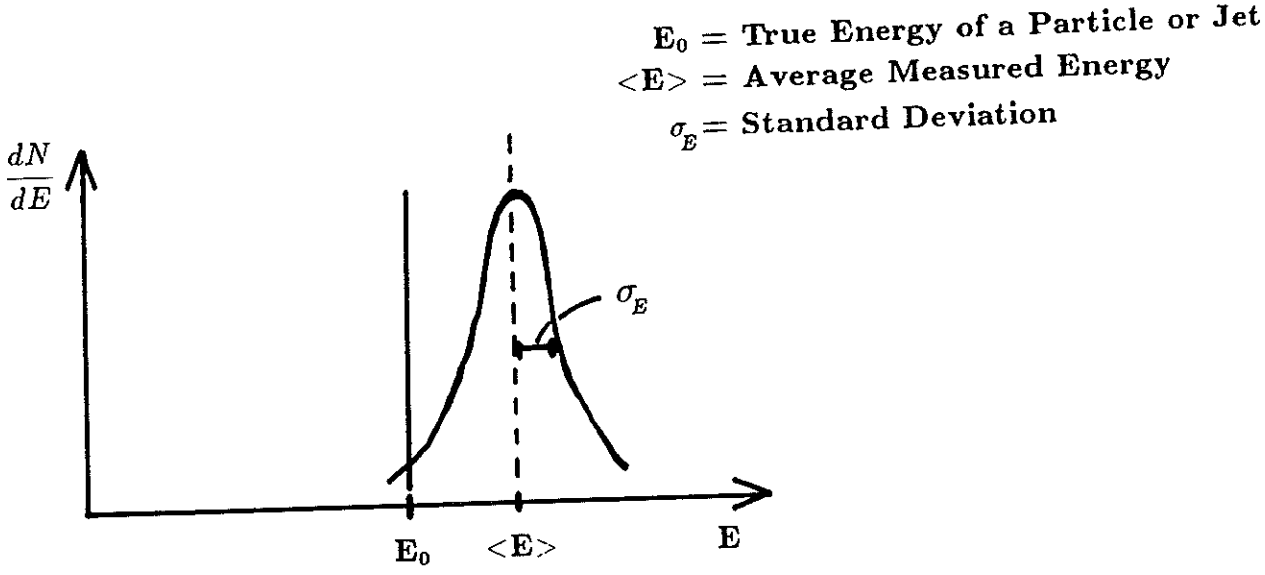

Fig. 6.1 Energy measurement with a calorimeter; E_0 = true energy of the incoming particle or jet, <E> = average value of the measured energy distribution, σ_E = standard deviation ($\hat{=}$ resolution); The calibration is perfect if E_0 = <E>.

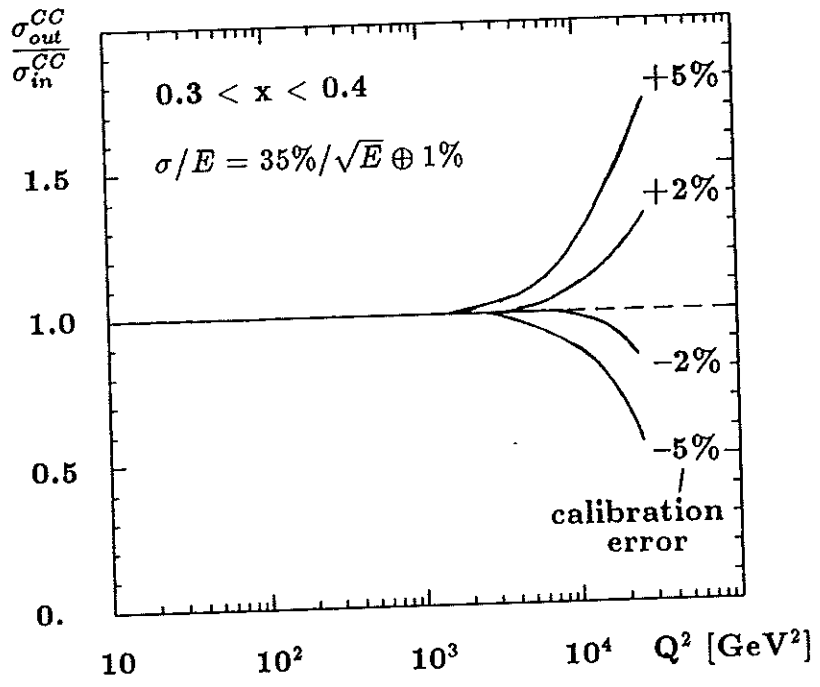

Fig. 6.2 Influence of the calibration error on the cross section, where σ_{in} and σ_{out} denote the cross section without and with calibration error.

In the ZEUS calorimeter the following calibration methods are used:

Uranium Radioactivity	–	the source of the signal is distributed in the calorimeter and is stable in space and time;
Beam Particles	–	for the absolute energy calibration use the ratio $\frac{(particle\ energy)}{(uranium\ signal)}$ (measured at CERN, FNAL, and with cosmic muons);
^{60}Co – Source Scans	–	quality control on local uniformity;
Light Flasher – System	–	linearity of photomultipliers and readout electronics;
Charge Injectors	–	balance of gains of all electronic channels;
Physics Reactions	–	particles with known energies measured in ZEUS.

Figure 6.3 illustrates the combination of the different calibration tools in the ZEUS calorimeter and the readout.

The light flasher system consists of a laser system which provides light flashes via light fibres to all photomultipliers. The complete readout system from the photomultipliers onwards can be checked by this system. The linearity up to the highest signals, the timing of all channels and the photoelectron yield can be determined [MIT90], [BAM90].

The charge injectors are coupled to the front–end cards to check the readout chain from the front–end cards onwards and to balance the gain of all electronic channels.

In the following section the influence of mechanical tolerances on the calorimeter calibration is discussed. Then the calibration with the radioactivity of the uranium and uniformity measurements with a pointlike radioactive source for quality control on local uniformity are presented. At the end of this chapter results on the beam calibration of FCAL and RCAL modules at the CERN SPS are presented and discussed.

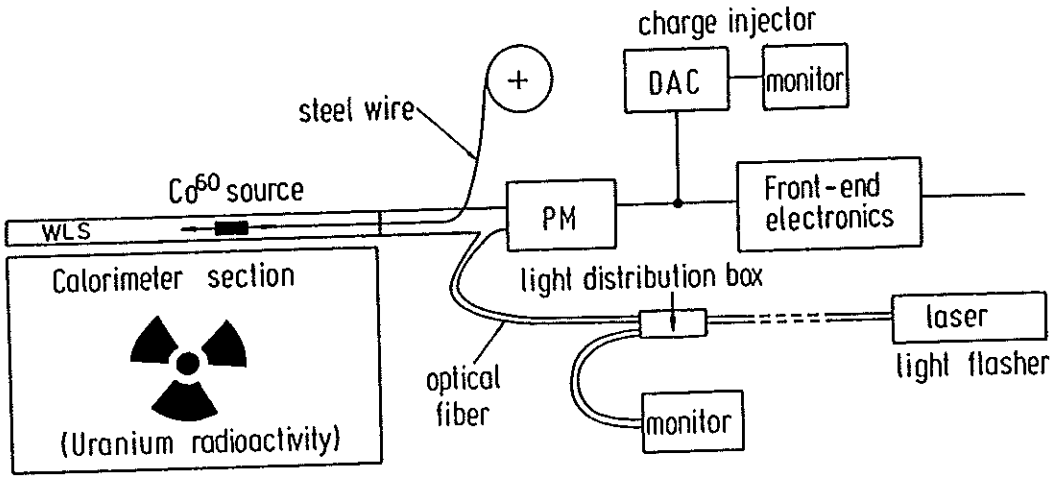

Fig. 6.3 Sketch of the various calibration tools in the ZEUS calorimeter.

6.3 Influence of Mechanical Tolerances on the Calorimeter Calibration

6.3.1 Uranium Plates – Tolerances

The uranium plates have been rolled by MSC in the USA. For FCAL and RCAL they have been clad with a steel foil at CRNL in Canada. The plates have maximum dimensions of 4600mm x 200mm x 3.3mm and weight of 60kg. The uranium plate thickness was measured with a precision of 0.02mm.

An increase of the DU plate thickness by 1% increases the particle energy deposition in the uranium approximately by 1%, thus about 1% less energy is seen in the scintillator and the signal from particles is reduced by about 1%. But there is no significant influence on the UNO signal [AND91].

This shows that a 1% thickness tolerance averaged over several uranium plates in the calorimeter is allowed (0.035mm). This precision has been achieved by collaboration with industry and requiring a high quality control standard.

Figure 6.4 presents the thickness distributions of the uranium plates of different calorimeter sections with an allowed tolerance per plate of ±0.15mm for FEMC and ±0.2mm for FHAC1. Averaged over several uranium layers (e.g. 25 plates in 1λ) the desired tolerance is achieved.

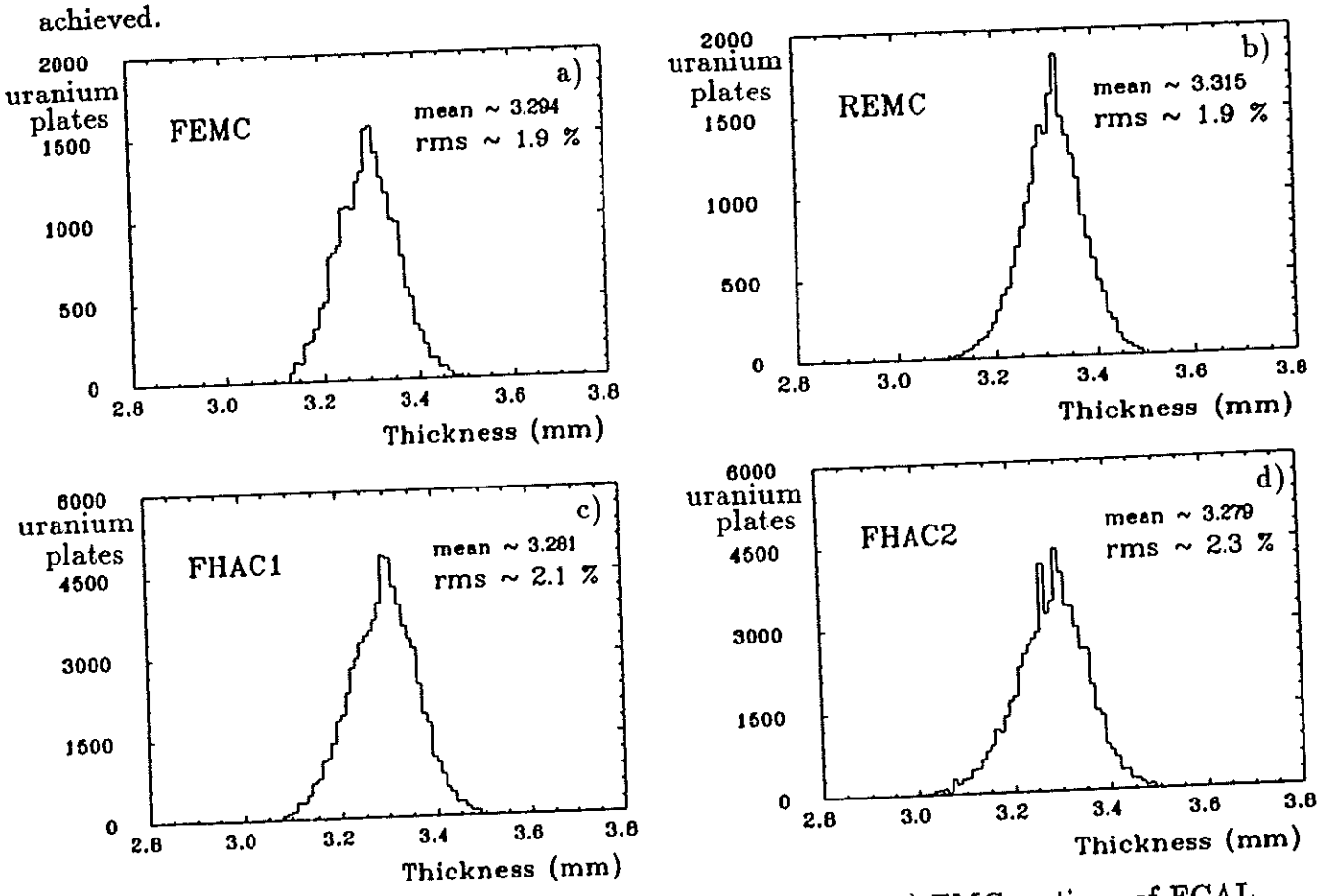

Fig. 6.4 Thickness distributions of uranium plates for a) EMC sections of FCAL, b) EMC sections of RCAL, c) HAC1 and d) HAC2 sections of FCAL.

6.3.2 Scintillator Plates – Tolerances

The scintillator plates have been manufactured by Kyowa in Japan. They have been cut, polished and wrapped at DESY. The final scintillator plates have dimensions of 200 (50)mm x 200mm x 2.6mm (≈150000 plates). Their thickness and light yield have been measured.

In a scintillator plate which is 1% thicker than nominal, approximately 1% more particle energy is deposited in the scintillator; thus the measured signal increases by about 1%. In contrast, the increase of the UNO signal is significantly smaller [AND91]. This shows that a thickness tolerance of about 1% averaged over several scintillator plates in the calorimeter is allowed (0.025mm).

The thickness distributions of scintillator plates selected for the different sections of the FCAL are shown in Fig. 6.5. The distribution of the FEMC (a) tiles shows an rms of 1.1%, FHAC1 (c) 2.4% and FHAC2 (d) 2.5%. The allowed thickness tolerances per plate have been ±0.1mm for FEMC and ±0.2mm for FHAC1 and FHAC2.

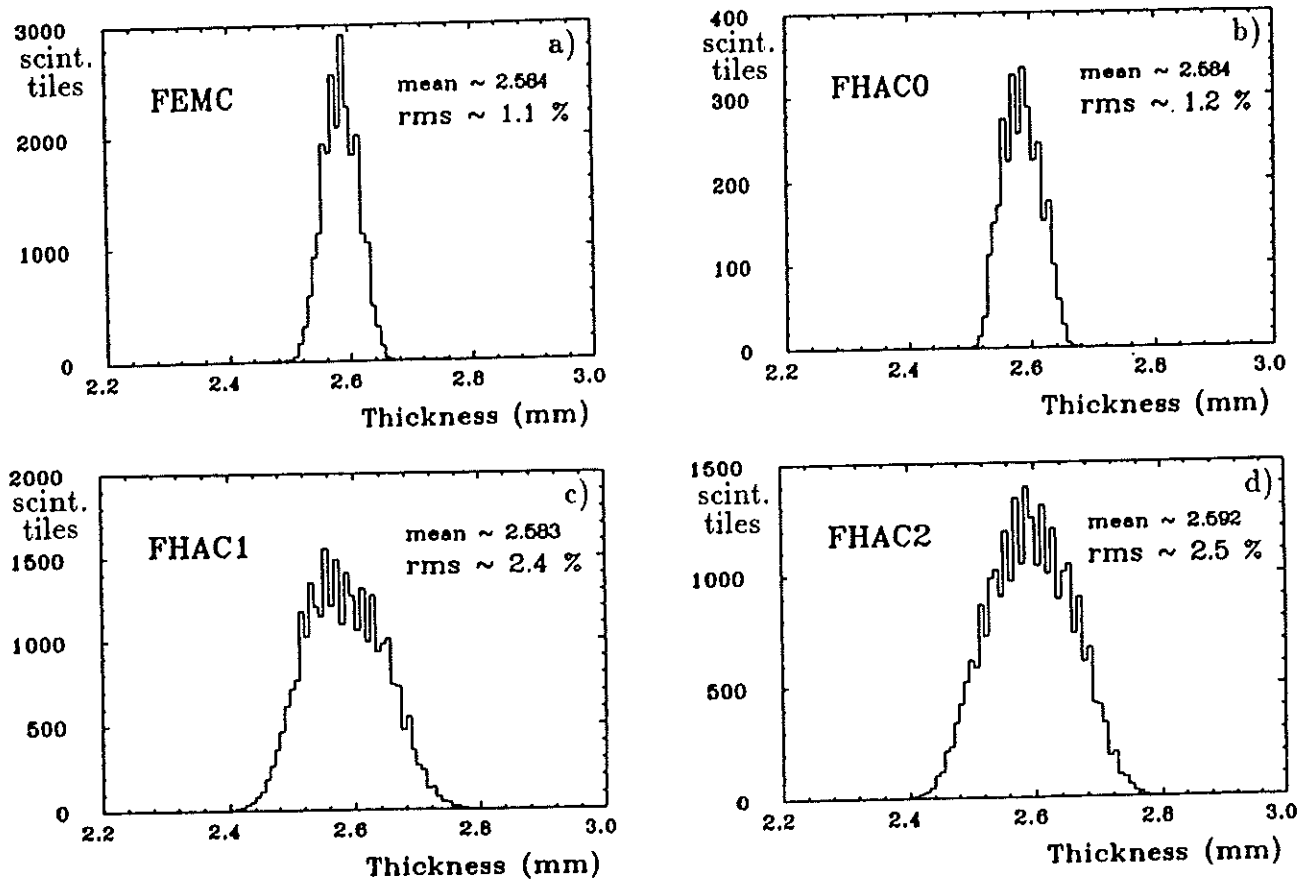

Fig. 6.5 Thickness distributions for samples of scintillator tiles belonging to a) EMC, b) HAC0, c) HAC1 and d) HAC2 sections of FCAL.

6.3.3 Influence of Mechanical Tolerances on the Calibration

A detailed discussion of the influence of scintillator, uranium and Fe–cladding thickness tolerances on the calorimeter calibration with respect to the calibration using the radioactivity of the uranium is presented in [AND91].

The electron sampling fraction can be expressed by:

$$e = \left(\frac{e}{mip}\right)\frac{\epsilon_s s}{\epsilon_u u + \epsilon_c c + \epsilon_s s} \quad ,$$

with e/mip = the ratio between the sampling fractions of electrons (4%) and minimum ionizing particles (6.6%), u, c, s = the nominal sampling thicknesses of uranium, cladding and scintillator (3.3mm, 2 x 0.2mm and 2.6mm) and ϵ_u, ϵ_c, ϵ_s the corresponding energy losses dE/dx (20.7MeV/cm, 11.7MeV/cm and 2.0MeV/cm).

The effect of the thickness variations, Δs, Δu, Δc, on the electron response is given by:

$$\frac{\Delta e}{e} = f_s^e\frac{\Delta s}{s} + f_u^e\frac{\Delta u}{u} + f_c^e\frac{\Delta c}{c} \quad ,$$

with f_s^e= 0.93, f_u^e=–0.87 and f_c^e=–0.06 for a single layer in the EMC sections (Table 6.1a).

The radiation dose rate of a uranium plate behind an absorber of thickness t can be described by [KLA87]:

$$Dose(t) \sim Ae^{-t/a} + Be^{-t/b} \quad ,$$

with A $\approx$ 1.95mGy/h and B $\approx$ 0.05mGy/h, a_s = 1.24mm and b_s = 36mm for scintillator and a_c = 0.17mm and b_c = 6.5mm for iron.

After integration over the dose rate the effect of thickness variations in the signal of the uranium radioactivity (UNO) can be expressed for single layers by:

$$\frac{\Delta(\mathrm{UNO})}{\mathrm{UNO}} = f_s^{uno}\frac{\Delta s}{s} + f_c^{uno}\frac{\Delta c}{c} \quad ,$$

with f_s^{uno}= 0.40, f_c^{uno}=–0.99 and $f_u^{uno} \approx$ 0.05 for the EMC sections.

Assuming that the deviations from the nominal value are uncorrelated between different plates of the calorimeter, the effect of the thickness tolerances on e/UNO for a complete EMC section can be determined by:

$$\frac{\Delta(\mathrm{e/UNO})}{\mathrm{e/UNO}} = F_s\frac{\Delta s}{s} \oplus F_u\frac{\Delta u}{u} \oplus F_c\frac{\Delta c}{c} \quad with \quad F_s = \left[\sum_i (f_s^e\epsilon_i - f_s^{uno}\epsilon_{uno})^2\right]^{1/2} \quad ,$$

where F_s= 0.21, F_u= 0.25 and F_c= 0.18 at 10GeV and approximately energy independent.

With the measured thickness tolerances (Δt/t) presented in the previous sections, a value of about 0.6% is expected for Δ(e/UNO).

The influence of thickness tolerances for EMC and HAC sections on the different ratios e/UNO, h/UNO and μ/UNO are summarized in Table 6.1a and 6.1b. For the EMC (HAC) sections Δ(h/UNO) $\approx$ 0.4% (0.3%) and $\Delta(\mu/\mathrm{UNO}) \approx$ 0.3% (0.2%) are calculated.

These estimations are in agreement with the experimental results obtained from the beam calibration presented in chapter 6.6.

Ratio	EMC	f^e	f^{uno}	F	$\Delta t/t$	$\Delta(e/UNO)$
e/UNO	s	+0.93	+0.40	0.21	1.1%	0.2%
	u	−0.87	+0.05	0.25	1.9%	0.5%
	c	−0.06	−0.99	0.18	1.8%	0.3%
	total					0.6%

Ratio	EMC	f^h	f^{uno}	F	$\Delta t/t$	$\Delta(h/UNO)$
h/UNO	s	+0.93	+0.40	0.10	1.1%	0.1%
	u	−0.87	+0.05	0.18	1.9%	0.3%
	c	−0.06	−0.99	0.18	1.8%	0.3%
	total					0.4%

Ratio	EMC	f^μ	f^{uno}	F	$\Delta t/t$	$\Delta(\mu/UNO)$
μ/UNO	s	+1.00	+0.40	0.12	1.1%	0.1%
	u	–	+0.05	0.01	1.9%	0.0%
	c	–	−0.99	0.19	1.8%	0.3%
	total					0.3%

Table 6.1a Influence of thickness tolerances for EMC sections on the ratios: e/UNO, h/UNO and μ/UNO.

Ratio	HAC	f^h	f^{uno}	F	$\Delta t/t$	$\Delta(h/UNO)$
h/UNO	s	+0.94	+0.53	0.05	2.4%	0.1%
	u	−0.82	+0.13	0.11	2.1%	0.2%
	c	−0.11	−1.53	0.16	1.3%	0.2%
	total					0.3%

Ratio	HAC	f^μ	f^{uno}	F	$\Delta t/t$	$\Delta(\mu/UNO)$
μ/UNO	s	+1.00	+0.53	0.05	2.4%	0.1%
	u	–	+0.13	0.01	2.1%	0.0%
	c	–	−1.53	0.17	1.3%	0.2%
	total					0.2%

Table 6.1b Influence of thickness tolerances for HAC sections on the ratios: h/UNO and μ/UNO.

6.4 Calibration with the Radioactivity of the Uranium

Many factors that affect the calorimeter signal cancel in the ratio $\frac{(particle\ signal)}{(uranium\ signal)}$.

The uranium signal (UNO) from the radioactivity of the depleted uranium (98.1% ^{238}U, 0.2% ^{235}U, 1.7% Nb) of the ZEUS calorimeter is used for:

1) monitoring of the photomultipliers (a total of 12000),
2) intercalibration of the calorimeter sections and
3) the absolute calibration scale.

Figure 6.6 presents the main decay lines of the decay chain of $^{238}_{92}$U into $^{234}_{92}$U, where the numbers in brackets indicate the energy in MeV of the emitted particles. The uranium signal is composed of β particles with a maximum energy of 2.3 MeV and γ rays with energies in the range from 10 to 1000 keV. The α particles (4.2 MeV) are absorbed in the cladding.

At the surface of 3mm thick uranium plates 2600counts/(cm^{2}s) have been measured for β particles above 10keV, with an average energy of 200keV, and 442counts/(cm^{2}s) for γ rays above 60keV, with an average energy of 500keV [PEG85].

Due to the large fraction of low energy electrons the radiation dose rate is reduced by about 70% after 0.2mm Fe–cladding and by about 90% after 0.4mm. Tolerances of 2μm in the thickness of the cladding change the signal by about 1%. Therefore Fe–foils have been selected for the cladding with thickness tolerances of 1–2μm.

Because of the long lifetime of uranium nuclei ($4.5 \cdot 10^9$y), the radioactivity of the uranium yields an extremely stable signal for the calibration of the calorimeter.

At the beginning of data taking the high voltages of the photomultipliers are set by the UNO signal to give a specified signal.

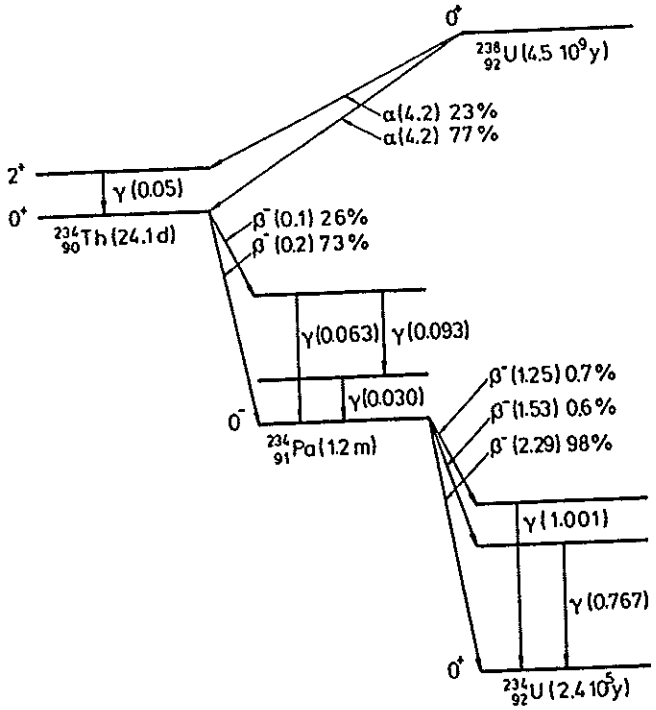

Fig. 6.6 Decay chain of $^{238}_{92}U$ into $^{234}_{92}U$, including only the main decay lines and indicating the energy in MeV of the emitted particles.

6.5 Uniformity Measurements with a Pointlike Radioactive Source

A pointlike radioactive source (^{60}Co, 2 mCi) with a length of 1mm and a diameter of 0.7mm is moved under computer control along the tower structure of a module and the calorimeter signal is measured. From this measurement local information is gained on: each scintillator plate, the calorimeter uniformity along the wavelength shifter and on stacking or installation errors [AND91], [KRÜ91], [GLO91].

The measurement device is described in Fig. 6.7. A trolley is installed on top of the front face of an FCAL or RCAL module, which is placed on its backframe. At each tower position a ^{60}Co – source is moved along the tower structure while the calorimeter signal is measured. Tubes have been installed inside the calorimeter modules, through which ^{60}Co – sources can be moved along the wavelength shifters also when the calorimeter is completely installed in the ZEUS detector.

Figure 6.8 shows the ratio of $\frac{(source\ signal)}{(uranium\ signal)}$ versus the source position along an FEMC section. For each single scintillator plate a separate signal is measured. Two large dips are observed in the FEMC, which correspond to the positions of the two gaps reserved for the silicon detectors (HES).

A corresponding scan with the ^{60}Co – source along an FHAC section, consisting of 80 scintillator plates, is presented in Fig. 6.9. The uniformity over the whole FHAC tower is within a few %.

Figure 6.10 shows a scan over an FHAC section with a large dip in the plateau region. A plastic strip was found between the scintillator plates and the wavelength shifter. After removing the plastic strip the uniformity of the FCAL section was in good shape.

All FCAL and RCAL modules have been checked by this procedure. Problems due to stacking or installation errors were found and have been repaired.

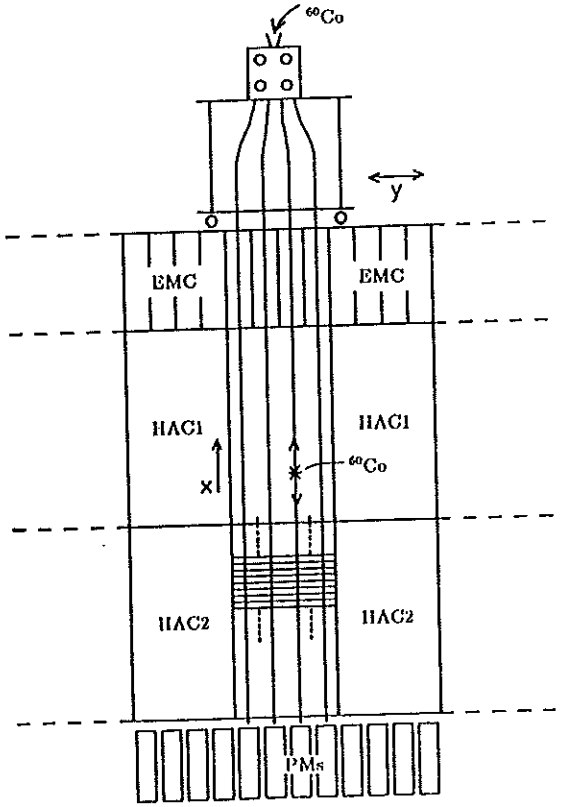

Figure 6.7
View of the ^{60}Co – source measurement device for quality control on local uniformity.

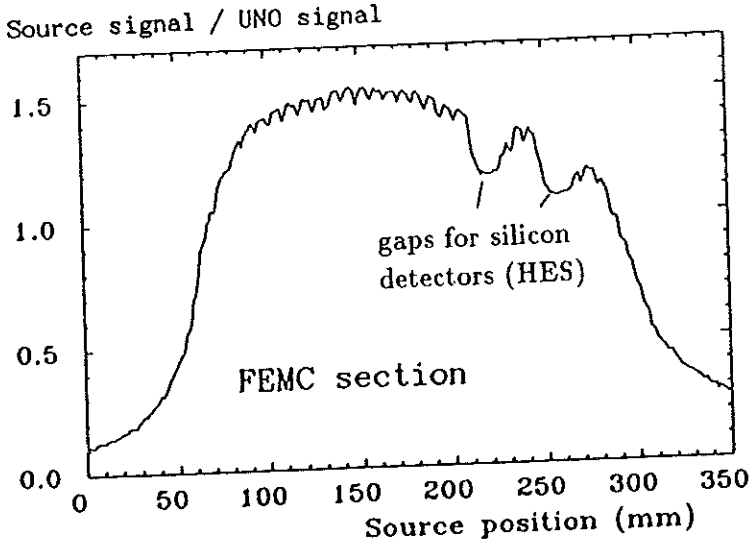

Figure 6.8
Calorimeter scan with a Co^{60} – source along an FEMC section. The source signal is given in units of the UNO signal.

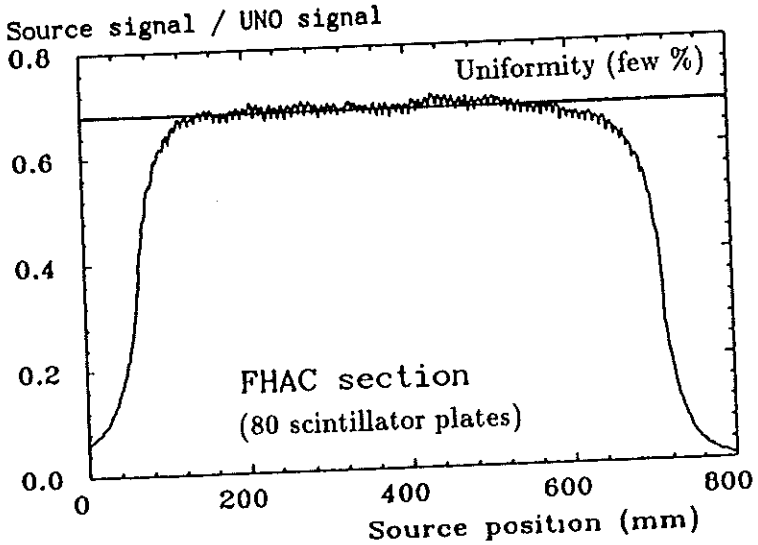

Figure 6.9
Calorimeter scan with a Co^{60} – source along an FHAC section. The source signal is given in units of the UNO signal.

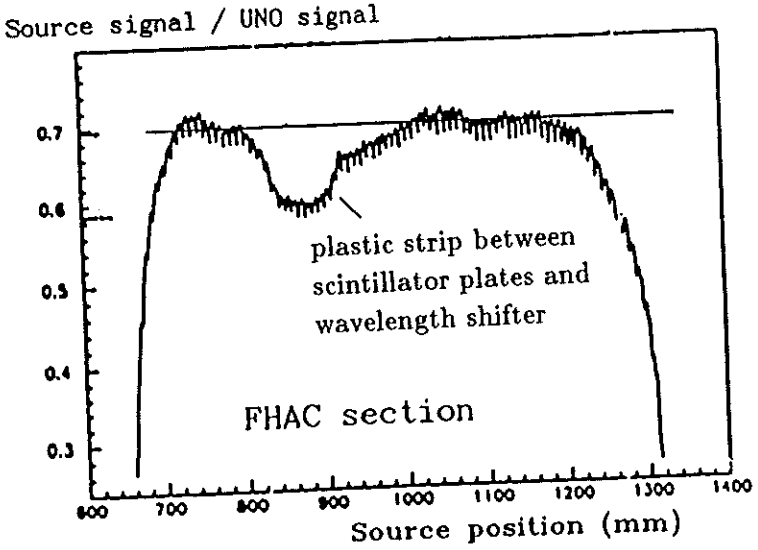

Figure 6.10
Calorimeter scan with a Co^{60} – source along an FHAC section. The dip disappeared after a plastic strip was removed, which was found between the scintillator plates and the wavelength shifter.

6.6 Beam Calibration of Calorimeter Modules at the CERN SPS

6.6.1 The Experimental Set Up for the Beam Calibration

The beam calibration of FCAL and RCAL modules was performed at the CERN SPS in the X5 beam line (West–Hall). Electrons, hadrons and muons were available in the momentum range from 15GeV/c to 110GeV/c.

A sketch of the calibration stand is shown in Fig. 6.11. An FCAL module with a weight of 12t and a length of 5m is bolted in horizontal position on top of the calibration stand [AND91]. It can be moved under computer control in the xy– plane and the total front face of the calorimeter module can be scanned with beam particles. A picture of the calibration stand is presented in Fig. 6.12.

The complete DAQ system is sketched schematically in Fig. 6.13. The movement of the test stand and the HV of the photomultipliers are controlled by the Slow Control Tasks installed on a 68020 microprocessor, which can be accessed from the main computer, a MicroVax 3600.

The readout electronics consists of a shaping–sampling–pipelining scheme [SIP89], [HER91], [AND91]. The PM signals are integrated and shaped such that the rise and fall times are longer than 96ns. The pulse is then sampled in steps of 96ns and the samples are stored for digitization (Fig. 6.14). The data from events selected by the trigger can be picked up inside an analog pipeline and transferred from the analog pipeline to a buffer. The pipelines and buffers are integrated micro electronics which are part of the front–end cards.

Each front–end card contains the readout for 12 channels (PMs). The signal of each PM is split into 4 parts described in Fig. 6.15. One channel for the measurement of the UNO signal (I_{UNO}), one channel with 'high gain' (Q_H) for the range from 0 to 20GeV/c, one with 'low gain' (Q_L) up to 400GeV/c and one channel for the trigger. The effective dynamic range is equivalent to 16.5 bits for a precise measurement from mips up to the highest expected signals.

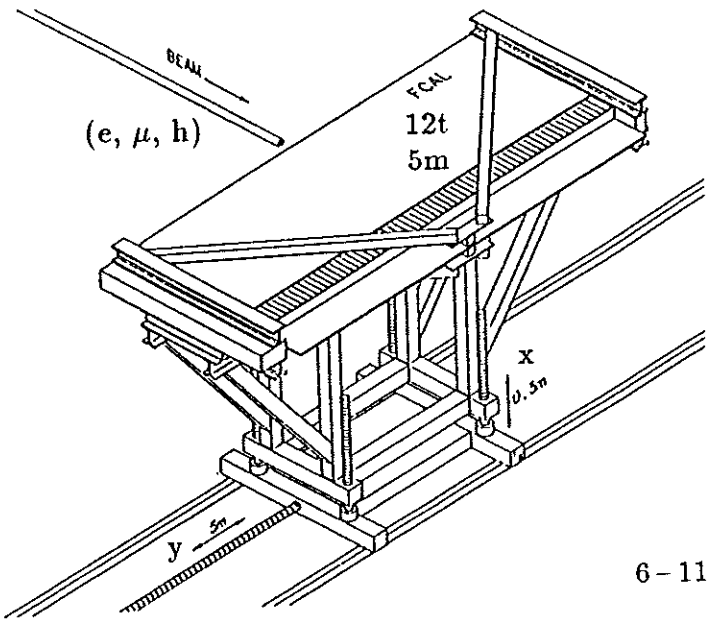

Figure 6.11
Sketch of the movable calibration stand with an FCAL module in horizontal position for testing.

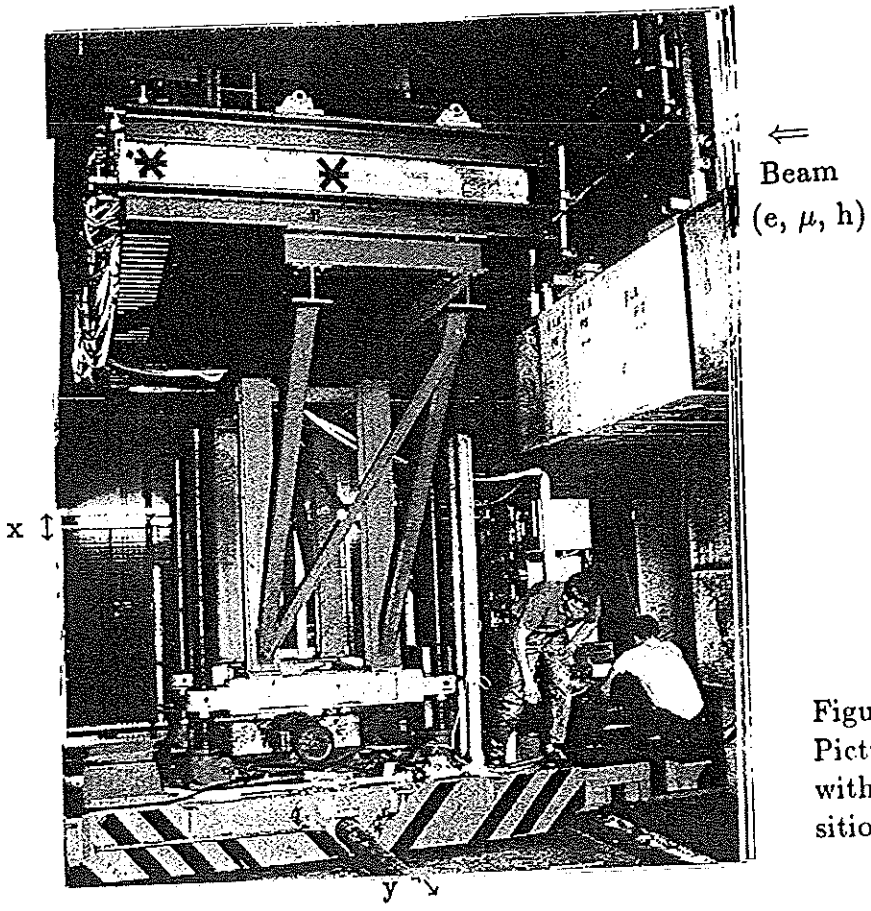

Figure 6.12
Picture of the movable calibration stand with an FCAL module in horizontal position for testing.

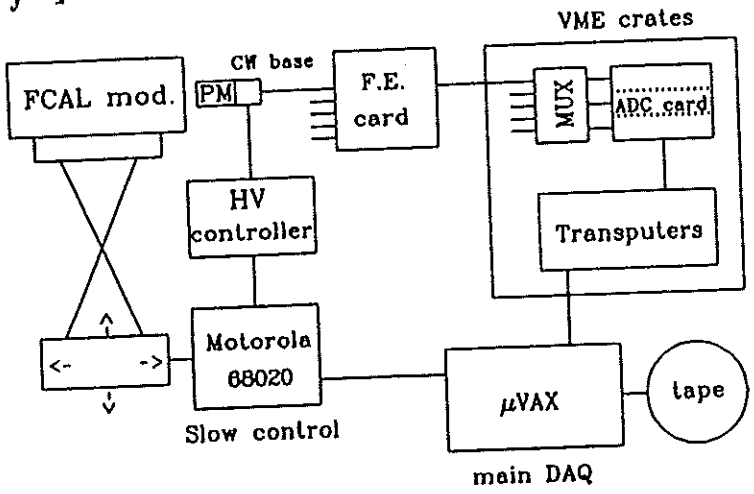

Fig. 6.13 Schematics of the data acquisition setup.

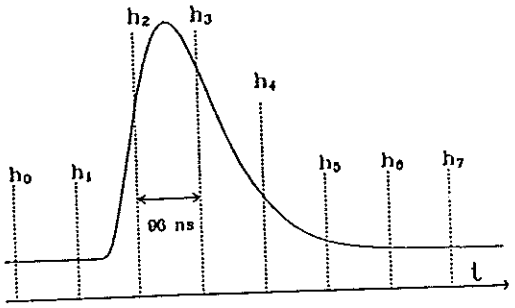

Figure 6.14
Pulse after shaper with 8 samples.

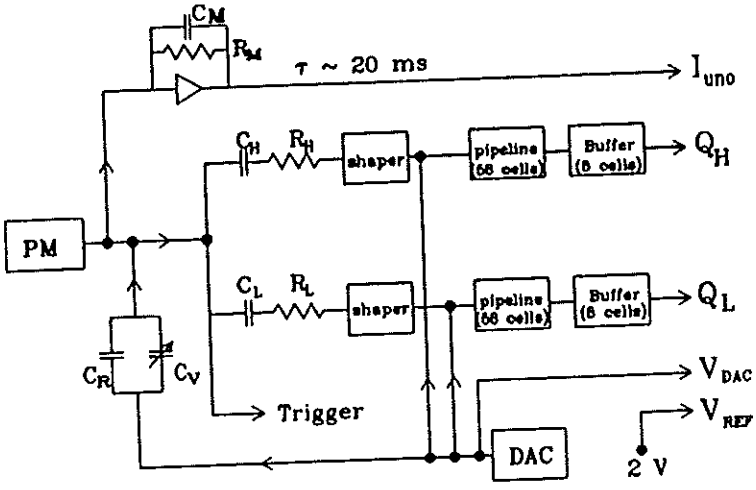

Figure 6.15
Schematics of a front-end card.

6.6.2 General Experimental Results

In this section a selection is presented of important general experimental results gained on the final FCAL and RCAL modules tested at CERN.

Energy scans have been performed with electrons in the momentum range from 15GeV/c to 110GeV/c. The deviation from linearity is less than 1% for FCAL1 and up to 2% for RCAL1 (Fig. 6.16). The energy resolution of electrons measured with FCAL1 and RCAL1 is about $17.5\%/\sqrt{E}$ and degrades slightly with increasing momentum to $19\%/\sqrt{E}$ at 100GeV/c.

The vertical (x) and horizontal (y) positions of the module installed on top of the calibration stand w.r.t. the beam axis were determined by 15GeV/c electron scans with an accuracy of $\Delta x \approx \pm 1$mm and $\Delta y \approx \pm 3$mm (Fig. 6.17).

The uniformity of the modules in the horizontal direction was measured with 15GeV/c electrons with perpendicular incidence on the calorimeter. Figure 6.18 shows the results of the uniformity scans for FCAL1 and RCAL1. The dips every 5cm in module FCAL1 are in the order of 4% due to the gaps of about 0.5mm between the scintillator tiles. With smaller beam dimensions within 300μm the dips increase to 10%. In module RCAL1 similar dips of about 7% are observed every 10cm (Fig. 6.18b). But as pointed out already in chapter 5.3 in the real detector the incident particles will have angles larger than 40mrad and the dips will be essentially smeared out.

Further results are the light yield for the FEMC sections of about 110 photoelectrons/GeV /PM and for the REMC sections of about 140 photoelectrons/GeV/PM corresponding to 1.4 and 1.7 p.e./mip/layer/PM respectively [AND91], [KRÜ89b].

The time resolution for electrons is better than 1ns above 15GeV/c and degrades at lower momenta due to noise (Fig. 6.19). The time resolution for muons is about 4ns in the EMC sections.

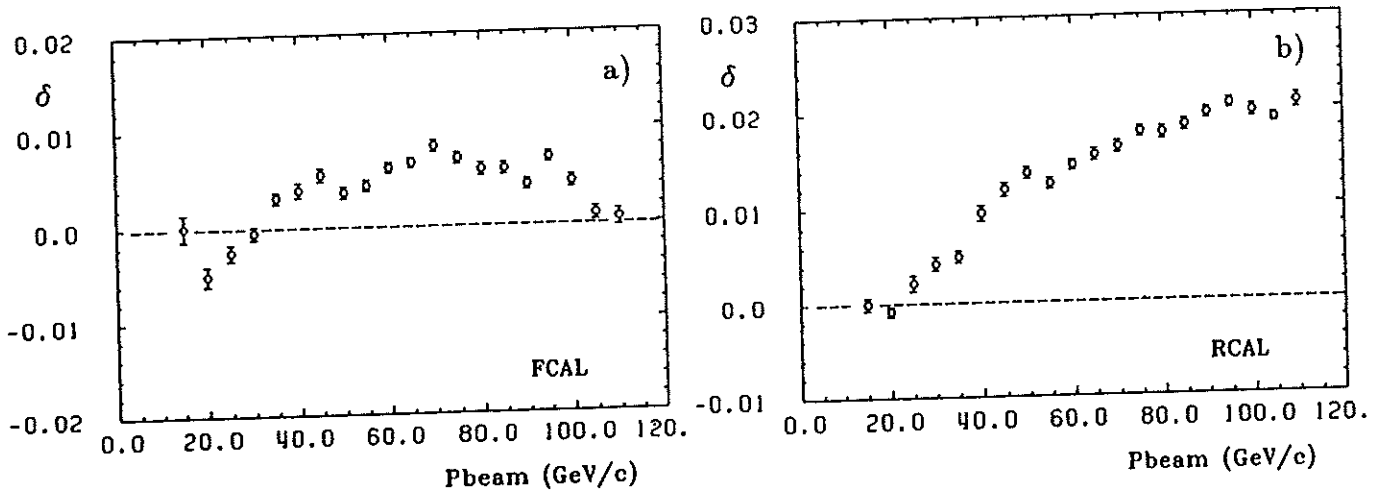

Fig. 6.16 Deviation from linearity for a) FCAL1 and b) RCAL1 as a function of the electron beam momentum, where $\delta = (Q/p)/(Q_0/p_0) - 1$ with Q_0 and p_0 the calorimeter charge and beam momentum at 15GeV/c.

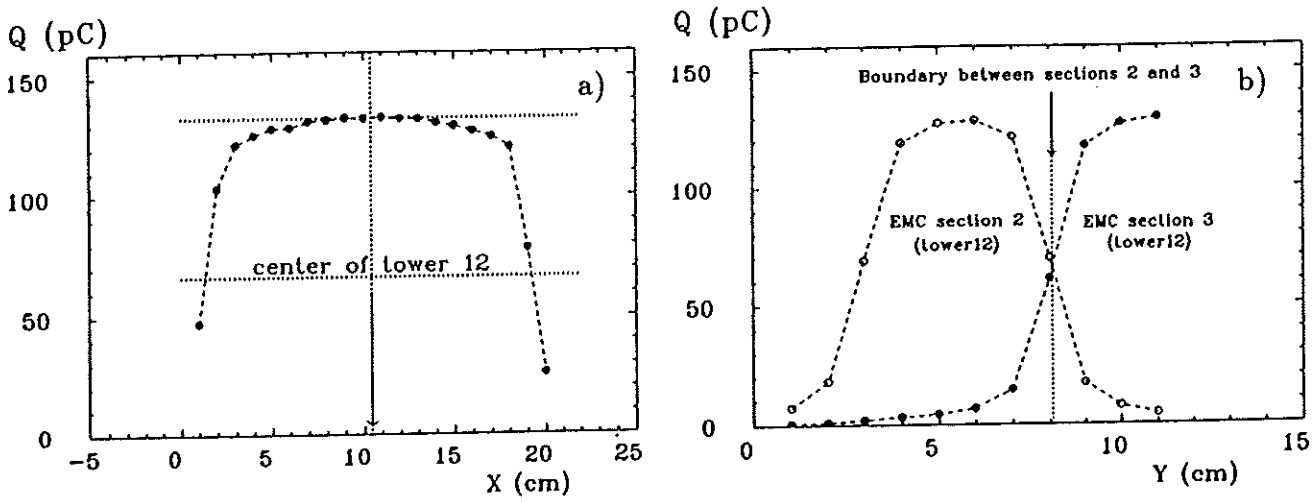

Fig. 6.17 Module scans with 15GeV/c electrons a) in vertical (x) and b) in horizontal (y) direction, in order to determine the position of the calorimeter module.

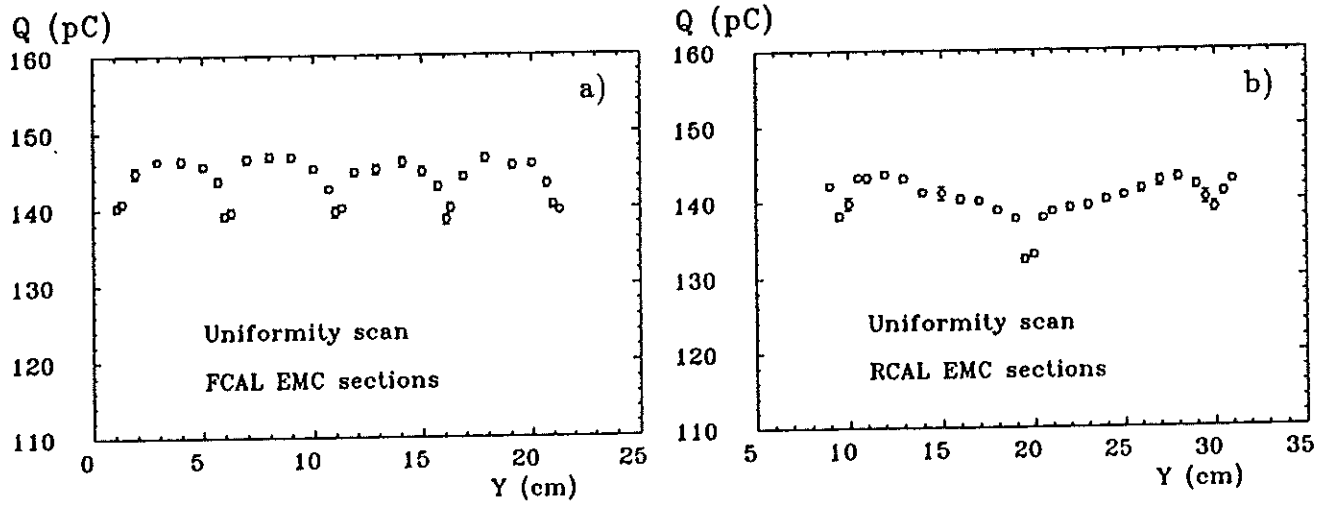

Fig. 6.18 Uniformity scans with 15 GeV/c electrons in horizontal (y) direction a) in module FCAL1 and b) in module RCAL1.

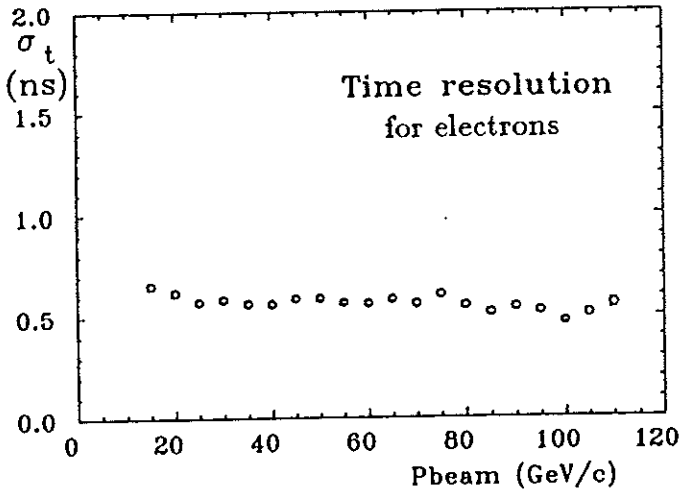

Fig. 6.19 Time resolution for electrons as a function of the beam momentum for an FCAL module.

6.6.3 Results on the Beam Calibration

The beam calibration has been performed with electrons, pions and muons at momenta of 15GeV/c and 100GeV/c at the CERN SPS. Systematic scans were taken over the entrance surfaces of 10 modules; 6 FCAL modules with 24 towers (900 EMC channels $\hat{=}$ 36% and 552 HAC channels $\hat{=}$ 30%) and 4 RCAL modules with 24 towers (328 EMC channels $\hat{=}$ 23% and 184 HAC channels $\hat{=}$ 20%) [AND91], [KRÜ90b], [KRÜ91].

At the beginning of a calibration cycle the gains of all photomultipliers were adjusted to give a specified signal from the uranium radioactivity (UNO calibration). After this adjustment all modules gave the same response to electrons and hadrons.

An electronics calibration cycle was performed for each module (Table 6.2). Then four 'beam–on' calibration cycles were taken with electrons, muons and hadrons at 15GeV/c or 100GeV/c as described in Table 6.3 and typically every 8 hours a 'beam–off' calibration cycle was taken in particular to measure the UNO currents and the gains of the electronics (Table 6.4).

After an initial run–in phase the time required for the calibration of one FCAL (RCAL) module was 5 (4) days.

The absolute calibration scale defined by the ratio $\frac{(particle\ signal)}{(uranium\ signal)}$ was determined.

The mean electron response, **e**, for the 74 EMC towers of an FCAL module (FNL4) is shown in Fig. 6.20a. The typical spread of e and μ is about 1% within one module and 0.5% from module to module. The statistical error for individual towers is in the order of 0.3% to 0.4%.

The typical spread of the hadronic response, **h**, is 1.1% within one module and 1% from module to module (Fig. 6.20b).

Figures 6.21a and 6.21b show the distributions of the mean response of 15GeV/c electrons (a) and 100GeV/c hadrons (b) for all measured FCAL towers.

These distributions show, that particles at a fixed energy yield the same signal to within 1% for all measured FCAL towers and that the calibration error is smaller than about 1%.

A calibration done in 12/89 and repeated in 4/90 shows an excellent stability: the difference of the response ratio of electrons to uranium radioactivity is 0.4%.

For all modules, those tested with beam as well as those not tested in beam, the calibration from the uranium signal has been cross checked with cosmic muons.

Step	Run Type	Events/Run	Runs	Comments
1	DC	50	2	ADC/V conversion
2	V_{inj}(0 V)	50	58	pipeline cell pedestals
3	V_{inj}(2 V)	50	58	pipeline cell gains
4	V_{inj}	50	8	pipeline cell linearity
5	Q_{inj}	100	2	pulse slopes
6	Q_{inj}	100	8	pulse linearity
7	Q_{inj}	100	2	ground check

Table 6.2 The electronics calibration cycle performed for each module.

Scan Number	Particles	E(GeV/c)	Events per Run	Runs F12(F11)	Runs R12(R11)	Sensitive Sections
1	electrons	15	2000	74(80)	40(42)	EMC(H/L)
2	electrons	100	2000	74(80)	40(42)	EMC(L)
	+ muons		2000			EMC(H)
3	hadrons	100	5000	23	23	HAC(L)
	+ muons		10000			HAC(H)
4	electrons	15	2000	74(80)	40(42)	EMC(H/L)

Table 6.3 The 'beam-on' test cycle performed for each module.

Scan Number	Run Type	Events per Run	Runs (FCAL)	Runs (RCAL)	Comments
1	UNO	1000	7	4	I_{uno} measurement
2	Q_{inj}(10 pC)	1000	7	4	gains for Q_{inj}
3	Q_{inj}(80 pC)	1000	7	4	gains for Q_{inj}
4	Random	1000	7	4	pedestals for beam
5	LED(AC)	1000	7	4	PM monitoring
6	LED(DC)	1000	7	4	PM monitoring
7	laser	1000	7	4	PM monitoring

Table 6.4 The 'beam-off' calibration cycle performed every 8 hours.

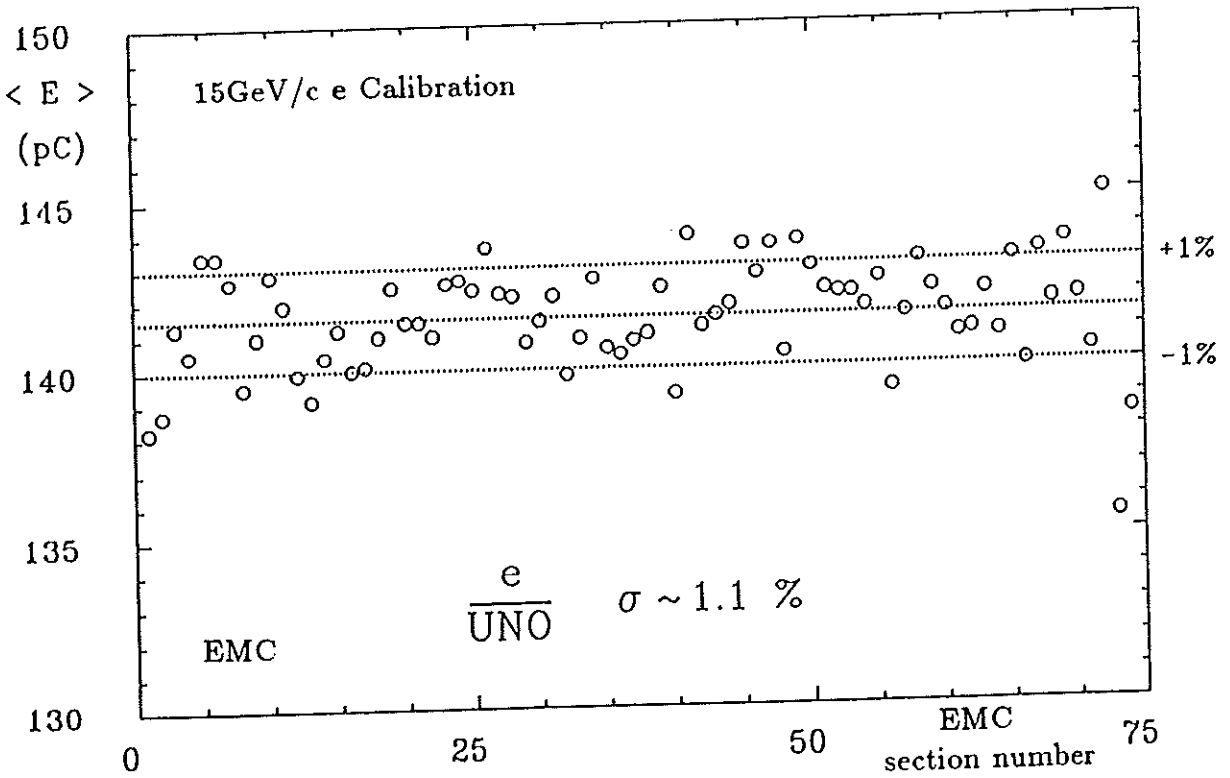

Fig. 6.20a Average response of 15GeV/c electrons for 74 EMC sections of one FCAL module after UNO calibration.

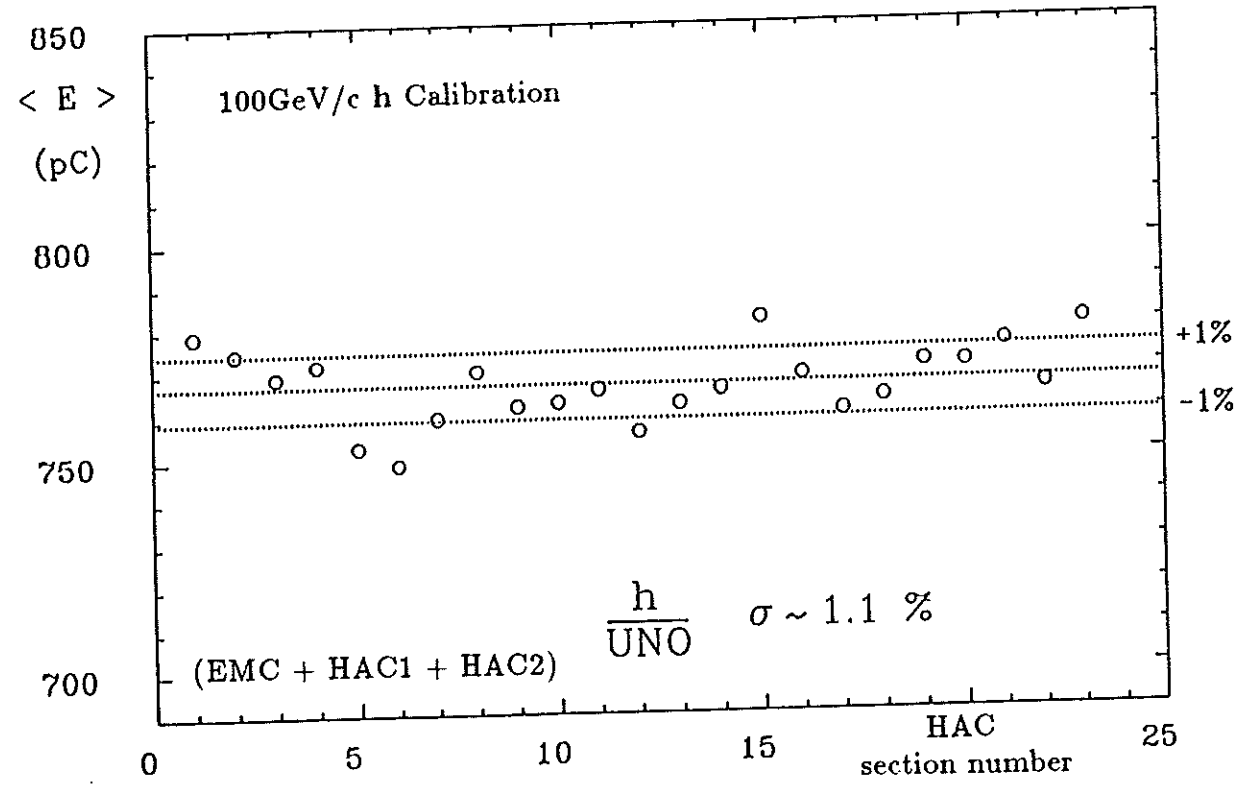

Fig. 6.20b Average response of 100GeV/c hadrons for 23 supertowers (EMC+HAC1+ HAC2) of one FCAL module after UNO calibration.

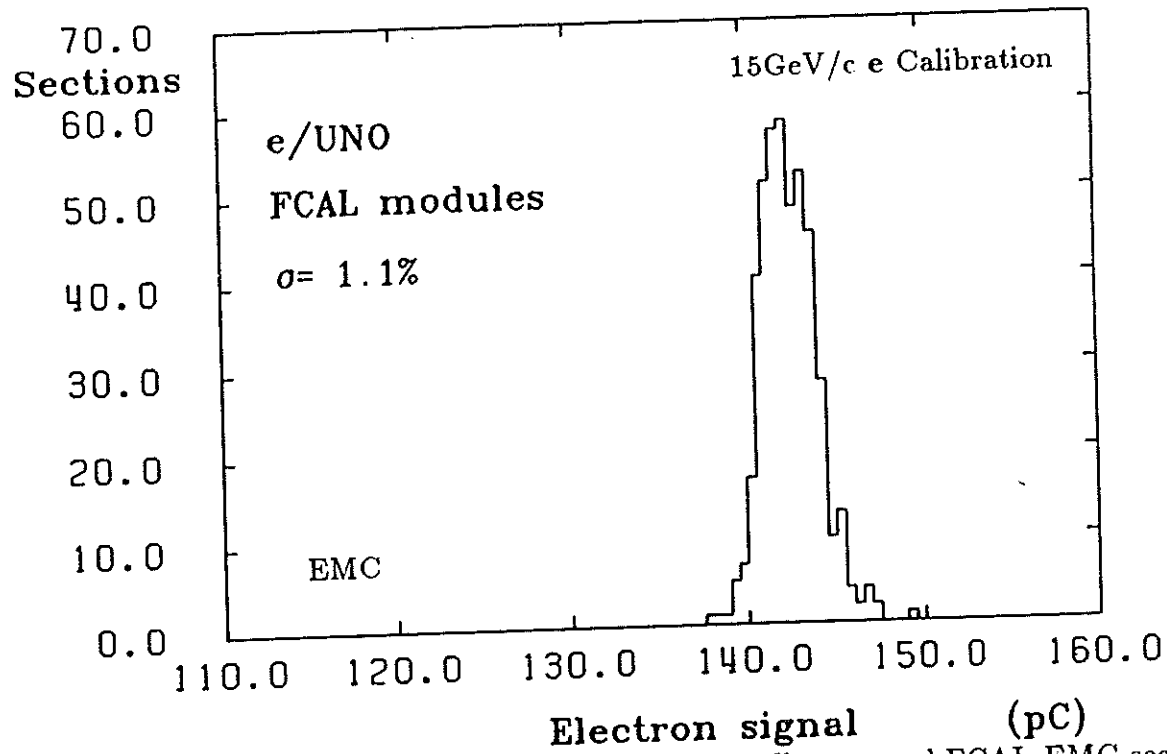

Fig. 6.21a Average response of 15GeV/c electrons for all measured FCAL EMC sections after UNO calibration.

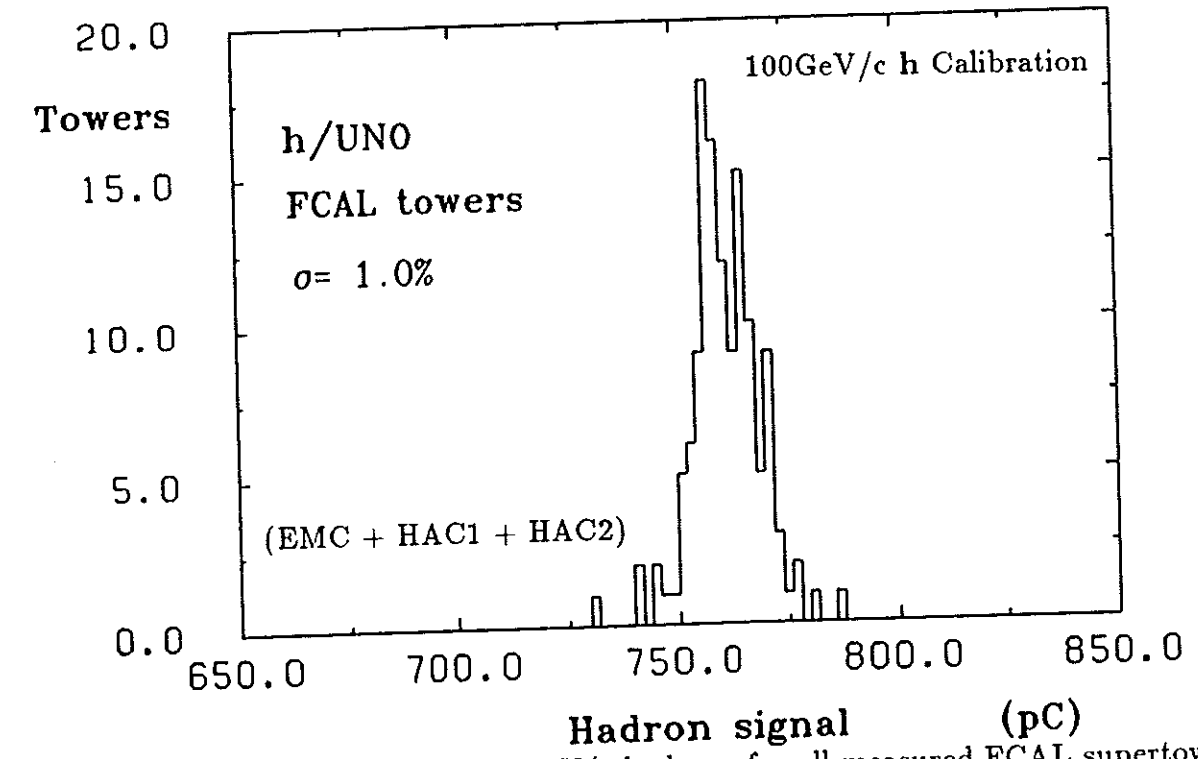

Fig. 6.21b Average response of 100GeV/c hadrons for all measured FCAL supertowers (EMC+HAC1+HAC2) after UNO calibration.

Chapter 7

Summary and Conclusions

The ZEUS collaboration has built a large detector at the new electron–proton collider HERA at DESY in order to study the interactions of 30GeV electrons and 820GeV protons in the newly opened kinematic region of very high momentum transfer up to $Q^2 \approx 40000 GeV^2$ and a centre of mass energy of 314GeV.

The high resolution uranium scintillator calorimeter represents the central component of the ZEUS detector. A large effort has been invested in calorimeter research and development. Many prototype calorimeters have been built and calorimeter tests have been performed by the ZEUS calorimeter group to optimize the parameters of the calorimeter.

The final ZEUS forward and rear calorimeter modules have a width of 20cm, a depth of up to 2m, a height varying 2.2m to 4.6m and a weight of up to 12t. They have a sandwich sampling structure of 3.3mm thick depleted uranium plates interleaved with 2.6mm thick plastic scintillator tiles throughout the whole calorimeter and wavelength shifter readout with associated photomultipliers. The calorimeter has a longitudinal segmentation into an electromagnetic ($25X_0$ or 1λ deep) and one or two hadronic sections (3λ – 6λ deep) with a tower structure of about 5cm x 20cm in the electromagnetic and about 20cm x 20cm in the hadronic sections.

The main characteristics of the ZEUS uranium scintillator calorimeter are the following:

A high energy resolution of $35\%/\sqrt{E}$ for hadrons and jets and $18\%/\sqrt{E}$ for electrons. Compensation (e/h = 1, the same signal size for electrons and hadrons) has been achieved at pion energies above 2GeV.

The three calorimeter sections, forward, barrel and rear, cover the full solid angle (4π hermeticity) and yield precise measurements of position of particles and jets ($\sigma_x \approx 1.2$cm for 100GeV hadrons) and an angular resolution of better than 10mrad, when combined with the interaction point.

The measured pulses are shorter than the bunch crossing time of 96ns and the time resolution is better than 1ns for energy deposits above 15GeV.

The readout electronics achieves a pedestal stability of about 3MeV and a gain stability of 0.5% over a period of 1 week. The photomultiplier gains can be monitored to within 0.5% by measuring the uranium activity every 8 hours.

The calorimeter response to electrons is linear within ±1% from 15GeV/c to 110GeV/c for the XP1911 photomultipliers and better than 2% for the R580 photomultipliers up to 110GeV/c.

The average light yield is 110 photoelectrons/GeV/PM for the FEMC sections and 140 photoelectrons/GeV/PM for the REMC sections. These values correspond to 1.4 and 1.7 photoelectrons/mip/layer/PM respectively. The attenuation length of the scintillator tiles is about 70cm.

The noise is 8, 10 and 13MeV for FEMC, REMC and HAC high gain channels respectively. For a complete FCAL tower (EMC+HAC1+HAC2) it is 47MeV (high gain). In the high gain the noise is dominated by uranium noise and in the low gain by electronic noise, where it amounts to 84MeV per photomultiplier channel.

By careful fabrication of all individual components of the ZEUS calorimeter and high quality control, the desired performance has been achieved. The uranium radioactivity has been found to be an invaluable tool for the calibration and monitoring of the response of the calorimeter modules. The absolute calibration scale has been determined with 15GeV electrons for the calorimeter modules calibrated at the CERN SPS and is valid for all FCAL and RCAL modules. An absolute calibration with an accuracy of about 1% has been obtained.

References

[ABR81] **Abramowicz, H. et al.;**
The Response and Resolution of an Iron–Scintillator Calorimeter for Hadronic and Electromagnetic Showers between 10GeV and 140GeV;
Nucl. Instr. and Meth. **180** (1981) 429–439

[ABR90] **Abramowicz, H. et al.;**
Intercalibration of the ZEUS Backing Calorimeter with the Uranium Calorimeter;
ZEUS Note 90–88, August 8, 1990

[ACO90] **Acosta, D. et al.;**
Results of Prototype Studies for a Spaghetti Calorimeter;
Nucl. Instr. and Meth. **A294** (1990) 193;
CERN/LAA/HC 90–008 (1990);
CERN–PPE/91–11 (1991)

[AGO89] **d'Agostini, G. et al.;**
Experimental Study of Uranium Plastic Scintillator Calorimeters;
NIKHEF–H/88–4; Nucl. Instr. and Meth. **A274** (1989) 134–144

[AKE85] **Akesson, T. et al.;**
Properties of a Fine–Sampling Uranium–Copper Scintillator Hadron Calorimeter;
Nucl. Instr. and Meth. **A241** (1985) 17–42

[AKE87] **Akesson, T. et al.;**
Performance of the Uranium/Plastic Scintillator Calorimeter for the HELIOS Experiment at CERN;
Nucl. Instr. and Meth. **A262** (1987) 243–263

[ALI90] **Ali, A.;**
Tiefinelastische Prozesse und Physik bei HERA;
Lectures given at the Herbstschule Maria Laach, September 4–14, 1990

[AMA81] **Amaldi, U.;**
Fluctuations in Calorimetry Measurements;
Physica Scripta **23** (1981) 409–424; reprint in [FER87]

[AND86] **Anders, B. et al.;**
Performance of a Uranium–Scintillator Calorimeter;
DESY 86–105 (1986)

[AND87] **Anders, B. et al.;**
DPG–Conference, Zürich (1987)

[AND90] **Andresen, A. et al.;**
Response of a Uranium–Scintillator Calorimeter to Electrons,
Pions and Protons in the Momentum Range 0.5 – 10 GeV/c;
DESY 89–149 (1989); Nucl. Instr. and Meth. **A290** (1990) 95–108

[AND90a] **Andresen, A.;**
Algorithmen zur Rekonstruktion der Achse hadronischer Schauer;
Diploma Thesis, Hamburg (1990)

[AND91] **Andresen, A. et al.;**
Construction and Beam Test of the ZEUS Forward and Rear Calorimeter;
DESY 91–026 (1991); Nucl. Instr. and Meth. **A309** (1991) 101–142

[AND91a] **Andresen, A. and Kröger, W.;**
Rekonstruktion von Position und Winkel hadronischer Schauer
mit dem ZEUS Kalorimeter;
DPG–Conference, Aachen, 12.3.91

[ARM83] **Armstrong, T.W. et al.;**
An Investigation of Fission Models for High–Energy Radiation
Transport Calculations;
Jül–1859 (1983)

[BAK88] **Bakken, J.A. et al.;**
Nucl. Instr. and Meth. **A270** (1988) 397–402; **A275** (1989) 81–88;
Nucl. Instr. and Meth. **A280** (1989) 25–35

[BAM90] **Bamberger, A. et al.;**
The Laser/LED System for the FCAL/RCAL;
ZEUS Note 90–119 (1990)

[BAR90] **Barreiro, F. et al.;**
Measurements of Longitudinal and Transverse Profiles for Hadron Showers
in the Range 10–100GeV and Comparisons with Monte Carlo Simulations;
DESY 89–171 (1989); Nucl. Instr. and Meth. **A292** (1990) 259–278

[BEH90] **Behrens, U. et al.;**
Test of the ZEUS Forward Calorimeter Prototype;
DESY 89–128 (1989); Nucl. Instr. and Meth. **A289** (1990) 115–138

[BEH90a] **Behrens, U.;**
Vergleich von Monte–Carlo–Simulationen und experimentellen Ergebnissen
für ein hadronisches Uran–Szintillator–Sampling Kalorimeter;
Ph. D. Thesis, Hamburg (1990)

[BER87] **Bernardi, E.;**
On the Optimization of the Energy Resolution of Hadron Calorimeters;
DESY F1–87–01 (1987); Ph. D. Thesis, Hamburg (1987)

[BER87a] **Bernardi, E. et al.;**
Performance of a Compensating Lead–Scintillator Hadronic Calorimeter;
DESY 87–41 (1987); Nucl. Instr. and Meth. **A262** (1987) 229–242

[BIR60] **Birks, J.B.;**
Scintillation Counters;
Pergamon Press, Oxford 1960.
The Theory and Practice of Scintillation Counting;
Pergamon Press, Oxford 1964

[BLÜ87] **Blümlein, J. et al.;**
Structure Functions, Quark Distributions and Λ_{QCD} at HERA;
Proceedings of the HERA Workshop, Vol. 1 p.67;
Editor R.D. Peccei, DESY, Hamburg, October 12–14, 1987

[BÖC81] **Böck, R.K. et al.;**
Parametrization of the Longitudinal Development of Hadronic Showers in Sampling Calorimeters;
Nucl. Instr. and Meth. **186** (1981) 533–539

[BOT81] **Botner, O.;**
New Ideas in Calorimetry;
Physica Scripta **23** (1981) 556–563

[BRA85] **Brau, J. and Gabriel, T.A.;**
Monte Carlo Studies of Uranium Calorimetry;
Nucl. Instr. and Meth. **A238** (1985) 489–495.
Theoretical Studies of Hadronic Calorimetry for High Luminosity, High Energy Colliders;
Nucl. Instr. and Meth. **A279** (1989) 40–56

[BRA88] **Braunschweig, W. et al.;**
Results from a Test of a Pb–Cu Liquid Argon Calorimeter;
Nucl. Instr. and Meth. **A265** (1988) 419–434

[BRI88] **Brinkmann, R.;**
HERA;
DESY HERA 88–03 (1988)

[BRÜ85] **Brückmann, H.;**
Proceedings of the Workshop on Compensated Calorimetry;
CALT 68 1305, Pasadena, September 1985

[BRÜ86] **Brückmann, H. et al.;**
Hadron Sampling Calorimetry, A Puzzle of Physics;
DESY 86–155 (1986); Nucl. Instr. and Meth. **A263** (1988) 136–149

[BRÜ87] **Brückmann, H. et al.;**
On the Theoretical Understanding and Calculation of Sampling Calorimeters;
DESY 87–064 (1987)

[BUO86] **Buon, J. and Steffen, K.;**
HERA Variable–Energy "Mini" Spin Rotator and Head–On EP Collision with Choice of Electron Helicity;
Nucl. Instr. and Meth. **A245** (1986) 248–261

[CAL89] **Caldwell, A. et al.;**
Development of the Front End Electronics for the
ZEUS High Resolution Calorimeter ;
Proceedings of the Workshop on Calorimetry for the Supercollider,
Tuscaloosa, Alabama, March 13–17, 1989.
Design and Implementation of a High Precision Readout System
for the ZEUS Calorimeter ;
submitted to Nucl. Instr. and Meth., October 1991

[CAS83] **Cashmore, R.J.;**
Exotic Phenomena at HERA;
Proceedings of the Workshop "Experimentation at HERA",
NIKHEF, Amsterdam, June 6–11, 1983; DESY HERA 83/20 (1983)

[CAS85] **Cashmore, R.J. et al.;**
Exotic Phenomena in High Energy ep Collisions;
Physics Reports **122** (1985) 275

[CAT87] **Catanesi, M.G. et al.;**
Hadron, Electron and Muon Response of a Uranium–Scintillator Calorimeter;
Nucl. Instr. and Meth. **A260** (1987) 43–54

[CHA72] **Chandler, K.C. and Armstrong, T.W.;**
Operating Instructions for the High–Energy Nucleon–Meson Transport Code
HETC;
Oak Ridge National Laboratory Report ORNL–4744 (1972)

[CLO87] **Cloth, P. et al.;**
The High Energy Radiation Transport System HERMES;
KFA–Jül–Report 1987

[CLO87a] **Cloth, P. et al.;**
Monte Carlo Simulation of Test 35 with HERMES;
KFA–Jül–Report 1987

[COL90] **Colas, J. et al.;**
Calorimetry at the LHC;
Proceedings of the Large Hadron Collider Workshop,
Editors: G. Jarlskog and D. Rein, Aachen, October 4–9, 1990;
CERN 90–10, Vol. I, p. 370–419; DESY 90–136 (1990)

[COO87] **Cooper–Sarkar, A.M.;**
Measurement of the Longitudinal Structure Function
and the Small x Gluon Density of the Proton;
Proceedings of the HERA Workshop, Vol. 1 p.231;
Editor R.D. Peccei, DESY, Hamburg, October 12–14, 1987

[COR87] **Cornet, F. et al.;**
Sensitivity of W' and Z' Searches at HERA;
Proceedings of the HERA Workshop, Vol. 2 p.771;
Editor R.D. Peccei, DESY, Hamburg, October 12–14, 1987

[COR90] **Corriveau, F.;**
private communication

[DAN90] **Dannemann, A.**;
Experimentelle Untersuchungen des intermodularen Signalverhaltens
im ZEUS–Prototyp–Kalorimeter;
Diploma Thesis, Hamburg (1990)

[DIE89] **Dierks, K. et al.**;
First Results from a Lead–Scintillator Calorimeter;
ZEUS Note 89–32 (1989)

[DIE90] **Dierks, K.**;
Entwicklung eines präzisen Hadron–Kalorimeters;
DESY F35–90–01 (1990); Ph. D. Thesis, Hamburg (1990)

[DRE90] **Drews, G. et al.**;
Experimental Determination of Sampling Fluctuations in Uranium
and Lead Hadronic Calorimeters;
DESY 89–159 (1989); Nucl. Instr. and Meth. **A290** (1990) 335–345

[ECF79] **ECFA 1979**;
Proceedings of the Study of an ep Facility for Europe;
Editor: U. Amaldi, DESY, Hamburg, April 2–3, 1979;
DESY Report 79/48 (1979)

[ECF81] **ECFA 1981**;
Résumé of the Discussion Meeting "Physics with ep Colliders in View of HERA";
Wuppertal, October 2–3, 1981;
DESY–HERA 81/18 (1981)

[ECF83] **ECFA 1983**;
Proceedings of the Workshop "Experimentation at HERA";
NIKHEF, Amsterdam, June 9–11, 1983;
DESY–HERA 83/20 (1983)

[ECF89] **ECFA Study Week**;
Proceedings of the ECFA Study Week on Instrumentation Technology for
High–Luminosity Hadron Colliders;
Editors: E. Fernandez and G. Jarlskog, Barcelona, September 14–21, 1989;
CERN 89–10, Vol. 1+2

[EIC83] **Eichten, E.J. et al.**;
New Tests for Quark and Lepton Substructure;
Phys. Rev. Lett. **50** (1983) 811–814

[ENG86] **Engelen, J. et al.**;
Performance of a Hadron Test Calorimeter for the ZEUS Experiment;
NIKHEF–H/86–18, November 1986

[ERN91] **Ernst, M.**;
Electron–Hadron Separation in a ZEUS FCAL Prototype
Including HES Diodes;
ZEUS Note 91–42 (1991)

[FAB75] **Fabjan, C.W. and Willis W.J.**;
Hadron Cascades in Iron and Uranium;
Phys. Lett. **60B** (1975) 105–108

[FAB77] **Fabjan, C.W. et al.**;
Iron Liquid–Argon and Uranium Liquid–Argon Calorimeters for Hadron Energy Measurement;
Nucl. Instr. and Meth. **141** (1977) 61–80

[FAB82] **Fabjan, C.W. and Ludlam, T.**;
Ann. Rev. Nuc. Part. Sci. 32, (1982) 335

[FAB85] **Fabjan, C.W.**;
Calorimetry in High–Energy Physics;
CERN–EP/85–54, reprint in [FER87]

[FAB89] **Fabjan, C.W. and Wigmans, R.**;
Energy Measurement of Elementary Particles;
CERN–EP/89–64 (1989); Rep. Prog. Phys. **52** (1989) 1519–1580

[FAB91] **Fabjan, C.W. et al.**;
Electron Drift Velocity and Characteristics of Ionization of Alpha and Beta Particles in Liquid Argon Doped with Ethylene for LHC Calorimetry;
CERN–PPE/91–171, October 1991

[FEL87] **Feltesse, J.**;
Measurement of Inclusive Differential Cross Sections;
Proceedings of the HERA Workshop, Vol. 1 p.33;
Editor R.D. Peccei, DESY, Hamburg, October 12–14, 1987

[FER87] **Ferbel, T.**;
Experimental Techniques in High Energy Physics;
Addison–Wesley Publishing Company (1987)

[FLA85] **Flauger, W.**;
Simulation of the Transition Effect in Liquid Argon Calorimeters;
Nucl. Instr. and Meth. **A241** (1985) 72–75

[FÜR90] **Fürtjes, A.**;
Verhalten des ZEUS Uran–Szintillator–Kalorimeters für niederenergetische Teilchen mit Energien von 0.2 - 10.0 GeV;
DESY F35–90–02 (1990); Diploma Thesis, Münster (1990)

[GAB85] **Gabriel, T.A. et al.**;
ORNL/TM–9270, Oak Ridge, January 1985;
IEEE Trans. Nucl. Sci. **NS–32(1)**, February 1985;
Gabriel, T.A.; Codes, Models and Cross Sections for Use in Analysing Compensated Calorimeters;
Proceedings of Workshop on Compensated Calorimetry,
Pasadena, September 10–11, 1985; CALT–68–1305

[GAB89] **Gabriel, T.A.;**
Detectors for the Superconducting Super Collider Design Concepts, and Simulation;
Proceedings of the Workshop on Calorimetry for the Supercollider, Tuscaloosa, Alabama, March 13–17, 1989

[GEN87] **Gennis, M.;**
Entwurf und Test eines elektromagnetischen Kalorimeters;
DESY F14–87–02 (1987); Diploma Thesis, Hamburg (1987)

[GLO91] **Gloth, G.;**
Uniformitätsmessungen am ZEUS–Kalorimeter mit Hilfe von radioaktiven Präparaten und ihre Analyse;
Diploma Thesis, Hamburg (1991)

[HER81] **HERA Proposal;**
A Proposal for a large Electron–Proton Colliding Beam Facility at DESY;
DESY HERA 81–10 (1981)

[HER87] **HERA Workshop;**
Proceedings of the HERA Workshop, Vol. 1+2;
Editor R.D. Peccei, DESY, Hamburg, October 12–14, 1987

[HER91] **HERA Workshop;**
Proceedings of the HERA Workshop;
DESY, Hamburg, 1991

[HER91a] **Hervas, L.;**
The Pipelined Readout for the ZEUS Calorimeter;
DESY F35D–91–01 (1991); Ph.D. Thesis, Madrid (1991)

[HIL87] **Hilger, E.;**
The ZEUS Uranium–Scintillator Calorimeter for HERA;
Nucl. Instr. and Meth. **A257** (1987) 488–498

[HOF82] **Hofmann, W. et al.;**
Characteristics of Lead–Scintillator Sampling Shower Counters for the Detection of Electrons and Photons in the Energy Range 70MeV to 6GeV;
Nucl. Instr. and Meth. **195** (1982) 475–482

[HOL78] **Holder, M. et al.;**
Performance of a Magnetized Total Absorption Calorimeter between 15GeV and 140GeV;
Nucl. Instr. and Meth. **151** (1978) 69–80

[ING87] **Ingelman, G. et al.;**
Deep Inelastic Physics and Simulation;
Proceedings of the HERA Workshop, Vol. 1 p.3;
Editor R.D. Peccei, DESY, Hamburg, October 12–14, 1987

[JAC79] **Jacquet, F. and Blondel, A. et al.;**
Detection and Study of the Charged Current Event;
Proceedings of the Study of an ep Facility for Europe;
Editor U. Amaldi, DESY, Hamburg, April 2–3, 1979;
DESY 79/48 (1979)

[KAI86] **Kaiser, H.;**
Design of Superconducting Dipole for HERA;
Presented at the 13th International Conference on High Energy Accelerators, Novosibirsk, USSR, August 7–11, 1986;
DESY HERA 1986–14 (1986)

[KAW91] **Kawulski, N.;**
Vergleich zwischen experimentellen Daten und Simulation im ZEUS Kalorimeter;
DESY F35–91–01 (1991); Diploma Thesis, Hamburg (1991)

[KLA87] **Klanner, R.;**
Thickness Tolerance on Fe–Cladding;
ZEUS Note 87–011 (1987)

[KLA88] **Klanner, R.;**
Test Program for the ZEUS Calorimeter;
Nucl. Instr. and Meth. **A 265** (1988) 200–209

[KLA89] **Klanner, R. and Wolf, G.;**
Das ZEUS–Präzisionskalorimeter für HERA;
Physikalische Blätter 45 (1989) Nr.9

[KLA91] **Klanner, R.;**
Eichung des ZEUS–Kalorimeters mit 1% Genauigkeit;
DESY, Talk, 10.4.1991

[KLE84] **Kleinknecht, K.;**
Detektoren für Teilchenstrahlung;
Teubner, Stuttgart 1984

[KÖL89] **Köll, O.;**
Auswertung von Testmessungen mit einem Prototypen des ZEUS Vorwärts–Kalorimeters;
Diploma Thesis, Hamburg (1989)

[KOS92] **Kose, R.;**
private communication (January 1992)

[KRÖ91] **Kröger, W.;**
Studies of Particle Jets with an Interaction Trigger ... ;
Ph.D. Thesis, Hamburg, in preparation.
DPG–Conference, Aachen, 12.3.91

[KRÖ92] **Kröger, W. et al.;**
The Interaction Trigger ... ;
DESY report, in preparation

[KRÜ85] **Krüger, J.;**
Hadronische Korrelationen in der tiefinelastischen Myon–Proton–Streuung;
WU B–DI 85–4 (1985); Ph.D. Thesis, Wuppertal (1985)

[KRÜ86a] **Krüger, J.**;
Untersuchung der longitudinalen Entwicklung hadronischer Schauer;
DPG–Conference, Heidelberg, 18.3.86

[KRÜ86b] **Krüger, J.**;
Shower Development in a Uranium/Scintillator Calorimeter (WA78)
and the Requirements for the Hadron Calorimeter of the ZEUS Detector;
ZEUS Note 86–019 (1986)

[KRÜ87a] **Krüger, J.**;
Hadronkalorimetrie bei ZEUS;
Seminar Talk, Hamburg University, 20.2.87

[KRÜ87b] **Krüger, J.**;
Untersuchung von Einflüssen auf das Auflösungsvermögen und
das e/π–Verhältnis bei einem Uran–Szintillator Kalorimeter;
DPG–Conference, Zürich, 19.3.87

[KRÜ87c] **Krüger, J.**;
Kalorimetrie bei ZEUS;
Seminar Talk, Hamburg University, 16.12.87

[KRÜ88a] **Krüger, J.**;
Hadronische Energieauflösung von Uran– und Blei–Szintillator Kalorimetern;
DPG–Conference, Freiburg, 18.3.88

[KRÜ88b] **Krüger, J.**;
Energiemessung in den HERA – Experimenten H1 und ZEUS
— Kalorimetrie bei hohen Energien — ;
DESY Talk, Hamburg, 18.5.88

[KRÜ88c] **Krüger, J.**;
High Resolution Hadron Calorimetry for the ZEUS Detector at DESY;
Seminar Talks given at:
Stanford Linear Accelerator Center (SLAC), Stanford, USA, 2.8.88;
Lawrence Berkeley Laboratory (LBL), Berkeley, USA, 3.8.88;
Fermi National Accelerator Laboratory (FNAL), Batavia, USA, 8.8.88;
Brookhaven National Laboratory (BNL), Brookhaven, USA, 10.8.88

[KRÜ89a] **Krüger, J.**;
The Heart of ZEUS — Description of the Uranium–Scintillator Calorimeter;
DESY Journal 2–88, Hamburg (1989)

[KRÜ89b] **Krüger, J.**;
Untersuchung der Lichtausbeute eines Blei–Szintillator Testkalorimeters
— Optimierung und Qualitätskontrolle des ZEUS Kalorimeters;
DPG–Conference, Bonn, 13.3.89

[KRÜ89c] **Krüger, J.**;
Response of the ZEUS Uranium Scintillator Calorimeter to Pions, Protons and Electrons for Kinetic Energies from ≈ 0.2 GeV to 10 GeV and Study of the Calorimeter Uniformity;
EPS–Conference, Madrid, Spain, 7.9.89;
published in the Proceedings of the Europhysics Conference on High–Energy Physics, Madrid, Spain, 6 – 13 September 1989, Nuclear Physics B (Proc. Suppl.) 16 (1990) 513–516

[KRÜ89d] **Krüger, J.**;
HERA – New Large Electron–Proton Colliding Beam Facility at DESY;
Contribution to New Detectors in Elementary Particle Physics;
Seminar, Hamburg University, 1.11.89

[KRÜ90a] **Krüger, J.**;
Der Einfluß von Material vor einem Kalorimeter auf die Energieauflösung;
DPG–Conference, Hamburg, 21.3.90

[KRÜ90b] **Krüger, J.**;
The ZEUS Uranium Scintillator Calorimeter;
Seminar Talk, Kazimierz, Poland, 31.5.90;
published in the Proceedings of the XIII Warsaw Symposium on Elementary Particle Physics; Kazimierz, Poland, 28 May – 1 June 1990

[KRÜ90c] **Krüger, J.**;
Criteria for the Length of a High Resolution Hadron Calorimeter;
Talk, ECFA–LHC Calorimeter Group, CERN, Genf, 18.7.90

[KRÜ90d] **Krüger, J.**;
Length of Calorimeters and Effect of Absorbers in Front of Calorimeters;
Talk, ECFA, LHC – Workshop, Calorimetry, Aachen, 4.10.90;
published in the Proceedings of the ECFA, LHC – Workshop;
Aachen, Germany, 4 – 9 October 1990

[KRÜ90e] **Krüger, J.**;
Length of Calorimeters and Effect of Absorbers in Front of Calorimeters;
DESY 90–163 (1990)

[KRÜ91] **Krüger, J.**;
Calibration of the ZEUS Uranium Scintillator Calorimeter;
Proceedings of the "5th Pisa Meeting on Advanced Detectors",
Isola d'Elba, La Biodola, May 26–31, 1991

[KÜS91] **Küster, H.**;
The H1 Liquid Argon Calorimeter;
DESY Journal 1–91, Hamburg (1991)

[LEI92] **Leich, A.**;
private communication

[LHC90] **Large Hadron Collider Workshop**;
Proceedings of the Large Hadron Collider Workshop;
Editors: G. Jarlskog and D. Rein, Aachen, October 4–9, 1990;
CERN 90–10, Vol. I–III

[LLE77] **LLewellyn–Smith, C.H. and Wiik, B.H.;**
DESY Report 77/36 (1977)

[LOH83] **Lohrmann, E. and Meß, K.–H.;**
Remarks on the Kinematics of e–p Collisions in HERA;
DESY HERA 83–08 (1983)

[LOH83a] **Lohrmann, E.;**
Einführung in die Elementarteilchenphysik;
Teubner, Stuttgart 1983

[LOH85] **Lohmann, W. et al.** ;
CERN 85–54 (1985)

[LOH87] **Lohrmann, E.;**
The HERA Machine – Status and Opportunities;
Contribution to the Eighth Vanderbilt International High Energy Physics Conference, Nashville, Tennessee, October 1987;
DESY F35D–87–01 (1987)

[LOH90] **Lohrmann, E.;**
private communication [AND90a]

[LON75] **Longo, E. and Sestili, I.;**
Monte Carlo Calculation of Photon–Initiated Electromagnetic Showers in Lead Glass;
Nucl. Instr. and Meth. **128** (1975) 283–307

[LON83] **Longo, E.;**
Currents and Structure Functions;
Proceedings of the Workshop on Experimentation at HERA, NIKHEF, Amsterdam, June 9–11, 1983;
DESY Report HERA 83/20 (1983) p.285

[LUN52] **Lund Monte Carlo** ;
T. Sjöstrand, M. Bengtsson; Comput. Phys. Commun. **39** (1986) 347;
T. Sjöstrand, M. Bengtsson; Comput. Phys. Commun. **43** (1986) 367;
M. Bengtsson, T. Sjöstrand; Phys. Lett. **185B** (1987) 435

[L3Y83] **L3 Collaboration;**
L3 Technical Proposal, May 1983

[MAR87] **Martyn, H.–U.;**
Contact Terms and Substructure at HERA;
Proceedings of the HERA Workshop, Vol. 2 p.801;
Editor R.D. Peccei, DESY, Hamburg, October 12–14, 1987

[MEI90] **Meinke, R.;**
Superconducting Magnet System for HERA;
Presented at the 1990 Applied Superconductivity Conference, Snowmass Village, Colorado, September 24–28, 1990;
DESY HERA 90–17 (1990)

[MES88] **Meß, K.–H. and Schmüser, P.;**
Superconducting Accelerator Magnets;
Lectures given at the joint CERN – Accelerator School – DESY,
Course on Superconductivity in Particle Accelerators,
Hamburg, May 30 – June 3, 1988;
DESY HERA 89–01 (1989)

[MIT90] **Mitchell, J. et al.;**
Status of the FCAL/RCAL Laser Calibration System;
ZEUS Note 90–104 (1990)

[MUS92] **Musgrave, B.;**
private communication

[NEL85] **Nelson, W.R., Hirayama, H. and Rogers, D.W.O.;**
The EGS4 Code System;
SLAC – Report – 165 (1985)

[OPA83] **OPAL Collaboration;**
The OPAL Detector Technical Proposal;
CERN/LEPC/83–4 (1983)

[PDG90] **Particle Data Group;**
Review of Particle Properties;
Phys. Lett. **B239** (1990)

[PEG85] **Pegel, C. and Prause, H.;**
Radiation from Thick Plates of Depleted Uranium;
Hamburg University, Zyklotron–S2/85 (1985)

[PES89] **Del Peso, J. and Ros, E.;**
On the Energy Resolution of Electromagnetic Sampling Calorimeters;
Nucl. Instr. and Meth. **A276** (1989) 456–467

[PET86] **Peters, J.H.;**
Untersuchungen an einem Uran–Szintillator Kalorimeter
mit Elektronen und Hadronen;
DESY F14–86–03 (1986); Diploma Thesis, Hamburg (1986)

[PIS91] **Pisa Meeting;**
Frontier Detectors for Frontier Physics;
Proceedings of the 5^{th} Pisa Meeting on Advanced Detectors;
Elba, La Biodola, May 26–31, 1991

[POE89] **Poelz, G.;**
Status of HERA and its Detectors H1 and ZEUS;
Proceedings of the XII Warsaw Symposium on Elementary Particle Physics;
Kazimierz, Poland, 29 May – 2 June, 1989

[REH85] **Rehak, P.;**
Proceedings of the Workshop on Compensated Calorimetry;
CALT 68 1305, Pasadena, September 1985

[ROS52] **Rossi, B.**;
High–Energy Particles;
Prentice–Hall, Eaglewood Cliffs, 1952

[SAX87] **Saxon, D.H.**;
Development of the ZEUS Detector;
RAL–87–113, DESY–87–165, December 1987

[SCH90] **Schmüser, P.**;
The Proton–Electron Storage Ring Facility HERA;
DESY Journal 3–90, November 8, 1990;
Zur Fertigstellung von HERA;
Physikalische Blätter, Band 46, Nr. 12, December 1990, 470–474

[SIP89] **Sippach, W. et al.**;
Development of the Front–End Electronic for the ZEUS
High Resolution Calorimeter;
IEEE Trans. Nucl. Sci. NS–36 (1989) 465

[SÖD90] **Söding, P.**;
HERA – Status and Physics Programme;
Talk given at the ECFA Large Hadron Collider Workshop,
Aachen, 4–9 October 1990

[STE71] **Sternheimer, R.M. et al.**;
General Expression for the Density Effect for the Ionization Loss
of Charged Particles;
Phys. Rev. B3 (1971) 3681–3692

[STE84] **Sternheimer, R.M. et al.**;
Density Effect for the Ionization of Charged Particles
in Various Substances;
At. Data Nucl. Data Tables 30 (1984) 261–271

[STI87] **Stirling, W.J.**;
Summary of the Results from Study Group 2 – QCD at HERA;
Proceedings of the HERA Workshop, Vol. 1 p.185;
Editor R.D. Peccei, DESY, Hamburg, October 12–14, 1987

[STÖ83] **Stoer, J.**;
Einführung in die Numerische Mathematik;
Springer–Verlag 1983

[STR91] **Straver, J.**;
Design, Construction and Beam Tests of the High Resolution
Uranium Scintillator Calorimeter for ZEUS;
NIKHEF, Amsterdam, Ph.D. Thesis, March 6, 1991

[TIE89] **Tiecke, H.**;
Contribution of Intrinsic and Sampling Fluctuations
to the Total Hadronic Energy Resolution;
Nucl. Instr. and Meth. **A277** (1989) 42–45

[TIE92] **Tiecke, H.;**
private communication

[TSA74] **Tsai, Y.S.;**
Pair Production and Bremsstrahlung of Charged Leptons;
Rev. Mod. Phys. **46** (1974) 815–851

[VIN86a] **de Vincenci, M. et al.** ;
Experimental Study of Uranium–Scintillator and Iron–Scintillator Calorimetry in the Energy Range 135 – 350GeV;
Nucl. Instr. and Meth. **A243** (1986) 348–360

[VIN86b] **de Vincenci, M. et al.** ;
Performance of a Sampling Calorimeter with Alternate U and Fe Absorbers;
Nucl. Instr. and Meth. **A248** (1986) 326–330

[VOS87] **Voss, G.A.;**
Status of the HERA–Project;
Proceedings of the 1987 International Symposium on Lepton and Photon Interactions at High Energies, Hamburg, 27–31 July 1987;
Edited by W. Bartel and R. Rückl, (1987) p.525

[WEG89] **Wegener, D.;**
Hadronkalorimeter – Entwicklung und Anwendungen;
Physikalische Blätter 45 (1989) Nr. 9

[WIG87] **Wigmans, R.;**
On the Energy Resolution of Uranium and Other Hadron Calorimeters;
CERN–EP/86–141 (1986); Nucl. Instr. and Meth. **A259** (1987) 389–429

[WIG87a] **Wigmans, R.;**
International Conference on Advances in Experimental Methods for Colliding Beam Physics;
SLAC, NIKHEF–H/87–8 (1987)

[WIG88] **Wigmans, R.;**
The Spaghetti Calorimeter Project at CERN;
Proceedings of the Workshop on Detectors at pp Colliders,
Snowmass (1988)

[WIG89] **Wigmans, R.;**
The Spaghetti Calorimeter Project at CERN;
Proceedings of the Workshop on Calorimetry for the Supercollider,
Tuscaloosa, Alabama, March 13–17, 1989

[WIG91] **Wigmans, R.;**
Advances in Hadron Calorimetry;
CERN–PPE/91–39, submitted to Annual Review of Nucl. and Part. Science

[WII88] **Wiik, B.H.;**
Design and Status of the HERA Superconducting Magnets;
Talk given at the World Congress on Superconductivity,
Houston – Texas, February 22–24, 1988;
DESY HERA 88–05 (1988)

[WII89] **Wiik, B.H.;**
HERA Status;
Talk given at the 1989 Particle Accelerator Conference,
Chicago, March 20–23, 1989;
DESY HERA 89–11 (1989)

[WII90] **Wiik, B.H.;**
The Status of HERA;
Report at the EPAC 90 – 2nd European Particle Accelerator Conference,
Nice, June 12–16, 1990;
DESY HERA 90–11 (1990)

[WIP90] **Wipf, S.L.;**
Superconducting Cable for HERA;
Talk given at the 1990 Intl. Industr. Symp. on the Super Collider,
Miami Beach, Florida, March 16, 1990;
DESY HERA 90–15 (1990)

[WOL86] **Wolf, G.;**
HERA: Physics, Machine and Experiments;
DESY 86–089 (1989)

[WOL86b] **Wolff, S.;**
Superconducting Magnets for HERA;
Presented at the 13th International Conference on High Energy Accelerators,
Novosibirsk, USSR, August 7–11, 1986;
DESY HERA 1986–12 (1986)

[WOL88] **Wolf, G.;**
HERA–Experiment ZEUS, Status Report;
DESY, HERA Bulletin Nr. 13, June 1988

[WOL89] **Wolf, G.;**
ZEUS – Experiment;
DESY, HERA Bulletin Nr. 17, September 1989

[WOL90] **Wolf, G.;**
Das ZEUS–Experiment bei HERA;
Talk given at Innerbetriebliche Fortbildung, DESY, 23.5.90

[WOL90a] **Wolf, G.;**
Experimental Horizons for Structure Function Measurements;
Proceedings of the Workshop on Hadron Structure Functions
and Parton Distributions;
Fermilab, April 26–28, 1990

[ZEU85] **ZEUS Collaboration;**
ZEUS a Detector for HERA, Letter of Intent;
DESY, June 1985

[ZEU86] **ZEUS Collaboration;**
The ZEUS Detector, Technical Proposal;
DESY, March 1986

[ZEU87] **ZEUS Collaboration;**
The ZEUS Detector, Status Report 1987 (Blue Book);
Editor J. Krüger, DESY, PRC 87–02, September 1987

[ZEU88] **ZEUS Collaboration;**
The ZEUS Detector, Status Report 1988;
DESY, ZEUS Note 88–089, August 1988

[ZEU89a] **ZEUS Collaboration;**
The ZEUS Detector, Status Report 1989 (Blue Book);
Editor E. Ros, DESY, March 1989

[ZEU89b] **ZEUS Collaboration;**
The ZEUS Detector, Progress Report 1989;
DESY, ZEUS Note 89–093, August 1989

[ZEU90] **ZEUS Collaboration;**
The ZEUS Detector, Progress Report 1990;
DESY, ZEUS Note 90–087, August 1990

[ZEU91] **ZEUS Collaboration;**
The ZEUS Detector, Status Report 1991 (Blue Book);
DESY, in preparation

[ZEU91a] **ZEUS Collaboration;**
Proposal for a Hadron–Electron Separator in the ZEUS Forward and Barrel Calorimeters;
ZEUS–Note 91–044, May 13, 1991

List of Figures and Tables

Figures

Fig. 2.21 $F_2(x,Q^2)$ structure function calculations for $1GeV^2 < Q^2 < 10^5 GeV^2$ accessible at HERA compared to measurements of different fixed target experiments.

Fig. 2.22 Event rates for NC scattering at HERA with $L = 500pb^{-1}$ calculated with Lund–LEPTO and EHLQ structure functions.

Fig. 2.23 Event rates for CC scattering at HERA with $L = 500pb^{-1}$ calculated with Lund–LEPTO and EHLQ structure functions.

Fig. 2.24 Gluon bremsstrahlung in eq–scattering.

Fig. 2.25 Two different gluon distributions superimposed on measurements expected for data from the ZEUS detector (Q^2=50GeV^2).

Fig. 2.26a Electron scattering on composite quarks.

Fig. 2.26b Composite electron and quark scattering by constituent interchange.

Fig. 2.26c Influence of a contact interaction with $\Lambda_H = 1$ TeV on the structure function $F_2(x,Q^2)$ compared to the standard model. The full curves correspond to $(V-A)_l$ x $(V-A)_q$, the dashed one to $(V-A)_l$ x $(V+A)_q$.

Fig. 2.27 Ratio of the cross sections of $\sigma(W_1 + W_2)$ to $\sigma(W_1)$.

Fig. 2.28 Neutral current cross sections for left and right handed $e^{\mp}$.

Fig. 2.29 Contributions of photon gluon fusion in NC events.

Fig. 2.30 Polar diagram of the kinematics for the final lepton and the current jet with lines of constant x and Q^2. Connecting a given (x,Q^2) point with the origin gives the laboratory momentum vectors, as shown by the example for x=0.5, Q^2=5000GeV^2.

Fig. 2.31 Monte Carlo simulated neutral current (NC) and charged current (CC) events.

Fig. 2.32 Areas in the x,Q^2–plane that can be measured with calorimeters of indicated resolution assuming the Longo criteria.

Fig. 2.33 Artist view of the ZEUS detector showing its internal structure.

Fig. 2.34 Section of the ZEUS detector along the beam.

Fig. 2.35 Section of the ZEUS detector perpendicular to the beam.

Fig. 2.36 Installation of the superconducting solenoid.

Fig. 2.37 Magnetic field measurements of the superconducting solenoid (1.8 T); open circles measured, full lines calculated with TOSCA.

Fig. 2.38 Layout of the ZEUS Uranium Scintillator Calorimeter; FCAL = Forward Calorimeter, BCAL = Central Calorimeter, RCAL = Rear Calorimeter, EMC and HAC = electromagnetic and hadronic sections.

Fig. 2.39 Front view of FCAL assembled from 24 modules of various depth in λ.

Fig. 2.40 Front view of FCAL with transverse segmentation seen from the IP.

Fig. 2.41 Internal structure of an FCAL module.

Fig. 2.42 Mechanical details of a large FCAL module.

Fig. 2.43 Details of the optical readout scheme.

Fig. 2.44 Readout of the scintillator light with wavelength shifters.

Fig. 2.45 The stacking machine, assembling the first FCAL prototype module, in York (Canada).

Fig. 2.46 Two FCAL wavelength shifter cassettes ready for installation.

Fig. 2.47 A fully stacked FCAL module at NIKHEF before WLS installation and mounting of the tension straps.

Fig. 2.48 Section through the BCAL perpendicular to the beam axis. Each BCAL module covers an angle wedge of 11.25^0 in ϕ and is tilt by 2.5^0.

Fig. 2.49 Internal structure of a BCAL module.

Fig. 2.50 The BCAL stacking machine at Argonne containing a fully stacked module.

Fig. 2.51 Black printed correction pattern for an EMC scintillator tile and the uniformity before and after correction.

Fig. 2.52 Uniformity of a FHAC1 WLS measured with a xenon lamp a) before and b) after correction.

Fig. 2.53 Emission spectrum of SCSN–38; Absorption spectra of K27 and Y7 in PMMA; Emission spectra of K27 and Y7 in PMMA and spectral sensitivity of a trialcali photocathode.

Fig. 2.54 View into the ZEUS detector after installation of the FCAL.

Fig. 2.55 Pulse height distributions measured in one Si diode plane after $3.3X_0$ in the FCAL prototype for 5 GeV hadrons and electrons identified by Cherenkov counters.

Fig. 2.56 Scatter plot of calorimeter information versus HES energy for 5 GeV beam particles. The indicated cuts yield clean electron and hadron samples.

Fig. 2.57 Elements of the Backing Calorimeter module assembly.

Fig. 2.58 Correlation between the energy measured in the BAC prototype calorimeter E_{BAC} and the FCAL prototype calorimeter E_{FCAL} for 100 GeV hadrons.

Fig. 2.59 Vertical section through the inner detector along the beam axis.

Fig. 2.60 Cell structure of the Vertex Detector.

Fig. 2.61 A 45^0 sector of the CTD consisting of 9 superlayers with 8 sense wires per superlayer.

Fig. 2.62 Equipotentials and electron drift trajectories in superlayer 1.

Fig. 2.63 The assembled vessel of the CTD at Oxford.

Fig. 2.64 Internal structure of one FTD chamber consisting of 3 layers.

Fig. 2.65 Cell structure of one FTD layer.

Fig. 2.66 Number of wire layers hit per track in CTD and CTD+FTD as a function of the θ angle.

Fig. 2.67 Internal structure of one TRD module.

Fig. 2.68 Radial cut through one TRD module.

Fig. 2.69 Vertical section through the Forward Muon Detector along the beam axis.

Fig. 2.70 Photo of the opened FMUON toroids.

Fig. 2.71 One full plane of FMUON drift chambers (DC1, DC2, DC3, DC4).

Fig. 4.11 Cherenkov ADC spectrum for a hadron sample identified by the calorimeter.

Fig. 4.12 Efficiency for hadrons as function of the Cherenkov signal.

Fig. 4.13 Distribution of the shower vertex position for 30 GeV.

Fig. 4.14 Average energy deposit of muons as function of the module number.

Fig. 4.15 Energy measured in the iron scintillator calorimeter part versus the energy measured in the uranium scintillator calorimeter part after intercalibration.

Fig. 4.16 Hadron, electron and muon response in the uranium part at 30 GeV.

Fig. 4.17 Hadron and electron response in the uranium part for various beam energies.

Fig. 4.18 e/π–ratio at 30 GeV as a function of the ADC gating time.

Fig. 4.19 Longitudinal shower profiles for beam momenta of 5 to 210 GeV for all events.

Fig. 4.20 Longitudinal shower profiles for beam momenta of 5 to 210 GeV for events with shower vertices in the first module.

Fig. 4.21 Cumulative distributions of longitudinal shower profiles for all events.

Fig. 4.22 Cumulative distributions of longitudinal shower profiles for events with shower vertex in the first module.

Fig. 4.23 Energy deposit in individual modules $[0.45\lambda_{int}]$ for 20 GeV jets.

Fig. 4.24a Energy deposit in individual modules $[0.45\lambda_{int}]$ for 40 GeV jets.

Fig. 4.24b Energy deposit in two individual modules $[0.9\lambda_{int}]$ for 40 GeV jets.

Fig. 4.25 Energy deposit in individual modules $[0.45\lambda_{int}]$ for 135 GeV jets.

Fig. 4.26 Longitudinal shower profiles of LUND jets ($x > 0.1$, $y > 0.6$; 20GeV - 160GeV jets) plus electromagnetic and hadronic parts as function of the calorimeter depth λ_{CAL} using the shower development measured for single particles.

Fig. 4.27 Longitudinal shower profiles as function of the calorimeter depth λ_{CAL} for 40 GeV and 135 GeV LUND jets.

Fig. 4.28 Section of the ZEUS calorimeter system along the beam.

Fig. 4.29 Maximum jet energy as a function of the polar angle θ with respect to the proton direction at HERA.

Fig. 4.30a Fraction of single particles with a shower containment of x_{con} as function of the calorimeter depth λ_{CAL} for 10 GeV.

Fig. 4.30b Fraction of 'jets' (ST-VX in 1.mod) with a shower containment x_{con} as function of the calorimeter depth λ_{CAL} for 10 GeV.

Fig. 4.31a Fraction of single particles with a shower containment of x_{con} as function of the calorimeter depth λ_{CAL} for 20 GeV.

Fig. 4.31b Fraction of 'jets' (ST-VX in 1.mod) with a shower containment x_{con} as function of the calorimeter depth λ_{CAL} for 20 GeV.

Fig. 4.32a Fraction of single particles with a shower containment of x_{con} as function of the calorimeter depth λ_{CAL} for 30 GeV.

Fig. 4.32b Fraction of 'jets' (ST-VX in 1.mod) with a shower containment x_{con} as function of the calorimeter depth λ_{CAL} for 30 GeV.

Fig. 4.33a Fraction of single particles with a shower containment of x_{con} as function of the calorimeter depth λ_{CAL} for 40 GeV.

Fig. 4.33b Fraction of 'jets' (ST-VX in 1.mod) with a shower containment x_{con} as function of the calorimeter depth λ_{CAL} for 40 GeV.

Fig. 4.34a Fraction of single particles with a shower containment of x_{con} as function of the calorimeter depth λ_{CAL} for 135 GeV.

Fig. 4.34b Fraction of 'jets' (ST-VX in 1.mod) with a shower containment x_{con} as function of the calorimeter depth λ_{CAL} for 135 GeV.

Fig. 4.35a Fraction of single particles with a shower containment of x_{con} as function of the calorimeter depth λ_{CAL} for 210 GeV.

Fig. 4.35b Fraction of 'jets' (ST-VX in 1.mod) with a shower containment x_{con} as function of the calorimeter depth λ_{CAL} for 210 GeV.

Fig. 4.36 Fraction of LUND jets with a shower containment of x_{con} as function of the calorimeter depth λ_{CAL} for 135 GeV.

Fig. 4.37 Fraction of events with 95% containment in the calorimeter for all events.

Fig. 4.38 Fraction of events with 95% containment in the calorimeter for events with shower vertex in the first module.

Fig. 4.39a Calorimeter depth (U/Scin) as a function of the polar angle θ required for a shower containment of 95% for 90% of single particles and WA78 'jets'.

Fig. 4.39b Depth in absorption length of the high resolution calorimeter as a function of the polar angle θ in the vertical plane. The dotted line indicates the length needed to contain 95% of the energy for 90% of the jets with the maximum energy allowed by HERA kinematics.

Fig. 4.40 Calorimeter design of a high resolution calorimeter (a), (veto readout section (b),) PM Boxes (c) and backing calorimeter (d).

Fig. 4.40a Fraction of energy deposition in the DU/Scint. + BAC calorimeters ($1 - \frac{E_{PM}}{E_{TOT}}$) for 40GeV jets with $E_{BAC} = 4\% - 5\%$; $\lambda_{CAL} = 5.4\lambda$.

Fig. 4.41 Fraction of 40 GeV 'jets' as function of $1 - \frac{E_{PM}}{E_{TOT}}$ for $E_{BAC} < 2\%$ of the shower energy; $\lambda_{CAL} = 5.4\lambda$.

Fig. 4.42 Fraction of 40 GeV 'jets' as fct. of $1 - \frac{E_{PM}}{E_{TOT}}$ for $E_{BAC} = 4\% - 5\%$ of the shower energy; $\lambda_{CAL} = 5.4\lambda$.

Fig. 4.43 Fraction of 40 GeV 'jets' additionally outside $i \cdot \sigma_{35}$ as function of the calorimeter depth for $E_{BAC} < 2\%$ of the shower energy.

Fig. 4.44 Fraction of 135 GeV 'jets' additionally outside $i \cdot \sigma_{35}$ as function of the calorimeter depth for $E_{BAC} < 2\%$ of the shower energy.

Fig. 4.45 Fraction of 40 GeV 'jets' as function of the shower energy in the BAC (E_{BAC}); $\lambda_{CAL} = 5.4\lambda$.

Fig. 4.46 Fraction of 135 GeV 'jets' as function of the shower energy in the BAC (E_{BAC}); $\lambda_{CAL} = 7.2\lambda$.

Fig. 4.47a Calorimeter depth for 80% of single hadrons as function of the energy for different fractions of shower containment.

Fig. 5.16 Pulse height distributions for e^+, π^+ and p with a momentum of 0.5 GeV/c. Gaussian fits are overlayed.

Fig. 5.17 e/h–ratio as a function of the momentum for π^+, π^- and p.

Fig. 5.18 e/h–ratio as a function of the kinetic energy for π^+, π^- and p.

Fig. 5.19 The energy resolution for π^+, π^- and p as a function of the kinetic energy E_K.

Fig. 5.20 Calorimeter response to 5GeV/c electrons (a) and 5GeV/c hadrons (b) as a function of the beam impact position at the boundary between two calorimeter modules for various angles of incidence (0mrad, 40mrad, 80mrad).

Fig. 5.21 Location of the Pb foil between modules 2 and 3 of the FCAL prototype.

Fig. 5.22 Calorimeter response to 30GeV/c electrons as a function of the beam impact position for various angles of incidence and thicknesses of Pb foils between modules 2 and 3.

Fig. 5.23 Contribution of the different calorimeter sections to the total signal of 30GeV/c electrons for 40mrad beam incidence a) without and b) with a 2mm thick Pb foil between modules 2 and 3.

Fig. 5.24 Shift of the electron response for 5GeV/c (a) and 30GeV/c (b) due to the non–uniformity at the boundary between two calorimeter modules as a function of the angle of beam incidence for various thicknesses of Pb foils.

Fig. 5.25 R.m.s. of the response distribution for the same conditions as for Fig. 5.24. These values indicate the direct contribution to the electron energy resolution.

Fig. 5.26 Calorimeter response to 5GeV/c electrons as a function of the calorimeter position in vertical direction over the spacers at the module boundary.

Fig. 5.27 Calorimeter response to 5GeV/c electrons as a function of the calorimeter position in vertical direction over the central region of the EMC sections.

Fig. 5.28 Material in front of the high resolution ZEUS uranium scintillator calorimeter in units of radiation lengths [X_0] as a function of the polar angle θ (as estimated in ZEUS 88–52).

Fig. 5.29 Pulse height spectra of 5GeV/c electrons and 5GeV/c pions without and with 9cm, 18cm and 27cm Al absorber in front of the FCAL prototype.

Fig. 5.30 Pulse height spectra of 30GeV/c electrons and 30GeV/c pions without and with 9cm, 18cm and 27cm Al absorber in front of the FCAL prototype.

Fig. 5.31 Ratio of the mean signal height with absorber (<Q>) and without absorber ($<Q_0>$) as function of the absorber thickness.

Fig. 5.32 Ratio of the standard deviation with absorber ($<\sigma>$) and without absorber ($<\sigma_0>$) as function of the absorber thickness.

Fig. 5.33 Ratio of the mean signal height with absorber (<Q>) and without absorber ($<Q_0>$) as a function of the momentum for various thicknesses of absorber in front of the FCAL prototype.

Fig. 5.34 Ratio of the mean signal height (<Q>) and the kinetic energy E_K as a function of the momentum for various thicknesses of absorber in front of the FCAL prototype.

Fig. 5.35 Experimental set up of the interaction trigger, aluminum absorber and presampler in front of the FCAL prototype at the CERN SPS.

Fig. 5.36 Particle multiplicities for interactions in the Be–target of the interaction trigger compared to single beam particles (Be–target removed).

Fig. 5.37 Correlation plot of the jet energy E_{Cal} measured in the FCAL prototype versus the charged particle multiplicity after 10cm Al absorber for 100GeV jets.

Fig. 5.38 Influence of an Al absorber on the average response to particle jets ($\frac{E_{Cal}(x)}{E_{Cal}(x=0)}$ – 1) as a function of the Al absorber thickness x[cm] for 50GeV and 100GeV jets without and with correction by the multiplicity measured with the trigger system and the presampler.

Fig. 5.39 Influence of an Al absorber on the energy resolution of particle jets ($\frac{\sigma}{E_{Cal}}(x)/\frac{\sigma}{E_{Cal}}(x=0)$ – 1) as a function of the Al absorber thickness x[cm] for 50GeV and 100GeV jets without and with correction by the multiplicity measured with the trigger system and the presampler.

Fig. 5.40 Lateral spread of 30GeV/c hadron showers. Each cell represents a 20cm x 20cm tower. The beam is incident in the middle of the central tower.

Fig. 5.41 Fraction of energy deposited by hadron showers in the different calorimeter sections as a function of the beam momentum.

Fig. 5.42 Distance δx between the centre of an EMC tower and the transverse centre of shower gravity.

Fig. 5.43 The signal ratio E_R/E_L of the right and left photomultipliers as a function of the distance δx to the centre of the tower.

Fig. 5.44 Horizontal position reconstruction for 5GeV/c electrons under normal incidence showing a) the shift in the average position and b) the position resolution.

Fig. 5.45 Horizontal position reconstruction for 5GeV/c hadrons under normal incidence showing a) the shift in the average position and b) the position resolution.

Fig. 5.46 Vertical position reconstruction for 5GeV/c electrons under normal incidence showing a) the shift in the average position and b) the position resolution.

Fig. 5.47 Vertical position reconstruction for 5GeV/c hadrons under normal incidence showing a) the shift in the average position and b) the position resolution.

Fig. 5.48 Position resolution of the transverse centres of gravity in EMC, HAC1 and HAC2 as a function of the hadron energy at θ angles of 0mrad and 200mrad with an impact position in the middle of tower 10 (see Fig. 5.50).

Fig. 5.49 Description of the coordinate system used for the parametrization of the longitudinal centres of gravity in one EMC section.

Fig. 5.50 Matrix of impact positions over the central entrance face of the FCAL prototype calorimeter.

Fig. 5.51 Correlation plots of the energies deposited in EMC, HAC1 and HAC2 and the transverse centres of shower gravity for 75GeV/c hadrons at θ = 200mrad.

Fig. 5.52 Parametrizations of the longitudinal centres of shower gravity for EMC, HAC1 and HAC2 for 75GeV/c hadrons at θ = 200mrad.

Fig. 5.54 Determination of the θ angles of the axis of particle showers with the FCAL prototype at CERN SPS.

Fig. 5.55 Fraction of energy deposited in the towers (20cm x 20cm) of EMC, HAC1 and HAC2 of a 100GeV/c hadron with a θ angle of beam incidence of 200mrad in x–direction.

Fig. 5.56 Fractions of θ angles reconstructed from the different calorimeter sections as a function of the energy of the hadron shower without interaction point. Each reconstructed θ angle is counted only once.

Fig. 5.57 Angular resolution as a function of the energy of the hadron shower determined by method 1 (parametrization) at θ = 200mrad without interaction point. The fractions of hadron showers are indicated in brackets.

Fig. 5.58 Angular resolution as a function of the energy of the hadron shower determined by method 2 (PLSP–algorithm) at θ = 200mrad without interaction point. The fractions of hadron showers are indicated in brackets.

Fig. 5.59 Angular resolution as a function of the energy of the hadron shower at θ = 200mrad for combinations of EMC + IP, HAC1 + IP and HAC2 + IP. The fractions of hadron showers are indicated in brackets.

Fig. 6.1 Energy measurement with a calorimeter and the description of calibration.

Fig. 6.2 Influence of the calibration error on the cross section, where σ_{in} and σ_{out} denote the cross section without and with calibration error.

Fig. 6.3 Sketch of the various calibration tools in the ZEUS calorimeter.

Fig. 6.4 Thickness distributions of uranium plates for a) EMC sections of FCAL, b) EMC sections of RCAL, c) HAC1 and d) HAC2 sections of FCAL.

Fig. 6.5 Thickness distributions for samples of scintillator tiles belonging to a) EMC, b) HAC0, c) HAC1 and d) HAC2 sections of FCAL.

Fig. 6.6 Decay chain of $^{238}_{92}U$ into $^{234}_{92}U$, including only the main decay lines and indicating the energy in MeV of the emitted particles.

Fig. 6.7 View of the ^{60}Co – source measurement device for quality control on local uniformity.

Fig. 6.8 Calorimeter scan with a Co^{60} – source along an FEMC section. The source signal is given in units of the UNO signal.

Fig. 6.9 Calorimeter scan with a Co^{60} – source along an FHAC section. The source signal is given in units of the UNO signal.

Fig. 6.10 Calorimeter scan with a Co^{60} – source along an FHAC section. The dip disappeared after a plastic strip was removed, which was found between the scintillator plates and the wavelength shifter.

Fig. 6.11 Sketch of the movable calibration stand with an FCAL module in horizontal position for testing.

Fig. 6.12 Picture of the movable calibration stand with an FCAL module in horizontal position for testing.

Fig. 6.13 Schematics of the data acquisition setup.

Fig. 6.14 Pulse after shaper with 8 samples.

Fig. 6.15 Schematics of a front-end card.

Fig. 6.16 Deviation from linearity for a) FCAL1 and b) RCAL1 as a function of the electron beam momentum, where $\delta = (Q/p)/(Q_0/p_0) - 1$ with Q_0 and p_0 the calorimeter charge and beam momentum at 15GeV/c.

Fig. 6.17 Module scans with 15GeV/c electrons a) in vertical (x) and b) in horizontal (y) direction, in order to determine the position of the calorimeter module.

Fig. 6.18 Uniformity scans with 15 GeV/c electrons in horizontal (y) direction a) in module FCAL1 and b) in module RCAL1.

Fig. 6.19 Time resolution for electrons as a function of the beam momentum for an FCAL module.

Fig. 6.20a Average response of 15GeV/c electrons for 74 EMC sections of one FCAL module after UNO calibration.

Fig. 6.20b Average response of 100GeV/c hadrons for 23 supertowers (EMC+HAC1+HAC2) of one FCAL module after UNO calibration.

Fig. 6.21a Average response of 15GeV/c electrons for all measured FCAL EMC sections after UNO calibration.

Fig. 6.21b Average response of 100GeV/c hadrons for all measured FCAL supertowers (EMC+HAC1+HAC2) after UNO calibration.

Tables

Composition of the ZEUS Collaboration

Spokesman: G. Wolf
Deputy Spokesman: J. Martin

October 1991

The collaboration includes the following institutions and physicists:

CANADA	
University of Manitoba	F. Ikraiam, J. Mayer, G. Smith
McGill University	F. Corriveau, D. Gilkinson, D. Hanna, W. Hung, J. Mitchell P. Patel, L. Sinclair, D. Stairs, M.St. Laurent
University of Toronto	D. Bailey, D. Bandyopadhyay, D. Barillari, F. Benard, S. Bhadra, M. Brkic, B. Burow, F. Chlebana, M. Crombie, G. Hartner, G. Levman, J. Martin, R. Orr, J. Prentice, C. Sampson, R. Teuscher, T.S. Yoon
York University	W. Frisken, Y. Iga
GERMANY*	
Bonn University	A. Bargende, J. Crittenden, H. Dabbous, B. Diekmann, J. Gajewski, G. Geitz, A. Grunenberg, B. Gutjahr, H. Hartmann, J. Hartmann, D. Haun, K. Heinloth, E. Hilger, H.-P. Jakob, St. Kramarczyk, M. Kückes, A. Mass, H. Müsch, E. Paul, R. Schattevoy, B. Schneider, H.-L. Schneider, R. Wedemeyer, M. Zachara
DESY	J.K. Bienlein, C. Coldewey, A. Dannemann, K. Dierks, W. Dorth, G. Drews, P. Erhard, I. Fleck, A. Fürtjes, R. Gläser, T. Haas, L. Hagge, D. Hasell, H. Hultschig, G. Jahnen, P. Joos, M. Kasemann, R. Klanner, W. Koch, U. Kötz, A. Kotanski, H. Kowalski, A. Ladage, B. Löhr, D. Lüke, J. Mainusch, O. Manczak, M. Momayezi, S. Nickel, D. Notz, I. Park, K.U. Pösnecker, M. Rohde, A. Savine, U. Schneekloth, J. Schröder, W. Schütte, W. Schulz, F. Selonke, E. Tscheslog, W. Vogel, T. Woeniger, G. Wolf, C. Youngman
DESY-Zeuthen	K. Deiters, H.J. Grabosch, A. Leich, C. Rethfeldt, S. Schlenstedt
Freiburg University	A. Bamberger, A. Freidhof, T. Poser, G. Theisen
Hamburg University, I. Institute of Exp.Phys. II. Institute of Exp.Phys.	U. Behrens, U. Holm, H. Kammerlocher, B. Krebs, K. Wick W. Kröger, J. Krüger, E. Lohrmann, M. Nakahata, N. Pavel, G. Poelz, T. Tsurugai, B.H. Wiik

KFA Jülich	P. Cloth, D. Filges, R.D. Neef, N. Paul, C. Reul, H. Schaal, G. Sterzenbach
Siegen University	E. Badura, H. Chaves, M. Rost, R.J. Seifert, A.H. Walenta, W. Weihs, G. Zech
ISRAEL	
Tel-Aviv University	R. Heifetz, A. Levy, D. Zer-Zion
Weizmann Institute***	C. Glasman, Y. Eisenberg, U. Karshon, A. Montag, D. Revel, A. Shapira
ITALY	
Bologna INFN and University	F. Arzarello, G. Barbagli, G. Bari, M. Basile, L. Bellagamba, D. Boscherini, G. Bruni, P. Bruni, M. Chiarini, G. Cara Romeo, L. Cifarelli, F. Cindolo, F. Ciralli, A. Contin, S. D'Auria, C. Del Papa, F. Fiori, F. Frasconi, P. Giusti, G. Iacobucci, G. Laurenti, Q. Lin, B. Lisowski, G. Maccarrone, A. Margotti, T. Massam, R. Nania, V. O'Shea, F. Palmonari, G. Sartorelli, M. Scioni, R. Timellini, M. Willutzky, A. Zichichi
Cosenza University	M. Schioppa, G. Susinno
Florence University	R. Casalbuoni, E. Celeghini, S. De Curtis, D. Dominici, S. De Gennaro, F. Francescato, M. Nuti, P. Pelfer, R. Salimbeni, U. Vanni
Frascati INFN	G. Anzivino, R. Casaccia, S. De Pasquale, B. Dulach, I. Laakso, S. Qian, L. Votano
L'Aquila University	R. Scrimaglio
Padua University	R. Brugnera, R. Carlin, F. Dal Corso, M. De Giorgi, U. Dosselli, C. Fanin, F. Gasparini, S. Limentani, M. Morandin, M. Posocco, L. Stanco, R. Stroili, C. Voci
Rome University	M. Bonori, U. Contino, G. D'Agostini, M. Guida, M. Iacovacci, M. Iori, S. Mari, G. Marini, M. Mattioli, D. Monaldi, A. Nigro
Turin University	
Turin I	C. Aglietta, P. Antonioli, G. Badino, A. Castellina, M. Dardo, W. Fulgione, P. Galeotti, L. Panaro, O. Saavedra, G.C. Trinchero, S. Vernetto
Turin II	D. Allasia, M. Arneodo, M. Costa, M.I. Ferrero, L. Lamberti, S. Maselli, C. Peroni, A. Solano, A. Staiano
JAPAN	
INS, Tokyo University	T. Hasegawa, M. Hazumi, T. Ishii, S. Kasai, M. Kuze, Y. Nagasawa, M. Nakao, H. Okuno, K. Tokushuku, T. Watanabe, S. Yamada
Tokyo Metropolitan University	M. Chiba, R. Hamatsu, T. Hirose, S. Kitamura, S. Nagayama, Y. Nakamitsu

NETHERLANDS	
NIKHEF-Amsterdam	S. Bentvelsen, A. Dake, J. Engelen, P. de Jong, P. Kooijman, H. van der Lugt, A. Tenner, H. Tiecke, H. Uijterwaal, J. Vermeulen, L. Wiggers, E. de Wolf, R. van Woudenberg
POLAND	
Institute of Nuclear Physics, Cracow	J. Chwastowski, A. Dwurazny, A. Eskreys, Z. Jakubowski, K. Piotrzkowski, L. Zawiejski
Inst. of Phys. and Nucl. Tech., Acad. of Mining and Metall., Cracow	K. Eskreys, K. Jeleń, D. Kisielewska, T. Kowalski, J. Kulka, M. Przybycien, E. Rulikowska-Zarebska, L. Suszycki
Phys. Dept., Jagellonian University, Cracow	A. Kotanski
Inst. of Exp. Phys., Warsaw Univ. and Inst. for Nucl. Studies	H. Abramowicz, M. Adamus, K. Charchula, J. Ciborowski, K. Genser, G. Grzelak, M. Krzyzanowski, K. Muchorowski, R.J. Nowak, J.M. Pawlak, K. Stojda, A. Stopczyński, R. Szwed, T. Tymieniecka, R. Walczak, A.K. Wróblewski, J.A. Zakrzewski, A.F. Zarnecki
SPAIN	
Univ. Autonoma Madrid	F. Barreiro, G. Cases, L. Hervas, L. Labarga, J. del Peso, J. Terron, J.F. de Troconiz
UNITED KINGDOM	
Bristol University	D.G. Cussans, M. Dyce, H.F. Fawcett, B. Foster, R. Gilmore, G.P. Heath, T.J. Llewellyn, J. Malos, C.J.S. Morgado, T.L. Short, R.J. Tapper, S. Wilson
Glasgow University	N.H. Brook, P.J. Bussey, A.T. Doyle. J.R. Forbes, C. Raine, D.H. Saxon
Imperial Coll. London	T.C. Bacon, J. Giddings, C. Markou, D. McQuillan, D.B. Miller, M.M. Mobayyen, T.J. Mortimer, A. Vorvolakis
University Coll. London	F.W. Bullock, T.W. Jones, A. Khan, J. Lane, G.J. Lush, P.L. Makkar, G. Nixon, S.F. Salih, J. Shulman
Oxford University	G. Blair, M.G. Bowler, I.M. Butterworth, R.J. Cashmore, A.M. Cooper-Sarkar, R.C.E. Devenish, D.M. Gingrich, P.M. Hallam-Baker, N. Harnew, T. Khatri, M. Lancaster, K.R. Long, P. Luffman, P. Morawitz, J. Nash, N.C. Roocroft, A. Weidberg, F.F. Wilson
Rutherford Applet. Lab.	J.C. Hart, N.A. McCubbin, T.P. Shah

USA	
Argonne National Lab.	M. Derrick, D. Krakower, S. Magill, B. Musgrave, J. Repond, R. Stanek, R. Talaga, T. Throh
Brookhaven Nat. Lab.	B. Radeka, R. Rau
Columbia University	A. Bernstein, A. Caldwell, D. Chen, I. Gialas, A. Parsons, S. Ritz, F. Sciulli, L. Wai, S. Wang, Fang Xu, Jun Xu
Iowa University	T. Bienz, H. Kreutzmann, U. Mallik, M. Roco
Louisiana State Univ.	L. Chen, R. Gunashinga, R. Imlay, N. Kartik, H.-J. Kim, R. McNeil, W. Metcalf
Ohio State University	B. Bylsma, L.S. Durkin, C. Li, T.Y. Ling, K. McLean, S.K. Park, T.A. Romanowski, R. Seidlein
Pennsylvania State Univ.	J.N. Lim, B.Y. Oh, J. Whitmore
Santa Cruz University	N. Cartiglia, C. Heusch, B. Hubbard, K. O'Shaughnessy, H.F. Sadrozinski, A. Seiden
Virginia Tech.	K. Blankenship, B. Lu, L.W. Mo
Wisconsin University	I. Ali, B. Behrens, U. Camerini, C. Fordham, C. Foudas, A. Gossiou, K. Iordanidis, M. Lomperski, R.J. Loveless, D.D. Reeder, W.H. Smith, S. Silverstein

*
This work has been supported by the German Federal Minister for Research and Technology (BMFT) under the contract numbers 054 BN 17, 054 BN 27, 054 FR 17, 054 HH 17, 054 HH 25, 054 SI 77.

**
This work has partially been supported by the research programs CPBP 01.06 and 01.09 G–MEN–III/90. The Polish members wish to thank the DESY directorate for the financial support and the hospitality extended to them while working at DESY.

***
Supported by the MINERVA Foundation, München.

ZEUS Kollaboration

Arbeiten der Gruppen von DESY, Hamburg I und Hamburg II

Stand 1.2.1990

Sprecher: G. Wolf, Technischer Koordinator: B. Löhr, Sicherheit: G. Poelz
Sekretariat: Frau U. Büchler, Frau I. Harm

Technische Koordination B. Löhr

D. David
G. Etgens (Krakau)
H. Gharavi
H. Hasson
J. Hauschildt
K. Hillebrandt
G. Knust
R. Lehmann
K. Löffler
C. Muhl
S. Richter
H. Sabath
S. Schulze
V. Sturm
K. Westphal
H. Wolter
W. Zierold
E. Zimmer-
Nixdorf (W)
ZEUS - Halle
T. Winch (ZEUS)
F. Czempik (MEA)
O. Kaul (MEA)

Supraleitende Magnete

Kontrollen/Betrieb
D. Notz
C. Szadkowski
Stromversorgung
P. Joos
O. Kaul
Kältebox
H. Hultschig
Feldrechnung
F. Corriveau

Verkabelung

G. Knust

Gasversorgung

B. Löhr
D. Miller (RAL)

Kalorimeter R. Klanner

Szintillatorfertigung

M. Rohde
A. Chmielinski (Kraka
N. Feind
B. Owczarek (Krakau)
H.H.Sabath

WLS Fertigung

U. Holm
W. Grell
R. Mohrmann
H. Prause
K. Wick

Fotoröhren

T. Ishii
F. Göthe
M. Rohde
R. Wawszczak

DESY - Strahltests

K. Dierks, G. Drews
U. Holm

Elektronik

U. Kötz
J. Berger
G. Cases
L. Hervas (Madrid)
A. Maniatis
A. Seidman(< 2/90)
H.J. Schirmacher
W. Schulz
H. Wolter
D. Zer-Zion

Co - Quellen

D. Hanna (McGill)
K. Wick
D. Gilkinson (McGill)
U. Holm
H. Kammerlocher
B. Krebs
H. Prause

Höhenstrahltests

F. Selonke
U. Behrens
K. Dierks
A. Fürtjes
G. Oldhaver
T. Pwalam
H.R. Roth

CERN-Tests, Eichung

J. Krüger
G. Drews
J. Hauschildt
U. Kötz
W. Kröger
H. Kammerlocher
K. Löffler
E. Ros
R. Salomon
T. Tsurugai

Strahlrohr

E. Lohrmann
A. Maniatis
C. Muhl
G. Pölz
W. Rüter (WI)

Polarisation

R. Klanner
E. Lohrmann
M. Lomperski (Wisconsin)
P. Patel (McGill)

Racks

C. Youngman
N. Feind

Crates

D. Notz
H. Quehl (F56)

HES

W. Koch
K.U. Pösnecker
G. Jahnen
M. Johannsen
H. Lenzen
M. Momayezi
R. Rau

BAC

R. Walczak
Z. Golebiewski (Wars
J. Zajac (Krakau)

Datennahme

C. Youngman
W. Amian (Jülich)
M. Dieckvoss
G. Drews
P. Erhard
T. Ishikawa (Tokyo)
H. Kammerlocher
A. Kotanski
R. Martens
D. Notz
I. Park

EVB

W. Vogel
U. Behrens
F.-O. Lohmann
T. Woeniger

Rekonstruktion

H. Kowalski
H. Abramowicz
R. Gläser
H. Greßmann
C. Günther
T. Haas
A. Levy (Tel Aviv)
E. Lohrmann
N. Pavel
J. delPeso (Madrid)
T. Poser (Freiburg)
A. Solano (Turin)
E. Tscheslog

Acknowledgements

A detector of the size and the complexity of the ZEUS detector can be built successfully only with the strong effort of many people. Therefore I would like to thank all participants of the various groups, who made this work possible.

I am very grateful to all my colleagues and friends of the ZEUS calorimeter group for their dedicated and enthusiastic effort during many years in calorimeter research and development and many calorimeter tests performed at CERN and DESY.

For the fruitful and excellent cooperation I warmly acknowledge A. Andresen, Prof. Dr. A. Bamberger, Dr. U. Behrens, Dr. E. Bernardi, Dr. G. Blair, B. Burow, G. Cases, Dr. J.A. Crittenden, A. Dannemann, Prof. Dr. M. Derrick, Dr. K. Dierks, Dr. G. Drews, Prof. Dr. J. Engelen, C. Farrow, Dr. H.F. Fawcett, A. Freidhof, A. Fürtjes, Dr. D. Gilkinson, Prof. Dr. R. Hamatsu, Prof. Dr. D. Hanna, Dr. T. Hasegawa, Dr. D. Hasell, Dr. L. Hervás, Dr. U. Holm, Prof. Dr. T. Ishii, H. Kammerlocher, Dr. W. Koch, Dr. U. Kötz, Dr. M. Krämer, B. Krebs, W. Kröger, Dr. B. Löhr, Dr. D. Lüke, Prof. Dr. J. Martin, Dr. J. Mitchell, Prof. Dr. B. Musgrave, Prof. Dr. A. Odian, Prof. Dr. P. Patel, Dr. G. Poelz, Prof. Dr. R. Rau, Prof. Dr. D.D. Reeder, Dr. M. Rohde, Prof. Dr. T.A. Romanowski, Dr. E. Ros, Dr. W. Schulz, Prof. Dr. F. Sciulli, Dr. F. Selonke, Dr. J. Straver, Dr. H. Tiecke, Dr. T. Tsurugai, Dr. W. Vogel, Dr. J. Whitmore, Prof. Dr. K. Wick and Dr. C. Youngman.

For the technical support during the long time of calorimeter constructions and tests, I cordially thank in particular the Herren N. Feind, J. Hauschildt, K. Löffler, H. Sabath, V. Sturm and K. Westphal.

I gratefully acknowledge Prof. Dr. E. Hilger, who introduced me many years ago to the interesting field of calorimeter research and development and Dr. G. Wolf, spokesman of the ZEUS collaboration, for innumberable conversations with respect to the ZEUS calorimeter and beyond and his permanent scientific support, so that it was always a pleasure for me to participate in the ZEUS experiment.

I warmly acknowledge Dr. R. Klanner, coordinator of the ZEUS calorimeter, for the excellent and successfull cooperation during many years of research, development and tests for the ZEUS calorimeter at CERN and DESY, and for many interesting discussions on various aspects of experimental physics.

In particular I am very grateful to Prof. Dr. E. Lohrmann for his continuous support of my research work in calorimetry, for the possibility to participate in the ZEUS calorimeter tests at CERN and in numerous international conferences and meetings, and for encouraging me to write this report.

I want to thank all ZEUS members who contributed in one way or another to this report, in particular I thank Dr. R. Klanner and Dr. G. Wolf for the careful reading and commenting of the manuscript.

Finally I would like to thank the DESY directorate, in particular Prof. Dr. P. Söding and Prof. Dr. V. Sörgel, who provided such excellent conditions for research in experimental high energy physics, that I always enjoyed working at DESY for the ZEUS collaboration.